Springer Series in Materials Science 309

Anming Hu *Editor*

Laser Micro-Nano-Manufacturing and 3D Microprinting

Springer

Springer Series in Materials Science

Volume 309

The Springer Series in Materials Science covers the complete spectrum of materials research and technology, including fundamental principles, physical properties, materials theory and design. Recognizing the increasing importance of materials science in future device technologies, the book titles in this series reflect the state-of-the-art in understanding and controlling the structure and properties of all important classes of materials.

More information about this series at http://www.springer.com/series/856

Anming Hu
Editor

Laser Micro-Nano-Manufacturing and 3D Microprinting

Springer

Editor
Anming Hu
University of Tennessee
Waterloo, ON, Canada

ISSN 0933-033X ISSN 2196-2812 (electronic)
Springer Series in Materials Science
ISBN 978-3-030-59312-4 ISBN 978-3-030-59313-1 (eBook)
https://doi.org/10.1007/978-3-030-59313-1

This Springer imprint is published by the registered company Springer Nature Switzerland AG
The registered company address is: Gewerbestrasse 11, 6330 Cham, Switzerland

Preface

Manufacturing is the basis of modern economics and society. The modern pursuit of high quality of life requires the revolution of modern manufacturing and engineering to produce products with unprecedented complex structures and properties. Reducing the costs in materials and energy, and enhancing freedom in design while continuously improving the performance at the device and system level remain major technological challenges. Micro- and nano-manufacturing, especially 2D and 3D microprinting, has emerged as effective solutions for the development of the Internet of things (IoTs), 5G/6G communication, portable electronics, artificial intelligence, and automated driving.

Lasers are powerful tools for various machining processes. For precision manufacturing at a micro-to-nano-scale, the fundamental understanding of light-nanomaterial interaction is crucial. The basic energy and mass transporting govern the relevant machining procedures. Unlike the macroworld, the unique properties and principles will be dominant in a microworld and nanoworld, such as the surface energy becomes dominant compared to volume energy and capillary force will overcome the gravitational force. This leads to the size effect of melting and innovative assembly strategy of nanomaterials. These must be further considered in precision micro-to-nano-manufacturing. On the other hand, with the blooming of laser technologies, laser enables work using tunable wavelengths, pulses, shapes, powers and other processing parameters. Especially due to the extensive availability of cheaper semiconductor laser and fiber laser, laser-based manufacturing becomes versatile in 2D-3D printing. Moreover, laser-based micro-nano-manufacturing can be integrated with other advanced manufacturing tools to address intellectual and green manufacturing. This makes laser-based micro-nano-manufacturing very unique and promising for microelectronics, energy, environment application.

In this book, we first introduce the fundamental of light-nanomaterial interaction, the size effect, the scaling of nanomaterials, and the surface plasmonic excitation of nanomaterials. For photonic manufacturing, we mainly compare the photothermal effect induced by long pules (long than 1 picosecond) or continue wave laser to the nonthermal effect induced by an ultrafast pulsed laser (shorter than 1 picosecond).

Subsequently, we review two kinds of key techniques for micro-to-nano-manufacturing: various micro-to-nano-manipulations and nanojoining. Based on these reviews, we introduce the latest progress on innovative molecular devices, near-field manufacturing, and super-resolution manufacturing.

In Chap. 2, Minlin Zhong and Peixun Fan present a comprehensive overview of the state of the art and current challenges of antireflection surface micro-nano-structures (SMNS), especially those fabricated by laser. The antireflection performances of the fabricated SMNS demonstrate in detail different multiscale structures. They also discuss the great application prospects of these SMNS.

In Chap. 3, Casas and Kautek focus on one potential approach to surpass the optical diffraction limit by introducing "Apertureless Scanning Near-Field Optical Lithography." In this method, a scanning probe microscope tip is illuminated by a focused laser beam and the electromagnetic field is strongly enhanced in the vicinity of the tip's apex. This may generate nanomodifications on a solid surface in close proximity to the tip. In this chapter, they review the thermal effects that allow distinguishing the underlying physical mechanisms: near-field optical enhancement and/or thermal surface modification.

In Chap. 4, Compagnini et al. review the basic principles of pulsed laser-induced nanoparticle synthesis in liquid. Two kinds of materials are focused as case studies, porous graphene, and TiO_2 nanoparticles. Biosensing and photocatalytic degradation by these materials are discussed.

Sano et al. introduce laser peening, as a surface modification technology using laser-driven shock compression to improve the properties of metals such as hardness, residual stress, fatigue properties, and corrosion resistance. A femtosecond laser-driven shock wave in solids enables peening without sacrificial overlay under atmospheric conditions. A brief explanation of a formation mechanism of a femtosecond laser-driven shock wave in solids including interactions of femtosecond laser pulse with metals and femtosecond laser ablation of metals, and applications of the femtosecond laser peening without sacrificial overlay under atmospheric conditions on aluminum alloy and iron are described in this chapter.

Feng Chen et al. review the laser processing of optical waveguides. The focused ultrashort pulses interact with the bulk matrix, resulting in modification of the refractive index of the localized regions. Both positive and negative index changes have been successfully utilized to generate waveguiding effects. Owing to the capability and feasibility of direct femtosecond laser writing, a number of waveguide devices have been fabricated in versatile optical materials, which brings out intriguing applications in many areas.

Guoying Feng et al. overview the laser processing microfluidics. Microfluidic channels are the key components of a micro-total analysis system (μ-TAS). Photolithography is a major method of microfluidic channels fabrication which is actually a two-dimensional planar fabrication technology. They argued that the fabrication of three-dimensional (3D) microfluidic structures by photolithography-based techniques requires additional stacking and bonding, leading to an increase in complexity and cost. A main method for achieving 3D microfluidic structures in transparent substrates is to use Femtosecond Laser Direct Writing is demonstrated.

Sugioka et al. focus on laser direct writing of microfluidic devices and nano-scale additive manufacturing. Microfluidic devices with three-dimensional (3D) configurations and multiple functionalities are exceptionally useful for on-chip construction of artificial biological environments and 3D manipulation of bio-species in microscale spaces. Direct writing of 3D microstructures having designable functionalities with femtosecond lasers allows the production of microfluidic, micro-optic/photonic and microelectronic elements, which can be monolithically integrated into a single glass substrate for the fabrication of high-performance biochips. The principles of fs laser direct writing manufacture of microfluidic, optofluidic, electro-fluidic, and ship-in-a-bottle biochips are introduced herein. Practical techniques and recent advances are reviewed. In addition, possible future directions in this field are discussed.

In Chap. 9, Zergioti et al. cover the laser-induced forward transfer as a prosing additive manufacturing. This chapter discusses the fundamental theory supporting laser printing and specifically laser-induced forward transfer that is a direct non-contact and non-destructive laser printing technique in an aim to provide a complete overview of the printing mechanism and the jetting dynamics, while potential applications are also presented. This chapter is also focused on the evolution of the technique toward additive manufacturing as well as industrialization activities that have risen in the last five years.

Kirihara reviews that artificial dendrite structures with dendritic geometries and spatially ordered micro-cavities are successfully fabricated using three-dimensional stereolithographic printing and ultraviolet laser. The metal and ceramic nanoparticles are dispersed in photosensitive liquid resins to obtain thixotropic pastes. Solid electrolyte dendrites of yttria-stabilized zirconia have been fabricated for fuel cell miniaturization. Subsequently, metallodielectric photonic crystals with diamond lattice structures are printed and demonstrated. Moreover, artificial bones of hydroxyapatite scaffolds were modeled to realize excellent biocompatibility. The graded porous structures in the artificial bones were processed.

In the last chapter, Wilhelm et al. report that laser processing technologies for micro-/nano-structuring of electrode materials in improving the electrochemical performance and operational lifetime of lithium-ion cells. Different types of laser structuring are used on metallic current collectors and thin or thick film electrodes. For thin metallic current collector foils, at anode and cathode sides, the self-organized structuring by laser-induced periodical surface structures and laser interference methods is successfully applied for improving electrode film adhesion and cell impedance. For thin and thick film electrode layers, direct laser ablation with structure sizes down to the micrometer range and high aspect ratios is found most powerful in order to create three-dimensional (3D) cell architectures with benefits regarding cell performance and a homogenous wetting of composite electrodes with liquid electrolyte. A huge impact of laser formed 3D batteries regarding capacity retention and cell lifetime at high charging and discharging rates is detected. A further improvement of 3D battery performance due to an operation in high potential regime and for advanced high energy silicon anode material has been achieved by joining of laser structuring and thin film passivation either of

active particles before laser patterning or by passivating of complete 3D electrodes after laser processing. The impact of 3D architectures on lithium distribution and chemical degradation processes in 2D batteries is studied.

We hope this book can provide a fundamental yet comprehensive overview of the state of the art of laser micro-nano-manufacturing and 3D microprinting. It can be utilized as an instructive book for graduate students and senior undergraduates to grasp the latest developments in this field. It can also be a reference for researchers and engineers to quickly access a great number of research articles in this direction. It is necessary to mention that there are lots of important fields are excluded in this book due to the width and depth of laser processing. Meanwhile, due to rapid growth and new insight in this field, it is inevitable to have some mistakes in the current version. The correction from the readers is welcome and will be integrated in the future editing. Finally, I owe special thanks to all authors for their great efforts in preparing corresponding chapter. It was my great honor to work with all those who have collaborated, shared, reviewed, helped, explained, and, in general, taught me about this interdisciplinary field. I would thank Viradasarani Natarajan and Zachary Evenson, who help to coordinate, organize and discuss, and edit this book.

Knoxville, TN, USA Anming Hu

Contents

Contributors

Shi Bai Advanced Laser Processing Research Team, RIKEN Center for Advanced Photonics, RIKEN, Wako, Saitama, Japan

Denzel Bridges Department of Mechanical, Aerospace and Biomedical Engineering, University of Tennessee Knoxville, Knoxville, TN, USA

Feng Chen School of Physics, State Key Laboratory of Crystal Materials, Shangdong University, Jinan, China

Giuseppe Compagnini Dipartimento di Scienze Chimiche, Università di Catania, Catania, Italy

Marcello Condorelli Dipartimento di Scienze Chimiche, Università di Catania, Catania, Italy

Javier R. Vázquez de Aldana Grupo de Investigación en Aplicaciones del Láser y Fotónica, Departamento de Física Aplicada, University of Salamanca, Salamanca, Spain

Yangbao Deng All-Solid-State Energy Storage Materials and Devices Key Laboratory of Hunan Province, College of Information and Electronic Engineering, Hunan City University, Yiyang, China

Luisa D'Urso Dipartimento di Scienze Chimiche, Università di Catania, Catania, Italy

Ignacio Falcón Casas Department of Physical Chemistry, University of Vienna, Vienna, Austria

Peixun Fan School of Materials Science and Engineering, Laser Materials Processing Research Center, Tsinghua University, Beijing, China

Guoying Feng Institute of Laser and Micro/Nano-Engineering, College of Electronics and Information Engineering, Sichuan University, Cheng'du, China

Simona Filice Dipartimento di Scienze Chimiche, Università di Catania, Catania, Italy;
Istituto per la Microelettronica e Microsistemi, Consiglio Nazionale delle Ricerche, Catania, Italy

Roberto Fiorenza Dipartimento di Scienze Chimiche, Università di Catania, Catania, Italy

Petronela Gotcu Karlsruhe Institute of Technology, IAM-AWP, Karlsruhe, Germany

Anming Hu Department of Mechanical, Aerospace and Biomedical Engineering, University of Tennessee Knoxville, Knoxville, TN, USA

Wolfgang Kautek Department of Physical Chemistry, University of Vienna, Vienna, Austria

Soshu Kirihara Joining and Welding Research Institute, Osaka University, Ibaraki City, Japan

Carmelo La Rosa Dipartimento di Scienze Chimiche, Università di Catania, Catania, Italy

Joong Kee Lee Department of Energy and Environmental Engineering, Korea University of Science and Technology, Daejeon, Republic of Korea;
Center for Energy Convergence, Green City Research Institute, Korea Institute of Science and Technology, Seoul, Republic of Korea

Guang Li Institute of Laser and Micro/Nano-Engineering, College of Electronics and Information Engineering, Sichuan University, Cheng'du, China

Ruozhou Li College of Electronic and Optical Engineering & College Microelectronics, Nanjing University of Post and Telecommunications, Nanjing, China

S. Papazoglou School of Applied Mathematical and Physical Sciences, National Technical University of Athens, Athens, Greece

Wilhelm Pfleging Karlsruhe Institute of Technology, IAM-AWP, Karlsruhe, Germany

Tomokazu Sano Division of Materials and Manufacturing Science, Graduate School of Engineering, Osaka University, Suita, Osaka, Japan

Silvia Scalese Istituto per la Microelettronica e Microsistemi, Consiglio Nazionale delle Ricerche, Catania, Italy

Salvatore Scirè Dipartimento di Scienze Chimiche, Università di Catania, Catania, Italy

Hans Jürgen Seifert Karlsruhe Institute of Technology, IAM-AWP, Karlsruhe, Germany

Felix Sima RIKEN Center for Advanced Photonics, RIKEN, Wako, Saitama, Japan;
CETAL, National Institute for Lasers, Plasma and Radiation Physics (INFLPR), Magurele, Ilfov, Romania

Peter Smyrek Karlsruhe Institute of Technology, IAM-AWP, Karlsruhe, Germany

Koji Sugioka RIKEN Center for Advanced Photonics, RIKEN, Wako, Saitama, Japan

Zhuping Wang Institute of Laser and Micro/Nano-Engineering, College of Electronics and Information Engineering, Sichuan University, Cheng'du, China

Yao Xiao Institute of Laser and Micro/Nano-Engineering, College of Electronics and Information Engineering, Sichuan University, Cheng'du, China

Jian Xu RIKEN Center for Advanced Photonics, RIKEN, Wako, Saitama, Japan; School of Physics and Electronic Science, East China Normal University, Shanghai, China

Yongchao Yu Department of Mechanical, Aerospace and Biomedical Engineering, University of Tennessee Knoxville, Knoxville, TN, USA

I. Zergioti School of Applied Mathematical and Physical Sciences, National Technical University of Athens, Athens, Greece

Lingyue Zhang Department of Mechanical, Aerospace and Biomedical Engineering, University of Tennessee Knoxville, Knoxville, TN, USA

Yijing Zheng Karlsruhe Institute of Technology, IAM-AWP, Karlsruhe, Germany

Minlin Zhong School of Materials Science and Engineering, Laser Materials Processing Research Center, Tsinghua University, Beijing, China

Weiping Zhou School of Physics and Electronic Science, Hunan University of Science and Technology, Xiang'tan, China

Chapter 1
Introduction to Laser Micro-to-Nano Manufacturing

Anming Hu, Ruozhou Li, Shi Bai, Yongchao Yu, Weiping Zhou, Denzel Bridges, Yangbao Deng, and Lingyue Zhang

Abstract Laser-based micro-to-nanomanufacturing becomes attractive in surface engineering, precising machining and 2D and 3D microprinting. This chapter introduces the fundamental of light-nanomaterial interaction, the size effect and scaling of nanomaterials and the surface plasmonic excitation of nanomaterials. We focus on the unique features of energy and mass transporting at a nanoscale under photonic excitation. For photonic manufacturing, we mainly compare the photothermal effect induced by long pulse (long than 1 picosecond) or continue wave laser to the nonthermal effect induced by an ultrafast pulsed laser (shorter than 1 picoseconds). We review various laser-based processing, such as, photonic reduction, sintering, laser direct writing and laser carbonization. Subsequently we reviewed two kinds of key techniques for micro-to-nanomanufacturing: various micro-to-nano manipulations and nanojoining. On the basis of these reviews, we introduce latest progresses on innovative molecular devices, near-field manufacturing and super-resolution manufacturing.

A. Hu (✉) · Y. Yu · D. Bridges · L. Zhang
Department of Mechanical, Aerospace and Biomedical Engineering, University of Tennessee Knoxville, 1512 Middle Drive, Knoxville, TN 37996, USA
e-mail: a2hu@uwaterloo.ca

R. Li
College of Electronic and Optical Engineering & College Microelectronics, Nanjing University of Post and Telecommunications, Nanjing 210023, China

S. Bai
Advanced Laser Processing Research Team, RIKEN Center for Advanced Photonics, RIKEN, 2-1 Hirosawa, Wako, Saitama 351-0198, Japan

W. Zhou
School of Physics and Electronic Science, Hunan University of Science and Technology, Xiang'tan 411201, China

Y. Deng
All-Solid-State Energy Storage Materials and Devices Key Laboratory of Hunan Province, College of Information and Electronic Engineering, Hunan City University, Yiyang 413000, China

A. Hu (ed.), *Laser Micro-Nano-Manufacturing and 3D Microprinting*, Springer Series in Materials Science 309, https://doi.org/10.1007/978-3-030-59313-1_1

1.1 Introduction

Laser has become a powerful and versatile tool for manufacturing various mechanical, energy, optoelectronic and biomedical devices with a precision down to a micro- and nano-size [1–3]. To enable a precise engineering and manufacturing it is a linchpin to understand the fundamentals of laser-matter interaction, specially at a small scale [4–6]. Due to the scaling law and the size effect, many materials will behave quite different from their bulk counterparts. Meanwhile, the principles of micro-optics and nanophotonics, which govern the propagation and further manipulation of light and laser (i.e., high single color, extremely strong and aligned light) and the optics at a macro scale are fundamentally disparate. This point has to be considered for micro-to-nano manufacturing. Due to the blooming development of both nanotechnology and nanophotonics, micro- and nanomanufacturing based on laser technology is demonstrating the bright perspective for the extensive application in emerging consumable electronics, flexible, portable and wearable electronics, big data, Internet of things (IoTs).

Traditionally, a pulse period shorter than a nanosecond (10^{-9} s) is named as ultrafast laser. Since the invention of chirped pulse amplification, femtosecond (10^{-15} s) lased laser has attracted extensive interests for precision machining [7]. It has found that limited heating diffusion on the surrounding region of the processed area is one of pronounced features of ultrafast laser processing [8, 9]. By employing a femtosecond ultraviolet laser, polymethyl methacrylate was ablated without the formation of a heat-affect zone [10, 11]. Comparing to the ablation with a nanosecond pulsed laser, the ablation threshold using a femtosecond and or a picosecond laser was also reduced significantly. These features encourage the high-precision manufacturing using various materials, such as biological tissues, semiconductors and other dialectical materials [12]. For an ultrafast interaction, the absorption of photons stimulates the carriers within hundred femtoseconds (fs), which is too short to disturb lattice since the electron-phonon coupling typically occurs in range of 1-100 ps [13, 14]. Meanwhile, an ultrafast pulse width is less than 1 ps. Thus, in an ideal case, ultrafast excitation only occurs within the focal spot. However, for a laser pulse with duration of nanoseconds or longer, the thermal diffusion cannot be neglectable [15]. On the other hand, the nonlinear multiphoton absorption is another important aspect of ultrafast laser processing. The probability of multiphoton absorption can be significantly increased with the extremely high laser peak intensity of tightly focused ultrashort laser pulses since the probability is a power function of the peak intensity [16, 17]. The highly localized nonlinear effect of ultrashort laser may lead to a super-resolution processing beyond the optical diffraction limit and thereby strong absorption can even occur in a transparent material [18, 19]. This multiphoton absorption of ultrafast laser not only permits the surface processing, but also permits the internal microfabrication of transparent materials, such as glass and polymer [20, 21]. Due to the unique multiphoton excitation and the aforementioned highly localized thermal processing, ultrafast laser is found unprecedent application for precise micro-to-nanomanufacturing.

This chapter is organized as follows: starting from the absorption, ionization and surface plasmonic excitation we will briefly review the fundamentals of laser-matter interaction based on a electron-hole plasma frame. We will specially discuss the differences of two kinds of laser, ultrafast pulsed laser and long pulsed or continuous-wave laser interacting with a dielectric material and metal. Based on these physical pictures, we will introduce unique electromagnetic properties of nanomaterials through the scaling law, and then we will briefly overview nanophotonics and plasmonics. In the Sect. 1.4, we will focus on the unique thermal and nonthermal phenomena dominantly induced by long laser pulses and short pulses, separately. In the following two sections, we can review two key fields for micro-to-nanomanufacturing, i.e., nanomanipulation and nanojoining. At last, we will review the latest progress on the nanomanufacturing overcoming the optical diffraction limit.

1.2 Laser-Matter Interaction: Absorption and Ionization

Light-matter interaction is based on the photonic energy is reflected (and/or scattered) by the surface and the absorption of molecules. According to the Lambert-Beer law, the transmittance T can be expressed as (1.1.1)

$$T = I/I_0 = e^{-\alpha x} \tag{1.1.1}$$

where, x is the width of media, I_0, I and I' stand for incident, transmitted and reflected light intensities, respectively. Thus, the interaction only happens in the surface layer (the penetration layer) $L \sim 1/\alpha$ for a non-transparent material. Figure 1.1 shows a light transmitting material with absorption coefficient, α. For graphite, this depth is about 30 nm for 620 nm light [22]. For aluminum, the penetration depth is about 15 nm at 308 nm [23] (Palik 1985). The conventional absorption spectroscopy measures the absorbance $A = Ln(I_0/I) = \alpha x$.

The primary laser-matter interaction process thus involves the excitation of electrons from their equilibrium states to higher energy levels by photo-absorption. Since the light is an electromagnetic wave, the physics of interaction can be described in a better picture by electromagnetic theory. We suppose that a material fills half-space at $x > 0$, overlapped by the skin depth (optical penetration depth) $l = \frac{c}{\omega\kappa}$, where k is the imaginary part of the refractive index and ω the light frequency. At a low laser

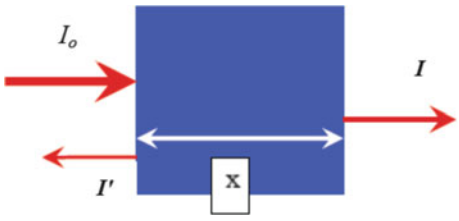

Fig. 1.1 Absorption, transmission and reflection in a planar sample

power (i.e., the laser power lower than the ablation threshold) for a visible to infrared light (at this band, the intra-band absorption can be neglect. For a ultraviolet wavelength, the Loranz-Drude approximation is needed [24, 25] for electron excitation due to the intra-band absorption), the material state can be described by a dielectric function in the Drude approximation

$$\varepsilon = 1 - n_e \frac{\langle \sigma \rangle}{\omega}(i + \omega\tau_m) = 1 - \frac{\omega^2 p_e}{\omega(\omega + i v_m)}$$
$$\varepsilon^{1/2} = n + ik \tag{1.1.2}$$

Here n_e is the electron density, ω_{pe} is the frequency of electron plasma under excitation, $\omega_{pe} = (4\pi e^2 n_e/m)^{1/2}$, v_m is an effective collision frequency of electrons with the lattice (ions). The corresponding absorbance, reflection coefficient, and transmittance, A, R, and T, are given by

$$R = \left|\frac{1 - \sqrt{\varepsilon}}{1 + \sqrt{\varepsilon}}\right| = \frac{4\mathrm{Re}\sqrt{\varepsilon}}{\left|1 + \sqrt{\varepsilon}\right|^2}$$
$$T = \left|\frac{2\mathrm{Re}\sqrt{\omega}}{1 + \sqrt{\omega}}\right|$$

and $A = 1 - R \approx 4\mathrm{Re}\left(\frac{\sqrt{\varepsilon}}{|\varepsilon|}\right) \approx 2\frac{v}{\omega}\left(\frac{n_e}{n_e}\right)^{1/2}$ here $n_e = \pi mc^2/(e^2\lambda^2)$ is the critical density.

We will further consider the surface plasmonic excitation (ω_{pe}) in details in the Sect. 1.3.2. Here, let us first consider photonic-induced ionization at a short light wavelength or a high laser power. For a conventional photoelectron effect, the electron energy is linear dependent on the photonic energy when the photonic energy is higher than a threshold potential. For a transparent dielectric material, there is limited absorption when the photon energy is smaller than the energy gap E_g of dielectric material. Nonlinear absorption mechanism allows photonic-induced ionization. According to the laser intensity and the wavelength, there are three mechanisms for ionization, i.e., tunneling ionization [26], multiphoton ionization [27] and avalanche ionization induced by inverse Bremsstrahlung [28]. Shown in Fig. 1.2, the boundary for the first two cases is described by the Kelddysh parameter [29].

$$\gamma = \frac{\omega}{e}\sqrt{\frac{m_e c n \varepsilon_0 E_g}{I}} \tag{1.1.3}$$

where e is the electron charge, m_e is the effective electron mass and c is the light velocity. When the laser intensity is high and thereby lowers the potential barrier while at a low photon energy (light frequency is low) the electron can pass through the potential barrier through quantum tunneling. As the laser wavelength is short, the electron is more easily excited through a multiphoton absorption. The study displayed that $\boldsymbol{\gamma} \ll 1$, a tunnel ionization is dominant meanwhile the multiphoton absorption

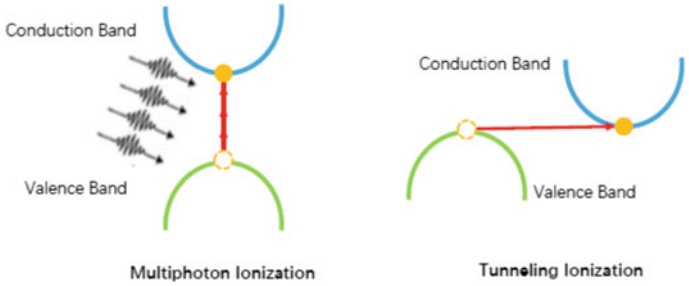

Fig. 1.2 Multiphoton ionization and tunneling ionization

is governed at $\boldsymbol{\gamma} \gg 1$. When $\boldsymbol{\gamma}$ is approximated near 1, two mechanisms may occur simultaneously [29]. Besides, the non-resonant nth order multiphoton ionization rate [30] is

$$P_i = \sigma_n \left(\frac{I}{\hbar\omega} \right)^n \tag{1.1.4}$$

where σ_n is the generalized nth order cross section and I is the peak laser intensity. Therefore, at a long light wavelength, the multiphoton ionization rate can be improved at an extremely high laser intensity.

Electrons at the conduction band can also absorb photon energy through an inverse Bremsstrahlung. When the electrons are enough hot (the kinetic energy is higher the energy gap), they can excite the electrons from the valent band to the conductive band through impaction and then generate two free electrons at the bottom of conductive band (Fig. 1.3). If the intensive laser field constant presents, this excitation of the initial electrons will be repeated and result in a large amount of free electrons. This impact-induced ionization is called the avalanche ionization [31]. And the initial

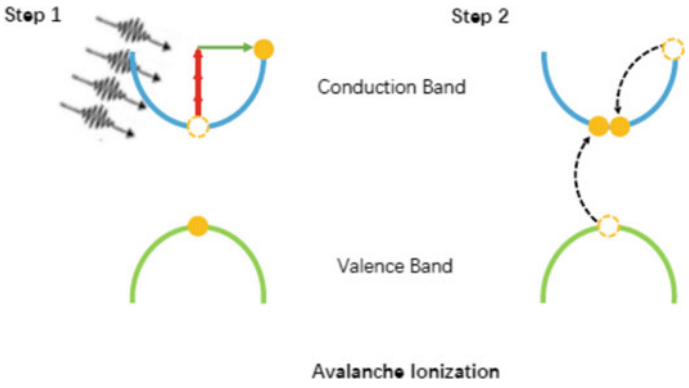

Fig. 1.3 Avalanche ionization through inverse Bremsstrahlung excitation

excited electrons can originate from the thermal excitation of impurity and/or from tunneling and multiphoton ionization. The avalanche ionization causes the significant increase of free electron density. Meanwhile, the laser heat enhances the plasma frequency ω_{pe} approaching the laser frequency. This subsequently yields a stronger resonant absorption and improves the free electron density to a critical value $n_e = \pi mc^2/(e^2\lambda^2)(\sim 10^{22}\ \mathrm{cm}^3)$.

For a practical photonic excitation with a high laser power, these ionizations may synergically exist. For example, with a 100 fs pulse excitation, multiphoton ionization creates a substantial amount of free electrons. When the electron density approaches $10^{17}\ \mathrm{cm}^{-3}$, the collisional ionization rate begins to exceed the multiphoton ionization rate [31]. When this electron density approaches $10^{22}\ \mathrm{cm}^{-3}$, a critical electron density, the reflectivity dramatically increases [32]. The maximum density was thus limited to $10^{22}\ \mathrm{cm}^{-3}$, which corresponds to approximately 10% of the total valence-band population [32].

A lattice softening has been theoretically expected when 10% of the valence electrons are excited into the conduction band [33, 34]. This lattice softening eventually leads to lattice melting, as predicted by ab initio molecular-dynamic calculation [35, 36] and observed experimentally by time-resolved reflectivity [37]. Such melting is an ultrafast phenomenon and is not a consequence of conventional thermal heat transfer.

1.3 Laser-Nanomaterial Interaction

1.3.1 Scaling Law

Nanomanufacturing is further based on the laser-nanomaterials interaction. When the size decreases from a macroscale to a nanoscale, some negligible properties at a macroscopic world become dominant. Although some macroscopic principles are still valid at a microsize, nanomaterials behave very unique. Specially, the quantum effect is critical at an interatomic range or very close to the surface, i.e., within a few nanometers distance. At this size range, a tiny nanoparticle is conventionally named as a quantum dot. The scaling law is a useful method to observe nanoworld based on our knowledge of the macroworld. The scaling law displaying the relation between physical quantities, allows to investigate physical principles and variations in the macro-, micro- and nanoworlds [38].

Size-Effect For a solid material, it is well known that surface atoms have fewer bonds than internal atoms. Less energy is thus needed for them to leave the surface. Considering n balls with an even diameter of R closely compacted in a 2D plane, it is easily to calculated that the total volume is $4n/3\mathrm{R}^3$, while the surface area is $n\,R^2$. The surface/volume ratio is $3/(4R)$, which will significantly increases when R decreases. For a rough estimation, there are about 0.3% atoms presented at the surface for a 1 Â µm particle. However, 87.5% atoms will occupy the surface state in a 2 nm

particle! According to thermodynamics estimation, a large surface/volume leads to a size depression effect of the particle melting temperature [39, 40]. Accordingly to classical Gibbs-Thomson equation, the melting point of particles ($T_m(d)$) can be expressed as follows [41]

$$T_m(d) = T(\infty)\left(1 - \frac{4\sigma_{sl}}{H_f \rho_s d}\right) \tag{1.1.5}$$

where d stands for the particle diameter, $T(\infty)$ is the bulk melting point, σ_{sl} is the solid-liquid interface energy, H_f is the bulk heat of fusion, ρ_s density of solid and d is the particle size. In a practical situation, particle surfaces have a high concentration of defects [40]. As a result, the surface atomic mobility is higher than the inner atoms. Nanoparticles can even demonstrate more activated behaviors at a temperature lower than its melting temperatures. Shi et al. indiced a surface melting model to describe the thermal stability of nanoparticles and/or a 2D system [42],

$$T_m(d) = T_m(\infty)\exp\left[-\frac{\alpha - 1}{\frac{d}{3h} - 1}\right] \tag{1.1.6}$$

where h is the monolayer height of the surface atoms, r is the particle diameter, α is a material constant, relevant to the surface vibration energy. Considering a surface diffusion is a thermally activated, thus $D(d, T)$ can be written in the Arrhenius law

$$D(d, T) = D_o(d)\exp\left[-\frac{E(d)}{RT}\right] \tag{1.1.7}$$

where D_0 is the intrinsic diffusion coefficient, R is the ideal gas constant. $E(d)$ is the diffusion barrier. Assuming $D_0(d) \sim D_0(\infty)$ and

$$\frac{E(d)}{E(\infty)} \approx \frac{T_m(d)}{T_m(\infty)}$$

Combining with the Arrhenius law, one can obtain the thermally activated diffusion coefficient as a function of particle diameter [43]

$$D(d, T) = D_0(d)\exp\left[-\frac{E(\infty)}{RT}\exp\left[-\frac{\alpha - 1}{\frac{d}{3h} - 1}\right]\right] \tag{1.1.8}$$

This indicates the diffusion is remarkably enhanced at a nanoscale. Equations (1.1.5) and (1.1.8) will significantly influence the nanomanufacturing. In brief, (1.1.5) indicates a the nanomanufacturing does not require a high energy. For example, compared to a welding at the macroscale is a Kilo Joule to Mega Joule procedure, a nanojoining only needs a nanojoule energy [44]. Soldering or even brazing at a nanoscale can be even realize by a innovative self-heating procedure

Table 1.1 Displays the typical forces as a scale of L [50]

Force type	Scaling
Surface tension	l^1
Electrostatic force	l^2
Fluid force	l^2
Weight/inertia	l^3
Electromagnetic force (for constant current density)	l^4
Van de Waal's force	l^1

[44–46]. Equation (1.1.8) further indicates numerical involving mass transporting occurs at a lower temperature, even at a room temperature [47]. Therefore, it is understood that a joining of nanowire does not need any heat at room temperature [47, 48]. Furthermore, (1.1.8) demonstrates the nanomanufacturing is a surface engineering with a size range less than 100 nm [5, 6, 16]. It is notable that compared to (1.1.5) successfully explain lots of experiment, (1.1.8) has not well established by experimentally investigation [49].

Scaling Laws of Mechanics Let us consider mechanical properties varying with a typical linear dimension L. It is obvious that the geometric area S is proportional to L^2 and the volume V varies with L^3. For a weight which is dependent on the volume, thus the weight varies with L^3. The buoyancy force is dependent on the surface and proportional to L^2. The S/V is 10^{-4}/mm for an elephant while this value is 10^{-1}/mm for a dragonfly. This can explain why the dragonfly can fly while an elephant cannot (Table 1.1).

This scaling behavior will significantly influence the nanomanufacturing. It is well known that robotic arms are extensively used in a modern automation assembly line. As shown in Fig. 1.4, this operation cannot be realized in a nanomanufacturing since the robotic arm cannot grasp and then release a nanoscale building block. For a nanoparticle, its weight is pretty smaller than the tension force with the surface of robotic arm. This means that once the particle absorbs by the robotic fingers due to the surface it will sticks on the arm. The gravity cannot separate it from the fingers. A robotic manipulation cannot be completed. Thus, a manipulation has to be addressed for nanomanufacturing. We will discuss this in Sect. 1.5.

Scaling Laws of Fluidics are important for inkjet based 3D printing, sensing in liquid and biomedical applications. When a body with a diameter of d falls into a viscous liquid, the friction force and the gravity will make the body falling in a constant velocity, v_c, $v_c = 4\rho g d^2/18\eta d\ v_c$, where η is the viscosity of the liquid and ρ is the density of liquid.

$$v_c \sim L^2$$

$$\tau \sim L^2$$

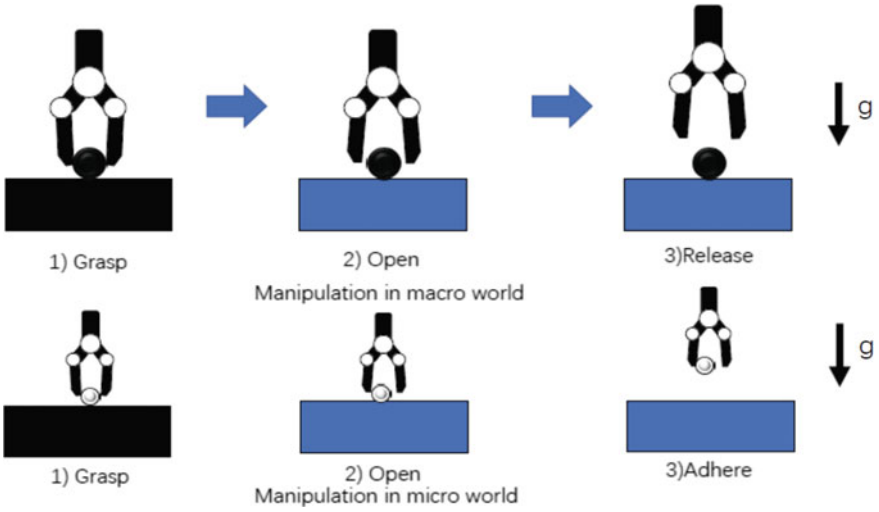

Fig. 1.4 Manipulation difference in a macroworld and a nanoworld

where τ is the transient time. The flux mode can be identified by the Reynold number R_e, $R_e = \rho v L/\eta$. If $v \sim L$, then

$$R_e \sim L^2$$

For a particle travels a distance L by diffusion in a diffusion time $\tau_d = \alpha D$, where α is a geometrical constant and D is the diffusion constant. One can obtain,

$$\tau_d \sim L^2$$

For liquid passes through a needle with a diameter of α, if the needle length is L and the flow rate is Q, the pressure drop through the needle will be

$$\Delta P = \frac{8\mu l Q}{\pi \alpha^4} \sim L^{-3}$$

According this scaling law, for a 30 μm in diameter and 3 cm long needle with a flow rate of 1 microliter per min the pumping pressure is 1.5 atm, but for a 0.3 μm in diameter needle the pumping pressure has to be more than 1.5×10^6 atm!

Scaling Law of Electromagnetics The nanomanufacturing and the operation of nanodevices are frequently involve the electromagnetic properties. Table 1.2 displays the scaling laws of the popular electromagnetic variables.

When the voltage remains constant and L varies, the electrical field E_{el} obviously changes $E_{el} \sim L^{-1}$. The magnetic field intensity in a solenoid with n turns of wire, of the length L, is defined as $B = n\mu I/L$, then $B \sim L$. The magnetic energy stored in the solenoid is

Table 1.2 Scaling laws of electromagnetic variables [51]

Electric quantity	Index, α in L^{α}
Current, I	2
Voltage, V	1
Resistance, R	−1
Capacitance, C	1
Inductance, L	1
Power, P	2

$B_{\text{mag}} = B^2V/2\mu$, V is the volume of the solenoid. One can get

$$B_{\text{mag}} \sim L^5$$

Scaling Laws of Optics are surely critical for laser nanomanufacturing. When light shines on the particle with a length of L, the reflective wave diverges. The divergence angle $\approx \lambda/L$. Hence,

$$\boldsymbol{\theta} \sim L^{-1}$$

This indicates a scattering light will have a very wide solid angle. For photolithography, the optical diffraction limitation with a fixed numerical aperture (NA) lens is

$$d \sim L \approx 2\lambda/(\boldsymbol{\pi}\text{NA}) \tag{1.2.1}$$

Therefore, a shorter wavelength is required for machining a small size of electrical component of integrated circuit chips. For a nanomanufacturing, an electrical ultraviolet (EUV) light source is required for photolithography.

These scaling laws have comprehensive influences of nanophotonic devices and laser-based nanomanufacturing. While microsized optical fibers possess superior performance for telecommunication with reduced lose and band width, submicrosize photonic devices, like, ring-shape resonant cavity, Fabry-Perot laser demonstrate limited quality factors and significant loss. These have to be considered for developing all-optics photonic devices and circuits [52]. In contract, metallic nanomaterials display potential to build plasmonic devices and circuits for light manipulation and confinement at a nanoscale. Through simulation, we have demonstrated several hybrid nanophotonic devices by integrating photonic circuits and plasmonic cavity or boundaries [53–55]. In the following sections we will first discuss how the light excites surface plasmonic resonance on a metallic nanoparticle and then illuminate how the light propagates along an optical fiber and a metallic nanowire. These fundamentals will form the foundation to understand, design and manufacture hybrid nanophotonic-plasmonic devices.

1.3.2 Surface Plasmonic Excitation of Nanoparticles

Surface Plasmons are coherent and collective electron oscillations bounded at the interface between two materials with positive and negative real part of dielectric functions respectively [24]. Fig. 1.5 shows the local electrical filed enhancement due to surface plasmonic excitation. The inherent subwavelength nature of surface plasmons enables significant spatial confinement of light energy and thereby dramatically strengthen the interaction between photons and materials. [56, 57] The enhanced light–matter interactions create fast-developing fields on plasmon-enhanced Raman spectroscopy [58, 59], photocatalysis [60], photothermal [61, 62], photovoltaic [63], fluorescence [64], nonlinear optics [65], etc.

The interaction of plasmonic material with light can be generally regard as the interaction of photons with the free electron gas inside the materials. Over a wide frequency range, the optical properties of plasmonic material can be linked to the well-known Drude approximation [66], where a gas of free electrons of number density moves against a fixed background of positive ion cores [24]. Here, electron-electron interactions and details of the lattice potential are simplified by using the effective mass of the electrons instead, under the hypothesis that the band structure is incorporated into the effective mass in some certain degree. The electrons oscillates with the applied light at an angular frequency ω, and their motion is damped via the relaxation time of the free electron gas τ. The dielectric function of plasmonic material can be write as

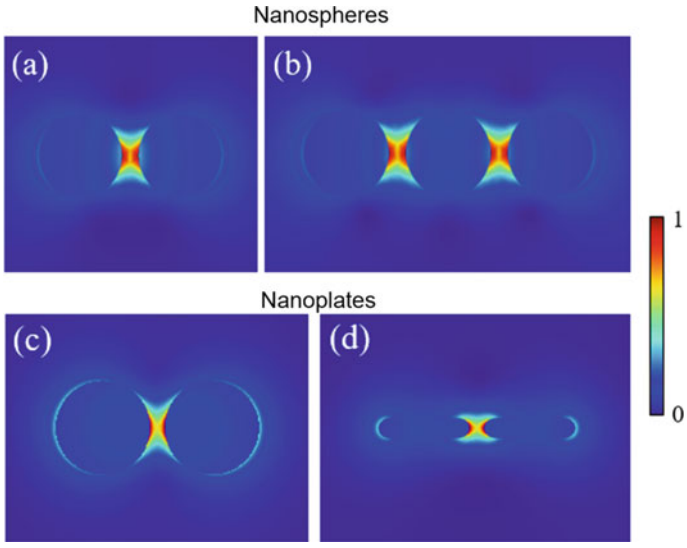

Fig. 1.5 The field distributions of localized surface plasmon resonances (LSPRs) in gold nanospheres and nanoplates

$$\varepsilon(\omega) = 1 - \frac{\omega_p^2}{\omega(\omega + j\gamma\omega)} \tag{1.2.2}$$

where ω_p is the plasma frequency of the free electron gas, $\gamma \sim 1/\tau$ is the impact frequency and τ is the characteristic impacting time.

Clearly the dielectric function of plasmonic material includes a complex form. The real and imaginary components $\varepsilon(\omega) = \varepsilon_r(\omega) + \varepsilon_i(\omega)$ are given by

$$\varepsilon_r(\omega) = 1 - \frac{\omega_p^2\tau^2}{1 + \omega^2\tau^2} \tag{1.2.3}$$

$$\varepsilon_i(\omega) = \frac{\omega_p^2\tau^2}{\omega\left(1 + \omega^2\tau^2\right)} \tag{1.2.4}$$

where the imaginary components of the complex dielectric function implies the attenuation of the lights inside the plasmon materials.

Note that this approximation is not adequate for high angle frequencies, where interband transitions occur [67]. This phenomenon is considerable at visible optical band for noble metals, where photons are efficient in inducing interband transitions [24]. For some of the noble metals such as gold and silver, this effect even occurs at an optical wavelength around 1 μm. The electrons from the filled band below the Fermi surface are excited to higher bands, and ultimately leads to a consequence of an increased damping.

By introducing the complex dielectric function of plasmon material, the interaction of plasmon materials with light can be generally described through classical electromagnetic field theory based on macroscopic Maxwell's equations. This theory is valid even when the spatial scale of the plasmon material is down to several nanometers, though quantum mechanics should be taking into account at sub-nanometer scale reign. In this chapter we limit our description within the realms of the classical theory. However, we have to be open mind for unexpected phenomena with the strong dependence of the properties on frequency and material characteristics.

Surface plasmons can be divided into two categories, i.e., localized surface plasmons (LSPs) and surface plasmon polaritons (SPPs). LSPs are non-propagating excitations of the conduction electrons of plasmonic structures by the light [68]. For metal or some certain kind of semiconductor nanoparticles with dimensions smaller than the incident light wavelength, LSPs can be excited by direct optical excitation. On the other hand, SPPs are electromagnetic excitations propagating at the interface and evanescently confined in the perpendicular direction [69, 70]. With the wavevector matching, SPPs can also be excited and propagated along a metallic nanowire that served as a subwavelength plasmonic waveguide, which is discussed in the next section.

Here, let us consider a small, isolated metal particle with its size comparable to the penetration depth of the incident electromagnetic field into the metal. Therefore the external electromagnetic field can penetrate into the particle and shift the free

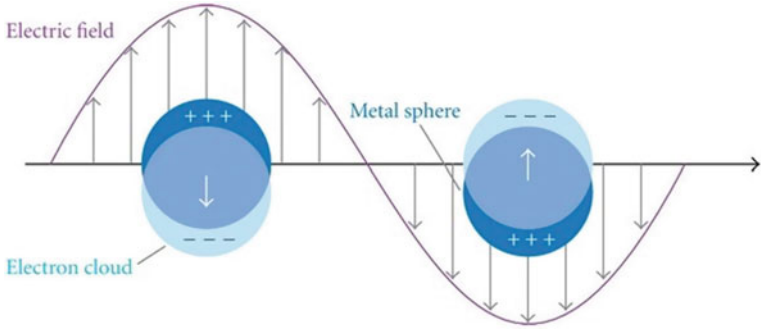

Fig. 1.6 Diagram of localized surface plasmon resonances (LSPRs) (Reprinted with permission from [71]. Copyright 2019. Hindawi Publishing Corporation)

conduction electron cloud with respect to the metal lattice and leads to a localized restoring field within the particle. The periodical shift of the electrons and change of the restoring field create coherent, resonant oscillations of the electron gas related to the exciting electromagnetic field. This phenomenon is called localized surface plasmon resonances (LSPRs) (Fig. 1.6).

Quasistatic Approximation can be used to describe LSPs in nanoparticles whose sizes are significant small compare with the wavelength of the exciting light [24]. Therefore exciting light can be regarded as a homogeneous field and the retardation over the particle volume can be neglected. Consider a homogeneous, isotropic sphere located at the origin in a uniform, static, homogeneous electric field $\boldsymbol{E}_0$, surrounding by an idea non-absorbing, isotropic medium with dielectric constant ε_m. Here we define the polarizability α via $\boldsymbol{p} = \varepsilon_0 \varepsilon_\mathrm{m} a \mathbf{E}_0$, where $\boldsymbol{p}$ is the dipole moment at the particle. By casting the Laplace equation, the complex polarizability is given by

$$\alpha = 4\pi a^3 \frac{\varepsilon(\omega) - \varepsilon_\mathrm{m}}{\varepsilon(\omega) + 2\varepsilon_\mathrm{m}} \tag{1.2.5}$$

where a and $\varepsilon(\omega)$ are the diameter and the dielectric function of the sphere of the sphere, respectively. The distribution of the electric field can be expressed as

$$\boldsymbol{E}_\mathrm{in} = \frac{3\varepsilon_\mathrm{m}}{\varepsilon(\omega) + 2\varepsilon_\mathrm{m}} \boldsymbol{E}_0 \tag{1.2.6}$$

$$\boldsymbol{E}_\mathrm{out} = \boldsymbol{E}_0 + \frac{3\boldsymbol{n}(\boldsymbol{n} \cdot \boldsymbol{p}) - \boldsymbol{p}}{4\pi \varepsilon_0 \varepsilon_\mathrm{m}} \frac{1}{r^3} \tag{1.2.7}$$

where $\boldsymbol{r}$ is the position vector point from the center of the sphere to the outside, $\boldsymbol{n}$ is the unit vector. The corresponding cross sections for scattering and absorption C_sca and C_abs are given by

$$C_{\text{sca}} = \frac{k^4}{6\pi}|\alpha|^2 = \frac{8\pi}{3}k^4a^6\left|\frac{\varepsilon - \varepsilon_{\text{m}}}{\varepsilon + 2\varepsilon_{\text{m}}}\right|^2 \tag{1.2.8}$$

$$C_{\text{abs}} = \text{Im}[\alpha] = 4\pi ka^3\text{Im}\left[\frac{\varepsilon - \varepsilon_{\text{m}}}{\varepsilon + 2\varepsilon_{\text{m}}}\right] \tag{1.2.9}$$

where $k = \frac{2\pi}{\lambda}$ is the wave vector of the exciting light. The extinction cross section can be defined as $C_{\text{ext}} = C_{\text{sca}} + C_{\text{abs}}$, i.e.

$$C_{\text{ext}} = 9\frac{\omega}{c}\varepsilon_{\text{m}}^{3/2}V\frac{\varepsilon_2}{[\varepsilon_1 + 2\varepsilon_{\text{m}}]^2 + \varepsilon_2^2} \tag{1.2.10}$$

When the particle diameter matches $a << \lambda$, the cross sections for scattering and absorption C_{sca} and C_{abs} scale with a^3 and a^6, respectively. Clearly all the scattering, both absorption and extinction of the particle are resonantly enhanced due to the LSPRs.

Quasistatic approximation can be relaxed to more complex geometrical shapes. For example, an ellipsoid with semiaxes specified by $\frac{x^2}{a_1^2} + \frac{x^2}{a_2^2} + \frac{x^2}{a_3^2} = 1$, where $a_1 \leq a_2 \leq a_3$, the polarizabilities α_i along the principal axes $i = 1,2,3$ can be written as

$$\alpha_i = 4\pi a_1a_2a_3\frac{\varepsilon(\omega) - \varepsilon_{\text{m}}}{3\varepsilon_m + 3L_i(\varepsilon(\omega) - \varepsilon_{\text{m}})} \tag{1.2.11}$$

where the geometrical factor L_i can be expressed as

$$L_i = \frac{a_1a_2a_3}{2}\int_0^\infty \frac{\text{d}q}{\left(a_i^2 + q\right)f(q)} \tag{1.2.12}$$

$$f(q) = \sqrt{\left(q + a_1^2\right)\left(q + a_2^2\right)\left(q + a_3^2\right)} \tag{1.2.13}$$

Despite only account for small plasmon structures with dipolar LSP modes, the quasistatic approximation still reveals the main profiles of the LSPs, i.e., the great field enhancement in the near field, and the significant scattering and absorption characteristics. The characteristics of LSPs can be influenced by the following factors, the shape and the size of the nanostructure (Figs. 1.7, 1.8), the dielectric function of the plasmon material and the dielectric function of the surrounding medium. Also, the excitation of the LSPs can be anisotropic for more complex plasmon structures with respect of the polarization of the exciting light (Fig. 1.9) [72].

Mie theory [73], based on the superposition of different eigenmodes which are dipolar or multipolar in character, provides a more exact analytical theoretical descripting of the absorption and scattering of light by spheres, especially for the spheres with a larger size, where the quasistatic approximation is not accurate. For more complex plasmon structures or the coupling among multiple structures, numerical computation protocols, such as, finite-different time-domain (FDTD) or finite

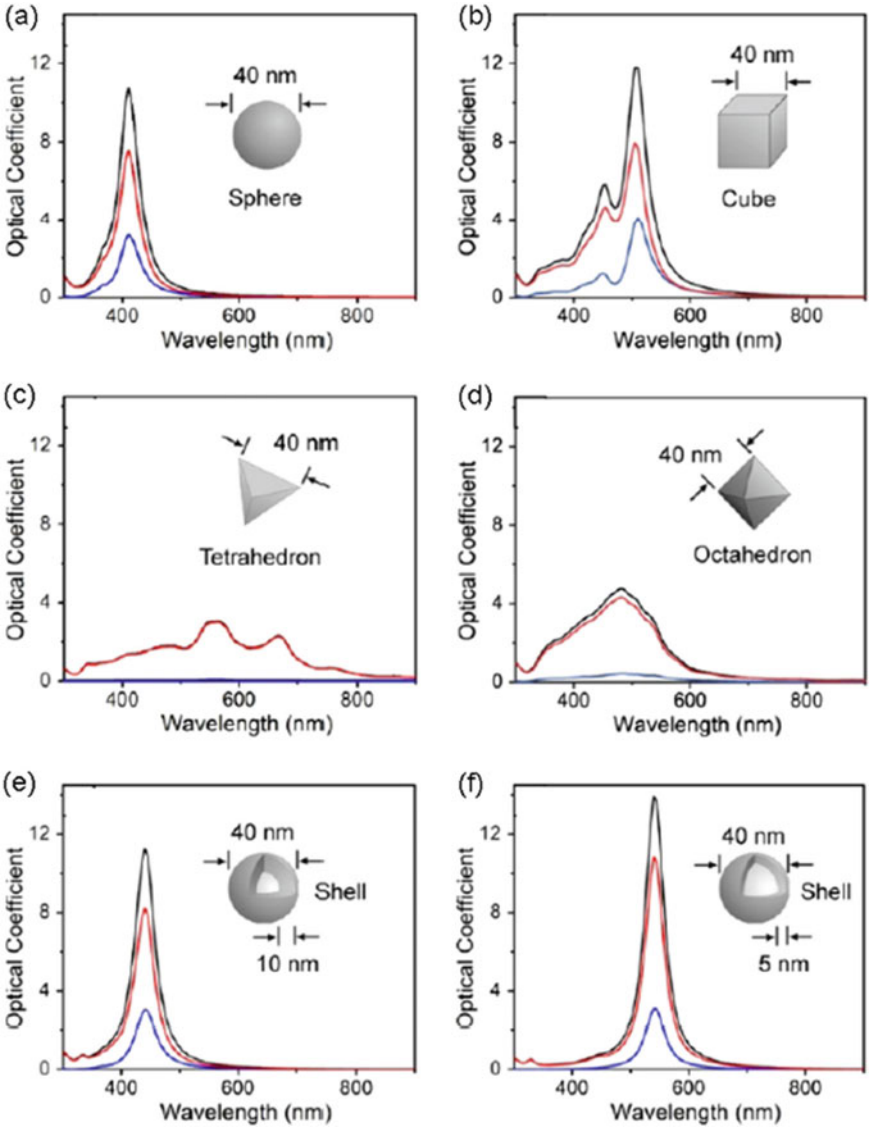

Fig. 1.7 The extinction spectra of nanoparticles in a variety of shapes. (Reprinted with permission from [74]. Copyright 2019 American Chemical Society)

element method (FEM), are more preferred to calculate the field distributions of the LSPs [24].

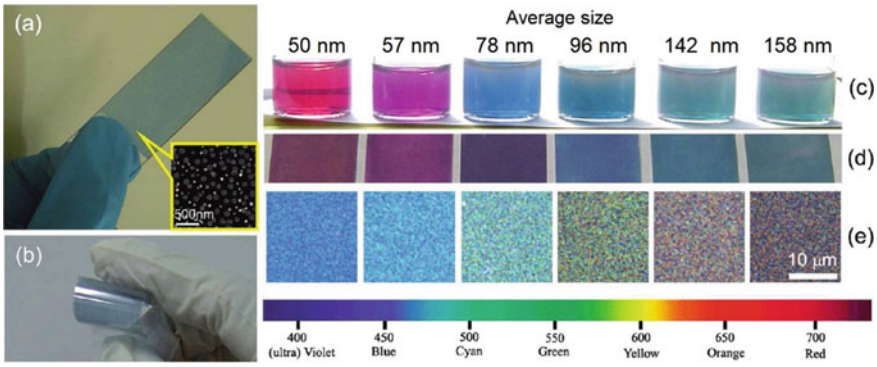

Fig. 1.8 The extinction spectra of silver nanoplates in a variety of sizes. (Reprinted with permission from [75]. Copyright 2011 American Chemical Society)

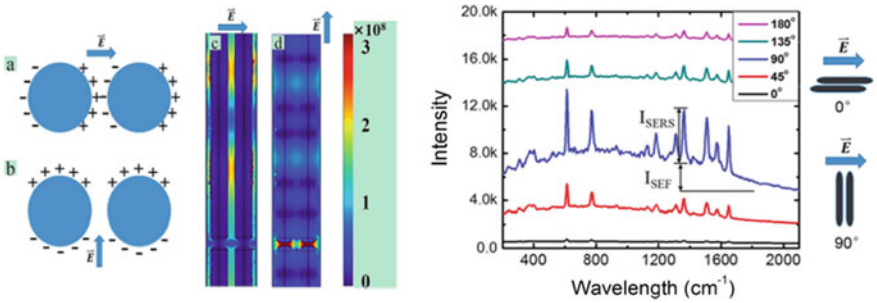

Fig. 1.9 The polarization dependence of the LSPs for nanoparticles in orthogonal directions. (Reprinted with permission from [76]. Copyright 2015 Royal Society of Chemistry)

1.3.3 Propagation Along an Optical Nanofiber (Optical Mode) and Metallic Nanowire (Plasmonic Mode)

Conventional dielectric fibers can guide electromagnetic modes with the core diameter thicker than the cut-off diameter. The lateral mode size in a dielectric fiber is limited by the diffraction limit to the order of λ/n, and will restrict higher degrees of miniaturization. Shown in Fig. 1.10, when the fiber diameter d is decreased, the evanescent fields of the fundamental mode extend deeper into the surrounding medium, which will degenerate the field confinement. Further decreasing the fiber diameter eventually turns the guided mode into a bulk plane-wave in the medium surrounding the fiber. The smallest mode size of conventional dielectric fiber is thus limited to a micrometer scale [77, 78].

Optical Nanofibers are one-dimensional (1D) nanoscale optical fibers with diameters in subwavelength scale (several hundred nanometers or less) respect to the guided light [79]. Compared with commercial glass fibers with diameters from several

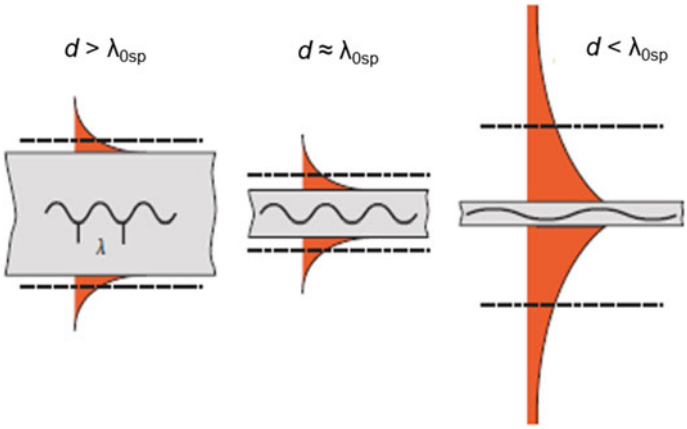

Fig. 1.10 The guided modes of the dielectric fibers with a variety of diameters. (Reprinted with permission from [77]. Copyright 2010. Springer Nature)

micrometers to hundreds of micrometers, optical nanofibers enable subwavelength or even deep subwavelength light guiding, and illustrate merits such as high optical confinement, strong field enhancement, small size and light weight. High optical confinement enables optical circuits with tight mode size, low loss sharp bends and short optical paths, which will be in favor of the minimization and condensing of optical or photonic devices, and may promote low-threshold or low-power optical nonlinear effects. Strong field enhancement will offer enhanced light-matter interactions at the nanofiber surroundings, and naturally promote the applications such as high sensitivity and fast response optical sensing. The steep gradient of the evanescent fields can provide large gradient force for optical trapping or deep potential wells for cold atom trapping and guiding.

Two mechanisms are mainly involved to realize subwavelength light guiding in optical nanofibers, high index difference for optical dielectric nanofibers and/or surface plasmon polaritons for plasmonic fibers.

High Index Difference is commonly utilized to construct optical dielectric nanofibers which supports optical waveguide modes. Shown in Fig. 1.11, a nanofiber consist a dielectric core with its refractive index n_1 significant higher than the index n_2 of the surrounding claddings such as vacuum, air and water. The guided light in optical dielectric nanofibers obtain the law for the conventional dielectric fibers. The mode size still contained by the diffraction limit. However, utilizing high-index core materials and high index difference ($\Delta n = n_1 - n_2$) can remarkably reduce the mode size and extend the optical fibers from micro scale to nano reign. A typical refractive index difference of an optical nanofiber ($\Delta n > 2$) is obviously higher than that of commercial optical fiber ($\Delta n \approx 0.01$).

The waveguiding properties for an optical nanofiber can be deduced from the Helmholtz equations

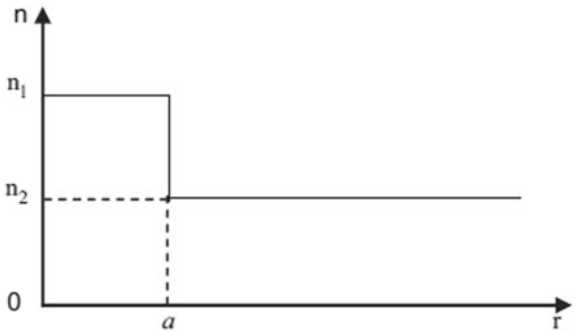

Fig. 1.11 Index profile of dielectric optical nanofibers. (Reprinted with permission from [79]. Copyright 2012. Elsevier Inc.)

$$\begin{aligned}\left(\nabla^2 + n^2k^2 - \beta^2\right)\boldsymbol{E} &= 0,\\ \left(\nabla^2 + n^2k^2 - \beta^2\right)\boldsymbol{H} &= 0\end{aligned} \tag{1.2.14}$$

where k is the wave vector of the light in vacuum and β is the propagation constant. Therefore the modes HE_{vm} and EH_{vm} can be expressed by the equations [79]:

$$\left\{\frac{(J'U)_v}{(UJU)_v + \frac{K'_v}{WK_v}\left\{\frac{(J'U)_v}{(UJU)_v + \frac{n_2^2K'_v}{n_1^2WK_v} = \left(\frac{v\beta}{kn_1}\right)^2\left(\frac{V}{UW}\right)^4}\right\}}\right\} \tag{1.2.15}$$

The $TE_{0\mathrm{m}}$ modes is given by

$$\left\{\frac{J_1(U)}{UJ_0(U)} + \frac{K_1(W)}{WK_0(W)}\right\} = 0 \tag{1.2.16}$$

The $TM_{0\mathrm{m}}$ modes is given by

$$\left\{\frac{n_1^2J_1(U)}{UJ_0(U)} + \frac{n_2^2K_1(W)}{WK_0(W)}\right\} = 0 \tag{1.2.17}$$

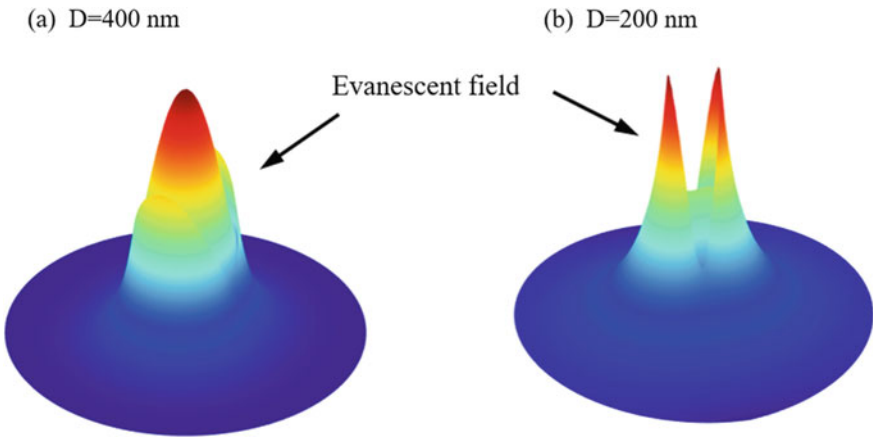

Fig. 1.12 Mode field distributions of dielectric optical nanofibers with thicknesses of **a** 400 nm and **b** 200 nm, respectively.

in which

$$U = a(k_0^2 n_1^2 - \beta^2)^{1/2}$$
$$W = a(\beta^2 - k_0^2 n_2^2)^{1/2}$$
$$V = k_0 a\left(n_1^2 - n_2^2\right)$$

J_v and K_v is the Bessel function of the first kind and the modified Bessel function of the second kind.

Figure 1.12 demonstrates the field distributions of nanofibers with diameters of 400 and 200 nm. A thinner nanofiber leads to a larger fractional evanescent fields which intrigue new opportunities for nanoscale light manipulation [80].

Surface Plasmon Polaritons (SPPs) are the coherent longitudinal charge oscillations of the conduction electrons coupled to the electromagnetic field at the interface of a metal and a dielectric, and are able to propagate along the interface [24]. Electromagnetic waves can be tightly confined around the interface in evanesce waves form with exponential distributions outwards from the dielectric-metal interfaces to both sides of metal and dielectric. [70] For plasmonic nanofibers, the fields decay exponentially in both the metal core and surrounding medium. The optical properties of SPPs can be deduced from Maxwell's equations of macroscopic electromagnetism and solve Helmholtz equation. The electromagnetic waves propagation along z directions matches the equations

$$\beta^2 + k_x^2 + k_y^2 = \varepsilon_\mathrm{m}\mu_0\omega^2 \tag{1.2.18}$$

$$\beta^2 - \kappa_x^2 - \kappa_y^2 = \varepsilon_\mathrm{d}\mu_0\omega^2 \tag{1.2.19}$$

where β is the propagation constant of the SPP mode, k_x, k_y, κ_x and κ_y are the component of the wavevector perpendicular to the interface in the two media, i.e., the metal cladding and surrounding dielectric. Note that, surface plasmons typically involve complex ε_m with negative real part and large imaginary part of ε_m. The k_x and k_y can be imaginary, making it possible to confine and guide the light beyond the beyond the diffraction limit in plasmon nanofibers like metal nanowires [81, 82] (Fig. 1.13).

The mode pattern of SPP can be much smaller than the optical propagation modes. When the diameter d of the plasmonic nanofiber is reduced below the wavelength λ_{0sp} of the SPP, there is significant reduction in the phase and group velocities, and thereby localization occurs [77]. It is possible to reduce the mode size of the guided SPP down to a few nanometers. Shown in Fig. 1.14, the diameter of plasmonic waveguide, $2a$, can be much smaller than $\lambda/(2n)$, the so-called optical diffraction limit.

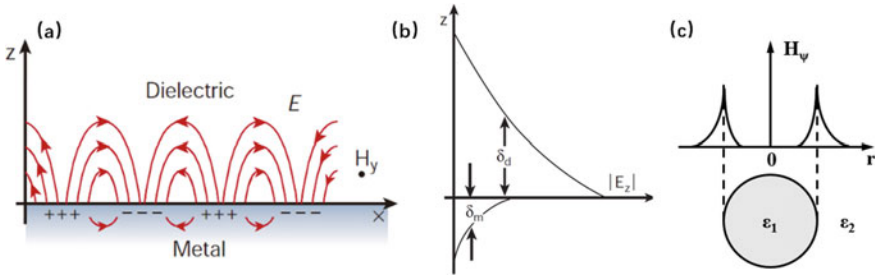

Fig. 1.13 Diagram of Surface plasmon polaritons (SPPs), **a** charge oscillations of the conduction electrons coupled to the electromagnetic field (Reprinted with permission from [69]. Copyright 2003. Springer Nature), field distributions of SPP modes propagate along, **b** a dielectric-metal interface (Reprinted with permission from [69]. Copyright 2003. Springer Nature.), and **c** a metal nanowire, showing the exponential distributions of the evanesce waves outwards from the dielectric-metal interface (reprinted with permission from [83] ©The Optical Society)

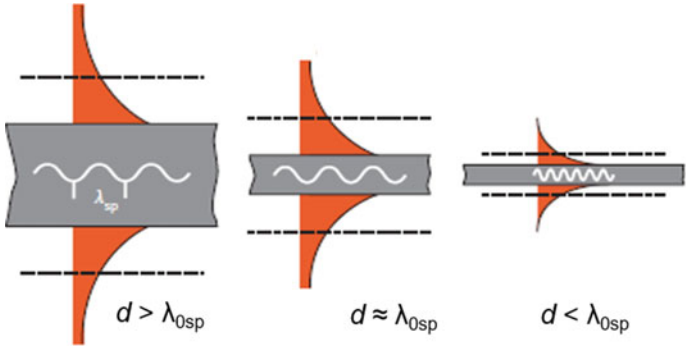

Fig. 1.14 The guided SPP modes of the metal nano wires with a variety of diameters (Reprinted with permission from [77]. Copyright 2010. Springer Nature)

The dielectric fiber, as we discussed in Fig. 1.10, on the contrary, with an extending of the evanescent fields, dramatically enlarges the mode sizes and eventually lose the effective confinement with a decreasing fiber diameter.

The dispersion relation of SPPs obeys the equation

$$\beta = k_0 \sqrt{\frac{\varepsilon_d \varepsilon_m}{\varepsilon_d + \varepsilon_m}} \tag{1.2.20}$$

in which $k_0 = \frac{\omega}{c}$ is the wavevector of the light in vacuum, ε_m an ε_d are the dielectric functions of the metal and the surrounding dielectric. The wavevector of the SPP mode $k_{sp} = \beta$ is obvious smaller than that of the light in vacuum. Therefore unlike LSPs, SPPs cannot be launched directly by incident light due to the momentum mismatch between the photons and plasmons. Techniques such as prism coupling, lens focusing, nanowire coupling and electron excitation were developed for the exciting of SPPs (Fig. 1.15).

Figure 1.16 demonstrates SPPs propagates along metal nanowires. With a bright spot of the exciting light at one end of a nanowire, dimmer spot can be observed at

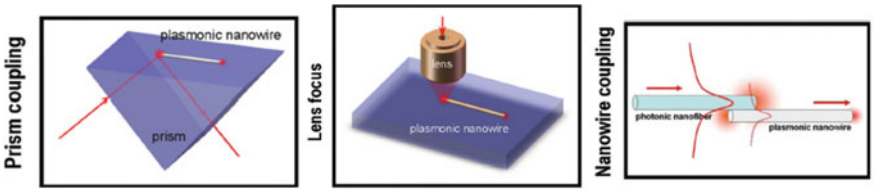

Fig. 1.15 Several techniques for the exciting of SPPs such as prism coupling, lens focusing and nanowire coupling (Reprinted with permission from [81]. Copyright 2013, Wiley-VCH)

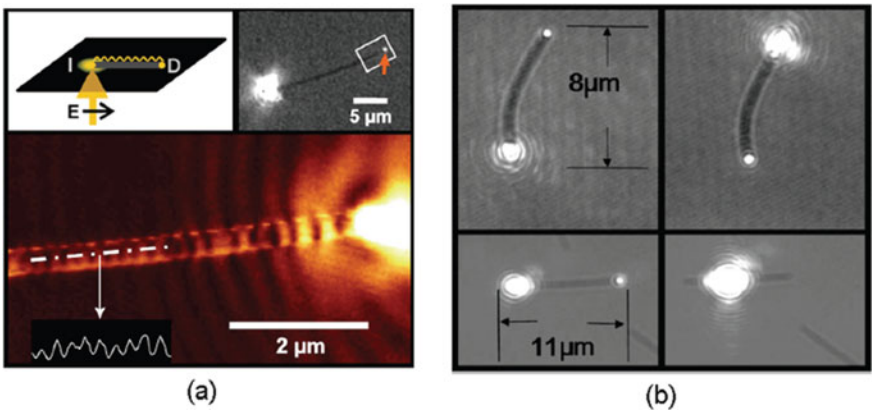

Fig. 1.16 SPPs propagates along metal nanowires (**a** Reprinted with permission from [84]. Copyright 2004 American Physical Society. **b** Reprinted with permission from [85]. Copyright 2006. American Chemical Society)

the other. The propagation of the SPP modes are limited by the attenuation due to the absorption in metal [84, 85].

The propagation length of SPP is given by

$$\delta_{sp} = \frac{1}{2k''_{sp}} = \frac{c}{\omega}\left(\frac{\varepsilon_d + \varepsilon'_m}{\varepsilon_d \varepsilon'_m}\right)^{\frac{3}{2}} \frac{\left(\varepsilon'_m\right)^2}{\varepsilon''_m} \tag{1.2.21}$$

in which k''_{sp} is the imaginary part of the complex SPP wavevector $k_{sp} = k'_{sp} + ik''_{sp}$, ε'_m and ε''_m are the real and imaginary parts of the complex dielectric function of the metal

$$\varepsilon_m = \varepsilon'_m + i\varepsilon''_m. \tag{1.2.22}$$

The propagation length of a SPP mode is strictly dominated by the mode size. For a silver nanowire, the propagation length typically ranges from hundreds of nanometers to several micrometers (Fig. 1.15). This characteristic sets the upper size limit for any photonic circuit based on SPPs.

To extend the propagation length, hybrid plasmon mode involve together with optical waveguide modes and SPP modes, and combine the superiority from both high index difference and SPPs [86, 87]. Fig. 1.17 demonstrates two configurations involves hybrid plasmon modes. Figure 1.18 shows subwavelength devices based on plasmonic circuits: plasmonic route, logic gate and the hybrid nanophononic circuits.

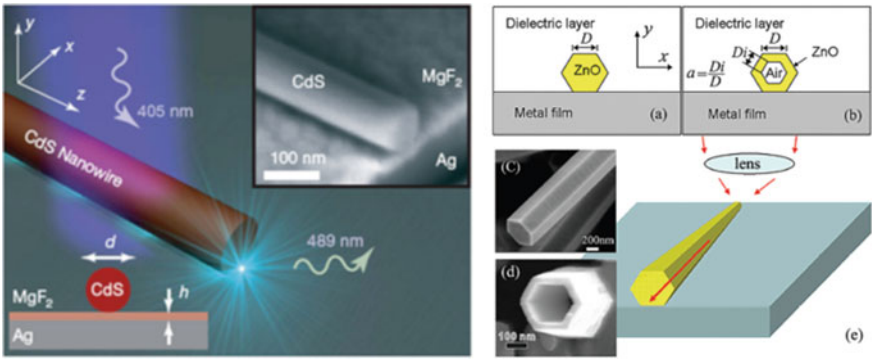

Fig. 1.17 Configurations involves hybrid plasmon modes (**a** Reprinted with permission from [87]. Copyright 2009. Springer Nature. **b** Reprinted with permission from [53]. Copyright 2010. American Institute of Physics Publishing)

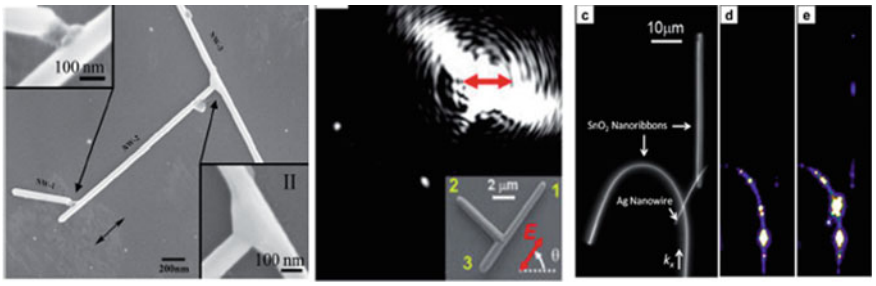

Fig. 1.18 Subwavelength devices using plasmonic nanofibers: plasmonic route (Reprinted with permission from [88]. Copyright 2016. Institute of Physics publications), logic gate (Reprinted with permission from [89]. Copyright 2010. American Chemical Society) and hybrid nanophotonic circuits (Reprinted with permission from [90]. Copyright 2009. Proceedings of the National Academy of Sciences)

1.3.4 Nanocomposite Absorption and Photothermal Effect

Photothermal effect is a well-known phenomenon that involves light absorption and heat generation. Nanocomposites consisting of metal nanostructures and other dielectrical/polymer materials, are considered as efficient and localized light-driven heat sources due to the huge absorption cross sections, effective light concentration and strong absorption medium due to large Ohmic losses of light-induced surface plasmons [61]. The heat from surface plasmons is generated from two parts, metal nanostructures and the surrounding dielectrics.

Photothermal effects in metal nanostructures arise from the exciting of surface plasmons. Surface plasmons can decay nonradiatively, which create energetic carriers, referred as "hot" carriers (electrons and/or holes) [91]. Following Landau damping, the athermal distribution of electron–hole pairs decays through two pathways, re-emission of photons or carrier multiplication caused by electron–electron interactions. Then the hot carriers will redistribute their energy by electron–electron scattering processes, subsequently generate heat through a Joule effect (i.e., electron-lattice scattering), and eventually transfer to the surroundings of the metal nanostructure through thermal conduction [92].

Since the heat originates from Joule effects, the heat power density distribution ($q(\boldsymbol{r}, t)$) in the metal nanostructure is given by [93]

$$q(\boldsymbol{r}, t) = \boldsymbol{j}(\boldsymbol{r}, t) \cdot \boldsymbol{E}(\boldsymbol{r}, t) \tag{1.2.23}$$

in which $\boldsymbol{j}(\boldsymbol{r}, t)$ and $\boldsymbol{E}(\boldsymbol{r}, t)$ are the complex amplitude of the electronic current density and the complex electric field intensity inside the metal, respectively. The equation can be write as

$$q(\boldsymbol{r}) = \frac{1}{2}\varepsilon_0 \omega \,\mathrm{Im}[\varepsilon(\omega)]|\boldsymbol{E}(\boldsymbol{r})|^2 \tag{1.2.24}$$

Obviously, the imaginary part ($\mathrm{Im}[\varepsilon(\omega)]$) of the dielectric functions of the nanostructure, represents the loss in the nanostructure, and contributes to the heat generation.

Surrounding the metal nanostructures, organic or inorganic mediums serve as the dielectrics which affect the field distributions of the surface plasmons and in turn impact the light absorption and heat generation processes. The absorption of light by the surrounding medium also contribute to the heat generations to some extent.

The total heat power p can be obtained from

$$p = \oint_v q(\boldsymbol{r})\mathrm{d}V \tag{1.2.25}$$

where the integral runs over the metal nanostructure volume V.

Let us consider a silver/organic nanocomposite cluster (Fig. 1.19), which consists of layered silver nanoplates with 3 nm-thick polyvinylpyrrolidone (PVP) shell capped on each of the nanoplate. The surface plasmons is extremely localized within the ultra-small volume between two silver nanoplates due to the strong plasmon coupling effect [94], whereas very limited electric field distribute in silver [75]. The heat, on the other hand, generates mainly in the silver reign due to the strong absorption in metal. However, the heat generated in PVP is several orders of magnitude smaller

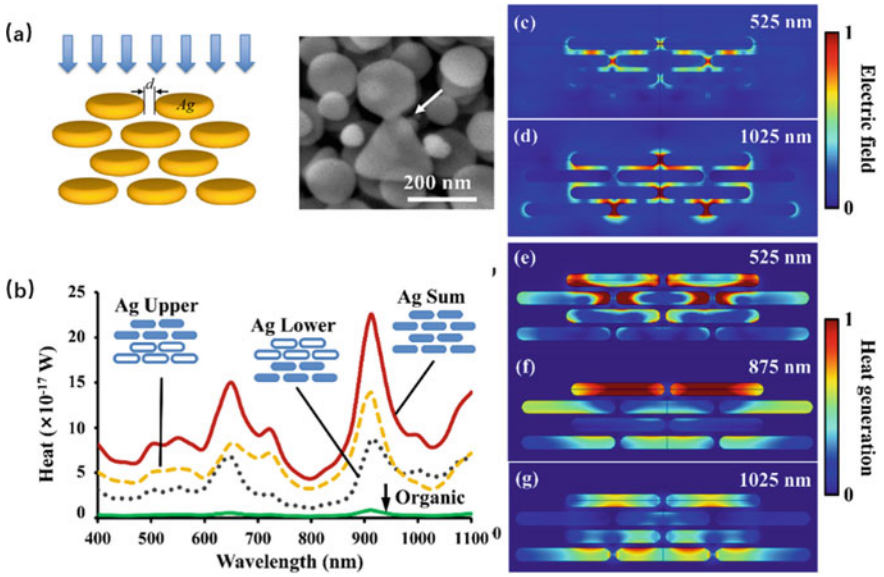

Fig. 1.19 Photothermal effect in a silver/polyvinylpyrrolidone (PVP) nanocluster, **a** diagram of the setup and SEM images of silver nanoplates, **b** calculated heat generation as a function of wavelength, electric field distributions with light wavelengths of **c** 525 nm and **d** 1025 nm, and heat distributions at wavelengths of **e** 525 nm, **f** 875 nm and **g** 1025 nm, respectively (Reprinted with permission from [95]. Copyright 2015 Royal Society of Chemistry)

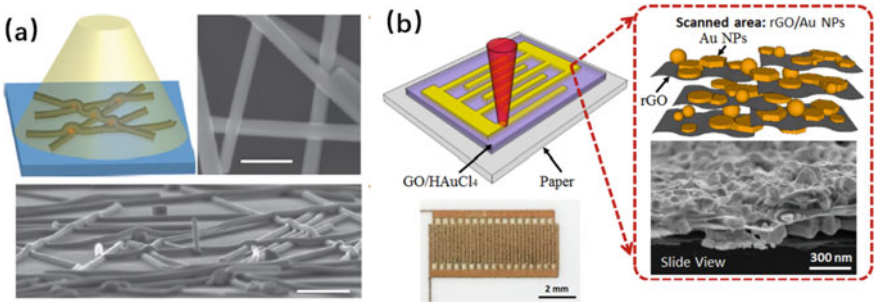

Fig. 1.20 Applications of photothermal effects, **a** photonic sintering (Reprinted with permission from [94]. Copyright 2012. Springer Nature.), **b** laser direct writing (Reprinted with permission from [98]. Copyright 2015 Royal Society of Chemistry)

than that generated in silver. Also, similar to Ag nanowires, heat generation is highly localized and self-contained in the junction point, creating "hot spots". Despite the heat at the hot spots can rapidly spread to the whole Ag nanoplate because of the high thermal conductivity of silver, the heat could be contained in several to hundreds nanometers scale depended on the size and shape of the nanostructures [61].

Besides the aforementioned merits, such as, highly localized heating and efficient light conversion, light-induced heat generation can be well controlled by multiple factors: material absorption involving material, geometrical morphology, size, etc., and incident light properties, such as light intensity, dose, polarization, direction, spectra and even pulse parameters for pulsed light sources. For example, the photothermal effects shows strong wavelength dependency in the silver/PVP nanocluster. The peaks in the heat-wavelength curves (Fig. 1.19b) typically reveals the strong surface plasmon resonance as well as the high efficient heat generation. Therefore, photothermal effects in nanocomposites naturally stimulate vast physical processes and chemical reactions with unprecedented spatial and temporal controls [94, 96]. Shown in Fig. 1.20, applications of photothermal effects have been extend to the fields as photothermal therapy [97, 100], laser direct writing [98], photonic sintering [94], solar energy harvesting [62], surface modification [99], and so on.

1.4 Photothermal Versus Photonic Nonthermal Manufacturing

1.4.1 Photonic Sintering

Photonic sintering is critical for printed electronics and 3D printing. Compared to conventional thermal sintering photonic sintering is a local effect by highly selected

surface plasmonic excitation. As aforementioned, the locally excited plasmonic resonance can only heat the adjacent particles with the narrowest gap. Besides, plasmonic sintering is more energy efficient by selected wavelength for excitation than the thermal sintering. The most unique feature of photonic sintering is "smart" and self-terminated: once the adjacent particles are fused together the new plasmonic excitation will automatically move to the new adjacent positions which usually locate at the edge of a pore [94, 101, 102]. Thus, the particle fusion induced by plasmonic sintering will lead to the eventual disappearance of pores.

The nature of photonic sintering that photothermally induced diffusion. For the diffusion, the liquid phase diffusion is much faster than a solid-state diffusion since the diffusivity in a liquid is much higher than in a solid [103]. As discussed in Sect. 1.1.2, the surface atoms are much activated than the inner atoms due to less bonding and the surface defects [40]. As a result, the sintering temperature can be much lower than the melting point of a particle. The onset sintering temperature as a function of the melting temperature can be written as

$$T_s(d) = \alpha T_m(d) \tag{1.3.1}$$

where the d is the particle diameter. For microparticles, α ranges from 0.5 to 0.8 [40], but for nanoparticles, this value decreases to 0.1–0.3 [45]. This indicates that the sintering of nanoparticles can occur at a very low temperature, only 10% of the melting point. This explains nanomaterials can be joined even at a room temperature without external heating [47]. Considering a possible surface melting of nanoparticle and thereby associated a liquid phase sintering, sintering of nanoparticles for 2D to 3D printed electronics and functional mechanical components are extremely attracted in micro-to-nanomanufacturing.

Diffusion Mechanisms Based on a conventional sintering theory, the driving force for sintering is dependent on the curvature of two touched particles, i.e., (Fig. 1.21)

$$\sigma = \gamma\left(\frac{1}{R_1} + \frac{1}{R_2}\right) \tag{1.3.2}$$

where γ is the specific surface energy, R_1 and R_2 are principle radii of two spherical particles. For two identical particles with a radium of r, the neck size can be expressed a function of r [104],

$$\frac{x}{r} = \left(\frac{Bt}{r^m}\right)^{1/n} \tag{1.3.3}$$

where t is the sintering holding time, B is a temperature-dependent sintering function, and the values of m and n are defined by individual diffusion mechanisms. Three dominant mechanisms have been discussed as the surface diffusion, grain boundary diffusion and the lattice diffusion. If sintering is driven by surface diffusion, (1.3.3) becomes

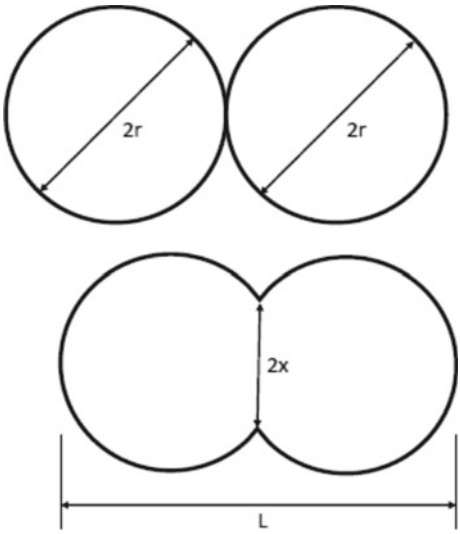

Fig. 1.21 sintering of two particles with the identical radiums

$$\left(\frac{x}{r}\right)_{\text{surf}} = \left(\frac{4.17\delta D_s \gamma_{sv} \Omega t}{RTr^4}\right)^{1/6} \tag{1.3.4}$$

where δ is the surface layer thickness and is estimated as 0.3 nm for Ag [105]) D_s is the surface diffusion coefficient calculated by (2), δ_{sv} is the bulk solid-vapor interfacial surface energy and is estimated as 1.14 J/m^2 for Ag [106]) and Ω is the molar volume (10.3 cm^3/mol for Ag). If sintering is driven by grain boundary diffusion, (1.3.3) becomes

$$\left(\frac{x}{r}\right)_{\text{gb}} = \left(\frac{32\omega D_{\text{gb}} \gamma_{sv} \Omega t}{RTr^4}\right)^{1/6} \tag{1.3.5}$$

where w is the grain boundary width and is estimated as 0.5 nm for Ag [105]) and D_{gb} is the grain boundary diffusion coefficient, which can be calculated by (1.1.8). For lattice diffusion sintering, (1.3.3) becomes

$$\left(\frac{x}{r}\right)_{\text{l}} = \left(\frac{42.05 D_l \gamma_{sv} \Omega t}{RTr^3}\right)^{1/4.78} \tag{1.3.6}$$

where D_l is the lattice diffusion coefficient calculated by (1.1.8). $D_s = 5 \times 10^3$ m^2/s) for surface diffusion, $D_{\text{gb}} = 1.2 \times 10^5$ m^2/s) for grain boundary diffusion, and $D_l = 4.4 \times 10^5$m^2/s) for volume diffusion [107]. $E(\infty)$ is bulk activation energy and is equal to ($E(\infty) = 2.661 \times 10^5$J/mol), ($E(\infty) = 9 \times 10^4$ J/mol), and ($E(\infty) = 18.5 \times 10^4$J/mol) for surface diffusion, grain boundary diffusion, and lattice diffusion, respectively [107, 108]). Dependent on different materials, particle size, particle shape and local temperatures, one of these or two, even three of them may involve the

underlying diffusion. It is possible to identify these mechanisms by characterizing the neck variation as a function of time. Nevertheless, there is limited experimental analyses by these models. The molecular dynamics simulations display remarkable differences from these models [107, 108]. The further investigation is desired to verify these models at a nanoscale.

It is extensively to use a pulsed light rather than a continue wave (constant) light for photonic sintering. With a constant energy output, a pulsed laser indicates a higher peak, which allows a deep penetration since the penetration is proportional to the input power. Besides, the pulsed laser allows the photothermal energy dissipation with a pulse gap for cooling. For sintering of printed circuit with pulsed light, because of the absorption difference of printed materials and substrates, it is possible to limit the thermal effect on the oriented layer only by choosing the proper wavelength. The metallic particles mainly absorb a visible or infrared light while the plastic/paper absorbs a ultraviolet light. It is thus reasonable to use a long-wavelength light for photonic sintering to avoid the thermal accumulation onto the plastic/paper substrate. This feature has advantage because one can print circuits onto a cheap plastic and/or paper substrates for flexible and/or stretchable devices for wearable/portable electronics [101, 109]. On the other hand, it is worth noting that the plasmonic resonant frequency is proportional to the anisotropy of nanomaterials. This means that the resonant wavelength has a blue-shift while the sintering processing [5, 75]. Thus, if the photonic sintering is completed by integrating different light sources, one should put a longer light sources before a short light source. Figure 1.22 shows a practical photonic sintering system by combining three kinds of pulsed light for sintering of printed Cu circuits [110].

The single sintering will gradually lead to the decrease of resistance. However, due to the inhomogeneous distribution of grain size as well as the diffusion is influenced by grain orientations and impurity on the grain boundaries, it is naturally predicted that there are large variation of local resistivity [111]. Thus, the global resistivity of printed circuits will dependent on several factors including the scattering from grain boundaries and surface roughness. It is extensively expressed the resistivity as follows [112],

$$\rho = \rho_{\mathrm{b}} + \rho_{\mathrm{im}} + \frac{\rho_{\mathrm{gb}}\sigma_{\mathrm{gb}}}{R} + \frac{\rho_{\mathrm{s}}s}{h} \tag{1.3.7}$$

where ρ_{b} is the bulk resistivity, ρ_{im} is due to the impurity scattering, this 3rd term is the resistivity due to the scattering of grain boundaries, R is the grain size and σ_{gb} is the grain boundary width, ρ_{gb} is the specific boundary resistivity and the last term comes from the surface scattering with s the surface roughness, h the film thickness and ρ_{s} the specific surface resistivity. Microstructure observation can determine σ_{gb} and R. Atomic force microscopy measurements can determine the surface roughness. During the transient temperature can be measured by a high speed infrared (IR) camera. Assuming the ρ_{b} and ρ_{im} unchanged during curing, one can deduce the resistivity arising from grain boundaries and surface scattering at different

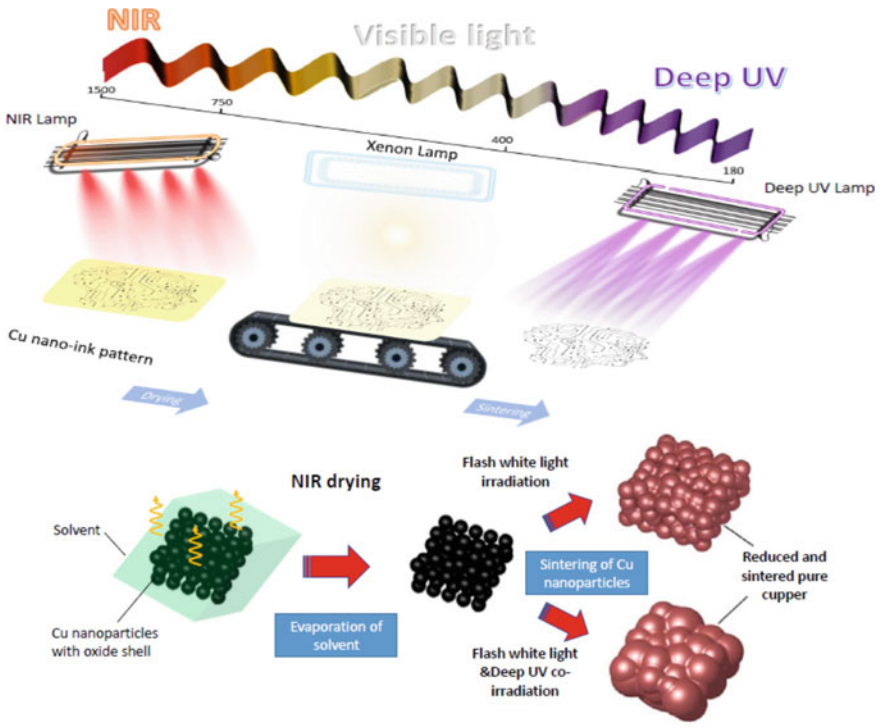

Fig. 1.22 Photonic sintering with different light sources. Adapted from [110]

temperatures. From the relationship between the microstructure and resistivity one can easily optimize the processing window of photonic sintering.

1.4.2 Ultrafast Laser Versus Long Pulsed and Continue Wave Laser Direction

Although laser has been extensively employed for precise manufacturing down to a nanoscale the physics procedure of laser-matter interaction will be significantly influenced by laser pulse widths since the relevant energy and mass transfers will take different characteristic times. To elucidate these procedures is critical to optimize laser-based manufacturing. Before we discuss nanomaterials processed by different lasers let us first check the physics model for laser-matter interaction with different pulse widths.

Two-Temperature Model for Different Pulsed Lasers According to a one-dimensional, two-temperature diffusion model [113, 114] the energy of low intensity

short laser pulses is absorbed by free electrons due to inverse Bremsstrahlung (Joule heat). The evolution of the absorbed energy involves thermalization within the electron gas (electron subsystem), energy transfer to the lattice and thermal diffusion in the lattice. These processes can be expressed as:

$$C_{\mathrm{e}}\frac{\partial T_{\mathrm{e}}}{\partial t} = \frac{\partial Q(z)}{\partial Z} - \gamma(T_{\mathrm{e}} - T_{\mathrm{l}}) + S \tag{1.3.8}$$

$$C_{\mathrm{l}}\frac{\partial T_{\mathrm{l}}}{\partial t} = \gamma(T_{\mathrm{e}} - T_{\mathrm{l}}) \tag{1.3.9}$$

$$Q(Z) = -k_{\mathrm{e}}\frac{\partial T_{\mathrm{e}}}{\partial z}, \quad S = I(t)A\alpha\exp(-\alpha Z) \tag{1.3.10}$$

here z is the direction of energy propagation perpendicular to the target surface, $Q(z)$ is the heat flux, S is the laser source function, $I(t)$ the laser intensity, $A = 1 - R$ is the surface transmissivity and α is the absorption coefficient. C_{e} and C_{l} are the specific heat of the electron and lattice subsystems with $C_{\mathrm{e}} = aT_{\mathrm{e}}$ where a is a constant, γ is the electron-lattice coupling parameter, and k_{e} is electron thermal conductivity. In (1.3.8) we should consider three characteristic time scales: τ_{e}, τ_{i}, and τ_{L}. $\tau_{\mathrm{e}} = C_{\mathrm{e}}/\gamma$ is the electron cooling time, $\tau_i = C_{\mathrm{l}}/\gamma$ is the lattice heating time and τ_{L} the laser pulse width. Following previous studies [9, 115], the laser pulses can be separated into three kinds of time regimes.

Femtosecond Pulses For a fs pulse, the laser width is much shorter than the electron cooling time, $\tau_{\mathrm{L}} \ll \tau_{\mathrm{e}} \sim 1$ ps. Then, $C_{\mathrm{e}}T_{\mathrm{e}}/t \gg \gamma T_{\mathrm{e}}$, and electron-lattice coupling can be neglected. If $D_{\mathrm{e}}\tau_{\mathrm{L}} < \alpha^{-2}$, where $D_{\mathrm{e}} = k_{\mathrm{e}}/C_{\mathrm{e}}$ is the electron thermal diffusivity, the electron heat conduction term can be neglected and (1.3.8) reduces to

$$C_e'\frac{\partial T_{\mathrm{e}}^2}{\partial t} = 2I_\alpha\alpha\exp(-\alpha z) \tag{1.3.11}$$

and gives

$$T_{\mathrm{e}}(t) = \left(T_0^2 + \frac{2I_\alpha\alpha}{C_{\mathrm{e}}'}t\exp(-\alpha z)\right)^{1/2} \tag{1.3.12}$$

here it is assumed that $I(t) = I_0$ and $I_a = AI_0$, while $T_0 = T_{\mathrm{e}}(0)$ is the initial temperature. $C_{\mathrm{e}}' = C_{\mathrm{e}}/T_{\mathrm{e}}$ is a constant when T_{e} remains smaller than the Fermi energy (in temperature). At the end of the laser pulse the electron temperature is given by

$$T_{\mathrm{e}}(\tau_{\mathrm{L}}) \approx \left(\frac{2F_\alpha\alpha}{C_{\mathrm{e}}'}\right)^{\frac{1}{2}}\exp\left(-\frac{z}{\delta}\right) \tag{1.3.13}$$

where $T_e(\tau_L) \gg T_0$, $F_a = I_a \tau_L$ is the absorbed laser fluence, and $\delta = 2/\alpha$ is the skin depth. After the laser pulse the electrons are rapidly cooled due to energy transfer to the lattice and heat conduction into the bulk. Since the electron cooling time is very short, (1.3.9) can be written as $T_i \sim T_e(\tau_L)t/\tau_i$ (neglecting the initial lattice temperature). The maximum lattice temperature can be estimated from the average cooling time of the electrons,

$$\tau_e^a \sim \frac{\tau_e}{2} = C_e^{'} \frac{T_e(\tau_e)}{2\gamma}$$

and is given by

$$T_l \sim T_e^2(\tau_L) \frac{C_e^{'}}{2C_l} \approx \frac{F_a a}{C_l} \exp(-az) \tag{1.3.14}$$

Significant evaporation will occur when $C_i T_i > \rho L_v$, where ρ is the density and L_v is the specific heat of evaporation. Using (1.3.14), we can express the condition of strong evaporation as $F_a \geq F_{th} \exp(az)$, where $F_{th} \sim \rho L_v/\alpha$ is the threshold laser fluence with fs pulses. Then the ablation depth per pulse L is

$$L \approx \alpha^{-1} \ln\left(\frac{F_a}{F_{th}}\right) \tag{1.3.15}$$

Such a logarithmic dependence of the ablation depth per pulse has been confirmed by the ablation of copper in vacuum using 150 fs laser pulses (780 nm, Momma et al. 1997) and in the ablation of highly oriented pyrolytic graphite (HOPG) with 120 fs pulses [16, 116]. It is notable that this penetration depth, standing for the influence regime of hot electrons, may be larger than the optical penetration depth described in formula (1.1.1).

Picosecond Pulses For a ps pulse, $\tau_e \sim 1$ ps $< \tau_L < \tau_i \sim 10$ ps. At times $t \gg \tau_e$, $C_e T_e/t \ll \gamma T_e$, (1.3.8) becomes quasi-stationary, (1.3.8)–(1.3.10) reduce to

$$\frac{\partial}{\partial z}\left(\frac{k_e \partial T_e}{\partial z}\right) - \gamma(T_e - T_l) + I_a a \exp(-az) = 0 \tag{1.3.16}$$

$$T_l = \frac{1}{\tau_l} \int_0^t \exp\left(-\frac{t-\theta}{\tau_l}\right) T_e(\theta) \mathrm{d}\theta + T_0 \tag{1.3.17}$$

The integral corresponds to the temperature increase of the lattice. At $t \ll \tau_i$, (1.3.17) can be simplified due to the quasi-stationary character of the electron temperature. Neglecting T_0, we get

$$T_l \approx T_e\left(1 - \exp\left(-\frac{t}{\tau_l}\right)\right) \approx \left(\frac{t}{\tau_l}\right) T_e \tag{1.3.18}$$

It is obvious that in the ps regime the lattice temperature remains much lower than the electron temperature. Thus the lattice temperature can be omitted in (1.3.16). When the condition $k_e T_e \alpha^2 \ll \gamma T_e$ is fulfilled (1.3.16) and (1.3.11) are very simple. The electron and lattice temperatures at the end of a ps pulse are given by

$$T_e \approx \frac{I_a a}{\gamma} \exp(-az) \tag{1.3.19}$$

$$T_l \approx \frac{F_a a}{C_l} \exp(-az) \tag{1.3.20}$$

Note that the obtained lattice temperature is governed by the electron cooling time. Thus, in fs and ps regimes (1.3.14), (1.3.19) and (1.3.20) give the same expression for the lattice temperature. This indicates that a logarithmic dependence of the ablation depth on laser fluence is also found in the ps regime. However, this conclusion is based on an assumption that the electron heat conduction is negligible. This is a very crude approximation since the electron heat conduction and the formation of melted zone must be related in ps ablation.

Nanosecond Pulses Ablation with ns pulses can be modeled with the condition $\tau_i \sim 10$ ps $\ll \tau_L$. In this case, the electron and lattice temperatures are equal, $T_e = T_l = T$ and (1.3.8)–(1.3.10) reduce to

$$\frac{C_l \partial T}{\partial t} = \frac{\partial}{\partial z\left(\frac{k_0 \partial T}{\partial z}\right)} + I_a a \exp(-az) \tag{1.3.21}$$

There are many experimental and theoretical studies on the processes involved in laser heating and irradiation with long pulses [117]. In this regime the target surface is first heated to the melting point and then to the vaporization temperature. During the interaction the dominant energy loss is heat conduction into the solid target. The heat penetration depth is given by $l \sim (Dt)^{1/2}$, where $D = k_0/C_i$ is the thermal diffusivity. Note that for a long pulse, $D_L \gg 1/\alpha^2$. The energy deposited inside the target per unit mass is given by $E_m \sim It/\rho l$. Evaporation occurs when $E_m \sim L_v$ at t_{th}, where L_v is the specific heat of evaporation. So, the condition for strong evaporation becomes, $E_m > L_v$ (or $\tau_L > t_{th}$) and

$$\begin{aligned} I &\geq I_{th} \sim \frac{\rho L_v D^{1/2}}{\tau^{1/2}} \\ F &> F_{th} \sim \rho L_v D^{1/2} \tau_l^{1/2} \end{aligned} \tag{1.3.22}$$

for the laser intensity and the fluence, respectively. A striking characteristic is that the threshold laser fluence depends on the square root of the laser pulse width. A deviation of the damage threshold from the $\tau^{1/2}$ scaling with short pulses has been clearly evident by ablation of fused silica by infrared (1053 nm) and visible (526 nm) laser radiation [118].

In summary of this section, fs pulses trigger a nonthermal ablation mechanism since both the electron-lattice thermal coupling and thermal diffusion to the lattice take longer time than the pulse width. ns pulses allow thermal equilibrium to occur between the electrons and the lattice.

Comparative Study Between Ultrashort Laser and Continue Wave Laser Interacted with 1-D Nanowire Due to the size effect, thermal diffusion in a nanoscale will be quite different from the aforementioned macroscale. Besides, the energy radiation, reflection and dissipation to the environment have to be considered. To understand the local melting of a Cu nanowire (Cu NW) using a focused laser beam, we recently conducted a comparative study with 1030 nm FS laser and 532 nm continuous-wave (CW) green laser at different power and atmosphere conditions [6]. To support the experimental observation and explain the difference between two types of laser irradiation, we examined computational modeling of the temperature distribution of CuNW. For the simulation, we model CuNW as a circular rod with a length of 30 μm and a diameter of 200 nm and assume that laser is irradiated at the tip of a modeled NW, and the temperature is distributed only along the length (defined as x direction) as shown in Fig. 1.23.

A one-dimensional (1-D) heat diffusion model and the finite difference method are employed for the thermal analysis of two types of laser irradiation: femtosecond laser (FS) and a continue wavelength laser at 532 nm (CW). In the case of CW laser, assuming a steady heat supply, the single-temperature model is used to calculate the temperature distribution and its evolution. In contrast, simulations of FS laser irradiation consider the electron and lattice temperatures (T_e and T_l), separately, (i.e., the aforementioned two-temperature model) due to the time-dependent heat flow from electrons to lattice.

Single-Temperature 1-D Heat Diffusion Model The temperature distribution in Cu nanowire (CuNW) and its evolution during the CW laser heating are calculated by using the single-temperature 1-D heat diffusion model and the finite difference

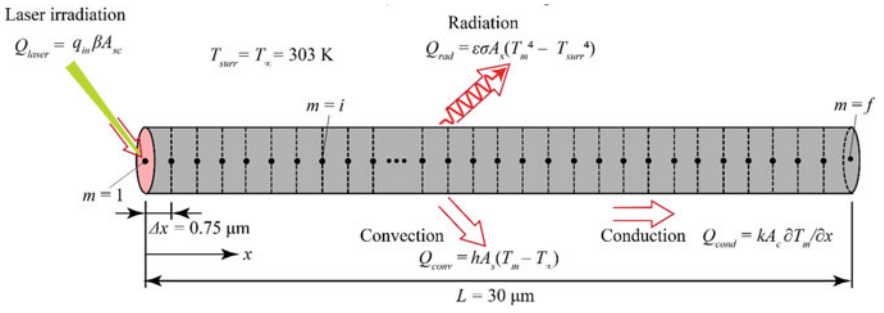

Fig. 1.23 Computational model of 30 μm long CuNW for 1-D heat diffusion equation solved with finite difference method simulation. Convection and radiation heat transfer are considered as the experiment occurred in the ambient atmosphere. The heat source from laser is considered at the tip (first nodal point) of the CuNW [6]

method. The energy balance in control volume of each nodal point (m) is used as the following governing equation [119, 120]:

$$Q_{\text{laser}} + Q_{\text{cond}} - Q_{\text{conv}} - Q_{\text{rad}} = \Delta E_{\text{st}}, \tag{1.3.23}$$

where Q_{laser} is the heat addition by laser and considered for the first nodal point ($m = 1$ or $x = 0$) only, Q_{cond} is the net heat conduction flow to the neighboring nodes, Q_{conv} and Q_{rad} are the convection and radiation heat loss through the CuNW surface, and ΔE_{st} is the change of stored heat in the control volume of each node. Here, for simplification, this analysis excludes heat dissipation through the substrate. This omission of the CuNW/substrate conduction heat transfer is because its inclusion can impose excessive complexities (from contact shape, roughness, and interfacial transport) although their influence is not significant (due to roughness and smaller actual contact area) and can be included in other surface heat dissipation terms (Q_{conv} and Q_{rad}). Q_{laser} is given as the product of laser heat flux q_{in}, absorptance (ratio of the absorbed to the incident radiant power) β, and the first node surface area, i.e., $Q_{\text{laser}} = q_{\text{in}}\, \beta A$, and our simulations employ $q_{\text{in}} = 4.46 \times 10^{10}$ W/m^2 for CW laser and $\beta = 0.5$ at the wavelength of CW laser (532 nm) [121]. Q_{cond} is calculated using nodal temperatures (T_{m}) and Cu thermal conductivity, $k = 400$ W/m K with 1-D Fourier heat conduction equation [119]. The convection and radiation heat transfer are calculated as $Q_{\text{conv}} = hA(T_{\text{m}} - T_{\infty})$ and $Q_{\text{rad}} = \varepsilon\sigma A(T_{\text{m}}^4 - T_{\text{surr}}^4)$ [119]. Here, σ represents the Stefan-Boltzmann constant, and we use room temperature for the surrounding and ambient air temperatures ($T_{\text{surr}} = T_{\infty} = 303$ K), convection coefficient of $h = 2000$ W/m^2 K, and Cu emissivity of $\varepsilon = 0.07$ [122]. Lastly, specific heat capacity, $c = 385$ J/kg K and density $\rho = 8960$ kg/m^{-3} of Cu are used for the calculation of the stored thermal energy change, i.e., $\Delta E_{\text{st}} = \rho Vc(\partial T_{\text{m}}/\partial t)$, where V is the control volume of nodal point m.

Two-Temperature Model for 1-D Nanowire With a short pulse of high-intensity laser irradiation, nonequilibrium between electron and lattice systems dynamically changes, and to address this nonequilibrium dynamics, electron and lattice temperatures of CuNW (T_{e} and T_{l}) are separately calculated. As in the analysis of CW laser, 1-D model and FDM are employed, but for each nodal point, the thermal energy balances for electron and lattice are considered, given by [13]:

$$\text{for electron } T_{\text{e}},\ Q_{\text{laser}} - Q_{\text{el}\to\text{latt}} + Q_{\text{el,cond}} = \Delta E_{\text{el}}, \text{ and} \tag{1.3.24}$$

$$\text{for lattice } T_{\text{l}},\ Q_{\text{el}\to\text{latt}} + Q_{\text{latt,cond}} - Q_{\text{conv}} - Q_{\text{rad}} = \Delta E_{\text{latt}}. \tag{1.3.25}$$

Here, the laser heat addition ($Q_{\text{laser}} = q_{\text{in}}\beta A$) is applied to the first node as in the CW laser simulation but considered only in T_{e} analysis [13, 123]. At the wavelength of FS laser (1030 nm), β has been reported as 0.06 [121]. During a pulse with 300 fs of duration, we assume a constant laser heat flux, $q_{\text{in}} = 1.77 \times 10^{17}$ W/m^2, which ensures the employed average power of FS laser (5 mW) considering 1 μm of laser

beam diameter and 120 kHz of pulse repetition rate. Heat flow from electron to the lattice, $Q_{el \rightarrow latt}$ is calculated using the electron-lattice coupling coefficient (g, W/m^3 K) from the literature [124] and the difference between T_e and T_l, i.e., $Q_{el \rightarrow latt} = gV(T_e - T_l)$. Conduction heat flow and stored thermal energy change for electron and lattice [$Q_{el,cond}$ and ΔE_{el} in (2) and $Q_{latt,cond}$ and ΔE_{latt} in (3)] are calculated using the electron thermal conductivity, $k_e = 385$ W/m K, lattice thermal conductivity, $k_l = 17$ W/m K, [125] temperature-dependent electron volumetric heat capacity C_e (J/m^3 K) from [124] and lattice volumetric heat capacity, $C_l = 3.45 \times 10^6$ J/m^3 K for Cu [125]. Convection and radiation (Q_{conv} and Q_{rad}) are included in the T_l analysis only and calculated as the single-temperature modeling using the same properties.

Figure 1.24 shows SEM images of laser-irradiated CuNWs under different processing conditions. Two kinds of laser beams, either a 130 fs pulse laser or 532 nm continue wavelength green laser, was focused by a long working distance 100× microscope lens with an NA of 0.8. After focusing, the diameter of the laser beam spot applied to the substrate was around 1 μm. The experiments were accomplished at room temperature and ambient atmosphere. Figure 1.24a-represent an experiment result for FS laser with an average laser power of 35 mW and Fig. 1.24d–f represent experiment results for CW laser at the same average power of 35 mW. Obviously, at the same average laser power, two laser irradiations create significant differences. For the FS laser, explosive deformations can be observed on both substrate and CuNW after the laser process by comparing Fig. 1.24a–c. The silicon wafer substrate is damaged, and a large number of Si and Ag nanoparticles splash around in the vicinity of the irradiation area (about ten micrometers). A large particles-aggregation appears on top of the NW. However, there is no structural and surface deformation on other parts of the nanowire. On the other hand, at the same laser power condition, the CW laser produced a different effect from that with the FS laser. Comparing Fig. 1.24d, e,

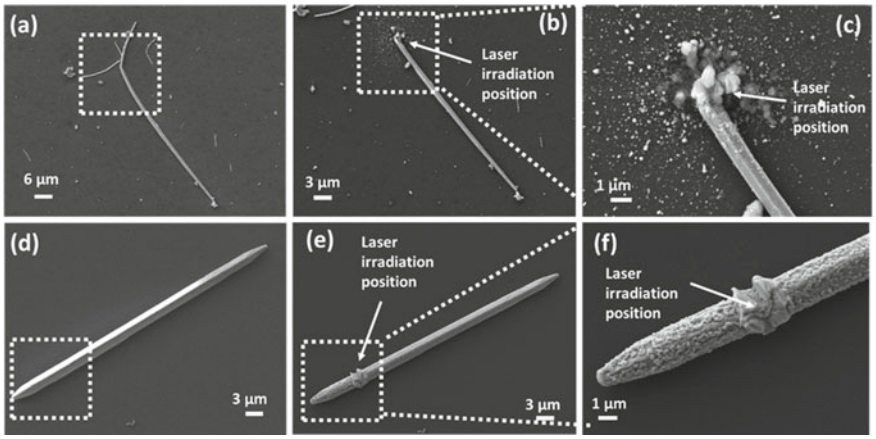

Fig. 1.24 SEM images of CuNW **a** before and **b** after FS laser irradiation, and **c** enlarged image of FS laser irradiation area. CuNW images (**d**) before and (**e**) after CW laser irradiation and **f** enlarged image of the CW laser irradiation area [6]

CW laser cannot break a CuNW at all but create a very clear surface deformation on the nanowire. As shown in Fig. 1.24f, at the laser-focused position, CuNW is partially melted at high temperatures induced by laser irradiation, and then the melted wire solidifies and crystalizes again after the laser is off. Furthermore, this thermal effect is propagated along the CuNW, and cause the increase of surface roughness of the entire nanowire (see Fig. 1.24f). In a sharp contrast, the surface of the un-irradiated area is kept as clean and smooth before and after FS laser irradiation. However, after CW laser irradiation, a clear surface change can be observed even in the un-irradiation area. Because the CuNW was exposed to air, serious oxidation could occur on the surface due to the heat-induced by CW laser, which will be further confirmed by the chemical analysis later. This oxidization has been confirmed by checking the oxygen distribution before and after the CW laser irradiation [6]. FS laser is an ultrafast high repetition pulse laser, with an average laser power of 35 mW, it can generate a peak power density of 1.24×10^{14} W/cm^2. On the other hand, with 35mW power, CW laser only generates a power density of 4.46×10^6 W/cm^2. Meanwhile, from the aforementioned theoretical analysis, for an ultrafast interaction, the absorption of photons stimulates electrons within a hundred femtoseconds (fs), which is too short to disturb lattice. The absorbed energy was thus transferred from electrons to the lattice by electron-lattice scattering after the laser pulse [13, 14]. The thermal coupling between free electrons and lattices typically occurs within 100 ps, depending on the electron-phonon coupling strength of different materials. The typical electron-phonon coupling time of hundred femtoseconds is much shorter than the heat transfer period by thermal conduction. Therefore, the thermal diffusion to the laser-irradiated surrounding area for a FS laser is very limited [15].

According to our computational simulations [6] with the CW laser (35 mW) irradiation (at $x = 0$), heat is accumulated, increasing temperature of CuNW with heating time (t), and the heat is dissipated along the length of CuNW (i.e., in the x-direction) in a nanosecond scale, as shown in Fig. 1.25a. With the CW laser heating longer than 0.5 μs, the temperature rises beyond the Cu melting point ($T_{\mathrm{m,Cu}} =$ 1368 K [126]), and a large portion of CuNW has a temperature above the oxidation temperature (1073 K) [127, 128]. Figure 1.25b displays that the thermally affected zone (i.e., the heated portion of the CuNW where the temperature is above the oxidation temperature) extends to 10 μm after 1 μs of heating time. It can be inferred that with the increase of irradiation time, the whole CuNW will be heated above the oxidation temperature. This explains that the oxidization of the entire CuNW with a CW laser observed from the experiment conducted in an ambient atmosphere in our study.

With the FS pulse laser irradiation at $x = 0$, the electron temperature (T_e) reaches a very high peak value (~27.5×10^4 K) within the pulse duration (~300 fs), and then it decays rapidly, releasing their energy to phonons (or lattice). The electron-lattice interaction causes the rise of local T_l [129], and T_e reaches almost equilibrium with T_l shortly (<20 ps) after the pulse at $x = 0$ (Fig. 1.25c). The lattice temperature (T_l) rises and decreases, and for most of the wire (>27 μm), it stays below the Cu melting point (Fig. 1.25d). A non-thermal ablation is expected at the beginning of the irradiated zone (<1 μm, close to the focus spot size) as the lattice temperature

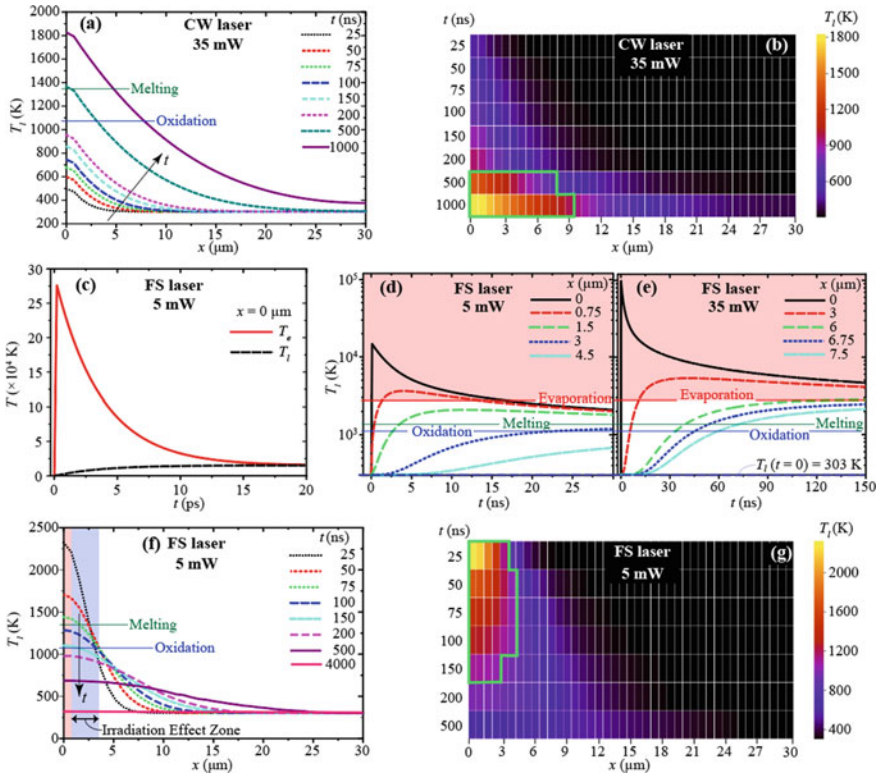

Fig. 1.25 **a** Temperature distribution and **b** heatmap of a modeled CuNW with respect to the distance from the heating area (x; the length direction) at a different heating time (t) when using the CW laser irradiation. **c** Electron and lattice temperatures of the first nodal point (T_e and T_l at $x = 0$) in a short time period after the FS laser pulse (with an average power of 5 mW) starts (< 20 ps). Time evolution of lattice temperature (T_l) from the beginning of a laser pulse (300 fs) at five different locations (i.e., $x = 0$, 0.75, 1.5, 3.0, and 4.5 μm) of CuNW with average FS laser power of **d** 5 mW and **e** 35 mW. (f) Temperature distribution and **g** heatmap of CuNW in the x-direction at different t when using the FS laser with 5 mW average power. The regions surrounded by green lines in (**b**) and (**f**) are above the oxidation temperature and vulnerable to oxidation [6]

is above the evaporation temperature of Cu (T_{ev} = 2840.15 K [130]), as shown in Fig. 1.25d. It is important to point out that such heat is very localized and maintained in a very short time period; T_l can be above the melting point less than 100 ns only near the heating region (x < 3 μm). FS laser irradiation with an average power of 35 mW as in the CW laser is expected to induce ablation of the much larger area, as Fig. 1.25e shows up to 6 μm of CuNW with a higher temperature than T_{ev}. With an average power of 5 mW, T_l drops below the oxidation temperature in 150 ns after a laser pulse, and the entire CuNW will be cooled close to room temperature before the next laser pulse comes (t = 8.33 μs with 120 kHz), as indicated by Figs. 1.25f, g. As T_l is maintained below the oxidation temperature in most regions (x > 4 μm),

we expect no significant oxidation even the experiment is conducted in an ambient atmosphere [6]. Even if thermal melting and oxidation exist, they are limited to a very local region (near the irradiated region) less than 3 μm. This simulation result is identical to the experiments, indicating that FS laser irradiation effect zones are about 2.5–4 μm with different laser powers [6].

In summary, computational simulations using 1-D heat diffusion equation and finite difference method (FDM) were performed to gain an insight into metal-laser interactions with different lasers. Simulation studies on lasers have established contrasting melting behaviors of metal under laser irradiations, which may pave the way to use the ultrashort laser for innovative nonthermal welding of nanowires and relevant devices development.

1.4.3 Photonic Reduction

Photonic reduction of metal salt has been developed as an effective method to form metal nanoparticles. The morphology of metal nanoparticles can be controlled by the various photonic parameters, such as, intensity, frequency, pulse width and polarization, etc. Generally, the photonic reduction of metal salt is realized by single-photon and two/multiphoton absorption induced photochemical reaction.

Single-photon Reduction and Two/Multiphoton Reduction For metal salt solution, the energy of a single photon in near-ultraviolet (3.11–6 eV), visible (3.11–1.78 eV) and infrared region (<1.78 eV) is not enough to photodecomposition of water (>6.5 eV) leading to the production of e^- to reduce metal ions [131]. Therefore, reducing reagent is needed for reducing reaction. As one typical reducing agent for silver salt reduction, citrate is extensively used for the synthesis of silver nanoparticles [132]. The process of photoreduction on silver ions by citrate is known as,

$$\text{Citrate} \xrightarrow{h\nu} \text{acetone} - 1, 3 \text{ - dicarboxylate} + CO_2 + e^-$$
$$Ag^+ + e^- \rightarrow Ag^0$$

In addition, small silver clusters Ag_n ($n = 2$–8) could be formed by continuous photoreduction,

$$\text{Citrate} + Ag_n \xrightarrow{h\nu} \text{acetone - 1, 3 - dicarboxylate} + CO_2 + Ag_n^-$$
$$Ag_n^- + Ag^+ \rightarrow Ag_{n+1}$$

By inducing the reducing agent, the metal ions may be also reduced by a photothermal effect. For example, the copper ions can be reduced by ethylene glycol during laser irradiation. The temperature of copper precursor increases to 250 °C by laser irradiation, which will result in the ethylene glycol decomposes into acetaldehyde [133]. The –CHO group of acetaldehyde can reduce the copper ions to

copper.

$$
\begin{aligned}
&2\mathrm{HO(CH_2)2} \xrightarrow{-\mathrm{H_2O}} 2\mathrm{C_2H_4O} \\
&\xrightarrow{\mathrm{Cu(OH)(NO_3)}} \mathrm{C_4H_6O_2} + 2\mathrm{H^+} + 2\mathrm{e^-} + \mathrm{Cu^{2+}} + \mathrm{OH^-} + \mathrm{NO_3^-} \\
&\rightarrow \mathrm{C_4H_6O_2} + \mathrm{Cu} + \mathrm{H_2O} + \mathrm{HNO_3} \\
&\rightarrow \mathrm{C_4H_6O_2} + \mathrm{Cu} + \frac{1}{2}\mathrm{H_2O} + \mathrm{NO_2} + \frac{1}{4}\mathrm{O_2}
\end{aligned}
$$

There are lots of reducing reagents suitable for different ion reduction. The reduction potential will gradually increase from ethylene glycol, polyvinylpyrrolidone (PVP), sodium citrate, ascorbic acid, sodium hypophosphite, sodium boron hydrate, and hydrazine hydrate. For a higher reduction potential, a lower temperature is required for reduction. On the other hand, some polymers can work as the capping layer to protect nanoparticles or limit the crystal growth in a certain direction and thereby to control the nanocrystal orientation. The experiments show that PVP is easily absorbed onto the (110) plane, while poly(methacrylic acid) (PMAA) and poly(acrylic acid) (PAA) tend to attach to (111) and (100) planes, respectively. Therefore, it is widely to use PVP with different molecule masses to grow silver nanowires [101] and nanoplane [95]. Ethan et al. have successfully grown (100) silver nanoplates with PMAA [134] and silver nanowire with nanodisc piling chains has been fabricated with PAA [135].

If the photon intensity is high enough to trigger two/multiphoton absorption, the metal salt can be converted to metal nanoparticles by photoreduction without any reducing agent [136]. Solvated electrons can be generated through a double photon excitation. This transient electron can reduce silver ions [137]. Furthermore, at the focal spot of a tightly focused laser beam, the energy absorbed during the transition (three-photon absorption) can exceed 7 eV. The water is photodecomposed and produces e^-, OH• and H• radicals. The metal ions can be therefore reduced to their zero valence state,

$$
\begin{aligned}
&\mathrm{Ag^+} + \mathrm{e^-} \rightarrow \mathrm{Ag^0} \\
&\mathrm{Ag^+} + \mathrm{H} \rightarrow \mathrm{Ag^0} + \mathrm{H^+}
\end{aligned}
$$

However, the efficiency of the photodecomposition of water is very low that only ~10% of silver ions can be reduced after 1 h [131]. It should be noted that the photon energy should surpass the threshold of multiphoton absorption which means high energy density is needed. It indicates that for laser processing, the multiphoton absorption usually occurs at an area in the center of beam focal spot. Therefore, the size of the reactive area may smaller than the focus spot, which may fabricate quantum dots with a size smaller than the optical diffraction.

Selectivity of Photonic Reduction for Wavelength Interestingly, the shape of nanoparticles synthesized by photonic reduction can be controlled by different wavelength illumination. Typically, the shape of nanoparticles is a sphere under

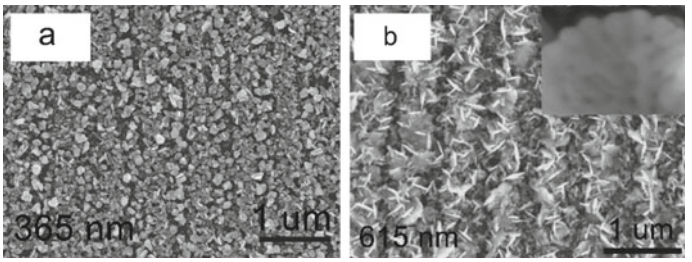

Fig. 1.26 SEM images of Ag film photoreduced by **a** 365 nm light and (**b**) 615 nm light [132]

short-wavelength illumination (Fig. 1.26a). In opposite, the shape of nanoparticles converted to a plate (disk) under long-wavelength illumination (Fig. 1.26b).

This phenomenon can be explained by the surface plasmon-enhanced photonic reduction. Briefly, in the case of short-wavelength illumination, the surface plasmon mode is dominantly transverse. Thus, short-wavelength light acts as feedback irradiation making the particle grow spherical. Conversely, as the longitudinal plasmon absorbs the longer wavelength irradiation more strongly, this longer particle axis grows preferentially, resulting in a plate-like shape [138].

1.4.4 Laser Direct Writing and Interference Lithography

Laser Direct Writing Laser direct writing provides high flexibility with non-contact and maskless fabrication processes, which significantly reduces the fabrication cost. Since laser direct writing can achieve a one-step fabrication combing local processing with patterning, the manufacturing efficiency is significantly enhanced. Figure 1.27 shows one schematic for laser direct writing setup. The setup has four basic elements to realize direct writing, including laser source, beam expander, focus lens (objective

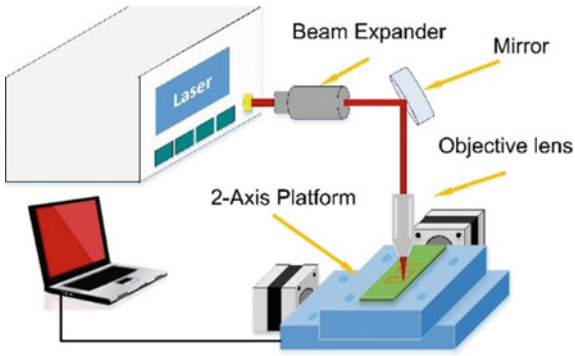

Fig. 1.27 Schematic for laser direct writing setup

lens), and translation motorized stage (multi-axis platform). Using high numerical - aperture objective lens and piezo stage stages, laser direct wiring have the fabrication resolution down to the sub-micrometer dimension.

Laser Interference Lithography Although laser direct writing has advantages as the aforementioned, laser interference lithography is suitable for the fabrication of periodic pattern due to high fabrication efficiency. Figure 1.28 shows a schematic of laser interference lithography setup using two inferred beams split by a beam splitter and the SEM image of periodic metal nanoparticle array fabricated by laser interference lithography. The period of interference pattern fabricated by laser interference lithography can be calculated by the following:

$$p = \frac{\lambda/2}{\sin(\theta)}$$

where P is the period of the interference pattern, λ is the laser wavelength and θ is the angle of the two interference beams. Also, by controlling the laser parameters such as beam intensity, the number of inferred beam and phase of a wavefront, periodic nanodots, and nanopolygon array can be fabricated by laser interference lithography. For multibeam interference lithography, the interference pattern can be calculated by the following equations:

$$I(x, y, z) = \int \left| \sum_{n=1,2,3....}^{N} E_n(E_{n0}, x, y, z, k_n, \theta_{\text{int}}, \varphi_n, \omega_n, \alpha_n, t) \right|^2 \mathrm{d}t \qquad (1.3.26)$$

where n is the number of laser beams, θ_{int} is the polar angle, φ is the azimuthal angle, α is the phase shift. For example, Fig. 1.29 shows the interference pattern at $\alpha = 0$ and $\alpha = \pi$, which indicates the shape of the pattern is ring and square, respectively [140]

It is worth mentioning that another method to fabricate periodic structure by laser is the laser-induced periodic surface structure (LIPSS). The orientation of the periodic structure of LIPSS is perpendicular/parallel (based on the fabrication conditions) to the laser polarization. Therefore, the two-dimensional periodic nanostructure can

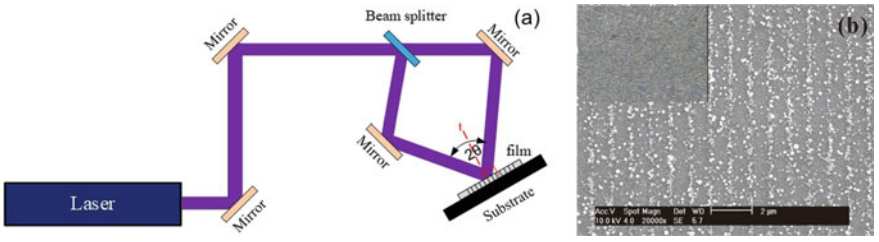

Fig. 1.28 **a** Schematic of laser interference lithography setup and **b** SEM images of periodic metal nanoparticle array fabricated by laser interference lithography [139]

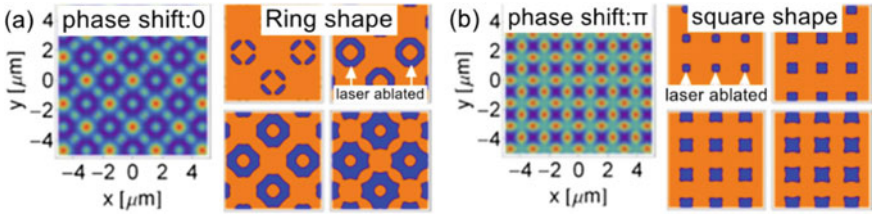

Fig. 1.29 Interference patterns as the phase shift. **a** 0 and **b** π using laser interference lithography (Figure adapted from [140])

be fabricated by orthogonally double laser exposure [141]. Such a nanostructure is successfully used for in situ on-line real-time pollutant monitoring of water.

1.4.5 Laser Ablation, Trimming, and Drilling

Extreme conditions, such as a high-temperature and high-pressure plasma state, generated by laser provide unique access to materials science and manufacturing. New materials and new phases synthesized via femtosecond laser-induced micro-explosions have appeared as a very attractive research topic [142]. As aforementioned procedure of Sect. 1.1.2, electron ejection due to ultrafast laser-matter interaction will lead to a Coulomb explosion of positively charged ions after laser-induced vaporization of electrons [4, 16]. This Coulomb explosion is confined in a microscale space in the vicinity of the focal spot. High-temperature and high-pressure conditions can thus be used for the synthesis of new materials. Hu reported that *sp*-bonded carbon chains (polyyne) can be formed on a graphite surface using femtosecond laser irradiation associated with the formation of amorphous tetrahedral carbon (diamond-like carbon) [16]. This *sp*-bonded carbon chain species can be precursors for various carbon allotropes, including carbon nanotubes, fullerenes, and carbynes [143]. Rapp reported a new tetragonal polymorph of silicon induced by confined microexplosions [144]. On the other hand, this Coulomb explosion can also occur in a liquid by focusing femtosecond into an organic solvent. Polyyne molecules are evident in such an environment [143, 145, 146]. However, polyyne molecules are unstable in a laser-thermal conduction, thus a nonthermal interaction induced by femtosecond is favorited for polyyne synthesis. Moreover, the mechanical shock wave induced by fs laser pulses can be used as a powerful surface peening tool for metals [147]. Femtosecond laser peening research without using a sacrificed layer was motivated by the process simplicity and localized shock pressure attainable with fs pulses in comparison to ns laser peening. More recently, strengthened mechanical properties in terms of high compressive residual stress and hardness enhancement were reported in fs laser peening of aluminum [148] and steel [149] free from a protective coating and a transparent overlay. Hence, it can be said that ultrafast laser is innovative for

materials synthesis and surface engineering but more research is needed in these directions.

Femtosecond laser-induced water spliting and coal gasification have been reported for facile synthesis of porous graphene and graphene quantum dots [150, 151]. The underlying dynamics is not yet established but taking a critical role for large scale synthesis of quantum dots. Femtosecond laser direct writing is also employed for device fabrication though the laser-induced reduction of graphene oxide. The reduction should be correlated to both the photonic thermal effect and multiphotonic absorption [98]. Recently we studied laser trimming of alloy stripes with femtosecond laser and nanosecond pulsed laser. The precision cutting for precisive resistance adjustment is realized by femtosecond laser trimming [152].

Multiphoton absorption of ultrafast laser is extensively used for drilling high aspect ratio microchannel or holes in transparent materials which the linear absorption is limited [1]. Recently we reported the microball lens by forming the microcavity in polymer [21]. Shown in Fig. 1.30, a wide angle imaging is demonstrated with

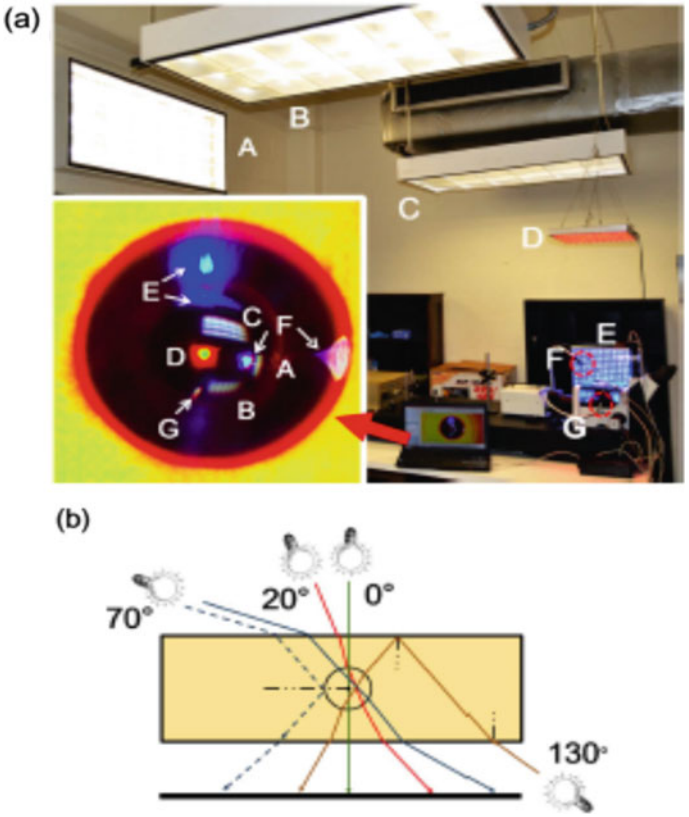

Fig. 1.30 Super-wide imaging by cavity microball lens. **a** Super-wide imaging taken by an inverted microscope. **b** Schematic for the super-angle-imaging of embedded microball lens [21, 153]

a micro-cavity ball lens combined with an inverter microscope. The photothermal modified optical index convex lens is also formed by precisely controlling laser power [153].

1.5 Micro-to-Nano Manipulation

The size effect and the scaling law make the nanoworld is quite different from the micro- and macroworld. Shown in Fig. 1.31, the volume force, such as gravity, scaling to L^3 will be negligible at microscale by compared to surface forces, scaling to L^2, like electrostatic force and pressure and friction force. The manipulation operating in the macroworld cannot thus work for a microscopic assembly. Furthermore, the linear force, such as surface tension is much stronger than a surface force. Therefore, a microtool cannot be used for a nanomanipulation. As a result, nanoscopic assembly methods have to be developed before a nanomanufacturing can be implemented.

In vacuum and/or ambient atmosphere, a metallic tip, such as a tungsten tip, is usually used for manipulating a microscale building block. However, for a nanomaterial, certain attachment-detachment procedures are required. For example, to prepare a TEM sample preparing by focused ion beam (FIB), the cut piece has to attach to the tip by the first deposition a carbon film to join the TEM sample and tip together, and then the separation of them by cutting carbon film by FIB again after the tip displacement with a 3D programmed platform. Cox et al. used this method to construct an "ATI" logo with carbon nanotubes [154].

Magnetic force allows the manipulation and orientation in both air and liquid environment without contacting. The magnetic force acting on a nanoparticle can be expressed as

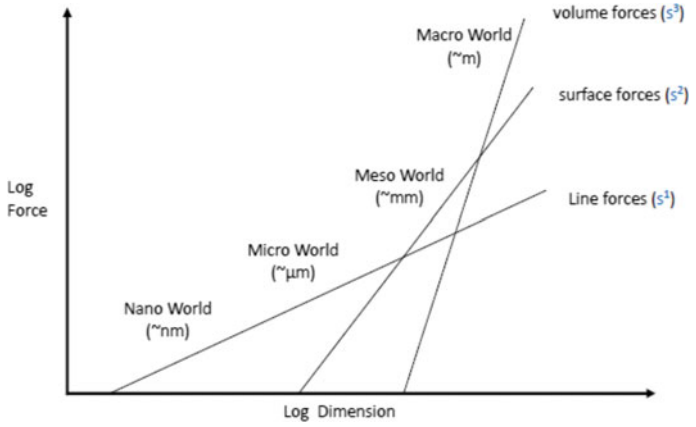

Fig. 1.31 Scaling laws of different forces at macro-, meso-, micro- and nanoworld

$$F_{\mathrm{m}} = V_{\mathrm{m}} \Delta\chi \nabla \left(\frac{1}{2} B \cdot H \right) \tag{1.4.1}$$

where the $\frac{1}{2} B \cdot H$ is the energy density of the magnetic field, V_{m} is the volume of the particle, $\Delta\chi$ is the effective susceptibility of the particle (assumed in water), if > 0, the magnetic force will cause the displacement of a nanoparticle. For placing a nanowire in a uniform magnetic field, the torque $_{\mathrm{m}}$ acted on the nanowire can be expressed as [155]

$$\tau_{\mathrm{m}} = m \times H = M_s \pi r^2 H L \sin\theta_l \tag{1.4.2}$$

where M_{s} is the saturation magnetization and m is the magnetic moment of the nanowire, $_{\mathrm{L}}$ is the angle between the nanowire and the magnetic field. The friction torque generated by liquid can be calculated through the following equation [155],

$$\tau_{\mathrm{d}} = \frac{1}{3} \omega_{\mathrm{w}} \pi \eta L^3 C \tag{1.4.3}$$

where $_{\mathrm{w}}$ is the angular rotation speed, C is the geometric factor. Then the rotation equation of nanowire driven by the magnetic field can be written by

$$I \alpha_{\mathrm{w}}(t) = \tau_{\mathrm{m}} - \tau_{\mathrm{d}} \tag{1.4.4}$$

where the a_{w} is the mass density of nanowire and I is the moment of inertia of nanowire.

In liquid optical tweezer is one popular tool for micromanipulation. In principle, optical tweezers generate forces by the optical gradient field. At the vicinity of the focal point, two forces will be generated: pick-up force $F\ \nabla$ and scattering force F_{s} [156].

$$F_{\nabla} = 2\pi a^3 \frac{\sqrt{\varepsilon_0}}{c} \left(\frac{\varepsilon - \varepsilon_0}{\varepsilon + 2\varepsilon_0} \right) \nabla |S| \tag{1.4.5}$$

$$F_{\mathrm{s}} = \frac{8}{3} \pi (ka)^4 a^2 \frac{\sqrt{\varepsilon_0}}{c} \left(\frac{\varepsilon - \varepsilon_0}{\varepsilon + 2\varepsilon_0} \right)^2 \mathrm{S} \tag{1.4.6}$$

where the s is Poynting vector, $s = 1/\mathrm{ExB}$, ε, and ε_0 are the dielectric coefficients of the particle and the medium, a is the particle diameter. $F_{\bigtriangledown}$ is scaling to a^3 and F_{s} scaling to a^6. At the microsize, F_{d} will be larger than F_{s}. A microscale building block is easily entrapped by a focal light. However, at a nanoscale, $F_{\bigtriangledown}$ will decrease rapidly and therefore, cannot effectively grasp a nanoparticle. For a nanoparticle, a near-field plasmonic tweezer has been developed [157], where the surface plasmonic field provides an entrapped force to grasp a metallic nanoparticle. However, optical tweezer, as a non-contact tool, is very practical for cell manipulation and other biomedical applications. To grasp a nanowire, a multipoint optical tweezer is invented

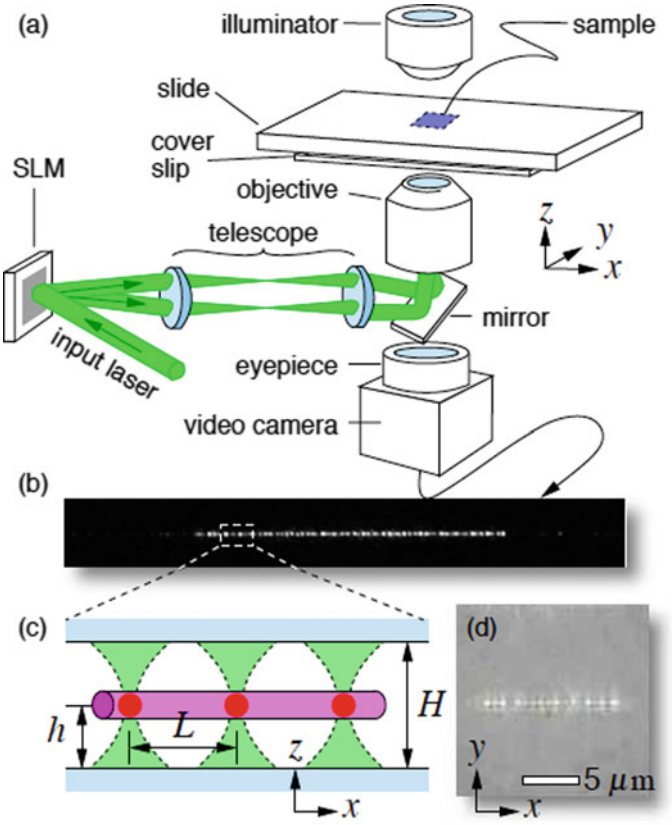

Fig. 1.32 Multifocal point optical tweezer (Reprinted with permission from [156] ©The Optical Society)

[156]. Shown in Fig. 1.32, through splitting light into a multibeam using a liquid crystal mirror and then focus several points onto a nanowire, a nanowire can be effectively picked up [156]. Through synchronously rotating the focal points the nanowire can be rotated.

Electric interaction is another popular tool for manipulation in liquid. For charged ions, the DC (direct current) electrical field will directly drive the displacement of ions. However, for a charged particle suspended in an electrolyte solution (Fig. 1.33), the electrical double layer phenomenon will make it similar to a neutral particle. According to the Stern model, the zeta potential can be expressed as

$\zeta = \varphi(z)e^{\kappa z}$, where the $\kappa$is a constant relevant to the electrical double layer thickness, which at least spreading over a Debye length λ_D.

$$\lambda_D = \kappa^{-1} = \sqrt{\frac{\varepsilon_d \kappa_B T}{\sum_i q_i^2 c_i^2}} \tag{1.4.7}$$

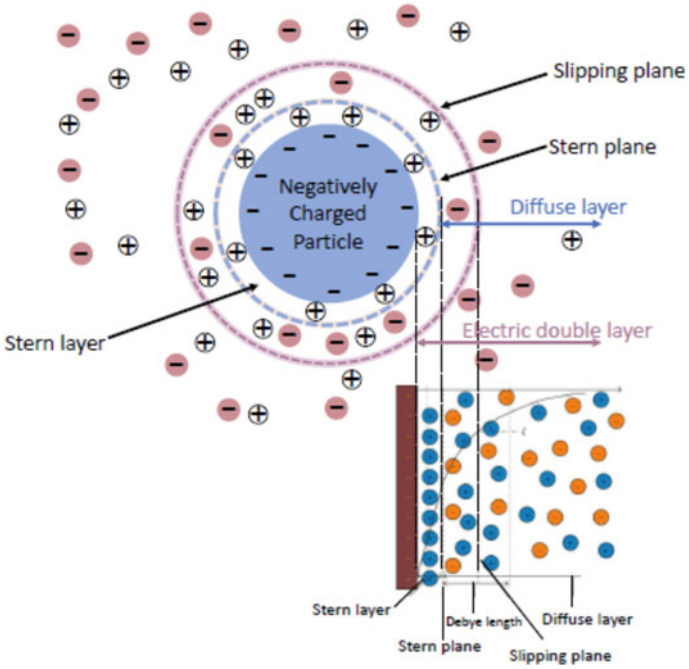

Fig. 1.33 Electrical double layers around a charged particle in an electrolyte solution

where $_{d}$ is the dielectric permittivity of the solution, K_B is the Boltzmann constant, q_i is the electrolyte charge, C_i is the concentration of electrolyte. For pure water, $_{D}$ is about 700 nm but in salted water, the double layer can be as thin as 10 nm. When the charged particle, the associated electrical double layer structure will move accordingly, the effective mass of the charged particle thus significantly increases. In this case, the dielectric interaction between the electrical field and electrical dipolar moment of particles will result in a driving force. Dielectrokinetics results in three kinds of effects: dielectrophoresis (DEP), electro-osmosis (EO), and electrothermal effect (ET). Because the electrical field can be generated by either DC (direct current) or AC (alternative) current source, electrokinetics can respectively be DCEK and ACEK. DCEK requires a high voltage to drive electrokinetic flow, an electrochemical reaction or a bubble can be easily formed in liquid during DCEK. In contrast, ACEK induced changes of fluidic polarity and thus effectively drive the transporting of liquid and suspended particles. ACK is thus extensively employed for manipulation.

For a DEP, a force will exert on a dielectric particle when it is subjected to a non-uniform electrical field. This force does not require the particle to be charged. All particles exhibit dielectrophoretic activity in the presence of electric fields. However, the strength of the force depends strongly on the medium and particles' electrical properties, on the particles' shape and size, as well as on the frequency of the electric field. Shown in Fig. 1.34, DEP force in a conducting dielectric medium can be written

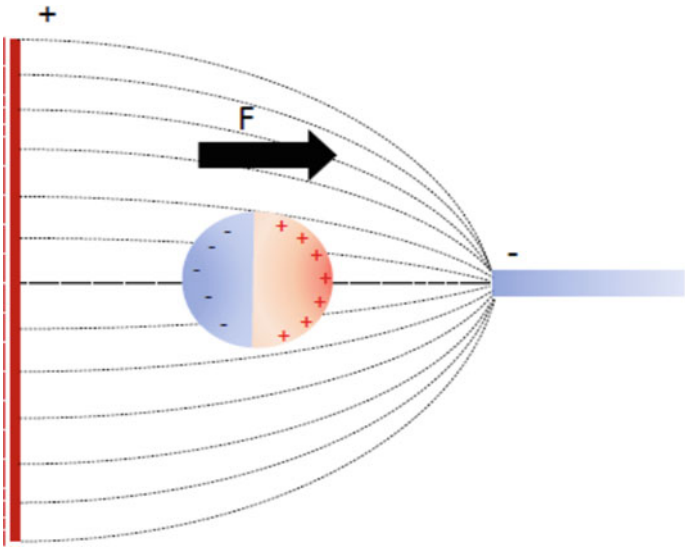

Fig. 1.34 Dielectrical forces acting on a particle in an electrical field

as

$$F_{\mathrm{DEP}} = \pi r^2 l \varepsilon_{\mathrm{m}} k(\omega) \left(\vec{E}_{\mathrm{r}} \cdot \nabla \vec{E}_{\mathrm{r}} \right) = \pi r^2 l \varepsilon_{\mathrm{m}} k(\omega) \nabla |E_{\mathrm{r}}| \tag{1.4.8}$$

$$k(\omega) = \mathrm{Re}\left[\frac{\varepsilon_{\mathrm{n}}^* - \varepsilon_{\mathrm{m}}^*}{\varepsilon_{\mathrm{m}}^*} \right] \tag{1.4.9}$$

$$\varepsilon^* = \varepsilon - i \frac{\sigma}{\omega} \tag{1.4.10}$$

where $\varepsilon_{\mathrm{n}}^*$ is the complex permittivity of particle and $\varepsilon_{\mathrm{m}}^*$ is for medium, ε is the dielectric constant, σ is electrical conductivity and ω is the field frequency, E_{r} is the root mean square of the external excitation field E. For a positive DEP, the particle will move toward to high field region and the negative DEP drives the particle to move away from high field region. In our recent works [6], both Cu nanowires and T_{e} nanowires are aligned by DEP at a certain frequency range and voltage.

ACEO is a phenomenon of induced-charge electro-osmosis of liquid, where the fluidic flow is generated by the action of an electric field on its induced ion diffusion near a polarizable surface. The ion's attachment and accumulation to the electrode surface will cause the capacitance change. Thus, ACEO is extensively used for sensing in liquid [158].

Since ACEO is caused by the counter-ions migration with or against the electric field, which produces fluidic motion due to fluidic viscosity, it is expected that the fluidic flow velocity will keep changing due to the ion migration. At a low

applied voltage (<100 mV), the time-average displacement of ACEO as a function of frequency can be expressed as

$$u \propto \frac{\varepsilon V^2}{\eta(1+\delta)L\left[\frac{\omega}{\omega_c}+\frac{\omega_c}{\omega}\right]^2} \tag{1.4.10}$$

where η is the viscosity of the fluid, ε is the permittivity of fluid, V is the applied voltage, L electrode spacing, δ is the ratio of the diffuse-layer to compact-layer capacitances (both assumed constant). The peak frequency is at the scale of the RC charging time

$$\omega_c \propto \frac{D(1+\delta)}{\lambda L} \tag{1.4.11}$$

where λ is the Debye screening length and D is a characteristic ionic diffusivity. At a high voltage, a Faradic charging occurs at the particle surface [159]. The aforementioned model is not appropriated. ACEO has applied to manipulate the microparticle and cells [160]. The application of ACEO for nanomanipulation is still unclear.

ACET refers to fluid motion resulting from temperature gradients in the fluid induced by an AC electric field. The fluid velocity based on the thermal gradient [160, 161] can be expressed as

$$|u| \approx 3 \times 10^{-3}\left(\frac{\varepsilon V^2}{\eta\sigma}\right)\left(\frac{\partial T}{\partial y}\right) \tag{1.4.12}$$

where V is the voltage, σ is electrical conductivity, η is the viscosity of fluid, ε is permittivity of fluid and $\frac{\partial T}{\partial y}$ is the local thermal gradient along axis y. Unlike Joule heating, the ACET velocity has a quadratic relationship with voltage [162]. The electrothermal force can be expressed as below [163]

$$F_{ET} = \frac{1}{2}\frac{\varepsilon(\alpha-\beta)}{1+(\omega\tau)^2}(\nabla T \cdot E)E - \frac{1}{4}\varepsilon\alpha|E|^2\nabla T \tag{1.4.13}$$

where $\alpha = \frac{1}{\varepsilon}\left(\frac{\partial\varepsilon}{\partial T}\right)$, $\beta = \frac{1}{\sigma}\left(\frac{\partial\sigma}{\partial T}\right)$, is the angular frequency of the AC electrical field, and. For aqueous solutions and temperatures around 293 K, a and beta can be estimated as $-0.4\%\ \mathrm{K}^{-1}$ and $2\%\ \mathrm{K}^{-1}$, respectively [164]. Therefore, the aforementioned equation can be simplified as [165]

$$F_{ET} = -0.012 \cdot \frac{\varepsilon|E|^2}{1+(\omega\tau)^2} \cdot \nabla T - 0.001\nabla T \cdot \varepsilon|E|^2 \tag{1.4.14}$$

ACET is extensively applied in microsystems for mixing, pumping of fluids, and microparticles manipulation [166]. Nanoparticle manipulation and/or in a nanofluid is relatively less studied.

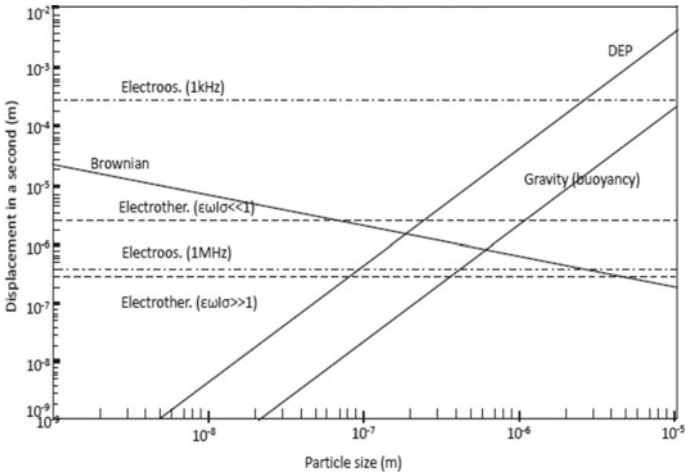

Fig. 1.35 Diagram of various motion mechanisms and forces in liquid [165]

Figure 1.35 displays various dielectric force versus gravity, buoyancy, and Brownian motion. For effective manipulation, DEP works for a microparticle or a nanowire with a length in micrometer. However, for a nanoparticle and/or quantum dots, ACEO is especially powerful to suppress the Brownian motion.

It is possible to combine an electrical field driving and an optical tweezer principle and form a so-called optoelectrical tweezer (OET). Shown in Fig. 1.36 is the principle of OET [167]. Light excises a transparent amorphous Si film and causes the increase of local conductivity. The local conductive Si electrode and transparent top-electrode form a 3D electric field for electrical driving. By scanning light, this field can be programmed and patterned for particle manipulation. Micro-and nano-robots become innovative tools for nanomanipulation.

Fig. 1.36 Principle of an optoelectrical tweezer [167]

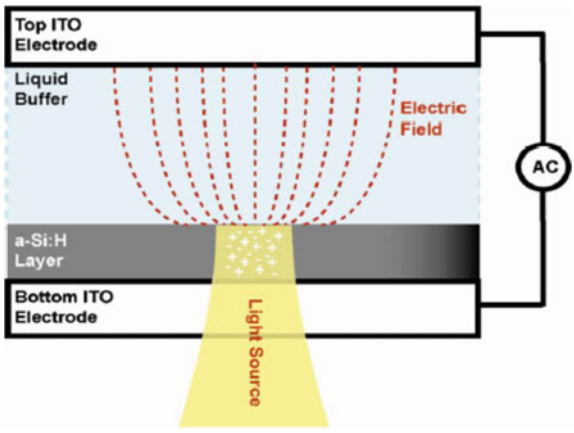

Numerical innovative methods have been investigated for particle manipulation. Microrobots have been proposed for manipulation [168]. It is facile to generate a microbubble by laser heat and use this bubble as a microrobot for particle manipulation [169]. Recently, such a microrobot has been demonstrated to enable 3D assembly of a micromechanical device [170]. Surface tension and LB methods are also used for nanowire alignment [76]. Large-area photonic crystal can be formed through self-assembly [171]. Laser-induced front transfer can be a powerful tool for nanomaterial transporting and manipulation. The last chapter of this book will focus on this method.

1.6 Nanojoining and Molecular Devices

1.6.1 Overview of Nanojoining

Welding of nanomaterials is essential manufacturing of functional nanoelectronics [172], including nanocircuits [173], light-gated nanowire transistors [174], nano waveguides and nanophotonic circuits and nanoplasmonic devices for quantum computation [5, 89, 175]. To realize a nanoscale joining, various methods have been developed to join nanomaterials, such as mechanical riveting [176, 177], mechanical pressure [178, 179], adhesive bonding [180, 181], cold welding [45, 47, 48], Joule heating [182–185], thermal annealing [95, 186–188], soldering and brazing [189–195], and laser (laser-induced plasmonic) welding [196–198].

Table 1.3 Various conventional joining methods versus nanojoining innovations

Conventional catalogue	Nanojoining
Mechanical joining	Mechanical clamping [176] Von der Waals force [177] Pressure [178, 179]
Adhesive joining	CNT/epoxy, polymer [180, 181]
Solid-state bonding	Diffusion/sintering/cold welding [47, 48] Electron/ion beam [199, 200] Ultrasonic welding [201]
Soldering/brazing	Resistance soldering [185] Active brazing [192] Self-powered brazing [195] Laser brazing [193] Vacuum brazing [194, 202] Transient liquid phase bonding [195]
Fusion welding	Resistance spot welding [182] Laser welding [196] Ultrafast nonthermal welding [6, 198]

Table 1.3 shows a comparison between conventional joining techniques and nanojoining innovations [41]. Solid-state diffusion driven by surface energy has enabled welding of two bare Au nanowires in vacuum at room temperature [47] and joining of two silver nanowires after removal of the surface-capping amorphous layer at an ambient atmosphere [48]. However, this solid-state diffusion is difficult to achieve joining with an arbitrary angle unless applying the external excitation energy, such as a head-to-side joining (T-shape) since the capping layer on the sidewall is thicker than the layer at the wire head [48]. Although the Joule heating was proposed to join metallic nanowires in case of contact wires [182, 183], the so-called nanoscopic resistance spot welding can be only applied to conductive nanowires. A mechanical pressing with nanoindentation was also developed to join nanowires to the substrate [178, 179]. Unfortunately, this press will significantly deform the wire head. On the other hand, the substrate can be also deformed seriously by Joule heating, mechanical pressure and thermal annealing unless the processing parameters, e.g., current, pressure, and temperature, are accurately controlled. Compared with these joining methods, photonic sintering was conducted for joining metal nanowires at arbitrary contact angles, which enables non-contact processing and good thermal management to minimize the damage of the substrate and nanomaterials. Due to self-localized plasmonic excitation [94], this plasmonic heat can lead to the perfect joining of adjacent and/or contact nanowires. A continuous-wave laser was reported to braze the crossed NWs [196], which is similar to autogenous laser brazing for metal microjoining [203]. However, laser joined metal NWs display a polycrystalline nature with lots of defects at the joined regions [88, 197, 204]. This is quite different from a self-oriented joining with solid-state diffusion where a clear lattice matching is founded. Femtosecond laser joining and a laser-healing of cutting wires has shown possible epitaxial recrystallization or enhanced grain orientation [88, 204, 205]. Therefore, precise control of laser parameters based on the understanding of the interaction of laser and nanowires is critical to improve nanojoining quality for innovative applications. As shown in Fig. 1.37, recent experiments by comparing femtosecond laser to continuous-wave laser and computation simulation and modeling have demonstrated

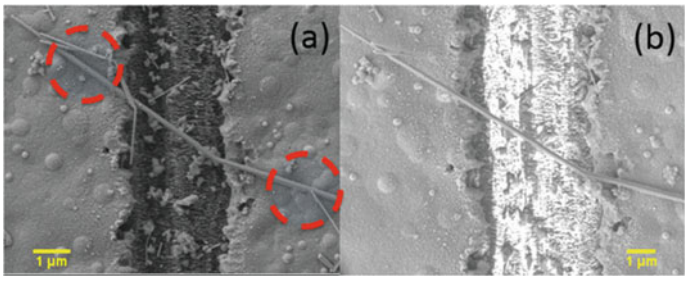

Fig. 1.37 Femtosecond laser joining of single Cu nanowire onto silver nanofilms printed by an aerosol printer [198]. The groove is cut by femtosecond laser. The groove width is 4 μm. **a** Before laser joining. Two dashed circles indicate the joining site. **b** After laser joining. The thin Cu nanowires indicated by circles in (**a**) were blown away by laser illumination

the success welding of metallic nanowires [6, 206]. However, the further work to join dissimilar nanowires, such as, metallic oxide nanowires still needs extensive research [197].

1.6.2 Molecular Electronics

Transistor, which is one of the essential components in integrated circuits, controls the flow of electrons by customizing the voltage that applied. In 2004 Ghost et al. predicted to realize an evolutional solid-state molecular transistor by the electrostatic regulation of the molecular orbital energy of a single molecule [207]. Electrostatic and conformational interactions are two possible mechanisms for field-effect molecular transistors. Electrostatic component leads to the thermal limit in the absence of tunneling. In their research, it shows that only if the molecular dipole moment μ is close to qt_{ox}, where t_{ox} represents the thickness of the oxide isolation layer, the conformational field effect can take a major role. Take advantage of that, if a large molecular dipole along a suitable direction is established, the conformational transition can be achieved. Soon after, Ahm et al. [208] have suggested another approach, in which internal electrostatic charge density can be adjusted by using an external node to control the charge transfer across the metal electrodes and the molecules. Transistor action can be achieved by aligning the molecular energy levels and the Fermi level of the leads. Remarkably, researchers have developed molecular transistors by gold nanowire wires [209]. In this research, an approximately 100 nm gold nanowire was patterned by electron beam lithography on top of an aluminum gate electrode. As an active device, a 1,4-benzenedithiol (BDT) with a delocalized aromatic ring as a π-conjugated molecule was coated on the gold nanowire surface, which acted as a channel material.

Diodes are another crucial component of integrated circuits that conduct current only in one direction when they are forward biased. Usually, a diode is composed of two kinds of semiconductor materials to form a P-N junction. Currently, two types of molecular diodes have been reported: rectifying diodes and resonant tunneling diodes. In 1974, Aviram and Rater discussed the possibility of a rectifier, which provided a foundation for current works on molecular rectifying diodes [210]. In their research, a donor π-system and an acceptor π-system linked by a σ-bonded tunneling bridge. This behavior has been identified by a hemi-quinone molecule, as shown in Fig. 1.38 [211]. For resonant tunneling diodes (RTD), electrons can pass through the resonant state at different energy levels; these diodes can be used as oscillators and switches [212]. For molecular RTDs, methylene groups or aliphatic groups are attached to both sides of a benzene ring, which leads to creating a potential barrier. To create a functional device, electrodes need to be able to pass through this potential barrier. However, the unoccupied energy level of the benzene ring does not match the energy level of the electrode. In this case, the transistor remains in the "off" state. The transistor can be turned to an "on" state, by varying the applied voltage [213]. To design a proper molecule device, computation modeling is facile and time-effective.

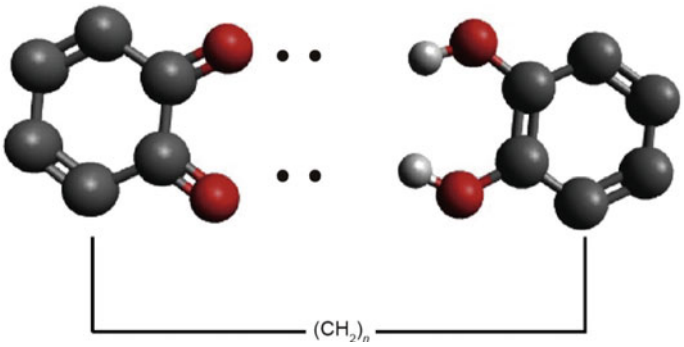

Fig. 1.38 a schematic of a hemi-quinone molecular structure [211]

Currently, the Hartree–Fock self-consistent field theory and the density functional theory (DFT) are two main theories used in developing a theoretical fundamental for molecular electronic devices.

Based on the concept of molecular electronic devices, molecular capacitors/memory units are developed as well. Jurow et al. have been reported a detailed review of porphyrins, which elucidated a potential for using these molecules in the fabrication of molecular capacitors [214]. Coming to molecular diodes and molecular transistors, molecular devices functional on dielectrics material and tunable dielectric constant are desired. In 2007, Chen et al. reported a hafnium dioxide (HfO_2) based metal-insulator-molecule-metal device [215]. A HfO_2 dielectric layer was deposited by an atomic layer deposition process. Although new studies provide an excellent potential for deployment of the molecular capacitor, current understanding of the molecular mechanism of the capacitor are not yet well experimentally established.

On the other hand, to establish a complete molecular electronic system, the development of molecular isolator and conductive wire is also necessary. For any integrated circuit, the isolator plays a significant role in regulating the flow of current. Many molecular with specific functional groups can be used as molecular insulator material. Currently, aliphatic organic molecular is considered as the best molecular insulator [216]. In aliphatic organic molecular, there are only σ bonds existing. By inserting these molecules between electrodes, it is very easy to break the pass current flow. Similar to the isolator, the concept of the molecular wire is crucial when dealing with the molecular electronics system. Different from molecular isolators, molecular wire requires high electrical conductivity. There are two primary types of molecular wires can be classified: saturated chains and conjugated chains [16, 217]. The main difference between the two chains is that whether atoms are connected with single bonds or connected by alternate single and double bonds [218]. In the development of molecular wire, CNTs are considered as a widely acceptable material [219].

1.6.3 1D (Nanowire and Nanotube) and 2D Material in Molecular Electrodes

1D and 2D materials are very promising building blocks for molecular electronics; especially, the carbon-based material plays a significant role in the design process and device fabrication. The first demonstration of carbon nanotubes (CNT) used in a field-effect transistor has been reported in 1998 [220]. A single wall CNT (SWCNT) was positioned on top to bridge two gold electrodes, which were fabricated on a SiO_2 film grown on a silicon wafer. Two gold electrodes act as source and drain electrodes, and the wafer itself was used as the gate electrode ("back-gate"). These CNT-FETs behaved as p-type FETs with ON/OFF current ratio of $\approx 10^5$ [221]. The further improvement of current conductance across the metal -molecule interface is a great technical challenge in a molecular transistor [222, 223]. It has been proved that the Schottky barrier between nanotube and metal contact leads to limit the current flow, which reduces molecular conductivity [224]. In terms of this issue, Javey et al. provided a valuable idea to reduce the barrier by placing a palladium contact with SWCNT [225]. The research shows that palladium has a high work function and an exceptional wetting interaction with CNTs, these properties can effectively reduce the contact resistance. Furthermore, metallic and semiconductor property of CNTs can be strengthened by controlling its geometric features during growth [226].

CNT has also become an indispensable material in other molecular devices. In 2004, Dragoman et al. discussed the possibility of using semi-conductive SWCNT for a molecular diode. As reported, the semi-conductive SWCNT yields better performance than the usual semiconductor hetero-structured RTD [227]. In their design, the barrier height was controlled by the DC voltage applied to the gate and the gap of intra-electrodes. Pandey et al. bridged pseudopeptide between two semi-conductive CNT and created a based molecular RTD (Fig. 1.39) [228]. As claimed in this system, no special bistable properties of the molecule are required and can exhibit longer reliability than bistable molecules, which is known as molecules that can be switched reversibly between two stages, such as magnetic [229], electrical properties [230], or optical properties [231]. Except for carbon-based materials, metal and metal oxide nanowire/nanotube-based 1D material have also been developed for molecular devices. In 2017 Madini et al. provide a new theoretical framework for molecular capacitor by introducing a single-walled boron nitride nanotube (SWBNNT) inside

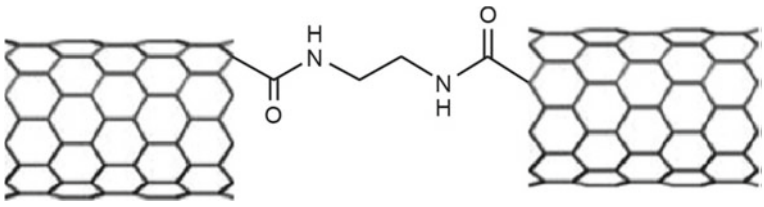

Fig. 1.39 Schematic of the CNT–pseudopeptide–CNT [228]

of anther SWBNNT [232]. Green et al. reported a 160-kilo-byte molecular electronic memory pattern, which fabricated by over 1400 Ti nanowires [233]. These molecular device patterns were configured to form a fully functional random-access memory circuit for storing and retrieving information.

Graphene is a typical 2D material providing valuable mechanical, electronic, chemical, and optical properties. At the same time, graphene is recognized as an ideal candidate for molecular junction [234, 235]. Wang et al. evident graphene as the ideal electrode through a comparative study to PEDOT:PSS and gold in molecular devices [235]. In their report, graphene has better transport characteristics and contact conductance. Nowadays, graphene is extensively applied in multiple molecular electric devices, such as conducting electrode in memory devices [236], field-effect transistors [236], and dye-sensitized solar cells [237].

1.6.4 Fabrication of Molecular Devices

In the process of molecular devices fabrication, pre-patterning, and precise manipulation of nanomaterials are required as very critical processes. Usually, e-beam lithography and chemical vapor deposition for in situ growth are the main tools for these procedures [238, 239]. With the development of molecular devices, some novel approaches have been established. As aforementioned the laser as a tool for precision machining has considerably contributed to the nanoscale process, such as laser-induced plasmonic nano joining [5, 6], nanoscale ablation [240], and etching [141, 241]. The precision machining property of laser processing has also been applied in molecular electrical devices as well. Maurice et al. reported a low-temperature process for nanogap creating in graphene [242]. In this study, a tightly focused femtosecond laser was used to induce a pre-patterned defect in graphene. After the laser process, an electro-burn process was applied to generate a gap with tens nanometer wide. During this process, the defected area could locally generate a dynamic hot spot, further facilitate the burn of graphene and eventually yield a nano-size gap. As a result, the nanogap width is 36.4 ± 18.5 nm (as presents in Fig. 1.40). A few nanometer gap as a basic architecture allows a single molecule to be inserted to create molecular transistors [243, 244], DNA sequencers [245, 246], and sensors [247]. Therefore, develop a nanogap fabrication process is essential in the field of molecular electronics.

Currently, the development of molecular electronics using DNA molecules as the building blocks or template for growth nanostructure has gained a huge interest. The key to using DNA as a scaffold for electronic circuits is to effectively transform the DNA molecules into conductive wires, which is called DNA metallization [248]. Typically, DNA-templated electronics is a two-step process; First, establish metallic nucleation centers on DNA molecules, which can be approached by binding metal ions or complexes to the DNA and their subsequent reduction, or by directly placing small metallic particles to the DNA. Once metallic nucleation centers were formed, using these centers as catalysts for selective deposition of metal along with

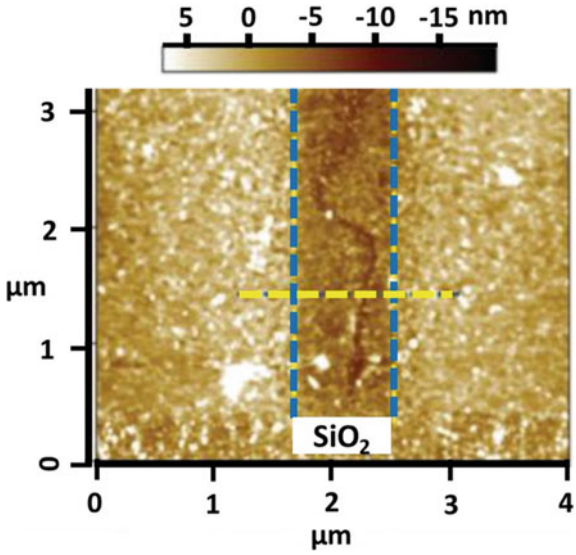

Fig. 1.40 AFM height image of a graphene device after laser pre-patterning and electroburning Modified from [242]

the DNA molecular template, which leads to creating a conductive metallic wire by bridging gaps between nucleation sites. Various metals have been employed including silver [249], palladium [250], platinum [251] and gold [252]. The disadvantage of this metallization method is the non-uniformity over the entire DNA scaffold. To address the uniformity problem, sequence-specific molecular lithography was further developed [253]. In molecular lithography, masks used in conventional photolithography is replaced by the information encoded in the DNA molecules. In 2003 Keran et al. reported a caritative process for assembly a CNT along with a pre-designed template on a DNA substrate [254]. In this research, a framework of using DNA and homologous genetic recombination for CNT self-assembly is established. By using homologous recombination, which is a protein-mediated reaction between two DNA molecules, a CNT was localized at a desired DNA scaffold molecule. *RecA* protein from *Escherichia coli* bacteria was used in the process. After CNT was localized, DNA molecule is metallized by $AgNO_3$. Conductive metallic wires were formed by silver reduction along the DNA. In here, *RecA* act as a protector to protects the active area of the transistor against metallization. Subsequently, electroless gold plating was applied using the silver clusters as nucleation centers to create a highly conductive gold electrode. Figure 1.41 shows an SEM image of an individual SWNT contacted by two DNA-templated gold nanowires.

Although current approaches of making DNA-templated wires have shown a promising development, it is still facing a difficulty in the production of smaller-scale nanostructures and devices, which is the major drawback [255]. To overcome this problem, better methods to realize conductance based on DNA scaffolds have to be developed. The laser-induced photochemistry is probably a promising solution.

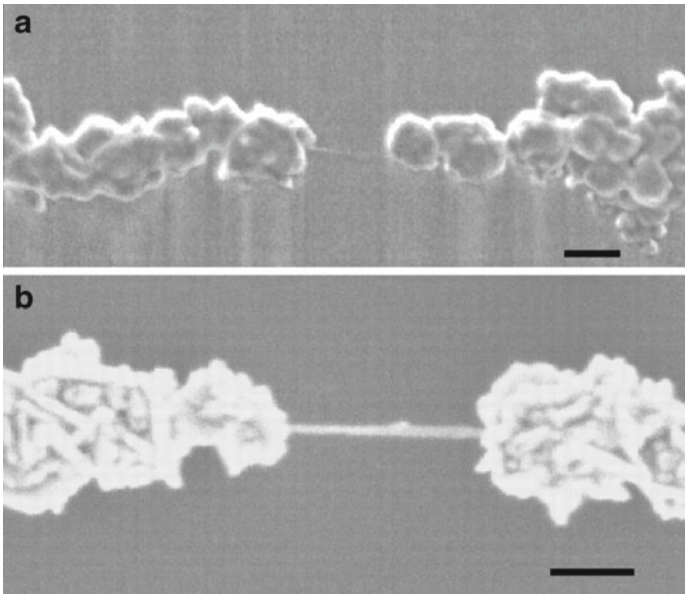

Fig. 1.41 A DNA-templated carbon nanotube FET and metallic wires contacting it. SEM images of SWNTs contacted by self-assembled DNA-templated gold wires. **a** An individual SWNT. **b** A rope of SWNTs. Scale bars, 100 nm [254]

1.7 Ultrafast Laser Near- and Super-Resolution Manufacturing

For decades, the ultrafast laser has been successfully used in cutting, drilling, welding, cleaning, surface modification, micromachining, and additive manufacturing [256]. Super-resolution processing is always one of the attractive goals of precision laser processing. Super-resolution laser manufacturing technology refers to technology that manufactures or processes dimensions smaller than the optical diffraction limit of the laser system ($\sim\lambda/(2n.\sin\alpha)$). At present, the smallest voxel size is about 50 nm, which is equivalent to 0.5 million dots per inch (dpi) in today's 2D graphics printing [257]. Although this value is already more than ten times smaller than the laser wavelength used, they are insufficient to manufacture many components compared to an electron beam with a resolution of a few nanometers, which is frequently required for a molecular device. Therefore, many innovative methods are still under development to further increase the resolution.

1.7.1 Two-Photon Direct Writing

The two-photon direct writing technology based on femtosecond laser has been developed to prepare micro/nanostructures. Two-photon absorption means that organic material molecules can simultaneously absorb two photons, with the same or different frequencies, and then be excited from a low energy state to a higher energy state. This two-photon direct writing technology enables the feature size of 3D printing down to submicron, thereby promoting the trend of miniaturization. The theoretical manufacturing size of TPP is about $\lambda/(2.7n.\sin\alpha)$, smaller than the single-photon diffraction limit [18]. Gissibl demonstrated the application of direct writing and testing by two-photon direct laser writing with a target of approximately 100 μm multilens and verified its high performance and functionality for quantitative measurement of modulation transfer function and aberrations [258]. Liao proposed a technique based on two-photon polymerization (TPP) for the preparation of precise and customizable hollow three-dimensional microstructure devices [259]. Different from traditional manufacturing technology, direct laser writing with TPP manufacturing scheme can better control all geometric characteristics of the manufactured architecture both interiorly and exteriorly. Two-photon printing is also used in the biological field. Worthington used the two-photon direct writing technique to print topological patterns with different feature sizes to study their effects on cell differentiation. This technique demonstrates a fast manufacturing of terrain surfaces with well-defined shapes with a resolution of less than 3 μm [260].

1.7.2 Near-Field Manufacturing

Another powerful nanofabrication using lasers with a spatial resolution beyond the optical diffraction limit is to use near-field technology, that is, evanescent waves manufacturing near scattering objects, which can achieve sub-diffraction limited focusing (minimum ~10 nm) [261]. In the near-field optical phenomenon, the evanescent wave becomes more important than free space far-field wave. The characteristic of the evanescent wave is that its amplitude decays rapidly in at least one direction of space. The light can be confined to a lateral dimension far less than half of the wavelength. There are a few near-field laser nanomanufacturing technologies as follows.

Particle lens array (PLA) technology uses an array of two-dimensional (2D) small particles as a lens array. The array is then used to convert the laser beam into a near-field parallel focused multiple enhancement optical spot. The efficiency of this method is very high. As the lens array covers a large area, millions of nanostructures can be prepared by irradiating with laser pulse only once. This makes it an ideal method for nanofabrication of large-area surfaces [262]. With 140 nm dielectric particles and 248 nm laser light source, PLA can obtain smaller features with a resolution as low as 30 nm [263].

Laser coupled near-field scanning optical microscopy tip can prepare arbitrary-shaped nanofeatures by controlling the path of the needle tip, as shown in Fig. 1.42. In a scanning near-field optical microscope (SNOM), a very small fiber tip (usually 50 nm) is used to scan while approaching the target surface (10–20 nm), which produces a high-resolution evanescent energy field at the tip [19]. Using this method a resolution of 35 nm can be obtained, corresponding to $\lambda/10$ [264].

Plasma lithography (PL) technology is the use of surface plasmon ultrashort wavelength characteristics combined with field positioning for nanolithography. Surface plasmons can produce high-precision patterns to realize a subwavelength resolution in the optical near-field with metal masks [265]. The lithography mask is usually composed of a silver film perforated with a 2D nanohole array. Numerical studies have shown that this method can achieve a lithographic resolution of 20 nm by using light at a wavelength of 365 nm through a silver mask. The experiment proves that the half-pitch resolution of nanolithography is as low as 60 nm [266, 267]. Dong proposed a surface plasmon interference lithography technique that uses a deep ultraviolet plasma structure to form ultra-high-resolution periodic nanopatterns in photoresists. The resolution of the generated pattern can thus be adjusted by changing the refractive index and thickness of the photoresist [268]. It is proved by numerical methods that one-dimensional and two-dimensional patterns with a half-pitch resolution of 14.6 nm can be generated. In addition, the half-pitch resolution of the generated pattern can be as low as 13 nm, using a high refractive index photoresist.

1.7.3 Stimulated Emission Depletion (STED) Manufacturing

In 1994, Hell and Wichmann provided a revolutionary proposal to ultimately break Abbe's resolution limit in fluorescence microscopy [269]. In their proposal, the fluorophore at the outer edge of the point spread function (PSF) is deliberately switched off by a mechanism of stimulated emission depletion (STED). Here, a second laser beam is focused into a special ring-shape, deactivating a surrounding part of the excited molecules, thereby limiting the effect of the excitation laser to a small volume at the central spot. In this case, the observation region does not have any fundamental diffraction limits. STED-nanoscopy has been proven to achieve resolutions below 10 nm [270]. In 2014, Stefan Hell was awarded the Nobel Prize in Chemistry, because of the diffraction barrier is eliminated in the optical fluorescence microscope, through the concept of stimulated emission depletion (STED) [270]. This STED concept can also be applied to optical super-resolution manufacturing. Figure 1.43 shows typical setups of STED microscopy and STED lithography. In a typical STED principle, the diameter of the exposure area can be calculated by the formula [271, 272]

$$d \approx \frac{\lambda}{2n\sin\alpha\sqrt{1 + bI_{\mathrm{STED}}/I_{\mathrm{S}}}} \tag{1.6.1}$$

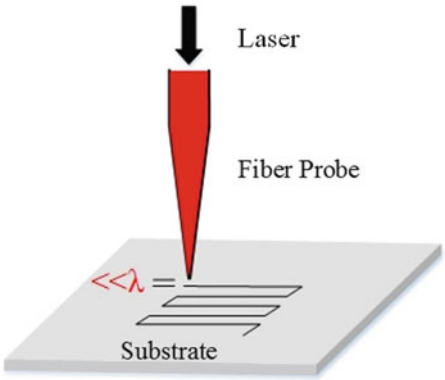

Fig. 1.42 A schematic diagram of laser coupled scanning near field optical microscopy tip [19]

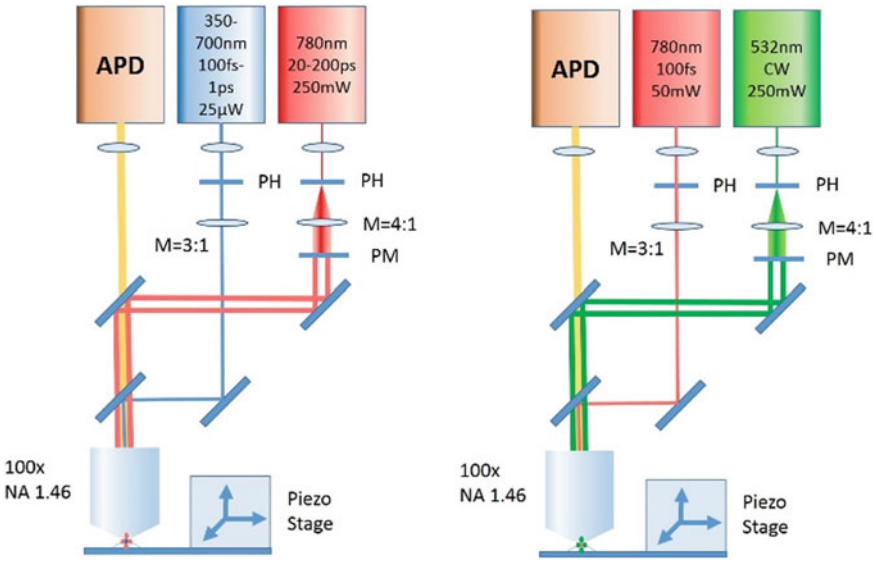

Fig. 1.43 Set up of STED microscopy (left) and STED lithography (right) [19]

where $n\sin\alpha$ is the numerical aperture, b is a systematic coefficient dependent on the beam shape, I_{STED} is the intensity of the depletion light, and I_{s} is the switching intensity at which half of the radicals will be depleted through stimulated emission. It can be easily understood that one can reduce the exposure area by increasing $I_{\mathrm{STED}}/I_{\mathrm{S}}$ ratios. Wollhofen proposed new limitations on the lateral resolution and feature size of the STED lithography technology with two-photon STED direct laser writing. The minimum lateral width can be prepared up to 55 nm, the width of separated twin lines can reach 120 nm [273]. Vitukhnovsky demonstrated the advantages of STED-inspired nanolithography for the preparation of metals and hybrid

nanostructures [274]. Compared with the direct laser writing method, they demonstrated that the use of STED nanolithography can greatly reduce the lateral size of the line. Using optically STED lithography, sub-diffraction-limited acrylate nanoanchors were prepared [275]. Acrylic nanopatches with a diameter of 60–70 nm prepared by STED enhanced two-photon polymerization are easily functionalized by antibodies at the single-molecule level. He proposed a control method of 45 nm wire based on direct laser writing with STED, which has a rod-shaped effective focal point. In traditional standard direct laser writing, a donut-shaped depletion focus is usually used, and the minimum line width is limited to 55 nm. In this work, they push this limit to the sub-50 nm size with a rod-like effective focal point, which is a combination of Gaussian excitation focusing and twin-oval depletion focusing [276]. Furthermore, Gan has demonstrated deep sub-diffraction optical beam lithography with a 9 nm feature size based on the STED mechanism [277].

1.8 Summary and Outlooks

A laser is a crucial tool for precise micro-to-nano manufacturing. For various applications the understanding of fundamentals between the laser and material interaction is basic. With the development of ultrafast laser available for a shorter pulse, higher peak power, and tunable wavelength at a wider band, the laser manufacturing enables versatile processing with a higher precision beyond the optical diffraction limit.

The basic interaction of laser and materials involves in energy absorption. At a micro-to-nanoscale, this physical procedure includes surface plasmon excitation and surface electron excitation. At a periodic approximately equal to or shorter than the electron-lattice coupling time, typically a couple of picoseconds, the so-called Coulomb explosion, and nonthermal melting will occur due to the surface electron vaporization. This localizes the thermal effect to the size similar to the optical penetration depth. This is the current physical basis for precision manufacturing using an ultrafast laser.

At a nanoscale, the physical properties of materials will be quite different from their bulk counterparts. The micro-to-nano manufacturing leads to the mass transfer at these scopes. The surface properties will be dominant due to the size effect and the scaling laws. The nanoparticles can be melt and sintered at a pretty low temperature, even close to room temperature. The involved surface liquid phase and enhanced surface diffusion will bring new mechanisms to the manufacturing and materials science.

Due to these new features, laser-based micro-to-nanomanufacturing is especially effective and powerful for printed electronics, such as flexible/stretchable electronics, 3D microprinting for portable electronics at current big data, Internet of things, next-generation computation and artificial intelligent era. It will create extensive opportunities in energy, environment, sensing, and biomedical applications.

With the further development of laser-based micro-to-nano manufacturing, it can be expected that molecular devices with high manufacturing and manipulation will

be research hot topics. These fields should base on hybrid manufacturing which may involve interdisciplinary techniques and disruptive concepts, such as near-field manufacturing and super-resolution manufacturing. It is believed that these progress may pave the way for science and technique evolution for post-Si and post-Moore's law and beyond.

Acknowledgements This book chapter is partially based on the lectures of Dr. Anming Hu presented at the course of "introduction to micro-to-nanomanufacturing" at the University of Tennessee Knoxville (UTK) for the period of 2014 to 2019. Some materials are modified from the students' presentations and course exercises. The contribution from all students is therefore recognized. The authors are also grateful to Dr. Seungha Shin (UTK) for numerical simulation and computation simulation, Dr. Jayne Wu (UTK) for ACEK mechanism, and Dr. Feng-yuan Zhang (UTK) for the scaling theory. The cited research work was supported by numerical funds. These supports are also sincerely grateful by the authors.

References

1. S. Lei, X. Zhao, X. Yu, A. Hu, S. Vukelic, M.B.G. Jun, H.-E. Joe, Y.L. Yao, Y.C. Shin. Ultrafast laser applications in manufacturing processes: a state-of-the-art review. J. Manuf. Sci. Eng. **142** (2020)
2. Y. Yu, S. Bai, S. Wang, A. Hu, Ultra-short pulsed laser manufacturing and surface processing of microdevices. Engineering **4**, 779–786 (2018)
3. Y. Yu, S. Wang, D. Ma, P. Joshi, A. Hu, Recent progress on laser manufacturing of microsize energy devices on flexible substrates. JOM **70**, 1816–1822 (2018)
4. A. Hu, Interaction of nanosecond and femtosecond laser pulses with carbon: deposition of carbon films having novel compositions. Thesis, UWSpace (2008)
5. A. Hu, P. Peng, H. Alarifi, X. Zhang, J. Guo, Y. Zhou, W. Duley, Femtosecond laser welded nanostructures and plasmonic devices. J. Laser Appl. **24**, 042001 (2012)
6. Y. Yu, Y. Deng, M.A. Al Hasan, Y. Bai, R.-Z. Li, S. Deng, P. Joshi, S. Shin, A. Hu. Femtosecond laser-induced non-thermal welding for a single Cu nanowire glucose sensor. Nanoscale Adv. **2**, 1195–1205 (2020)
7. D. Strickland, G. Mourou, Compression of amplified chirped optical pulses. Optics Commun. **56**, 219–221 (1985)
8. M.F. Yanik, H. Cinar, H.N. Cinar, A.D. Chisholm, Y. Jin, A. Ben-Yakar, Functional regeneration after laser axotomy. Nature **432**, 822 (2004)
9. C. Momma, B.N. Chichkov, S. Nolte, F. von Alvensleben, A. Tünnermann, H. Welling, B. Wellegehausen, Short-pulse laser ablation of solid targets. Opt. Commun. **129**, 134–142 (1996)
10. R. Srinivasan, E. Sutcliffe, B. Braren, Ablation and etching of polymethylmethacrylate by very short (160 fs) ultraviolet (308 nm) laser pulses. Appl. Phys. Lett. **51**, 1285–1287 (1987)
11. S. Küper, M. Stuke, Femtosecond UV excimer laser ablation. Appl. Phys. B **44**, 199–204 (1987)
12. N. Bärsch, K. Körber, A. Ostendorf, K.H. Tönshoff, Ablation and cutting of planar silicon devices using femtosecond laser pulses. Appl. Phys. A **77**, 237–242 (2003)
13. S.S. Wellershoff, J. Hohlfeld, J. Güdde, E. Matthias, The role of electron–phonon coupling in femtosecond laser damage of metals. Appl. Phys. A **69**, S99–S107 (1999)
14. R.R. Gattass, E. Mazur, Femtosecond laser micromachining in transparent materials. Nat. Photon. **2**, 219–225 (2008)
15. K. Sugioka, Y. Cheng, Ultrafast lasers—reliable tools for advanced materials processing. Light: Sci. Appl. **3**, e149–e149 (2014)

16. A. Hu, M. Rybachuk, Q.B. Lu, W.W. Duley, Direct synthesis of sp-bonded carbon chains on graphite surface by femtosecond laser irradiation. Appl. Phys. Lett. **91**, 131906 (2007)
17. C. Zheng, A. Hu, T. Chen, K.D. Oakes, S. Liu, Femtosecond laser internal manufacturing of three-dimensional microstructure devices. Appl. Phys. A **121**, 163–177 (2015)
18. J. Fischer, M. Wegener, Three-dimensional optical laser lithography beyond the diffraction limit. Laser Photon. Rev. **7**, 22–44 (2013)
19. W. Zhou, D. Bridges, R. Li, S. Bai, Y. Ma, T. Hou, A. Hu, Recent progress of laser micro-and nano manufacturing. Sci. Lett. J **5**, 228 (2016)
20. S. Küper, M. Stuke, Ablation of UV-transparent materials with femtosecond UV excimer laser pulses. MRS Proc. **129**, 375 (1988)
21. C. Zheng, A. Hu, K.D. Kihm, Q. Ma, R. Li, T. Chen, W.W. Duley, Femtosecond laser fabrication of cavity microball lens (CMBL) inside a PMMA substrate for super-wide angle imaging. Small **11**, 3007–3016 (2015)
22. K. Seibert, G.C. Cho, W. Kütt, H. Kurz, D.H. Reitze, J.I. Dadap, H. Ahn, M.C. Downer, A.M. Malvezzi, Femtosecond carrier dynamics in graphite. Phys. Rev. B **42**, 2842–2851 (1990)
23. D.E. Aspnes, E.D. Palik, *Handbook of optical constants of solids* (Academic, New York, 1985), pp. 89–112
24. S.A. Maier, *Plasmonics: Fundamentals and Applications* (Springer, 2007)
25. A. Vial, A.-S. Grimault, D. Macías, D. Barchiesi, M.L. de la Chapelle, Improved analytical fit of gold dispersion: Application to the modeling of extinction spectra with a finite-difference time-domain method. Phys. Rev. B **71**, 085416 (2005)
26. C.B. Schaffer, A. Brodeur, E. Mazur, Laser-induced breakdown and damage in bulk transparent materials induced by tightly focused femtosecond laser pulses. Measure. Sci. Technol. **12**, 1784–1794 (2001)
27. L. Sheng-hsien, F. Yuichi, (*Advances in Multi-photon Processes and Spectroscopy* (World Scientific, 2004)
28. Y.L. Yao, H. Chen, W. Zhang, Time scale effects in laser material removal: a review. Int. J. Adv. Manuf. Technol. **26**, 598–608 (2005)
29. L.V. Keldysh, Ionization in the field of a strong electromagnetic wave. Sov. Phys. JETP **20**, 1307–1314 (1965)
30. P. Lambropoulos, *Multiphoton Ionization of Atoms* (Academic Press, 1984)
31. B.C. Stuart, M.D. Feit, S. Herman, A.M. Rubenchik, B.W. Shore, M.D. Perry, Nanosecond-to-femtosecond laser-induced breakdown in dielectrics. Phys. Rev. B **53**, 1749–1761 (1996)
32. K. Sokolowski-Tinten, D. von der Linde, Generation of dense electron-hole plasmas in silicon. Phys. Review B **61**, 2643–2650 (2000)
33. P. Stampfli, K.H. Bennemann, Theory for the instability of the diamond structure of Si, Ge, and C induced by a dense electron-hole plasma. Phys. Rev. B **42**, 7163–7173 (1990)
34. P. Stampfli, K.H. Bennemann, Dynamical theory of the laser-induced lattice instability of silicon. Phys. Rev. B **46**, 10686–10692 (1992)
35. P.L. Silvestrelli, A. Alavi, M. Parrinello, D. Frenkel, Ab initio molecular dynamics simulation of laser melting of silicon. Phys. Rev. Lett. **77**, 3149–3152 (1996)
36. P.L. Silvestrelli, A. Alavi, M. Parrinello, D. Frenkel, Structural, dynamical, electronic, and bonding properties of laser-heated silicon: An ab initio molecular-dynamics study. Phys. Rev. B **56**, 3806–3812 (1997)
37. D.H. Reitze, H. Ahn, M.C. Downer, Optical properties of liquid carbon measured by femtosecond spectroscopy. Phys. Rev. B **45**, 2677–2693 (1992)
38. M. Wautelet, Scaling laws in the macro-, micro- and nanoworlds. Eur. J. Phys. **22**, 601–611 (2001)
39. C. Yang, C.P. Wong, M.M.F. Yuen, Printed electrically conductive composites: conductive filler designs and surface engineering. J. Mat. Chem. C **1**, 4052–4069 (2013)
40. K. Lu, Sintering of nanoceramics. Int. Mat. Rev. **53**, 21–38 (2008)
41. Y. Ma, H. Li, D. Bridges, P. Peng, B. Lawrie, Z. Feng, A. Hu, Zero-dimensional to three-dimensional nanojoining: current status and potential applications. RSC Adv. **6**, 75916–75936 (2016)

42. F.G. Shi, Size dependent thermal vibrations and melting in nanocrystals. J. Mater. Res. **9**, 1307–1314 (1994)
43. Q. Jiang, S.H. Zhang, J.C. Li, Grain size-dependent diffusion activation energy in nanomaterials. Solid State Commun. **130**, 581–584 (2004)
44. P. Peng, A. Hu, A.P. Gerlich, G. Zou, L. Liu, Y.N. Zhou, Joining of silver nanomaterials at low temperatures: processes, properties, and applications. ACS Appl. Mater. Interfaces. **7**, 12597–12618 (2015)
45. A. Hu, J.Y. Guo, H. Alarifi, G. Patane, Y. Zhou, G. Compagnini, C.X. Xu, Low temperature sintering of Ag nanoparticles for flexible electronics packaging. Appl. Phys. Lett. **97**, 153117 (2010)
46. D. Bridges, C. Rouleau, Z. Gosser, C. Smith, Z. Zhang, K. Hong, J. Cheng, Y. Bar-Cohen, A. Hu, Self-powered fast brazing of Ti–6Al–4 V using Ni/Al reactive multilayer films. Appl. Sci. **8**, 985 (2018)
47. Y. Lu, J.Y. Huang, C. Wang, S. Sun, J. Lou, Cold welding of ultrathin gold nanowires. Nat. Nanotechnol. **5**, 218–224 (2010)
48. P. Peng, L. Liu, A.P. Gerlich, A. Hu, Y.N. Zhou, Self-oriented nanojoining of silver nanowires via surface selective activation. Particle Particle Syst. Character. **30**, 420–426 (2013)
49. K. Dick, T. Dhanasekaran, Z. Zhang, D. Meisel, Size-dependent melting of silica-encapsulated gold nanoparticles. J. Am. Chem. Soc. **124**, 2312–2317 (2002)
50. A. Ghosh, B. Corves. *Introduction to Micromechanisms and Microactuators* (Springer, 2015)
51. K.E. Drexier, in *Nanosystems* (Wiley, 1992, Chap. 2)
52. K. Liu, S. Sun, A. Majumdar, V.J. Sorger, Fundamental scaling laws in nanophotonics. Sci. Rep. **6**, 37419 (2016)
53. X.-Y. Zhang, A. Hu, T. Zhang, X.-J. Xue, J.Z. Wen, W.W. Duley, Subwavelength plasmonic waveguides based on ZnO nanowires and nanotubes: a theoretical study of thermo-optical properties. Appl. Phys. Lett. **96**, 043109 (2010)
54. X. Zhang, T. Zhang, A. Hu, Y. Song, W.W. Duley, Controllable plasmonic antennas with ultra narrow bandwidth based on silver nano-flags. Appl. Phys. Lett. **101**, 153118 (2012)
55. X.-Y. Zhang, A. Hu, J.Z. Wen, T. Zhang, X.-J. Xue, Y. Zhou, W.W. Duley, Numerical analysis of deep sub-wavelength integrated plasmonic devices based on semiconductor-insulator-metal strip waveguides. Opt. Express **18**, 18945–18959 (2010)
56. H. Raether, in *Surface Plasmons on Smooth and Rough Surfaces and on Gratings* (Springer 1988), pp. 4–39
57. Z. Fang, X. Zhu, Plasmonics in Nanostructures. Adv. Mater. **25**, 3840–3856 (2013)
58. Y. Fang, N.-H. Seong, D.D. Dlott, Measurement of the distribution of site enhancements in surface-enhanced raman scattering. Science **321**, 388 (2008)
59. P. Peng, H. Huang, A. Hu, A.P. Gerlich, Y.N. Zhou, Functionalization of silver nanowire surfaces with copper oxide for surface-enhanced Raman spectroscopic bio-sensing. J. Mater. Chem. **22**, 15495–15499 (2012)
60. W. Hou, S.B. Cronin, A review of surface plasmon resonance-enhanced photocatalysis. Adv. Funct. Mater. **23**, 1612–1619 (2013)
61. G. Baffou, R. Quidant, C. Girard, Heat generation in plasmonic nanostructures: influence of morphology. Appl. Phys. Lett. **94**, 153109 (2009)
62. C. Ma, J. Yan, Y. Huang, C. Wang, G. Yang, The optical duality of tellurium nanoparticles for broadband solar energy harvesting and efficient photothermal conversion. Sci. Adv. **4**, eaas9894 (2018)
63. C. Clavero, Plasmon-induced hot-electron generation at nanoparticle/metal-oxide interfaces for photovoltaic and photocatalytic devices. Nat. Photon. **8**, 95–103 (2014)
64. T. Neumann, M.L. Johansson, D. Kambhampati, W. Knoll, Surface-plasmon fluorescence spectroscopy. Adv. Funct. Mat. **12**, 575–586 (2002)
65. G.I. Stegeman, J.J. Burke, D.G. Hall, Nonlinear optics of long range surface plasmons. Appl. Phys. Lett. **41**, 906–908 (1982)
66. P. Drude, Zur Elektronentheorie der Metalle. Ann. Phys. **306**, 566–613 (1900)

67. S. Link, M.A. El-Sayed, Shape and size dependence of radiative, non-radiative and photothermal properties of gold nanocrystals. Inte. Rev. Phys. Chem. **19**, 409–453 (2000)
68. E. Petryayeva, U.J. Krull, Localized surface plasmon resonance: nanostructures, bioassays and biosensing—A review. Anal. Chim. Acta **706**, 8–24 (2011)
69. W.L. Barnes, A. Dereux, T.W. Ebbesen, Surface plasmon subwavelength optics. Nature **424**, 824–830 (2003)
70. K. Welford, Surface plasmon-polaritons and their uses. Opt. Quant. Electron. **23**, 1–27 (1991)
71. Y. Hong, Y.-M. Huh, D.S. Yoon, J. Yang, Nanobiosensors based on localized surface plasmon resonance for biomarker detection. J. Nanomater. (2012)
72. A. Agrawal, S.H. Cho, O. Zandi, S. Ghosh, R.W. Johns, D.J. Milliron, Localized surface plasmon resonance in semiconductor nanocrystals. Chem. Rev. **118**, 3121–3207 (2018)
73. G. Mie, Beiträge zur Optik trüber Medien, speziell kolloidaler Metallösungen. Ann. Phys. **330**, 377–445 (1908)
74. H. Yu, Y. Peng, Y. Yang, Z.-Y. Li, Plasmon-enhanced light–matter interactions and applications. NPJ Comput. Mater. **5**, 45 (2019)
75. X.-Y. Zhang, A. Hu, T. Zhang, W. Lei, X.-J. Xue, Y. Zhou, W.W. Duley, Self-assembly of large-scale and ultrathin silver nanoplate films with tunable plasmon resonance properties. ACS Nano **5**, 9082–9092 (2011)
76. W. Zhou, A. Hu, S. Bai, Y. Ma, D. Bridges, Anisotropic optical properties of large-scale aligned silver nanowire films via controlled coffee ring effects. RSC Adv. **5**, 39103–39109 (2015)
77. D.K. Gramotnev, S.I. Bozhevolnyi, Plasmonics beyond the diffraction limit. Nat. Photon. **4**, 83–91 (2010)
78. M. Born, E. Wolf, *Principle of Optics*, 7th edn (World Scientific, Cambridge, 1999)
79. L. Tong, F. Zi, X. Guo, J. Lou, Optical microfibers and nanofibers: a tutorial. Opt. Commun. **285**, 4641–4647 (2012)
80. L. Tong, J. Lou, E. Mazur, Single-mode guiding properties of subwavelength-diameter silica and silicon wire waveguides. Opt. Express **12**, 1025–1035 (2004)
81. X. Guo, Y. Ma, Y. Wang, L. Tong, Nanowire plasmonic waveguides, circuits and devices. Laser Photon. Rev. **7**, 855–881 (2013)
82. Y. Fang, Z. Li, Y. Huang, S. Zhang, P. Nordlander, N.J. Halas, H. Xu, Branched silver nanowires as controllable plasmon routers. Nano Lett. **10**(5), 1950–1954 (2010)
83. J. Takahara, S. Yamagishi, H. Taki, A. Morimoto, T. Kobayashi, Guiding of a one-dimensional optical beam with nanometer diameter. Opt. Lett. **22**, 475–477 (1997)
84. H. Ditlbacher, A. Hohenau, D. Wagner, U. Kreibig, M. Rogers, F. Hofer, F.R. Aussenegg, J.R. Krenn, Silver nanowires as surface plasmon resonators. Phys. Rev. Lett. **95**, 257403 (2005)
85. A.W. Sanders, D.A. Routenberg, B.J. Wiley, Y. Xia, E.R. Dufresne, M.A. Reed, Observation of plasmon propagation, redirection, and fan-out in silver nanowires. Nano Lett. **6**, 1822–1826 (2006)
86. R.F. Oulton, V.J. Sorger, D.A. Genov, D.F.P. Pile, X. Zhang, A hybrid plasmonic waveguide for subwavelength confinement and long-range propagation. Nat. Photon. **2**, 496–500 (2008)
87. R.F. Oulton, V.J. Sorger, T. Zentgraf, R.-M. Ma, C. Gladden, L. Dai, G. Bartal, X. Zhang, Plasmon lasers at deep subwavelength scale. Nature **461**, 629–632 (2009)
88. L. Lin, L. Liu, P. Peng, G. Zou, W.W. Duley, Y.N. Zhou, In situ nanojoining of Y-and T-shaped silver nanowires structures using femtosecond laser radiation. Nanotechnology **27**, 125201 (2016)
89. Y. Fang, Z. Li, Y. Huang, S. Zhang, P. Nordlander, N.J. Halas, H. Xu, Branched silver nanowires as controllable plasmon routers. Nano Lett. **10**, 1950–1954 (2010)
90. R. Yan, P. Pausauskie, J. Huang, P. Yang, Direct photonic–plasmonic coupling and routing in single nanowires. Proc. Natl. Acad. Sci. **106**, 21045 (2009)
91. A.D. Semenov, G.N. Goltsman, R. Sobolewski. Hot-electron effect in superconductors and its applications for radiation sensors. Supercond. Sci. Technol. **15**, R1–R16 (2002)
92. S. Link, M.A. El-Sayed, Spectral properties and relaxation dynamics of surface plasmon electronic oscillations in gold and silver nanodots and nanorods. J. Phys. Chem. B **103**, 8410–8426 (1999)

93. A.O. Govorov, W. Zhang, T. Skeini, H. Richardson, J. Lee, N.A. Kotov, Gold nanoparticle ensembles as heaters and actuators: melting and collective plasmon resonances. Nanoscale Res. Lett. **1**, 84 (2006)
94. E.C. Garnett, W. Cai, J.J. Cha, F. Mahmood, S.T. Connor, M. Greyson Christoforo, Y. Cui, M.D. McGehee, M.L. Brongersma. Self-limited plasmonic welding of silver nanowire junctions. Nat. Mat. **11**, 241–249 (2012)
95. R.-Z. Li, A. Hu, D. Bridges, T. Zhang, K.D. Oakes, R. Peng, U. Tumuluri, Z. Wu, Z. Feng, Robust Ag nanoplate ink for flexible electronics packaging. Nanoscale **7**, 7368–7377 (2015)
96. J. Qiu, W.D. Wei, Surface plasmon-mediated photothermal chemistry. J. Phys. Chem. C **118**, 20735–20749 (2014)
97. A. Csaki, F. Garwe, A. Steinbrück, G. Maubach, G. Festag, A. Weise, I. Riemann, K. König, W. Fritzsche, A parallel approach for subwavelength molecular surgery using gene-specific positioned metal nanoparticles as laser light antennas. Nano Lett. **7**, 247–253 (2007)
98. R.Z. Li, R. Peng, K.D. Kihm, S. Bai, D. Bridges, U. Tumuluri, Z. Wu, T. Zhang, G. Compagnini, Z. Feng, A. Hu, High-rate in-plane micro-supercapacitors scribed onto photo paper using in situ femtolaser-reduced graphene oxide/Au nanoparticle microelectrodes. Energy Environ. Sci. **9**, 1458–1467 (2016)
99. L. Röntzsch, K.-H. Heinig, J.A. Schuller, M.L. Brongersma, Thin film patterning by surface-plasmon-induced thermocapillarity. Appl. Phys. Lett. **90**, 044105 (2007)
100. J.M. Stern, J. Stanfield, W. Kabbani, J.-T. Hsieh, J.A. Cadeddu, Selective Prostate cancer thermal ablation with laser activated gold nanoshells. J. Urol. **179**, 748–753 (2008)
101. R.-Z. Li, A. Hu, T. Zhang, K.D. Oakes, Direct writing on paper of foldable capacitive touch pads with silver nanowire inks. ACS Appl. Mater. Interfaces. **6**, 21721–21729 (2014)
102. Y. Huang, Y. Tian, C. Hang, Y. Liu, S. Wang, M. Qi, H. Zhang, J. Zhao, Self-limited nanosoldering of silver nanowires for high-performance flexible transparent heaters. ACS Appl. Mater. Interfaces. **11**, 21850–21858 (2019)
103. R.M. German, P. Suri, S.J. Park, Review: liquid phase sintering. J. Mater. Sci. **44**, 1–39 (2009)
104. F.E. Kruis, K.A. Kusters, S.E. Pratsinis, B. Scarlett, A simple model for the evolution of the characteristics of aggregate particles undergoing coagulation and sintering. Aerosol Sci. Technol. **19**, 514–526 (1993)
105. W.K. Lee, R.L. Eadie, G.C. Weatherly, K.T. Aust, A study of the sintering of spherical silver powder—II. The initial stage. Acta Metall. **26**, 1837–1843 (1978)
106. M.I. Alymov, E.I. Maltina, Y.N. Stepanov, Model of initial stage of ultrafine metal powder sintering. Nanostruct. Mater. **4**, 737–742 (1994)
107. H.A. Alarifi, M. Atis, Z. Ouml, C. Gbreve, A. Hu, M. Yavuz, Y. Zhou. Molecular dynamics simulation of sintering and surface premelting of silver nanoparticles. Mater. Tran. **54**, 884–889 (2013)
108. H.A. Alarifi, M. Atiş, C. Özdoğan, A. Hu, M. Yavuz, Y. Zhou, Determination of complete melting and surface premelting points of silver nanoparticles by molecular dynamics simulation. J. Phys. Chem. C **117**, 12289–12298 (2013)
109. W. Zhou, S. Bai, Y. Ma, D. Ma, T. Hou, X. Shi, A. Hu, Laser-direct writing of silver metal electrodes on transparent flexible substrates with high-bonding strength. ACS Appl. Mater. Interf. **8**, 24887–24892 (2016)
110. H.-J. Hwang, K.-H. Oh, H.-S. Kim, All-photonic drying and sintering process via flash white light combined with deep-UV and near-infrared irradiation for highly conductive copper nano-ink. Sci. Rep. **6**, 19696 (2016)
111. J.R. Greer, R.A. Street, Thermal cure effects on electrical performance of nanoparticle silver inks. Acta Mater. **55**, 6345–6349 (2007)
112. S. Mypati, S.R. Dhanushkodi, M. McLaren, A. Docoslis, B.A. Peppley, D.P.J. Barz, Optimized inkjet-printed silver nanoparticle films: theoretical and experimental investigations. RSC Adv. **8**, 19679–19689 (2018)
113. M. Kaganov, E. Lifshitz, L. Tanatarov, Relaxation between electrons and the crystalline lattice. Soviet Phys.-JETP **4**, 173–178 (1957)

114. S. Anisimov, B. Kapeliovich, T. Perelman, Electron emission from metal surfaces exposed to ultrashort laser pulses. Zh. Eksp. Teor. Fiz. **66**, 375–377 (1974)
115. B.N. Chichkov, C. Momma, S. Nolte, F. von Alvensleben, A. Tunnermann, Appl. Phys. A **63**, 109 (1996)
116. M.D. Shirk, P.A. Molian, Ultra-short pulsed laser ablation of highly oriented pyrolytic graphite. Carbon **39**, 1183–1193 (2001)
117. W.W. Duley (*UV Lasers: Effects and Applications in Materials Science* (Cambridge University Press, 2005)
118. M.D. Perry, B.C. Stuart, P.S. Banks, M.D. Feit, V. Yanovsky, A.M. Rubenchik, Ultrashort-pulse laser machining of dielectric materials. J. Appl. Phys. **85**, 6803–6810 (1999)
119. T.L. Bergman, F.P. Incropera, D.P. DeWitt, A.S. Lavine, *Fundamentals of Heat and Mass Transfer* (Wiley, 2011)
120. J.H. Lienhard, *A Heat Transfer Textbook* (Courier Dover Publications, 2019)
121. D. Bergström, The absorption of laser light by rough metal surfaces (2008)
122. Z. Yang, J. Hao, S. Yuan, S. Lin, H.M. Yau, J. Dai, S.P. Lau, Field-effect transistors based on amorphous black phosphorus ultrathin films by pulsed laser deposition. Adv. Mater. **27**, 3748–3754 (2015)
123. L.L. Taylor, R.E. Scott, J. Qiao, Integrating two-temperature and classical heat accumulation models to predict femtosecond laser processing of silicon. Opt. Mater. Express **8**, 648–658 (2018)
124. Z. Lin, L.V. Zhigilei, V. Celli, Electron-phonon coupling and electron heat capacity of metals under conditions of strong electron-phonon nonequilibrium. Phys. Rev. B **77**, 075133 (2008)
125. Y. Wang, Z. Lu, X. Ruan, First principles calculation of lattice thermal conductivity of metals considering phonon-phonon and phonon-electron scattering. J. Appl. Phys. **119**, 225109 (2016)
126. S.W. Holman, R.R. Lawrence, L. Barr (1895)
127. U. Nerle, M.K. Rabinal, Thermal oxidation of copper for favorable formation of cupric oxide (CuO) semiconductor. IOSR J. Appl. Phys. **5**, 1–7 (2013)
128. M. Kaur, K.P. Muthe, S.K. Despande, S. Choudhury, J.B. Singh, N. Verma, S.K. Gupta, J.V. Yakhmi, Growth and branching of CuO nanowires by thermal oxidation of copper. J. Cryst. Growth **289**, 670–675 (2006)
129. J.K. Chen, D.Y. Tzou, J.E. Beraun, Numerical investigation of ultrashort laser damage in semiconductors. Int. J. Heat Mass Transf. **48**, 501–509 (2005)
130. Y. Bentor, *Periodic Table: Copper*. http://www.chemicalelements.com/elements/cu.html
131. J.P. Abid, A.W. Wark, P.F. Brevet, H.H. Girault, Preparation of silver nanoparticles in solution from a silver salt by laser irradiation. Chem. Commun. 792–793 (2002). https://doi.org/10.1039/b200272h
132. S. Bai, Y.-H. Lin, X.-P. Zhang, W.-P. Zhou, T. Chen, Y. Ma, T.-X. Hou, D. Bridges, K.D. Oakes, A. Hu, Two-step photonic reduction of controlled periodic silver nanostructures for surface-enhanced Raman spectroscopy. Plasmonics **10**, 1675–1685 (2015)
133. S. Bai, S. Zhang, W. Zhou, D. Ma, Y. Ma, P. Joshi, A. Hu, Laser-assisted reduction of highly conductive circuits based on copper nitrate for flexible printed sensors. Nano-Micro Lett. **9**, 42 (2017)
134. E. Marzbanrad, A. Hu, B. Zhao, Y. Zhou, Room temperature nanojoining of triangular and hexagonal silver nanodisks. J. Phys. Chem. C **117**, 16665–16676 (2013)
135. J. Bai, Y. Qin, C. Jiang, L. Qi, Polymer-controlled synthesis of silver nanobelts and hierarchical nanocolumns. Chem. Mater. **19**, 3367–3369 (2007)
136. C.L. Thomsen, D. Madsen, J. Tho/gersen, J.R. Byberg, S.R. Keiding, Femtosecond spectroscopy of the dissociation and geminate recombination of aqueous CS2. J. Chem. Phys. **111**, 703–710
137. C.R. Wang, A. Hu, Q.B. Lu, Direct observation of the transition state of ultrafast electron transfer reaction of a radiosensitizing drug bromodeoxyuridine. J. Chem. Phys. **124**, 241102 (2006)

138. M. Maillard, P. Huang, L. Brus, Silver nanodisk growth by surface plasmon enhanced photoreduction of adsorbed [Ag +]. Nano Lett. **3**, 1611–1615 (2003)
139. S. Bai, W. Zhou, Y. Lin, Y. Zhao, T. Chen, A. Hu, W.W. Duley, Ultraviolet pulsed laser interference lithography and application of periodic structured Ag-nanoparticle films for surface-enhanced Raman spectroscopy. J. Nanopart. Res. **16**, 2470 (2014)
140. Y. Nakata, Y. Matsuba, K. Murakawa, N. Miyanaga, Change of interference pattern using fundamental and second-harmonic wavelengths by phase shift of a beam. Appl. Phys. A **117**, 207–210 (2014)
141. S. Bai, D. Serien, A. Hu, K. Sugioka, 3D microfluidic surface-enhanced Raman spectroscopy (SERS) chips fabricated by all-femtosecond-laser-processing for real-time sensing of toxic substances. Adv. Funct. Mater. **28**, 1706262 (2018)
142. S.M. Yalisove, K. Sugioka, C.P. Grigoropoulos, Advances and opportunities of ultrafast laser synthesis and processing. MRS Bull. **41**, 955–959 (2016)
143. A. Hu, J. Sanderson, A.A. Zaidi, C. Wang, T. Zhang, Y. Zhou, W.W. Duley, Direct synthesis of polyyne molecules in acetone by dissociation using femtosecond laser irradiation. Carbon **46**, 1823–1825 (2008)
144. L. Rapp, B. Haberl, C.J. Pickard, J.E. Bradby, E.G. Gamaly, J.S. Williams, A.V. Rode, Experimental evidence of new tetragonal polymorphs of silicon formed through ultrafast laser-induced confined microexplosion. Nat. Commun. **6**, 7555 (2015)
145. A.A. Zaidi, A. Hu, D.E. Henneke, W.W. Duley, Femtosecond laser irradiation of liquid alkanes: mechanism of polyyne formation. Chem. Phys. Lett. **723**, 151–154 (2019)
146. A.A. Zaidi, A. Hu, M.J. Wesolowski, X. Fu, J.H. Sanderson, Y. Zhou, W.W. Duley, Time of flight mass spectrometry of polyyne formation in the irradiation of liquid alkanes with femtosecond laser pulses. Carbon **48**, 2517–2520 (2010)
147. T. Matsuda, T. Sano, K. Arakawa, O. Sakata, H. Tajiri, A. Hirose, Femtosecond laser-driven shock-induced dislocation structures in iron. Appl. Phys. Express **7**, 122704 (2014)
148. T. Sano, T. Eimura, R. Kashiwabara, T. Matsuda, Y. Isshiki, A. Hirose, S. Tsutsumi, K. Arakawa, T. Hashimoto, K. Masaki, Femtosecond laser peening of 2024 aluminum alloy without a sacrificial overlay under atmospheric conditions. J. Laser Appl. **29**, 012005 (2017)
149. J.D. Majumdar, E.L. Gurevich, R. Kumari, A. Ostendorf, Investigation on femto-second laser irradiation assisted shock peening of medium carbon (0.4% C) steel. Appl. Surface Sci. **364**, 133–140 (2016)
150. P. Russo, A. Hu, G. Compagnini, W.W. Duley, N.Y. Zhou, Femtosecond laser ablation of highly oriented pyrolytic graphite: a green route for large-scale production of porous graphene and graphene quantum dots. Nanoscale **6**, 2381–2389 (2014)
151. P. Russo, A. Hu, G. Compagnini, Synthesis, properties and potential applications of porous graphene: a review. Nano-Micro Lett. **5**, 260–273 (2013)
152. Q. Su, S. Bai, J. Han, Y. Ma, Y. Yu, Y. Deng, M. Wu, C. Zheng, A. Hu, Precise laser trimming of alloy strip resistor: a comparative study with femtosecond laser and nanosecond laser. J. Laser Appl. **32**, 022013 (2020)
153. C. Zheng, A. Hu, R. Li, D. Bridges, T. Chen, Fabrication of embedded microball lens in PMMA with high repetition rate femtosecond fiber laser. Opt. Express **23**, 17584–17598 (2015)
154. D.C. Cox, R.D. Forrest, P.R. Smith, V. Stolojan, S.R.P. Silva, Study of the current stressing in nanomanipulated three-dimensional carbon nanotube structures. Appl. Phys. Lett. **87**, 033102 (2005)
155. K. Keshoju, H. Xing, L. Sun, Magnetic field driven nanowire rotation in suspension. Appl. Phys. Lett. **91**, 123114 (2007)
156. E.R. Dufresne, D.G. Grier, Optical tweezer arrays and optical substrates created with diffractive optics. Rev. Sci. Instrum. **69**, 1974–1977 (1998)
157. B.J. Roxworthy, K.C. Toussaint, Femtosecond-pulsed plasmonic nanotweezers. Sci. Rep. **2**, 660 (2012)
158. C. Cheng, S. Wang, J. Wu, Y. Yu, R. Li, S. Eda, J. Chen, G. Feng, B. Lawrie, A. Hu, Bisphenol a sensors on polyimide fabricated by laser direct writing for onsite river water monitoring at attomolar concentration. ACS Appl. Mater. Interfaces. **8**, 17784–17792 (2016)

159. W. Jie, Biased AC electro-osmosis for on-chip bioparticle processing. IEEE Trans. Nanotechnol. **5**, 84–89 (2006)
160. J. Wu, Y. Ben, D. Battigelli, H.-C. Chang, Long-range AC electroosmotic trapping and detection of bioparticles. Ind. Eng. Chem. Res. **44**, 2815–2822 (2005)
161. M. Lian, N. Islam, J. Wu, AC electrothermal manipulation of conductive fluids and particles for lab-chip applications. IET Nanobiotechnol. **1**, 36–43 (2007)
162. A. GonzÁLez, A. Ramos, H. Morgan, N.G. Green, A. Castellanos, Electrothermal flows generated by alternating and rotating electric fields in microsystems. J. Fluid Mech. **564**, 415–433 (2006)
163. M. Stubbe, J. Gimsa, A short review on AC electro-thermal micropumps based on smeared structural polarizations in the presence of a temperature gradient. Colloids Surfaces A: Physicochem. Eng. Aspects **376**, 97–101 (2011)
164. G. Baysinger, L.I. Berger, R.N. Goldberg, H.V. Kehiaian, K. Kuchitsu, *CRC Handbook of Chemistry and Physics* (National Institute of Standards and Technology, 2015)
165. J. Wu, Interactions of electrical fields with fluids: laboratory-on-a-chip applications. IET Nanobiotechnol. **2**, 14–27 (2008)
166. A. Salari, M. Navi, T. Lijnse, C. Dalton, AC electrothermal effect in microfluidics: a review. Micromachines **10**, 762 (2019)
167. A. Jamshidi, Optoelectronic manipulation, assembly, and patterning of nanoparticles (2009)
168. X. Xing, J. Zheng, C. Sun, F. Li, D. Zhu, L. Lei, X. Cai, T. Wu, Graphene oxide-deposited microfiber: a new photothermal device for various microbubble generation. Opt. Express **21**, 31862–31871 (2013)
169. L. Dai, Jiao, L. Liu, in *Presented at 2016 IEEE 16th International Conference on Nanotechnology (IEEE-NANO), 22–25 Aug. 2016* (2016)
170. L. Dai, Z. Ge, N. Jiao, L. Liu, 2D to 3D manipulation and assembly of microstructures using optothermally generated surface bubble microrobots. Small **15**, 1902815 (2019)
171. E.C.H. Ng, K.M. Chin, C.C. Wong, Controlling inplane orientation of a monolayer colloidal crystal by meniscus pinning. Langmuir **27**, 2244–2249 (2011)
172. W. Lu, C.M. Lieber, in *Nanoscience and Technology: A Collection of Reviews from Nature Journals* (World Scientific 2010), pp. 137–146
173. H. Yan, H.S. Choe, S. Nam, Y. Hu, S. Das, J.F. Klemic, J.C. Ellenbogen, C.M. Lieber, Programmable nanowire circuits for nanoprocessors. Nature **470**, 240–244 (2011)
174. J. Kim, H.-C. Lee, K.-H. Kim, M.-S. Hwang, J.-S. Park, J.M. Lee, J.-P. So, J.-H. Choi, S.-H. Kwon, C.J. Barrelet, H.-G. Park, Photon-triggered nanowire transistors. Nat. Nanotechnol. **12**, 963–968 (2017)
175. C. Rewitz, G. Razinskas, P. Geisler, E. Krauss, S. Goetz, M. Pawłowska, B. Hecht, T. Brixner, Coherent control of plasmon propagation in a nanocircuit. Phys. Rev. Appl. **1**, 014007 (2014)
176. T. Gong, Y. Zhang, W. Liu, J. Wei, C. Li, K. Wang, D. Wu, M. Zhong, Connection of macro-sized double-walled carbon nanotube strands by bandaging with double-walled carbon nanotube films. Carbon **45**, 2235–2240 (2007)
177. K.P. Yung, J. Wei, B.K. Tay, Formation and assembly of carbon nanotube bumps for interconnection applications. Diamond Related Mater. **18**, 1109–1113 (2009)
178. T. Tokuno, M. Nogi, M. Karakawa, J. Jiu, T.T. Nge, Y. Aso, K. Suganuma, Fabrication of silver nanowire transparent electrodes at room temperature. Nano Res. **4**, 1215–1222 (2011)
179. P. Peng, W. Guo, Y. Zhu, L. Liu, G. Zou, Y.N. Zhou, Nanoscale wire bonding of individual ag nanowires on au substrate at room temperature. Nano-Micro Lett. **9**, 26 (2017)
180. Z. Gu, Y. Chen, D.H. Gracias, Surface tension driven self-assembly of bundles and networks of 200 nm diameter rods using a polymerizable adhesive. Langmuir **20**, 11308–11311 (2004)
181. T. Gong, Y. Zhang, W. Liu, J. Wei, Y. Jia, K. Wang, D. Wu, M. Zhong, Reinforcing the bandaged joint of double-walled carbon nanotube strands by intercalation of epoxy resin. Mater. Lett. **62**, 4431–4433 (2008)
182. H. Tohmyoh, S. Fukui, Self-completed Joule heat welding of ultrathin Pt wires. Phys. Rev. B **80**, 155403 (2009)

183. T.-B. Song, Y. Chen, C.-H. Chung, Y. Yang, B. Bob, H.-S. Duan, G. Li, K.-N. Tu, Y. Huang, Y. Yang, Nanoscale joule heating and electromigration enhanced ripening of silver nanowire contacts. ACS Nano **8**, 2804–2811 (2014)
184. A.T. Bellew, H.G. Manning, C. Gomes da Rocha, M.S. Ferreira, J.J. Boland, Resistance of single Ag nanowire junctions and their role in the conductivity of nanowire networks. ACS Nano **9**, 11422–11429 (2015)
185. A. Vafaei, A. Hu, I.A. Goldthorpe, Joining of individual silver nanowires via electrical current. Nano-Micro Lett. **6**, 293–300 (2014)
186. Y. Akada, H. Tatsumi, T. Yamaguchi, A. Hirose, T. Morita, E. Ide, Interfacial bonding mechanism using silver metallo-organic nanoparticles to bulk metals and observation of sintering behavior. Mater. Trans. **49**, 1537–1545 (2008)
187. H. Alarifi, A. Hu, M. Yavuz, Y.N. Zhou, Silver nanoparticle paste for low-temperature bonding of copper. J. Electron. Mater. **40**, 1394–1402 (2011)
188. J.S. Oh, J.S. Oh, J.H. Shin, G.Y. Yeom, K.N. Kim, Nano-welding of Ag nanowires using rapid thermal annealing for transparent conductive films. J. Nanosci. Nanotechnol. **15**, 8647–8651 (2015)
189. Ç.Ö. Girit, A. Zettl, Soldering to a single atomic layer. Appl. Phys. Lett. **91**, 193512 (2007)
190. Y. Peng, T. Cullis, B. Inkson, Bottom-up nanoconstruction by the welding of individual metallic nanoobjects using nanoscale solder. Nano Lett. **9**, 91–96 (2009)
191. Q. Cui, F. Gao, S. Mukherjee, Z. Gu, Joining and interconnect formation of nanowires and carbon nanotubes for nanoelectronics and nanosystems. Small **5**, 1246–1257 (2009)
192. Y. Ma, H. Li, L. Yang, A. Hu, Reaction-assisted diffusion bonding of $Ti_6A_{l4}V$ alloys with Ti/Ni nanostructured multilayers. J. Mater. Process. Technol. **262**, 204–209 (2018)
193. Mafune, J. Am. Chem. Soc. **125**, 1636 (2003)
194. C. Ma, S. Xue, D. Bridges, Z. Palmer, Z. Feng, A. Hu, Low temperature brazing nickel with Ag nanoparticle and Cu-Ag core-shell nanowire nanopastes. J. Alloys Compd. **721**, 431–439 (2017)
195. D. Bridges, R. Xu, A. Hu, Microstructure and mechanical properties of Ni nanoparticle-bonded Inconel 718. Mater. Des. **174**, 107784 (2019)
196. S. Dai, Q. Li, G. Liu, H. Yang, Y. Yang, D. Zhao, W. Wang, M. Qiu, Laser-induced single point nanowelding of silver nanowires. Appl. Phys. Lett. **108**, 121103 (2016)
197. L. Lin, G. Zou, L. Liu, W.W. Duley, Y.N. Zhou, Plasmonic engineering of metal-oxide nanowire heterojunctions in integrated nanowire rectification units. Appl. Phys. Lett. **108**, 203107 (2016)
198. Y. Deng, Y. Bai, Y. Yu, S. Deng, Y. Tian, G. Zhang, C. Zheng, J. Wu, A. Hu, Laser nanojoining of copper nanowires. J. Laser Appl. **31**, 022414 (2019)
199. M. Terrones, F. Banhart, N. Grobert, J.C. Charlier, H. Terrones, P.M. Ajayan, Molecular junctions by joining single-walled carbon nanotubes. Phys. Rev. Lett. **89**, 075505 (2002)
200. H. Shehla, A. Ishaq, Y. Khan, I. Javed, R. Saira, N. Shahzad, M. Maaza, Ion beam irradiation-induced nano-welding of Ag nanowires. Micro Nano Lett. **11**, 34–37 (2016)
201. C. Chen, L. Yan, E.S.-W. Kong, Y. Zhang, Ultrasonic nanowelding of carbon nanotubes to metal electrodes. Nanotechnology **17**, 2192–2197 (2006)
202. S. Hausner, S. Weis, B. Wielage, G. Wagner, Low temperature joining of copper by Ag nanopaste: correlation of mechanical properties and process parameters. Welding World **60**, 1277–1286 (2016)
203. G. Satoh, C. Qiu, S. Naveed, Y. Lawrence Yao, Strength and phase identification of autogenous laser brazed dissimilar metal microjoints. J. Manuf. Sci. Eng. **137** (2015)
204. S.J. Henley, M. Cann, I. Jurewicz, A. Dalton, D. Milne, Laser patterning of transparent conductive metal nanowire coatings: simulation and experiment. Nanoscale **6**, 946–952 (2014)
205. H. Yang, J. Lu, P. Ghosh, Z. Chen, W. Wang, H. Ye, Q. Yu, M. Qiu, Q. Li, Plasmonic-enhanced targeted nanohealing of metallic nanostructures. Appl. Phys. Lett. **112**, 071108 (2018)
206. Y. Li, Y. Li, L. Feng, G. Lu, Metal alloy nanowire joining induced by femtosecond laser heating: A hybrid atomistic-continuum interpretation. Int. J. Heat Mass Transfer **150**, 119287 (2020)

207. A.W. Ghosh, T. Rakshit, S. Datta, Gating of a molecular transistor: electrostatic and conformational. Nano Lett. **4**, 565–568 (2004)
208. C.H. Ahn, A. Bhattacharya, M. Di Ventra, J.N. Eckstein, C.D. Frisbie, M.E. Gershenson, A.M. Goldman, I.H. Inoue, J. Mannhart, A.J. Millis, A.F. Morpurgo, D. Natelson, J.-M. Triscone, Electrostatic modification of novel materials. Rev. Modern Phys. **78**, 1185–1212 (2006)
209. H. Song, Y. Kim, Y.H. Jang, H. Jeong, M.A. Reed, T. Lee, Observation of molecular orbital gating. Nature **462**, 1039–1043 (2009)
210. A. Aviram, M.A. Ratner, Molecular rectifiers. Chem. Phys. Lett. **29**, 277–283 (1974)
211. A.R.I. Aviram, P. Roland, The effect of electric fields on double-well-potential molecules. Ann. N.Y Acad. Sci. **852**, 339–348 (1998)
212. E.R. Brown, J.R. Söderström, C.D. Parker, L.J. Mahoney, K.M. Molvar, T.C. McGill, Oscillations up to 712 GHz in InAs/AlSb resonant-tunneling diodes. Appl. Phys. Letters **58**, 2291–2293 (1991)
213. J.C. Ellenbogen, J.C. Love, Architectures for molecular electronic computers. I. Logic structures and an adder designed from molecular electronic diodes. Proc. IEEE **88**, 386–426 (2000)
214. M. Jurow, A.E. Schuckman, J.D. Batteas, C.M. Drain, Porphyrins as molecular electronic components of functional devices. Coord. Chem. Rev. **254**, 2297–2310 (2010)
215. Z. Chen, B. Lee, S. Sarkar, S. Gowda, V. Misra, A molecular memory device formed by HfO_2 encapsulation of redox-active molecules. Appl. Phys. Lett. **91**, 173111 (2007)
216. M.J. Kumar, Molecular diodes and applications. Recent Patents Nanotechnol **1**, 51–57 (2007)
217. N.J. Tao, in *Nanoscience and Technology: A Collection of Reviews from Nature Journals* (World Scientific 2010), pp. 185–193
218. A. Hu, Q.B. Lu, W.W. Duley, M. Rybachuk, Spectroscopic characterization of carbon chains in nanostructured tetrahedral carbon films synthesized by femtosecond pulsed laser deposition. J. Chem. Phys. **126**, 154705 (2007)
219. S.J. Tans, M.H. Devoret, H. Dai, A. Thess, R.E. Smalley, L.J. Geerligs, C. Dekker, Individual single-wall carbon nanotubes as quantum wires. Nature **386**, 474–477 (1997)
220. P. Avouris, Molecular electronics with carbon nanotubes. Acc. Chem. Res. **35**, 1026–1034 (2002)
221. R. Martel, T. Schmidt, H.R. Shea, T. Hertel, P. Avouris, Single- and multi-wall carbon nanotube field-effect transistors. Appl. Phys. Lett. **73**, 2447–2449 (1998)
222. K. Sotthewes, V. Geskin, R. Heimbuch, A. Kumar, H.J.W. Zandvliet, Research update: molecular electronics: the single-molecule switch and transistor. APL Mater. **2**, 010701 (2014)
223. C. Joachim, J.K. Gimzewski, R.R. Schlittler, C. Chavy, Electronic transparence of a single C_{60} molecule. Phys. Rev. Lett. **74**, 2102–2105 (1995)
224. S. Heinze, J. Tersoff, R. Martel, V. Derycke, J. Appenzeller, P. Avouris, Carbon nanotubes as Schottky barrier transistors. Phys. Rev. Lett. **89**, 106801 (2002)
225. A. Javey, J. Guo, Q. Wang, M. Lundstrom, H. Dai, Ballistic carbon nanotube field-effect transistors. Nature **424**, 654–657 (2003)
226. M.M.J. Treacy, T.W. Ebbesen, J.M. Gibson, Exceptionally high Young's modulus observed for individual carbon nanotubes. Nature **381**, 678–680 (1996)
227. D. Dragoman, M. Dragoman, Terahertz oscillations in semiconducting carbon nanotube resonant-tunneling diodes. Physica E: Low-Dimens. Syst. Nanostruct. **24**, 282–289 (2004)
228. R.R. Pandey, N. Bruque, K. Alam, R.K. Lake. Carbon nanotube—molecular resonant tunneling diode. Phys. Status Solidi (a), **203**, R5–R7 (2006)
229. S. Venkataramani, U. Jana, M. Dommaschk, F.D. Sönnichsen, F. Tuczek, R. Herges, Magnetic bistability of molecules in homogeneous solution at room temperature. Science **331**, 445–448 (2011)
230. S. Di Motta, E. Di Donato, F. Negri, G. Orlandi, D. Fazzi, C. Castiglioni, Resistive molecular memories: influence of molecular parameters on the electrical bistability. J. Am. Chem. Soc. **131**, 6591–6598 (2009)
231. Y. Li, H. Li, Y. Li, H. Liu, S. Wang, X. He, N. Wang, D. Zhu, Energy transfer switching in a bistable molecular machine. Org. Lett. **7**, 4835–4838 (2005)

232. M.S. Madani, M. Monajjemi, H. Aghaei, M. Giahi, Thin double wall boron nitride nanotube: nano-cylindrical capacitor. Orient. J. Chem. **33**, 1213–1222 (2017)
233. J.E. Green, J. Wook Choi, A. Boukai, Y. Bunimovich, E. Johnston-Halperin, E. DeIonno, Y. Luo, B.A. Sheriff, K. Xu, Y. Shik Shin, H.-R. Tseng, J.F. Stoddart, J.R. Heath, A 160-kilobit molecular electronic memory patterned at 1011 bits per square centimetre. Nature **445**, 414–417 (2007)
234. J.R. Pinzon, A. Villalta-Cerdas, L. Echegoyen, in *Unimolecular and Supramolecular Electronics I* (Springer 2011), pp. 127–174
235. G. Wang, Y. Kim, M. Choe, T.-W. Kim, T. Lee, A new approach for molecular electronic junctions with a multilayer graphene electrode. Adv. Mater. **23**, 755–760 (2011)
236. J. Liu, Z. Yin, X. Cao, F. Zhao, A. Lin, L. Xie, Q. Fan, F. Boey, H. Zhang, W. Huang, Bulk heterojunction polymer memory devices with reduced graphene oxide as electrodes. ACS Nano **4**, 3987–3992 (2010)
237. X. Wang, L. Zhi, K. Müllen, Transparent, conductive graphene electrodes for dye-sensitized solar cells. Nano Lett. **8**, 323–327 (2008)
238. M. Freitag, M. Radosavljevic, Y. Zhou, A.T. Johnson, W.F. Smith, Controlled creation of a carbon nanotube diode by a scanned gate. Appl. Phys. Lett. **79**, 3326–3328 (2001)
239. M.A. Hughes, K.P. Homewood, R.J. Curry, Y. Ohno, T. Mizutani, An ultra-low leakage current single carbon nanotube diode with split-gate and asymmetric contact geometry. Appl. Phys. Lett. **103**, 133508 (2013)
240. T. Tsuji, T. Kakita, M. Tsuji, Preparation of nano-size particles of silver with femtosecond laser ablation in water. Appl. Surf. Sci. **206**, 314–320 (2003)
241. M. Hörstmann-Jungemann, J. Gottmann, D. Wortmann, Nano-and microstructuring of SiO_2 and sapphire with fs-laser induced selective etching. J. Laser Micro/Nanoeng. **4**, 135–140 (2009)
242. A. Maurice, L. Bodelot, B.K. Tay, B. Lebental, Controlled, low-temperature nanogap propagation in graphene using femtosecond laser patterning. Small **14**, 1801348 (2018)
243. F. Prins, A. Barreiro, J.W. Ruitenberg, J.S. Seldenthuis, N. Aliaga-Alcalde, L.M.K. Vandersypen, H.S.J. van der Zant, Room-temperature gating of molecular junctions using few-layer graphene nanogap electrodes. Nano Lett. **11**, 4607–4611 (2011)
244. Q. Xu, G. Scuri, C. Mathewson, P. Kim, C. Nuckolls, D. Bouilly, Single electron transistor with single aromatic ring molecule covalently connected to graphene nanogaps. Nano Lett. **17**, 5335–5341 (2017)
245. H.W.C. Postma, Rapid sequencing of individual DNA molecules in graphene nanogaps. Nano Lett. **10**, 420–425 (2010)
246. J. Prasongkit, A. Grigoriev, B. Pathak, R. Ahuja, R.H. Scheicher, Transverse conductance of DNA nucleotides in a graphene nanogap from first principles. Nano Lett. **11**, 1941–1945 (2011)
247. W. Kubo, S. Fujikawa, Au double nanopillars with nanogap for plasmonic sensor. Nano Lett. **11**, 8–15 (2011)
248. E. Braun*, K. Keren, From DNA to transistors. Adv. Phys. **53**, 441–496 (2004)
249. E. Braun, Y. Eichen, U. Sivan, G. Ben-Yoseph, DNA-templated assembly and electrode attachment of a conducting silver wire. Nature **391**, 775–778 (1998)
250. J. Richter, M. Mertig, W. Pompe, I. Mönch, H.K. Schackert, Construction of highly conductive nanowires on a DNA template. Appl. Phys. Lett. **78**, 536–538 (2001)
251. R. Seidel, M. Mertig, W. Pompe, Scanning force microscopy of DNA metallization. Surface Interface Anal. **33**, 151–154 (2002)
252. K. Keren, R.S. Berman, E. Braun, Patterned DNA metallization by sequence-specific localization of a reducing agent. Nano Lett. **4**, 323–326 (2004)
253. K. Keren, M. Krueger, R. Gilad, G. Ben-Yoseph, U. Sivan, E. Braun, Sequence-specific molecular lithography on single DNA molecules. Science **297**, 72–75 (2002)
254. K. Keren, R.S. Berman, E. Buchstab, U. Sivan, E. Braun, DNA-templated carbon nanotube field-effect transistor. Science **302**, 1380–1382 (2003)

255. Y. Ye, L. Chen, X. Liu, U.J. Krull, DNA and microfluidics: building molecular electronics systems. Anal. Chim. Acta **568**, 138–145 (2006)
256. L. Li, M. Hong, M. Schmidt, M. Zhong, A. Malshe, B. Huis in't Veld, V. Kovalenko, Laser nano-manufacturing—State of the art and challenges. CIRP Ann. **60** 735–755 (2011)
257. C. Barner-Kowollik, M. Bastmeyer, E. Blasco, G. Delaittre, P. Müller, B. Richter, M. Wegener, 3D laser micro- and nanoprinting: challenges for chemistry. Angewandte Chemie Int. Edn. **56**, 15828–15845 (2017)
258. T. Gissibl, S. Thiele, A. Herkommer, H. Giessen, Two-photon direct laser writing of ultracompact multi-lens objectives. Nat. Photon. **10**, 554–560 (2016)
259. C. Liao, W. Anderson, F. Antaw, M. Trau, Two-photon nanolithography of tailored hollow three-dimensional microdevices for biosystems. ACS Omega **4**, 1401–1409 (2019)
260. K.S. Worthington, A.-V. Do, R. Smith, B.A. Tucker, A.K. Salem, Two-photon polymerization as a tool for studying 3D printed topography-induced stem cell fate. Macromol. Biosci. **19**, 1800370 (2019)
261. Z.B. Wang, N. Joseph, L. Li, B.S. Luk'Yanchuk, A review of optical near-fields in particle/tip-assisted laser nanofabrication. Proc. Inst. Mech. Eng. Part C: J. Mech. Eng. Sci. **224**, 1113–1127 (2010)
262. W. Guo, Z.B. Wang, L. Li, D.J. Whitehead, B.S. Luk'yanchuk, Z. Liu, Near-field laser parallel nanofabrication of arbitrary-shaped patterns. Appl. Phys. Lett. **90**, 243101 (2007)
263. S.M. Huang, M.H. Hong, B.S. Luk'yanchuk, Y.W. Zheng, W.D. Song, Y.F. Lu, T.C. Chong, Pulsed laser-assisted surface structuring with optical near-field enhanced effects. J. Appl. Phys. **92**, 2495–2500 (2002)
264. J.W. Kingsley, S.K. Ray, A.M. Adawi, G.J. Leggett, D.G. Lidzey, Optical nanolithography using a scanning near-field probe with an integrated light source. Appl. Phys. Lett. **93**, 213103 (2008)
265. W. Srituravanich, N. Fang, C. Sun, Q. Luo, X. Zhang, Plasmonic nanolithography. Nano Lett. **4**, 1085–1088 (2004)
266. W. Srituravanich, S. Durant, H. Lee, C. Sun, X. Zhang, Deep subwavelength nanolithography using localized surface plasmon modes on planar silver mask. J. Vacuum Sci. Technol. B: Microelectron. Nanometer Struct. Process. Measure. Phenomena **23**, 2636–2639 (2005)
267. Z.-W. Liu, Q.-H. Wei, X. Zhang, Surface plasmon interference nanolithography. Nano Lett. **5**, 957–961 (2005)
268. J. Dong, J. Liu, G. Kang, J. Xie, Y. Wang, Pushing the resolution of photolithography down to 15 nm by surface plasmon interference. Sci. Rep. **4**, 5618 (2014)
269. S.W. Hell, J. Wichmann, Breaking the diffraction resolution limit by stimulated emission: stimulated-emission-depletion fluorescence microscopy. Opt. Lett. **19**, 780–782 (1994)
270. E. Rittweger, K.Y. Han, S.E. Irvine, C. Eggeling, S.W. Hell, STED microscopy reveals crystal colour centres with nanometric resolution. Nature Photon. **3**, 144–147 (2009)
271. B. Harke, P. Bianchini, F. Brandi, A. Diaspro, Photopolymerization inhibition dynamics for sub-diffraction direct laser writing lithography. Chem. Phys. Chem. **13**, 1429–1434 (2012)
272. B. Harke, J. Keller, C.K. Ullal, V. Westphal, A. Schönle, S.W. Hell, Resolution scaling in STED microscopy. Opt. Express **16**, 4154–4162 (2008)
273. R. Wollhofen, J. Katzmann, C. Hrelescu, J. Jacak, T.A. Klar, 120 nm resolution and 55 nm structure size in STED-lithography. Opt. Express **21**, 10831–10840 (2013)
274. A.G. Vitukhnovsky, D.A. Chubich, S.P. Eliseev, V.V. Sychev, D.A. Kolymagin, A.S. Selyukov, Advantages of STED-inspired 3D direct laser writing for fabrication of hybrid nanostructures. J. Russian Laser Res. **38**, 375–382 (2017)
275. M. Wiesbauer, R. Wollhofen, B. Vasic, K. Schilcher, J. Jacak, T.A. Klar, Nano-anchors with single protein capacity produced with STED lithography. Nano Lett. **13**, 5672–5678 (2013)
276. X. He, T. Li, J. Zhang, Z. Wang, STED direct laser writing of 45 nm width nanowire. Micromachines **10**, 726 (2019)
277. Z. Gan, Y. Cao, R.A. Evans, M. Gu, Three-dimensional deep sub-diffraction optical beam lithography with 9 nm feature size. Nat. Commun. **4**, 2061 (2013)

Chapter 2
Ultrafast Laser Enabling Versatile Fabrication of Surface Micro-nano Structures

Minlin Zhong and Peixun Fan

Abstract Surface micro-nano structures play an important role in realizing various functions at solid surfaces and interfaces. Ultrafast lasers, especially the new-generation high-repetition rate high-power ultrafast lasers, have been proven to be powerful and versatile tools in enabling the fabrication of surface micro-nano structures. Taking the antireflection property as the key and cut-in point, this chapter presents a brief overview on the state-of-the-art and current challenges on the fabrication of surface micro-nano structures. Special focus will be placed on our achievements in the recent years in developing ultrafast laser-based approaches for the general, scalable, and controllable construction of surface micro-nano functional structures, including nanoscale structures, micro-nano dual-scale structures, and macro-micronano-nanowire multiscale structures, and the unique antireflection performances realized by these surface micro-nano structures. This chapter intends to offer readers an integrated tour of ultrafast laser fabrication techniques for surface micro-nano structures and an outlook on their great application potentials.

2.1 Introduction

The research on surface micro-nano structures (SMNSs) on solids is an important route for extending surface engineering studies towards micro-nano scales and also an indispensable branch of the international frontier research of nano science and technology. Investigations of SMNS originate from the observance of fascinating structural properties in nature as well as the research efforts devoted to understanding the mechanisms behind them. Through billions of years of evolution, biological systems routinely produce micro-nano structured surfaces with useful properties [1–4], such as the self-cleaning effect of lotus leaves by micropapillae and branch-like nanostructure [5], the structural colors of butterfly wings by periodic hierarchical

M. Zhong (✉) · P. Fan
School of Materials Science and Engineering, Laser Materials Processing Research Center, Tsinghua University, Beijing, China
e-mail: zhml@tsinghua.edu.cn

A. Hu (ed.), *Laser Micro-Nano-Manufacturing and 3D Microprinting*, Springer Series in Materials Science 309, https://doi.org/10.1007/978-3-030-59313-1_2

microstructures [6, 7], and the antireflection (AR) performance of moth eyes by two-dimensional sub-wavelength structures [7]. All of these amazing surface structures have aroused devouring curiosity of scientists as well as engineers to learn from nature and provided enormous inspiration for them to mimicking these unprecedented properties for the real-world applications. Currently, the research of SMNS has involved multiple disciplines and provided an effective bridge connecting surface engineering techniques to advanced materials, functional surfaces, and intelligent devices, exhibiting great potentials in wide practical fields.

As a typical representative of the properties of SMNS, optical antireflection has essential importance for a variety of critical applications like solar energy utilization, optoelectronic devices, infrared imaging, stealth, aerospace, etc. Thus, it has been being one of the focuses of worldwide research on SMNS. Since there have been many research and review articles introducing the physical fundamentals of antireflection effect within the past few years [8–10], we will not go deep into the details on that in this chapter. Instead, taking the AR properties as a main reference, we pay special emphasis on the fabrication of various SMNS with different geometrical features, aiming to provide a general description on the relationships among fabrication process, SMNS features, as well as their properties.

In order to fully explore the potential of SMNS, the primary research task is to prepare desired surface micro-nano structural features just according to the application requirements. Over the years, most of the conventional micro-nano fabrication methods including both the top-down and bottom-up strategies have been utilized for producing SMNS [11–14], as shown in Fig. 2.1. Among that, pulsed laser ablation has shown superior advantages in flexible, non-contact, and highly controllable material processing without obvious material dependence, making it very promising in forming micro-nano structures on solid surfaces. In the past decades, various types of pulsed lasers spanning over the timescale of ns to fs and the wavelength range

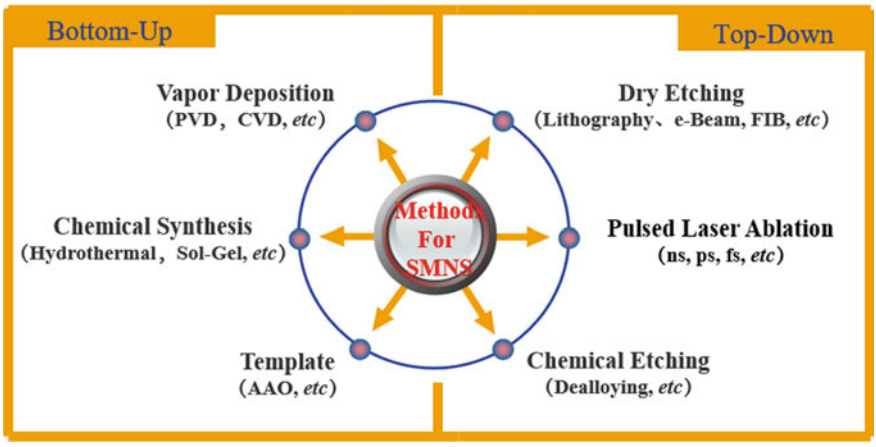

Fig. 2.1 Bottom-up and top-down strategies and the corresponding main methods for fabricating SMNS

of ultraviolet (UV) to infrared have been used in the fabrication of SMNS [15–17]. Laser-assisted surface micro-nano structuring has been increasingly investigated, aiming at the tailoring of surface functionality of variety of materials [18–20], etc.

In comparison with the continuous wave and long pulse (ns ~ ms) lasers, ultrafast lasers with pulse duration in the timescale of ps and fs ranges can induce a unique cold processing effect, based on which the heat affect zone on processed materials can be greatly reduced [21]. Attributing to this advantage, higher processing precision down to the sub-microscale can be realized, and thus, fabrication of SMNS can be conducted in a more controllable manner. The research on ultrafast laser can date back to the 1980s. In the early stage, the mainstream ultrafast lasers are those with narrow pulse durations in the range of 50–150 fs. However, the pulse repetition rates as well as laser power of such kinds of ultrafast lasers are usually limited, making them mainly suitable for fundamental research. Over the nearly past decade, high repetition rate (up to MHz) and high power (up to 10^2–10^3 W) ultrafast lasers keep emerging out, which can fabricate the SMNS in a greatly increase processing efficiency. Although the pulse durations of these kinds of ultrafast lasers are not so narrow as the former types, they can indeed provide not only scientific instruments for fundamental physical and chemical research, but also industrial tools for practical engineering applications.

In recent years, based on these new generation high repetition rate high power ultrafast lasers, we paid special research efforts on developing laser-assisted new methods in general, scalable and controllable construction of metal surface micro-nano functional structures, as shown in Fig. 2.2. Taking the antireflection property as the key and cut-in point, we get deep into the study of photon absorption, transfer, storage, and conversion within the metal surface micro-nano structures. The potential

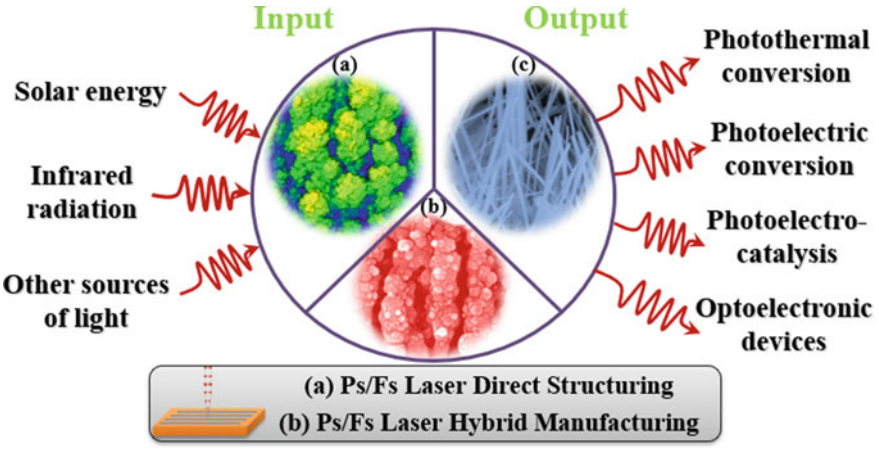

Fig. 2.2 Schematic of research roadmap on laser-assisted construction of metal surface micro-nano structures for photon absorption and conversion applications

applications of the proposed new methods as well as the prepared metal surface micro-nano structures in the fields like photothermal conversion, photoelectrocatalysis, and optoelectronic devices are explored.

In the present chapter, a brief overview of the state-of-the-art and current challenges of antireflection SMNS, especially those fabricated by laser, is provided first. After that, the specific methods we developed with high repetition rate high power ultrafast lasers for fabricating SMNS on metals are introduced in Sect. 2.3. The antireflection performances of the fabricated SMNS are demonstrated in detail in the following part, which is further organized into three sections according to the scale features of SMNS: (Sect. 2.4) antireflection of nanoscale structures, (Sect. 2.5) antireflection of micro-nano dual-scale structures, and (Sect. 2.6) antireflection of multiscale structures. In the last Sect. 2.7, some representative applications of the SMNS we constructed are presented. This chapter intends to offer readers both an integrated tour of laser fabrication technologies for SMNS and a basic realization of their great application prospects.

2.2 Overview of Research

2.2.1 Micro-nano Structures on Semiconductor Surfaces for Antireflection

Silicon is the most widely used semiconductor material. The antireflection structures on Si surfaces are essential for enhancing their light absorption and improving their performances particularly in photovoltaic and photodetector fields. In 1999, Eric Mazur et al. [22] in Harvard University produced conical spike arrays on silicon surfaces through fs laser irradiation and reduce its surface reflectance down to below 10% in the spectrum of UV (0.25 μm) to the near-infrared (2.5 μm), which is called "Black Silicon". After that, a number of similar shaped Si surface structures with varied geometrical dimensions have been fabricated, not only by lasers but also by other methods, in order to continuously improve their antireflection properties [23, 24]. In 2007, for example, Huang et al. [25] prepared arrayed Si nanotips with a base diameter of ~200 nm and lengths up to 16,000 nm through plasma etching, achieving highly efficient antireflection performances over through the ultrabroad spectrum range from 0.25 to 200 μm.

Encouraged by the success of antireflection SMNS on Si, the research on antireflection SMNS on other semiconductor materials has also been extensively conducted, especially on the gallium-based semiconductors like GaAs [26], GaN [27], GaP [28], etc. Song et al. [26] use a two-beam laser interference method to fabricate closely packed and aspect-ratio-controlled subwavelength grating structures on GaAs surfaces, the measured reflectance values of which are below 5% over a wide wavelength range of 300–1100 nm.

2.2.2 *Micro-nano Structures on Metal Surfaces for Antireflection*

Guo et al. [29–32] from the University of Rochester conducted pioneering work on turning highly reflective metal surfaces to be highly absorptive through the fabrication of surface micro-nano structures via fs laser irradiation, producing the so-called black metals, e.g., black platinum, gold, tungsten, titanium, and aluminum. The broadband absorption, typically around 85–95% over the wavelength spectra from UV to near-infrared (NIR), i.e., 0.25–2.5 μm, was attributed to periodic groove structures covered with finer sub-structures at micro- and nanoscales, as shown in Fig. 2.3. Such sub-structures were spontaneously formed during laser ablation with femtosecond pulses.

Guo et al. [32] also have extended their studies on the antireflection properties of metal SMNS to longer wavelength ranges and found that the fs laser-produced SMNS can still be useful in bringing the surface reflectance down to lower values in relative to the intrinsic metal surfaces in the mid-infrared (MIR) and even far-infrared (FIR) spectrum regions, as shown in Fig. 2.4. However, obvious increasing trend in surface reflectance with wavelength was observed.

Many other scientists and researchers have also devoted their efforts to continuously improve the antireflection properties of fs laser formed SMNS and reduce the metal surface reflectance to lower levels [33–35]. For example, Iyengar et al. [35] used a fs laser to produce conical microstructures on Ti surfaces, of which the surface reflection combined with scattering was reduced to low values of ~3% over a broad spectral (0.4–1.6 μm) and angular range (0–60°), with a lowest total reflection of ~1.8% being achieved at certain wavelengths.

Usually, the processing speeds of conventional fs lasers are in the magnitude of μm s^{-1}, making it a rather time-consuming process to fabricate the black metals by simply focusing the fs laser beams on to the sample surfaces. In order to increase

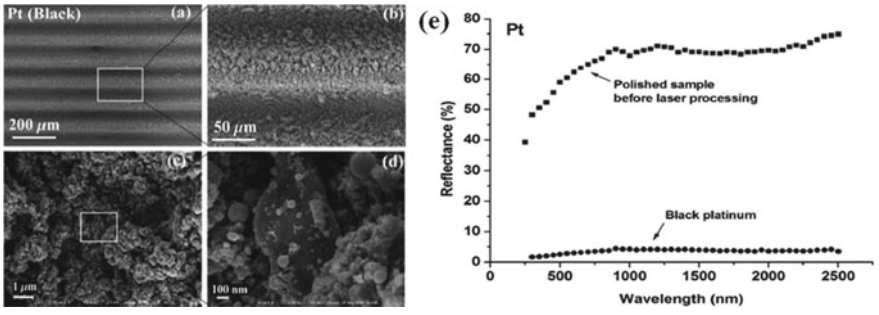

Fig. 2.3 **a**–**d** SEM images showing surface structures of the black platinum produced by fs laser; **e** spectral reflectance of the black and polished platinum samples. Reproduced from [29] with permission from the American Institute of Physics

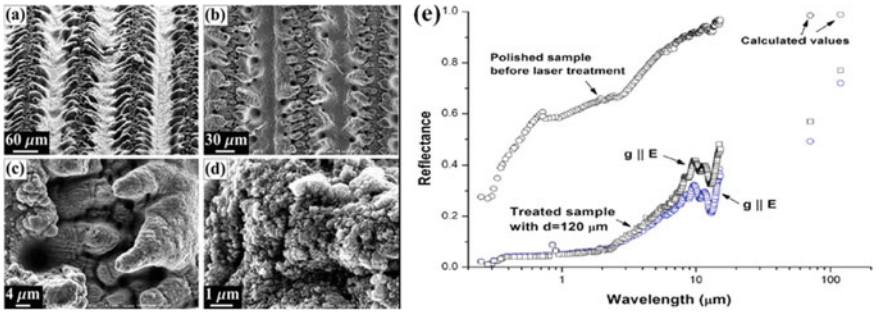

Fig. 2.4 **a–d** SEM images showing surface structures of fs laser processed titanium sample; **e** spectral reflectance as a function of wavelength for both the fs laser processed and the polished titanium samples. Reproduced from [32] with permission from the American Institute of Physics

the processing efficiency, Paivasaari et al. [36, 37] proposed a four-beam interferometric fs laser ablation approach and fabricated hole-array structures on stainless steel and copper surfaces. Although almost total absorption was obtained for stainless steel sample in the 200–2300 nm spectrum, a gradual increase of reflectance to ~50% was observed for copper samples at the wavelength of 800 nm. It is worth noting that nanosecond laser has also been used for blackening copper [38], where steady absorption above 97% in the spectral range of 250–750 nm was realized by forming highly organized periodic microstructures. However, a nearly linear increase of reflectance up to 30% occurred between 750 and 2500 nm.

The antireflection properties of nanoscale structures fabricated by fs laser on metal surfaces have also been investigated. Because their dimensions are comparable with the visible spectrum wavelengths, selective optical responses are usually performed by the nanoscale structures [30]. Dusser et al. [39] created oriented nanostructures on the metal surface, namely nanoripples, which are typically in the range of visible spectrum and smaller than the laser wavelength. Colorful surface effect was induced which was further utilized to generate specific color patterns as shown in Fig. 2.5.

2.2.3 Challenges

The capabilities to harvest light, and correspondingly to eliminate the surface reflection over broadband spectrum without obvious wavelength dependence, are essential for various critical applications. Also, it is one of the major and shared goals of the continuous advances in different antireflection strategies, including from the conventional quarter-wavelength ($\lambda/4$) films to the multilayered film stacks for destructive interference [8, 40]; from the directly moth-eye mimics to nanowire/porous-based dielectric structures for gradient refractive index [41, 42]; from single-scale metallic micro or nano features to multiscale hierarchical structures for light trapping [43, 44]; and from rigorously designed and fabricated metamaterials to their pattern and

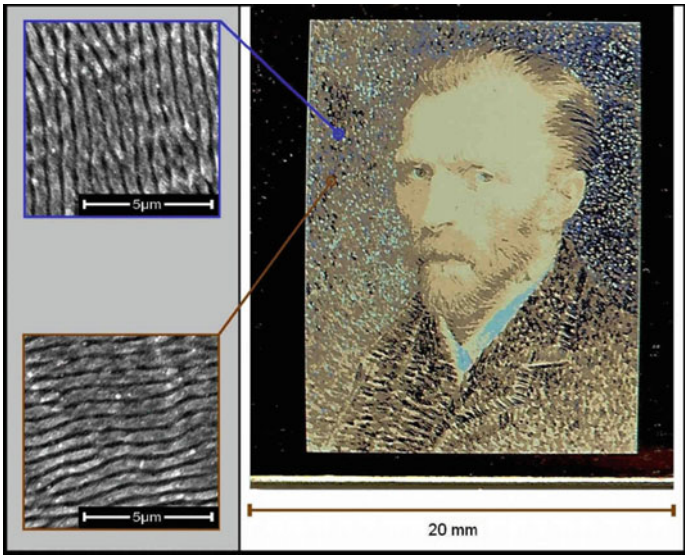

Fig. 2.5 Color effects (on the right) resulting from controlled nanostructures formed by fs laser irradiation on stainless steel surface; SEM images (on the left) of controlled nanostructures with two different orientations. Reproduced from [39] with permission from The Optical Society

dimension varied counterparts for exciting resonance in ε and μ individually [45, 46]. In addition to that, various novel light-harvesting strategies are still emerging for now [47–50].

It is well known that landmark achievement on antireflection research has been achieved by the coatings of vertically aligned carbon nanotubes, reaching ultralow reflectance (<1%) over ultrabroadband spectrum ranges (from UV to far-infrared) [51, 52]. Besides, we have talked in Sect. 2.2.1 that by fabricating nanotip arrays on silicon surfaces, ultrabroadband light harvesting over the UV to THz spectrum ranges has also been realized. Compared to that, however, the research on antireflection properties of metal surfaces is still unsatisfactory. Surface engineering methods to reach antireflection on metal surfaces, meeting both broadband effectiveness and ultralow reflectance requirements, are still in great need.

From the viewpoint of micro-nano structure manufacturing, great challenges exist in the designable, predictable, controllable, as well as scalable fabrication of surface micro-nano structures until now. Beyond that, it is the continuous pursuit of researchers to further develop general strategies and techniques for fabricating surface micro-nano structures on various materials.

Based on this background, our research is aiming to tune the light manipulation properties of metal surface via SMNS constructed by the new generation high repetition rate high power ultrafast lasers (ps and fs). Correspondingly, the following sections will introduce in detail the recent progresses we achieve on the fabrication, functionalization, and application of metal surface micro-nano structures.

2.3 Fabrication of Metals Surface Micro-nano Structures

2.3.1 Fabrication of Metal Surface Nanoripples and Nanoparticles

The formation of LIPSS (i.e., laser-induced periodic surface structures) under laser irradiation is a well-known phenomenon and has been being studied since years ago. As a special type of LIPSS, nanoripples with spatial periodicities obviously shorter than the irradiation laser wavelengths have exhibited many unique physical properties and thus attracted numerous research interests. With the high repetition rate high power ultrafast lasers, we have also produced nanoripples on metal surfaces. Figure 2.6a shows a typical SEM image of these nanoripples. Through continuous laser scanning where the adjacent laser tracks were partially overlapped to each other, continuous and long ripples perpendicular to the linear polarization vector of the laser beam can be produced. Figure 2.6b shows a AFM image of the nanoripples, which have clear contours. From the cross-sectional profile shown in Fig. 2.6c, it can be seen that the nanoripples have an average height of 270 ± 22 nm and an average periodicity of 750 ± 31 nm, which is significantly smaller than the wavelength of laser utilized (1064 nm).

Another major type of nanoscale feature generated by the high repetition rate high power ultrafast lasers is nanoparticles. Our investigations show that the nanoparticle distributions on metal surfaces can be effectively controllable by sequentially changing the ultrafast laser processing parameters. Figure 2.7 demonstrates typical morphologies of nanoscale features produced under ultrafast laser on copper, where nanoparticles are found to be existing together with irregular surface nanostructures. Most nanoparticles are spherical in shape, with their diameters varying from a few to over a hundred nanometers. Those nanoparticles distribute randomly over the nanostructured copper surfaces, with no obvious orientations. With a relatively lower scanning speed, like 2000 mm s^{-1}, and correspondingly higher energy input per area, more abundant nanoparticles tend to be produced, covering the areas both around and among the surface nanostructures.

Statistical analysis on the radius distribution of the nanoparticles was made (see Fig. 2.8). Most of nanoparticles on the nanostructured copper surfaces are smaller than 100 nm in radii. Besides, the radius distributions are pretty narrow, with over 80% of the nanoparticles having a radius below 60 nm for all studied conditions. As the scanning speed decreases, two evolution trends ban be observed. On the one hand, the number densities of nanoparticles in all radius ranges increase simultaneously, resulting in an obvious increase in the total number of nanoparticles from near 50 to about 125 per 10 μm^2. On the other hand, the mean radius of nanoparticles is kept almost constant, showing only a slight increase from 42 to 48 nm. As a consequence, the mean distance between these nanoparticles decreases obviously from ~400 to ~200 nm. Nanoparticle features with similar distributions have also been produced on other metal surfaces like steel, titanium, aluminum, etc. It is well known that metallic nanoparticles can induce unique localized surface plasmon resonance effect,

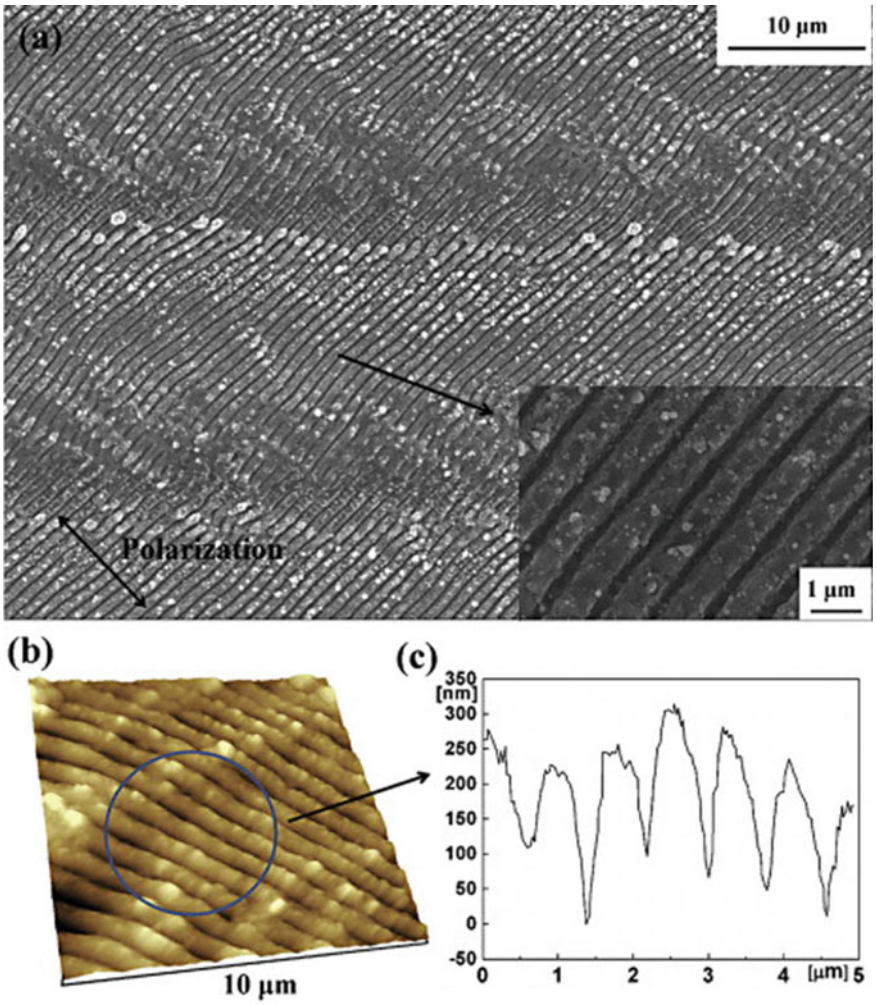

Fig. 2.6 **a** SEM micrograph of nanoripples on copper surface formed by an ultrafast laser; **b** AFM image of the nanoripples; **c** cross-sectional profile of the nanoripples. Reproduced from [53] with permission from Elsevier

for which the response wavelength of nanoparticles is determined by their shapes, diameters, as well as distances. In this consideration, the ultrafast laser micro-nano structuring gives us a good candidate for tuning the optical responses of metal surfaces via controlling the distributions of produced nanoparticles.

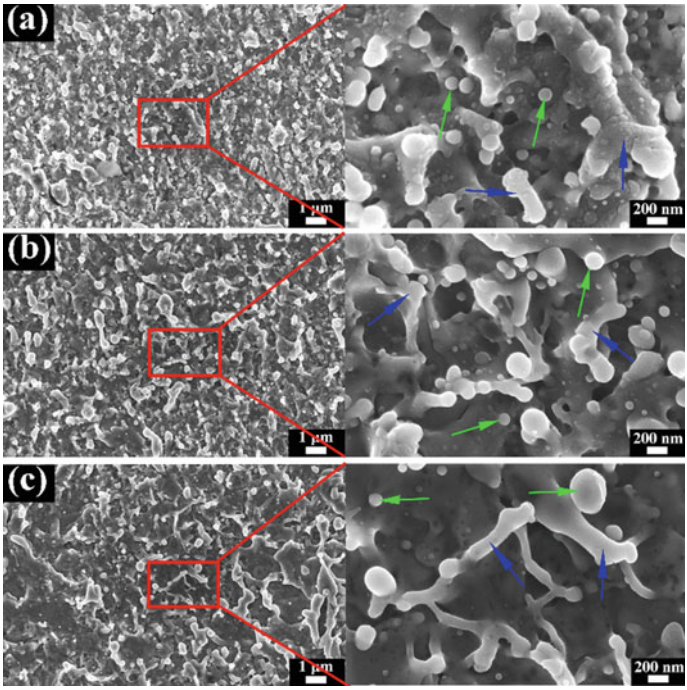

Fig. 2.7 **a**–**c** SEM images of surface features on copper fabricated with a scanning speed of 2000, 3000, and 5000 mm s^{-1}, respectively. The green arrows refer to the nanoparticles while the blue arrows refer to the surface nanostructures. Reproduced from [54] with permission from the American Institute of Physics

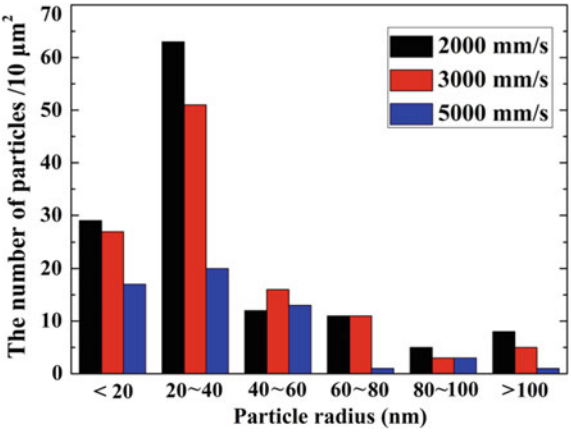

Fig. 2.8 Distribution histograms of nanoparticles on the ultrafast laser nanostructured copper surfaces. Reproduced from [54] with permission from the American Institute of Physics

2.3.2 *Fabrication of Metal Surface Micro-nano Dual-scale Structures*

When more laser energies, i.e., higher laser fluence and more laser pulses, are input into metal surfaces, different kinds of microscale structures can be fabricated by the high power high repetition rate ultrafast lasers. On the surfaces of the microscale structures, there covers abundant nanoscale features, naturally forming the unique micro-nano dual-scale hierarchical structures.

One representative type of structural features for demonstrating this is surface particle structures. As laser energy input increases, particle structures with sequential size changes from nano scale to micro scale have been successfully fabricated. Here, we classify them into five categories: the nano particles with sizes varying from tens (~10^1) to hundreds (~10^2) nm (as discussed in Sect. 2.3.1), the sub-micro particles with sizes in the range of 0.5–1 μm, the fine-micro particles with sizes in the range of 1–10 μm, the microparticles of 10–50 μm in sizes, and the coarse-micro particles larger than 50 μm, as shown in Fig. 2.9. Despite that all these sample surfaces are dominated by particle features, differences in their structural constitutions can be observed. The nano and sub-micro particles are single-scale structures, while the surfaces of microscale particles are covered by sub-microscale features, constituting dual-scale hierarchical structures. Moreover, only the particle feature exists on the nano and sub-micro particle dominating surfaces, while micro pores and voids occupy the space among particles in the three microscale particle dominating surfaces. As the particle sizes change from fine-micro to coarse-micro, the dimensions of the pores also change.

The microparticle size and surface porosity of the three dual-scale particle structures have also been statistically analyzed. As illustrated in Fig. 2.10, the average particle size increases from ~7 μm for the fine-micro particle structures to ~56 μm for the coarse-micro particle structures; meanwhile, the surface porosity shows an obvious decrease from ~54 to ~21%. Therefore, it demonstrates that the coarsening of particle structures will compress the space of pores and voids on metal surfaces, which will alternately influence their optical responses as indicated by the starred curve in Fig. 2.10.

Figure 2.11 shows the typical SEM images of another representative type of ultrafast laser fabricated surface micro-nano dual-scale structures, i.e., the arrayed structures, demonstrating their evolution with laser scanning intervals. As a reference, the diameter of the ultrafast laser focal spot for this particular investigation is ~30 μm. With the scanning interval increasing from smaller to greater than of the focal spot, three kinds of structures were formed on copper surfaces. When scanning intervals were much smaller than the focal spot, the entire metal surfaces were scanned and modified by laser more than once. As a result, irregular coral-like surface structures composed of micro-cavities with random orientations were fabricated (Fig. 2.11a). Such micro-cavities consist of large hollows with dimensions of 30–100 μm where small holes with dimensions of 1–30 μm were embedded, with micro protrusions and particles surrounding them, forming a unique kind of porous structure. When

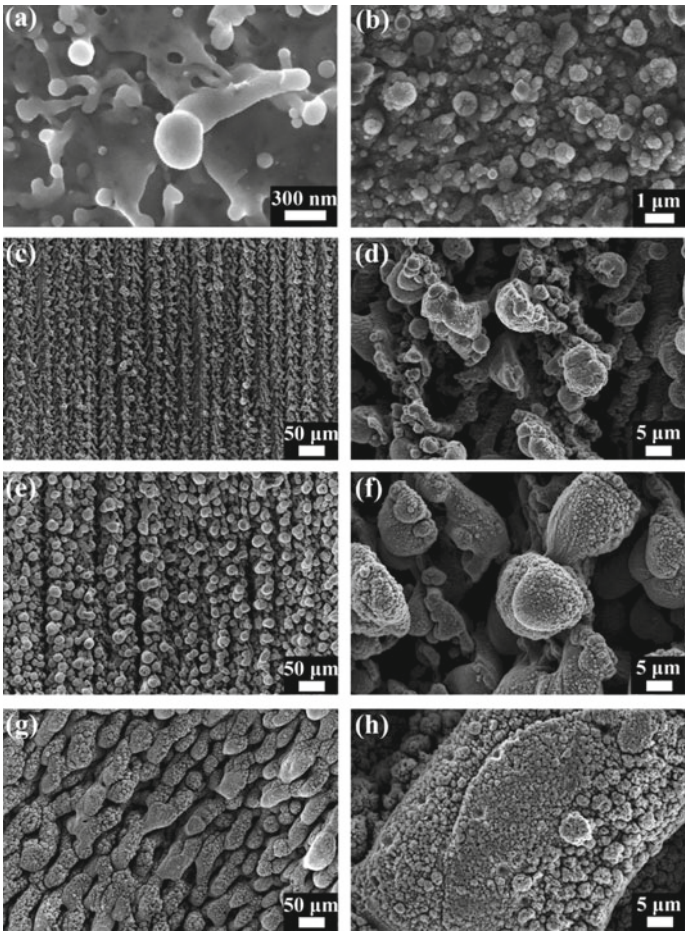

Fig. 2.9 SEM images of surface particle structures with different sizes fabricated by ultrafast laser. **a** Nano particles; **b** sub-micro particles; **c**, **d** fine-micro particles; **e**, **f** micro particles; **g**, **h** coarse-micro particles. Reproduced from [55] with permission from Elsevier

scanning intervals were equivalent to the focal spot, regularly distributed surface structures began to form and uniform hole-array structures with dimension of ~20 μm were produced (Fig. 2.11b). When scanning intervals were larger than the focal spot, only a certain portion of the metal surfaces can be directly irradiated by laser, through which arrayed bell mouth-like structures with plateau-like areas among them were generated (Fig. 2.11c).

It can be seen that not only the dimensions but also the topological forms of SMNS can be easily controllable by adapting the ultrafast laser processing parameters. Thus, large flexibility is offered to us by the high repetition rate high power ultrafast lasers for fabricating the desired SMNS for targeted optical performances.

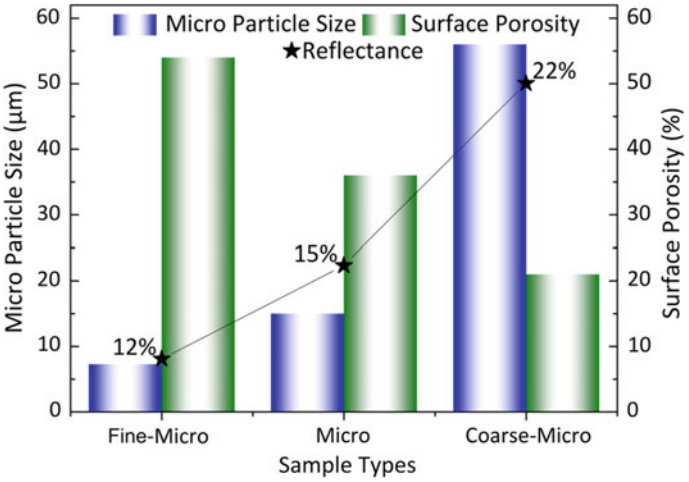

Fig. 2.10 Statistics of the particle size and surface porosity of the micro-nano dual-scale particle structures. Reproduced from [55] with permission from Elsevier

2.3.3 Construction of Metal Surface Macro-micronano-Nanowire Multiscale Structures

As one of the most promising materials for energy conversion and storage, the direct synthesis of oxide nanowires on conductive substrates and their assembly into three-dimensional (3D) self-supporting architectures are of great importance for the improvement of their functions. We have proposed and experimentally demonstrated a top-down and bottom-up combined fabrication strategy, which has the outstanding advantages for preparing 3D self-supporting macro-micronano-nanowire multiscale architectures directly on metal substrates in a well-controlled fashion.

As shown in the schematics in Fig. 2.12a, such a combined approach starts from the ultrafast laser structuring of metal surfaces (Procedure 1). Through this procedure, versatile surface micro-nano structures can be directly generated on bulk metals (Structure 1). After that, the bulk metal samples with the micro-nano structures premade by ultrafast laser are heated in a horizontal-tube furnace for thermal oxidation (Procedure 2). Within this process, the premade micro-nano structures play the role of precursor, which defines the microscopic environment where the metal-oxide nanowires are synthesized. All the structural elements involved in such a combined approach, from the bulk metal substrate, to the ultrafast laser fabricated micro-nanoscale features, and to the oxide nanowires, together construct a macro-micronano-nanowire multiscale architecture (Structure 2).

As a demonstration, Fig. 2.12b–e shows the nanowires grown in situ on the ultrafast laser made one dimensional (1D) periodic structures on Cu surface. The nanowires, with lengths over 10 μm, grow perpendicularly to the sidewalls of the micro gratings and extend to the free space. The chemical composition of the

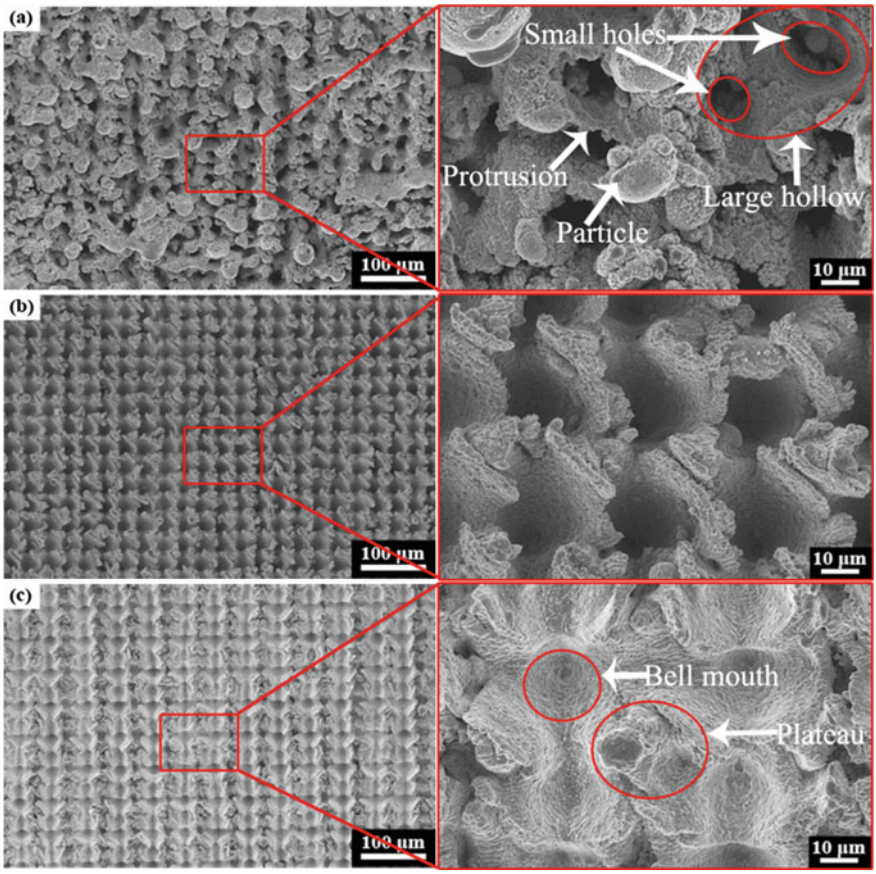

Fig. 2.11 SEM images of ultrafast laser fabricated SMNS on Cu with different scanning intervals: **a** 5 μm, **b** 30 μm, and **c** 50 μm. Reproduced from [56] with permission from The Optical Society

nanowires was analyzed via EDS and XRD characterizations, which identified a main phase constitution of cupric oxide. Serving as a transitional bridge, the relatively larger scale gratings connect the oxide nanowires with the underneath metal substrates and also play the role of skeleton which supports the integrated surface architectures. Resembling the grass taking root in the soil, the oxide nanowires are tightly connected with the skeleton resulting from the in situ growing process. The precursor structures and the nanowires are naturally combined without obvious interface characteristics, making the constructed architectures an intact and robust structural system.

With different types of precursor structures introduced by ultrafast laser, the microscopic environment for growing oxide nanowires also differs. As an illustration, we have intentionally fabricated two kinds of 1D periodic structures through adapting the ultrafast laser structuring process, as shown in Fig. 2.13. Despite that the two grating

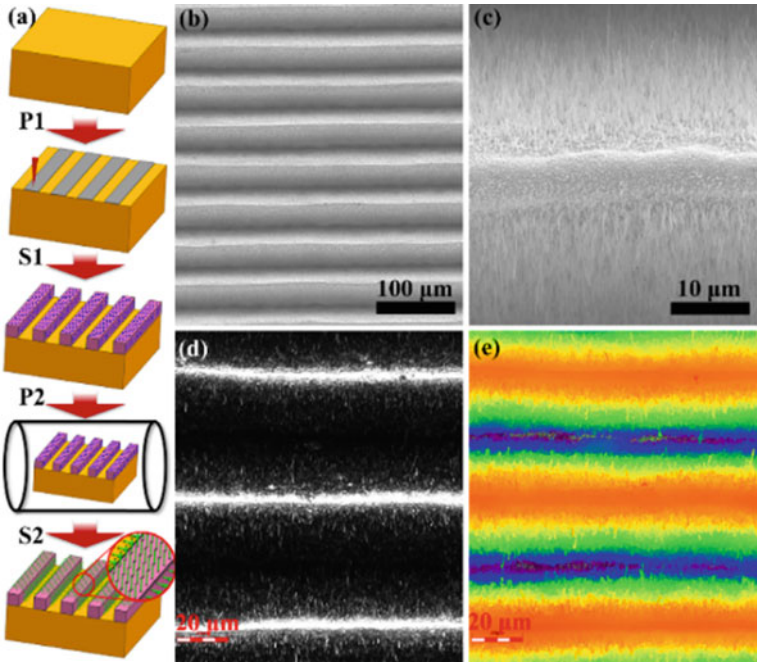

Fig. 2.12 **a** Schematics of the top-down and bottom-up combined fabrication strategy (P1-Procedure 1, S1-Structure 1, P2-Procedure 2, S2-Structure 2). **b**, **c** SEM images of the nanowires grown on the laser fabricated 1D periodic structures. **d**, **e** 3D laser confocal microscope images for the structures in (**b**, **c**) in gray and color charts. Reproduced from [57] with permission from The Royal Society of Chemistry

structures are similar at the microscale, their surfaces are covered with different nanoscale features. Specifically, nano ripples cover the micro gratings in Fig. 2.13a, while nano particles cover the micro gratings in Fig. 2.13e. Massive papillae exist on the former gratings, which are finer and more homogeneous than the particles on the latter gratings. After thermal oxidation, both kinds of 1D periodic structures can grow out oxide nanowires but with distinguishing characteristics. On the micro gratings covered by nano ripples, the oxide nanowires are thinner (50–80 nm in diameter) and longer, which distribute densely on the whole grating surfaces. Due to their high length/diameter ratios, some nanowires even bend at the wire top. In contrast, the nanowires on the micro gratings covered by particle features are thicker (130–250 nm in diameter) and have a relatively sparser distribution; however, they have higher stiffness and look straighter. Such an influence of the precursor structures on the geometries and distributions of oxide nanowires to grow can be utilized for preparing multiscale structures with desired hierarchical features, which is also the advantages of the top-down and bottom-up combined fabrication strategy.

The precursor effect discussed above can also be used for selectively growing oxide nanowires on designated surface areas. For instance, a pattern of “TSINGHUA

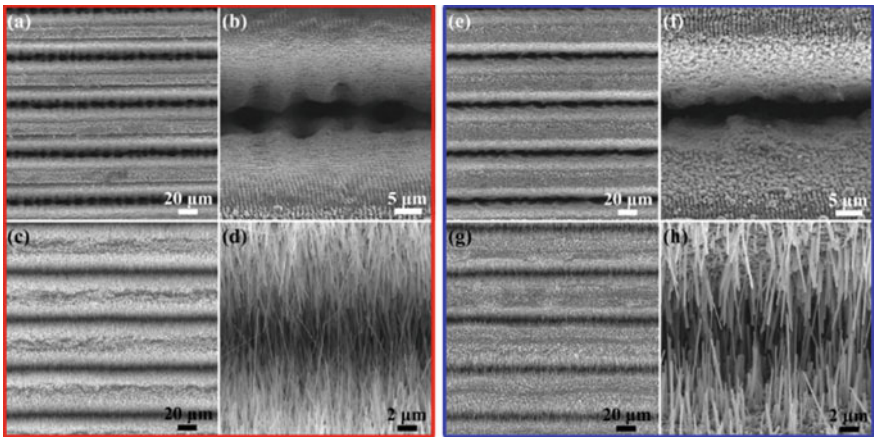

Fig. 2.13 SEM images of nanowires grown on different types of 1D periodic structures fabricated by ultrafast laser. The 1D periodic microscale structures covered with nanoscale ripples in (**a**, **b**) and covered with nanoscale particles in (**e**, **f**); (**c**, **d**); and (**g**, **h**) show nanowires grown on the structures in (**a**) and (**e**), respectively. Reproduced from [57] with permission from The Royal Society of Chemistry

UNIVERSITY" has been made on Cu surface, and the results after thermal oxidation are shown in Fig. 2.14. As can be found, all surface areas with the premade micro-nano structures can grow out numerous and well-aligned oxide nanowires, with multiscale architectures being constructed. Compared to that, the surface areas that were not pre-structured by ultrafast laser can seldom produce oxide nanowires. It is verified that the ultrafast laser structuring can activate metal surfaces to provide microscopic environment from which oxide nanowires preferentially grow.

Based on the above knowledge, the spatial distribution of nanowires can be directly designed by intentionally controlling the dimensions and patterns of the premade structures. For example, two-dimensional (2D) periodic structures with different periodicities, like micro cone arrays, have been fabricated via ultrafast laser. After thermal oxidation, remarkable 3D macro-micronano-nanowire hierarchical structures are successfully prepared, as shown in Fig. 2.15. Specifically, when the periodicities of the arrayed micro cones gradually increase from Fig. 2.15a–c to 2.15e, the potion of surface areas covered by the nanowires decreases. One of the distinguishing advantages of ultrafast laser structuring is that it is a program-controlled approach, which makes the content and distribution of oxide nanowires on metal surfaces also programmable. This is crucial for the achievement of desired physical–chemical properties for various practical applications.

In addition, with the capability of facilitating the growth of oxide nanowires and seamlessly connecting them with larger scale metal structures as well as bulk metal substrates, more kinds and more complex 3D multiscale architectures have been facilely constructed, including 2D periodic structures with spindle-like units, fractal structures composed of particle clusters, and vivid helical structures, as shown

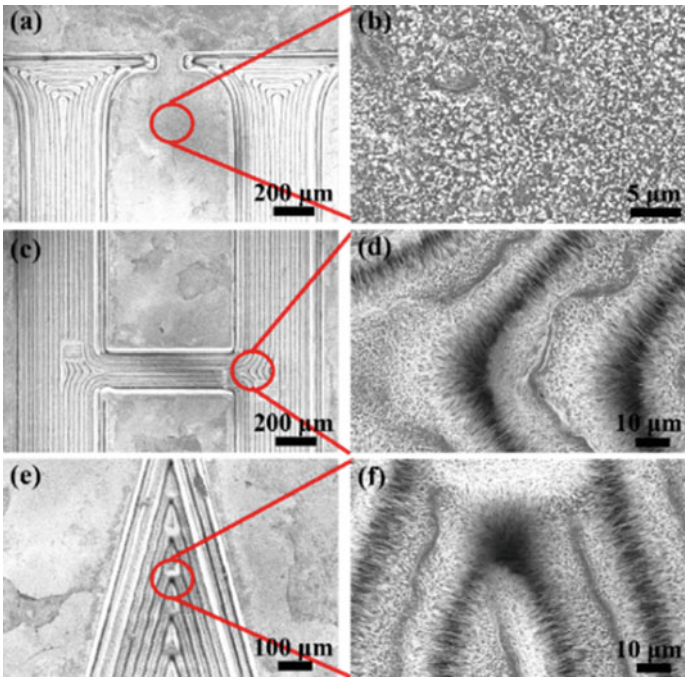

Fig. 2.14 SEM images of nanowires grown on a Cu surface partially structured by ultrafast laser: **a**, **b** unstructured areas; **c**, **d** areas structured in the pattern of letter "H"; **e**, **f** areas structured in the pattern of letter "A". Reproduced from [57] with permission from The Royal Society of Chemistry

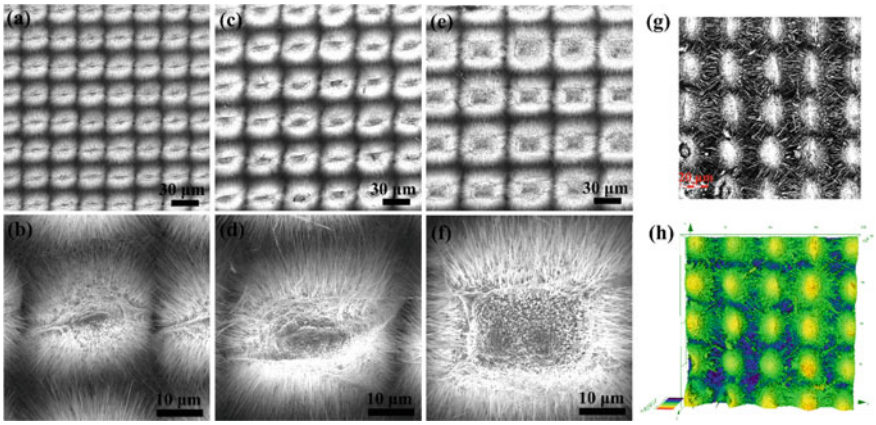

Fig. 2.15 SEM images of nanowires grown on 2D periodic structures of different periodicities fabricated by ultrafast laser: **a**, **c**, **e** in low and **b**, **d**, **f** in high magnifications. **g**, **h** 3D confocal microscope images for structures in (**a**) in gray and colorful charts. Reproduced from [57] with permission from The Royal Society of Chemistry

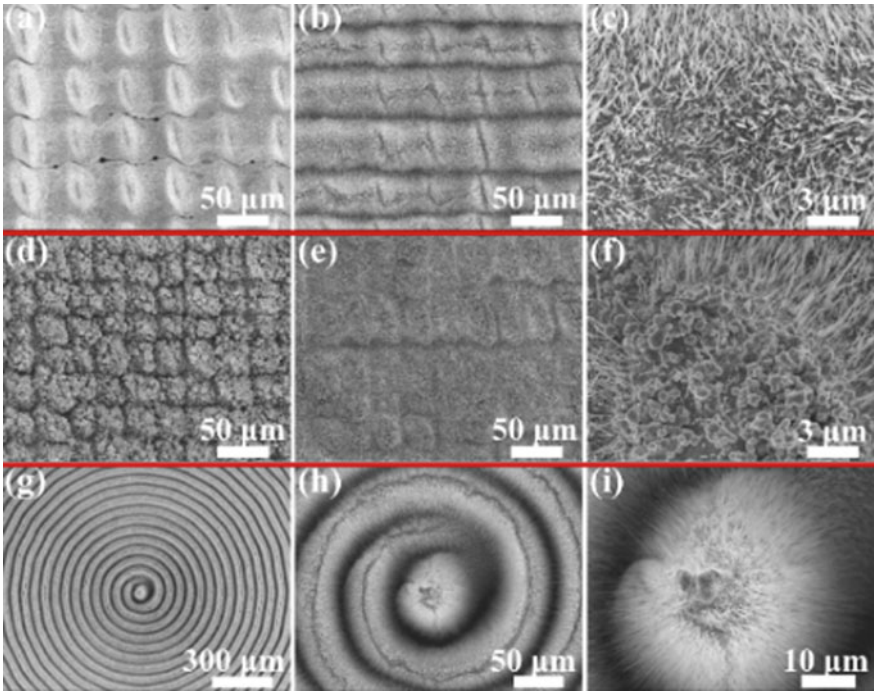

Fig. 2.16 SEM images of nanowires grown on various SMNS produced by ultrafast laser: **a** before and **b**, **c** after growth of nanowires on spindle-like structures; **d** before and **e**, **f** after growth of nanowires on particle cluster structures; **g**, **h**, **i** nanowires grown on helical structures. Reproduced from [57] with permission from The Royal Society of Chemistry

in Fig. 2.16. Although the structural forms of premade micro-nano structures are strikingly different for them, they have succeeded in growing oxide nanowires out of their surfaces without exception.

Another advantage of the ultrafast laser structuring is that it is a unique technique without obvious material dependence. Also, thermal oxidation is an approach that has been widely used for synthesizing nanostructures and nanomaterials with various oxide compositions. On the basis, the ultrafast laser structuring and thermal oxidation combined strategy can be generally applied for the creation of 3D self-supporting architectures on various solid surfaces.

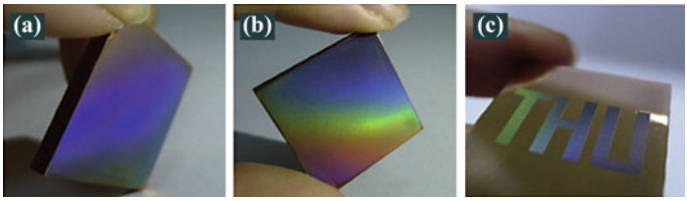

Fig. 2.17 **a**, **b** Photographs of the ultrafast laser fabricated large area (25×25 mm^2) nanoripples on Cu surfaces; **c** photograph of colorful words produced on Cu surfaces. Reproduced from [53] with permission from Elsevier

2.4 Antireflection of Metal Surface Nanoscale Structures

2.4.1 Rainbow-Like Colors of Metal Surface via Nanoripples

As mentioned in Sect. 2.3.1, continuous long and uniformly distributed nanoripples have been produced on metal surfaces in large area by overlapped laser scanning step by step. Figure 2.17 shows that the large area nanoripples perform various colors at different viewing angles, which is a typical optical response of grating type nanostructures in the visible spectrum. Due to the advantageous flexibility of the laser surface structuring method, colorful words can be produced on metal surfaces by scanning particular selected areas. Such an unique kind of rainbow-like structural colors may find applications in the fields of color display, decoration, and identification of codes.

2.4.2 Sequential Colorization of Metal Surfaces via Nanoparticles

Also in Sect. 2.3.1, it has been discussed that the nanoparticle distributions on metal surfaces can be facially tuned by adapting ultrafast laser processing parameters. This characteristic can also be utilized to arouse selective surface antireflection performances of metal surfaces in the visible wavelength range and thus form a colorization effect on metal surfaces.

In particular, under optimized laser parameters, the original shining Cu surfaces can be turned into colorful appearances sequentially varying from black to brown, yellow, green, blue, purple, and pink only when the ultrafast laser scanning speeds are tuned from 100 to 200, 500, 1000, 2000, 3000, and 5000 mm s^{-1}, as demonstrated in Fig. 2.18.

In contrast to the structural colors induced by nanoripples, the colors of nanoparticles will not change with viewing angles (see Fig. 2.19). Besides, reflection spectra of surface nanoparticles have been measured under different incident angles, with the overall trend of the reflection spectra with wavelength remaining consistent except the slight difference in their curve levels. Therefore, it indicates that the selective

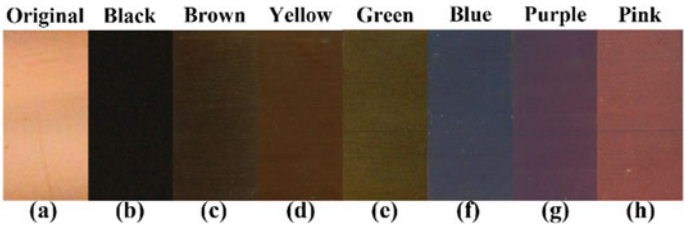

Fig. 2.18 Photographs of polished and ultrafast laser colorized copper surfaces. The scanning speeds for samples **b**–**h** were 100, 200, 500, 1000, 2000, 3000, and 5000 mm s^{-1}, respectively. The area of all sample surfaces is 10 × 20 mm^2. Reproduced from [58] with permission from the American Institute of Physics

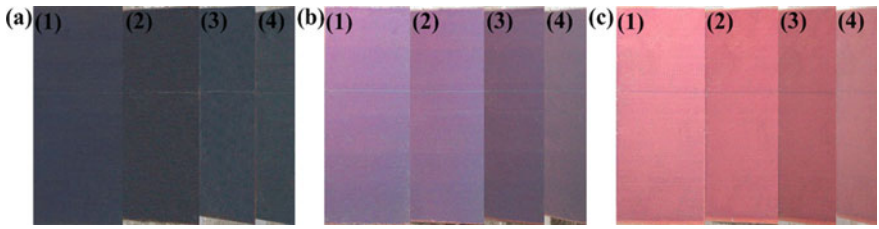

Fig. 2.19 Photographs of the nanostructured copper surfaces at different viewing angles. Samples **a**–**c** correspond to samples **a**–**c** in Fig. 2.7, respectively. The sample tilting angles in (1)–(4) were 0°, 30°, 45°, and 60°, respectively. The area of all sample surfaces is 10 × 25 mm^2. Reproduced from [54] with permission from the American Institute of Physics

spectral responses of nanoparticles in the visible spectrum are irrelevance to the incident angle of the incoming light.

Similar results have also been achieved on other metal surfaces (see Fig. 2.20), sufficiently proving the general applicability of the ultrafast laser sequential colorization method via producing surface nanoparticles.

2.4.3 Colorful Self-cleaning Metal Surfaces via Nanoscale Structures

In addition to the colorization effect, the nanoscale structures on metal surfaces can also render them excellent superhydrophobic as well as self-cleaning properties. Taking the nanoripples, for example, an apparent contact angle up to 153.9 ± 3.2° and a small sliding angle of 11 ± 3° can be realized between their surface and the water droplets, showing obvious superhydrophobicity (see Fig. 2.21). The water droplets could effortlessly move away even when the surface was only slightly tilted, which is attributed to the large amount of nanoscale structural features presenting on the surface.

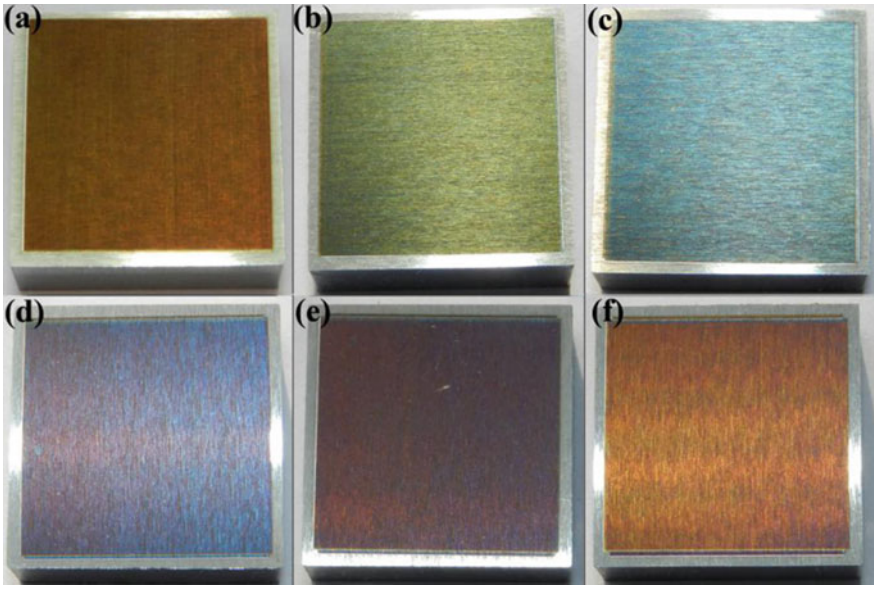

Fig. 2.20 Photographs of ultrafast laser colorized steel surfaces. The scanning speeds for samples **a**–**f** were 1000, 1500, 2000, 2500, 3000, and 3500 mm s^{-1}, respectively. The area of all sample surfaces is 20 × 20 mm^2. Reproduced from [59] with permission from Laser Institute of America

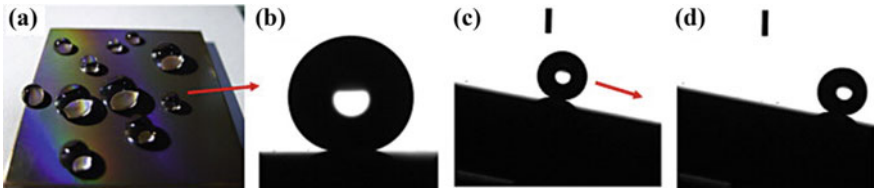

Fig. 2.21 **a**, **b** Optical image of water droplets on a colorful metal surface treated by ultrafast laser; **c**, **d** photographs of a water droplet rolling down when the sample was tilted. Reproduced from [53] with permission from Elsevier

2.5 Antireflection of Metal Surface Micro-nano Dual-scale Structures

2.5.1 Tunable Antireflection via Metal Surface Particle Structures

The reflection spectra of particle structures of different dimensions in the UV–VIS-NIR spectrum range were plotted in Fig. 2.22a. The single-scale nanoparticles show characteristic peaks and valleys in its reflection spectrum in the visible range, as

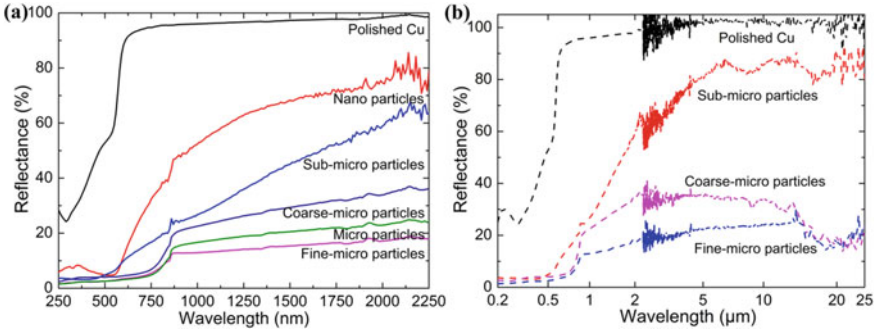

Fig. 2.22 Reflection spectra of the ultrafast laser fabricated surface particle structures in the **a** UV–VIS-NIR and **b** UV-MIR wavelength ranges. Reproduced from [55] with permission from Elsevier

discussed in Sect. 2.4. Approaching into longer wavelengths, the spectrum of the Cu nanoparticles ascends rapidly and tends to steady at a certain level. In contrast, the sub-micro particle structure displays a nearly linear response in its surface reflection to incident light with wavelength around 500–2000 nm. The three micro scale particle structures show similar evolution trends on their surface reflection spectra. In specific, they have achieved broadband antireflection, with their surface reflectance drastically and steadily reduced relative to the polished Cu surface. For the micro scale particles of different sizes, their reflection spectra have been lowered to different levels. The surface average reflectance increases from ~12% for the fine-micro particles to ~22% for the coarse-micro particles, which is positively related to the evolution tendency of particle sizes and negatively related to that of the surface porosity (see Fig. 2.10).

We further measured the optical reflection of the sub-micro, fine-micro, and coarse-micro particles in even longer wavelength spectra (i.e., the MIR range), as presented in Fig. 2.22b. Overall, a continuing evolution trend is shown in all the reflection spectra as in the UV–VIS-NIR spectrum. Specifically, it can be observed that the reflection curve of the sub-micro particles reaches a high level and shows a similar changing trend as the polished Cu surface in the MIR range. The reflectance of the coarse-micro particles firstly rises to a high level of ~40% and then drops back to a similar level as the fine-micro particles after the wavelength of ~15 μm. It is only the fine-micro particles which preserve steady low surface reflectance lower than 20% over through the studied spectrum range of 0.2–25 μm, providing a promising candidate for broadband light absorption and electromagnetic shielding which demands antireflection properties without apparent wavelength dependence.

Figure 2.23 demonstrates the relationships among antireflection properties, particle sizes, and amounts of ultrafast laser pulses input. A constant increase is shown in the particle size from the nano scale ones to the coarse-micro scale ones. However, the most effective antireflection, i.e., minimum surface reflectance over broad wavelength spectrum, is achieved by the particle structure with a medium dimension. Thus, the structural form and dimension need to be adjusted according to the property requirements. The ultrafast lasers offer excellent capabilities in realizing

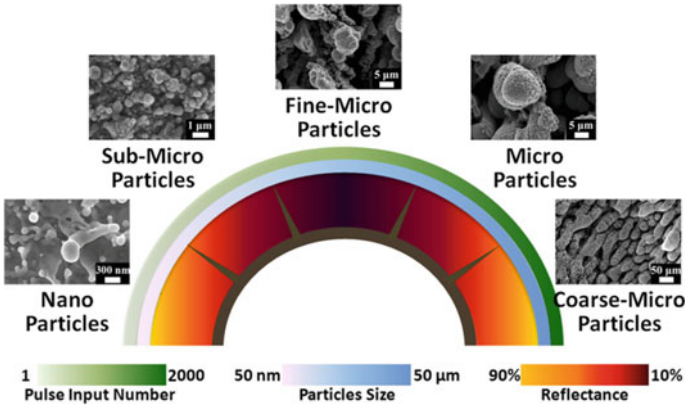

Fig. 2.23 Schematic diagram of the evolution of antireflection properties of ultrafast laser fabricated surface particle structures with respect to the particle sizes. Reproduced from [55] with permission from Elsevier

such an adjustment feasibly and facilely. As validated in our research, the reflection on copper surfaces has been tuned from 10 to 90% in spectral level and from UV to MIR in spectrum range.

2.5.2 Ultrabroadband Antireflection of Micro-nano Dual-scale Structures

The reflection spectra of arrayed micro-nano dual-scale structures in the UV–VIS-NIR spectrum range were shown in Fig. 2.24. As can be seen, the ultrafast laser processing parameters (scanning interval (I), for example) indeed have obvious influence on metal surface reflection via forming different forms of SMNS. The lowest reflectance was obtained with lower scanning intervals, with over 97% absorptance in the UV and visible spectral regions and over 90% absorptance in average in the UV–VIS-NIR regions being obtained. Due to the decreased reflectance in the visible region, the initial shining surface of the polished Cu sample turns to be black. With scanning intervals equivalent to and larger than the laser focal spot, the produced SMNS exhibits weakened antireflection properties especially in the infrared region. This is a natural result caused by the reduction of light trapping structural features presenting on Cu surfaces from the porous coral-like structures to uniform hole arrays then to the open bell mouth-like structures.

Moreover, the dual-scale structural architectures of the ultrafast laser-produced antireflection SMNS make them now only effective for short wavelength spectrum but also effective for much longer infrared wavelength ranges, as shown in Fig. 2.25a, b. Actually, through carefully adapting the ultrafast laser micro-nano structuring process and thus, highly random to the features, the average reflectance

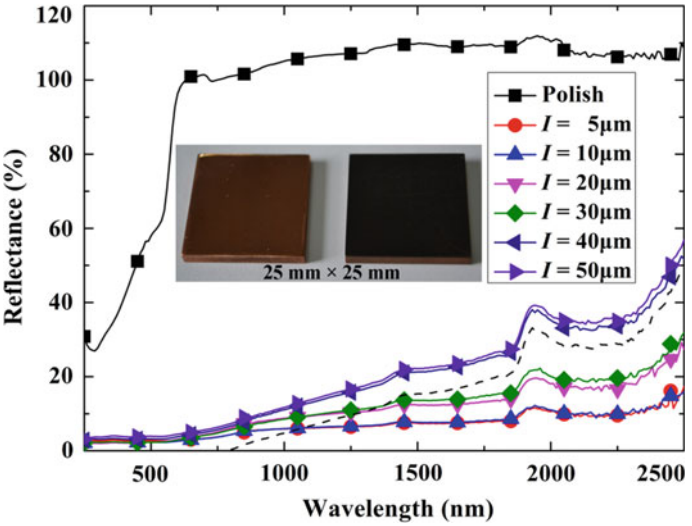

Fig. 2.24 Reflectance of ultrafast laser-produced SMNS on Cu as a function of wavelength (*I* is short for scanning intervals). The inset shows the photographs of polished Cu (on the left) and blackened Cu (on the right) samples. Reproduced from [56] with permission from The Optical Society

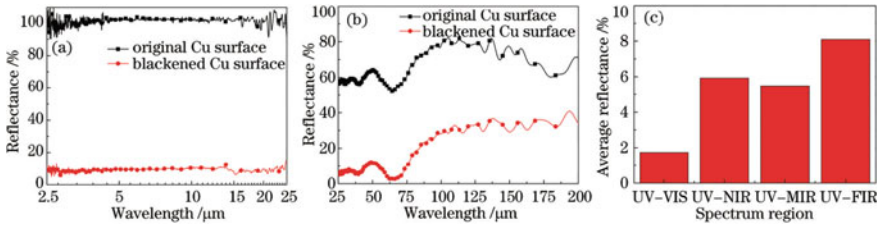

Fig. 2.25 **a** Hemispherical reflectance of original Cu and "black" Cu surfaces in mid-infrared regions; **b** specular reflectance of original Cu and "black" Cu surfaces in far-infrared regions; **c** average reflectance of ultrafast laser fabricate Cu SMNS in different wavelength ranges. Reproduced from [60] with permission from Chinese Laser Press

of metal surfaces in the UV–VIS, UV-NIR, UV-MIR, and UV-FIR regions have been reduced down to around 2%, 6%, 5%, and 8%, respectively, exhibiting ultra-broadband highly effective antireflection properties (see Fig. 2.25c). Besides, these antireflection performances show little change within the incident angle range of 0–60°. To the best of our knowledge to date, this is the broadest and the most stable optical antireflection performances ever reported on metal surfaces.

For the sake of practical applications, we performed different aging tests for the ultrafast fabricated ultrabroadband antireflection SMNS, including the high temperature aging, the Xe light aging, and the salt spray aging tests. No apparent changes in the structural features and chemical compositions have been observed after the tests.

Attributing to that, no degradation on the antireflection properties has occurred, confirming the stability of the ultrafast fabricated SMNS. Therefore, it is demonstrated that the ultrafast laser fabricated antireflection SMNS is advantageous for both its wavelength-independent antireflection performance and its structural robustness, which has essential importance for practical applications.

2.5.3 General Broadband Antireflection of Metal Surfaces via Micro-nano Dual-scale Structures

In addition to Cu, the micro-nano antireflection structures can be conveniently made on other kinds of metal substrates by the high repetition rate high power ultrafast laser in high efficiencies. As shown in Fig. 2.26, we have successfully produced black Al SMNS, black Ti SMNS, and black steel SMNS, whose total reflectance in the UV–VIS-NIR spectrum regions significantly decreases down to around 10%, 5%, and 5%, respectively. Thus, the high repetition rate high power ultrafast laser micro-nano structuring approach is proved to be generally applicable in forming desired SMNS on metal surfaces to realize highly effective optical functions.

2.6 Antireflection of Metal Surface Macro-micronano-nanowire Multiscale Structures

2.6.1 Enhanced IR Antireflection of Metal Surfaces via Multiscale Structures

Here, the 2D periodic surface structural architectures are taken as an example for demonstrating the antireflection properties of the produced macro-micronano-nanowire multiscale structures. When a scanning interval of 40 μm was used with other optimized ultrafast laser conditions, micro cone arrays uniformly distributing on the Cu surface in a periodicity of 40 μm were fabricated, among which were regular micro holes (Fig. 2.27a). These micro cones are covered by plenty of nanoscale features, e.g., nano particles and nano corrugations. After thermal oxidation, oxide nanowires with a dense and uniform distribution radially grow out from the outer surface of the micro cones, turning the micro cones to be fluffy and the micro holes to be blurry, as shown in Fig. 2.27c.

The antireflection properties of the 2D periodic Cu multiscale structures in the MIR region (2.5–25 μm) were measured by a mid-infrared spectroscope equipped with an integrating sphere. As presented in Fig. 2.28, the polished Cu surface without any SMNS has high reflectance throughout the MIR spectrum. With the micro cone arrays fabricated above, the hemispherical reflectance of Cu surface shows a 20–30 percentage-point decrease in comparison with the polished one. However, the

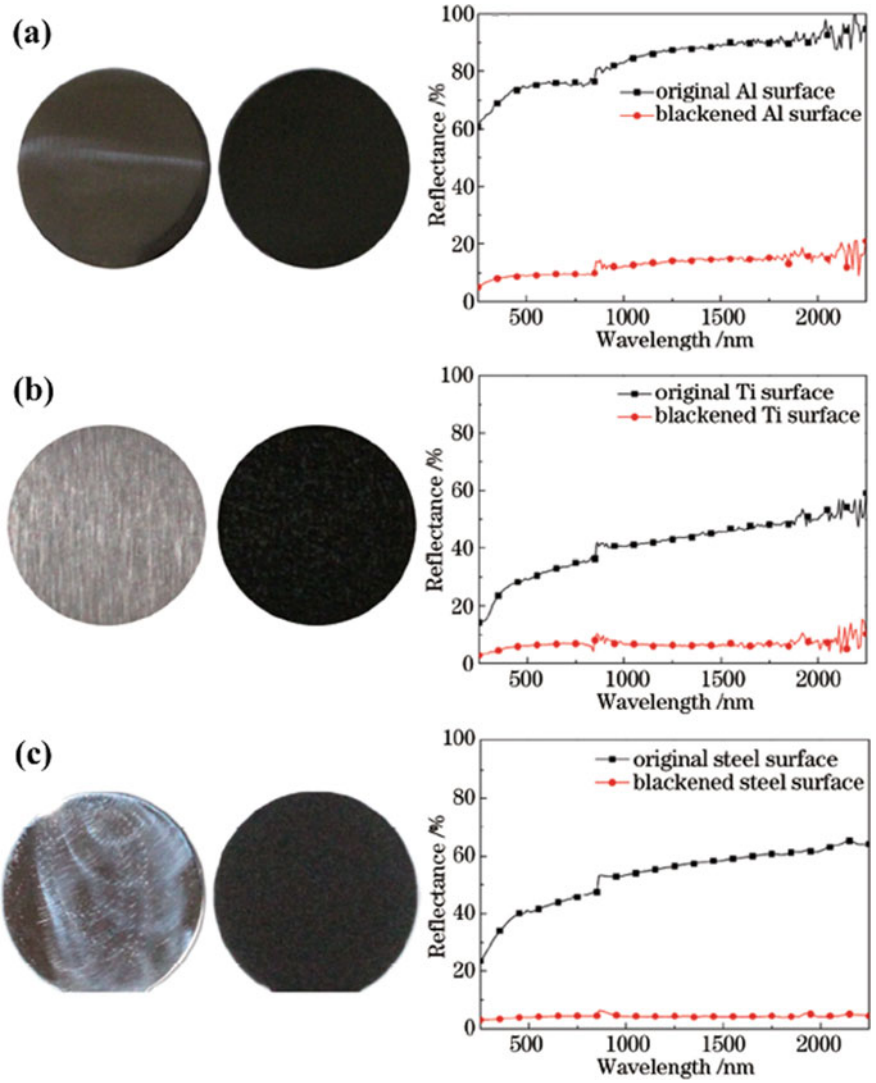

Fig. 2.26 Ultrafast laser fabricated black metal surfaces and their reflection spectra: **a** "Black" Al, **b** "Black" Ti, **c** "Black" Steel. Reproduced from [60] with permission from Chinese Laser Press

surface reflection is still at an approximately equal level at different wavelengths, with the reflectance curve remaining a steady line within the whole studied spectrum. Further, after the growth of oxide nanowires, the hemispherical reflectance declines abruptly over the whole studied wavelength range, with some deep reflectance valleys emerging. Particularly, at the wavelengths around 15–16 μm, the surface reflectance drops to a minimum value of ~2%, achieving a reduction by a factor ~38 and ~48 with respect to the micro cones without nanowires and the polished Cu surface,

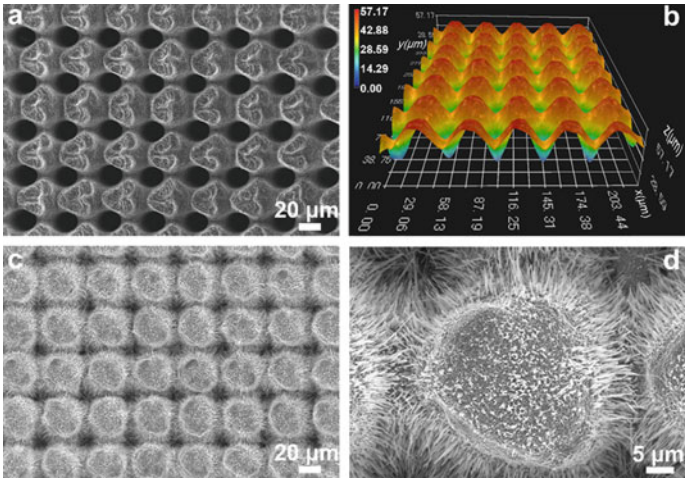

Fig. 2.27 Microscopic characterization of the micro-nano structures as well as nanowires on the ultrafast laser structured Cu surface. Reproduced from [61] with permission from the American Chemical Society

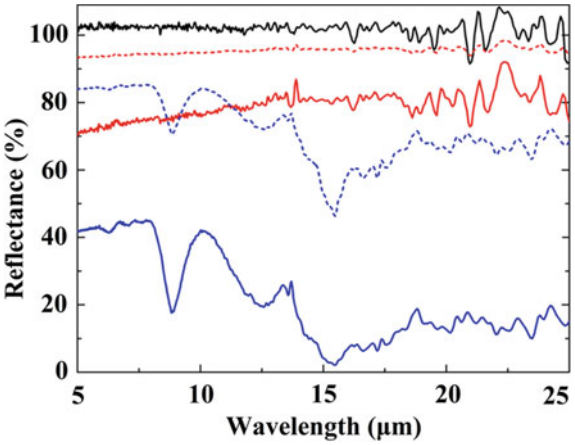

Fig. 2.28 Enhanced IR antireflection via the oxide nanowires grown on ultrafast laser fabricated SMNS. The black, red, and blue solid lines correspond to the measured hemispherical reflectance for the polished Cu surface, the structured Cu surface without oxide nanowires, and the structured Cu surface with oxide nanowires, respectively. Reproduced from [61] with permission from the American Chemical Society

respectively. Given that the bulk Cu is opaque to the infrared light, this yields a 98% absorbance, suggesting that a near-unity infrared antireflection property has been realized.

Furthermore, attributing to the isotropic and symmetric distribution of the Cu SMNS, this broadband infrared antireflection property shall be independent from the incident angles or polarizations of the incoming light. A simulation study on the hemispherical reflectance of the Cu micro cone structures with oxide nanowires at oblique incident angles has been conducted. Also, the specular reflectance of the same Cu SMNS has been experimentally measured at variable incidence angles in the MIR region. The results validate that neither the simulated hemispherical reflectance nor the measured specular reflectance have apparent change at different incident angles up to 60°. It is demonstrated that the multiscale hierarchical structures fabricated via the top-down and bottom-up combined approach can provide us unique infrared antireflection properties.

2.6.2 Mechanism of Enhanced IR Antireflection of Multiscale Structures

Within the macro-micronano-nanowire multiscale structures, the relatively larger features, e.g., micro cones, function as the skeleton of the entire surface architectures. Since these micro cones have spacings between them that are larger than the wavelengths of incident light investigated in this chapter, they can perform the multiple internal reflection and geometrical light trapping effect, which is the main reason accounting for the improved antireflection properties of ultrafast laser fabricated SMNS compared to the polished surfaces. Specifically, the number that the internal reflection occurs for an incident light before escaping the SMNS is determined by their geometrical dimensions. And the overall reflectance of the SMNS should be the product of reflectance for each internal reflection of the incident light within the SMNS.

Here, for the sake of brevity, we assume that the reflectance for each internal reflection is the same, termed as $R0$. Then, the difference between $R0$ of the micro cone arrays without nanowires and that with nanowires is mainly triggered by the oxide nanowire features. It is known that the oxide nanowires can induce phonon dissipation and eliminate the energy of incident photons, resulting in a lower $R0$. Then, the reduced $R0$ gets multiplied through the multiple internal reflection among the micro structures produced by ultrafast laser, reaching a much lower overall surface reflectance, as schematically indicated by the thickness difference of the arrows in Fig. 2.29c, d.

The macro-micronano-nanowire multiscale structures combine the phonon dissipation effect of the oxide nanowires with the light trapping effect of the larger scale metal structural features. Indeed, it is reasonable to regard the whole multiscale structure as an effective medium between the metal surface and the free space. The oxide nanowires are metallurgically connected to the bulk metal through the micro-nano structures produced by ultrafast laser. A gradual and seamless transition in structural features from the nanowires to the micro-nanostructures and to the original

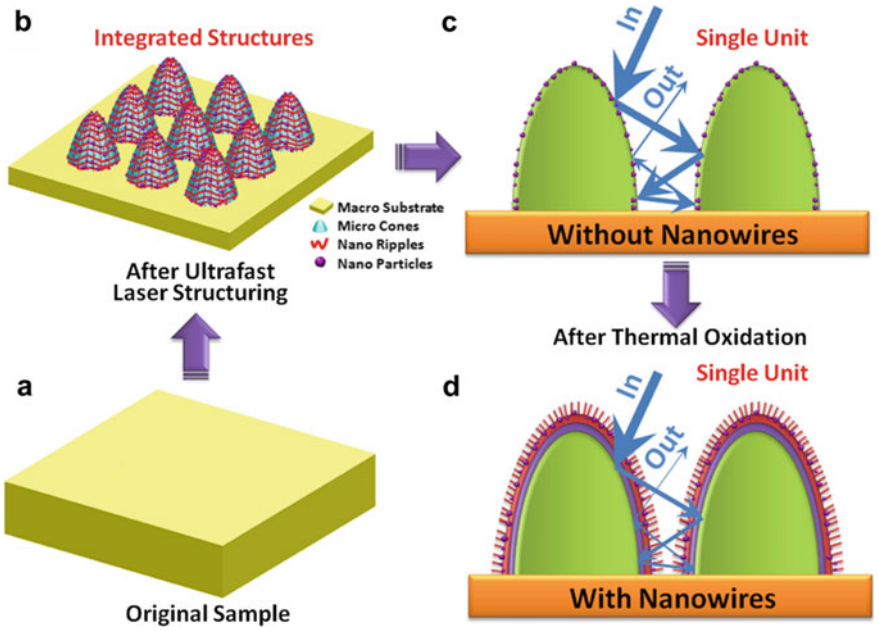

Fig. 2.29 Schematic of the strategy to enhance the antireflection performance of metal SMNS by growing oxide nanowires on their surfaces. **a** Blank Cu sample; **b** integrated micro cone arrays; **c**, **d** unit structure from the micro cone arrays showing the multiple internal reflection effect, where the blue arrows represent the traveling of incident light among the micro cones. Reproduced from [61] with permission from the American Chemical Society

bulk substrate was established. Attributing to that, the multiscale structures play the role of an excellent effective medium, which can dramatically diminish the surface reflection in a broadened wavelength range, giving rise to remarkable antireflection properties.

2.6.3 Tunability of IR Antireflection of Multiscale Structures

The macro-micronano-nanowire hierarchical structures as well as their antireflection performances can be facilely controlled by the ultrafast laser structuring process. As an example, micro cones with a denser distribution than those in Fig. 2.27 and micro petals are fabricated by changing the laser scanning intervals to 30 μm and 50 μm, respectively (Fig. 2.30a, b). After thermal oxidation, nanowires are grown on both their surfaces regardless of their specific morphologies (Fig. 2.30c, d.)

Analog results as in Fig. 2.28 can be observed in the reflection spectra of the denser micro cones and the micro petals (Fig. 2.31a), especially when considering the reflectance difference between the structures with and without nanowires. However,

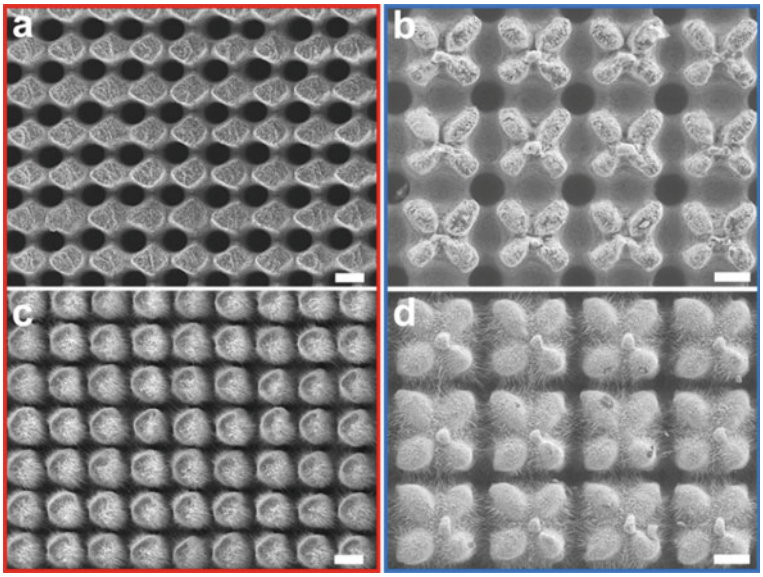

Fig. 2.30 Microstructure characterizations of modified Cu SMNS with a periodicity of 30 μm (**a**, **c**) and 50 μm (**b**, **d**). All scale bars are equal to 20 μm. Reproduced from [61] with permission from the American Chemical Society

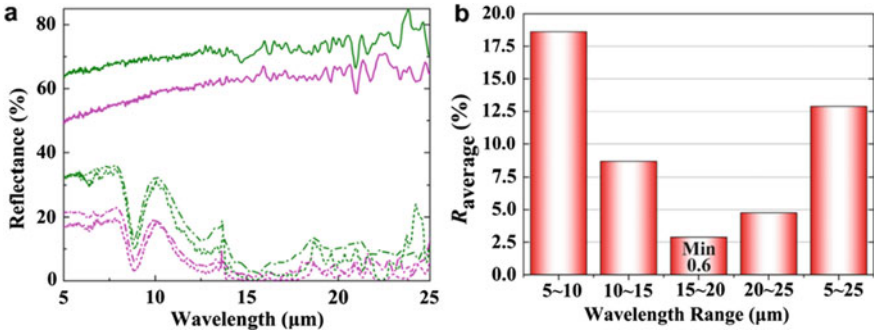

Fig. 2.31 Broadband near-unity antireflection of the modified SMNS in the MIR spectrum, **a** hemispherical reflectance of Cu SMNS with periodicity of 30 μm (magenta lines) and 50 μm (olive lines) **b** average reflectance in different wavelength ranges of Cu SMNS with nanowires with a periodicity of 30 μm. Reproduced from [61] with permission from the American Chemical Society

the reflection spectra of both the denser micro cones and the micro petals have reached obviously lower levels than those in Fig. 2.28. In particular, the reflectance from both structures with nanowires decreases to below 10% in a broad spectrum. The denser micro cones and the micro petals achieve enhanced antireflection performances through a similar physical mechanism. The smaller spacing between the adjacent cones in the denser micro cone arrays and the unique morphology of the micro petals

can both provide Cu surfaces with more effective light trapping effects and consequently reach lower reflectance. For the denser micro cone arrays with nanowires, a reflectance valley of ~0.6% at around the wavelength of 17 μm has been realized, which is one of the lowest experimental results reported on metal surfaces to the best of our knowledge to date. In addition to that, such a near-unity infrared antireflection property has no obvious wavelength dependence, which is broadband effective with hemispherical reflectance steadily below 3% attained over the 14–18 μm wavelength range. In Fig. 2.31b, it is further shown that the average reflectance within the 10–15, 15–20, and 20–25 μm spectra is all below 10%, indicating that nearly 90% of surface reflection has been eliminated by the macro-micronano-nanowire multiscale antireflection structures.

2.7 Applications and Outlook

2.7.1 Photothermal Conversion

As mentioned in Sect. 2.1, we aim to study the photon absorption as well as conversion properties of the metal surface micro-nano structures. It has been shown in the former sections that SMNS with outstanding antireflection properties over broad spectrum as well as broad incident angle ranges has been successfully fabricated through the ultrafast laser-assisted micro-nano structuring approaches we developed. Such extraordinary antireflection properties can greatly enhance the photon trapping capability of metal surfaces and improve their photo absorption efficiency. After that, the absorbed photon energies can be utilized through various means, among which photothermal conversion is one most direct way. In this section, we take the photothermal conversion process as an application instance of the excellent antireflection SMNS we fabricated.

Here, we selected four kinds of typical SMNS for comparison. As shown in Fig. 2.32a–d, when the four kinds of SMNS are produced, the Cu surfaces get darker gradually from Structure 1 to Structure 4, indicating increased light absorption on Cu surfaces. Based on the SEM and laser confocal microscope characterizations, these structures can be classified into two groups. Structures 1 and 2 are constituted of uniform arrays of micro cones as well as micro holes among them. Both the cones and holes have clear contours. On the surfaces of the micro cones, there exist plenty of submicro scale features like corrugations and particles. Structure 2 has higher cones and deeper holes than Structure 1, which is accountable for the contrast in their brightness under the same SEM conditions. Structures 3 and 4 feature with particles ranging from nano to micro scales, which distribute randomly and hierarchically on the copper surfaces and are a highly disordered structural form. Particularly in Structure 4, the particle architectures are more prominent while the minimum structural features are

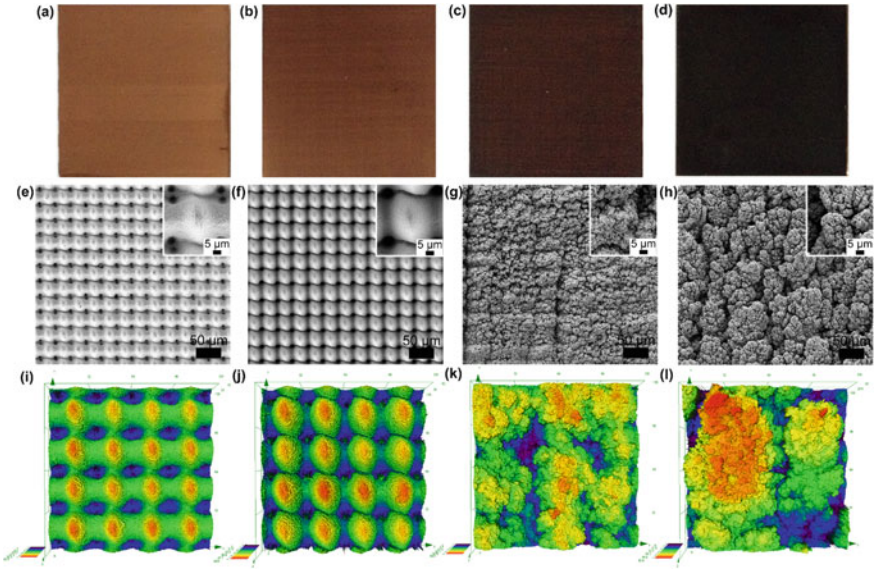

Fig. 2.32 Photographs (top row), SEM images (middle row), and 3D laser confocal microscope images (bottom row) for four kinds of SMNS fabricated by ultrafast laser on Cu. From left column to right: Structure 1, Structure 2, Structure 3, and Structure 4. Reproduced from [62] with permission from The Royal Society of Chemistry

smaller and more shape-diversified, through which a unique kind of cauliflower-shaped architecture has been constructed whose branches and shrubs are formed by clusters of smaller particles.

The light absorption properties of these four SMNS on Cu are shown in Fig. 2.33a. Intrinsically, the polished Cu surface has strong light reflection. The reflection spectrum decreases gradually from Structure 1 to Structure 4, consistent with the changing

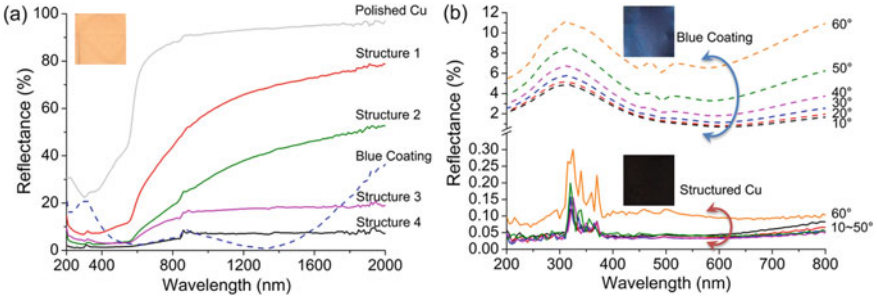

Fig. 2.33 **a** Measured hemispherical reflectance for four kinds of micro-nano structures as well as blue coating on Cu surfaces, **b** comparison of the measured specular reflectance as a function of wavelength and incident angle between Structure 4 and blue coating. Reproduced from [62] with permission from The Royal Society of Chemistry

of brightness on the four Cu surfaces in Fig. 2.32. Compared to the uniform micro cone arrays, the disordered particle aggregates can absorb light more effectively. Specifically, Structure 2 reaches higher light absorption than Structure 1 while Structure 4 reaches higher light absorption than Structure 3. In particular, a steady broadband spectrum with below 10% reflectance from UV to the infrared regions is obtained in Structure 4. An average hemispherical reflectance of ~2% has been realized in the spectrum of 200–800 nm, suggesting that ~98% of the irradiated solar energy in this wavelength range can be collected by the structure. In contrast, the light trapping capability of Structure 4 is even more significant than the commercial antireflection blue coating over broader spectrum ranges.

Further, the specular reflectance under varied incident angles is measured. At higher incident angles, the reflection spectra of the blue coating rise to higher levels successively (see Fig. 2.33b). Compared to that, the reflection spectra of Structure 4, namely the ultrafast laser fabricated cauliflower-shaped structure, stay at much lower levels at all incident angles tested, with no increment being observed till the incident angle of 50°. Even at the incident angle of 60°, its specular reflectance spectrum is only around 0.1%. Such results illustrate that the SMNS fabricated by ultrafast laser, particularly the cauliflower-shaped hierarchical structure, can benefit applications of light absorption with their remarkable capabilities of broadband antireflection without sensitivity to incident angles.

The enhanced light absorption properties of the ultrafast laser fabricated SMNS are more intuitively validated by their thermograms under the irradiation of a solar simulator (analogue to the AM 1.5 Global condition). As shown in Fig. 2.34, all the copper sample surfaces look similar at the starting point under the infrared view. Only slight contrast can be observed between the sample surfaces and the circumjacent environment. After being irradiated for 10 min, obvious differences on their appearances are shown. The temperature rise on the polished Cu surface is very insignificant. The blue coating gets a little more temperature rise but still far from significant. For the SMNS fabricated by ultrafast laser, the grouping characteristics, in accordance with discussed in their structural forms in Fig. 2.32, are also illustrated in their infrared thermograms. The uniform micro cone arrays obtain limited temperature increments, while the disordered hierarchical particle aggregates manifest distinct temperature rises. The latter show bright white appearances instantly when irradiated by the sunlight. Such performances persist at incident angles of 0–60°. Although the heating capabilities of the ultrafast laser fabricated SMNS seem to weaken at higher incident angles, the cauliflower-shaped structure presents the most prominent heating effect all the time. Therefore, it is verified that the unique cauliflower-shaped Cu SMNS is an efficient medium for absorbing solar light and converting it to heat.

For further demonstrating the solar harvesting and the photothermal conversion capabilities of the SMNS produced by ultrafast laser, a water evaporation experiment has been conducted. As Fig. 2.35a shows, the copper samples are employed to absorb the incident light and convert it to thermal energy. Driven by the heated Cu surfaces, accelerated evaporation occurs in the surrounding water. Through such a water evaporation test, the light-to-heat conversion properties of the samples studied can be more

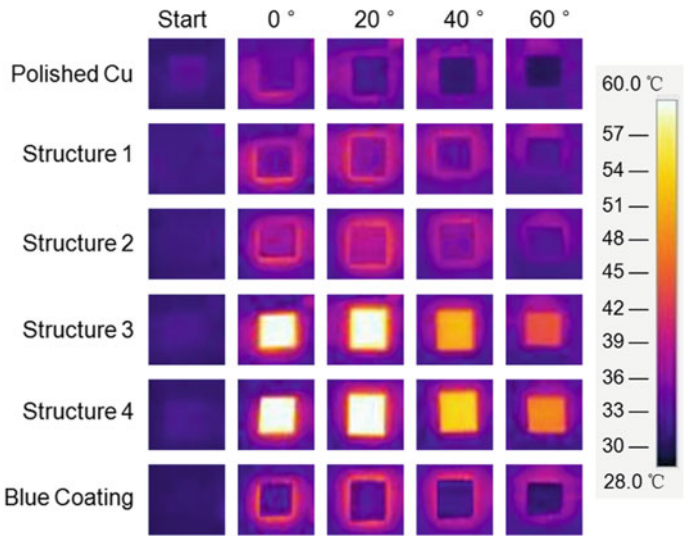

Fig. 2.34 Infrared thermograms of different Cu surfaces after irradiation in varied incident angles for 10 min at a radiation power density of 1 kW m^{-2}. The initial conditions of all sample surfaces (marked as Start) are also shown for comparison. Reproduced from [62] with permission from The Royal Society of Chemistry

comprehensively evaluated, with their overall photothermal conversion efficiencies being measured. Figure 2.35b indicates that when higher light absorptance is reached by the ultrafast laser structured Cu surfaces, higher overall photothermal conversion efficiencies can also be achieved, yielding stronger water evaporation. Within the different types of SMNS, the cauliflower-shaped structure presents a highest overall conversion efficiency of ~62%, realizing a more than twofold enhancement in the solar water evaporation process. Thus, it is confirmed that the cauliflower-shaped copper SMNS can be significantly effective in absorbing the incoming light energy and transferring it to the surrounding substances.

2.7.2 Outlook

Besides photothermal conversion, the ultrafast laser fabricated metal surface micro-nano structures can also find applications in many other fields, especially in the energy-related and optoelectronic areas. For example, our study has shown that nickel surfaces with multiple kinds of micro-nano dual-scale structures can exhibit significantly improved electrocatalytic water splitting performances; titanium surfaces with "macro-micronano-nanowire" multiscale structures can double the photocatalytic degradation efficiency of Ti–TiO_2 material system; copper surfaces with pit arrayed micro-nano hierarchical structures can achieve a SERS enhanced factor of ~10^5; etc.

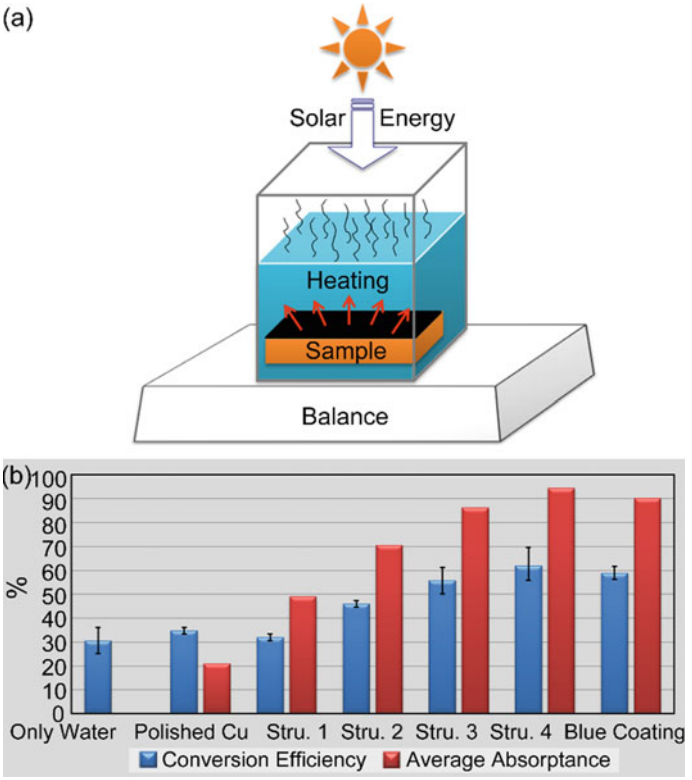

Fig. 2.35 Photothermal conversion of the ultrafast laser fabricated SMNS, **a** schematic of the water evaporation experiment, **b** comparison of the overall photothermal conversion efficiencies and the average absorptance within 200–2000 nm range between different samples. Reproduced from [62] with permission from The Royal Society of Chemistry

Furthermore, both the metal and metal-oxide hybrid micro-nano structures display superhydrophobicity and self-cleaning properties, rendering them the potential to be applied in practical environments. More research efforts should be paid in future to explore the application potential of laser fabricated SMNS in various fields and fully utilize the outstanding physical–chemical properties they have exhibited.

Ultrafast lasers, especially the new generation high repetition rate high power ultrafast lasers, have been proven to be powerful and versatile tools in enabling the fabrication of micro-nano structures on metal surfaces. It can be anticipated that they should also be quite effective for the surface functionalization of many other kinds of materials including semiconductors, dielectrics, ceramics, biomaterials, etc. Also, they provide us a lot more possibilities for precisely processing low-dimensional nanomaterials. The related research and investigations are currently being conducted by scientists from worldwide.

Last but not the least, innovations on laser-based, laser-assisted, and laser-hybrid strategies and methods, especially on the preparation principles and techniques for general, scalable, and controllable construction of surface micro-nano functional structures, are always welcomed.

References

1. C. Neinhuis, W. Barthlott, Characterization and distribution of water-repellent, self-cleaning plant surfaces. Ann. Bot-Lond. **79**, 667–677 (1997)
2. K. Liu, L. Jiang, Multifunctional integration: from biological to bio-inspired materials. ACS Nano **5**(9), 6786–6790 (2011)
3. B. Dean, B. Bhushan, Shark-skin surfaces for fluid-drag reduction in turbulent flow: a review. Phil. Trans. R. Soc. A **368**, 4775–4806 (2010)
4. X. Gao, L. Jiang, Water-repellent legs of water striders. Nature **432**, 36 (2004)
5. K. Koch, W. Barthlott, Superhydrophobic and superhydrophilic plant surfaces: an inspiration for biomimetic materials. Phil. Trans. R. Soc. A **367**, 1487–1509 (2009)
6. A.R. Parker, H.E. Townley, Biomimetics of photonic nanostructures. Nat. Nanotechnol. **2**, 347–353 (2007)
7. P. Vukusic, J.R. Sambles, Photonic structures in biology. Nature **424**, 852–855 (2003)
8. H.K. Raut, V.A. Ganesh, A.S. Nair et al., Anti-reflective coatings: a critical, in-depth review. Energy Environ. Sci. **4**, 3779–3804 (2011)
9. L. Yao, J. He, Recent progress in antireflection and self-cleaning technology—from surface engineering to functional surfaces. Prog. Mater Sci. **61**, 94–143 (2014)
10. A. Deinega, I. Valuev, B. Potapkin et al., Minimizing light reflection from dielectric textured surfaces. J. Opt. Soc. Am. A **28**(5), 770–777 (2011)
11. S. Tsoi, E. Fok, J.C. Sit et al., Surface functionalization of porous nanostructured metal oxide thin films fabricated by glancing angle deposition. Chem Mater. **18**, 5260–5266 (2006)
12. A. Nakajima, K. Hashimoto, T. Watanabe et al., Transparent superhydrophobic thin films with self-cleaning properties. Langmuir **16**, 7044–7047 (2000)
13. P.L. Taberna, S. Mitra, P. Poizot et al., High rate capabilities Fe3O4-based Cu nano-architectured electrodes for lithium-ion battery applications. Nat. Mater. **5**, 567–573 (2006)
14. T. Ito, S. Okazakl, Pushing the limits of lithography. Nature **406**, 1027–1031 (2000)
15. L. Li, M.L. Hong, M. Schmidt et al., Laser nano-manufacturing—state of the art and challenges. CIRP Ann-Manuf. Technol. **60**(2), 735–755 (2011)
16. T.C. Chong, M.H. Hong, L.P. Shi, Laser precision engineering from micro fabrication to nanoprocessing. Laser Photon. Rev. **4**(1), 123–143 (2010)
17. M.J. Abere, M.L. Zhong, J. Kruger, J. Bonse, Ultrafast laser-induced morphological transformations. MRS Bull. **41**(12), 969–974 (2016)
18. I. Etsion, State of the art in laser surface texturing. J. Tribol.-Trans. ASME **127**(1), 248–253 (2005).
19. J.Y. Long, P.X. Fan, D.W. Gong et al., Superhydrophobic surfaces fabricated by femtosecond laser with tunable water adhesion: from lotus leaf to rose petal. ACS Appl. Mater. Interfaces **7**, 9858–9865 (2015)
20. C. Kerse, H. Kalaycıoğlu, P. Elahi et al., Ablation-cooled material removal with ultrafast bursts of pulses. Nature **537**, 84–89 (2016)
21. X. Liu, D. Du, G. Mourou, Laser ablation and micromachining with ultrashort laser pulses. IEEE J. Quantum Electron. **33**(10), 1706–1716 (2002)
22. C. Wu, C.H. Crouch, L. Zhao et al., Near-unity below-band-gap absorption by microstructured silicon. Appl. Phys. Lett. **78**(13), 1850–1852 (2001)
23. J. Escarré, K. Söderström, M. Despeisse et al., Geometric light trapping for high efficiency thin film silicon solar cells. Sol. Energy Mater. Sol. Cells **98**, 185–190 (2012)

24. H. Xu, N. Lu, D. Qi et al., Biomimetic antireflective Si nanopillar arrays. Small **4**(11), 1972–1975 (2008)
25. Y.F. Huang, S. Chattopadhyay, Y.J. Jen et al., Improved broadband and quasi-omnidirectional anti-reflection properties with biomimetic silicon nanostructures. Nat. Nanotechnol. **2**, 770–774 (2007)
26. Y.M. Song, S.Y. Bae, J.S. Yu et al., Closely packed and aspect-ratio-controlled antireflection subwavelength gratings on GaAs using a lenslike shape transfer. Opt. Lett. **34**(11), 1702–1704 (2009)
27. C.H. Chiu, P. Yu, H.C. Kuo et al., Broadband and omnidirectional antireflection employing disordered GaN nanopillars. Opt. Express **16**(12), 8748–8754 (2008)
28. S.L. Diedenhofen, R.E. Algra, E.P.A.M. Bakkers, J.G.Rivas, Mimicking moth's eyes for photovoltaic applications with tapered GaP nanorods, in *Proceedings of SPIE 7772, Next Generation (Nano) Photonic and Cell Technologies for Solar Energy Conversion, 77720M* (2010)
29. A.Y. Vorobyev, C. Guo, Femtosecond laser blackening of platinum. J. Appl. Phys **104**, 053516 (2008)
30. A.Y. Vorobyev, C. Guo, Colorizing metals with femtosecond laser pulses. Appl. Phys. Lett. **92**, 041914 (2008)
31. T.Y. Hwang, A.Y. Vorobyev, C. Guo, Formation of solar absorber surface on nickel with femtosecond laser irradiation. Appl Phys a **108**, 299–303 (2012)
32. A.Y. Vorobyev, A.N. Topkov, O.V. Gurin et al., Enhanced absorption of metals over ultrabroad electromagnetic spectrum. Appl. Phys. Lett. **95**, 121106 (2009)
33. H. Huang, L.M. Yang, S. Bai, J. Liu, Blackening of metals using femtosecond fiber laser. Appl. Opt. **54**, 324–333 (2015)
34. B. Zheng, W. Wang, G. Jiang, X. Mei, Fabrication of broadband antireflective black metal surfaces with ultra-light-trapping structures by picosecond laser texturing and chemical fluorination. Appl. Phys. B **122**, 180 (2016)
35. V.V. Iyengar, B.K. Nayak, M.C. Gupta, Ultralow reflectance metal surfaces by ultrafast laser texturing. Appl. Optics **49**(31), 5983–5988 (2010)
36. K. Paivasaari, J.J.J. Kaakkunen, M. Kuittinen et al., Enhanced optical absorptance of metals using interferometric femtosecond ablation. Opt. Express **15**(21), 13838–13843 (2007)
37. J.J.J. Kaakkunen, K. Paivasaari, M. Kuittinen et al., Morphology studies of the metal surfaces with enhanced absorption fabricated using interferometric femtosecond ablation. Appl. Phys. A **94**, 215–220 (2009)
38. G. Tang, A.C. Hourd, A. Abdolvand, Nanosecond pulsed laser blackening of copper. Appl. Phys. Lett. **101**, 231902 (2012)
39. B. Dusser, Z. Sagan, H. Soder et al., Controlled nanostructures formation by ultrafast laser pulses for color marking. Opt. Express **18**, 2913–2924 (2010)
40. M.A. Kats, R. Blanchard, P. Genevet, F. Capasso, Nanometre optical coatings based on strong interference effects in highly absorbing media. Nat. Mater. **12**, 20–24 (2013)
41. J.Q. Xi, M.F. Schubert, J.K. Kim et al., Optical thin-film materials with low refractive index for broadband elimination of Fresnel reflection. Nat. Photon. **1**, 176–179 (2007)
42. P. Spinelli, M.A. Verschuuren, A. Polman, Broadband omnidirectional antireflection coating based on subwavelength surface Mie resonators. Nat. Commun. **3**, 692 (2012)
43. J. Escarré, K. Söderström, M. Despeisse et al., Geometric light trapping for high efficiency thin film silicon solar cells. Sol. Energy Mater. Sol. Cells. **98**, 185–190 (2012)
44. C.F. Guo, T. Sun, F. Cao et al., Metallic nanostructures for light trapping in energy-harvesting devices. Light-Sci. Appl. **3**, e161 (2014)
45. N.I. Landy, S. Sajuyigbe, J.J. Mock et al., Perfect metamaterial absorber. Phys. Rev. Lett. **100**, 207402 (2008)
46. C.M. Watts, X. Liu, W.J. Padilla Metamaterial electromagnetic wave absorbers. Adv. Mater. **24,** OP98-OP120 (2012)
47. T. Søndergaard, S.M. Novikov, T. Holmgaard et al., Plasmonic black gold by adiabatic nanofocusing and absorption of light in ultra-sharp convex grooves. Nat. Commun. **3**, 969 (2012)

48. T.V. Teperik, F.J. García de Abajo, A.G. Borisov et al., Omnidirectional absorption in nanostructured metal surfaces. Nat. Photon. **2**, 299–301 (2008)
49. Y. Yao, J. Yao, V.K. Narasimhan et al., Broadband light management using low-Q whispering gallery modes in spherical nanoshells. Nat. Commun. **3**, 664 (2012)
50. S.L. Diedenhofen, G. Vecchi, R.E. Algra et al., Broad-band and omnidirectional antireflection coatings based on semiconductor nanorods. Adv. Mater. **21**, 973–978 (2009)
51. Z.P. Yang, L. Ci, J.A. Bur et al., Experimental observation of an extremely dark material made by a low-density nanotube array. Nano Lett. **8**(2), 446–451 (2008)
52. K. Mizuno, J. Ishii, H. Kishida et al., A black body absorber from vertically aligned single-walled carbon nanotubes. PNAS **106**(15), 6044–6047 (2009)
53. J.Y. Long, P.X. Fan, M.L. Zhong et al., Superhydrophobic and colorful copper surfaces fabricated by picosecond laser induced periodic nanostructures. Appl. Surf. Sci. **311**, 461–467 (2014)
54. P.X. Fan, M.L. Zhong, L. Li et al., Angle-independent colorization of copper surfaces by simultaneous generation of picosecond-laser-induced nanostructures and redeposited nanoparticles. J. Appl. Phys. **115**, 124302 (2014)
55. P.X. Fan, M.L. Zhong, B.F. Bai et al., Tuning the optical reflection property of metal surfaces via micro–nano particle structures fabricated by ultrafast laser. Appl. Surf. Sci. **359**, 7–13 (2015)
56. P.X. Fan, M.L. Zhong, L. Li et al., Rapid fabrication of surface micro/nano structures with enhanced broadband absorption on Cu by picosecond laser. Opt. Express **21**, 11628–11637 (2013)
57. P.X. Fan, M.L. Zhong, B.F. Bai et al., Large scale and cost effective generation of 3D self-supporting oxide nanowire architectures by a top-down and bottom-up combined approach. RSC Adv. **6**, 45923–45930 (2016)
58. P.X. Fan, M.L. Zhong, L. Li et al., Sequential color change on copper surfaces via micro/nano structure modification induced by a picosecond laser. J. Appl. Phys. **114**, 083518 (2013)
59. P.X. Fan, M.L. Zhong, C. Lin et al., Sequential colorization of steel surface by ps laser texturing. Int. Congr. Appl. Lasers Electro-Opt. **1**, 700–705 (2013)
60. P.X. Fan, J.Y. Long, D.F. Jiang et al., Study on ultrafast laser fabrication of UV-FIR ultra-broadband antireflection surface micro-nano structures and their properties. Chin. J. Lasers **42**(8), 0806005 (2015)
61. P.X. Fan, B.F. Bai, J.Y. Long et al., Broadband high-performance infrared antireflection nanowires facilely grown on ultrafast laser structured Cu surface. Nano Lett. **15**, 5988–5994 (2015)
62. P.X. Fan, H. Wu, M.L. Zhong et al., Large-scale cauliflower-shaped hierarchical copper nanostructures for efficient photothermal conversion. Nanoscale **8**, 14617–14624 (2016)

Chapter 3
Apertureless Scanning Near-Field Optical Lithography

Ignacio Falcón Casas and Wolfgang Kautek

Abstract Optical nanolithography has experienced substantial advances in the last decades. Lithography resolution by optical methods has been historically limited by light diffraction. One potential approach to surpass this barrier is "apertureless scanning near-field optical lithography". In this method, a scanning probe microscope tip is illuminated by a focused laser beam and the electromagnetic field is strongly enhanced in the vicinity of the tip's apex. This may generate nanomodifications on a solid surface in close proximity with the tip. In this chapter, we review the thermal effects that allow distinguishing the underlying physical mechanisms: near-field optical enhancement and/or thermal surface modification.

3.1 Introduction

Since Synge proposed the first near-field microscope idea in 1928 [1], there have been multiple attempts to overcome the diffraction limit of light. In 1984, Pohl et al. [2] and Lewis et al. [3] independently developed the first scanning near-field optical microscope (SNOM), a combination of a scanning probe microscope (SPM) with a laser beam channeled into a tapered optical fibre, overcoming the diffraction limit [4–9]. Soon it was pointed out that a similar scheme could be used for subwavelength surface nanostructuring [10, 11]. The character of the evanescent near-field leads to a strong spatial electromagnetic field decay both in lateral and vertical directions. This near-field spatial confinement, combined with field enhancement are key elements for near-field optical nanolithography. Several experimental setups have been proposed and implemented during the last two decades, both for SNOM and scanning near-field optical lithography (NFOL). In aperture schemes [12–28], light from a laser source is delivered through an optical fibre with a nanometric hole (about 50–150

I. Falcón Casas · W. Kautek (✉)
Department of Physical Chemistry, University of Vienna,
Währinger Strasse 42, 1090 Vienna, Austria
e-mail: wolfgang.kautek@univie.ac.at

I. Falcón Casas
e-mail: nacmenarg@gmail.com

A. Hu (ed.), *Laser Micro-Nano-Manufacturing and 3D Microprinting*, Springer Series in Materials Science 309, https://doi.org/10.1007/978-3-030-59313-1_3

nm) at the end. The fibre end is used in scanning force microscope (SFM) mode and placed a few nanometers above the surface. Metallic coatings around the tappered fibre end are used to prevent light losses. In apertureless scanning near-field optical lithography [29], a laser beam is focused on a tip placed above a substrate. aNFOL exhibits advantages compared with aperture NFOL [6, 30]. Spatial resolution can be higher in the apertureless case since SPM tips with a radius of 5–10 nm are commercially available. In contrast, it is difficult to fabricate and reproduce fibre apertures smaller than 50 nm. Further, laser intensities are limited because of the danger of damage of the fibre. Small apertures also limit the intensity, with common transmission factors of about 10^{-5}. Finally, optical fibres may absorb in some regions of the spectrum, while apertureless schemes do not have this limitation. Experimental results of aNFOL have demonstrated the ability to generate nanostructures down to 10 nm. A thorough analysis of aNFOL always has to consider thermal effects produced by the laser-tip-substrate interaction.

Scanning probe lithography (SPL) involves mechanical, thermal, optical, electrostatic and chemical interactions between a probe and the surface as in the standard scanning force microscope (SFM), or different combinations of them [31]. Thermal scanning probe lithography (tSPL) e.g. is a thermomechanical direct-write method enabling fast turnaround fabrication of nanostructures. Heated SFM tips are employed to modify structural and chemical properties of surfaces [32, 33] as e.g. the self-amplified depolymerization of an organic resist into the gaseous phase [34].

In this chapter, an optical scanning probe lithography approach is discussed, in particular apertureless scanning near-field optical lithography (aNFOL). Thermal effects are reviewed in order to discriminate near-field optical enhancement effects from thermomechanical phenomena.

3.2 Fundamentals

This section focuses on the fundamentals of apertureless scanning near-field optical lithography (aNFOL), particularly tip enhancement and the relevant parameters of this process.

3.2.1 Near-Field Tip Enhancement

Near-field tip enhancement occurs when a sharp tip is illuminated by an electromagnetic field. This phenomenon has been attributed to several effects based on the principles of the lightning rod, antenna effect, dipole polarizability and plasmon resonance. Controlled by an SPM, the tip is positioned at a distance d from the substrate (typically, a few nanometres). In order to obtain an analytical solution, one can simplify the problem by replacing the tip by a sphere with radius r_0 equal to the tip radius at the apex. In this treatment, electrostatics is considered, neglecting

retardation effects. This assumption is justified because the size of the sphere (typically 10 nm) is much smaller than the laser wavelength. Applying the method of images, the substrate's surface is replaced by an imaginary sphere of radius r_0 at a distance $2(d + r_0)$ between the centres of both spheres. These two spheres form a dipole oriented perpendicular to the surface (z direction). A linear p-polarized laser beam, with an electromagnetic field $\boldsymbol{E}_0$ oscillating at frequency ω, forces this dipole to oscillate along the z direction. This may produce a large surface charge accumulation at the tip's apex. The total polarization is $\boldsymbol{P} = \alpha(\boldsymbol{E}_0 + \boldsymbol{E}_{\text{image}}) = \alpha^{\text{eff}}\boldsymbol{E}_0$, whose effective polarizability along the tip axis α^{eff} can be written as [35]:

$$\alpha^{\text{eff}} = \frac{\alpha(1+\beta)}{1 - \dfrac{\alpha\beta}{16\pi(d+r_0)^3}} \tag{3.1}$$

where $\alpha = 4\pi r_0^3 \dfrac{\varepsilon_t(\omega) - 1}{\varepsilon_t(\omega) + 2}$ is the sphere quasi-static polarizability and $\beta = \dfrac{\varepsilon_s(\omega) - 1}{\varepsilon_s(\omega) + 1}$ represents the quasi-static Fresnel reflection coefficient. ε_s and ε_t are the permittivities of the substrate and tip materials. From 3.1 and 3.2, one can see that the effective polarizability α^{eff} depends on geometrical factors (r_0, d) and on the permittivities of both tip and substrate (ε_t, ε_s).

In a similar fashion, one can consider a more realistic structure and replace the sphere by an elongated ellipsoid of axes a, b, whose geometry is closer to a real SPM tip. Following a similar procedure as before, one obtains an enhancement factor κ [36]:

$$\kappa = 1 + \frac{2\alpha\left(1/R_c^3 + \beta/(2d + R_c)^3\right)}{1 - \left(\alpha\beta/4(d + R_c)^3\right)} \tag{3.2}$$

with the radius of curvature of the tip's apex $R_c = b^2/a$ and the modified polarizability for an elongated ellipsoid $\alpha = R_c^3(\varepsilon - 1)/2$. For certain values of the parameters in (3.2), the enhancement factor κ can acquire high values leading to a strong enhancement of the electromagnetic field.

Numerical simulations predict the existence of near-field tip enhancement, with enhancement factors up to two orders of magnitude [30, 36–47]. This phenomenon has been confirmed by SNOM [43, 48, 49] and aNFOL (see Sect. 3.4) experiments. The enhanced electromagnetic field can be absorbed by the substrate below the tip enabling material modification when sufficient intensities/fluences are applied (Fig. 3.1).

3.2.2 *Parameters Affecting Near-Field Tip Enhancement*

Tip-sample distance is one crucial parameter regarding near-field enhancement, as it has been demonstrated in aSNOM, thermal near-field spectroscopy, and tip-enhanced

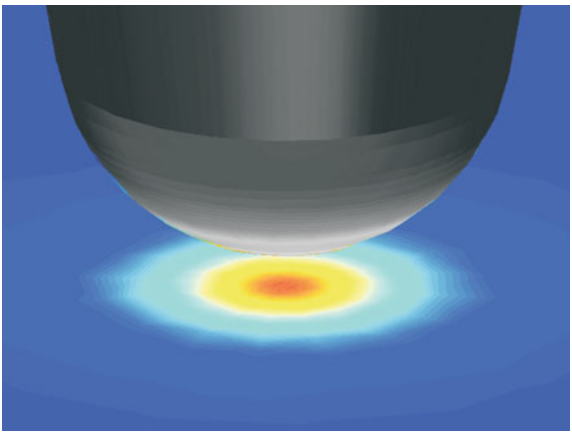

Fig. 3.1 Calculated field enhancement on a gold substrate induced by a silicon tip at a distance of 2 nm by the Boundary Element Method (BEM). The incident laser excites the tip from the left at an angle of 76°. The electric vector field is parallel to the major axis of the tip [51]

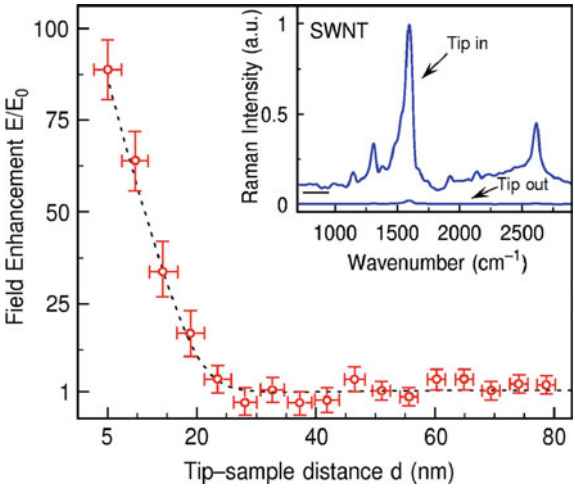

Fig. 3.2 Optical enhancement versus tip-sample-distance derived from the tip-enhanced Raman scattering experiment. Inset: Corresponding Raman spectra for single-wall carbon nanotubes (SWNTs) on a Au surface with the tip at $d = 5$ nm (Tip in) versus tip-sample distance exceeding the near-field interaction length scale (Tip out). Reprinted from [43] with permission of The Optical Society

Raman scattering (TERS). The evanescent nature of near-field elecromagnetic radiation produces an exponential decay of the intensity. The electrostatic dipole leads to an enhancement factor decaying as $1/d^3$ (3.1, 3.2). Simulations and experiments result in typical $1/e$ decay length values of the order of nanometres. For instance, a TERS (Fig. 3.2) [43] and an aSNOM experiment [48] exhibited an $1/e$ near-field decay length of about 20 nm. Simulations show that the near-field lateral confinement is controlled by the tip radius [6, 36, 50].

Another key parameter regarding the enhancement factor is laser polarization. A tip close to a surface generates a dipole oriented in the direction of the tip axis (Sect. 3.2.1). In order to efficiently excite this dipole, the laser electromagnetic field must oscillate along the tip axis. Laser illumination with linear *p*-polarization leads to a maximum enhancement of the near-field below the tip apex (Fig. 3.3). In contrast, for linear *s*-polarization illumination the enhancement factor decreases by several

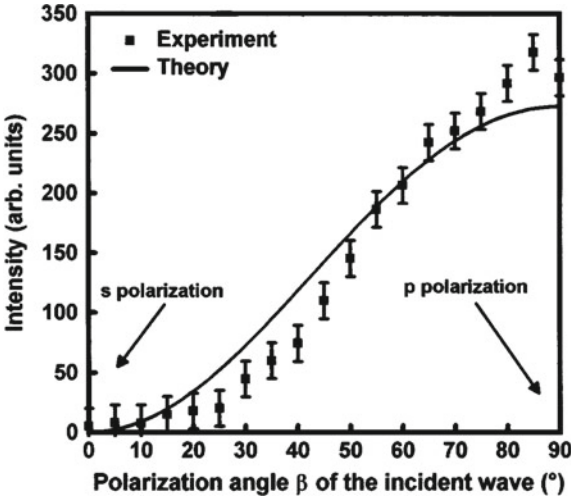

Fig. 3.3 Variations of the intensity scattered by the tip as a function of polarization angle β of the incident wave. Reprinted from [52] with permission of The Optical Society

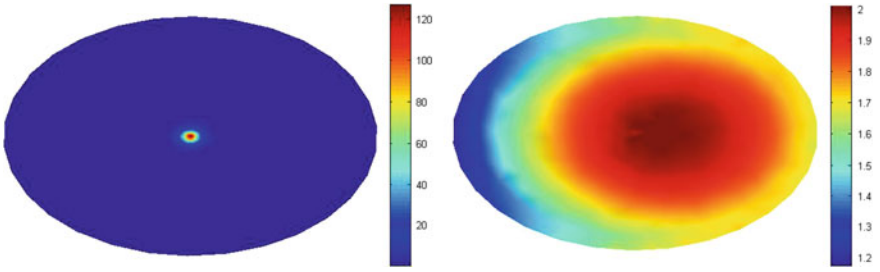

Fig. 3.4 Calculated field-enhancement for *p*-polarization (left) and *s*-polarization (right) [51]

orders of magnitude. This polarization dependence has been predicted in numerical simulations [44, 47, 51, 53–57] (Fig. 3.14) and confirmed by experiments [47, 50, 52].

Besides laser polarization, numerical simulations have shown that the enhancement factor depends on the angle of incidence of the laser beam with respect to the tip axis (Fig. 3.5). Various optimal angles for maximum enhancement have been reported, e.g. $\theta = 30°$ [44, 54], 40° [41] and 45° [43]. Further research has shown that the optimal angle also depends on the tip material, with $\theta = 40°$ for silicon and $\theta = 76°$ for gold-coated silicon tips [47].

The enhancement factor has been calculated for various metallic tip materials (Au, Ag, Cu and Al), wire radii, tip angles and laser wavelengths [46] (Fig. 3.6). Plasmon resonance peaks are observed at visible wavelengths. However, in the near-infrared region of the spectrum ($\lambda = 700$–1000 nm), the enhancement factor tends to increase monotonically with the wavelength, showing a similar tendency for all

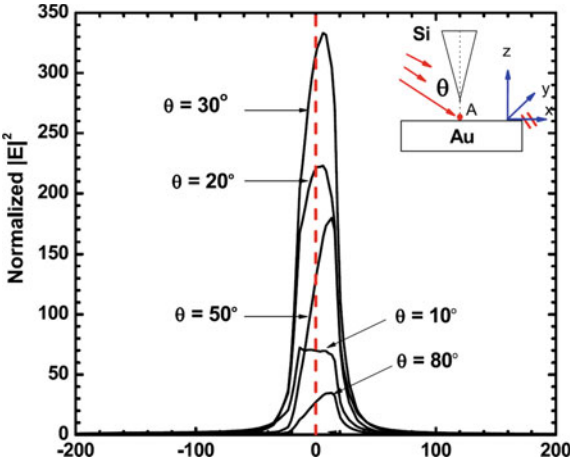

Fig. 3.5 Normalized E^2 intensity field distribution along x-direction on sample surface underneath the tip as a function of laser incident angle θ. The maximum intensity is about 333 at $\theta = 30°$. Reprinted from [44] with permission of Springer

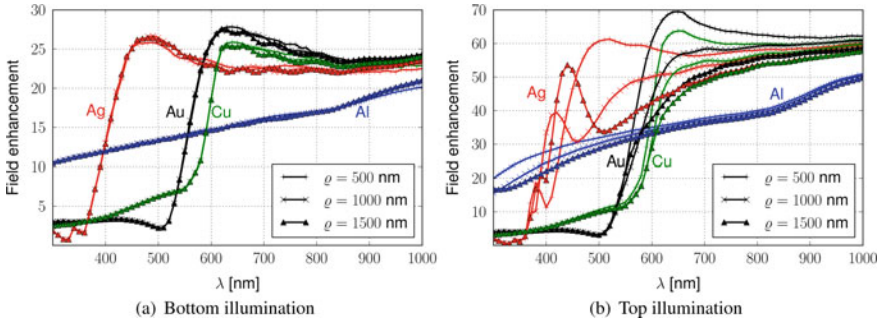

Fig. 3.6 Field enhancement for bottom and top illumination for several metallic tip and wire radii. A radially polarized laser beam is focused by a parabolic mirror on a metallic cylindrical wire. The wire has a diameter ρ, ending with a tapered conical tip. Reprinted from [46] with permission of The Optical Society

materials. Plasmon resonances are dominant in the visible region, while lightning rod and antenna effects seem to play a stronger role for longer wavelengths.

The tip radius also affects field enhancement related with the lightning rod effect. A smaller tip radius causes a higher surface charge accumulation leading to a stronger near-field enhancement. Various simulations show that the enhancement factor increases exponentially with the reciprocal of the tip radius [36, 41, 46, 50, 58]. Few studies exist on the influence of the laser spot size [46, 59].

In conclusion, the quantitative correlation of the laser polarization and the tip-sample distance with the near-field tip enhancement have been repeatedly reported. However, the influence of the tip radius, the angle of incidence, the laser wavelength, the spot size, and the tip materials, need further investigations.

3.3 Thermal Effects

The first articles in the aNFOL field claimed that nanostructured subwavelength features were produced due to pure near-field tip-enhancement effects. Those experiments were performed in vacuum with tip positions controlled by a scanning tunneling microscope (STM). However, it was questioned if thermal expansion of the STM tip may produce thermomechanical modifications on the surface. In order to distinguish between thermal and optical physical phenomena, thermal effects of laser illuminated tips must be carefully analyzed. Therefore, some of these aspects are reviewed in this section.

3.3.1 Tip Temperature

Since the tip is heated when it is illuminated by a laser beam, it is important to retrieve information about the tip temperature and heat distribution in an aNFOL experiment. On one hand, it may be used to discriminate between different structuring mechanisms. On the other hand, a high temperature may produce deformation or even destruction of the tip, thus affecting the reproducibility. For instance, the metallic coating of SFM silicon tips can be easily melted if the applied laser intensity is high enough.

The Raman line shift from a heated silicon tip [60] has been used as a method for tip temperature determination [59]. In this experiment, an SFM tip was illuminated by a Ti:Sa laser oscillator (with $\lambda = 800$ nm, $\tau = 50$ fs, pulse energy 2 nJ, repetition rate 80 MHz). The laser beam was focused on a 3–4 μm spot on the tip resulting in a maximum tip temperature of 550 °C for a laser power of 180 mW (Fig. 3.7).

The non-linear evolution of tip temperature with increasing laser power, was attributed to two-photon absorption of the tip. Using the same parameters as in the experiment, a tip temperature of about 500 °C was obtained for a laser fluence of 15 mJ/cm^2. The tip's apex reached thermal equilibrium after 50,000 pulses ($<$1 ms), with variations in temperature of a few degrees between consecutive laser pulses. This result suggests that femtosecond pulsed lasers working at high repetition rates and low energy per pulse can quickly lead to a thermomechanical steady state. In contrast, a temperature of about 3000 K was estimated for a tungsten SFM tip under a laser fluence of 100 mJ/cm^2 [61]. However, the temporal length of laser pulses was neglected in this calculation.

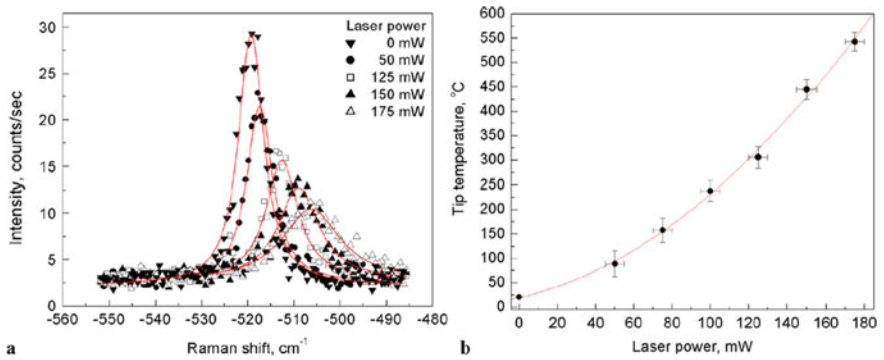

Fig. 3.7 **a** Laser power dependence of the Si Raman line shift and **b** tip temperature estimation following [60]. Reprinted from [59] with permission of Springer

Laser fluence and intensity influence on tip temperature for nanosecond laser pulses have been simulated [62] in agreement with experiments [63–65]. For a fluence of 10 mJ/cm and an intensity $I = 1$ MW/cm^2, a 10 ns laser pulse raises the tip temperature up to about 130 °C. A higher tip temperature value of about 400 °C was computed using the same fluence, but with a laser intensity $I = 100$ MW/cm^2 and $\tau = 0.1$ ns. However, for shorter pulses ($\tau < 10$ ps, $I > 1000$ MW/cm^2), the heat-diffusion length $l_T = \sqrt{\delta\tau}$ (with δ the material's thermal diffusivity) becomes shorter than the region heated by the enhanced field (which is about the radius of the tip). In this later case, the model fails and non-realistic temperatures of 8000°C were obtained. Recently, temperatures were obtained by measuring the thermal near-field emission of a laser-heated tip [66]. A continuous wave laser ($\lambda = 532$ nm) was focused onto a tip (laser spot size 10 μm) and the infrared radiation emitted was fitted to a blackbody spectrum. Temperatures of 420, 530, and 610 K were found for laser powers of 300, 500, and 800 mW, respectively.

3.3.2 Tip Thermal Expansion

First aNFOL experiments used STM devices, and succeeded in performing sub-wavelength features smaller than 100 nm [38, 39, 67, 68]. However, the near-field enhancement mechanism was questioned [69–73]. It was claimed that laser heating might produce a thermal expansion of the tip. In STM setups, the tip is about 1 nm above the surface. Therefore, a slight tip expansion of just a few nanometers is enough to make contact with the surface, thus opening the possibility of mechanical surface modification. This expansion is smaller for femtosecond pulses, but still enough to produce the tip-sample contact. Further research work by other authors agrees with STM tip thermal expansion of a few nanometers [61–64]. Furthermore, if the tip temperature is high enough, melting of the substrate surface may be possible.

3.3.3 Cantilever Thermomechanical Behaviour

On cantilever-based SFM-setups, it is important to determine the thermomechanical behaviour of the cantilever under laser illumination. When a tip is illuminated by a laser, heat is diffused along the cantilever structure and causing expansion. A heat gradient can lead to different expansion rates at different cantilever locations. This introduces modifications on the cantilever geometry and position. Longitudinal cantilever expansion leads to a displacement of the tip position, which may compromise the lateral resolution in nanolithography. Common silicon SPM cantilevers exhibit a metallic coating on the back side to improve its reflectivity for the positioning laser. This metallic layer has a different thermal expansion coefficient than silicon and causes a dramatic bending effect [74] (Fig. 3.8). This produces changes, not only in the longitudinal x direction, but also in the vertical z axis. Numerical calculations have shown that the shift in the z direction can reach several nanometres. SPM feedbacks have a typical response of 0.1–1 ms, while heat diffusion along the cantilever structure takes place in a shorter time scale. This phenomenon of pulse laser dependent thermomechanical cantilever displacements have to be considered in aNFOL applications at low pulse repetition rates. Femtosecond lasers run at MHz rates, however, can achieve a quick thermal equilibrium of the cantilever, mitigating issues related with cantilever expansion [74].

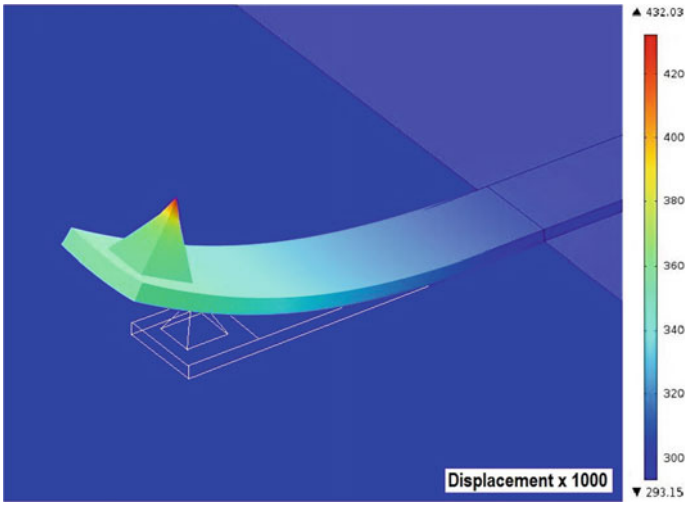

Fig. 3.8 Temperature profile and deformation of a cantilever heated to 432 K. The deformation is magnified 1000 times for better illustration. The white contours of the cantilever indicate the original position [74].

3.3.4 Non-contact Heat Transfer Between a Hot Tip and a Substrate

A hot tip can transfer heat to the substrate by conduction and radiation. Air molecules acquire kinetic energy via collisions due to the tip temperature and hit the substrate below the tip. Heat flux density between a silicon tip at a temperature of 800 K and a substrate can reach values up to 0.5 MW m^{-2} K^{-1} [75]. In this study, radiation contribution was neglected compared to air conduction.

However, radiation heat transfer must be considered. Near-field thermal radiation can be strongly enhanced when the tip and/or substrate materials support a plasmon excitation [76]. The thermal near-field radiation between nanostructures has been studied for different geometries [76, 77]. High values of near-field radiation heat transfer coefficient up to 1.0 MW m^{-2} K^{-1} were found [78]. The thermal near-field radiation between a heated silicon oxide micro-sphere and a vanadium oxide film substrate was measured in vacuum [79]. The micro-sphere temperature was varied between 100 and 200 °C, and conductances slightly above 10^3 W m^{-2} K^{-1} were found at a sphere-substrate distance of about 20 nm.

3.4 Experimental Results

3.4.1 Continuous Wave Lasers

There are numerous examples using continuous wave (cw) lasers as light sources for aNFOL. The spatial distribution of the near-field tip-enhancement has been determined by observing the surface topography of a polymer after CW laser irradiation [80]. A nanofilm of a positive photosensitive polymer (PMMA) mixed with a chromophore (Dispersed Red 1, DR1) was deposited on a glass substrate by spin coating. A cw Nd:VYO_4 diode laser ($\lambda = 532$ nm) irradiated a Co-coated silicon tip working in SFM tapping mode. The tip was positioned a few nanometers above the surface and 1 mW average power was applied to the tip during 20 s with a laser spot of 100 μm. Fringes with a period of about half of the laser wavelength were found on the polymer surface probably due to far-field interference. A nanobump of 40 nm width and few nanometers height was observed at the center of the circular fringes, indicating the presence of a singularity in the field distribution at the tip apex. Similar results were found using a cw fibre laser (808 nm) and a Pt tip [81].

Using a different approach, near-field tip-enhancement has been also exploited to pattern aluminium thin films by photo-thermally induced corrosion in water [82]. A cw Nd:YVO_4 diode laser with linear *p*-polarization illuminated a glass slide from the bottom in total reflection configuration. The surface of the glass was coated with a 20 nm thick aluminium film. The laser beam was focused on the aluminium surface and surface plasmons were excited leading to an enhanced near-field on the metal surface. Due to the localized nature of the near-field, only material close to the tip

apex was affected by heat-induced corrosion. This process was capable to pattern metallic films with aspect ratios of 1:2. Depth and width of the formed trenches were controlled by adjusting the SFM scanning speed. With an illumination laser power of 60 mW and a scanning speed of 136 nm/s, lines of 20 nm width and 5.5 nm depth were written on the film surface.

3.4.2 Nanosecond and Femtosecond Pulse Lasers

One of the first experiments in the field employed various STM-tip materials , such as Pt/Ir, W, Au and Ag-coated W, on a gold substrate [67]. With a Nd:YAG laser illumination (5 ns, $\lambda = 532$ nm) subwavelength surface modifications were achieved. Dot dimensions were found with a lateral size of 30–50 nm and 10–15 nm in height. Above a certain laser intensity threshold (10–20 MW/cm^2 for Ag and Ag-coated W tips and 30–80 MW/cm^2 for Pt/Ir tips), hillocks were observed with 100% probability. 10 nm width lines were created using a laser intensity close to the threshold (15 MW/cm^2). Laser polarization had a strong influence on the structuring process [39]. A laser polarization parallel to the tip axis led to a maximum effect. From this an optical near-field enhancement mechanism was concluded. Similar results were reported using an SFM cantilevered tip [38, 68].

Shortly after these experiments, contradictory explanations for the nanostructuring process were developed [71]. The observation of a transient increase of the tunneling current on a μs timescale was indicative of thermal expansion of the tip resulting a thermomechanical deformation of the substrate. Also femtosecond pulse irradiation led to the same conclusion [69] corroborated by further research work [70, 72, 73, 83].

STM devices were gradually replaced by SFM devices in aNFOL. A SFM tip does not need to be as close to the surface as in an STM.

A frequency-doubled Q-switched Nd:YAG laser ($\tau = 7$ ns) was focused onto a commercial silicon tip with a curvature of 12 nm [84]. Pits with a diameter of 28-40 nm and a depth of 4–10 nm were obtained on 50 nm thick gold films deposited on silicon at a laser intensity of 80 MW/cm^2. Protrusions around the pits suggested a thermomechanical mechanism. Feature sizes increased with the number of laser pulses, pulse energy and cantilever force. The nanofabrication process was attributed to a combination of near-field enhancement and mechanical indentation of the tip.

Recently, an aNFOL setup ($\lambda = 266$ nm and $\tau = 4$ ns) has been used to study the near-field structuring effect of tip materials and curvature on gold, tantalum and silicon substrates [85]. Surprisingly, only the conductive diamond-coated Si probe—with the highest tip radius—produced craters on the surface of gold and silicon samples. Crater diameter varied from 100 to 120 nm for single shot pulse irradiation. The diameter of craters did not change with the tip-sample distance and the laser fluence, only the depth of craters were affected. The ablated mass of the substrate increased with the number of laser pulses for all materials studied. However, crater depths reached a plateau for tantalum and silicon, after a certain number of laser

pulses. In contrast, for the gold substrate, the crater depth kept increasing with the number of pulses.

aNFOL experiments with nanosecond laser pulses can raise the tip temperature up to 350–800 °C, causing a tip expansion of a few nanometers [74, 86]. To exclude this phenomenon, the use of femtosecond lasers in aNFOL is an appealing alternative.

Nonlinear femtosecond aNFOL based on apertureless near-field two-photon lithography was performed on a 50 nm thick SU-8 photoresist film [87]. A Ti:Sa amplified laser with $\lambda = 790$ nm, $\tau = 120$ fs and a repetition rate of 1 kHz was combined with metallic SFM tips (Pt/Ir or Au) in contact mode. In a first step, the photoresist was exposed—without the SFM tip—to intensities ranging from 1 to 2 TW/cm^2, finding a feature formation threshold at 0.92 TW/cm^2 resulting in lateral dimensions of 300–400 μm. As the SU-8 photoresist does not absorb light at 790 nm, laser absorption was caused by nonlinear processes, e.g. multiphoton absorption. Two-photon polymerization of the photoresist was observed when the metal-coated tip was brought into contact with the surface, even at intensities as low as 0.15 TW/cm^2. This indicated a 7-fold near-field enhancement factor. Lateral widths of the created features were about 70 nm (Fig. 3.9). The size of the formed structures did not depend on the laser spot size. The influence of the scanning speed was tested, from 10 to 200 μm/s, with no apparent effect on the polymerization intensity threshold. However, experiments using a silicon nitride tip failed to produce observable structures, even at intensities as high as 1 TW/cm^2.

Based on a similar setup, a so-called "floating tip nanolithography" was developed to assure that the tip was not in contact with the substrate [88]. The cantilever of an SPM tip was forced to oscillate with a small amplitude (<1 nm) at a frequency far from the resonance frequency of the cantilever.

Silicon tips, with 20–30 nm coating layers of W_2Cr and a curvature of 30 nm were illuminated by a focused femtosecond laser beam ($\lambda = 800$ nm, $\tau = 100$ fs, spot size $w = 300$ μm and angle of incidence 17°) [61]. The same regenerative amplifier system was used without femtosecond injection to deliver nanosecond pulses ($\lambda = 800$ nm, $\tau = 9$ ns). Samples used were 20–30 nm thick metallic films, ranging from low to high melting points (In, Au, Cu, FeCr). An SFM contact mode generated craters with diameter of 20–30 nm and depths of several nanometers. The fluence threshold for femtosecond pulses was 2.5–1.5 times lower than that for nanosecond pulses. In the case of femtosecond irradiation, fluence threshold values for *p*-polarization (*s*-polarization) were 34 (67) and 75 (150) mJ/cm^2 for Au and FeCr, respectively. Therefore, the fluence threshold for *s*-polarization was 1.5–2.5 higher than for *p*-polarization. In addition, the fluence damage threshold oft he FeCr films at *p*-polarization did not vary with the tip-sample distances (5–40 nm). Therefore, a near-field enhancement structuring mechanism was excluded. To get an insight into the thermal processes involved, the tip thermal expansion caused by laser heating was estimated. For a laser fluence of 100 mJ/cm^2, the tip could reach temperatures of 3000 K leading to a thermal expansion of about 20 nm. Nanostructure formation was therefore attributed to thermomechanical effects, including melting of the substrate.

Commercial Si tips with 5–10 nm curvature were irradiated by a Ti:Sa laser amplifier ($\lambda = 800$ nm, $\tau = 83$ fs, 1 kHz repetition rate) in SFM contact mode in

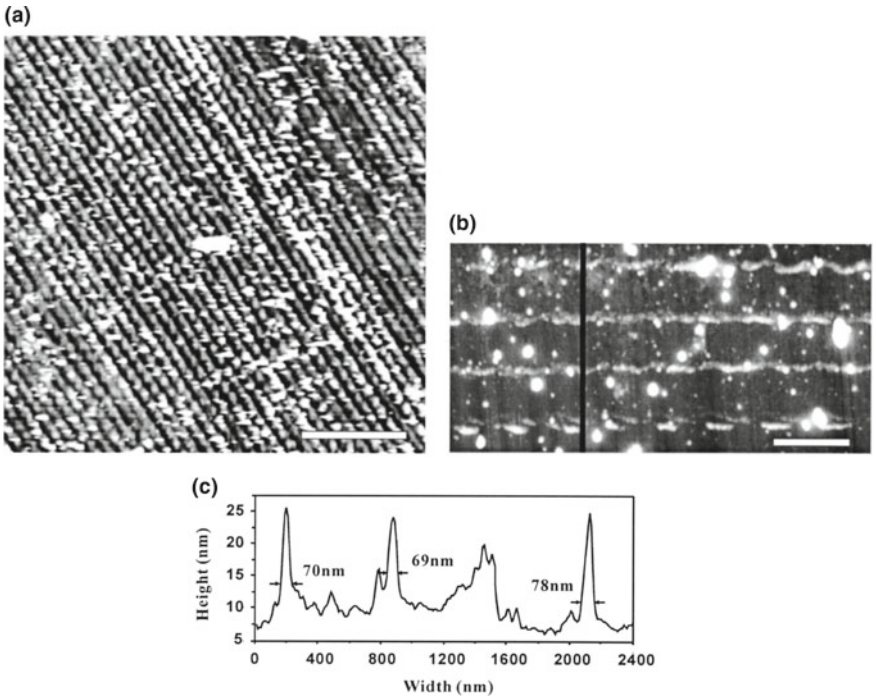

Fig. 3.9 SFM images of two-photon produced line structures in SU-8 using the field enhancement of the aSNOM tip with far-field intensities of **a** 0.9 TW/cm^2 and **b** 0.45 TW/cm^2. Panel **c** shows a crosssectional view (height profile) along the dark vertical line in (**b**), suggesting that two-photon apertureless near-field lithography can produce $\sim$72 $\pm$ 10 nm features using 790 nm light. The scale bars in **a** and **b** are 5 and 1 μm respectively. Reprinted from [87], with the permission of AIP Publishing

order to nanostructure gold films in ambient conditions [89]. Feature formation by indentation of the tip was not observed, due to the low pressure exerted by the low spring constant of cantilevers used. A *p*-polarized focused laser beam at grazing incidence versus the substrate resulted in lines with a minimum lateral width of 10 nm and 4–8 nm depth (Fig. 3.10a). Both width and depth of lines increased with the laser fluence (Fig. 3.10b). Various pattern shapes were structured on the substrate's surface, showing the versatility to control the shape, width and depth of lines, with a minimum feature lateral size of $\lambda/80$.

The amplitude and the phase of the cantilever oscillation were electronically monitored. When the tip approached to a distance of about 3 nm from the surface, a sudden change in the phase of the cantilever oscillation was detected. Thus, the tip-sample distance could be controlled with a precision of <1 nm. This allowed to rule out any effects caused by the contact between the hot tip and the substrate. A Ti:Sa laser oscillator with $\lambda = 800$ nm, $\tau = 20$ fs and repetition rate 80 MHz was employed. Lines of 20 nm width and 1 nm depth were written on a 15 nm gold film

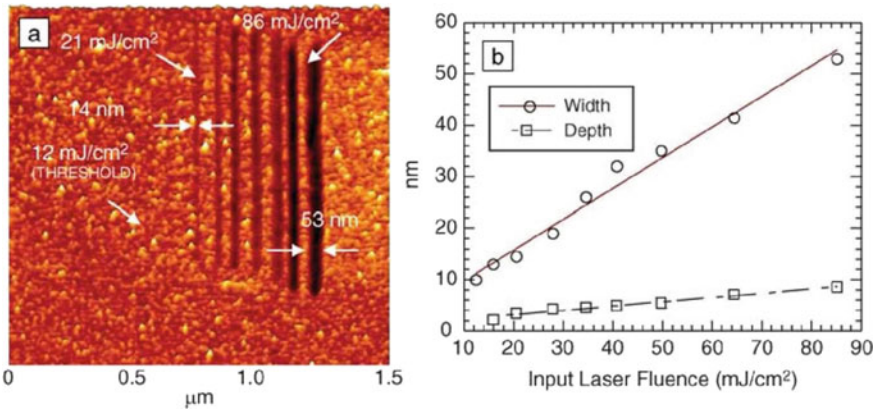

Fig. 3.10 Dependence of lateral feature size on a gold film on the laser fluence. Reprinted from [89], with the permission of AIP Publishing

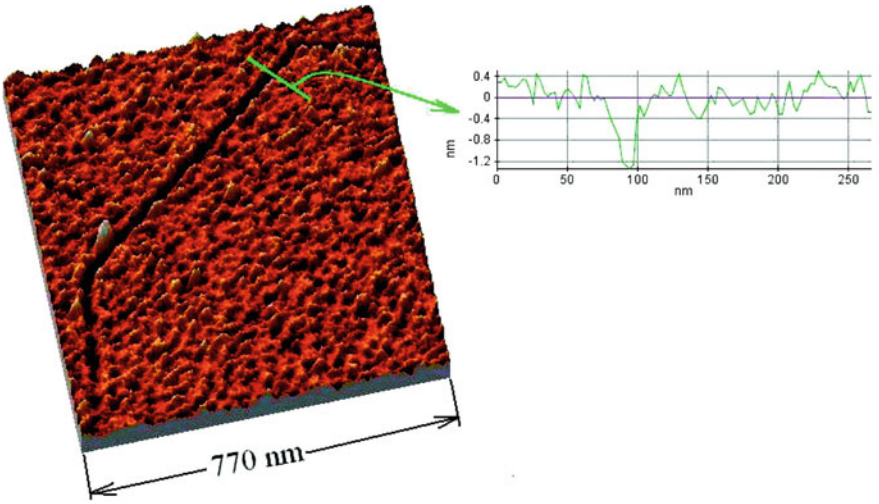

Fig. 3.11 Floating tip nanolithography on a gold film (15 nm of Au on a Si wafer with 2 nm of Cr buffer layer). Reprinted with permission from [88]. Copyright (2008) American Chemical Society

(Fig. 3.11). The tip temperature was below the melting point of gold, so that the hot tip effect (thermal substrate modification caused by the tip temperature) was ruled out. A comparison between hot tip and mechanical SFM lithography was undertaken at a photoresist (AZ4620). Mechanical SFM scratching produced material displacement to the edges of the formed lines. In contrast, hot tip lithography achieved the same resolution, but no material was deposited around the edges of the trenches. Two mechanisms were proposed to explain the observed nanolithography results.

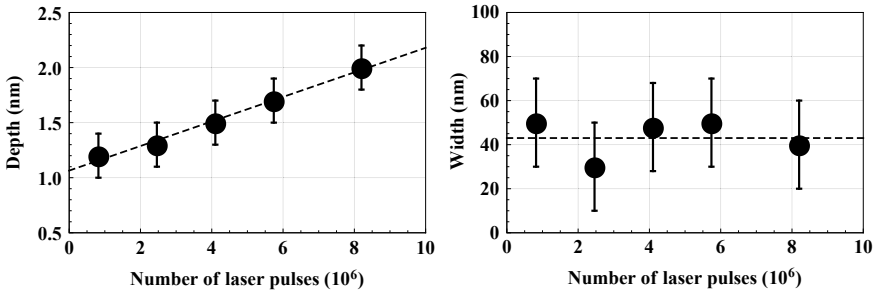

Fig. 3.12 Effect of the number of pulses on the depth and width of lines nanostructured on a photoresist (AZ4620) [90]

Hot tip interaction with the surface of the substrate led to melting/evaporation of the material, and electromagnetic near-field enhancement caused material ablation below the tip. A systematic study of the influence of the number of femtosecond laser pulses ($\lambda = 800$ nm, $\tau = 20$ fs, 82 MHz repetition rate), the operation mode (contact and noncontact SFM), and the polarization performed at high repetition rates on a photoresist (AZ4620) have been systematically analyzed [74, 90]. The tip-sample distance was precisely controlled down to 0.5 nm by using the "floating tip" technique. The crater depths increased with the number of pulses, whereas the the width was practically unaffected (Fig. 3.12). The influence of the laser power on the depth and width exhibited the same trend for both *p* and *s*-polarization (Figs. 3.13 and 3.14). No variation of the width was observed for both *p* and *s*-polarization when varying the tip-sample distance (Figs. 3.15 and 3.16). In contrast, the depth increased with the tip-sample distance for *p*-polarization, while it remained practically unaffected for *s*-polarization (Figs. 3.15 and 3.16). This results may show an indication that near-field enhancement is involved, since the structuring effect is expected to be stronger for *p*-polarization. In addition, the effect of laser polarization was tested on the same photoresist. If near-field enhancement is the dominant physical mechanism, one should expect greater feature depths for *p*-polarization based on simulations (Fig. 3.4). However, the experiments showed practically no depth difference between *p*-polarization and *s*-polarization. These results seem to indicate that thermal phenomena are superposed on optical enhancement processes.

3.4.3 Near-Field Enhancement Factor

In spite of the importance of the near-field enhancement factor $EF = |E|/|E0|$, difficulties kept prevailing in quantifying it experimentally. One way to measure it has consisted in the observation of the multiphoton polymerization of a photoresist around metallic nanostructures [91]. The laser fluence can be adjusted below the polymerization threshold, so that only regions where near-field enhancement occurs

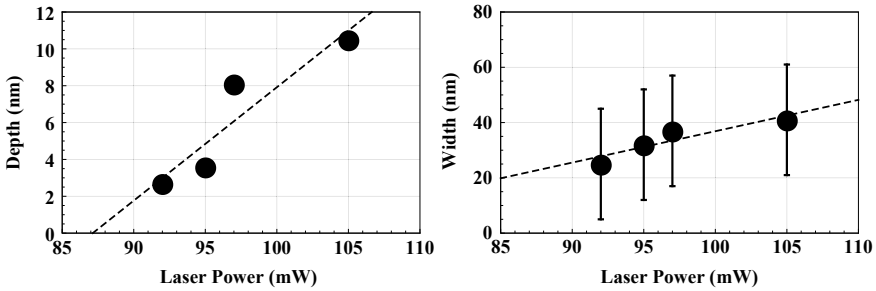

Fig. 3.13 Depth and width of structured lines on a photoresist (AZ4620) versus laser power for *p*-polarization [90]. Noncontact mode with the tip kept 8 nm above the surface. The tip-sample distance was calculated monitoring the phase of the cantilever's oscillations (according to [88])

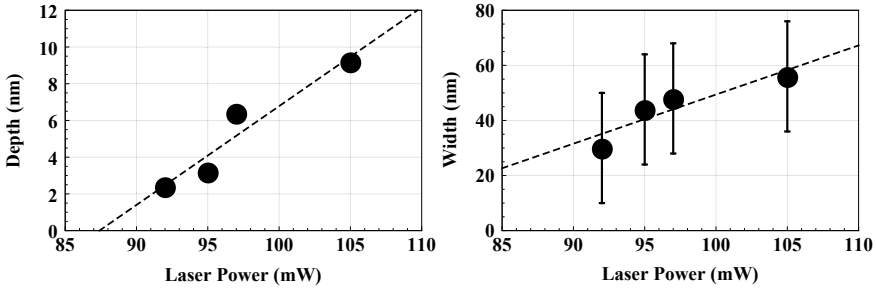

Fig. 3.14 Depth and width of structured lineson a photoresist (AZ4620) versus laser power for *s*-polarization [90]. Noncontact mode with the tip kept 8 nm above the surface. The tip-sample distance was calculated monitoring the phase of the cantilever's oscillations (according to [88])

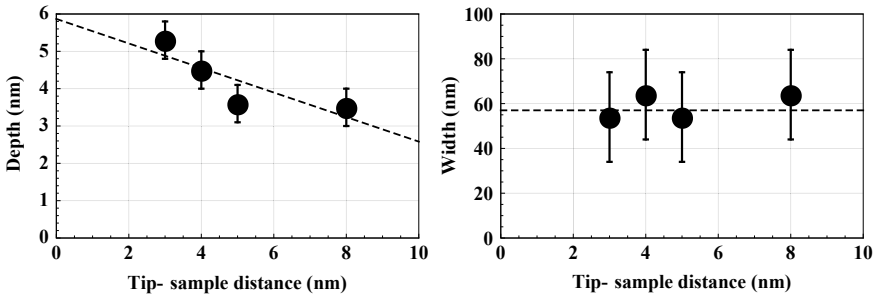

Fig. 3.15 Depth and width of structured lineson a photoresist (AZ4620) versus laser power, for *p*-polarization [90]. The tip-sample distance was calculated monitoring the phase of the cantilever's oscillations (according to [88])

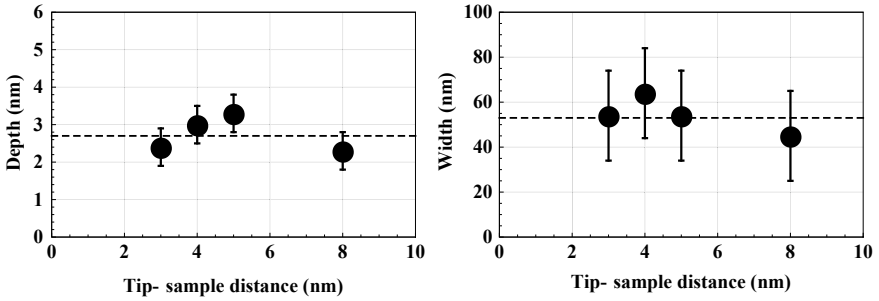

Fig. 3.16 Depth and width of structured lines on a photoresist (AZ4620) versus laser power, for *s*-polarization [90]. The tip-sample distance was calculated monitoring the phase of the cantilever's oscillations (according to [88]).

become polymerized. The sample is rinsed afterwards, removing any monomer remnants. By employing this method, a study on two-photon polymerization obtained a near-field enhancement factor $EF = 24$ around triangular nanostructures in a bow-tie configuration [92]. Remarkably, these values were independent of the laser power, irradiation time and spot size. A similar experiment had been previously undertaken [93], but it showed a lower enhancement factor $EF = 10$, according to FDTD simulations. The differences were attributed to various factors, as different substrate layers or variable sharpness values of nanofeatures. In a similar fashion, near-field marking of star-shaped gold nanoparticles by femtosecond laser pulses was used to estimate the near-field enhancement factor [94]. A maximum value $EF = 7.2$ was found around the metallic nanostructures. Recently, an experimental estimation of near-field tip-enhancement has been obtained [95]. Gold films were irradiated by infrared femtosecond pulses ($\lambda = 1040$ nm, $\tau = 150$ fs) in an apertureless scanning probe configuration. A threshold value for far-field modifications of the gold surface was found, allowing to estimate a near-field enhancement factor $EF = 7$, in agreement with simulations.

3.5 Conclusions

Scanning probe lithography is emerging as a potential technology in the field of nanolithography. Particularly apertureless scanning probe near-field optical lithography (aNFOL) showed the ability to surpass the light diffraction limit. The possibility of dealing with non-transparent samples, the flexibility regarding laser wavelength, and being able to work in ambient conditions make this technique a versatile option for nanotechnology. However, the productivity is limited as in other scanning probe techniques. This technique appears appealing to emerging fields like plasmonics and nano-optics due to the capability of producing nanostructures. The physical mechanisms responsible for aNFOL are still under discussion. Both plasmonic and

thermomechanical processes can contribute to various extents. Further research is needed to advance apertureless scanning probe near-field optical lithography to a better understanding and nanotechnological applicability.

References

1. E. Synge, Lond. Edinburgh Dublin Philos. Mag. J. Sci. **6**, 356–362 (1928)
2. D.W. Pohl, W. Denk, M. Lanz, Appl. Phys. Lett. **44**, 651–653 (1984)
3. A. Lewis, M. Isaacson, A. Harootunian, A. Muray, Ultramicroscopy **13**, 227–231 (1984)
4. R.C. Dunn, Chem. Rev. **99**, 2891–2927 (1999)
5. S. Kawata, in *Near-Field Optics and Surface Plasmon Polaritons*, ed. by S. Kawata (Springer, Berlin Heidelberg, 2001)
6. S. Patanè, P.G. Gucciardi, M. Labardi, M. Allegrini, La Rivista del Nuovo Cimento **27**, 1–46 (2004)
7. S. Kawata, V.M. Shalaev, *Tip Enhancement* (Elsevier, 2007)
8. L. Novotny, *Progress in Optics*, vol. 50 (Elsevier, 2007) Chap. 5, pp. 137-184
9. A. Hartschuh, Angew. Chem. Int. Ed. **47**, 8178–8191 (2008)
10. J. Wessel, J. Opt. Soc. Am. B **2**, 1538–1541 (1985)
11. H.J. Mamin, D. Rugar, Appl. Phys. Lett. **61**, 1003–1005 (1992)
12. V. Likodimos, M. Labardi, L. Pardi, M. Allegrini, M. Giordano, A. Arena, S. Patanè, Appl. Phys. Lett. **82**, 3313–3315 (2003)
13. T. Yatsui , M. Ohtsu, in *Progress in Nano-Electro-Optics I, Basics and Theory of Near-Field Optics*, ed. by M. Ohtsu (Springer, 2003), Chap. 1
14. S. Sun, G.J. Leggett, Nano Lett. **4**, 1381–1384 (2004)
15. G. Wysocki, J. Heitz, D. Bäuerle, Appl. Phys. Lett. **84**, 2025–2027 (2004)
16. Y. Lin, M.H. Hong, W.J. Wang, Y.Z. Law, T.C. Chong, Appl. Phys. A **80**, 461–465 (2005)
17. S. Noach, M. Manevich, N.P. Eisenberg, E.P. Fokin, T.V. Mihalina, Nanotechnology **16**, 775–778 (2005)
18. W.J. Wang, R. Zhao, L.P. Shi, X.S. Miao, P.K. Tan, M.H. Hong, T.C. Chong, Y.H. Wu, Y. Lin, J. Appl. Phys. **98**, 124313 (2005)
19. G.J. Leggett, Nano Biotechnol. **3**, 223–240 (2007)
20. S.-B. Wen, R. Greif, R.E. Russo, Appl. Phys. Lett. **91**, 251113 (2007)
21. V. Zorba, X. Mao, R.E. Russo, Appl. Phys. Lett. **95**, 041110 (2009)
22. D. Credgington, O. Fenwick, A. Charas, J. Morgado, K. Suhling, F. Cacialli, Adv. Funct. Mater. **20**, 2842–2847 (2010)
23. E. Flaxer, M. Klebanov, V. Lyubin, M. Manevich, S. Noach, in *Microscopy: Science, Technology, Applications and Education*, vol. 3, ed. by A. Mendez-Vilas, J. Diaz (2010), pp. 2103–2110
24. Z. Liu, E. ul Haq, J.K. Hobbs, G.J. Leggett, Y. Zhang, J.M.R. Weaver, C.J. Roberts, Microelectron. Eng. **88**, 2109–2112 (2011)
25. S. Sun, D.G. Thompson, D. Graham, G.J. Leggett, J. Mater. Chem. **21**, 14173 (2011)
26. E. McLeod, A. Ozcan, J. Lab. Autom. **17**, 248–254 (2012)
27. A.A. Kuchmizhak, Y.N. Kulchin, O.B. Vitrik, A.G. Savchuk, S.V. Makarov, S.I. Kudryashov, A.A. Ionin, Opt. Commun. **308**, 125–129 (2013)
28. S.M. Aghaei, N. Yasrebi, B. Rashidian, J. Nanomater. **2015**, 1–7 (2015)
29. A.A. Tseng, Opt. Laser Technol. **39**, 514–526 (2007)
30. L. Novotny, S.J. Stranick, Annu. Rev. Phys. Chem. **57**, 303–331 (2006)
31. R. García, A.W. Knoll, E. Riedo, Nat. Nanotechnol. **9**, 577–587 (2014)
32. D. Pires, J.L. Hedrick, A. De Silva, J. Frommer, B. Gotsmann, H. Wolf, M. Despont, U. Duerig, A.W. Knoll, Science **328**, 732–5 (2010)
33. P.C. Paul, A.W. Knoll, F. Holzner, M. Despont, U. Duerig, Nanotechnology **22**, 275306 (2011)

34. A.W. Knoll, D. Pires, O. Coulembier, P. Dubois, J.L. Hedrick, J. Frommer, U. Duerig, Adv. Mater. **22**, 3361–5 (2010)
35. B. Knoll, F. Keilmann, Nature **399**, 134–137 (1999)
36. J.L. Bohn, D.J. Nesbitt, A. Gallagher, J. Opt. Soc. Am. A **18**, 2998–3006 (2001)
37. Y. Inouye, S. Kawata, Opt. Lett. **19**, 159–161 (1994)
38. K. Dickmann, J. Jersch, F. Demming, Surf. Interface Anal. **25**, 500–504 (1997)
39. J. Jersch, F. Demming, L.J. Hildenhagen, K. Dickmann, Appl. Phys. A **66**, 29–34 (1998)
40. A.V. Zayats, Opt. Commun. **161**, 156–162 (1999)
41. R. Esteban, R. Vogelgesang, K. Kern, Nanotechnology **17**, 475 (2006)
42. R. Esteban, R. Vogelgesang, K. Kern, Phys. Rev. B **75**, 195410 (2007)
43. R.M. Roth, N.C. Panoiu, M.M. Adams, R.M. Osgood, C.C. Neacsu, M.B. Raschke, Opt. Express **14**, 2921–2931 (2006)
44. Z.B. Wang, B.S. Luk'yanchuk, L. Li, P.L. Crouse, Z. Liu, G. Dearden, K.G. Watkins, Appl. Phys. A **89**, 363–368 (2007)
45. W. Zhang, X. Cui, O.J.F. Martin, J. Raman Spectrosc. **40**, 1338–1342 (2009)
46. J. Mihaljevic, C. Hafner, A.J. Meixner, Opt. Express **21**, 25926–25943 (2013)
47. C. Huber, A. Trugler, U. Hohenester, Y. Prior, W. Kautek, Phys. Chem. Chem. Phys. **16**, 2289–2296 (2014)
48. L. Wang, X.G. Xu, Appl. Phys. Lett. **6**, 8973 (2016)
49. P. Dean, O. Mitrofanov, J. Keeley, I. Kundu, L. Li, E.H. Linfield, A.G. Davies, Appl. Phys. Lett. **108**, 091113 (2016)
50. P. Royer, D. Barchiesi, G. Lerondel, R. Bachelot, Phil. Trans. R. Soc. Lond. A **362**, 821–842 (2004)
51. C. Huber, A. Trugler, U. Hohenester, W. Kautek, Unpublished results
52. L. Aigouy, A. Lahrech, S. Grésillon, H. Cory, A.C. Boccara, J.C. Rivoal, Opt. Lett. **24**, 187–189 (1999)
53. L. Novotny, R.X. Bian, X.S. Xie, Phys. Rev. Lett. **79**, 645–648 (1997)
54. O.J.F. Martin, C. Girard, Appl. Phys. Lett. **70**, 705–707 (1997)
55. L. Novotny, E.J. Sánchez, X.S. Xie, Ultramicroscopy **71**, 21–29 (1998)
56. A. Downes, D. Salter, A. Elfick, J. Phys. Chem. B **110**, 6692–6698 (2006)
57. X. Chen, X. Wang, Nanotechnology **22**, 075204 (2011)
58. S. Thomas, M. Krüger, M. Förster, M. Schenk, P. Hommelhoff, Nano Lett. **13**, 4790–4794 (2013)
59. A.A. Milner, K. Zhang, V. Garmider, Y. Prior, Appl. Phys. A **99**, 1–8 (2010)
60. M. Balkanski, R.F. Wallis, E. Haro, Phys. Rev. B **28**, 1928–1934 (1983)
61. A. Kirsanov, A. Kiselev, A. Stepanov, N. Polushkin, J. Appl. Phys. **94**, 6822–6826 (2003)
62. P.I. Geshev, S. Klein, K. Dickmann, Appl. Phys. B **76**, 313–317 (2003)
63. V.A. Ukraintsev, J.T. Yates Jr., J. Appl. Phys. **80**, 2561 (1996)
64. S. Grafström, P. Schuler, J. Kowalski, R. Neumann, J. Appl. Phys. **83**, 3453 (1998)
65. S. Grafström, J. Appl. Phys. **91**, 1717 (2002)
66. B.T. O'Callahan, M.B. Raschke, APL Photon. **2**, 021301 (2017)
67. J. Jersch, K. Dickmann, Appl. Phys. Lett. **68**, 868–870 (1996)
68. J. Jersch, F. Demming, K. Dickmann, Appl. Phys. A **64**, 29–32 (1996)
69. J. Boneberg, H.J. Münzer, M. Tresp, M. Ochmann, P. Leiderer, Appl. Phys. A **67**, 381–384 (1998)
70. J. Boneberg, M. Tresp, M. Ochmann, H.J. Münzer, P. Leiderer, Appl. Phys. A **66**, 615–619 (1998)
71. I. Lyubinetsky, Z. Dohnálek, V.A. Ukraintsev, J.T. Yates Jr., J. Appl. Phys. **82**, 4115–4117 (1997)
72. R. Huber, M. Koch, J. Feldmann, Appl. Phys. Lett. **73**, 2521–2523 (1998)
73. V. Gerstner, A. Thon, W. Pfeiffer, J. Appl. Phys. **87**, 2574–2580 (2000)
74. C. Huber, Y. Prior, K. Wolfgang, Meas. Sci. Technol. **25**, 075604 (2014)
75. P.O. Chapuis, J.J. Greffet, K. Joulain, S. Volz, Nanotechnology **17**, 2978 (2006)
76. A.C. Jones, B.T. O'Callahan, H.U. Yang, M.B. Raschke, Prog. Surf. Sci. **88**, 349–392 (2013)

77. J.B. Pendry, J. Phys.: Condens. Matter **11**, 6621–6633 (1999)
78. B. Song, Y. Ganjeh, S. Sadat, D. Thompson, A. Fiorino, V. Fernández Hurtado, J. Feist, F.J. García Vidal, J.C. Cuevas, P. Reddy, E. Meyhofer, Nat. Nanotechnol. **10**, 253–258 (2015)
79. F. Menges, M. Dittberner, L. Novotny, D. Passarello, S. Parkin, M. Spieser, H. Riel, B. Gotsmann, Appl. Phys. Lett. **108**, 171904 (2016)
80. F. H'dhili, R. Bachelot, G. Lerondel, D. Barchiesi, P. Royer, Appl. Phys. Lett. **79**, 4019–4021 (2001)
81. J. Cui, L. Yang, H. Xie, Y. Wang, X. Mei, K. Wang, W. Wang, C. Hou, Integr. Ferroelectr. **169**, 124–132 (2016)
82. D. Haefliger, A. Stemmer, Ultramicroscopy **100**, 457–464 (2004)
83. M. Ochmann, H.J. Münzer, J. Boneberg, P. Leiderer, Rev. Sci. Instrum. **70**, 2049–2052 (1999)
84. Y.F. Lu, B. Hu, Z.H. Mai, W.J. Wang, W.K. Chim, T.C. Chong, Jpn. J. Appl. Phys. **40**, 4395–4398 (2001)
85. C. Jabbour, J.-L. Lacour, M. Tabarant, A. Semerok, F. Chartier, J. Anal. At. Spectrom. **31**, 1534–1541 (2016)
86. S.M. Huang, M.H. Hong, Y.F. Lu, B.S. Luk'yanchuk, W.D. Song, T.C. Chong, J. Appl. Phys. **91**, 3268–3274 (2002)
87. X. Yin, N. Fang, X. Zhang, I.B. Martini, B.J. Schwartz, Appl. Phys. Lett. **81**, 3663–3665 (2002)
88. A.A. Milner, K. Zhang, Y. Prior, Nano Lett. **8**, 2017–2022 (2008)
89. A. Chimmalgi, T.Y. Choi, C.P. Grigoropoulos, K. Komvopoulos, Appl. Phys. Lett. **82**, 1146–1148 (2003)
90. C. Huber, Y. Prior, W. Kautek, Unpublished results
91. C. Deeb, R. Bachelot, J. Plain, A.L. Baudrion, S. Jradi, A. Bouhelier, O. Soppera, K.J. Prashant, L. Huang, C. Ecoffet, L. Balan, P. Royer, ACS Nano **4**(8), 4579–4586 (2010)
92. T. Geldhauser, A. Kolloch, N. Murazawa, K. Ueno, J. Boneberg, P. Leiderer, E. Scheer, H. Misawa, Langmuir **28**(24), 9041–9046 (2012)
93. A. Sundaramurthy, P.J. Schuck, N.R. Conley, D.P. Fromm, G.S. Kino, W.E. Moerner, Nano Lett. **6**(3), 355–360 (2006)
94. S.H. Møller, J. Vester-Petersen, A. Nazir, E.H. Eriksen, B. Julsgaard, S.P. Madsen, P. Balling, Appl. Phys. A **124**, 210 (2018)
95. I. Falcón Casas, W. Kautek, Nanomaterials **8**, 536 (2018)

Chapter 4
Laser-Induced Synthesis and Processing of Nanoparticles in the Liquid Phase for Biosensing and Catalysis

Giuseppe Compagnini, Marcello Condorelli, Carmelo La Rosa, Luisa D'Urso, Salvatore Scirè, Roberto Fiorenza, Simona Filice, and Silvia Scalese

Abstract Laser ablation (LAL) and irradiation in liquids (LIL) are becoming two of the most studied and dominant ways of synthesis and modification for nanostructured materials. Such rapid development is due to a fast and economic way to obtain nanoparticles of any material. Starting from solid targets submerged in water or other liquids, it is possible to obtain noble metals, metal alloys, metal oxides, and graphene nanoparticles, simply by irradiating the target with a focused laser beam. Moreover, it is also possible to modify already existing nanoparticles, generating defects in their structures or reshaping them, through laser irradiation of their colloidal dispersion using an unfocused laser beam. In this chapter, a focus on the fundaments of laser ablation and modification in liquids is reported as well as some advances in the synthesis and modification of new nanostructures with their relative application in different fields of research such as bio-sensing, catalysis, and optoelectronics. The example of the synthesis of ultra-pure silver nanoparticles by LAL and their application as surface-enhanced Raman scattering (SERS) active substrate for biosensing application is provided. In such a study, it is possible to detect and characterize a protein involved in diabetes mellitus type 2 (amylin), at nanomolar concentration. LIL has been also considered to modify commercial TiO_2 and graphene oxide (GO) colloids. Such unconventional treatment has shown to enhance the performances of these two materials, towards photocatalytic water splitting and water purification applications, thanks to the modification of the morphology and oxygen functionalities of these materials. As an added value, the LIL of TiO_2 and GO is a more green technique and tunable methodology concerning conventional reduction methods. Laser irradiation of GO results in conferring to the material an antimicrobial activity not shown by the untreated one. Similarly, the performance in the photocatalytic H_2 production of laser-treated TiO_2 samples is examined pointing out that the TiO_2

G. Compagnini (✉) · M. Condorelli · C. La Rosa · L. D'Urso · S. Scirè · R. Fiorenza · S. Filice
Dipartimento di Scienze Chimiche, Università di Catania, Viale A. Doria 6, 95125 Catania, Italy
e-mail: gcompagnini@unict.it

S. Filice · S. Scalese
Istituto per la Microelettronica e Microsistemi, Consiglio Nazionale delle Ricerche, Zona industriale VIII Strada n. 5, 95121 Catania, Italy

A. Hu (ed.), *Laser Micro-Nano-Manufacturing and 3D Microprinting*, Springer Series in Materials Science 309, https://doi.org/10.1007/978-3-030-59313-1_4

structural modifications induced by the LIL process are fundamentals to strongly increase the photocatalytic performance.

4.1 Introduction

Research related to the production of nanoparticles and nanostructures of different size, shape, structure, and composition is on the rise due to their large applications in the different fields of science and technology [1–6]. Due to such an increasing request, the production of different types of nanoparticles stimulated the development of new strategies for their production by using different methodologies.

Many homemade vacuum machines have been built in various laboratories to produce clusters of different materials having a nanometric size. However, vacuum technologies require very good maintenance to obtain objects of high quality. For instance, impurities present in the fly zone between the source and the deposition plate may pollute the produced materials. Therefore, high vacuum conditions are strictly required.

On the other hand, classical wet chemistry has been by far used with a large number of different bottom-up approaches for nanomaterials fabrication involving fundamental building blocks of matter: atoms and molecules [7, 8].

An intriguing alternative is to work directly in the liquid phase to grow and/or modify nanosized materials using pulsed laser beams. In these cases, laser energy can be used to ablate solid targets in the so-called Pulsed Laser Ablation in Liquids technique (PLAL) or to modify previously synthesized colloidal dispersions, thus changing the shape, size, and composition of the nano-entities or activate reactive path for the formation of stable or metastable materials [9–14].

Regarding PLAL techniques, they involve a focused, high-power laser beam onto the surface of a solid target that is submerged beneath a liquid. The interaction of the laser with the target causes the surface to vaporize in the form of an ablation plume. This contains species such as atoms, ions, and clusters, traveling with high kinetic energy. The species in the plume collide and react with the molecules of the surrounding liquid, producing new compounds that contain atoms from both the original target and the liquid. Because of the intensity of the laser and the nanosecond timescales, the instantaneous temperature and pressure within the reaction volume can be extremely high (many thousands of Kelvin and tens of GPa). Such high-temperature, high-pressure, and high-density conditions provide a "brute force" method of synthesizing novel materials that have hitherto been inaccessible using milder, more conventional techniques. The mechanisms involved in the nucleation and phase transition of nanocrystals upon PLAL are not well understood. A recent review [15] gave an overview of nucleation thermodynamics, the phase transition, and the growth kinetics in the case of nanocrystals obtained by laser ablation of liquids.

Pulsed lasers have been also used to irradiate nanoparticles in liquid environments at fluences well below the ablation threshold (usually 0.1–0.5 J/cm^2). This has

received much attention for manipulating the morphology of nano-sized particles during or after their formation. Laser irradiation has been shown to cause fragmentation of nanometer-size silver and gold particles in aqueous solutions, size enlargement of spherical metal and semiconducting nanoparticles, transformation of gold nanorods into spheres as well as laser-induced alloying [16, 17]. The result of laser irradiation of metal nanoparticles is strongly dependent on experimental conditions. For instance, the Koshizaki group has published many papers showing a method to produce spherical submicrometer particles of different materials by laser irradiation of nanocolloids which has been previously grown by PLAL or by classical chemical syntheses [18, 19]. They have also shown that heating–melting–evaporation model can be successfully applied for many phenomena arising when colloidal nanoparticle interacts with pulsed laser beams. On the other hand, Compagnini et al. have successfully synthesized Au/Ag colloidal nano-alloys with a wide range of compositions by laser ablation of single metal targets in water and a re-irradiation of mixed colloidal suspensions [20, 21]. In this respect, control over the size and polydispersity of NPs can be achieved by modulation of the laser pulse width and fluency, but also through rational use of selected capping ligands with different affinity toward the nanoparticles surface.

In the following, we plan to briefly discuss some fundamentals regarding the interaction of the pulsed laser beam with a target material embedded in liquid environments and then propose a few examples in which nanomaterials are obtained and applied to biosensing, energy, and environmental applications.

4.2 Fundamentals

4.2.1 Liquid Phase Laser Ablation of Solid Targets

The mechanisms of ablation of any target by laser pulses in a liquid confining medium have been extensively described in the papers by Fabbro et al. [22, 23] and by Sakka et al. [24, 25]. Basically, a plume containing the material is produced at the solid–liquid interface in the place where the incident laser pulses impinge the target. A sketch of the sequence of this mechanism, with the possible involved reactions, is depicted in Fig. 4.1.

The laser-induced plasma expands adiabatically at a supersonic velocity, absorbing the residual part of the laser pulse. This fact determines the creation of a shock wave confined by the liquid environment, and the shock wave, therefore, induces extra pressure. Such a phenomenon is currently described as the formation of the so-called ‘cavitation bubble’. The extra pressure created in the plasma induces, in turn, an additional temperature increase, and this continuous process determines the conditions for a continual supply of the vaporizing species coming from the solid target. In synthesis, a thermodynamic state of higher temperature, higher pressure, and higher density is determined with respect to that of the initially generated plasma.

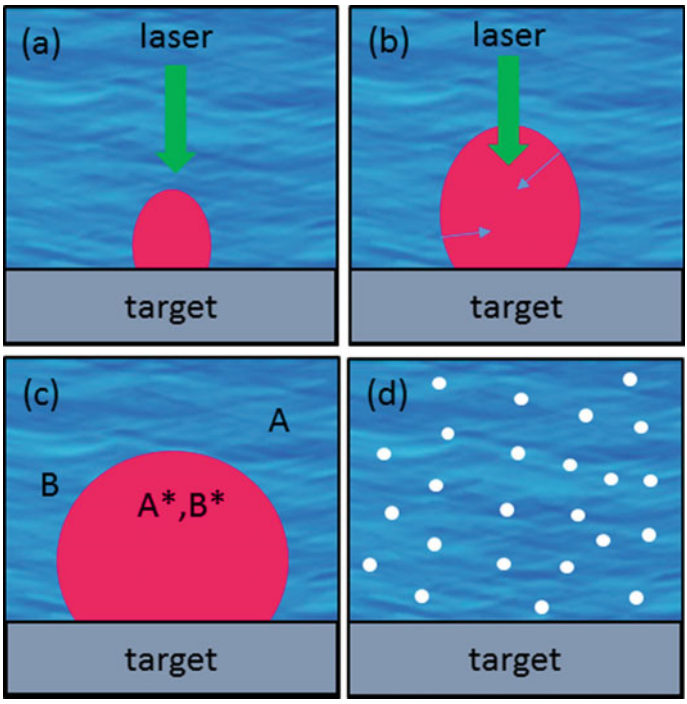

Fig. 4.1 Sequence of PLAL mechanism. The laser hits the target inducing a plasma plume (**a**) which expands into the liquid with a cavitation bubble carrying high temperatures and pressures (**b**). Meanwhile, a number of complex chemical reactions are ignited (**c**), leading to the final formation of nanostructures (**d**)

As an example, Berthe [26] reported a pressure of 2–2.5 GPa, when 50 ns, 0.308 μm wavelength pulses (by a XeCl excimer laser) are employed. With shorter pulse duration (3 ns), pressures up to 10 GPa have been reported.

Concerning density and temperature values, densities up to 10^{22}–10^{23} atoms/cm^3 and plume temperature reaching 4000–5000 K have been reported for the ablated species. During the evolution of the above-described processes, a series of chemical reactions may occur at the solid–liquid interface. Some of these are shown schematically in Fig. 4.1 (panel (c)). First types of reactions occur inside the laser-induced plasma. Here metastable conditions, as those generated by the high temperature and high pressure, take place and lead to the formation of exotic species.

Another kind of chemical reaction occurs at the interface between the laser-induced plasma and the confining liquid environment. The favorable thermodynamic conditions give the opportunity of high energy reactions between ablated species from the target and the molecules of the liquid medium. Reactions are also observed inside the liquid.

Indeed, the extremely high pressure generated in front of the plasma acts on the ablated species from the target at the interface and produces high energy chemical

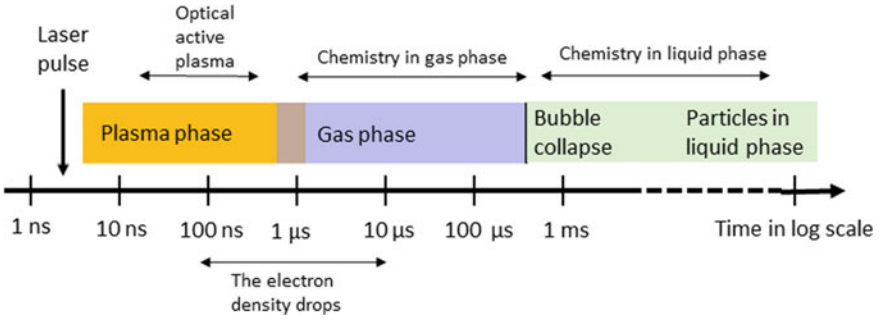

Fig. 4.2 The temporal of the PLAL phenomenon in the case of a nanosecond laser pulse

reactions between ablated atomic species and the liquid molecules inside the liquid phase. As reported by Yang, the evolution stage of plasma, generated by the pulsed laser ablation process of solid targets in liquid media, is represented by the cooling and condensation of generated species in the confining liquid as shown in the panel (d) of Fig. 4.1. The different types of condensation mechanisms will determine different results in material preparations. In particular, one part of the plasma will condense and deposit back on the solid target surface during the plasma quenching in the liquid phase. This process has the effect of depositing materials on the solid target, and it may be used to produce thin films of new materials, resulting from the above-described chemical reactions.

The temporal evolution of the phenomena is reported in Fig. 4.2 for a nanosecond pulse.

As previously reported, the study of the cavitation bubble is one of the most important issues to understand the evolution of the ablation processes and to predict the final results regarding the produced nanostructures.

Cavitation bubbles are generally studied by combining three complementary optical experimental methods with high temporal resolution providing details on the cavitation bubble formation, nucleation, growth, and dissipation dynamics. These are, namely, Optical Emission Spectroscopy for the plasma characterization, fast shadowgraph for plasma and cavitation dynamics, and laser scattering for the mechanisms of delivery of the produced materials in the liquid.

The shadowgraphy can be described as follows:

(i) the laser–target and the laser–plasma interactions,
(ii) the relaxation of the plasma with a characteristic lifetime correlated with the electron density drop,
(iii) the lifetime of the liquid-confined bubble,
(iv) the bubble collapse, and
(v) the aging in the liquid phase.

Coming back to the features of the final colloidal suspension, the reader can find several papers in which the formation of a plenty of different nanoparticles

are obtained using a variety of different laser pulses and target submerged in many liquids and solutions [9–14].

Here, we want to report and discuss a quite unusual experiment in which PLAL in water, using a titanium target, is performed using only a single nanosecond laser pulse. In this case, we plan to gain some information on the specific material produced, avoiding re-irradiation effects, typical in the case of the production of massive materials.

It is known that the repeated pulsed laser ablation of titanium in water gives the formation of a TiO_2 colloid with a mixture of anatase and rutile phases. Figure 4.3a shows the optical image of the crater onto the titanium plate used as a target, once the

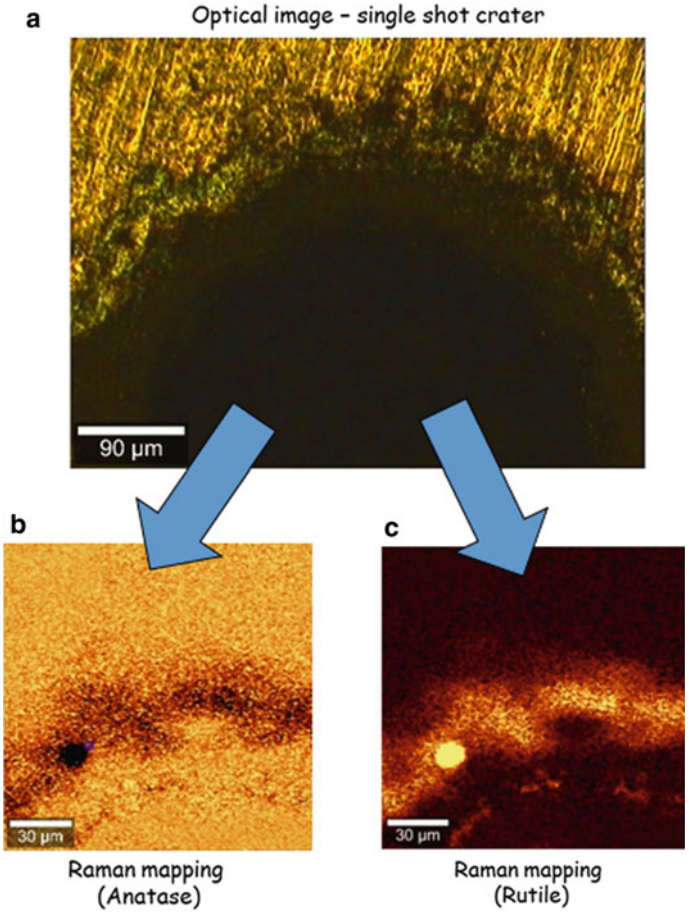

Fig. 4.3 Optical image of the crater created on a titanium plate after firing a nanosecond laser pulse (**a**). The corresponding Raman maps (**b** and c) refer to the presence of rutile and/or anatase nearby the crater

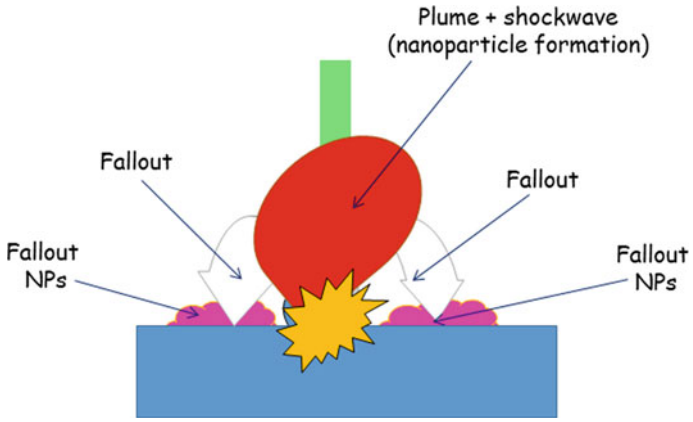

Fig. 4.4 Fallout nanoparticles are mostly in the rutile phase. This material is essentially not involved in the re-irradiation process

shot has been fired. The corresponding Raman maps (Fig. 4.3b, c) refer to the presence of rutile and/or anatase nearby the crater. Anatase is present nearly everywhere, while rutile has been found only in the vicinity or the crater borderline.

Such an anomaly can be explained using the sketch of Fig. 4.4 in which we depict a possible plume evolution.

After the ablation, the cavitation bubble and the plume push the embryonic material far away from the metallic surface, where pressure and temperature quench quite rapidly. Nucleated nanoparticles fallout in the vicinity of the crater border. The analysis evidences that the nanoparticles are mostly in the rutile phase. It is interesting to observe that this material is not involved in a re-irradiation process, in all those cases where repeated laser pulses are used for massive nanoparticles production.

Laser ablation in liquids then gives the possibility to obtain a large variety of nanosized materials directly embedded in the liquid phase. The colloidal suspensions have unique properties if compared with all the other chemical methods used to obtain them. Indeed such laser-generated colloidal nanoparticles are characterized by the following potential advantages:

(a) Versatility: compared to common chemical reduction or precipitation routes which rely on the availability of the respective precursors, this physicochemical laser ablation method allows for the production of nanoparticles from any base material (metal, alloy, semiconductor, ceramic) and in numerous liquids, including polymer-dissolving organic liquids or even ionic liquids.
(b) Availability of precursors: the solid raw material for laser-based nanoparticle production is easily available and often 5–10 times cheaper than commonly used metal–organic precursor compounds.
(c) Purity: the ligand-free synthesis method gives access to highly pure colloids resulting in a high nanoparticle surface activity—the particle surface is not blocked by the chemical ligands or residues of the reducing agents, which leads

to significant advantages for quality demanding nanotechnology applications in biomedicine and catalysis.

(d) Electroaffinity: laser-generated (noble) metal colloids are electron acceptors because of surface atom oxidation resulting in a relatively high particle surface charge. If this charge is not screened by impurities, the particles attract oxygen species and the resulting surface charge triggers electrostatic repulsion. At the same time, the Lewis-acidity of the inorganic nanoparticle makes it possible to achieve efficient electron-donative ligand adsorption.

(e) Defects: under controlled conditions, defect-rich materials and suboxides can be sythesized, potentially broadening the range of optical, semiconducting, or catalytic properties.

Besides the formation of nanomaterials by using an ablation process, power laser beams can be used to modify plenty of nanostructures which have been previously obtained using other methods. In this case, the laser energy triggers many possible phenomena such as fragmentation, melting, or surface functionalization.

4.2.2 Irradiation of Nanoparticles Colloids

Pulsed laser selective heating of existing nanoparticle colloids has been used by several authors in order to modify the structure and/or the chemical nature of a colloidal dispersion [27–30]. The case of noble metal colloids has been frequently treated. As an example, shape modification of gold NPs with pulsed lasers involves the interaction of laser radiation at a wavelength that is close to the localized surface plasmon resonance of the nanocrystals and/or the interband transitions.

The first investigations on the effect of nanosecond laser pulses on aqueous colloidal dispersions of spherical metal NPs showed that fragmentation and reshaping were the two main effects at high and low laser fluences, respectively. Later on, the influence of nanosecond and femtosecond laser pulses at different energies on colloidal gold nanorods, as well as the corresponding structural transformations, were studied. Femtosecond laser pulses at 800 nm led to reshaping of the anisotropic NPs into spheres while keeping constant the initial volume, whereas nanosecond pulses resulted predominantly in fragmentation of the Au NRs.

Recently Koshizaki has reported that suitable irradiation conditions produce spherical submicrometer particles of different materials. With this method, previously prepared NPs were irradiated by unfocused nanosecond laser pulses in different liquids. In the following Fig. 4.5 we report the result of our experiment which indicates that submicrometric spherical TiO_2 particles can be obtained in water suspension starting from random sized titania nanostructures.

The sphere formation mechanism is pretty intuitive [31]. When a colloidal solution is irradiated with a pulsed laser, only the solid particles are heated. The selective heating process depends on the laser energy absorption efficiency of the single solid particles, as well as that of the environment.

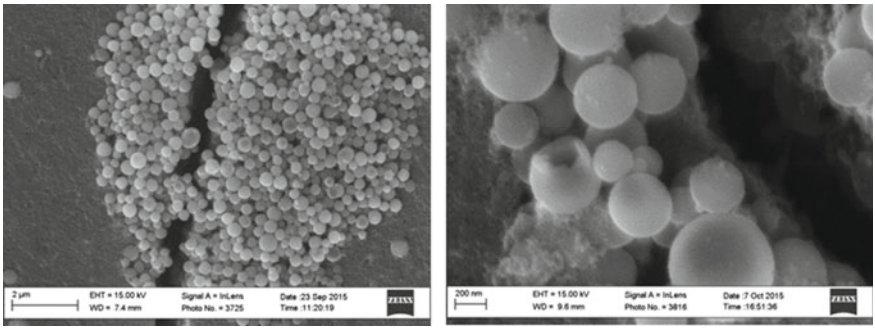

Fig. 4.5 Submicrometric spherical TiO_2 particles obtained in water suspension after the irradiation of randomly sized titania

If the laser energy absorbed is enough to melt them, their shape will change, due to surface tension. If the energy is high enough to completely melt the particles, they become spherical. However, if the energy is insufficient to melt whole particles, only the particle surface melts, resulting in surface smoothing. It is possible to predict the necessary conditions to form spheres, calculating the laser selective heating.

As it was shown in [27], the particle cooling characteristic times (both by irradiation and by boiling heat transfer) is around 10^{-4}–10^{-6} s, significantly shorter than the time between two consecutive pulses (10–1000 Hz repetition) but much longer than the pulse duration (<10^{-8} s). In such condition, it is possible to make all the calculations for one individual laser pulse. This is because we can neglect all the heat losses during the particle heating/melting time and neglect the inter-pulse effect. In such a case, the laser energy absorbed by a particle can be written as follow:

$$Q_{\text{abs}} = J\sigma_{\text{abs}}^{\lambda}(d_{\text{p}}) \tag{4.1}$$

where d_{p} is the diameter of the particle, J is the laser fluence and $\sigma_{\text{abs}}^{\lambda}$ is the particle absorption cross-section, which can be calculated by classical Mie theory. All the absorbed energy is consumed in the heating and melting processes of the particle, which can be expressed as:

$$Q_{\text{abs}} = \rho_{\text{p}}\frac{\pi d_{\text{p}}^3}{6}\left[C_{\text{p}}^{\text{s}}(T_{\text{m}} - T_0) + \Delta H_{\text{m}}\right] \tag{4.2}$$

where T_{m}, ρ_{P}, $C_{\text{p}}{}^{\text{s}}$, T_0 and ΔH_{m} are the melting temperature, the density of the particle, the heat capacities of the material, the ambient temperature, and the enthalpy of melting respectively.

By combining (4.1) and (4.2) one gets the relationship between particle diameter and critical laser energy density for particle melting.

Koshizaki has reported the results for such a calculation, indicating that the critical laser energy density strongly depends on particle size. With increasing laser fluence,

the size of the formed spheres also increases. This result agrees with our experimental results regarding titania.

4.3 Case Studies

We want now to discuss two typical applications of nanomaterials produced by using laser processing in liquids. In this respect, we want to stress both advantages and problems in the use of such a kind of synthetic method relatively to each of the applications proposed. The first example concerns with the use of laser-generated silver nanoparticles for protein biosensing through the use of the so-called Surface Enhanced Raman (SER) effect. The second is related to the possible modification of TiO_2 NPs and graphene oxide by laser irradiation of a colloidal solution. In this case, the modified nanoparticles are employed for several purpouses, such as the pollutant removal from water and photocatalytic water splitting applications.

We want to stress that the processing of nanomaterials through lasers in liquid environments can be considered as an added value with respect to other materials manipulation by conventional methods.

4.3.1 SERS Biosensing of Proteins

Surface-enhanced Raman spectroscopy (SERS) was originally discovered in the 1970s [32–35]. Almost 30 years after the discovery of SERS, interest in SERS has exploded. Thanks to exciting advances in techniques for preparing nanoparticles and to the laser and optics technology associated with measuring the Raman spectra, a number of important applications have been reported.

Under favorable circumstances, Raman enhancements as large as 14 orders of magnitude can be achieved [36]. This is a very high degree of enhancement, capable of single-molecule detection [37] and raises a great interest in creating an ultrasensitive sensing platform with molecular identification capabilities, especially as a sensor for biological molecules.

The large enhancement of the Raman scattering intensity has been explained by two mechanisms: the electromagnetic and chemical mechanisms. The former is attributed to the increase of the local electromagnetic field of the adsorbate because of the excitation of the surface plasmon on the metal surface. On the other hand, the chemical adsorption mechanism is attributed to short distance effects due to the charge transfer between the metal and the adsorbed molecule. Generally, the electromagnetic effect dominates and the chemical effect contributes to the enhancement only on one or two orders of magnitude.

A key role for the magnification is given by the so-called "hot spots" [38]. Hot spots are highly localized regions of intense local field enhancement caused by local surface plasmon resonances. They are generally formed within the interstitial crevices present

in metallic nanostructures (rough metal surfaces, tips, or cavities in nanoparticles agglomerations).

In this way the electromagnetic field of the light at the surface can be greatly enhanced under conditions of surface plasmon excitation; the amplification of both the incident laser field and the scattered Raman field through their interaction with the surface constitutes the electromagnetic SERS mechanism.

Applications of SERS effect to the sensor field is powered by its ability to identify chemical species and obtain structural information in a wide variety of fields including polymer and materials science, biochemistry and biosensing, catalysis, and electrochemistry One of the most important field in which SERS spectroscopy has been applied is biochemistry. With the development of proteomics, it is indispensable to develop new detection methods for high-throughput protein analysis. Most biological methods have the disadvantages of being very time-consuming, consuming large amounts of materials, and resulting in low product yield, which would be stumbling blocks for high-efficiency proteomics.

For fluorescence-based methods, broad emission spectra from molecular fluorophores make multiplexing impossible, and the drawback of susceptibility to photobleaching may greatly weaken their detection limits.

In contrast, SERS-based methods for biomolecules have great advantages over fluorescence-based methods in terms of photostability and spectral multiplexing. They are also much more sensitive than chemiluminescence-based methods. More and more studies have proved the great potential of SERS in protein identification and detection of protein-ligand interactions.

Here, SERS effect has been obtained by using silver NPs in solution produced by PLAL and the key role played by the PLAL in obtaining a large magnification is due to the absence of by-products after the NPs formation. Definitely each Ag NP is able to interact with the protein directly.

As an analyte, we have chosen an amyloidogenic protein called human Islet Amyloid PolyPeptide (hIAPP). Highly aggregated hIAPP deposits are considered the common feature of many degenerative pathologies such as Diabetes Mellitus type II, Parkinson, and Alzheimer [39–42].

Toxicity is often associated with the irreversible formation of amyloid fibers which are protein aggregates, rich in β-sheet structures [39]. Mounting experimental evidences suggest that toxicity is associated with non-specific pores within the cell membrane of the target [43, 44]. Generally, the pathway of fibril formation is mainly investigated using kinetic fluorescent ThT assay. From such assay, it is possible to recognize three different regions: a first region where no fluorescence is detected (the lag-phase); a second region where fluorescence increases (growth-phase) and a final region where fluorescence reaches a plateau. These three regions are associated with three different states of the protein.

Specifically, the presence of unstructured aggregates (oligomeric state) have been assigned to the first region [45], while the increase of ThT fluorescence in the second region is attributed to a self-assembling process of the amiloidogenic proteins forming fibrils [46].

Many structural characterizations are not satisfactory either for oligomers and fibrils. Indeed, since the oligomers show a fast-transient state, X-ray diffraction can merely assign amorphous structures, rich in β-sheet [47]. This especially in the early stage of fibril self-assembling pathway [39, 48].

A possible alternative is the use of highly sensible and chemical-specific techniques such as SERS [49, 50]. This has already been proposed for the detection of prefibrillar assemblies [51–53].

The introduction of SER active surfaces during the amyloid fibril formation can also alter (inhibit/promote) the nucleation-dependent fibrillogenesis mechanism. Recent investigations have in fact highlighted the influence of metal and polymeric nanoparticles in the amyloid fibril formation.

In this respect, Zhang et al. [54] reported that gold nanoparticles (NPs) catalyze the aggregation and growth of lysozyme, while Liao et al. [55] demonstrated that negatively charged gold NPs inhibit Alzheimer's amyloid-β fibrillation. Moreover, Brancolini et al. [56] showed that the interaction between proteins and citrate-capped gold NPs is weak in the physiological condition due to citrate presence.

Of course, chemical reduction of metal salts is one of the most frequently used methods for preparing colloidal metals in order to perform SERS in water protein solutions. Copper, Platinum, Palladium, Silver, and Gold colloids have been prepared by this method. The latter two are most often prepared by reduction of $AgNO_3$ or $HAuCl_4$. Sodium borohydride and sodium citrate are common reductants, although a number of other compounds have been used.

As previously mentioned, these procedures leave into the ambient a large number of unwanted impurities which limit the interaction and reactivity of the analyte with the naked surface and then the sensitivity of the surface-enhanced technique.

The fabrication procedures that are based on pulsed laser ablation in liquid (PLAL) are particularly interesting, because they permit preparation of stable and unprotected nanostructures even in pure solvents [10, 57]. Therefore, having in mind the above-mentioned applications, an investigation on the surface of PLAL-synthesized AgNPs, and on the possible means to control its characteristics, is important in view of proper tailoring of the colloid properties.

Figure 4.6a shows the Raman spectra for hIAPP in the prefibrillar structures and after the formation of amyloid fibrils at a protein concentration of 0.4 μM. The positions of the vibrational bands characterizing the secondary structure depend on inter and intramolecular protein interactions, including peptide-bond angles and hydrogen-bonding patterns.

Typically, a protein Raman spectrum is the result of three major vibrational modes in the range 1000–1800 cm^{-1}:

(a) amide bands (amide I, II, III) of the polypeptide backbone
(b) vibrations of aromatic amino acid residue
(c) vibrations of nonaromatic side chains.

As expected, at the beginning of the fibrillogenesis process, no protein signal is detected. At the end of the growth process, fibrils are well visible spectroscopically. Atomic Force Microscopy in tapping mode (Fig. 4.6b) determines the morphology

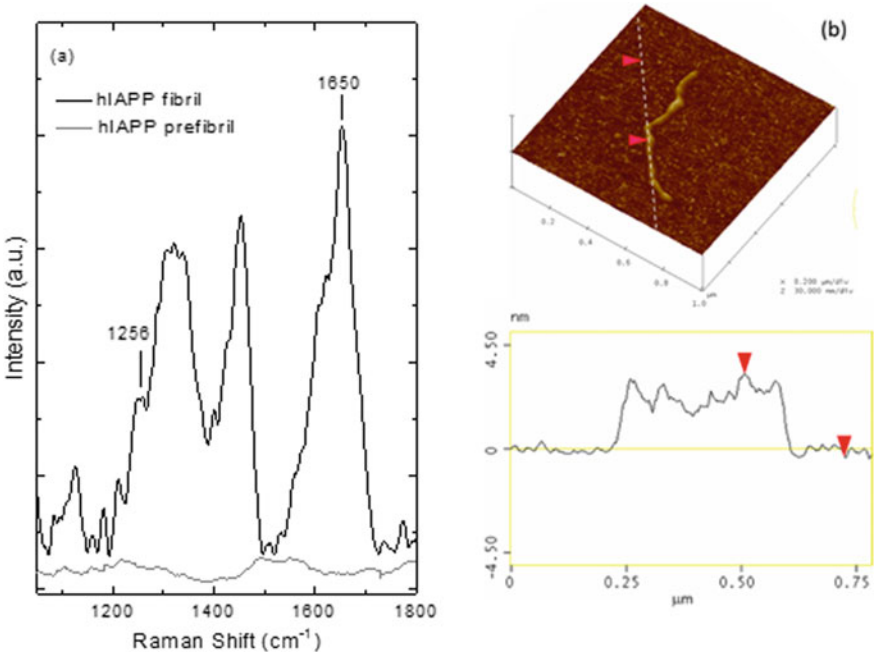

Fig. 4.6 **a** Normal Raman Spectra of hIAPP fibril (black line) and prefibril (gray line). **b** Section analysis and AFM image (2 µm × 2 µm) of a single fibril in aged hIAPP

of amyloid fibrils on a silicon substrate which has formed after an incubation time t > 24 h [44]. A section analysis has estimated the height of the fibril at about 3.4 ± 0.2 nm.

Regarding the Raman spectrum reported in Fig. 4.6, from here on we will discuss only the frequency of the amide I band ranging between 1630 and 1690 cm^{-1}. Indeed, in such spectral region, there is no overlapping with the vibrational modes of other functional groups. By contrast, amide III signals (1230–1270 cm^{-1}) lie at the same frequency range of CH and C–C.

As a matter of fact, the (normal) Raman spectrum of hIAPP clearly evidences the presence of fibrils with amide I in α-helix and β-sheet configurations. Secondary structures in α-helix configuration is usually unexpected in fibrils because of the conversion into β-sheet conformations. Their existence can be also confirmed by the detection of an amide III band at 1256 cm^{-1} [58–63].

Our previous ThT fluorescence assays have shown that after an incubation time of about 6 h, protein solutions (<1 µM) contain non-structured oligomers. After 6 h of incubation, the fibril growth process starts and the formation of mature fibrils completes after 24 h. The low protein concentration in the lag phase is the reason for the detection failure through (normal) Raman spectroscopy.

To enhance the sensitivity of the technique, we added some aliquots of PLAL generated colloidal Ag NPs to a 250 nM protein solution at different hIAPP incubation times (2, 6, and 24 h). The result is reported in Fig. 4.7.

If we consider the intensity ratio of (β-sheet)/(α-helix + r. coil), an increase of about 40% of the β-sheet by increasing the incubation time from 2 to 6 h is detected. A transformation of random coils structures and α-helices towards β-sheets ordered aggregates have been found.

After 2 h, amide I band results broadly, clearly indicating a mixture of α-helices, random coils and β-sheets. The SERS signals have almost the same integrated intensity areas. For clarity, we used three Lorentzian functions to deconvolve such a broad structure.

Since the vibrational spectra have been performed immediately after the nanoparticle introduction, we suppose their null (or negligible) contribution to the protein evolution.

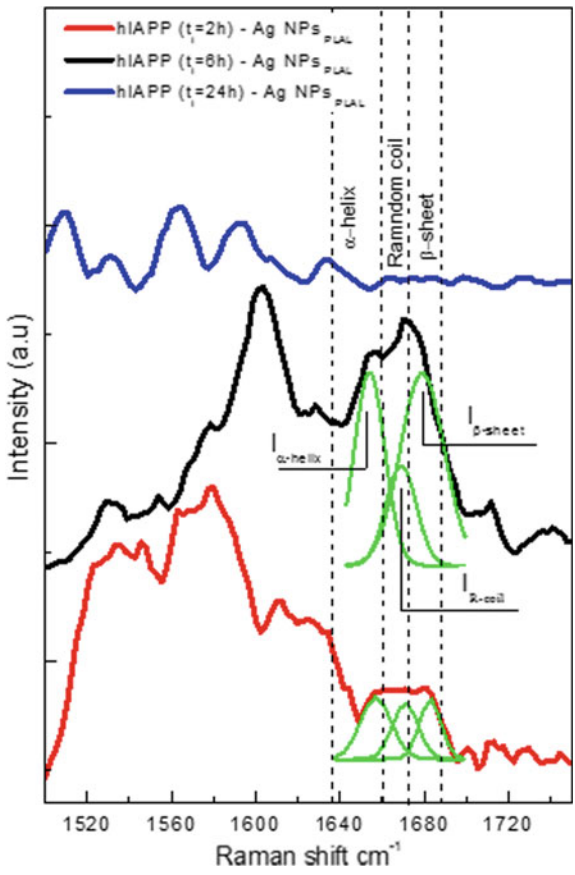

Fig. 4.7 SERS of hIAPP in presence of Ag NPs PLAL added after 2, 6, and 24 h. Lorentzian deconvolutions are also shown (green lines)

We want now to discuss a possible interaction of the metallic nanoparticle surfaces during the fibril growth to investigate a possible dual role of undecorated (PLAL produced) metal nanoparticles. For these reasons we mixed metal colloids at the beginning of the lag phase, leaving them throughout the evolution time and monitoring the SERS spectrum as time goes by. In this respect, we also want to compare the behavior of PLAL colloids with those of chemically prepared ones (salt reduction). In details, Ag, Au nanoparticles both prepared by the laser method and by the chemical route were added to a 250 nM protein as-prepared solution.

We have then monitored the fibrillogenesis process as function of the incubation time between 15 min and 24 h in the presence of PLAL silver nanoparticles.

Figure 4.8 shows significant SERS spectral changes after 1, 4, and 15 h. In all these cases every feature of interest is well resolved in the spectra.

Signals associated to the α-helix structures are detected after 1 h, α-helices, random coils and β-sheets are easily detected after 4 h, while after 15 h, random coils and β-sheets are the main features characterizing oligomers and prefibrils. This is consistent with a conversion of α-helix in β-sheet rich prefibrils. Finally, after an incubation time of 24 h most of the fibrils precipitate, preventing further spectroscopic observations in the amide I region. The remaining vibrational features could be associated to small peptide fragments interacting with silver nanoparticles. As reported in the literature [64], the absence of any band related to the secondary structure could be attributed to a parallel orientation of the remaining peptide backbone on silver colloid surface.

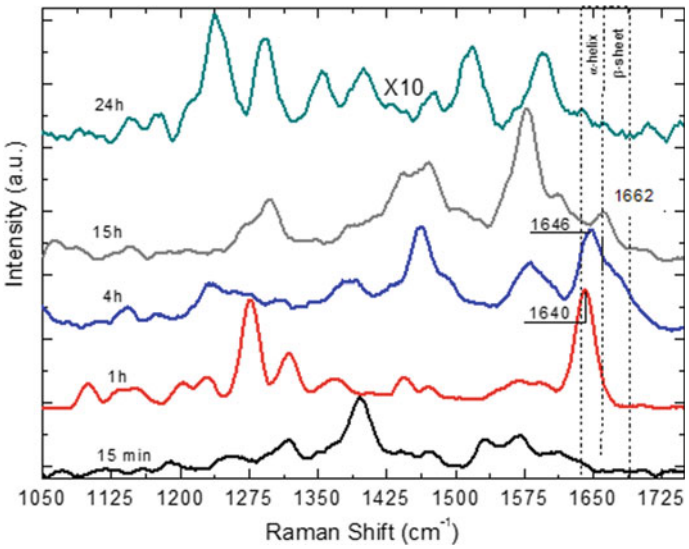

Fig. 4.8 SERS spectra of hIAPP induced by Ag NPs obtained by laser ablation in water, as function of the incubation time between 15 min and 24 h

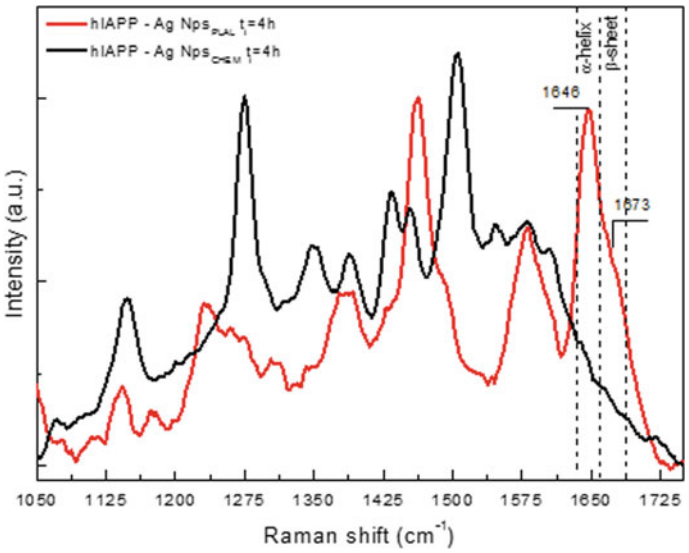

Fig. 4.9 SERS spectra of hIAPP (250 nM) in presence of Ag and Au NPs PLAL after an incubation time of 4 h

Figure 4.9 reports the same experiment conducted using silver nanoparticles obtained by chemical synthesis. The latter are obtained upon reaction of sodium borohydride with silver nitrate $AgNO_3$.

Unlike PLAL nanoparticles, no β-sheets are detected after the interaction with Ag NPs_{CHEM}. This different behavior could be attributed to a weak interaction between Ag NPs_{CHEM} and hIAPP responsible for a feeble Raman enhancement.

Specifically, in chemical synthesized silver colloids, borohydride anions are adsorbed onto nanoparticles surface. The presence of the resulting repelling forces plays a key role in the hIAPP-colloid interaction.

In summary, we have shown that uncapped and pure NPs produced by ablation in water exhibit highest sensitivity if compared with chemically produced ones and inhibit the structural arrangements of monomers and oligomers into a β-sheet structures, characteristic of fibrils [65].

4.3.2 Environmental Applications: Dye Removal, Antibacterial Activity, and Photocatalytic H_2 Production

Environmental pollution, energy production, and storage are current global challenges faced by human beings. Since the past two decades, the evolution of nanotechnology represents an ever-improving process in the design, discovery, creation, and

novel utilization of artificial nanoscale materials. To meet the major challenges in environmental sustainability, these nanomaterials in various hierarchical fashions are stimulating important practical applications in the environmental field sector. The rapid development in materials and catalysis science has led to significant advances in understanding the controlled synthesis and structure–activity relationship of the nanomaterials. The design, synthesis, and modification of novel nanomaterials allow for enhanced performance for environmental-related applications.

In this section, we intend to present three examples in which 'in water' laser irradiation of TiO_2 and Graphene Oxide (GO) colloids is able to enhance the performances towards photocatalytic water splitting and water purification (dye removal and antibacterial activity) applications, respectively.

Activated carbons are generally used as adsorbents for dyes removal because of their extremely high surface areas (1000 m^2/g on average) [66]. Several research groups specifically studied other new strategies for the synthesis of non-carbonaceous, low-cost adsorbents as TiO_2 nanowires, zeolites, zinc ferrite nanoparticles, or mesoporous Cu_2O submicro-spheres. Anyway, carbon-based materials remain the most attractive thanks to their properties such as structural diversity, chemical stability, and cost-effective synthesis. Recently, graphene and graphene oxide (GO) are drawing much attention as alternative materials for adsorption [67] of various substances such as dyes, heavy metals and phenols [68].

The large theoretical surface area (as high as 2630 m^2/g) of GO and the presence of the oxygen functional groups induce a negative charge on the surface that is responsible for the formation of stable aqueous colloids, and favors the adsorption of positively charged species, such as metal ions or cationic dyes [68–71]. Because of such properties graphene oxide and reduced graphene oxide (rGO) could be considered promising adsorbents for dyes like methylene blue (MB). In this contest, we have reported the reduction of GO sheets by the pulsed laser irradiation in liquid technique [72]. The main benefit of such technique with respect to the common reduction methods for GO, is the absence of chemical by-products during the synthesis making this method greener than chemical reduction processes.

GO was synthetized by a modified Hummers and Offeman's method [73]. The obtained sheets showed (AFM analysis) a thickness of ~0.7 nm, which agrees with standard thickness for such synthesis method reported in the literature for graphene oxide dispersions in water. The reason why GO layers result thicker than single-layer graphene sheets (0.34 nm) is due to the existence of the functional groups containing oxygen in the basal plane of the structure, to the roughness ascribed to sp^3 centers and to the presence of point defects in the carbon lattice.

GO was reduced by irradiating a GO solution with the second harmonic of a pulsed Nd:YAG laser with a pulse duration of 5 ns with a repetition rate of 10 Hz. The irradiation process was carried out, without any focusing lens, under strong stirring conditions, to ensure a homogeneous irradiation of the GO solution, at a constant fluence of 0.32 J/cm^2 for different times. With this experimental set up, we obtained stable solutions of rGO with different degree of reduction, depending on the time of irradiation and the degree of reduction was confirmed by several characterization analyses. We hypothesized that the reduction process under laser

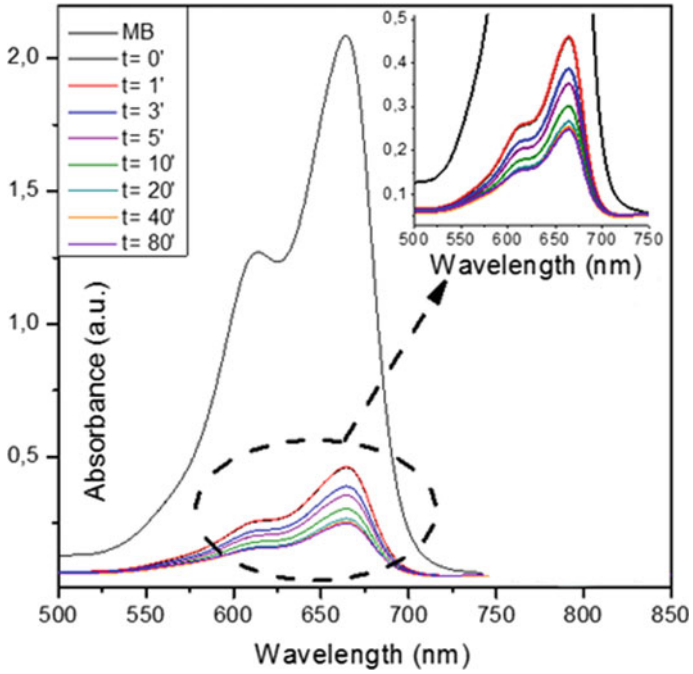

Fig. 4.10 UV-vis absorbance spectra of methylene blue in a reduced GO solution at different times

irradiation of the GO sheets takes place because GO is subjected to a mechanism similar to the solvo-thermal reduction of graphene oxide.

One of the main features of the obtained GO suspension is the stability toward clustering and precipitation. This property results to be critical if these systems are used for the removal of contaminants in wastewaters and it strongly depends on the effective surface charge related with the double layer around the GO sheets.

To study the stability of the laser-treated GO dispersion, zeta potential measurements were performed for the as-prepared GO and laser-irradiated one. GO prepared by the modified Hummers method has a zeta-potential of −63 mV and after laser irradiation, a decrease of the zeta-potentials up to −50 mV was observed. Even if these ζ-potential values result lower than as-prepared GO, the obtained rGO dispersions remain stable because ζ-potential values lower than −30 mV are generally considered to give sufficient mutual repulsion and ensure the stability of a dispersion.

After characterization, we tested GO and rGO (30 min. laser treatment) towards the absorption of methylene blue (MB). The result indicates that the GO/MB mixture became unstable and immediately an aggregation phenomenon occurred. Some aliquots of the mixed solution were taken at regular intervals of time, to calculate concentration of the residual MB by using a UV–Vis spectrophotometer, the spectra obtained are reported in Fig. 4.10. When GO (rGO) is added to the solu-

tion the concentration of the residual MB rapidly decreases until 40 min. Then an equilibrium is reached.

The amount of MB adsorbed (Q_t) at time t, was calculated according to the equation:

$$Q_t = [(C_0 - C_t)V]/m$$

where C_0 is the initial concentration of MB (mg/l), C_t is the amount of adsorbed MB on the adsorbent (mg/g), V is the volume of the solution (l) and m is the mass of adsorbent (g). The behavior has been reported in Fig. 4.11 for GO and rGO (30 min. irradiation).

Initially, very fast adsorption occurs reaching Q_t values of around 600 mg/g in a few seconds. After this stage, a slower adsorption stage occurs after about 3 min. The adsorption capacity reaches the equilibrium after 20 min. The fast adsorption stage is attributed to the adsorption of MB molecules on the surface of the adsorbents (Fig. 4.11).

Conversely, the slower adsorption process can be related to the intra-particle diffusion, suggesting that adsorption mechanism is quite complex and involves different steps. AFM investigations have evidenced that the increase of the adsorption capacity for laser-treated GO could be related to the presence of macro and meso-pores, which enhanced the adsorption process (higher adsorption capacity).

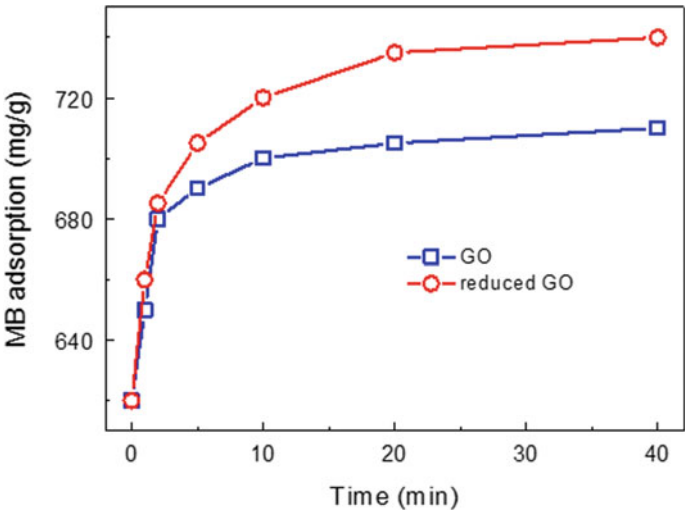

Fig. 4.11 MB adsorbed as a function of time using GO and reduced GO in water. A fast stage is followed by slower adsorption, lasting for about 3 min with an equilibrium after around 20 min. The fast adsorption stage is attributed to the adsorption of MB dyes on the external surface of the adsorbents

The antibacterial properties of laser-irradiated graphene oxide were recently demonstrated in a paper by Buccheri et al. [74]. The test was performed on *Escherichia coli* using both GO and laser-irradiated GO, showing that the higher antibacterial activity is obtained for GO irradiated at least for three hours. These properties seem to be correlated to the resulting morphology and size of laser-treated GO and independent of the kind and amount of oxygen functionalities. Indeed, X-ray photoelectron spectroscopy, Raman spectroscopy, dynamic light scattering, and scanning electron microscopy show a reduction of the GO flakes size after visible laser irradiation, preserving a considerable content of oxygen and hydrophilicity degree. SEM images of the bacteria after the exposure to the laser-irradiated GO flakes confirm membrane damage after interaction with the laser-modified GO, as shown in Fig. 4.12.

In addition, fish embryo toxicity test on zebrafish was performed and it displayed that neither mortality nor sub-lethal effects were caused by the different laser-treated GO solutions, even when the concentration was increased up to four times higher than the one effective to reduce the bacteria survival. The antibacterial properties and the absence of toxicity make the visible laser irradiation of GO a promising option for water purification applications.

We now come to the third case study, related to the possibility to enhance the hydrogen production through photocatalytic water splitting by laser irradiating titania colloids.

We would like to remind that photocatalysis is a process that uses light to activate a substance and modifies the rate of a chemical reaction without itself being changed.

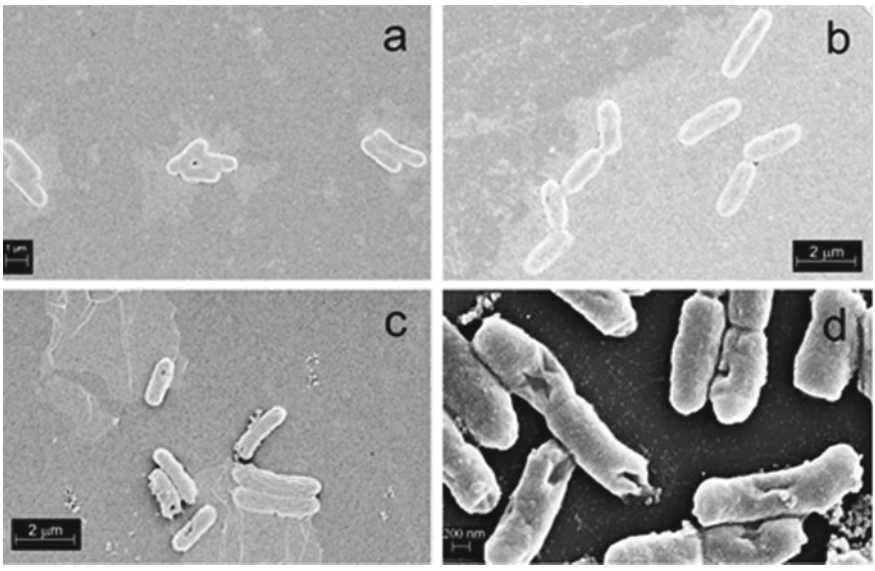

Fig. 4.12 SEM images of untreated E. coli (**a**) and of E. coli after 1 h of exposure to 30 mg/l of GO (**b**) or to 30 mg/l of laser-treated GO (**c** and **d**) (from [74])

The photocatalyst is the substance which can modify the rate of chemical reaction using light irradiation. Photocatalysis finds a large number of applications in many fields such as the removal of pollutants from water or air and hydrogen production. In particular, water treatment technology by photocatalysis is low cost, environmentally friendly, and sustainable, while photocatalytic water splitting for the production of hydrogen may become more competitive with respect to the conventional production method (hydrocarbon steam reforming) as the cost continues to decrease with the technology advancement.

Since the first report by Fujishima and Honda [75], photocatalytic water-splitting using titanium dioxide TiO_2 for hydrogen production offers a promising way for clean, low-cost, and environmentally friendly production of hydrogen by solar energy. Presently, the solar-to-hydrogen energy conversion efficiency is too low for the technology to be economically sound. The main barriers are the rapid recombination of photo-generated electron/hole pairs as well as backward reaction and the poor activation of TiO_2 by visible light. Some investigators studied the effects of addition of sacrificial reagents and carbonate salts to prohibit rapid recombination of electron/hole pairs and backward reactions. Other research focused on the enhancement of photocatalysis by modification of TiO_2 by means of doping of pure titania with metals [76–78], non-metals [79, 80] or the fabrication of TiO_2-based nanohybrids [81, 82].

In addition to above-mentioned methods, recent investigations have also demonstrated that the presence of defect-containing (blue) TiO_2 significantly improves the photocatalytic activity in the overall solar spectrum, including visible and UV [83, 84]. Blue titania surface defect states are composed by under-coordinated Ti^{4+} sites and oxygen vacancies which act as anchoring and charge injection/recombination sites, playing a crucial role in the electron injection and recombination dynamics. Literature presents several methods to dope TiO_2 with metals, non-metals, or combining it with carbon nanostructures that involve chemical processes with the possibility of introducing impurities inside the chemical structure of titania. In addition, treatment under vacuum or under reducing conditions and treatments by using hydrogen plasmas have been used for reducing titania and introducing defects. These methods unavoidably involve high processing temperatures (400–700 °C), vacuum systems, long processing times, and multistep operations. For these reasons, it is exceptionally desirable to explore simple and economic strategies to modify titanium dioxide with increased photocatalytic activity.

Pulsed lasers are powerful tools for the time-efficient preparation and/or modification of functional materials [85] and these are recently investigated for defects introduction in metal oxides semiconductors. Yang et al. obtained defective anatase by laser ablation of a titanium target in water by using a nanosecond 532 nm laser [86] or by using a near-IR laser [87]. Bulk defects such as oxygen vacancies of the LAL-synthesized titania samples were observed and these induced a clear blueshift and broadening of the band gap band in the Raman spectra. Besides nanoparticles formation by laser ablation, laser irradiation methods make it possible to modify the chemical/physical properties of nanoparticles directly dispersed in solution such as

their morphology and size, their chemical composition, or crystalline phase. Furthermore, laser irradiation in liquid resulting in NPs melting or fragmentation also induces defects in titania structure.

As previously demonstrated, 'in liquid' laser irradiation technique has been demonstrated to be an interesting method to easily increase the photocatalytic activity of TiO_2 and other nanomaterials towards the degradation of organic pollutants and water splitting application [88, 89]. It's an easy, low cost, eco-friendly, and tunable technique to modify inorganic semiconductors directly in water. Very recently, hydrogenated blue titania has been found to greatly enhance both solar absorption and photocatalytic methyl orange decomposition compared to the pristine TiO_2 [90]. Visible active titania colloids were obtained by UV laser irradiation of anatase NPs dispersed in ethanol and the as modified samples showed an higher photocatalytic activity either under UV and solar irradiation with respect to untreated material. The use of ethanol as solvent in the laser processes was found to be the best choice to improve the activity of TiO_2 sample under visible light. This is explained in more detail in the following paragraphs.

Here, we report a study on the use of laser irradiation in liquids for improving the photocatalytic activity of titanium dioxide [91]. We use laser irradiation for the introduction of defects inside titania (as Ti^{3+} and O-vacancies) to improve the photocatalytic activity of titania for water splitting. In this case, the proposed method can be 'built-in', since laser irradiation and hydrogen production can be performed in the same system at the same site. Indeed, laser irradiation is performed on aqueous titania dispersions which can be directly used for the subsequent water splitting process.

Unlike a conductor, a semiconductor like titania has well defined VB and CB. Energy difference between these two levels is said to be the band gap Eg. Without excitation, both the electrons and holes are in the valence band. When semiconductors are excited by photons with energy equal to or higher than their band gap energy level, electrons receive energy from the photons and are thus promoted from VB to CB. This reaction can be expressed as:

$$TiO_2 + h\upsilon \rightarrow h^+ + e^-$$

The photo-generated electrons and holes can undergo different processes shown in Fig. 4.13:

(i) the charge carriers successfully diffuse to the surface of TiO_2 and then act as oxidizing and/or reductant;
(ii) the charge carriers are trapped by the surface and/or bulk defect sites of TiO_2;
(iii) the separated charge carriers recombine and release the energy in the form of photon or heat in bulk and/or on the surface.

If H_2O splitting is desired, the CB level should be more negative than the hydrogen evolution level E_{H_2/H_2O} to initiate hydrogen production, while the VB should be more positive than water oxidation level E_{O_2/H_2O} for efficient oxygen production from water by photocatalysis [92]. On the other hand, during the degradation of an

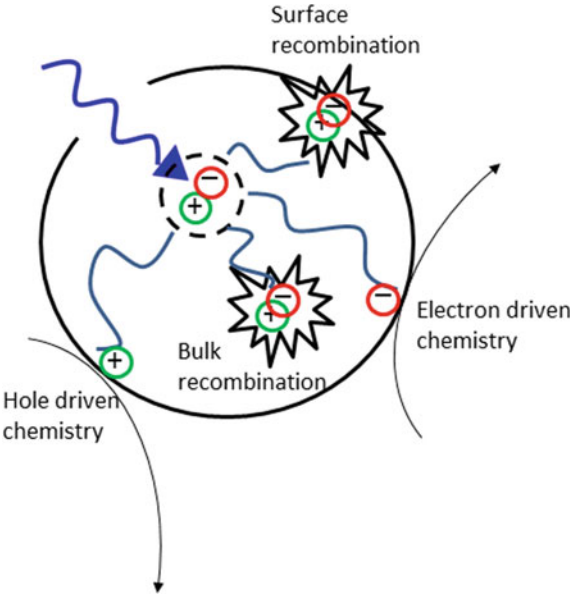

Fig. 4.13 Mechanisms of photocatalytic processes using a wide gap semiconductor oxide

organic compound, the holes in the valence band oxidize the organic contaminants while the electrons reduce it. As a consequence, the VB should be lower with respect to the potential level of the donor species so it can transfer an electron to the VB. The CB level should be higher with respect to the potential of the acceptor species so it can subtract the electron from the CB.

Anatase, rutile, and P25 (anatase/rutile mixed phase) water suspension have been irradiated under continuous stirring by the second harmonic (532 nm) radiation of a Nd:YAG pulsed laser system operating with a pulse duration of 5 ns and a repetition rate of 10 Hz. The laser beam size was around 28 mm^2, and it was directed toward the titania solution without any focusing lens. The titania suspension was irradiated homogeneously at a constant laser power up to 1.45 W (0.5 J/cm^2) for 30 min.

Immediately after the irradiation, the initially white suspension turns towards deep blue. The prepared samples were tested for photocatalytic water splitting under UV–Vis or Visible light. A detailed structural analysis of the colloids evidenced that upon irradiation the titania nanoparticles undergo a series of modifications, responsible for the enhanced catalytic performances. The change of color solution from white to blue indicated the formation of defects like reduced titanium Ti^{3+} and oxygen vacancies as confirmed by XPS analysis. These defects have consequences in the modification of the electronic structure reducing the energy gap of the material. A phase change from anatase towards rutile was also observed. However, this was inhibited for P25.

Photocatalytic H_2 production experiments demonstrate that pulsed laser irradiation increased the photocatalytic performances of the samples under UV and solar

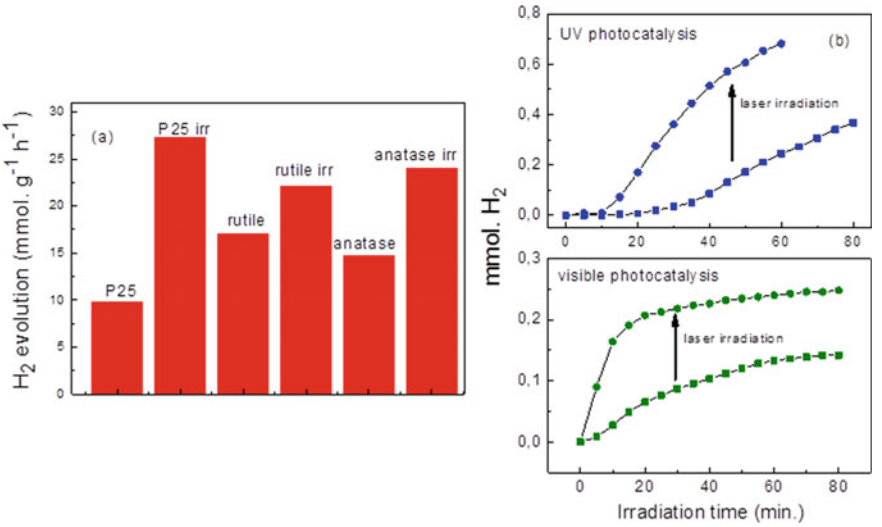

Fig. 4.14 **a** Amount of produced hydrogen under UV irradiation for different titania samples before and after laser irradiation process. **b** Amount of produced hydrogen under UV and Visible irradiation versus time for as received P25 and laser modified P25

actions. The induced magnification was long-living and provides a simple and environmentally friendly methodology. Figure 4.14a shows the overall hydrogen evolution as a function of time, comparing as received and irradiated rutile, anatase, and P25 samples at the maximum fluence. It is important to underline that the increase of laser fluence had a positive effect on the photocatalytic performance of titania which could be correlated to higher concentration of defects. The laser irradiation strongly enhanced the production rate up to a factor of three for P25 that showed the best performance, but also anatase and rutile samples increased their photocatalytic activity after laser irradiation. It is also possible to exclude a correlation between the increased activity and the phase change of titania from anatase to rutile. Indeed P25, which was the sample with the largest difference in the activity, did not exhibit any relevant change in the crystalline phase due to irradiation. In agreement with the theoretical studies reported by Zhao et al. [93] the same figure also evidences a higher rutile activity with respect to anatase.

Figure 4.14b reports the amount of produced hydrogen versus time of UV or Visible irradiation for the P25 as received and after laser irradiation. Under UV irradiation, the curves display an initial induction period lasting less than 10 min due to stabilization of lamp radiation and the saturation of water with evolved gases; a linear increment in which there is a maximum in the hydrogen production rate and finally a moderate decrease of the production rate after about one-hour irradiation due to a recombination of photo-generated electron/hole pairs or to a fast backward reaction (recombination of hydrogen and oxygen into water).

An enhancement of the hydrogen production is also obtained by irradiating the sample using visible light, shown also in Fig. 4.14b for P25. In this case, however, it is possible to note that the total amount of hydrogen production with visible light is considerably lower than that found with UV irradiation. This behavior is reasonable, considering the energy band-gap measurements. The hydrogen production yield for irradiated nanoparticles was compared with that obtained after a standard reduction procedure at 500 °C for 1 h in hydrogen atmosphere [30]. It can be seen that the photocatalytic performances in the H_2 reduced sample is much lower compared to laser irradiation. This confirms the laser irradiation process, not only as a lower cost and easier process with respect to standard reduction, but also as a more efficient approach in generating higher photocatalytic active samples.

In this regard, highly visible light photoactive titania colloids have been prepared by UV laser irradiation of anatase titania colloids in water or ethanol. The nature of solvent/titania interaction affects the induced modifications by laser processing and consequently the photocatalytic performances. In particular, theoretical calculations showed that water molecules only weakly interact with the titania surface resulting in the coexistence of surface oxygen vacancy defects, as confirmed by photoluminescence (PL) spectra, and OH groups on titania surfaces as shown by Fourier transform infrared spectra (FT-IR) spectrum. In this scenario, laser irradiation leads to the passivation of oxygen vacancies due to surface hydroxylation as confirmed both by PL and FT-IR spectra. These laser-induced modifications resulted in an increased photocatalytic activity under UV irradiation. A similar result was observed for samples laser-treated in ethanol; furthermore, a photocatalytic activity under solar irradiation was also conferred to anatase sample by laser processing in this solvent. Ethanol molecules completely passivate defects in anatase surface as confirmed by FT-IR spectra, theoretical calculations, and the quenching of visible emission band in PL spectra of colloids before the laser processing. In this case, the UV laser irradiation of anatase surface covered by ethanol moieties lead to higher degree of titania reduction due to the holes scavenger effect of ethanol itself. In addition, ethanol moieties adsorbed on titania surfaces are photooxidezed during the laser processing, as confirmed by FT-IR spectra resulting in the introduction of vacancies not susceptible to ethanol absorption and an indirect C doping of titania surface by the incorporation of carboxylated species obtained as by-products of ethanol moieties photoconversion. Under artificial solar light, this sample showed comparable performance respect to other TiO_2 composites tested in the same conditions and higher activity with respect to C doped titania samples.

These results point out the light on another advantage of the ‘in liquid’ laser irradiation process: a proper evaluation of the dispersing medium-semiconductor interaction allows to tune the process, in order to improve the photocatalytic activity of the semiconductor itself and extend it to visible light wavelength range. This is a very interesting aspect from a practical point of view.

Furthermore, in comparison to the other TiO_2-based samples [94] synthetized with structural and chemical modifications, for the photocatalytic hydrogen production the laser-treated TiO_2 was the best sample under UV irradiation, whereas under solar/visible light irradiation the TiO_2 chemically modified with other metals showed

the best results [94]. Further improvements in the laser irradiation process (for example changing the solvent of the irradiation process) can greatly ameliorate the photoactivity under visible light irradiation.

References

1. G. Schmid, *Nanoparticles: From Theory to Application* (Wiley, 2006)
2. S.K. Kulkarni, *Nanotechnology: Principles and Practices* (Springer, 2014)
3. D. Vollath, *Nanomaterials: An Introduction to Synthesis, Properties and Applications* (Wiley, 2012)
4. J. Jeevanandam, A. Barhoum, Y.S. Chan et al., Review on nanoparticles and nanostructured materials: history, sources, toxicity and regulations. Beilstein J. Nanotechnol. **9**, 1050–1074 (2018)
5. M. Shafiq, S. Anjum, C. Hano et al., An overview of the applications of nanomaterials and nanodevices in the food industry. Foods **9**, 148 (2020)
6. H. Wang, X. Liang, J. Wang et al., Multifunctional inorganic nanomaterials for energy applications. Nanoscale **12**, 14–42 (2020)
7. M. Rycenga, C.M. Cobley, J. Zeng et al., Controlling the synthesis and assembly of silver nanostructures for plasmonic applications. Chem. Rev. **111**, 3669–3712 (2011)
8. X. Zhang, A. Hu, T. Zhang et al., Self-assembly of large-scale and ultrathin silver nanoplate films with tunable plasmon resonance properties. ACS Nano **5**, 9082–9092 (2011)
9. D. Zhang, B. Gökce, S. Barcikowski, Laser synthesis and processing of colloids: fundamentals and applications. Chem. Rev. **117**, 3990–4103 (2017)
10. S. Barcikowski, G. Compagnini, Advanced nanoparticle generation and excitation by lasers in liquids. Phys. Chem. Chem. Phys. **15**, 3022–3026 (2013)
11. G.W. Yang, Laser ablation in liquids: applications in the synthesis of nanocrystals. Prog. Mater Sci. **52**, 648–698 (2007)
12. V. Amendola, M. Meneghetti, Laser ablation synthesis in solution and size manipulation of noble metal nanoparticles. Phys. Chem. Chem. Phys. **11**, 3805–3821 (2009)
13. F. Taccogna, M. Dell'Aglio, M. Rutigliano et al., On the growth mechanism of nanoparticles in plasma during pulsed laser ablation in liquids. Plasma Sources Sci. Technol. **26**, 045002 (2017) (10pp)
14. G. Yang, *Laser Ablation in Liquids: Principles and Applications in the Preparation of Nanomaterials* (Pan, Stanford, 2012)
15. V. Amendola, D. Amans, Y. Ishikawa et al., Room-temperature laser synthesis in liquid of oxide, metal-oxide core-shells and doped oxide nanoparticles. Chem. A Eur. J. **26**(42) (2020)
16. G. González-Rubio, A. Guerrero-Martínez, L.M. Liz-Marzán, Reshaping, fragmentation, and assembly of gold nanoparticles assisted by pulse lasers. Acc. Chem. Res. **49**, 678–686 (2016)
17. L. Delfour, T.E. Itina, Mechanisms of ultrashort laser-induced fragmentation of metal nanoparticles in liquids: numerical insights. J. Phys. Chem. C **119**, 13893–13900 (2015)
18. H. Wang, A. Pyatenko, K. Kawaguchi et al., Selective pulsed heating for the synthesis of semiconductor and metal submicrometer spheres. Angew. Chem. Int. Ed. **49**, 6361–6364 (2010)
19. H. Wang, A. Pyatenko, K. Kawaguchi et al., General bottom-up construction of spherical particles by pulsed laser irradiation of colloidal nanoparticles: a case study on CuO. Chem. Eur. J. **18**, 163–169 (2012)
20. G. Messina, M. Sinatra, V. Bonanni et al., Tuning the composition of alloy nanoparticles through laser mixing: the role of surface plasmon resonance. J. Phys. Chem. C **120**, 12810–12818 (2016)
21. G. Compagnini, E. Messina, O. Puglisi et al., Laser synthesis of Au/Ag colloidal nano-alloys: optical properties, structure and composition. Appl. Surf. Sci. **254**, 1007–1011 (2007)
22. R. Fabbro, P. Peyer, L. Berthe et al., Physics and applications of laser-shock processing. J. Laser Appl. **10**, 265–279 (1998)

23. L. Berthe, R. Fabbro, P. Peyer et al., Shock waves from a water-confined laser-generated plasma. J. Appl. Phys. **82**, 2826–2832 (1997)
24. T. Sakka, S. Yawanage, Y.H. Ogata et al., Laser ablation at solid–liquid interfaces: an approach from optical emission spectra. J. Chem. Phys. **112**, 8645–8653 (2000)
25. K. Saito, K. Takatani, T. Sakka et al., Observation of the light emitting region produced by pulsed laser irradiation to a solid–liquid interface. Appl. Surf. Sci. **197**, 56–60 (2002)
26. L. Berthe, A. Sollier, R. Fabbro et al., The generation of laser shock waves in a water-confinement regime with 50 ns and 150 ns XeCl excimer laser pulses. J. Phys. D Appl. Phys. **33**, 2142–2145 (2000)
27. D. Liu, C. Li, F. Zhou et al., Rapid synthesis of monodisperse au nanospheres through a laser irradiation-induced shape conversion, self-assembly and their electromagnetic coupling. Sci. Rep. **5**, 7686 (2015) (9pp)
28. Y. Chen, Y. Tseng, C. Yeh, Laser-induced alloying Au–Pd and Ag–Pd colloidal mixtures: the formation of dispersed Au/Pd and Ag/Pd nanoparticles. J. Mater. Chem. **12**, 1419–1422 (2002)
29. M.A. Buccheri, D. D'Angelo, S. Scalese et al., Modification of graphene oxide by laser irradiation: a new route to enhance antibacterial activity. Nanotechnology **27**, 245704 (2016) (12pp)
30. X. Li, A. Pyatenko, Y. Shimizu et al., Fabrication of crystalline silicon spheres by selective laser heating in liquid medium. Langmuir **27**, 5076–5080 (2011)
31. A. Pyatenko, M. Yamaguchi, M. Suzuki, Mechanisms of size reduction of colloidal silver and gold nanoparticles irradiated by Nd: YAG Laser. J. Phys. Chem. C **113**, 9078–9085 (2009)
32. M. Fleischmann, P.J. Hendra, A.J. McQuillan, Raman spectra of pyridine adsorbed at a silver electrode. Chem. Phys. Lett. **26**, 163–166 (1974)
33. D.L. Jeanmaire, R.P. Van Duyne, Surface Raman electrochemistry. Part 1. Heterocyclic, aromatic and aliphatic amines adsorbed on the anodised silver electrode. J. Electroanal. Chem. **84**, 1–20 (1977)
34. M.G. Albrecht, J.A. Creighton, Anomalously intense Raman spectra of pyridine at a silver electrode. J. Am. Chem. Soc. **99**, 5215–5219 (1977)
35. R.P. Van Duyne, Laser excitation of Raman scattering from adsorbed molecules on electrode surfaces. Chem. Biochem. Appl. Lasers **4**, 101–185 (1979)
36. E.C. Le Ru, E. Blackie, M. Meyer et al., Surface enhanced Raman scattering enhancement factors: a comprehensive study. J. Phys. Chem. C **111**, 13794–13803 (2007)
37. S. Nie, S.R. Emory, Probing single molecules and single nanoparticles by surface-enhanced Raman scattering. Science **275**, 1102–1106 (1997)
38. G. Chen, Y. Wang, M. Yang et al., Measuring ensemble-averaged surface-enhanced Raman scattering in the hotspots of colloidal nanoparticle dimers and trimers. Am. Chem. Soc. **132**, 3644–3645 (2010)
39. J.A. Hebda, A.D. Miranker, The interplay of catalysis and toxicity by amyloid intermediates on lipid bilayers: insights from type II diabetes. Biophysics **38**, 125–152 (2009)
40. F.E. Cohen, S.B. Prusiner, Pathologic conformations of prion proteins. Ann. Rev. Biochem. **67**, 793–819 (1998)
41. M. Pappalardo, M. Milardi, D. Grasso et al., Steered molecular dynamics studies reveal different unfolding pathways of prions from mammalian and non-mammalian species. New J. Chem. **31**, 901–905 (2007)
42. D. Milardi, M.F.M. Sciacca, M. Pappalardo et al., The role of aromatic side-chains in amyloid growth and membrane interaction of the islet amyloid polypeptide fragment LANFLVH. Eur. Biophys. J. **40**, 1–12 (2011)
43. R. Soong, J.R. Brender, P.M. Macdonald et al., Association of highly compact type II diabetes related islet amyloid polypeptide intermediate species at physiological temperature revealed by diffusion NMR spectroscopy. J. Am. Chem. Soc. **131**, 7079–7085 (2009)
44. S. Scalisi, M.F.M. Sciacca, G. Zhavnerko et al., Self-assembling pathway of HiApp fibrils within lipid bilayers. Chem. BioChem. **11**, 1856–1859 (2010)
45. P. Arosio, T.P.J. Knowles, S. Linse, On the lag phase in amyloid fibril formation. Phys. Chem. Chem. Phys. **17**, 7606–7618 (2015)

46. S.A. Hudson, T. Ecroyd, W. Kee et al., The thioflavin T fluorescence assay for amyloid fibril detection can be biased by the presence of exogenous compounds. FEBS **276**, 5960–5972 (2009)
47. R.N. Rambaran, L.C. Serpell, Amyloid fibrils. Prion **2**, 112–117 (2008)
48. M. Pannuzzo, D. Milardi, A. Raudino et al., Analytical model and multiscale simulations of Aβ peptide aggregation in lipid membranes: towards a unifying description of conformational transitions, oligomerization and membrane damage. Phys. Chem. Chem. Phys. **15**, 8940–8951 (2013)
49. V. Amendola, M. Meneghetti, S. Fiameni et al., SERS labels for quantitative assays: application to the quantification of gold nanoparticles uptaken by macrophage cells. Anal. Methods **3**, 849–856 (2011)
50. G. Grasso, L. D'Urso, E. Messina et al., A mass spectrometry and surface enhanced Raman spectroscopy study of the interaction between linear carbon chains and noble metals. Carbon **47**, 2611–2619 (2009)
51. I. ChoiYun, S. Huh, D. Erickson et al., Ultra-sensitive, label-free probing of the conformational characteristics of amyloid beta aggregates with a SERS active nanofluidic device. Microfluid. Nanofluid. **1**, 663–669 (2012)
52. D. Bhowmik, K.R. Mote, C.M. MacLaughlin et al., Cell-membrane-mimicking lipid-coated nanoparticles confer Raman enhancement to membrane proteins and reveal membrane-attached amyloid-β conformation. ACS Nano **9**, 9070–9077 (2015)
53. D. Kurouski, T. Deckert-Gaudig, V. Deckert et al., Surface characterization of insulin protofilaments and fibril polymorphs using tip-enhanced Raman spectroscopy (TERS). Biophys. J. **106**, 263–271 (2014)
54. D. Zhang, O. Neumann, H. Wang, V.M. Yuwono et al., Gold nanoparticles can induce the formation of protein-based aggregates at physiological pH. Nano Lett. **9**, 666–671 (2009)
55. Y. Liao, Y. Chang, Y. Yoshiike et al., Negatively charged gold nanoparticles inhibit Alzheimer's amyloid-β fibrillization, induce fibril dissociation, and mitigate neurotoxicity. Small **8**, 3631–3639 (2012)
56. G. Brancolini, A. Corazza, M. Vuano et al., Probing the influence of citrate-capped gold nanoparticles on an amyloidogenic protein. ACS Nano **9**, 2600–2613 (2015)
57. C. Rehbock, J. Jakobi, L. Gamrad et al., Current state of laser synthesis of metal and alloy nanoparticles as ligand-free reference materials for nano-toxicological assays. J. Nanotechnol. **5**, 1523–1541 (2014)
58. W.H. Moore, S. Krimm, Vibrational analysis of peptides, polypeptides, and proteins. II. β-poly(*L*-alanine) and β-poly(*L*-alanylglycine). Biopolymers **15**, 2465–2483 (1976)
59. W.L. Peticolas, Applications of Raman spectroscopy to biological macromolecules. Biochimie **57**(4), 417–428 (1975)
60. B.G. Frushour, P.C. Painter, J.L. Koenig, Vibrational spectra of polypeptides. J. Macromol. Chem. **15**, 29–115 (1976)
61. T.G. Spiro, B.P. Gaber, Laser Raman scattering as a probe of protein structure. Annu. Rev. Biochem. **46**, 553–572 (1977)
62. J.F. Rabolt, W.H. Moore, S. Krimm, Vibrational analysis of peptides, polypeptides, and proteins. 3. alpha-poly(*L*-alanine). Macromolecules **10**, 1065–1074 (1977)
63. J. Bandekar, S. Krimmt, Vibrational analysis of peptides, polypeptides, and proteins: characteristic amide bands of β-turns. Biophysics **76**, 774–777 (1979)
64. C. Cabaleiro-Lago, F. Quinlan-Pluck, I. Lynch et al., Inhibition of amyloid β protein fibrillation by polymeric nanoparticles. J. Am. Chem. Soc. **130**, 15437–15443 (2008)
65. L. D'Urso, M. Condorelli, O. Puglisi et al., Detection and characterization at nM concentration of oligomers formed by hIAPP, Aβ(1–40) and their equimolar mixture using SERS and MD simulations. Phys. Chem. Chem. Phys. **20**, 20588–20596 (2018)
66. A. Mendez, F. Fernandez, G. Gasco, Removal of malachite green using carbon-based adsorbents. Desalination **206**, 147–153 (2007)
67. M.Z. Iqbal, A.A. Abdala, Thermally reduced graphene: synthesis, characterization and dye removal applications. RSC Adv. **3**, 24455–24464 (2013)

68. S. Filice, M. Mazurkiewicz-Pawlicka, A. Malolepszy et al., Sulfonated pentablock copolymer membranes and graphene oxide addition for efficient removal of metal ions from water. Nanomaterials **10**, 1157 (2020)
69. M.J. Lü, J. Li, X.Y. Yang et al., Applications of graphene-based materials in environmental protection and detection. Chin. Sci. Bull. **58**, 2698–2710 (2013)
70. S. Scalese, I. Nicotera, D. D'Angelo et al., Cationic and anionic azo-dye removal from water by sulfonated graphene oxide nanosheets in Nafion membranes. New J. Chem. **40**, 3654–3663 (2016)
71. S. Yanga, S. Chena, Y. Changa, A. Caoa et al., Removal of methylene blue from aqueous solution by graphene oxide. J. Coll. Int. Sci. **359**, 24–29 (2011)
72. S.F. Spanò, G. Isgrò, P. Russo et al., Tunable properties of graphene oxide reduced by laser irradiation. Appl. Phys. A **117**, 19–23 (2014)
73. S. Park, R.S. Ruoff, Chemical methods for the production of graphenes. Nat. Nanotech. **4**, 217–224 (2009)
74. M.A. Buccheri, D. D'Angelo, S. Scalese et al.: Modification of graphene oxide by laser irradiation: a new route to enhance antibacterial activity. Nanotechnology **27**, 245704 (2016) (12pp)
75. A. Fujishima, K. Honda, Electrochemical photolysis of water at a semiconductor electrode. Nature **238**, 37–38 (1972)
76. A. Fuerte, M.D. Hernandez-Alonso, A.J. Maira et al.: Visible light-activated nanosized doped-TiO_2 photocatalysts. Chem. Comm. **24**, 2718−2719 (2001)
77. Z.W. Seh, S.H. Liu, M. Low et al., Au-TiO_2 photocatalysts with strong localization of plasmonic near-fields for efficient visible-light hydrogen generation. Adv. Mater. **24**, 2310–2314 (2012)
78. R. Fiorenza, M. Bellardita, L. Palmisano et al., A comparison between photocatalytic and catalytic oxidation of 2-propanol over Au/TiO_2–CeO_2 catalysts. J. Mol. Catal. A Chem. **415**, 56–64 (2016)
79. R. Fiorenza, M. Bellardita, L. D'Urso et al.: Au/TiO_2-CeO_2 catalysts for photocatalytic water splitting and VOCs oxidation reactions. Catalysts **6**, 121 (2016) (13pp)
80. R. Asahi, T. Morikawa, T. Ohwaki et al., Visible-light photocatalysis in nitrogen-doped titanium oxides. Science **293**, 269–271 (2001)
81. R. Fiorenza, M. Bellardita, S. Scirè, L. Palmisano, Photocatalytic H_2 production over inverse opal TiO_2 catalysts. Catal. Today **321–322**, 113–119 (2019)
82. J.B. Varley, A. Janotti, C.G. Van de Walle, Mechanism of visible-light photocatalysis in nitrogen-doped TiO_2. Adv. Mater. **23**, 2343–2347 (2011)
83. S. Filice, D. D'Angelo, S.F. Spanò et al., Modification of graphene oxide and graphene oxide–TiO_2 solutions by pulsed laser irradiation for dye removal from water. Mater. Sci. Semicond. Proc. **42**, 50–53 (2015)
84. Y. Shiraishi, H. Sakamoto, Y. Sugano et al., Pt–Cu bimetallic alloy nanoparticles supported on anatase TiO_2: highly active catalysts for aerobic oxidation driven by visible light. ACS Nano **7**, 9287–9297 (2013)
85. D. Zhang, J. Liu, P. Li et al., Recent advances in surfactant-free, surface-charged, and defect-rich catalysts developed by laser ablation and processing in liquids. ChemNanoMat **3**, 512–533 (2017)
86. L.H. Li, Z.X. Deng, J.X. Xiao, G.W. Yang, A metallic metal oxide (Ti_5O_9)-metal oxide (TiO_2) nanocomposite as the heterojunction to enhance visible-light photocatalytic activity. Nanotechnology **26** (2015)
87. J. Yan, P. Liu, C. Ma et al., Plasmonic near-touching titanium oxide nanoparticles to realize solar energy harvesting and effective local heating. Nanoscale **8**, 8826–8838 (2016)
88. X. Chen, D. Zhao, K. Liu et al., Laser-modified black titanium oxide nanospheres and their photocatalytic activities under visible light. ACS Appl. Mater. Interfaces **7**, 16070–16077 (2015)
89. S. Filice, G. Compagnini, R. Fiorenza et al., Laser processing of TiO_2 colloids for an enhanced photocatalytic water splitting activity. J. Colloid Interface Sci. **489**, 131–137 (2017)

90. G. Zhu, Y. Shan, T. Lin et al., Hydrogenated blue titania with high solar absorption and greatly improved photocatalysis. Nanoscale **8**, 4705–4712 (2016)
91. J. Tian, X. Hu, H. Yang et al., High yield production of reduced TiO_2 with enhanced photocatalytic activity. Appl. Surf. Sci. **360**, 738–743 (2016)
92. A.L. Linsebigler, G. Lu, J.T. Yates, Photocatalysis on TiO_2 surfaces: principles, mechanisms, and selected results. Chem. Rev. **95**, 735–758 (1995)
93. W.-N. Zhao, Z.-P. Liu, Mechanism and active site of photocatalytic water splitting on titania in aqueous surroundings. Chem. Sci. **5**, 2256–2264 (2014)
94. R. Fiorenza, S. Sciré, L. D'Urso et al., Efficient H_2 production by photocatalytic water splitting under UV or solar light over variously modified TiO_2-based catalysts. Int. J. Hydrogen Energy **44**, 14796–14807 (2019)

Chapter 5
Dry Laser Peening: Ultrashort Pulsed Laser Peening Without Sacrificial Overlay Under Atmospheric Conditions

Tomokazu Sano

Abstract Laser peening, or laser shock peening, is a surface modification technique using a laser-driven shock wave to improve mechanical properties of solids such as hardness, residual stress, fatigue properties, and corrosion resistance. An ultrashort pulsed laser-driven shock compression of solids enables peening without sacrificial overlay under atmospheric conditions, which is called Dry Laser Peening (DryLP). An ultrashort pulsed laser ablation of solids and the accompanying ultrashort pulsed laser-driven shock wave have an important role on the peening effects. Improvement of mechanical properties of base material and laser welded 2024 aluminum alloy using DryLP are described in this chapter.

5.1 Introduction

Laser peening, or laser shock peening, is a surface modification method using a laser-driven shock wave to improve mechanical properties such as hardness, residual stress, fatigue properties, and corrosion resistance [1–25]. A nanosecond pulsed laser is conventionally used as a laser peening tool in aerospace, automotive, medical, and nuclear industries. The solid which is irradiated by the nanosecond laser pulse transits into a gas or a plasma via a liquid, accompanied by a volume expansion. A shock wave is driven as a recoil force during the expansion on the surface and propagates into the material [2, 4]. The plastic deformation of the material via the shock wave contributes to the peening effect [1]. In the case using a laser pulse with a near infrared wavelength (~1.05 μm), the material's surface needs to be covered with a protective coating or a sacrificial layer such as a black paint or an aluminum tape to prevent the surface from melting or sustaining damage from the

T. Sano (✉)
Division of Materials and Manufacturing Science, Graduate School of Engineering, Osaka University, 2-1 Yamada-oka, Suita 565-0871, Osaka, Japan
e-mail: sano@mapse.eng.osaka-u.ac.jp

A. Hu (ed.), *Laser Micro-Nano-Manufacturing and 3D Microprinting*, Springer Series in Materials Science 309, https://doi.org/10.1007/978-3-030-59313-1_5

laser pulse. After the laser treatment, the remaining coating needs to be removed. laser peening without coating was developed using 532 nm wavelength lasers by optimizing process conditions, which has been applied to practical uses in nuclear industries [17]. However, the surface needs to be covered with a transparent medium such as water to suppress the plasma expansion and obtain a high amplitude of the shock wave sufficient to deform the material plastically for both wavelengths lasers. Although a micro laser shock peening process has been developed using the shorter wavelength of 355 nm with tens of nanosecond pulse width to suppress thermal damage, this process also requires both a coating and water [14]. The nanosecond laser process does not produce a sufficient shock wave without covering the surface with a plasma confinement medium. Although the applicability of laser peening will clearly be increased if a sacrificial overlay is not required, such a technique has yet to be realized for the nanosecond laser process.

The intensity of an ultrashort laser pulse, which is equivalent to the energy per unit time and unit area and is proportional to the square of the electric field intensity, is extremely high even at a low energy because the pulse width is extremely short [26]. Therefore, direct irradiation of a solid surface with an ultrashort laser pulse drives an intense shock wave that propagates into the solid [27–44]. A shock wave driven by the ultrashort laser pulse irradiated under atmospheric conditions deforms a material plastically, resulting in quenching metastable high-pressure phases [45–47] or forming a high density of dislocations [48–51]. Heat-affected and melted zones formed by an ultrashort laser pulse are much smaller than those produced by a nanosecond laser pulse due to its extremely short pulse width [52, 53]. Based on these features, peening without a sacrificial overlay under atmospheric conditions to improve mechanical properties was developed using an ultrashort laser pulse by optimizing process conditions [54], which was named Dry Laser Peening (DryLP) [55], although ultrashort laser peening of steel under water [56, 57] and ultrashort laser peen forming of thin metal sheet in air [58, 59] have been reported so far.

Dry laser peening of base metal and laser welded 2024 aluminum alloy are described in this chapter. Ultrashort pulsed laser ablation of solids and the accompanying shock wave plays an important role on the peening. Details of the ultrashort pulsed laser ablation of solids and the ultrashort laser-driven shock wave in solids are described in [60–76] and [77–83], respectively.

5.2 Dry Laser Peening of Base Metal of 2024 Aluminum Alloy

5.2.1 Experimental Methods

The material used was a precipitation-hardened 2024 aluminum alloy which is commercially used in the aerospace industry. A 2024-T351 aluminum alloy was used except for the fatigue tests, where a 2024-T3 aluminum alloy was used. The proof

stress of 2024-T351 and 2024-T3 alloys are 321 MPa and 334 MPa, respectively. The surface of the specimen to be irradiated by laser pulses was electropolished in 20% sulfuric acid–methanol electrolyte for 30 s to remove the work-strained layer.

Figure 5.1 schematically illustrates the experimental setup for dry laser peening. The specimen of 2024-T351 aluminum alloy specimen with the dimensions of 10 × 10 × 10 mm^3 was mounted on an *x*–*y* stage as shown in Fig. 5.1a. Femtosecond laser pulses (Spectra-Physics Inc., Spitfire) with a wavelength of 800 nm and a pulse width of 120 fs were focused using a plano-convex lens with a focal length of 70 mm and irradiated normal to the electropolished surface of the specimen in the air. Before the peening experiment, the depth etched by a single pulse of femtosecond laser was investigated as a function of pulse energy to select the peening conditions. The crater depth formed by femtosecond laser irradiation at a fixed position was measured using a laser microscope. The removed depth per pulse was estimated by dividing the crater depth by the number of irradiation pulses.

For the peening treatment, the aluminum specimen was moved in the *x*- and *y*- directions during laser irradiation as shown in Fig. 5.1b. A coverage C_v, which is expressed by $C_v = \pi D^2 N_p / 4$ where D is the spot diameter of the laser pulse irradiated and N_p is the number of pulses per unit square. N_p is varied by changing the moving speed in the *x*-direction and the pulse-to-pulse distance in the *y*-direction.

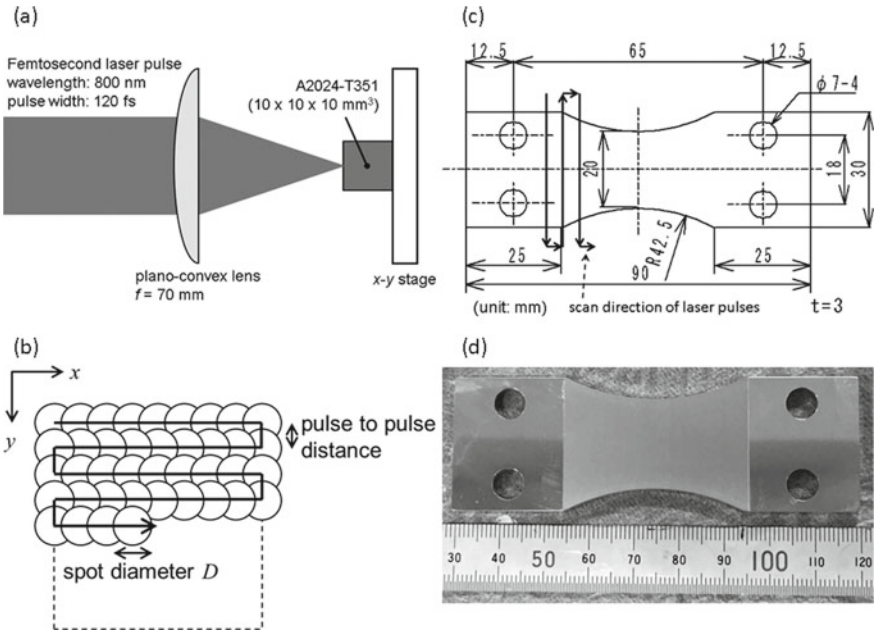

Fig. 5.1 Schematic illustrations of **a** the experimental setup for laser irradiation, **b** the scan direction of laser pulses for the setup shown in (**a**), and **c** shape and dimensions of fatigue test specimens and scan direction of laser pulses for fatigue specimens. Picture of fatigue test specimen corresponding to (**c**) is shown in (**d**) [54]

Based on the relationship between the removed depth and the pulse energy, five pulse energies of 5, 30, 75, 200, and 600 μJ, which corresponded to spot diameters of 12, 30, 40, 60, and 70 μm, respectively, and two different coverages of 692 and 2768% were chosen for peening treatment.

Surface morphology was observed using a scanning electron microscope (SEM, HITACHI S-3000H). Microstructure was observed using a transmission electron microscope (TEM, JEOL JEM-2010). For TEM observations, a small piece of the cross section was thinned by a 30 keV focused Ga-ion beam (HITACHI FB-2000). The residual stress on the laser-irradiated surface was measured from the Al(222) diffraction peak of CrKα X-rays (2.2897 Å) using a stress constant of − 96.89 MPa/degree, which was calculated using the Kröner model [84] with a single-crystal elastic stiffness ($C_{11} = 106.78$ GPa, $C_{12} = 60.74$ GPa, and $C_{44} = 28.21$ GPa) [85]. Thin layers of the surface were successively removed by electrolytic polishing to obtain the depth profile of the residual stress. The hardness of the cross section was measured using a nanoindentation system (ELIONIX ENT-1100a) with the applied load of 1 mN. Before the nanoindentation test, the cross section was polished by a 5 keV Ar-ion beam (JEOL SM-09010) to remove the work-hardened layer.

The shape and dimensions of the fatigue specimens of the 2024-T3 aluminum alloy are shown in Fig. 5.1c. The thickness of the specimen was 3 mm. Both top and bottom surfaces were mirror-finished in the same manner as the 2024-T351 specimens. Dry laser peening treatments were performed for both surfaces. Picture of fatigue test specimen after the dry laser peening treatment is shown in Fig. 5.1d. Plane bending tests were conducted at a cyclic speed of 1400 cycles/min with a constant strain amplitude and a stress ratio of $R = -1$ in the air at room temperature.

5.2.2 Results and Discussion

The relationships between the removed depth per pulse and the pulse energy is shown in Fig. 5.2. The gradient above 30 μJ is larger than that below 30 μJ, suggesting that a stronger shock pressure is driven above 30 μJ because the larger volume of the removed material creates a larger recoil force. Therefore, pulse energies of 5, 30, 75, 200 and 600 μJ, which are below, at, and above 30 μJ, were chosen for the peening experiments to confirm the existence of the threshold.

Figure 5.3 shows the SEM images of the laser-irradiated surface for the pulse energies of 30, 75, and 600 μJ and coverages of 692 and 2768%. Regardless of the condition, droplets are not observed, indicating that the femtosecond laser treatment creates a negligibly small molten layer.

The results of the residual stress measurements for surfaces of the femtosecond laser irradiated material with coverage of 692 and 2768% are shown in Fig. 5.4. Compressive residual stress is achieved above 30 μJ, which corresponds to the point where the gradient of the removed depth per pulse energy changes. This means that a pulse energy above 30 μJ sufficiently drives a shock wave to induce plastic deformation. A larger pulse energy gives a larger compressive stress for a given

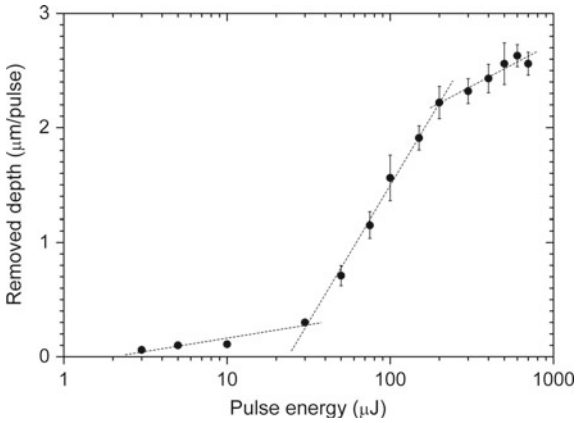

Fig. 5.2 Relationships between the removed depth per pulse and the pulse energy [54]

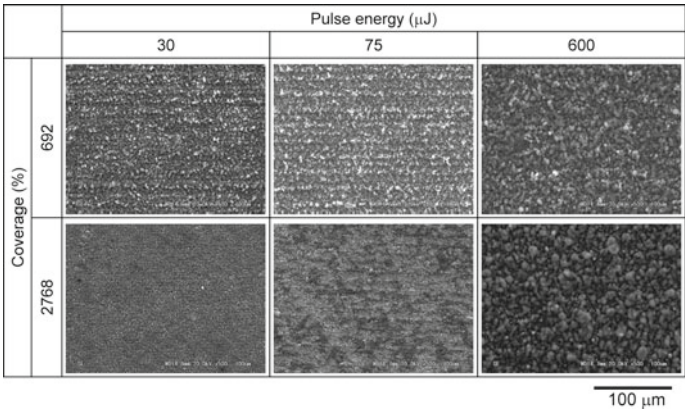

Fig. 5.3 SEM images of the surface of 2024-T351 specimen after dry laser peening [54]

coverage. The compressive stress for the coverage of 692% is slightly larger than that for the coverage of 2768% for the same pulse energy. Here, σ_x is larger than σ_y below 30 μJ, but this tendency is reversed above 75 μJ for given coverages. The depth profiling results of σ_x for 600 μJ and 2768% are shown in Fig. 5.4c. The maximum compressive residual stress around 300 MPa is attained at a depth of 4 μm from the surface. This value is almost equal to the 0.2% proof stress of 2024-T351 aluminum alloy [86] and the values obtained using other peening methods such as nanosecond laser peening, shot peening, or ultrasonic peening [87–91]. The compressive stress decreases to zero around 90 μm, which is around one tenth of the peened depth obtained by nanosecond laser peening.

The results of hardness measurements in the cross section of the laser irradiated specimen are shown in Fig. 5.5. The data in the hardened region are fit by polynomial

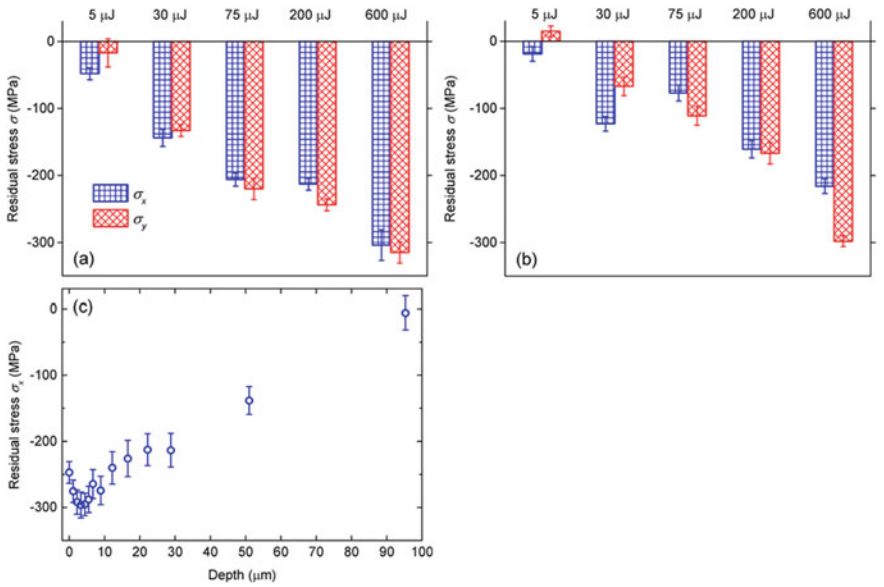

Fig. 5.4 Residual stress of the surface after femtosecond laser irradiation with a coverage of **a** 692% and **b** 2768%. Depth profile of the residual stress for the specimen irradiated with a pulse energy of 600 μJ and a coverage of 2768%. Error bars indicate measurement uncertainty [54]

curves. The maximum value of the curve is defined as the maximum hardness $H_{\max}$, of which corresponding depth is defined as the depth at the maximum hardness. The depth where the fitting curve matches the original hardness, which corresponds to the hardness at the depth of 40 μm, is defined as the hardened depth as well as the difference between the hardened depth and the depth at the maximum hardness as the thickness of the hardened region (Table 5.1). Most of the surface region has a hardness similar to the original material, which corresponds to the SEM observation shown in Fig. 5.3 where most the surface region consists of debris. The maximum hardness is almost the same for each condition. A larger pulse energy forms a thicker hardened region for a given coverage. For the pulse energy of 600 μJ, the thickness of the hardened region with a 692% coverage is larger than that with a 2768% coverage. A larger coverage induces more removed depth as well as increasing the thickness of the plastic deformed region. Therefore, a larger coverage does not necessarily form a thicker residual hardened region.

Both surfaces of the fatigue test specimen shown in Fig. 5.1c were peened using a pulse energy of 600 μJ and a coverage of 2768%. The relationship between stress amplitude and number of cycles to failure of dry laser-peened 2024-T3 aluminum alloy and base material is shown in Fig. 5.6. The fatigue life was improved as much as 38 times in comparison with base material at stress amplitude of 195 MPa. The fatigue strength at 2×10^6 cycles of the peened specimen was 58 MPa larger than that of the base material. Fracture surfaces of a dry laser peened specimen at a stress

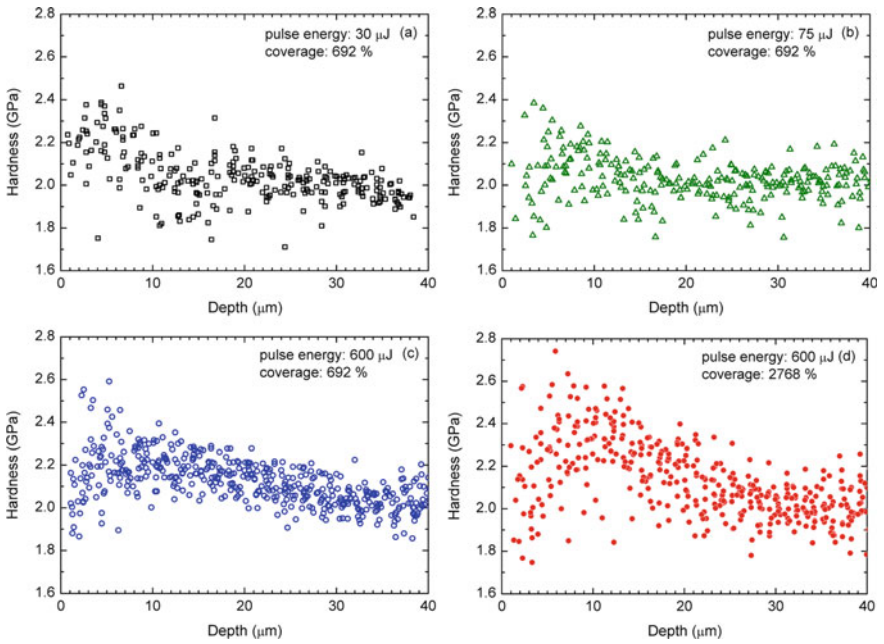

Fig. 5.5 Depth profile of the hardness in depth for the specimen irradiated by femtosecond laser pulses with **a** a pulse energy of 30 μJ and a coverage of 692%, **b** a pulse energy of 75 μJ and a coverage of 692%, **c** a pulse energy of 600 μJ and a coverage of 692%, and **d** a pulse energy of 600 μJ and a coverage of 2768% [54]

Table 5.1 Maximum hardness, depth at the maximum hardness, hardened depth, and thickness of the hardened region for each laser condition

Laser conditions pulse energy and coverage	Max hardness (GPa)	Depth at max. hardness (μm)	Hardened depth (μm)	Thickness of hardened region (μm)
30 μJ & 692%	4.4	14.3	9.9	4.4
75 μJ & 692%	8.0	16.9	8.9	8.0
600 μJ & 692%	10.2	35.2	25.2	10.2
600 μJ & 2768%	11.1	28.0	16.9	11.1

amplitudes of 280 and 195 MPa are shown in Fig. 5.7. Cracks initiated from the surface for a stress amplitude of 280 MPa. For a stress amplitude of 195 MPa, crack initiation sites were located around 160 μm deep from the surface. For the lower stress amplitude, it is suggested that crack initiation from the surface was suppressed because the surface layer with a thickness of 28 μm was hardened and 90 μm was compressive, resulting in the internal crack initiation.

Figure 5.8 shows the TEM image of the cross section of 2024-T351 aluminum alloy irradiated by a pulse energy of 600 μJ with a coverage of 2768%. The surface is

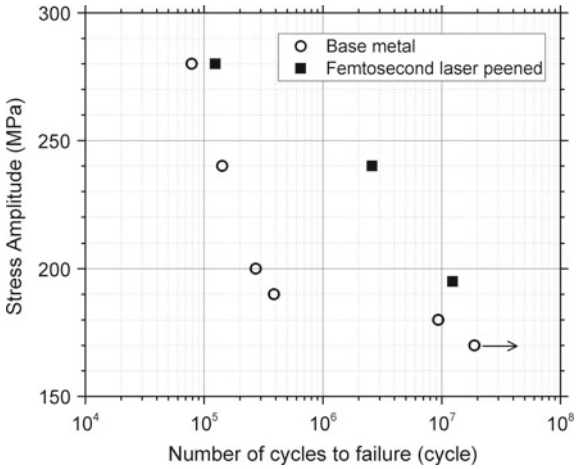

Fig. 5.6 Results of plane bending fatigue tests for specimens of dry laser-peened 2024-T3 aluminum alloy and base material [54]

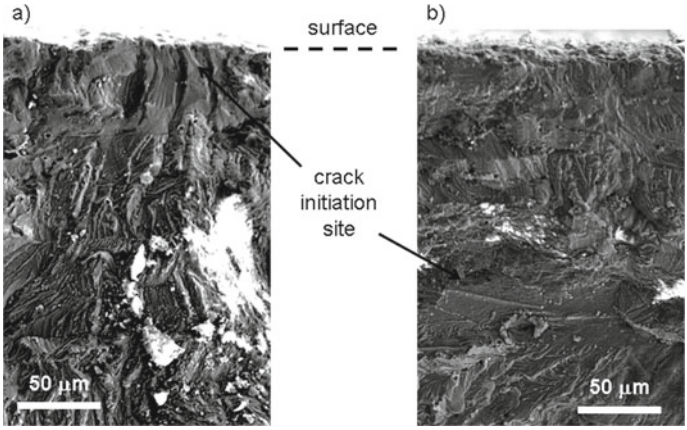

Fig. 5.7 Fracture surfaces of dry laser-peened 2024-T3 aluminum alloy at stress amplitude of **a** 280 MPa and **b** 195 MPa [54]

covered with a layer around 5 μm thick containing some voids, as shown in Fig. 5.8a. These voids would cause the lack of a hardness increase in the surface region over a thickness of several microns seen in Fig. 5.5. The magnified view of the interface between the surface layer and the lower solid material is shown in Fig. 5.8b. A clear grain boundary exists at the interface, suggesting that the surface layer was formed after melting and resolidification.

As shown in Fig. 5.4c, the residual stress in the top surface was compressive, even though the residual stress in a resolidified layer is generally tensile. As shown in Fig. 5.7b, cracks did not initiate from voids in the resolidified layer for a lower

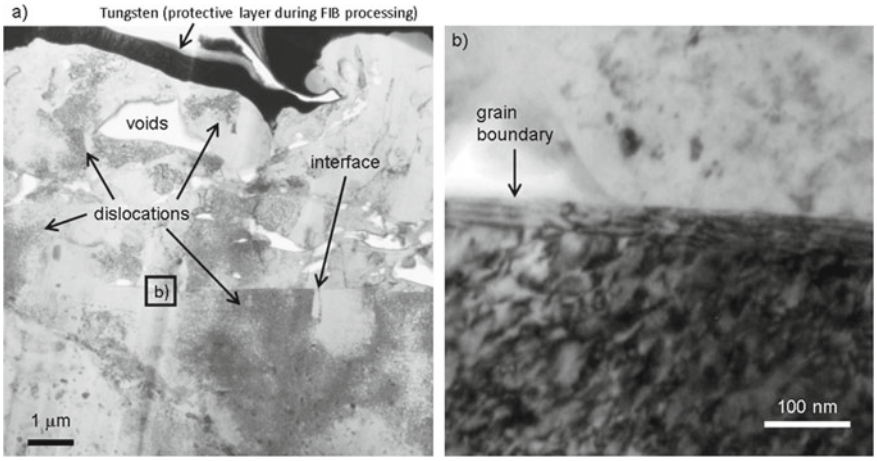

Fig. 5.8 **a** TEM image of the cross section of the femtosecond laser-irradiated 2024-T351 aluminum alloy with a pulse energy of 600 μJ and a coverage of 2768%. **b** Magnified view around the interface between the surface layer and the solid material [54]

stress amplitude, resulting in improved fatigue life at high cycles. A high density of dislocations exist in the upper resolidified layer as well as the solid material, indicating both layers were plastically deformed or peened by femtosecond laser-driven shocks. A shock front which is driven by a femtosecond laser pulse overtakes the heat front induced by the laser pulse, and finally forms a high density of dislocations in a region deeper than the heat affected zone [45, 48–51]. Under the dry laser peening condition for a coverage of 2768%, the shock front passes through about 2 nm thick molten layer and propagates into the resolidified layer which is formed by former laser pulses and the solid layer, resulting in providing peening effects on the material.

5.3 Dry Laser Peening of Laser Welded 2024 Aluminum Alloy

5.3.1 Introduction

LP is generally effective for improving the fatigue performance of arc-welded [92] and friction stir-welded joints [93–95]. The fatigue performance of welded precipitation-strengthened aluminum alloys, such as the 2000, 6000, and 7000 series, were worse than the corresponding base material (BM) because of the softening of the weld metal (WM), heat-affected zone (HAZ), and residual tensile stress on the surface after welding [96, 97]. Therefore, in recent years, friction stir welding (FSW) has been widely used to join precipitation-strengthened aluminum alloys because it results in only a small decrease in the strength of the weld joint and small

distortion of the joint after welding [98–100], although the welding speed is relatively low. Laser welding is a high-speed welding method that has been used for achieving high-productivity welding of precipitation-strengthened aluminum alloys [101, 102]. Although the weldability of 2024 aluminum alloy is generally low, fast full-penetration welding of this alloy using highly focused fiber laser achieved weld joints with smaller HAZ regions and no cracking [103]. However, areas of WM with reduced strength exist, and avoiding generation of blowholes in the laser-welded joints is difficult. Although the thickness with the compressive residual stress induced by DryLP process is almost one-tenth of conventional LP methods [54, 104], this method was shown to be effective for FSW-processed 7075-T73 aluminum alloy, where the stir zone, thermo-mechanically affected zone, and HAZ were softened, but no welding defects occurred, confirming that the fatigue performance was better than that of the BM at lower stress amplitude after DryLP treatment.

5.3.2 Experimental Methods

A 2024-T3 aluminum alloy with thickness of 3 mm was used. The original alloy had a 0.2% proof stress of 334 MPa, tensile strength of 464 MPa, and elongation of 21.8%.

A single-mode fiber laser (IPG Photonics, YLS-2000-SM, Japan, wavelength: 1070 nm, CW) was used for full-penetration bead-on-plate welding of the aluminum alloy, as shown in Fig. 5.9a. The fiber diameter was 14 μm and we used a laser power of 2.0 kW. The laser was focused on the alloy surface with a spot size of 54 μm. Ar was used for shielding gas with a flow rate of 30 L/min. A welding speed of 2.5 m/min was used. The top and bottom surfaces of the laser-welded specimens were observed using an optical digital microscopy (Hirox, KH-7700, Japan). The cross-section of the weld bead was observed using optical microscopy (Olympus, SZX7, Japan).

Then, the laser-welded specimens were subjected to DryLP in air. The peening was performed 15 months after welding to allow the completion of natural aging. As shown in Fig. 5.9b, c, femtosecond laser pulses with a wavelength of 800 nm, pulse duration of 130 fs, and pulse energy of 0.6 mJ (Spectra-Physics, Spitfire, Japan) were focused using a plano-convex lens with focal length of 70 mm onto the specimen. The laser pulses were overlapped, with a coverage of 692%, which was shown to be the most effective condition for DryLP of 2024-T3 aluminum alloy [54].

For the preparation of specimens for hardness tests, the weld reinforcement was removed and electropolished in 20% sulfuric acid–methanol electrolyte for 30 s to remove the work-strained layer before DryLP treatment. The hardness of the top surface was measured using a Vickers hardness tester (Mitsutoyo, HM-221, Japan) with a load of 1.96 N and loading time of 15 s.

For the preparation of specimens for residual stress measurement, DryLP treatment was conducted on as-welded specimens without removing the weld reinforcement. Depth profiling of the residual stress which was normal to the weld bead in the specimens was conducted nondestructively using the BL22XU beamline at SPring-8

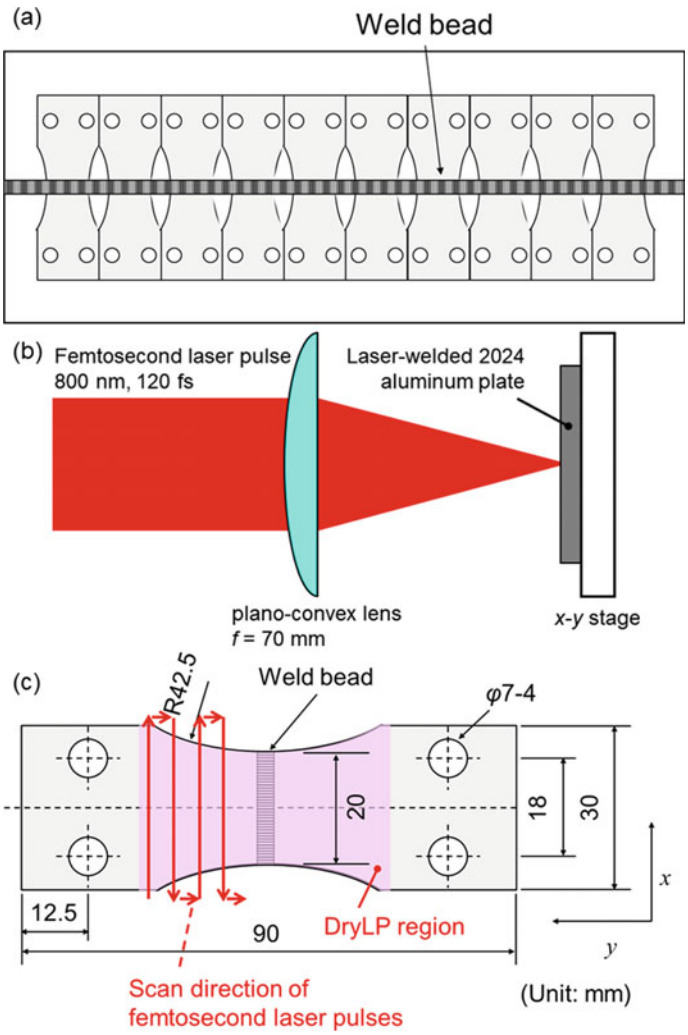

Fig. 5.9 Schematic illustrations of the experimental procedures. **a** Full-penetration bead-on-plate laser welding and preparation of fatigue test specimens cut from the laser-welded plate. **b** Dry laser peening (DryLP) process using femtosecond laser pulses. **c** Geometry of the fatigue test specimens with the weld bead located in the center. DryLP was performed using an *x*–*y* automatic stage which sequentially moved the specimen in a serpentine pattern, as indicated by the red arrows [55]

[105], using the strain scanning method [106] with monochromatic X-rays with a photon energy of 30.013 keV, as shown in Fig. 5.10. A CdTe detector was used for the measurements. The residual stress σ was estimated using $\sigma = E(d - d_0)/d_0$, where E is the Young's modulus of 61.7 GPa, d is the d-spacing of the (311) plane of aluminum in the welded or DryLPed specimens, and d_0 is the d-spacing of the (311) plane in the BM of 0.12196 nm. The d-spacing of the (311) plane parallel to the weld

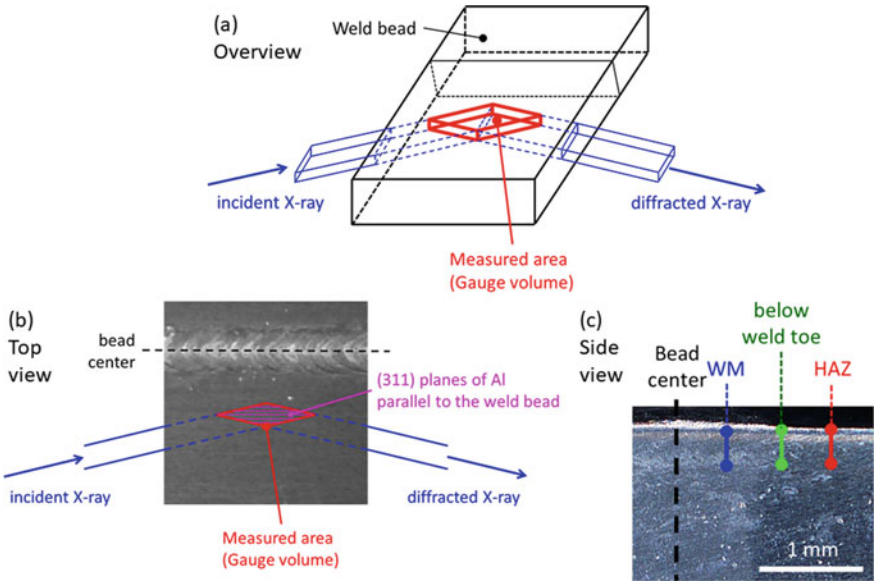

Fig. 5.10 Schematic illustrations of **a** overview, **b** top, and **c** side views of residual stress measurements using the strain scanning method with synchrotron X-rays [55]

bead in the gauge volume was measured, as shown in Fig. 5.10a, b. The widths of both the incident and receiving slits were 0.2 mm. For the surface measurements, the heights of these slits were 50 μm. For depth profiling, the slit heights, which determine the depth resolution, were 10 μm from the surface to a depth of 40 μm, and the slit heights were 30 μm deeper than a depth of 40 μm. The d-spacings of the (311) plane of the WM, below the weld toe, and in the HAZ were measured, as shown in Fig. 5.10c.

Four kinds of specimens for fatigue testing were prepared: (i) As-welded specimen; (ii) reinforcement-removed welded specimen; (iii) DryLPed welded specimen; and (iv) DryLPed reinforcement-removed welded specimen. The stress concentration influenced the fatigue properties of the as-welded specimen due to both reinforcements and undercuts. Hence, to investigate the stress concentration only influenced by the undercuts, the reinforcements were removed. The reinforcements were removed using diamond pastes with a particle size of 1 μm. These specimens were cut from the laser-welded specimen, as shown in Fig. 5.9a. DryLP was conducted on both surfaces of the laser-welded specimen, as shown in Fig. 5.9 b. Plane bending fatigue tests (PBF-30, Tokyo Koki, Tokyo, Japan) were conducted at a cyclic speed of 1400 cycles/min with a constant strain amplitude and a stress ratio of $R = -1$ in air at room temperature based on Little's method [107]. The stress ratio of $R = -1$ was selected to indicate the effectiveness of the DryLP more clearly because both surfaces were treated. The fracture surfaces were observed using optical microscopy (Olympus, SZX7, Japan) and scanning electron microscopy (SEM; Hitachi, S-3000H, Japan).

The microstructures were observed to estimate dislocation densities in the specimens using a transmission electron microscopy (TEM; JEOL JEM-2010, Japan) with an acceleration voltage of 200 kV. For TEM observations, a small piece of the cross-section was thinned using a 30-keV-focused Ga-ion beam (Hitachi, FB-2000A, Japan).

5.3.3 Results

Optical microscopy images of the top and bottom rear surfaces of the laser-welded specimens are shown in Fig. 5.11a, b. Although no cracks were observed on the surfaces, some pores existed on the top surface and some undercuts (indicated by yellow arrows in the figures) were found on both surfaces. The cross-section of the weld bead shows that full-penetration welding was achieved, where the reinforcement did not show any cracks (Fig. 5.11c). The bead widths on the top and rear surfaces were around 2.0 mm and 1.2 mm, respectively. The optical microscopy image of the bottom surface of the reinforcement-removed welded specimen is shown in Fig. 5.11d, where the yellow arrows indicate the undercuts.

The results of the hardness tests for the samples with the reinforcement removed are shown in Fig. 5.12. Before DryLP, the hardness of the BM was 138 HV, while

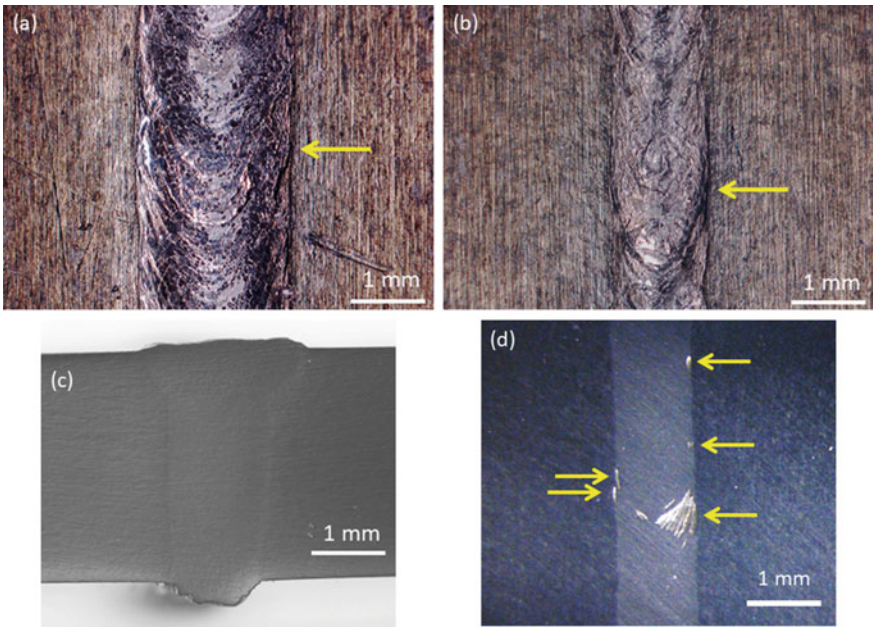

Fig. 5.11 Optical microscopy images of **a** top surface, **b** bottom surface, **c** cross-section of the laser-weld bead, and **d** bottom surface of reinforcement-removed welded specimen [55]

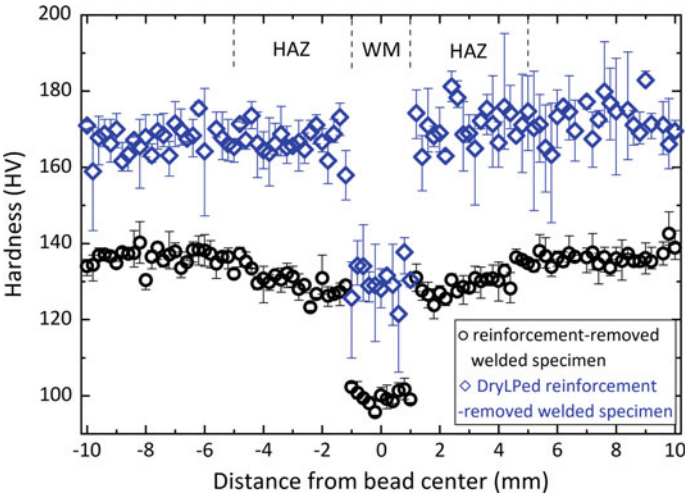

Fig. 5.12 Hardness distributions over the surfaces of welded samples with the reinforcement removed, before, and after DryLP treatment. Error bar indicates the maximum and minimum values [55]

that on the surface of the WM was ~100 HV. It was reported that this decrease in hardness is due to (i) the segregation of the strengthening elements such as magnesium, copper, and their intermetallic compounds; (ii) formation and growth of non-strengthening coarse precipitates; (iii) dissolution of strengthening precipitates; (iv) uniform re-distribution of precipitating elements; and (v) vaporization of low boiling point magnesium during heating and the following freezing due to the fast cooling rates [108–110], resulting in fewer precipitates being formed, even after natural aging for 15 months. The hardness of the HAZ in this specimen was around 130 HV (similar to the BM) because of the dissolution of precipitates and overaging [108, 111]. After DryLP, the hardness of all areas of the sample increased compared to that of the as-welded sample. The hardness of the WM was similar to that of the BM before peening, while the hardness of the HAZ and BM after DryLP was around 178 HV.

Residual stress curves of the top surface before and after DryLP treatment of the laser-welded specimens are shown in Fig. 5.13a. The residual stress in the WM and HAZ areas of the as-welded specimen were tensile, while other areas had compressive stresses, which is a typical residual stress distribution for welded joints. This tensile residual surface stress in the WM and HAZ areas changed to compressive stress after DryLP treatment, while the magnitude of the compressive residual stresses outside these areas increased. The depth profiles of the residual stress in the WM, below the weld toe, and in the HAZ before and after DryLP treatment are shown in Fig. 5.13b–d. The tensile residual stresses in the WM, below the weld toe, and in the HAZ were observed to a depth of ~300 μm from the weld center in the as-welded specimen. These tensile residual stresses inside the material between the surface and a depth of

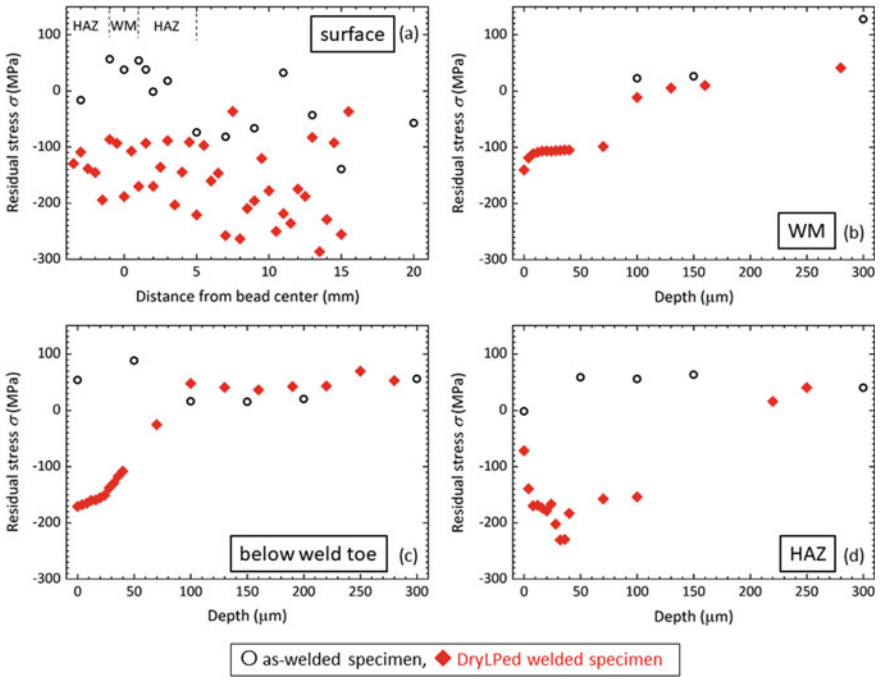

Fig. 5.13 **a** Residual stress distributions along the surface (up to 50-μm depth). Depth profiles of the residual stress in the **b** WM, **c** below the weld toe, and **d** in the HAZ of laser-welded specimens before and after DryLP [55]

~100 μm changed to compressive stresses after DryLP, which is comparable to the thickness of the compressive layer in the DryLPed BM [54].

The results of the fatigue tests are shown in Fig. 5.14. The fitted curves for each specimen were obtained using Stromeyer's expression, $\log(\sigma - a) = -b \log N + c$, where σ is the stress amplitude, N is the number of cycles to failure, and a, b, and c are the fitting parameters. The fatigue performances of the as-welded specimens with and without reinforcement were worse than that of the BM. Although the fatigue lives of these specimens at a stress amplitude of 180 MPa were almost the same, that of the reinforcement-removed welded specimen was shorter than that of the as-welded specimen at 120 MPa. After DryLP treatment, the fatigue performances of the specimens with and without reinforcement were enhanced to a similar degree. The fatigue life increased by a factor of almost two at a stress amplitude of 180 MPa and more than 50 times at 120 MPa, which indicates that the DryLP treatment is more effective at lower stress amplitudes.

Bright-field TEM images of the region ~10 μm below the surface in the WM of as-welded and DryLPed specimens (with reinforcement) are shown in Fig. 5.15. The incident electron beam direction was nearly parallel to the [110] direction of Al, where the {111} reflection of Al was excited. The dislocations were observed

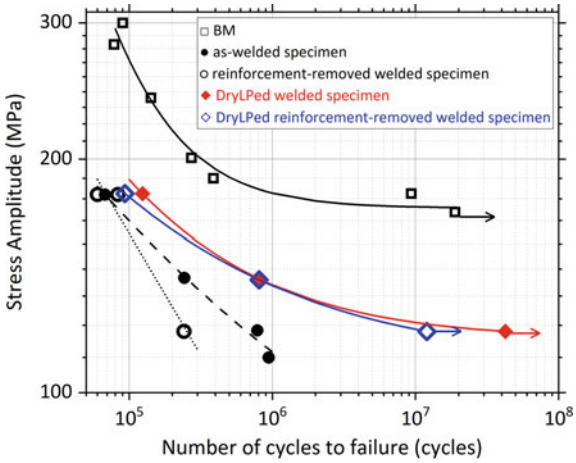

Fig. 5.14 Results of fatigue tests for the base material (BM) and as-welded specimens (with and without reinforcement) before and after DryLP treatment [55]

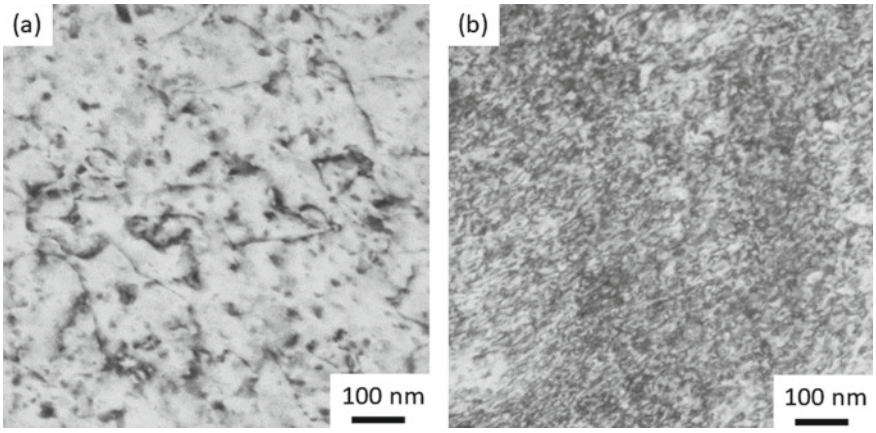

Fig. 5.15 TEM images of weld material (WM) microstructures in laser-welded specimens (with reinforcement) **a** before and **b** after DryLP treatment

as the darker areas. The dislocation density was estimated using Keh's equation, $\rho = \left(n_1/L_1 + n_2/L_2\right)/t$, where ρ is the dislocation density, n_1 and n_2 is the number of intersection points between the dislocation lines and the vertical and horizontal grid lines drawn on the TEM image, respectively, L_1 and L_2 is the total length of the vertical and horizontal grid lines, respectively, and t is the thickness of the TEM sample [112]. The dislocation densities of these samples before and after DryLP treatment were estimated as 1.0×10^{14} m^{-2} and 5.1×10^{14} m^{-2}, respectively. This indicates that DryLP plastically deformed the WM, resulting in hardening and inducing compressive residual stress.

5.4 Plastic Deformation Induced by Ultrashort Pulsed Laser-Driven Shock Wave

By taking the time derivative of the Orowan equation $\gamma = k\rho \mathbf{b}\bar{l}$ [113], $\mathrm{d}\gamma/\mathrm{d}t = k\mathbf{b}(\rho \mathrm{d}\bar{l}/\mathrm{d}t + \bar{l}\mathrm{d}\rho/\mathrm{d}t)$ is obtained, where γ is the plastic strain, ρ is the mobile dislocation density, b is the Burgers vector, $\bar{l}$ is the mean distance traveled by a dislocation, t is the time, and k is a proportionality constant. The plastic strain rate $\mathrm{d}\gamma/\mathrm{d}t$ is expressed by the sum of the term for the velocity of dislocations $\mathrm{d}\bar{l}/\mathrm{d}t$ and the generation of dislocations $\mathrm{d}\rho/\mathrm{d}t$. In shock compression above the Hugoniot elastic limit or high strain-rate deformation, the generation of dislocations dominates this phenomenon premising that the velocity of dislocations does not exceed the sound velocity. Dislocation nucleation takes place just behind the shock front to relieve the stress caused by the lattice mismatch between regions in front and behind the shock front [114]. In the case of conventional shocks, a part of the dislocations once generated behind the shock front and multiplied in a release process is annihilated due to residual heat, resulting in a residual density of one tenth of the highest density once induced. In the case of femtosecond laser-driven shock, the major part of the dislocations once induced remains due to much less dislocation annihilation because of negligible heat effects, resulting in massive peening effects. This appears to be the unique mechanism of dry laser peening without a sacrificial overlay under atmospheric conditions in comparison with other peening methods such as nanosecond laser peening, shot peening, and ultrasonic peening.

When a peak pressure of a shock wave exceeds a threshold that depends on a material, the pressure increases as a function of the time or the travel distance exhibits a single structure, where the plastic component overtakes the elastic component. The threshold stress for aluminum when the single structure of the shock front is clearly formed is 25 GPa [37]. It was reported that the single structure was observed in the surface layer of 500 nm in pure aluminum, which was irradiated using the intensity of 8.7×10^{12} W/cm^2 with the pulse duration of 150 fs [34]. Therefore, the shock wave with a single structure over 25 GPa should be driven and propagated in the 2024 aluminum alloy, which was irradiated at the intensity of 1.2×10^{14} W/cm^2 with the pulse duration of 130 fs in this research.

It was empirically observed that the strain rate η of the shock wave with the single structure was proportional to the fourth-power of the shock stress σ [115, 116]. For the aluminum alloy, $\eta = 9100\sigma^4$ has been reported [37]. Therefore, the strain rate η of 3.5×10^9 s^{-1} was obtained for the shock stress of 25 GPa. The dimensionless Bland number $B = 3hs\eta/8c$ was defined [115], where h is the sample thickness, c is the bulk sound velocity under normal pressure, and s is the slope of the u_p-u_s relation, $u_\mathrm{s} = c + su_\mathrm{p}$, where u_p is the particle velocity and u_s is the shock velocity. When B is greater than 1, steady-wave conditions are expected [37]. The thickness h was estimated to be 3.0 μm for $B = 1$, $\eta = 3.5 \times 10^9$ s^{-1}, $s = 1.338$, $c = 5.328$ km/s [117]. Therefore, the shock wave with the single structure propagates in the surface layer of 3.0 μm. The single structure splits into two structures, elastic and plastic waves,

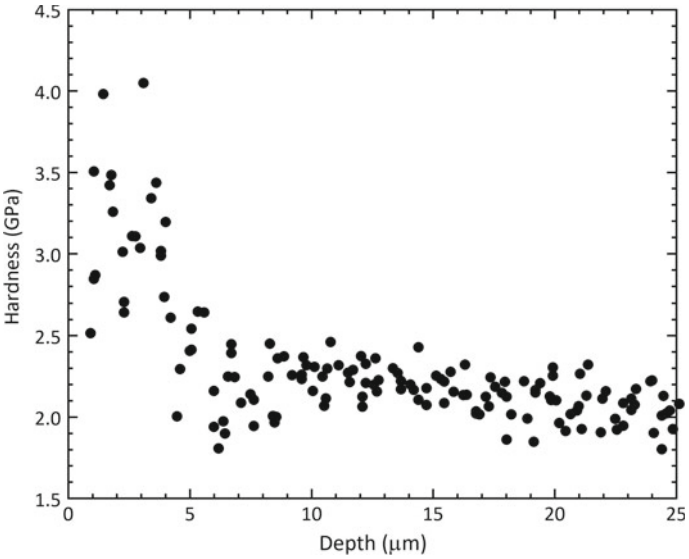

Fig. 5.16 Depth profile of hardness in the BM region in the DryLPed 2024 aluminum measured using nanoindentation [55]

at the depth of 3.0 μm, and the shock wave with the two-wave structure propagates into the deeper region.

Figure 5.16 shows the hardness in the BM region in the DryLPed 2024 aluminum alloy as a function of the depth measured using nanoindentation (ELIONIX, ENT-1100a, Japan) with an applied load of 1 mN and loading time of 2 s. The increase in hardness is more significant at a depth of 3 μm from the surface rather than depths of 3–20 μm, although the hardness increased in the surface layer with 20 μm thickness. The thickness of the significantly hardened layer of 3 μm corresponds to the thickness of 3.0 μm where the shock wave with the single structure propagates. This implies that the single structure induces plastic deformation more effectively, thereby increasing the hardness. A high-density-dislocation structure, shown in Fig. 5.15b, was formed in a layer where the shock wave with the single structure propagates, because dislocation generation, rather than dislocation multiplication, was dominant [54, 104, 114].

5.5 Concluding Remarks

DryLP method improves the fatigue properties of both base material and friction stir welded 7075-T73 aluminum alloy [106] and welded specimens with and without reinforcement almost equally. DryLP is expected to be more effective in improving the fatigue performance of laser-welded specimens with weld defects at lower stress

amplitudes. Combining high-speed laser welding with DryLP is expected to be a suitable strategy for replacing other welding processes, resulting in high productivity. This combination could be applied in various industrial fields, such as the automotive, rail, aircraft, and space industries.

In addition, DryLP method has a great potential to be applied in various fields where conventional peening methods cannot be used, as this process can be performed under ambient conditions without the use of a plasma confinement medium such as water or transparent materials. For example, a micro device such as Nano- or Micro-Electro Mechanical Systems can be peened by ultrashort laser pulses because the range of the heat-affected zone by the pulses is on the nano- to micrometer scale. Additionally, this method can be theoretically performed in a vacuum because there is no significant difference of the shock pressure between driven in a vacuum and in air, allowing this method to be used in space.

Acknowledgements This work was supported in part by MEXT Quantum Leap Flagship Program (MEXT Q-LEAP) Grant Number JPMXS0118068348, and JSPS KAKENHI Grant Numbers JP16H04247, JP16K14417, 19K22061, and 20H02048, The Amada Foundation, and The Light Metal Educational Foundation. This work was funded in part by ImPACT Program of Council for Science, Technology and Innovation (Cabinet Office, Government of Japan).

References

1. P. Fairand, B.A. Wilcox, W.J. Gallagher, D.N. Williams, J. Appl. Phys. **43**, 3893 (1972)
2. P. Fairand, A.H. Clauer, J. Appl. Phys. **50**, 1497 (1979)
3. A.H. Clauer, J.H. Holbrook, B.P. Fairand, *Shock Waves and High-Strain-Rate Phenomena in Metals* (Plenum Publishing Corporation, New York, 1981), pp. 675–703
4. R. Fabbro, J. Fournier, P. Ballard, D. Devaux, J. Virmont, J. Appl. Phys. **68**, 775 (1990)
5. P. Peyre, R. Fabbro, P. Merrien, H.P. Lieurade, Mater. Sci. Eng. A **210**, 102 (1996)
6. R. Fabbro, P. Peyre, L. Berthe, X. Scherpereel, J. Laser Appl. **10**, 265 (1998)
7. J.P. Chu, J.M. Rigsbee, G. Banaś, H.E. Elsayed-Ali, Mater. Sci. Eng. A **260**, 260 (1999)
8. P. Peyre, X. Scherpereel, L. Berthe, C. Carboni, R. Fabbro, G. Béranger, C. Lemaitre, Mater. Sci. Eng. A **280**, 294 (2000)
9. G. Hammersley, L.A. Hackel, F. Harris, Opt. Laser. Eng. **34**, 327 (2000)
10. J.-M. Yang, Y.C. Her, N. Han, A. Clauer, Mater. Sci. Eng. A **298**, 296 (2001)
11. C.S. Montross, T. Wei, L. Ye, G. Clark, Y.-W. Mai, Int. J. Fatigue **24**, 1021 (2002)
12. R.K. Nalla, I. Altenberger, U. Noster, G.Y. Liu, B. Scholtes, R.O. Ritchie, Mater. Sci. Eng. A **355**, 216 (2003)
13. I. Nikitin, B. Scholtes, H.J. Maier, I. Altenberger, Scripta Mater. **50**, 1345 (2004)
14. W. Zhang, Y.L. Yao, I.C. Noyan, ASME, , J. Manuf. Sci. Eng. **126**, 10 (2004)
15. C. Rubio-González, J.L. Ocaña, G. Gomez-Rosas, C. Molpeceres, M. Paredes, A. Banderas, J. Porro, M. Morales, Mater. Sci. Eng. A **386**, 291 (2004)
16. K. Ding, L. Ye, *Laser Shock Peening: Performance and Process Simulation* (Woodhead Publishing, Cambridge, 2006)
17. Y. Sano, M. Obata, T. Kubo, N. Mukai, M. Yoda, K. Masaki, Y. Ochi, Mater. Sci. Eng. A **417**, 334 (2006)
18. O. Hatamleh, J. Lyons, R. Forman, Int. J. Fatigue **29**, 421 (2007)
19. I. Nikitin, I. Altenberger, Mater. Sci. Eng. A **465**, 176 (2007)

20. A.W. Warren, Y.B. Guo, S.C. Chen, Int. J. Fatigue **30**, 188 (2008)
21. R.D. Tenaglia, D.F. Lahrman, Nat. Photonics **3**, 267 (2009)
22. C. Ye, S. Suslov, B.J. Kim, E.A. Stach, G.J. Cheng, Acta Mater. **59**, 1014 (2011)
23. Y. Zhang, J. Lu, K. Luo, *Laser Shock Processing of FCC Metals: Mechanical Properties and Micro-Structural Strengthening Mechanism* (Springer, New York, 2013)
24. X. Ren, *Laser Shocking Nano-Crystallization and High-Temperature Modification Technology* (Springer, New York, 2015)
25. Y. Liao, C. Ye, G.J. Cheng, Opt. Laser. Technol. **78**, 15 (2016)
26. D. Strickland, G. Mourou, Opt. Commun. **56**, 219 (1985)
27. R. Evans, A.D. Badger, F. Fallies, M. Mahdieh, T.A. Hall, P. Audebert, J.-P. Geindre, J.-C. Gauthier, A. Mysyrowicz, G. Grillon, A. Antonetti, Phys. Rev. Lett. **77**, 3359–3362 (1996)
28. K.T. Gahagan, D.S. Moore, D.J. Funk, R.L. Rabie, S.J. Buelow, Phys. Rev. Lett. **85**, 3205 (2000)
29. D.J. Funk, D.S. Moore, K.T. Gahagan, S.J. Buelow, J.H. Reho, G.L. Fisher, R.L. Rabie, Phys. Rev. B **64**, 115114 (2001)
30. D.S. Moore, K.T. Gahagan, J.H. Reho, D.J. Funk, S.J. Buelow, R.L. Rabie, T. Lippert, Appl. Phys. Lett. **78**, 40 (2001)
31. S.D. McGrane, D.S. Moore, D.J. Funk, R.L. Rabie, Appl. Phys. Lett. **80**, 3919 (2002)
32. S.I. Anisimov, N.A. Inogamov, Y.V. Petrov, V.A. Khokhlov, V.V. Zhakhovskii, K. Nishihara, M.B. Agranat, S.I. Ashitkov, P.S. Komarov, Appl. Phys. A **92**, 797 (2008)
33. M.B. Agranat, S.I. Anisimov, S.I. Ashitkov, V.V. Zhakhovskii, N.A. Inogamov, P.S. Komarov, A.V. Ovchinnikov, V.E. Fortov, V.A. Khokhlov, V.V. Shepelev, JETP Lett. **91**, 471 (2010)
34. S.I. Ashitkov, M.B. Agranat, G.I. Kanel, P.S. Komarov, V.E. Fortov, JETP Lett. **92,** 516 (2010)
35. V.V. Zhakhovskii, N.A. Inogamov, JETP Lett. **92**, 521 (2010)
36. V.V. Zhakhovsky, M.M. Budzevich, N.A. Inogamov, I.I. Oleynik, C.T. White, Phys. Rev. Lett. **107**, 135502 (2011)
37. J.C. Crowhurst, M.R. Armstrong, K.B. Knight, J.M. Zaug, E.M. Behymer, Phys. Rev. Lett. **107**, 144302 (2011)
38. V.H. Whitley, S.D. McGrane, D.E. Eakins, C.A. Bolme, D.S. Moore, J.F. Bingert, J. Appl. Phys. **109**, 013505 (2011)
39. A.A. Ionin, S.I. Kudryashov, S.V. Makarov, L.V. Seleznev, D.V. Sinitsyn, JETP Lett. **94**, 34 (2011)
40. M.M. Budzevich, V.V. Zhakhovsky, C.T. White, I.I. Oleynik, Phys. Rev. Lett. **109**, 125505 (2012)
41. B.J. Demaske, V.V. Zhakhovsky, N.A. Inogamov, I.I. Oleynik, Phys. Rev. B **87**, 054109 (2013)
42. S.I. Ashitkov, P.S. Komarov, M.B. Agranat, G.I. Kanel, V.E. Fortov, JETP Lett. **98**, 384 (2013)
43. J.C. Crowhurst, B.W. Reed, M.R. Armstrong, H.B. Radousky, J.A. Carter, D.C. Swift, J.M. Zaug, R.W. Minich, N.E. Teslich, M. Kumar, J. Appl. Phys. **115**, 113506 (2014)
44. J.C. Crowhurst, M.R. Armstrong, S.D. Gates, J.M. Zaug, H.B. Radousky, N.E. Teslich, Appl. Phys. Lett. **109**, 094102 (2016)
45. T. Sano, H. Mori, E. Ohmura, I. Miyamoto, Appl. Phys. Lett. **83**, 3498 (2003)
46. T. Sano, K. Takahashi, O. Sakata, M. Okoshi, N. Inoue, K.F. Kobayashi, A. Hirose, J. Phys. Conf. Ser. **165**, 012019 (2009)
47. M. Tsujino, T. Sano, O. Sakata, N. Ozaki, S. Kimura, S. Takeda, M. Okoshi, N. Inoue, R. Kodama, K.F. Kobayashi, A. Hirose, J. Appl. Phys. **110**, 126103 (2011)
48. M. Tsujino, T. Sano, T. Ogura, M. Okoshi, N. Inoue, N. Ozaki, R. Kodama, K.F. Kobayashi, A. Hirose, Appl. Phys. Express **5**, 022703 (2012)
49. T. Matsuda, T. Sano, K. Arakawa, A. Hirose, J. Appl. Phys. **116**, 183506 (2014)
50. T. Matsuda, T. Sano, K. Arakawa, O. Sakata, H. Tajiri, A. Hirose, Appl. Phys. Express **7**, 122704 (2014)
51. T. Matsuda, T. Sano, K. Arakawa, A. Hirose, Appl. Phys. Lett. **105**, 021902 (2014)
52. B.N. Chichkov, C. Momma, S. Nolte, F. von Alvensleben, A. Tunnermann, Appl. Phys. A **63**, 109 (1996)

53. R. Le Harzic, N. Huot, E. Audouard, C. Jonin, P. Laporte, S. Valette, A. Fraczkiewicz, R. Fortunier, Appl. Phys. Lett. **80**, 3886 (2002)
54. T. Sano, T. Eimura, R. Kashiwabara, T. Matsuda, Y. Isshiki, A. Hirose, S. Tsutsumi, K. Arakawa, T. Hashimoto, K. Masaki, Y. Sano, J. Laser Appl. **29**, 012005 (2017)
55. T. Sano, T. Eimura, A. Hirose, Y. Kawahito, S. Katayama, K. Arakawa, K. Masaki, A. Shiro, T. Shobu, Y. Sano, Metals **9** (2019)
56. H. Nakano, S. Miyauti, N. Butani, T. Shibayanagi, M. Tsukamoto, N. Abe, J. Laser Micro/Nanoeng. **4**, 35 (2009)
57. D. Lee, E. Kannatey-Asibu Jr., J. Laser Appl. **23**, 022004 (2011)
58. Y. Sagisaka, M. Kamiya, M. Matsuda, Y. Ohta, J. Mater, Process. Tech. **210**, 2304 (2010)
59. Y. Sagisaka, K. Yamashita, W. Yanagihara, H. Ueta, J. Mater, Process. Tech. **219**, 230 (2015)
60. G.L. Eesley, Phys. Rev. Lett. **51**, 2140 (1983)
61. J.G. Fujimoto, J.M. Liu, E.P. Ippen, Phys. Rev. Lett. **53**, 1837 (1984)
62. G.L. Eesley, Rev. B **33**, 2144 (1986)
63. R.W. Schoenlein, W.Z. Lin, J.G. Fujimoto, G.L. Eesley, Phys. Rev. Lett. **58**, 1680 (1987)
64. A.P. Kanavin, I.V. Smetanin, V.A. Isakov, Yu.V. Afanasiev, B.N. Chichkov, B. Wellegehausen, S. Nolte, C. Momma, A. Tunnermann, Phys. Rev. B **57**, 14698 (1998)
65. B. Rethfeld, A. Kaiser, M. Vicanek, G. Simon, Phys. Rev. B **65**, 214303 (2002)
66. D. Perez, L.J. Lewis, Phys. Rev. Lett. **89**, 255504 (2002)
67. D. Perez, L.J. Lewis, Phys. Rev. B **67**, 184102 (2003)
68. D. Bejan, G. RaseevPhys, Rev. B **55**, 4250 (1997)
69. M.I. Kaganov, I.M. Lifshitz, L.V. Tanatarov, Sov. Phys. JETP **4**, 173 (1957)
70. P.B. Allen, Phys. Rev. Lett. **59**, 1460 (1987)
71. J.I. Etcheverry, M. Mesaros, Phys. Rev. B **60**, 9430 (1999)
72. K. Sokolowski-Tinten, J. Bialkowski, A. Cavalleri, D. von der Linde, A. Oparin, J. Meyer-ter-Vehn, S.I. Anisimov, Phys. Rev. Lett. **81**, 224 (1998)
73. F. Vidal, T. Johnston, S. Laville, O. Bathelemy, M. Chaker, B.L. Drogoff, J. Margot, M. Sabsabi, Phys. Rev. Lett. **86**, 2573 (2001)
74. L.V. Zhigilei, B.J. Garrison, J. Appl. Phys. **88**, 1281 (2000)
75. C. Schafer, H.M. Urbassek, L.V. Zhigilei, Phys. Rev. B **66**, 115404 (2002)
76. S.I. Anisimov, B.L. Kapeliovich, T.L. Perel'man, Sov. Phys. JETP **39**, 375 (1974)
77. L.R. Veeser, J.C. Solem, Phys. Rev. Lett. **40**, 1391 (1978)
78. R.J. Trainor, J.W. Shaner, J.M. Auerbach, N.C. Holmes, Phys. Rev. Lett. **42**, 1154 (1979)
79. M. Koenig, B. Faral, J.M. Boudenne, D. Batani, A. Benuzzi, S. Bossi, C. Remond, J.P. Perrine, M. Temporal, S. Atzeni, Phys. Rev. Lett. **74**, 2260 (1995)
80. S.H. Glenzer, B.J. MacGowan, P. Michel, N.B. Meezan, L.J. Suter, S.N. Dixit, J.L. Kline, G.A. Kyrala, D.K. Bradley, D.A. Callahan, E.L. Dewald, L. Divol, E. Dzenitis, M.J. Edwards, A.V. Hamza, C.A. Haynam, D.E. Hinkel, D.H. Kalantar, J.D. Kilkenny, O.L. Landen, J.D. Lindl, S. LePape, J.D. Moody, A. Nikroo, T. Parham, M.B. Schneider, R.P.J. Town, P. Wegner, K. Widmann, P. Whitman, B.K.F. Young, B. Van Wonterghem, L.J. Atherton, E.I. Moses, Science **327**, 1228 (2010)
81. R. Pakula, R. Sigel, Phys. Fluids **28**, 232 (1985)
82. A. Ng, A. Forsman, P. Celliers, Phys. Rev. E **51**, 5208 (1995)
83. E. Tokunaga, A. Terasaki, T. Kobayashi, Opt. Lett. **17**, 1131 (1992)
84. E. Kröner, Z. Phys. **151**, 504 (1958)
85. N. Kamm, G.A. Alers, J. Appl. Phys. **35**, 327 (1964)
86. Z. Horita, T. Fujinami, M. Nemoto, T.G. Langdon, Metall. Mater. Trans. A **31A**, 691 (2000)
87. A.H. Clauer, C.T. Walters, S.C. Ford, *Lasers in Materials Processing*, vol. 7 (American Society for Metals, Metals Park, Ohio, 1983)
88. C.A. Rodopoulos, J.S. Romero, S.A. Curtis, E.R. de los Rios, P. Peyre, J. Mater. Eng. Perform. **12**, 414 (2003)
89. C.A. Rodopoulos, S.A. Curtis, E.R. de los Rios, J. SolisRomero, Int. J. Fatigue **26**, 849 (2004)
90. A. Ali, X. An, C.A. Rodopoulos, M.W. Brown, P. O'Hara, A. Levers, S. Gardiner, Int. J. Fatigue **29**, 1531 (2007)

91. A. Gariepy, F. Bridier, M. Hoseini, P. Bocher, C. Perron, M. Levesque, Surf. Coat. Tech. **219**, 15 (2013)
92. A.T. DeWald, J.E. Rankin, M.R. Hill, M.J. Lee, H.L. Chen, J. Eng. Mater. Technol. **126**, 465 (2004)
93. H. Omar, J. Mater. Eng. Perform **17**, 688 (2008)
94. O. Hatamleh, Int. J. Fatigue **31**, 974 (2009)
95. Y. Sano, K. Masaki, T. Gushi, T. Sano, Mater. Des. **36**, 809 (2012)
96. G. Bussu, P.E. Irving, Int. J. Fatigue **25**, 77 (2003)
97. C.D.M. Liljedahl, J. Brouard, O. Zanellato, J. Lin, M.L. Tan, Int. J. Fatigue **31**, 1081 (2009)
98. R. Nandan, T. DebRoy, H.K.D.H. Bhadeshia, Prog. Mater. Sci. **53**, 980 (2008)
99. C. Kulekci, A.S. Ik, E. Kaluc, Int. J. Adv. Manuf. Technol. **36**, 877 (2008)
100. M. Garware, G.T. Kridli, P.K. Mallick, J. Mater. Eng. Perform. **19**, 1161 (2010)
101. T. Dursun, C. Soutis, Mater. Des. **56**, 862 (2014)
102. E. Schubert, M. Klassen, I. Zerner, C. Walz, G. Sepold, J. Mater. Process. Technol. **115**, 2 (2001)
103. S. Katayama, H. Nagayama, M. Mizutani, Y. Kawahito, Weld. Int. **23**, 744 (2009)
104. T. Kawashima, T. Sano, A. Hirose, S. Tsutsumi, K. Masaki, K. Arakawa, H. Hori, J. Mater. Process. Technol. **262**, 111 (2018)
105. T. Shobu, K. Tozawa, H. Shiwaku, H. Konishi, T. Inami, T. Harami, J. Mizuki, A.I.P. Conf, Proc. **879**, 902 (2007)
106. T. Shobu, H. Konishi, J. Mizuki, K. Suzuki, H. Suzuki, Y. Akiniwa, K. Tanaka, Mater. Sci. Forum **524**, 691 (2006)
107. R.E. Little, in *Probabilistic Aspects of Fatigue,* ed. by R. Heller (ASTM International: West Conshohocken, 1972), pp. 29–42
108. J. Ahn, L. Chenb, E. Heb, C.M. Daviesa, J.P. Deara, J. Manuf. Process. **25**, 26 (2017)
109. J. Ahn, E. Heb, L. Chenb, J. Deara, C. Daviesa, J. Manuf. Process. **29**, 62 (2017)
110. B. Hu, I.M. Richardson, J. Laser Appl. **17**, 70 (2005)
111. C.E. Cross, D.L. Olson, S. Liu, *Aluminium Welding, Handbook of Aluminum; Dekker: New York*, vol. 1 (NY, USA, 2003)
112. A.S. Keh, *Interscience Publishers: New York* (NY, USA, 1962), pp. 213–233
113. E. Orowan, Proc. Phys. Soc. London **52**, 8 (1940)
114. M.A. Meyers, Scripta Metall. **12**, 21 (1978)
115. J.W. Swegle, D.E. Grady, J. Appl. Phys. **58**, 692 (1985)
116. D.E. Grady, J. Appl. Phys. **107**, 013506 (2010)
117. R.G. McQueen, S.P. March, J.W. Taylor, J.N. Fritz, W.J. Carter, *High-Velocity Impact Phenomena* ed. by R. Kinslow (Academic: New York, 1970), p. 293

Chapter 6
Direct Femtosecond Laser Writing of Optical Waveguides in Dielectrics

Feng Chen and Javier R. Vázquez de Aldana

Abstract By applying direct femtosecond laser writing, optical waveguides with diverse configurations can be produced in various transparent dielectrics, including glasses, single crystals, and ceramics. The focused ultrashort pulses interact with the bulk matrix, resulting in modification of refractive index of the localized regions. Both positive and negative index changes have been successfully utilized to generate waveguiding effects. Owing to the capability and feasibility of direct femtosecond laser writing, a number of waveguide devices have been fabricated in versatile optical materials, which brings out intriguing applications in many areas. In this chapter, we overview the fundamentals of the femtosecond laser writing of optical waveguides in optical dielectrics and introduce the recent applications in selected topics.

6.1 Introduction

Optical waveguides with compact geometries are basic components in integrated optics [1]. They are defined as regions or layers with high refractive index in comparison with their surroundings. In waveguides, the light fields can be confined in very small volumes, reaching relatively high intensities. The advantages of waveguide-based devices are twofolds: First, the diffraction-free light propagation enables beam guidance and tailoring in chip-scale devices, which leads to a number of applications in many areas; and second, the tight confinement of light fields brings out enhanced features of bulk features in waveguides [2]. In 1996, Davis et al. reported on the first femtosecond laser-written waveguides in a few family glasses [3], and numerous subsequent works have been performed towards waveguide fabrication in various transparent materials [4]. As of yet, direct femtosecond laser writing/inscription has

F. Chen (✉)
School of Physics, State Key Laboratory of Crystal Materials, Shangdong University, Jinan 250100, China
e-mail: drfchen@sdu.edu.cn

J. R. V. de Aldana
Grupo de Investigación en Aplicaciones del Láser y Fotónica, Departamento de Física Aplicada, University of Salamanca, Salamanca 37008, Spain

A. Hu (ed.), *Laser Micro-Nano-Manufacturing and 3D Microprinting*, Springer Series in Materials Science 309, https://doi.org/10.1007/978-3-030-59313-1_6

been used to successfully produce optical waveguides in glasses, single crystals, ceramics, and organic polymers, showing wide applicability of different materials [5–7]. In addition, compared with other techniques for waveguide fabrication, direct femtosecond laser writing possesses powerful three-dimensional (3D) processing capability of materials, which enables implementation of devices with various functionalities in dielectrics [8]. As a result, highly efficient miniaturized platforms based on laser-written waveguides have been realized for photonic signal processing towards diverse purposes [9].

The direct processing of dielectric materials by femtosecond laser contains two ways: longitudinal and transverse writing (see Fig. 6.1). The advantage of longitudinal writing is the preservation of laser beam symmetry, while the limitation of waveguide length exists due to the working distance of focusing lens in the system. The transverse writing is much more feasible and attracts much more attention of researchers. Expect to the writing geometries, the parameters of the femtosecond laser system are critical to the quality of the waveguide devices. And the beam shaping of the laser pulses (e.g., by some slits) is an efficient solution to control the waveguide geometries [9]. Moreover, the nature of different materials plays important roles in the waveguide properties. In crystalline materials, the fabrication of waveguides is much more complicated in comparison with amorphous bulks [6]. Nevertheless, a number of functionalized devices have been produced by direct femtosecond laser writing. They have shown potential applications in many aspects, e.g., telecommunication mode couplers [10], laser generations [11], frequency conversions [6], microfluidic chips [12], quantum information processing [13], astrophotonic devices [14], and so on. Osellame et al. edited a book which gave comprehensive overview of the femtosecond laser micromachining of photonic and microfluidic devices in transparent materials in 2012 [9]. Several new review articles were presented in direct femtosecond laser-written waveguides in distinguish focused topics, for examples, by Chen et al. [6], Choudhury et al. [15], and Meany et al. [13], respectively.

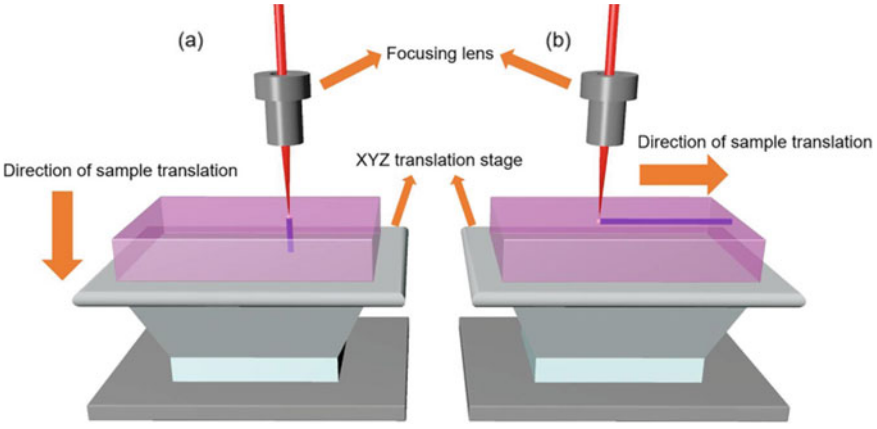

Fig. 6.1 Schematic plots of the **a** longitudinal and **b** transverse writing configurations

In this chapter, we review the fundamentals and new advances of femtosecond laser-written waveguides in dielectrics. Section 6.2 introduces the fundamentals of refractive index modification in dielectrics by femtosecond laser pulses. In Sect. 6.3, the geometries of different waveguides by laser writing are overviewed. In Sect. 6.4, we summarize, in a brief way, the dielectric materials applied for laser writing of waveguide devices. Several selected applications of laser-written waveguides are presented in Sect. 6.5 to indicate the state of the art of the research fields. Finally, in Sect. 6.6 a summary is given and an outlook of the future topics is presented.

6.2 Femtosecond Lasers Induced Refractive Index Changes

When ultrashort laser pulses are focused inside transparent dielectrics well localized and, to some extent, controlled material modifications can be induced. The high-intensity that can be reached in the focal region and the short temporal duration of the laser pulse (tens or a few hundreds of femtoseconds) are responsible for a very complex laser-matter interaction phenomenology. As the laser pulse intensity reaches 10^{12}–10^{13} W/cm^2, values that can be easily achieved with amplified laser systems, a larger number of electrons can be ionized through the so-called strong-field ionization processes [16]: multiphoton ionization (more efficient at low intensities) or tunnel ionization. Then, detached electrons form a plasma that continues interacting with the laser field, absorbing energy by inverse Bremsstrahlung and releasing more electrons by collisions (process called avalanche ionization) [17]. However, due to the short pulse duration, the laser–matter interaction finishes before a significant energy transfer between electrons and ions took place, and thus negligible thermal effects are induced: the irradiated area consists of a hot plasma of electrons and a "cold" lattice of ions. The evolution of such system once the interaction with the laser has finished is so complex that is still far from being completely understood and depends strongly on both the plasma as the material properties [18]. Once the equilibrium is again reached after the irradiation, localized modifications of the material may be found, directly linked to the ionized electron density that was reached in the material [19]. In fact, there are clear thresholds [20], in terms of the input pulse energy, to induce certain modification in each target (depending, of course, on the experimental conditions as focusing, pulse duration, wavelength, etc.).

For low pulse energies, a weak and smooth material modification is induced in the focal volume that changes the index of refraction in this area [3]. The first micro-analysis studies were done in glasses and suggest that a structural rearrangement of bonds takes place without destruction of the overall integrity of the glass [21]. This weak material modification is usually referred to as "Type-I modification" (following the classification scheme proposed in [22]) and can be associated with a positive or a negative refractive index change in the focal volume. Positive refractive index changes associated with Type-I modification are more frequently produced in glasses than in crystals, provided that densification is expected to be more easily induced in amorphous materials than in ordered crystalline structures. However, in glasses with

strong thermal expansion (such as BK7) the laser irradiation usually induces negative refractive index modifications. It should be noticed that Type-I modifications are liable to be completely or partially "erased" by thermal treatment of the sample after laser exposition [23].

As the pulse energy is increased and certain threshold is exceeded, severe optical damage will be induced in the irradiated region (see Fig. 6.2). In this case, the material modification (named "Type-II modification") is very complex, involves severe structural damage, and depends strongly on the dielectric target. In general, a refractive index decrease will be produced in the focal volume [24] that, in the case of glasses, it is linked with the generation of micro-explosions [25] in the region that achieved the largest plasma density: The plasma energy is transferred to the lattice thus generating a highly localized temperature that results in a micro-explosion and the creation of a subsequent micro-voids [26]. In the case of crystalline targets, the refractive index decrease is explained in terms of a local amorphization induced in that region [27] that is accompanied by the presence of defects and micro-voids [28]. Moreover, due to the shock wave produced from this area, a mechanical stress field is induced in the surrounding material, leading to a refractive index increase (compression) in this area [29]. The compressed region may appear at both lateral sides of the damage tracks, or at the apex of the track [30].

The pulse energy to produce one or the other modification type in a given material is strongly dependent on the experimental conditions, mainly the pulse duration and

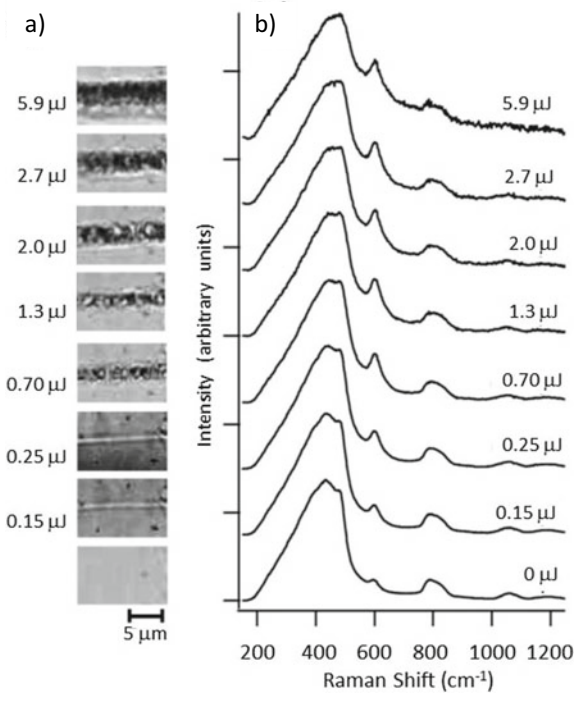

Fig. 6.2 Transition from Type-I to Type-II modifications induced in fused silica with 800 nm, 120 fs pulses at 1 kHz repetition rate as the pulse energy in increased. **a** Micrographs of the lines written in fused silica with different pulse energies. **b** Raman spectra of modified regions (Adapted from [21])

the focusing optics, thus requiring a careful initial characterization [31]. As reference values, for a tight focusing with NA 0.20–0.40, Type-I modifications are produced with few hundreds of nano-Joules, and Type-II appear as the pulse energy approaches the micro-Joule level (Fig. 6.2).

In addition to the described modifications, that can be induced with just a single femtosecond laser pulse, other effects may appear when the target is irradiated with a pulse train with certain repetition rate. In such case, when several pulses impinge on the same point of the target, the cumulative effect of all of them may produce a final modification that could not be induced with a single pulse [32]. Generally, this effect is related to the heat transferred by the laser pulse to the sample, and the key parameters are the repetition rate of the pulse train and the heat diffusion time of the target. In this way, we may distinguish between two irradiation regimes: thermal and non-thermal. In the thermal regime, the heating produced by one pulse overlaps with the heating produced by the subsequent one, leading to a very high local temperature increase by heat accumulation that may lead to the material melting and, therefore, to the local modification [33]. In the non-thermal regime, the time interval between subsequent pulses is large enough so that local heating is dissipated and no net temperature increase is produced at the end. The transition between both regimes takes place at a given repetition rate, the critical frequency, that can be estimated by [34]

$$f_{\text{crit}} = \frac{\alpha}{d^2} \tag{1}$$

with "d" being the diameter of the focal spot and "α" the thermal diffusivity of the sample. The onset of thermal effects for typical tight focusing conditions in dielectrics is in the range of tens/hundreds of kHz. In certain materials, glasses in particular, local melting generated in the thermal regime with large repetition rate lasers, such as femtosecond oscillators, has been demonstrated to produce a refractive index increase [32] that can be assimilated to that of Type-I modification. On the other hand, in crystals, the local heating produced in the thermal regime releases color centers and reduces the defect concentration of the laser tracks [35, 36].

6.3 Waveguide Geometries

The principle for waveguide fabrication in transparent dielectrics with femtosecond pulses is simple: It consists basically on the inscription of localized refractive index modifications along with the sample, thus forming "channels" with efficient light confinement properties [3] embedded in the substrate. However, there exist several

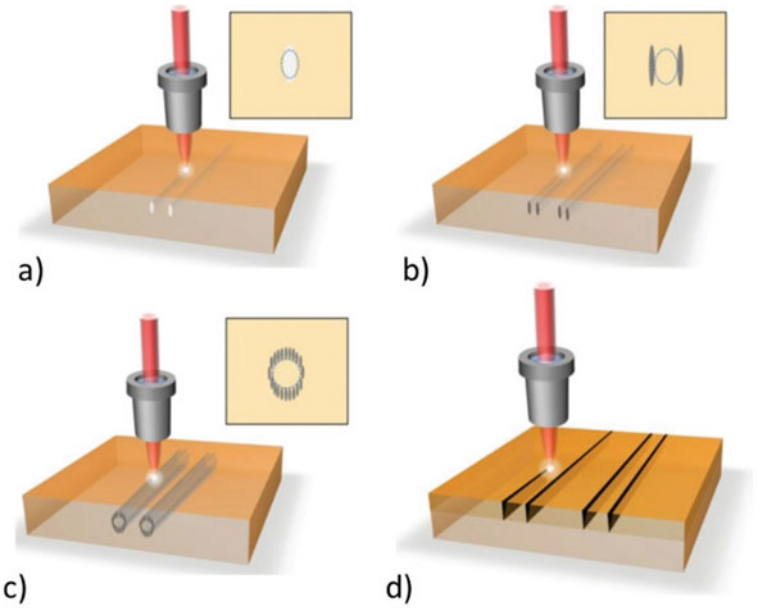

Fig. 6.3 Schematic of different fabrication procedures of fs-laser inscribed waveguides. **a** Waveguides based on Type-I modification. **b** Stress-induced waveguides based on Type-II modification. **c** Depressed-cladding waveguides based on Type-II modification. **d** Ridge waveguides. The insets indicate the cross-sectional sketches of the waveguides. The shadows represent the fs-laser-induced tracks, and the dashed lines indicate the spatial locations of the waveguide cores (Taken from [6])

strategies or approaches to get efficient waveguides, depending on the type of modification that is induced in the target material, or on the desired optical performance of the waveguide (i.e., monomode/multimode or dependence with polarization). Figure 6.3 shows sketches of the different approaches by femtosecond laser writing/micromachining.

6.3.1 Waveguides Based on Type-I Modification

Type-I modification has been extensively used to fabricate waveguides in materials where the refractive index modification induced by the laser is positive ($\Delta n > 0$): This is the case of most of the glasses and a few crystals (i.e., $LiNbO_3$ [29], Nd:YCOB [37], ZnSe [38], or BGO in the mid-IR [39]). The straightforward technique for waveguide inscription then consists of moving the sample with respect to the focus of the beam at certain velocity, thus producing a track with increased index of refraction along the sample in which light may be directly confined. With the aim of modifying the optical properties and performance of the waveguide, several parallel tracks can be inscribed [37, 40, 41], thus increasing the cross section of the modified region: This way the

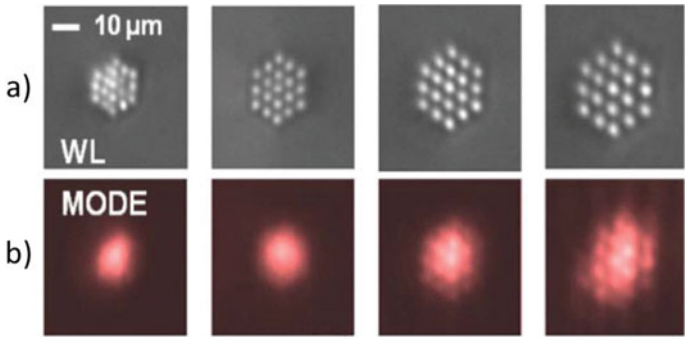

Fig. 6.4 **a** Microscopic white light pictures of hexagonal multicore waveguide arrays based on Type-I modification written with 130 mW, 140 fs pulses, at a scan velocity of 200 μm/s and different separations of the waveguides in fused silica. **b** Near-field modes of multi-core waveguides (Adapted from [43])

modal behavior can be finely controlled and optimized to the desired wavelength. Another alternative to obtain large area waveguides consists on the fabrication of waveguide arrays [42] with very small separation among them, such that the strong evanescent coupling allows the formation of a nearly continuous mode [43] (see Fig. 6.4).

Maybe the main advantage of the waveguides based on Type-I modification is the potential for the fabrication of 3D complex photonic circuits and devices [9, 44] (see Sect. 6.5.1). Since light is directly confined at the laser tracks, and no further damage is induced in the neighborhood of the waveguide, it is relatively simple to inscribe in the sample any arbitrary guiding geometry, as well as elements like splitters [39], combiners, or couplers [45].

Depressed-cladding waveguides. In materials where Type-I modification produces a refractive index decreased in the exposed region, there is an approach for the fabrication of optical waveguides. It consists of the inscription of many parallel laser tracks forming a modified cladding (with decreased index) and a central unexposed core where the light propagates through. In principle, this configuration supports only leaky modes [46] what means that only continuum radiation modes exist. However, when the width of the lower-index region is large, propagating modes very similar to confined modes are supported [47].

6.3.2 Waveguides Based on Type-II Modification

As discussed in the previous section, when the pulse energy is such that optical breakdown takes place, a more complex refractive index modification is induced in the sample. The index of refraction at the damage tracks typically decreases, making it impossible to inscribe a waveguide that confines light directly at the track. In this

case, there exist two approaches to get light confinement that has been extensively studied in crystals provided that, in most of them, Type-I modification with refractive index increase cannot be produced.

Stress-induced waveguides. The first one consists of making use of the refractive index increase that is produced at the surroundings of the damage track, caused by the mechanical stress and compression induced after the irradiation. In order to increase the refractive index change in this region and obtaining a better confinement of the light, two parallel laser scans are done along the sample at certain separation (~15–25 μm; see Fig. 6.4a) so that the waveguide is formed between the two damage tracks: this is the so-called double-scan technique [23, 29, 48]. A very interesting property of this fabrication approach is that the guiding region has not been directly exposed to the laser irradiation, and then the physical characteristics of the bulk are almost unaffected: This is crucial in many applications, particularly in crystals, that are based on the nonlinear or spectroscopic features of the material [49, 50]. Moreover, in comparison with waveguides based on Type-I modification, stress-induced waveguides are very stable even at high temperatures [51], making them very suitable for high-power applications. In addition to the simple "double-scan" technique, some approaches with more complexity have been developed in order to gain better confinement of the guided mode [52, 53] or to engineer the stress-field geometry [54].

Depressed-cladding waveguides. An alternative approach for the fabrication of optical waveguides based on Type-II modifications consists of the inscription of many parallel damage tracks forming a modified cladding and a central unexposed core where the light propagates through [55] (see Figs. 6.5a–c). In order to get a good optical performance, the separation between damage tracks must be very small (2–3 μm) and the scanning velocity very large in order to minimize the stress induced in the surroundings of the tracks. In this way, the refractive index profile is basically a cladding with decreased index (severe damage) and the central core keeps the index of the bulk. In principle, this configuration supports only leaky modes [46] what means that only continuum radiation modes exist. However, when the width of the lower-index region is large, propagating modes very similar to confined modes are supported.

Efficient depressed-cladding waveguides have been successfully fabricated in many crystalline materials [6] even with very low propagation losses. In similar manner to the behavior of "double-scan" waveguides, they have been demonstrated to preserve the spectroscopic properties at the waveguide core [56]. In addition, in most of the crystals, guidance features are independent of light polarization. Both properties make cladding waveguides very attractive for constructing active components as waveguide lasers [55, 57]. But the main advantage of cladding waveguides is that they can be designed with any arbitrary geometry and dimensions in order to tailor the modal behavior for the required wavelength, even in the mid-infrared [58], optimizing the coupling with external devices (i.e., optical fibers): In this sense, the most convenient geometry is circular, with typical diameters between 30 and 150 μm.

In addition to the "standard" cladding waveguides described above, different improvements have been introduced in the cladding designs. For instance, complex

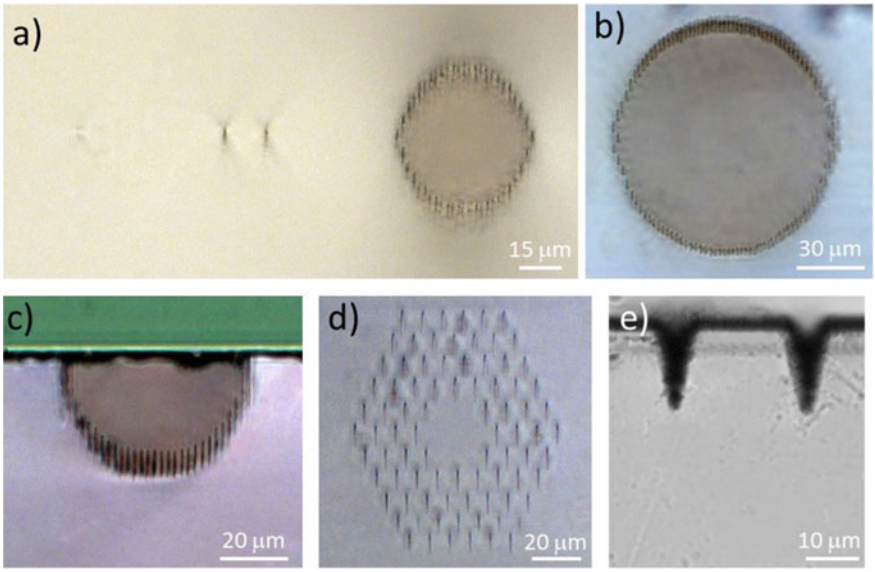

Fig. 6.5 Optical microscope images of different waveguides fabricated by femtosecond laser irradiation in the non-thermal regime (120 fs, 1 kHz, 800 nm). **a** Multiple scan waveguide based on Type-I modification (left), double-scan waveguide based on Type-II modifications (center), and circular cladding waveguide (right) inscribed in fused silica. **b** Circular cladding waveguide in NdYAG crystal. **c** Shallow cladding waveguide in NdYAG crystal. **d** Optical-lattice-like cladding waveguide in NdYAG crystal. **e** Ridge waveguides produced in ZnSe by swift ion irradiation and femtosecond laser ablation

damage tracks structures can be implemented in order to reduce losses and get better confinement for the two polarizations [59]. Dual-cladding waveguides, consisting of two concentric tubular structures, have been also used to improve the performance of miniaturized waveguide lasers [60]. Another family of waveguides is based on large claddings with a hexagonal optical-lattice-like structure of the damage tracks (Fig. 6.5d). These structures, in addition to offer very low propagation losses and isotropic behavior of the supported mode with polarization, allow the design of compact beam splitters and beam shapers [61, 62] making them very interesting for the integration of complex photonic devices.

Finally, it should be noted that cladding waveguides can be fabricated very shallow in the sample in such a way that the surface acts as waveguide boundary (see Fig. 6.5c). This is very interesting in the fabrication of devices that require an external interaction with the guided mode, for example in electro-optic devices, or in integrated Q-switched waveguide lasers [63].

6.3.3 Other Femtosecond Laser Writing Techniques

Fs-laser irradiation can be focused on the surface of a dielectric material leading to ultra-fast ablation (see for instance [64] and references therein), that consists in local material removal with minimal damage in the surroundings. Although the layer removed with a single laser pulse is typically of a few hundreds of nanometers [65], the incidence with multiple pulses allows the production of micro-holes or precise cuts in the sample surface [66]. This micro-machining tool offers a pathway to fabricate ridge waveguides on planar waveguide substrates (the planar waveguide previously fabricated by other techniques as ion-beam implantation): The fs-laser is used to precise micro-cuts in the planar surface, constructing ridges that confine light propagation in certain regions [67], thus forming channel waveguides with the desired lateral dimensions (see Fig. 6.5e). The technique has been applied to different crystals in order to fabricate frequency converters or waveguide lasers [68]. The main drawback of these waveguides is the roughness of the ablation grooves produced with the fs-laser, which introduces large propagation losses and degrades the modal profiles: To improve the performance, some post-processing treatments have been used, as thermal annealing [69] or ion-beam sputtering [67].

6.4 Materials

6.4.1 Glasses

Glasses are maybe the family of materials in which more research work on direct femtosecond laser inscription has been done. There are several reasons for that, such as the excellent optical properties and quality of many glasses, the stability of the material or the relatively low cost, among many others. However, maybe the most interesting property of glasses that make them very attractive for femtosecond laser waveguide inscription is the possibility to produce Type-I modifications with refractive index increase [3] in many of them, working both in the non-thermal regime (low repetition rate laser systems) and in the thermal regime (high repetition rate systems). Additionally, some of them show the possibility to produce selective chemical etching in the areas exposed to femtosecond laser irradiation [70], opens the door to a wide range of applications that mix several types of laser micro-processing, such as the fabrication of microfluidic or lab-on-a-chip devices [9].

Among the large amount of available glasses with optimal optical properties, some of them have concentrated most of the research efforts. Fused silica (amorphous SiO_2) is one of the most extensively studied materials regarding femtosecond laser irradiation and waveguide fabrication. It is available with excellent optical quality and shows a very wide transmission window. The techniques used for the inscription of optical waveguides are both single scan [3] or multiple scan [40], thus obtaining very low propagation loss in the visible and near-IR (0.12 dB/cm), or even in the

mid-IR [71] (1.3 dB/cm at 3.39 μm), with refractive index changes of the order of 1×10^{-3}. The excellent performance of the waveguides has allowed the implementation of complex photonic devices in fused silica. Planar Y-splitters [72] or multiple splitters [73] are the basic elements for the fabrication of complex photonic circuits, but the potential of femtosecond lasers for 3D inscription was exploited with the fabrication of nearly equalized 3D splitters [74]. Other 3D structures, as directional couplers in 3D [75], straight waveguide arrays [76], or fan-out devices [77] have been demonstrated in this material. Fused silica is one of the glasses that shows selective chemical etching, and integrated optofluidic devices have been fabricated on it [9]. In addition, the possibility to dope silicate glasses with active ions, such as Nd, has allowed the manufacturing of active waveguides [78].

Borosilicate glass is also an excellent substrate for the inscription of optical waveguides. For instance, complex 3D beam splitters (photonic lanterns) have been demonstrated in this glass [44] by the multi-scan approach, operating at 1539 nm with very low losses. Depressed-cladding structures have been also inscribed in borosilicate glass with a photonic-crystal hexagonal structure that modulates the spectral transmission of the waveguide, thus forming anti-resonant reflecting optical waveguides [79].

Phosphate glass is very interesting for its spectroscopic properties when it is doped with Nd, Yb, or Er:Yb. Different active devices such as waveguide lasers have been manufactured in Er:Yb phosphate glass by direct femtosecond laser inscription [80, 81] emitting at 1533.5 nm. It should be remarked that the waveguides inscribed in this glass exhibit very low propagation loss (0.24 dB/cm) [82].

Another glass with optimum properties is Foturan, a lithium aluminosilicate glass doped by silver and cerium oxides. This glass is photosensitive and shows selective chemical etching. The possibility to fabricate optical waveguides on it by femtosecond laser irradiation [83] makes it very attractive for manufacturing optofluidic devices [84]. ZBLAN (heavy metal fluoride glass) has been also used for the inscription of optical waveguides. Doped with Tm, waveguide lasers based on depressed-cladding structures have been obtained, emitting at 1.9 μm with prop loss of 0.22 dB/cm and 50% slope efficiency [85].

6.4.2 Single Crystals

Single crystals play significant roles in optics and photonics. According to their crystalline structures or functions, one can roughly classify the single-crystals into a few groups. As of yet, in addition to the normal optical crystals (e.g., quartz), the direct laser writing has been successfully applied to *functional* crystals, such as laser, nonlinear, and electrooptic crystals. Electrooptic crystals utilize the electrooptic effects to modulate the light behaviors in crystals on the phase, amplitude, and polarizations, engineering the light propagation, and multi-beam interactions for signal processing of photonic systems. Laser crystals are favorite gain media, which are widely used for laser generation and signal amplification. Nonlinear crystals are

key elements for light frequency conversion, realizing color changes, and new light sources for diverse applications.

The electrooptic crystal used for laser-written waveguides is $LiNbO_3$ [6]. Since $LiNbO_3$ is a multifunctional crystal, many efforts have been performed on it to study the guiding properties. Liao et al. reported on the modulation of light based on femtosecond laser inscribed $LiNbO_3$ (double-line) waveguides [86]. Other crystals such as LGS may be also used for EO modulation. Nevertheless, cost-effective modulators require low voltages of applied electrical fields, and in principle, the transverse dimension should be as compact as possible. Considering this factor, double-line structures may be better since the cross sections are much smaller than those of depressed-cladding waveguides [86].

Nonlinear crystals for frequency conversion of laser-written waveguides include birefringent crystals and periodically poled superlattices. Frequency doubling to generate second harmonics is one of the most important functions for nonlinear crystals based on Type-I or Type-II phase matching conditions. Laser-written waveguides in nonlinear crystals, such as KTP [87], BIBO [54, 88], GdCOB [37], $LiNbO_3$ [23], KDP [89], have been fabricated in both double-line and depressed-cladding geometries. In addition, by using periodically poled wafers in ferroelectrics, such as PPLN, PPLT, PPKTP, one can realize broadband SHG in laser-written waveguides. The mostly investigated wafer is PPLN. All the possible designs have been applied on PPLN, including single-line or multi-line Type-I, double-line Type-II, and depressed cladding configurations [90–92]. For PPKTP [93], only double-line structures have been investigated.

The laser crystals are doped by active ions into suitable bulk materials. The lasing wavelength depends on the atomic energy levels of specific active ions. For visible waveguide, lasing can be achieved by using Pr-doped crystals, including Pr:$SrAl_{12}O_{19}$ (at 644 nm) [94], Pr:YLF (at 604 nm) [53], Pr:YKF (at 610 and 645 nm) [95] waveguides. Another solution to generate visible laser is to use self-frequency-doubled crystals, which combine the nonlinear properties of bulk crystals and gain feature of the action ions in a single crystal, such as Nd:YAB [96], and Nd:YCOB [97]. In the near infrared regime, Ti-doped sapphire is for 700–900 nm tunable wavelength [98] while Nd- or Yb-doped systems are often used for 1 μm lasing. Nd- or Yb-doped YAG crystals [99, 100] and vanadates (YVO_4, $GdVO_4$) [57, 101] are favorite gain media. Other doped crystals are also investigated, such as Nd:GGG [50], Nd:LGS [102], Nd:KGW [103], Nd:KYW [104], Nd:$LiNbO_3$ [105]. The Tm-doped systems can generate lasing at 1.8–2 μm band. The reported result is Tm:KLuW cladding waveguides [106]. For typical mid-infrared wavelength regime, it is desirable to use laser-written waveguides in Cr or Fe-doped ZnSe or ZnS [107, 108], in which tunable lasing from ~2 to ~3 μm.

6.4.3 Ceramics

Transparent ceramics are polycrystalline materials. The monocrystalline partners of the ceramics are usually with cubic lattice structures. As of yet, rare-earth ion-doped YAG and yttria [109] are the investigated ceramics for femtosecond laser inscribed waveguides. Nd- or Yb-doped YAG ceramic waveguides have been used for efficient gain cavities to realize waveguide lasing at 1 μm [110], while Tm-doped YAG ceramics have been ascertained for 2 μm laser generation in waveguide cavity [111]. Also due to the working wavelength of the waveguides, Nd- or Yb-doped YAG waveguides can take the geometry of double line or claddings, while the Tm-doped YAG is only with depressed claddings because of the longer operation wavelength. As for the waveguide qualities, compared with the single-crystalline partners, the guiding behaviors and the laser-induced micrometric modifications are very similar in ceramics. This also results in similar laser performances of waveguide lasers between the gain cavities of single crystals and polycrystalline ceramics. Nevertheless, in principle, the ceramics possess the advantage of easy production of larger bulks, which may lead to larger waveguide wafers for the integration of more functions.

6.5 Selected Applications

6.5.1 3D Waveguide Devices

One of the most interesting features of femtosecond laser irradiation is the possibility to do true 3D micro-processing inside transparent dielectrics: The laser beam can be focused at any depth of the sample, thus allowing the strongly localized modification at arbitrary positions. This capability has opened the door to many novel and exciting applications [4], as nano-surgery [112], or additive/subtractive 3D nano-manufacturing [113]. Photonics and waveguide fabrication, in particular, have been specially benefited from this feature, provided that other manufacturing techniques (ion-beam implantation, Silica-on-Silicon or sol–gel) are restricted to planar or quasi-planar geometries. However, there exists a wide variety of applications that require 3D photonic circuits based on optical waveguides, in different scientific and technological fields such as astro-photonics or biomedicine.

For the fabrication of 3D photonic circuits, the most straightforward technique is the use of Type-I modifications (see Sect. 6.2) in such a way that guidance is directly produced at the focal volume with no further damage at the surroundings. This technique allows the implementation of low losses waveguide splitters/combiners in 3D [44], or the efficient coupling between neighbor waveguides through evanescent field [76], having both elements crucial importance for complex 3D devices. For instance, it has been demonstrated the direct integration of such waveguides in microfluidic

chips [9, 114, 115]. Moreover, due to the possibility to control the optical properties of the waveguides by the multi-scan technique, the 3D photonic circuits can be designed to operate even in the mid-infrared [116].

Most of these devices have been implemented in glass substrates (Sect. 6.4.1) due to the relative simplicity of the fabrication procedure in such targets. However, there is much interest in the integration of such structures in dielectric crystals [6] due to their impressive optical properties, as high transparency range, or nonlinear coefficients. Several research groups have been working towards the fabrication of complex photonic devices in crystals using femtosecond laser direct inscription, but most of the research work has been restricted to planar structures based on simple waveguides. This is due to the large complexity of the problem: On the one hand, Type-I modification typically produces a refractive index decrease (instead of an increase) in most of the crystals and, on the other hand, anisotropy in crystalline materials makes the fabrication highly sensitive to irradiation conditions [117]. In crystals in which a refractive index increase can be produced by Type-I modification, such as $LiNbO_3$, $Bi_4Ge_3O_{12}$, or $YCa_4O(BO_3)_3$, 3D devices such as waveguide arrays [37] or complex splitters [39, 118] have been demonstrated (see Fig. 6.6).

However, in other crystals, alternative techniques based on Type-II modifications must be used. Stress-induced waveguides (double-scan technique) are not very convenient for the fabrication of 3D optical devices mainly due to the difficulty to implement even simple splitters with this approach. Planar Y-branch splitters with rectangular depressed-cladding waveguides have been fabricated in surface of Nd:YAG [119] or buried in KTP [120]. For the inscription of true 3D devices, other techniques based on cladding structures have been also proposed. The use of hexagonal optical-lattice-like structures of the laser damage tracks has allowed the fabrication of efficient 3D splitters (1×2, 1×3, 1×4) by introducing certain defects in the lattice structure [62, 68, 121]. Such complex and monolithic structures

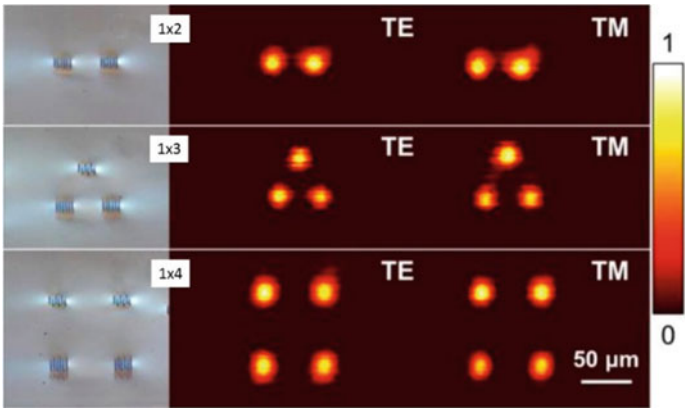

Fig. 6.6 3D splitters based on Type-I modifications produced in $Bi_4Ge_3O_{12}$ operating at 4 µm. Adapted from [37]

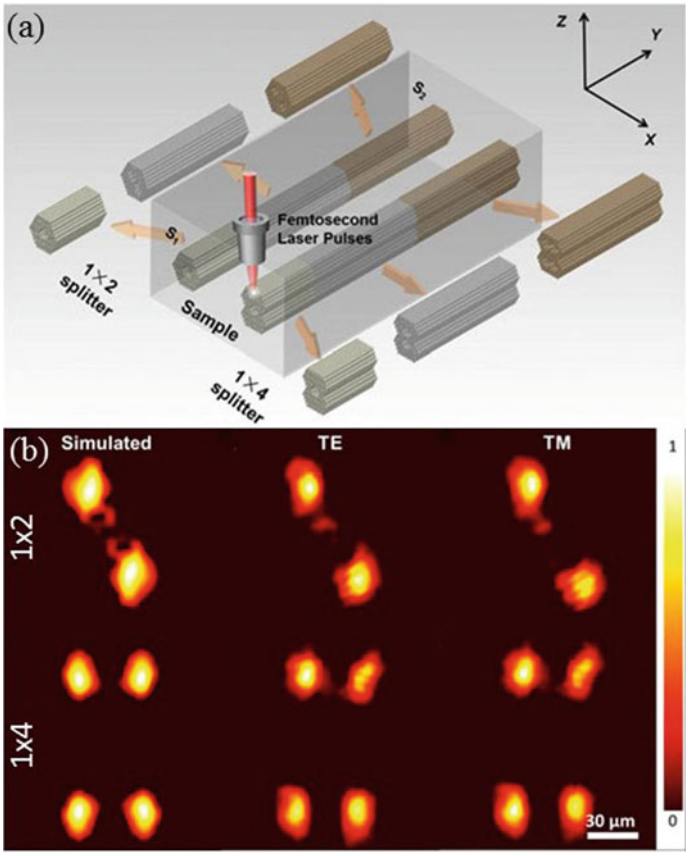

Fig. 6.7 3D splitters inscribed in NdYAG based on cladding hexagonal optical-lattice-like structures (Fig. 6.5d). **a** Schematic of the fabrication technique. **b** Output modes for 1 × 2 and 1 × 4 splitters. Adapted from [121]

(see Fig. 6.7) can be potentially integrated in any transparent dielectric, thus opening the way to arbitrarily complex 3D devices in crystals.

6.5.2 Electrooptic Devices

Electrooptic (EO) modulators are used to modulate the signal parameters (e.g., phase, intensities, and polarizations), which in practice are usually realized in waveguide-based platforms. One of the typical configurations is Mach–Zehnder interferometer (MZI), which was produced in laser-written $LiNbO_3$ waveguides. Liao et al. reported on a MZI waveguide modulator produced by femtosecond laser inscription in a *x*-cut MgO:$LiNbO_3$ wafer [86]. This structure was composed of channel waveguides

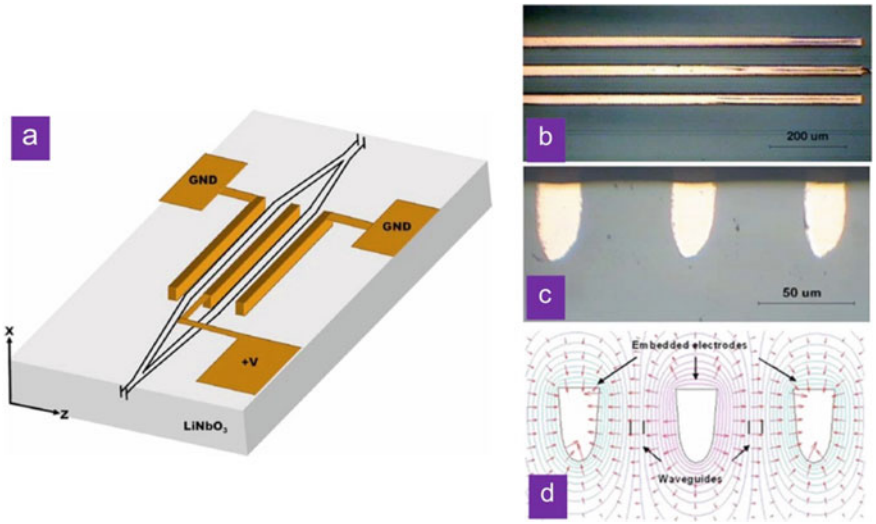

Fig. 6.8 Schematic of the MZI modulator design and cross-sectional views of the waveguides and electrodes [86]

with double-line geometry and embedded microelectrodes subsequently fabricated by femtosecond laser ablation and selective electroless plating. Figure 6.8 shows the schematic of the MZI modulator design and cross-sectional views of the waveguides and electrodes. The EO overlap integral of the MZI modulator was 0.95.

It was interesting to implement monolithic integration of frequency converter and MZ modulator in a single $LiNbO_3$ chip [122]. In this prototype, the electrodes were ablated out of a gold-layer sputtered onto the sample surface. The EO overlap integral of this MZI was 0.16, and the half-wave-voltage of the modulator was 23 V. In addition, tunable EO waveguide Bragg gratings in $LiNbO_3$ waveguides can be produced by femtosecond laser writing. Such waveguide grating was designed and realized for EO tuning at a wavelength around 1550 nm.

6.5.3 Waveguide Lasers and Amplifiers

Waveguide lasers and amplifiers are key gain devices in photonic systems. Waveguide lasers are the miniaturized light sources, which possess low lasing thresholds, comparable efficiencies, and compact geometries, in comparison with the bulk lasers. The substrates of dielectric waveguide lasers include doped glasses (see Sect. 6.4.1), crystals (Sect. 6.4.2) and ceramics (Sect. 6.4.3). By applying direct femtosecond laser writing, active waveguides with various geometries have been fabricated in gain media. In recent years, the research on waveguide lasers has been developed rapidly. Particularly, with laser-written waveguides as the gain cavities, a number

of solid-state waveguide systems for broadband lasing covering wavelength from visible till mid-infrared have been realized.

Visible waveguide lasing at red light wavelength band-based Pr-doped crystals waveguides reaches the output powers of tens of mW [53, 94, 95]. In the near infrared regime, the Ti:sapphire waveguide lasing from 700 to 870 nm was realized, with the maximum output power of 143 mW at 800 nm, and a slope efficiency of 23.5% [98]. Based on laser-written waveguides of Yb:YAG crystal, the recent work has shown the maximum output power to be ~5 W or even higher with the optimization of the optical pump system of waveguide lasers [123]. The slope efficiency of waveguide lasing at 1 μm also reaches high values close to the quantum limit. The reported results on 1.8–2 μm lasing band have been realized in Tm:YAG and Tm:KLuW cladding waveguides, and maximum output power of 93 and 46 mW was achieved, respectively [106, 111]. For typical mid-infrared wavelength regime, by using laser-written waveguides in Cr or Fe-doped ZnSe or ZnS, lasing from 2.5 μm has been realized with maximum output power of 5.1 W [107].

In addition to the continuous-wave waveguide lasing, people have developed Q-switched and mode-locked systems to achieve pulsed waveguide lasers, by using saturable absorbers (such as SESAMs, graphene, MoS_2, carbon nanotubes) [11]. The obtained repetition rate of the Q-switched waveguide lasers reaches MHz, and the maximum output power can be as high as a few watts [124]. The lasing at 2 μm with Q-switched mode-locking based on graphene reaches 7.8 GHz from a Tm:YAG ceramic waveguide [125]. Figure 6.9 shows typical pulsed lasing performance from a laser-written Nd:YVO_4 waveguide based on graphene Q-switching [126].

Another advantage of waveguide lasers over bulk systems is that lasing with tailored beam output can be realized in waveguides. By applying direct optical pump into the 3D waveguide in gain media, lasing generation at 1 μm with beam splitting (e.g., 1 × 2, 1 × 3, and 1 × 4) or ring-shaped transformation has been achieved in laser-written Nd or Yb-doped YAG waveguides [61, 121]. In addition, optical-lattice-like cladding structures based on Nd:YAP crystal is an ideal platform to get lattice-like lasing [117]. The powerful 3D microprocessing ability of direct femtosecond laser writing may offer more intriguing devices for lasing as miniature light sources.

Waveguide amplifiers are key devices in telecommunication systems. The amplification at C-band (centered at 1.55 μm) is of special importance to industries, and Er-doped glass waveguides are typically used as amplifiers, which are called "EDWA" (erbium-doped waveguide amplifier) in the communication systems. Direct femtosecond laser writing has been utilized to manufacture channel waveguides in a few glass families, including Er-doped or Er, Yb-codoped phosphates, oxyfluoride silicates, phospho-tellurites, bismuthates, and chalcogenides, to realize amplification at telecommunication bands [15]. Figure 6.10 shows the fiber-to-fiber net gain spectra under different pump powers in an Er-doped bismuthate glass waveguide for C-band. As pumped of 1050 mW at 980 nm, the amplifier exhibits a peak internal gain per unit length of 2.3 dB/cm at 1533 nm and a peak fiber-to-fiber net gain of 16.0 dB at 1533 nm [127].

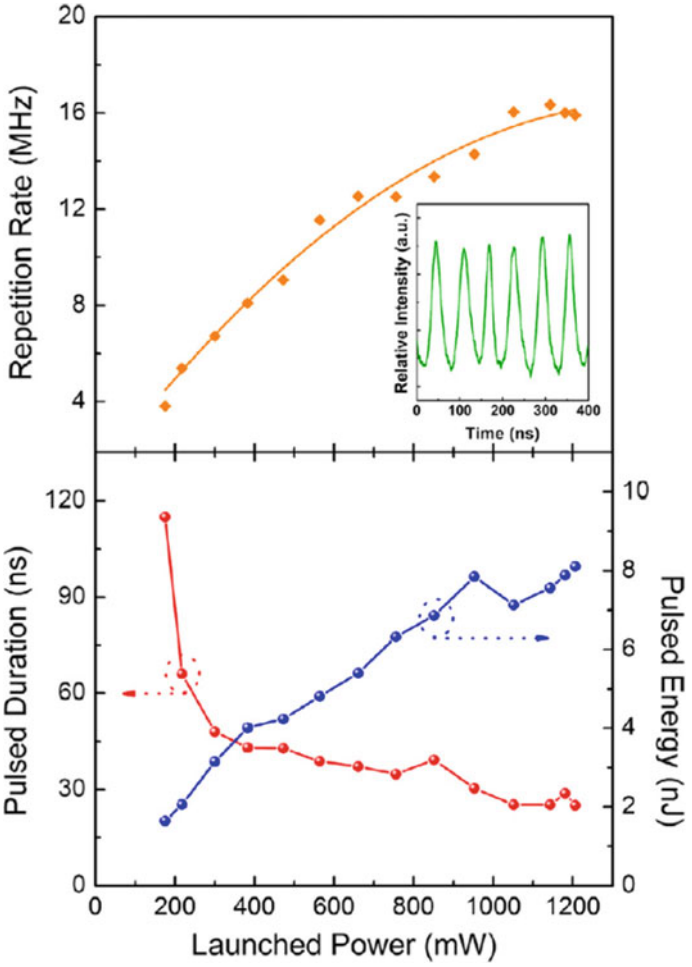

Fig. 6.9 Typical pulsed laser in a laser-written Nd:YVO_4 waveguide based on graphene Q-switching: repetition rate, pulse duration, and pulse energy versus launched pump power. The inset picture shows a typical pulse train [126]

6.5.4 Frequency Converters

Waveguides based on nonlinear crystals could be used to achieve second harmonic generation (SHG) with enhanced efficiencies in comparison with the bulks. The conversion efficiency depends not only on the bulk nonlinear features but also on the guiding properties of the structures. The laser-written waveguides have been used to realize SHG of light at a wavelength regime from ~400 to 790 nm through phase matching (PM) or quasi-phase matching (QPM) configurations. Since waveguides

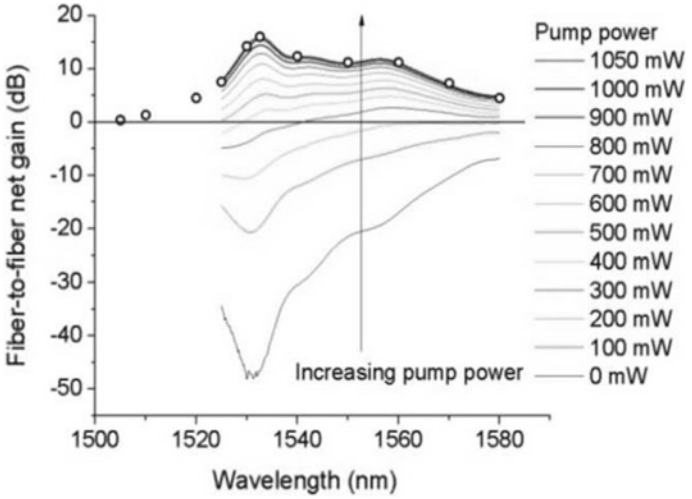

Fig. 6.10 Fiber-to-fiber net gain spectra under different pump powers in an Er-doped bismuthate glass waveguide for C-band [127]

based on Type-I modification (see Sect. 6.3) only support guidance along one polarization, SHG from such structures can only be realized under the QPM mechanism. Double-scan waveguides, and in general other waveguides based on Type-II modification, may support guidance along both orthogonal polarizations, which have been used for frequency doubling based on the PM or the QPM mechanisms.

Under pulsed laser pump, green light has been generated in laser-written waveguides in a few nonlinear crystals or domain-engineered materials, for examples, $LiNbO_3$, PPLN, KTP, PPKTP, and BiBO. The best conversion efficiency (η) reported for the PM SHG was 49% for a double-line $LiNbO_3$ waveguide [23], and highest output SH power (peak values) was 427 W for KTP cladding waveguide [87]. For the QPM SHG, in double-line PPLN waveguides a high value of $\eta = 58\%$ has been achieved, with 59 W output peak power of 532 nm light [91]. For PPKTP, η reached a maximum value as high as 47.4% and a peak power of green light of 252 W was generated [128]. For PPLN Type-I waveguides, the QPM SHG was realized with η of 6.5% W^{-1} cm^{-2}, while Type-I PPKTP waveguides possess η of 0.18% W^{-1} cm^{-2} for the blue light SHG [93]. In addition, Nie et al. reported on the SHG of 532-nm green light from a 3D optical-lattice-like beam splitter. The obtained conversion efficiency for the 3D SHG is even higher than that from the no-splitted channel waveguide [62]. Figure 6.11 shows the comparison of mode profiles of the KTP optical-lattice-like waveguides with 3D 1×4 splitting geometries and straight channels for SHG [62].

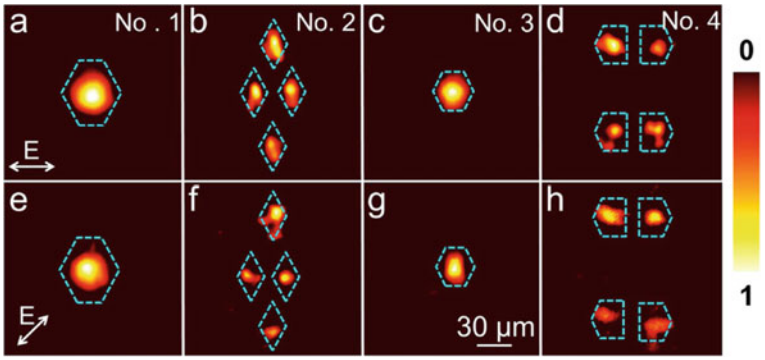

Fig. 6.11 SHG mode of the optical-lattice-like KTP cladding waveguides. Near-field modal profiles of optical-lattice-like cladding waveguides for straight channels and 1 × 4 at **a**–**d** 532 nm and **e**–**h** 1064 nm under 1064 → 532 nm green laser SHG configuration. The inserted arrows are the polarizations [62]

6.5.5 Microfluidic Chips

Lab-on-chip devices usually refer to the microfluidic chips for biological and chemical applications. The integration of optics and fluidics brings out significant development of the chip-scale devices, which is now defined as the term "Optofluidics" [129]. These chips allow the integration of necessary elements, mainly including buried waveguides for guided light probe and microscale channels for fluidics. In such devices, biological or chemical analytic capabilities have been enhanced, enabling promising applications such as nanoparticle trapping and manipulation, cell sorting, and refractive index sensing [129]. Due to the powerful 3D micromachining ability of direct laser writing, it is practical to integrate optical waveguides with 3D geometry into a monolithic chip combining microchannels of fluidics [12, 84]. The first work on this topic was reported by Applegate et al. [130] for cell sorting in a laser-written glass chip. To date, a number of novel designs have been proposed and functional devices have been prototyped and produced, mainly in glass substrates (Sect. 6.4.1). In these devices, the laser-written waveguides can be either straight or specially designed. The main function of the waveguides is to realize photons as light probes or trapping sources. To name a few, in some designs, to achieve refractive index sensing, the light fields in the waveguides are required to have direct interactions with the fluidics, which can be realized by MZI configuration of embedded 3D laser-written waveguides one-arm-crossed the microfluidic channel [115]. In this geometry, the light goes through the two arms with additional phase difference due to the refractive index of guided mode and reference arm, which is promising for highly sensitive chemical sensing (e.g., to detect biochemical molecules). One more recent example on real-time sorting of single cells was using double-Y-shaped microfluidic chip, in which the cell manipulation was realized in the specially designed channels by optical forces exerted through laser radiation emitted from optical waveguides

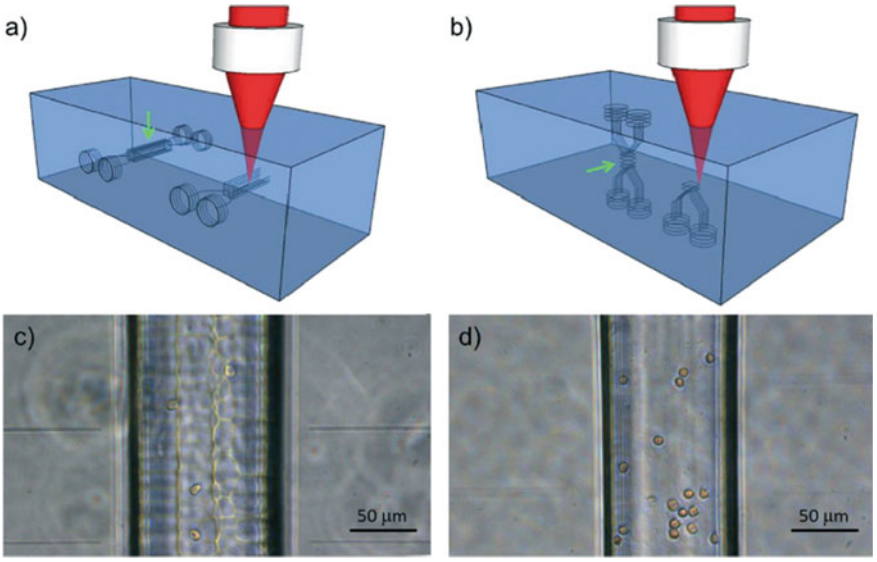

Fig. 6.12 Schematic rendering of the double-Y-shaped microfluidic circuit irradiation patterns and phase-contrast microscopy images of swollen red blood cells in the microchannels fabricated with the transverse and longitudinal writing geometries [131]

[131]. Figure 6.12 shows the schematic rendering of the double-Y-shaped microfluidic circuit irradiation patterns and phase-contrast microscopy images of swollen red blood cells in the microchannels fabricated with the transverse and longitudinal writing geometries [131].

6.5.6 Quantum Circuits

Quantum circuits are ideal platforms for quantum information processing. By applying direct femtosecond laser writing of glass (e.g., fused silica), 3D chip-scale devices containing designed waveguide structures have been fabricated to realize some functions, such as quantum computing and random walk [13]. One of the advantages of laser-written quantum circuits is the good overlap of single-mode fiber and waveguide channels, enabling high coupling efficiency of the devices. In addition, the 3D devices by laser writing utilize the bulk space, which leads to much compact design of the circuits. To date, there have been a number of applications based on laser-written glass waveguide wafers [132, 133]. A *qubit* (quantum bit) is the basic element of quantum information science, which can exist in superposition state of bit "0" and "1". Encoding a qubit by photons can be performed in the quantum chips by polarization or spatial mode encoding. This requires a set of low-loss waveguide channels with sufficient coupling effect of modal profiles,

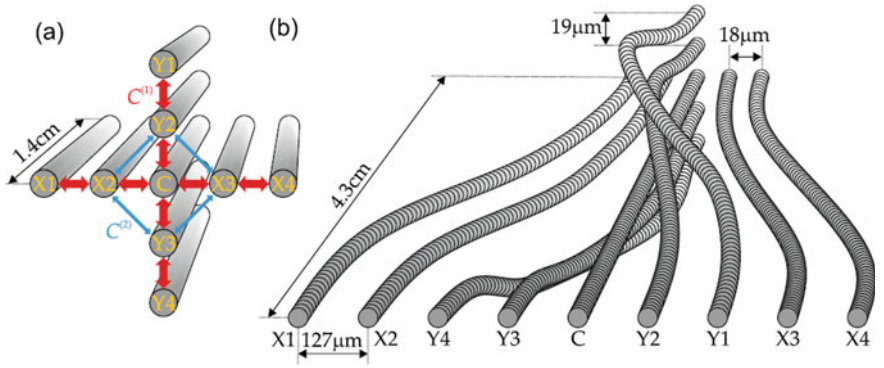

Fig. 6.13 Schematic of **a** laser-written 2D waveguide array and **b** the interface section of waveguide circuit for random walk of correlated photon pairs based on Swiss cross geometry [134]

which can be fabricated by direct laser writing of glasses with relative ease. The basic elements of these quantum circuits include waveguide couplers and waveguide arrays. Figure 6.13 shows a laser-written 2D waveguide array for random walk of correlated photon pairs [134]. The design of the circuit is based on a so-called Swiss cross array, in which different channels have special mode coupling in horizontal or/and vertical planes. In this photonic network, two-photon quantum walks of distinguishable and indistinguishable photon pairs can be realized. In addition, Corrielli et al. used laser-written waveguides in Pr:YSO crystal as platform and demonstrated the implementation of an integrated on-demand spin-wave optical memory, which opens perspectives for integrated quantum memories [135].

6.6 Summary and Outlook

In summary, the development of different strategies for the inscription of optical waveguides in transparent materials by direct femtosecond laser irradiation has allowed the integration of a large number of compact photonic devices in almost any desired transparent dielectric benefitting from its specific physical properties (nonlinear behavior, spectroscopic properties, transparency, and anisotropy). This research field is attracting more and more interest mainly due to the possibility to fabricate 3D photonic circuits and to integrate them in complex devices that combine several functionalities: compact lasers, lab-on-a-chip devices or complex beam shapers are only some examples.

The perspectives for this research field are very promising due to the development of novel femtosecond laser sources with high repetition rates, large pulse energy, and excellent performances, minimizing the fabrication times and allowing the efficient application of several micromachining techniques in a single-step procedure. Among the challenges to face within future, we should mention the necessity to improve

the performance of complex 3D devices in some specific materials, particularly for spectral ranges in the mid-infrared, or the integration of active optical waveguides in novel functional materials.

References

1. W. Sohler, H. Hu, R. Ricken, V. Quiring, C. Vannahme, H. Herrmann, D. Büchter, S. Reza, W. Grundkötter, S. Orlov, H. Suche, R. Nouroozi, Y. Min, Opt. Photon. News **19**, 24 (2008)
2. C. Grivas, Prog. Quant. Electron. **35**, 159 (2011)
3. K.M. Davis, K. Miura, N. Sugimoto, K. Hirao, Opt. Lett. **21**, 1729 (1996)
4. R.R. Gattass, E. Mazur, Nat. Photon. **2**, 219 (2008)
5. M. Ams, G.D. Marshall, P. Dekker, J.A. Piper, M.J. Withford, Laser Photon. Rev. **3**, 535 (2009)
6. F. Chen, J.R. Vazquez de Aldana, Laser Photon. Rev. **8**, 251 (2014)
7. S. Sowa, W. Watanabe, T. Tamaki, J. Nishi, K. Itoh, Opt. Exp. **14**, 291 (2006)
8. S. Nolte, M. Will, J. Burghoff, A. Tünnermann, Appl. Phys. A **77**, 109 (2003)
9. R. Osellame, G. Cerullo, R. Ramponi, *Femtosecond Laser Micromachining: Photonic and Microfluidic Devices in Transparent Materials* (Springer, Berlin, 2012)
10. S.M. Eaton, W. Chen, L. Zhang, H. Zhang, R. Iyer, J.S. Aitchison, P.R. Herman, I.E.E.E. Photon, Technol. Lett. **18**, 2174 (2006)
11. C. Grivas, Prog. Quant. Electron. **45–46**, 3 (2016)
12. K. Sugioka, Y. Cheng, Light Sci. Appl. **3**, e149 (2014)
13. T. Meany, M. Grafe, R. Heilmann, A. Perez-Leija, S. Gross, M.J. Steel, M.J. Withford, A. Szameit, Laser Photon. Rev. **9**, 363 (2015)
14. T.A. Birks, I. Gris-Sánchez, S. Yerolatsitis, S.G. Leon-Saval, R.R. Thomson, Adv. Opt. Photon. **7**, 107 (2015)
15. D. Choudhury, J.R. Macdonald, A.K. Kar, Laser Photon. Rev. **8**, 827 (2014)
16. M. Protopapas, Ch. Keitel, P. Knight, Rep. Prog. Phys. **60**, 389 (1997)
17. B. Stuart, M. Feit, S. Herman, A. Rubenchik, B. Shore, M. Perry, Phys. Rev. B **53**, 1749 (1996)
18. E. Gamaly, A. Rode, B. Luther-Davies, V. Tikhonchuk, Phys. Plasmas **9**, 949 (2002)
19. L. Sudrie, A. Couairon, M. Franco, B. Lamouroux, B. Prade, S. Tzortzakis, A. Mysyrowicz, Phys. Rev. Lett. **89**, 186601 (2002)
20. L. Sudrie, M. Franco, B. Prade, A. Mysyrowicz, Opt. Commun. **191**, 333 (2001)
21. J. Chan, T. Huser, S. Risbud, D. Krol, Opt. Lett. **26**, 1726 (2001)
22. J. L. Archambault, L. Reekie, P.S.J. Russel, Electron. Lett. **29**, 453 (1993)
23. J. Burgnoff, Ch. Grebing, S. Nolte, A. Tünnermann, Appl. Phys. Lett. **89**, 081108 (2006)
24. V. Apotolopoulos, L. Laversenne, T. Colomb, C. Depeursinge, R. Salathe, M. Pollnau, R. Osellame, G. Cerullo, P. Laporta, Appl. Phys. Lett. **85**, 1122 (2004)
25. E.N. Glezer, E. Mazur, Appl. Phys. Lett. **71**, 882 (1997)
26. R. Stoian, K. Mishchik, G. Cheng, C. Mauclair, C. D'Amico, J.P. Colombier, M. Zamfirescu, Opt. Mater. Exp. **3**, 1755 (2013)
27. T. Gorelik, M. Will, S. Nolte, A. Tuennermann, U. Glatzel, Appl. Phys. A **76**, 309 (2003)
28. S. Juodkazis, K. Nishimura, S. Tanaka, H. Misawa, E. Gamaly, B. Luther-Davies, L. Hallo, P. Nicolai, V. Tikhonchuk, Phys. Rev. Lett. **96**, 166101 (2016)
29. J. Burghoff, S. Nolte, A. Tünnermann, Appl. Phys. A **89**, 127 (2007)
30. B. McMillen, K. Chen, D. Jaque, Appl. Phys. Lett. **94**, 081106 (2009)
31. N. Nguyen, A. Saliminia, S. Chin, R. Vallée, Appl. Phys. B **85**, 145 (2006)
32. S. Eaton, H. Zhang, P. Herman, F. Yoshino, L. Shah, J. Bovatsek, A. Arai, Opt. Exp. **13**, 4708 (2005)

33. C. Schaffer, J. García, E. Mazur, Appl. Phys. A **76**, 351 (2003)
34. S. Juodkazis, H. Misawa, I. Maksimov, Appl. Phys. Lett. **85**, 5239 (2004)
35. A.H. Nejadmalayeri, P.R. Herman, Opt. Exp. **15**, 10842 (2007)
36. A. Benayas, W.F. Silva, A. Ródenas, C. Jacinto, J. Vázquez de Aldana, F. Chen, Y. Tan, R.R. Thomsom, N.D. Psaila, D.T. Reid, G.A. Torchia, A.K. Kar, D. Jaque, Appl. Phys. A **104**, 301 (2011)
37. A. Ródenas, A. Kar, Opt. Exp. **19**, 17820 (2011)
38. J.R. Macdonald, R.R. Thomson, S.J. Beecher, N.D. Psaila, H.T. Bookey, A.K. Kar, Opt. Lett. **35**, 4036 (2010)
39. R. He, I. Hernandez-Palmero, C. Romero, J.R. Vázquez de Aldana, F. Chen, Opt. Exp. **22**, 31293 (2014)
40. Y. Nasu, M. Kohtoku, Y. Hibino, Opt. Lett. **30**, 723 (2005)
41. R. Osellame, M. Lobino, N. Chiodo, M. Marangoni, G. Cerullo, Appl. Phys. Lett. **90**, 241107 (2007)
42. Th. Pertsch, U. Peschel, F. Lederer, J. Burghoff, M. Will, S. Nolte, A. Tünnermann, Opt. Lett. **29**, 458 (2004)
43. G. Cheng, C. D'Amico, X. Liu, R. Stoian, Opt. Lett. **38**, 1924 (2013)
44. R. Thomson, T. Birks, S. Leon-Saval, A. Kar, J. Bland-Hawthorn, Opt. Exp. **19**, 5698 (2011)
45. K. Suzuki, V. Sharma, J. Fujimoto, E. Ippen, Opt. Exp. **14**, 2335 (2005)
46. J. Hu, C. Menyuk, Adv. Opt. Photon. **1**, 58 (2009)
47. D. Lancaster, S. Gross, A. Fuerbach, H. Edendorff, T. Monro, M. Withford, Opt. Exp. **20**, 27503 (2012)
48. J. Siebenmorgen, K. Petermann, G. Huber, K. Rademaker, S. Nolte, A. Tunnermann, Appl. Phys. B **97**, 251 (2009)
49. A. Rodenas, G. Torchia, G. Lifante, E. Cantelar, J. Lamela, F. Jaque, L. Roso, Appl. Phys. B **95**, 85 (2009)
50. C. Zhang, N. Dong, J. Yang, F. Chen, J.R. Vázquez de Aldana, Q. Lu, Opt. Exp. **19**, 2503 (2011)
51. G. Torchia, A. Rodenas, A. Benayas, E. Cantelar, L. Roso, D. Jaque, Appl. Phys. Lett. **92**, 111103 (2008)
52. A. Benayas, W. Silva, C. Jacinto, E. Cantelar, J. Lamela, F. Jaque, J.R. Vázquez de Aldana, G. Torchia, L. Roso, A. Kaminskii, D. Jaque, Opt. Lett. **35**, 330 (2010)
53. S. Müller, T. Calmano, P. Metz, N. Hansen, C. Kränkel, G. Huber, Opt. Lett. **37**, 5223 (2012)
54. S.J. Beecher, R.R. Thomson, D.T. Reid, N.D. Psaila, M. Ebrahim-Zadeh, A.K. Kar, Opt. Lett. **36**, 4548 (2011)
55. A.G. Okhrimchuk, A.V. Shestakov, I. Khrushchev, J. Mitchell, Opt. Lett. **37**, 2248 (2005)
56. H. Liu, Y. Jia, J.R. Vázquez de Aldana, D. Jaque, F. Chen, Opt. Exp. **20**, 18620 (2012)
57. Y. Jia, F. Chen, J.R. Vázquez de Aldana, Opt. Exp. **20**, 16801 (2012)
58. Q. An, Y. Ren, Y. Jia, J.R. Vázquez de Aldana, F. Chen, Opt. Mater. Exp. **3**, 466 (2013)
59. H. Nguyen, A. Ródenas, J.R. Vázquez de Aldana, J. Martínez, F. Chen, M. Aguiló, M. Pujol, F. Diaz, Opt. Exp. **24**, 7777 (2016)
60. H. Liu, F. Chen, J.R. Vázquez de Aldana, D. Jaque, Opt. Lett. **38**, 3294 (2013)
61. Y. Jia, Ch. Cheng, J.R. Vázquez de Aldana, G. Castillo, B. del Rosal, Y. Tan, D. Jaque, F. Chen, Sci. Rep. **4**, 5988 (2014)
62. W. Nie, Y. Jia, J.R. Vázquez de Aldana, F. Chen, Sci. Rep. **6**, 22310 (2016)
63. H. Liu, Ch. Cheng, C. Romero, J.R. Vazquez de Aldana, F. Chen, Opt. Exp. **23**, 9730 (2015)
64. S. Harilal, J. Freeman, P. Diwakar, A. Hassanein, Femtosecond laser ablation: fundamentals and applications, in Laser-induced breakdown spectroscopy, Ed. by S. Murazzi, U. Perini (Springer, Berlin, 2014)
65. G. Dumitru, V. Romano, H. Weber, M. Sentis, W. Marine, Appl. Phys. A **74**, 729 (2002)
66. B. Chichkov, C. Momma, S. Nolte, F. Alvensleben, A. Tunnermann, Appl. Phys. A **63**, 109 (1996)
67. R. Degl'Innocenti, S. Reidt, A. Guarino, D. Rezzonico, G. Poberaj, P. Günter, J. Appl. Phys. **100**, 113121 (2006)

68. Y. Jia, Y. Tan, Ch. Cheng, J.R. Vázquez de Aldana, F. Chen, Opt. Exp. **22**, 12900 (2014)
69. G. Liu, R. He, Sh. Akhmadaliev, J.R. Vázquez de Aldana, Sh. Zhou, F. Chen, Nucl. Intrum. Meth. Phys. Res. B **325**, 43 (2014)
70. Y. Kondo, J. Qiu, T. Mitsuyu, K. Hirao, T. Yoko, Jpn. J. Appl. Phys. **38**, L1146 (1999)
71. J. Martínez, A. Ródenas, T. Fernández, J.R. Vázquez de Aldana, R. Thomson, M. Aguiló, A. Kar, J. Solís, F. Díaz, Opt. Lett. **40**, 5818 (2015)
72. D. Homoelle, S. Wielandy, A. Gaeta, N. Borrelli, C. Smith, Opt. Lett. **24**, 1311 (1999)
73. J.R. Liu, Z.Y. Zhang, S.D. Chang, C. Flueraru, C.P. Grover, Opt. Commun. **253**, 315 (2005)
74. S. Nolte, M. Will, J. Burghoff, A. Tuennermann, Appl. Phys. A **77**, 109 (2003)
75. W. Watanabe, T. Asano, K. Yamada, K. Itoh, J. Nishii, Opt. Lett. **28**, 2491 (2003)
76. Th. Pertsch, U. Peschel, F. Lederer, J. Burghoff, M. Will, S. Nolte, A. Tünnermann, Opt. Lett. **29**, 468 (2004)
77. R. Thomson, H. Bookey, N. Psaila, A. Fender, S. Campbell, W. MacPherson, J. Barton, T. Reid, A. Kar, Opt. Express **15**, 11691 (2007)
78. Y. Sikorski, A.A. Said, P. Bado, R. Maynard, C. Florea, K.A. Winick, Electron. Lett. **36**, 226 (2000)
79. S. Gross, M. Alberich, A. Arriola, M. Withford, A. Fuerbach, Opt. Lett. **38**, 1872 (2013)
80. R. Osellame, S. Taccheo, G. Cerullo, M. Marangoni, D. Polli, R. Ramponi, P. Laporta, S. De Silvestri, Electron. Lett. **38**, 964 (2002)
81. S. Taccheo, G. Della Valle, R. Osellame, G. Cerullo, N. Chiodo, P. Laporta, O. Svelto, A. Killi, U. Morgner, M. Lederer, D. Kopf, Opt. Lett. **29**, 2626 (2004)
82. G. Cerullo, R. Osellame, S. Taccheo, M. Marangoni, D. Polli, R. Ramponi, P. Laporta, S. De Silvestri, Opt. Lett. **27**, 1938 (2002)
83. V. Bhardwaj et al., J. Appl. Phys. **97**, 083102 (2005)
84. K. Sugioka, Y. Cheng, Lab Chip **12**, 3576 (2012)
85. D. Lancaster, S. Gross, H. Ebendorff-Heidepriem, K. Kuan, T. Monro, M. Ams, A. Fuerbach, M. Withford, Opt. Lett. **36**, 1587 (2011)
86. Y. Liao, J. Xu, Y. Cheng, Z. Zhou, F. He, H. Sun, J. Song, X. Wang, Z. Xu, K. Sugioka, K. Midorikawa, Opt. Lett. **33**, 2281 (2008)
87. N. Dong, F. Chen, J.R. Vázquez de Aldana, Phys. Status Solidi RRL **6**, 306 (2012)
88. Y. Jia, J.R. Vázquez de Aldana, C. Romero, Y. Ren, Q. Lu, F. Chen, Appl. Phys. Exp. **5**, 072701 (2012)
89. L.L. Huang, P. Salter, M. Karpinski, B. Smith, F. Payne, M. Booth, Appl. Phys. A **118**, 831 (2015)
90. S. Zhang, J. Yao, Q. Shi, Y. Liu, W. Liu, Appl. Phys. Lett. **92**, 231106 (2008)
91. J. Thomas, M. Heinrich, J. Burghoff, S. Nolte, A. Ancona, Appl. Phys. Lett. **91**, 151108 (2007)
92. S. Kroesen, K. Tekce, J. Imbrock, C. Denz, Appl. Phys. Lett. **107**, 101109 (2015)
93. S. Campbell, R.R. Thomson, D.P. Hand, A.K. Kar, D.T. Reid, C. Canalias, V. Pasiskevicius, F. Laurell, Opt. Exp. **15**, 17146 (2007)
94. T. Calmano, J. Siebenmorgen, F. Reichert, M. Fechner, A. Paschke, N. Hansen, K. Petermann, G. Huber, Opt. Lett. **36**, 4620 (2011)
95. T. Calmano, A. Sottile, P. W. Metz, D. Parisi, C. Kränkel, M. Tonelli, G. Huber, Advanced Solid State Lasers Conference 2015, paper AW1A.5
96. N. Dong, J. Martínez de Mendivil, E. Cantelar, G. Lifante, J. Vázquez de Aldana, G.A. Torchia, F. Chen, D. Jaque, Appl. Phys. Lett. **98**, 181103 (2011)
97. Y. Ren, J.R. Vázquez de Aldana, F. Chen, Opt. Express **21**, 11562 (2013)
98. C. Grivas, C. Corbari, G. Brambilla, P.G. Lagoudakis, Opt. Lett. **37**, 4630 (2012)
99. T. Calmano, J. Siebenmorgen, O. Hellmig, K. Petermann, G. Huber, Appl. Phys. B **100**, 131 (2010)
100. T. Calmano, J. Siebenmorgen, A. Paschke, C. Fiebig, K. Paschke, G. Erbert, K. Petermann, G. Huber, Opt. Mater. Exp. **1**, 428 (2011)
101. H. Liu, Y. Tan, J.R. Vázquez de Aldana, F. Chen, Opt. Lett. **39**, 4553 (2014)
102. Y. Ren, J.R. Vázquez de Aldana, F. Chen, H. Zhang, Opt. Exp. **21**, 6503 (2013)
103. X. Liu, S. Qu, Y. Tan, F. Chen, Appl. Opt. **50**, 930 (2011)

104. F.M. Bain, A.A. Lagatsky, R.R. Thomson, N.D. Psaila, N.V. Kuleshov, A.K. Kar, W. Sibbett, C.T.A. Brown, Opt. Exp. **17**, 22417 (2009)
105. Y. Tan, J.R. Vázquez de Aldana, F. Chen, Opt. Eng. **53**, 107109 (2014)
106. E. Kifle, X. Mateos, J.R. Vázquez de Aldana, A. Ródenas, P. Loiko, S.Y. Choi, F. Rotermund, U. Griebner, V. Petrov, M. Aguiló, F. Díaz, Opt. Lett. **42**, 1169 (2017)
107. S.A. McDaniel, A. Lancaster, J.W. Evans, A.K. Kar, G. Cook, Opt. Exp. **24**, 3502 (2016)
108. A. Lancaster, G. Cook, S.A. McDaniel, J. Evans, P.A. Berry, J.D. Shephard, A.K. Kar, Appl. Phys. Lett. **107**, 031108 (2015)
109. N. Dong, Y. Yao, F. Chen, J.R. Vazquez de Aldana, Phys. Status Solidi RRL **5**, 184 (2011)
110. A. Ródenas, A. Benayas, J.R. Macdonald, J. Zhang, D.Y. Tang, D. Jaque, A.K. Kar, Opt. Lett. **36**, 3395 (2011)
111. Y. Ren, G. Brown, A. Ródenas, S. Beecher, F. Chen, A.K. Kar, Opt. Lett. **37**, 3339 (2012)
112. A. Vogel, J. Noack, G. Huttman, G. Paltauf, Appl. Phys. B **81**, 1015 (2005)
113. K. Sugioka, Y. Cheng, Appl. Phys. Rev. **1**, 041303 (2014)
114. R. Osellame, V. Maselli, R. Martínez Vázquez, R. Ramponi, G. Cerullo, Appl. Phys. Lett. **90**, 231118 (2007)
115. A. Crespi, Y. Gu, B. Ngamsom, H. Hoekstra, Ch. Dongre, M. Pollnau, R. Ramponi, H. van den Vlekkert, P. Watts, G. Cerullo, R. Osellame, Lab Chip **10**, 1167 (2010)
116. A. Ródenas, G. Martin, B. Arezki, N. Psaila, G. Jose, A. Jha, L. Labadie, P. Kern, A. Kar, R. Thomson, Opt. Lett. **37**, 392 (2012)
117. W. Nie, R. He, Ch. Cheng, U. Rocha, J.R. Vázquez de Aldana, D. Jaque, F. Chen, Opt. Lett. **41**, 2169 (2016)
118. J. Lv, Y. Cheng, W. Yuang, X. Hao, F. Chen, Opt. Mater. Exp. **5**, 1274 (2015)
119. H. Liu, Ch. Cheng, C. Romero, J.R. Vázquez de Aldana, F. Chen, Opt. Exp. **23**, 9730 (2015)
120. M. Butt, H. Nguyen, A. Ródenas, C. Romero, P. Moreno, J.R. Vázquez de Aldana, M. Aguiló, R. Solé, M. Pujol, F. Díaz, Opt. Exp. **23**, 15343 (2015)
121. Y. Jia, Ch. Cheng, J.R. Vázquez de Aldana, F. Chen, J. Lightwave Technol. **34**, 1328 (2016)
122. S. Ringleb, K. Rademaker, S. Nolte, A. Tünnermann, Appl. Phys. B **102**, 59 (2011)
123. T. Calmano, S. Müller, IEEE J. Sel. Top. Quantum Electron. **21**, 401 (2015)
124. S. Hakobyan, V.J. Wittwer, K. Hasse, C. Kränkel, T. Südmeyer, T. Calmano, Opt. Lett. **41**, 4715 (2016)
125. Y. Ren, G. Brown, R. Mary, G. Demetriou, D. Popa, F. Torrisi, A.C. Ferrari, F. Chen, A.K. Kar, IEEE J. Sel. Top. Quantum Electron. **21**, 1602106 (2015)
126. R. He, J.R. Vázquez de Aldana, F. Chen, Opt. Mater. **46**, 414 (2015)
127. R.R. Thomson, N.D. Psaila, S.J. Beecher, A.K. Kar, Opt. Exp. **18**, 13212 (2010)
128. S. Zhang, J. Yao, W. Liu, Z. Huang, F. Lu, Electron. Lett. **46**, 1290 (2010)
129. X. Fan, I.M. White, Nat. Photon. **5**, 591 (2011)
130. R.W. Applegate, J. Squier, T. Vested, J. Oakey, D.W.M. Marr, P. Bado, M.A. Dugan, A.A. Said, Lab Chip **6**, 422 (2006)
131. T. Yang, P. Paiè, G. Nava, F. Bragheri, R. Martinez Vazquez, P. Minzioni, M. Veglione, M. Di Tano, C. Mondello, R. Osellamebc, I. Cristiania, Lab Chip **15**, 1262 (2015)
132. R.J. Chapman, M. Santandrea, Z. Huang, G. Corrielli, A. Crespi, M.-H. Yung, R. Osellame, A. Peruzzo, Nat. Commun. **7**, 11339 (2016)
133. A. Crespi, R. Ramponi, R. Osellame, L. Sansoni, I. Bongioanni, F. Sciarrino, G. Vallone, P. Mataloni, Nat. Commun. **2**, 566 (2011)
134. K. Poulios, R. Keil, D. Fry, A. Meinecke, D. Jasmin, F. Matthews, C. Jonathan, A. Politi, M. Lobino, M. Grafe, M. Heinrich, S. Nolte, A. Szameit, J.L. O'Brien, Phys. Rev. Lett. **112**, 143604 (2014)
135. G. Corrielli, A. Seri, M. Mazzera, R. Osellame, H. de Riedmatten, Phys. Rev. Appl. **5**, 054013 (2016)

Chapter 7
Micro-hole Arrays and Net-like Structure Fabrication via Femtosecond Laser Pulses

Guoying Feng, Guang Li, Zhuping Wang, and Yao Xiao

Abstract Femtosecond lasers are widely used in the fields of ultra-precision processing, microelectronic device manufacturing, medical, high-density information storage and recording, which are characterized by a small thermal effect and unique processing of transparent dielectric materials. In this chapter, we first theoretically analyzed the micromachining mechanism of dielectronic materials with femtosecond laser pulses. After reviewing the laser direct fabricating of micro-hole arrays on fused silica sheet, we focus on the latest progress of microchannels fabrication by femtosecond laser. We further discuss 3D microchannel structures to highlight the unique manufacturing using ultrafast laser.

7.1 Introduction

Femtosecond lasers can quickly and accurately focus energy into an area to be processed, while also quickly realize micro/nano-processing in the semiconductor, glass, metal, polymer, ceramics, plastics, resins, and other materials [1]. Lasers of this kind have been widely used in micro/nano-drilling, three-dimensional microchannel, waveguide, optical grating, optical memory, optical sensors, biotechnology, chemical technology, and medical applications as well as other fields. Compared with conventional processing methods, femtosecond laser micro/nanofabrication has the following advantages:

1. It has a very small heat-affected zone [2, 3], so a fine "cold" process can be achieved [4]. Due to the ultrashort timescale and the ultrahigh laser intensity coupled to the electron system, the electrons reach a very high temperature in a very short period of time before the electrons transfer energy to the lattice, but the material relaxation time (heat transfer between the electrons and the lattice) is far greater than the pulse duration of a femtosecond laser, which means that the

G. Feng (✉) · G. Li · Z. Wang · Y. Xiao
Institute of Laser and Micro/Nano-Engineering, College of Electronics and Information Engineering, Sichuan University, No. 24 South Section, 1 Yihuan Road, Cheng'du 610064, China
e-mail: guoing_feng@scu.edu.cn

A. Hu (ed.), *Laser Micro-Nano-Manufacturing and 3D Microprinting*, Springer Series in Materials Science 309, https://doi.org/10.1007/978-3-030-59313-1_7

matter in processed areas is still in a cold state during the femtosecond laser micromachining. Compared with long-pulse laser micromachining, the femtosecond laser has a small energy diffusion depth and reduced (but unavoidable) thermal effect during micromachining, which makes the machining accuracy higher and the processing edge relatively finer, so that it has realized "the cold" processing.
2. It can process a wide range of machinable materials, from metal or nonmetal to a biological cell. The high intensity femtosecond laser not only contributes linear absorption to the material matrix but also a strong nonlinear absorption. Thus, femtosecond lasers can be applied to both the interior and surface of many metals, dielectrics, semiconductors, and biological tissues in an effort to achieve material removal or processing.
3. Applications in real three-dimensional processing are achievable because the laser power density in the laser focus region is extremely high, while the laser power density in the unfocused region is not significant enough to cause material damage. Therefore, precise spatial localization can be achieved by adjusting the spatial orientation of the femtosecond laser. At the same time, the laser intensity at the focal point can reach a higher level relative to the light intensity at the non-focal point which is insufficient to cause ionization and multiphoton absorption. Therefore, femtosecond laser can achieve high-precision three-dimensional machining by focusing laser pulse inside of the transparent material.
4. The processing scale is smaller than the focal spot, achieving micro/nanofabrication. Femtosecond laser light intensity distribution is generally Gaussian type. The area processed by focused fs laser pulses is far smaller than the size of the spot. The processing size breaks through optical diffraction limit, which can achieve real sub-micron or even nano-scale processing, such as nano-cattle, gears, and micro-chain rotation [5].

The technology used in femtosecond laser micro-processing is mainly femtosecond laser direct writing (FLDW), projection preparation, and interference. Among them, FLDW technology is flexible and has a high degree of freedom which is widely used in a variety of point scanning, line scanning. The projection technique can be used to process any two-dimensional shapes on the surface of the material. In addition, interference can be harnessed in creating periodic three-dimensional structures, specifically, by multi-beam interference.

7.2 Theoretical Analysis of Femtosecond Pulse-Laser Micromachining

Femtosecond lasers have a high peak power and ultrashort pulse width which exhibits strong nonlinear effects during matter interaction. Thus, a large variety of materials can be processed by femtosecond lasers. However, the mechanisms of femtosecond laser interaction with various semiconductors, metals, ceramics, resins, as well as others do vary from material to material. The materials that can be processed by

femtosecond lasers can be separated into two categories: (1) metal materials (2) and non-metallic materials. Metal materials have good thermal and electric conductivity because of the existence of a large number of free electrons within the material, and metal materials have absorption characteristics for near-infrared and visible light, while transparent materials and semiconductors do not absorb these two bands of light. However, it will be a metal similar absorption material due to multi-photon ionization when femtosecond laser power density reaches a certain extent.

7.2.1 Interaction Principle Between Femtosecond Laser and Metallic Materials

Most of the metal materials are opaque to visible light. When the laser initially interacts with the metal, the energy is deposited at a penetration depth of $l_s = 1/\alpha$ (α is the absorption coefficient) [6]. Then the laser energy gradually spreads to the depth of $l_d = \sqrt{D\tau}$ (D is the thermal diffusion coefficient, and τ is the laser pulse width) during the process. If the material is processed by a long-pulse laser ($l_d > l_s$), the thermal diffusion effect is very obvious; however, when processed by an ultrashort pulse laser ($l_d < l_s$), the laser energy is unable to spread quickly which causes material directly evaporation around the focus. The laser heat-affected zone is very small during the process, allowing high-precision machining.

When there is a strong laser interaction with metal materials, the free electrons in the metal are all heated instantaneously. The high-temperature electrons transfer their energy to low-temperature particles via collision. The energy transfer time between electrons is in the order of 100 fs, during which time the high-temperature electrons can transfer energy to the non-laser affected region. Relaxation time (the collision heating time between electron and lattice) of the metal is in the order of picoseconds. The relaxation time of a metal material with strong electron–phonon coupling (e.g., Fe) is one to two orders shorter than that of metal with a weak electron–phonon coupling. However, the pulse width of a femtosecond laser is much smaller than the relaxation time, so there is not enough time to heat up the metal lattice during the process. Electrons are instantly heated up to high temperature, causing the electron and lattice to exist at different temperatures. So, a two-temperature model is used to replace the classical thermodynamic model in solving the changes of temperature in ion T_i and electron T_e during the process [7, 8],

$$C_e(T_e)\frac{\partial T_e}{\partial t} = K\nabla^2 T_e - g(T_e - T_i) + A(r,t) \tag{1}$$

$$C_i\frac{\partial T_i}{\partial t} = g(T_e - T_i) \tag{2}$$

where C_e and C_i are the specific heat capacity (per volume) of lattices and electrons, respectively, K is thermal conductivity, $A(r, t)$ is the corresponding heat source of laser pulse, and g is the electron and phonon coupling constant.

The main differences between long-pulse-laser and ultrashort-pulse-laser processing of metal materials are as follows: The thermal effect time of long-pulse-laser interaction with matter is determined by the laser pulse width, but the thermal effect time of ultrashort-pulse-laser interaction with matter depends on the relaxation time of the material. The electron temperature reaches extremely high temperatures during ultrashort-pulse-laser interaction, while the ion temperature is delayed. So, the interaction between femtosecond lasers and the material is "cold." The lattice temperature will still rise after the laser pulse has stopped. Laser thermal effects can be appropriately reduced but unable to be avoided by using ultrashort laser pulse interaction for micromachining. The main reasons that affect the precision of femtosecond laser micromachining include the melting of the material caused by lattice heating, the thermal infiltration caused by electron interaction, and the accumulation of molten material.

It should be noted that the dual-temperature model does not take into account the material nonlinear absorption effect; therefore, the dual-temperature model is only applicable to metal materials.

7.2.2 The Interaction of an Intense Femtosecond Laser Pulse with Dielectric Materials

7.2.2.1 Ionization Mechanism

The interaction between the laser and the solid matter is the stimulated process of valence electrons reaching their excited state by absorbing photons. The generation of stimulated processes can be single-photon resonance transitions, two-photon and high-order multi-photon transitions, tunnel ionization, and so on. The single-photon resonant transitions obey Beer's law, a linear process, while the others are nonlinear processes which are closely related to the intensity of the laser beam. Avalanche ionization and photoionization are the main reasons for the generation of free electrons, but their dominance in dielectric processing remains unclear.

1. Avalanche ionization process
   Avalanche ionization is a phenomenon in which free-charge carriers absorb laser energy after impact ionization occurs in the material. A small number of free electrons in the medium are used as seed electrons to absorb the laser photon energy and enhance their kinetic energy through inverse bremsstrahlung absorption. When the kinetic energy is larger than that of bound electrons, the electrons collide with the valence band electrons, causing the valence electrons to be excited to the conduction band, becoming free electrons and leading to the formation of an additional free electron. Thus, a seeded electron with higher

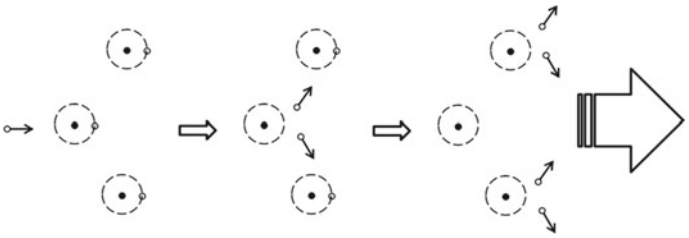

Fig. 7.1 Schematic of avalanche ionization

kinetic energy produces two free electrons with lower kinetic energy. At high laser power, the free electrons with lower kinetic energies continue to absorb the laser energy and become free electrons with higher kinetic energy. Thus, the electrons act as the new seeds and continue to collide with other valence electrons, producing more conduction band electrons. If the laser energy is continuously input, the above process will continue to cycle. The electron numbers in conduction band increase exponentially and show an "avalanche" of growth, which is called avalanche ionization process. When the free electron density generated via avalanche ionization reaches a critical value, the transparent dielectric rapidly absorbs the laser energy, eventually leading to the burning of the material. The process is shown in Fig. 7.1.

2. Photoionization process
   Photoionization refers to the process of direct ionization of a dielectric by a laser field. Photoionization in accordance with the laser frequency and intensity can be divided into multi-photon ionization and tunnel ionization. Transparent dielectrics typically have a broad bandgap, an energy transition that unable to be achieved by single-photon resonance linear absorption, and low-intensity lasers do not produce ablation. However, when the femtosecond laser with high peak energy density processes the dielectric, the bound electrons absorb the energy of multiple incident photons at the same time, and its kinetic energy, therefore, exceeds the bandgap of the dielectric and becomes a free electron. The process is called multi-photon ionization, as shown in Fig. 7.2. In addition, under the conditions of a strong laser field, the bound electrons can cross the barrier of the Coulomb field and become free electrons. This process is called tunneling ionization.

The dominance of multi-photon ionization and tunnel ionization can be determined by the Keldysh parameter γ, which is calculated as follows:

$$\gamma = \frac{\omega\sqrt{m\Delta}}{eE} \tag{3}$$

where ω is the laser frequency, m and e are the electron mass and charge, respectively, and Δ is the bandgap of SiO_2. When values γ is larger than 1.5, multi-photon

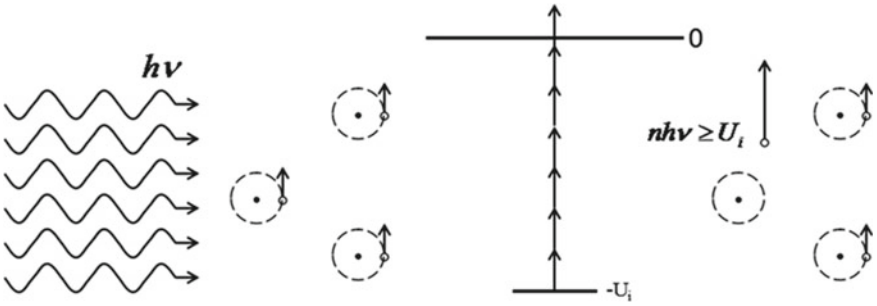

Fig. 7.2 Schematic of multi-photon ionization

ionization has dominated; on the contrary, tunnel ionization dominated; when γ *is* about 1.5, the two processes exist.

7.2.2.2 Material Removal Mechanism

Due to the extremely high peak power density of a femtosecond laser, the material removal mechanism is different from that of a long-pulse laser. At present, there are different views on the mechanism, and two main mechanisms are discussed: (1) electron–phonon collision causing the local temperature to rise above the vaporization temperature removing the material, (2) and Coulomb explosion, when the femtosecond laser is interacting with the dielectric, the extremely high peak power density will cause the electrons to escape from the surface area of the material. When the electrostatic force in the material is larger than the force between the lattices, the chemical bond will be broken and cause damage to the lattice, effectively removing the material, and this mechanism is the Coulomb explosion.

In the process of removing dielectric material via femtosecond laser interaction, it is not yet clear whether the dominant factor of the free electron generation is multi-photon ionization or avalanche ionization. Early studies suggest that multi-photon ionization provides seed electrons for avalanche ionization, and avalanche ionization is still the main cause of ablation, that is, multi-photon collision ionization theory. In recent years, the Fokker–Planck equation has been used to describe the evolution of free electrons. It has been shown that when the laser pulse width is less than 100 fs and the power density is more than 10^{14} J/cm^2, the ablation threshold is approximately equal to the threshold value calculated by considering the multi-photon ionization. The multi-photon ionization is so strong that the free electrons can reach the critical density before avalanche ionization, and multi-photon ionization dominates the ablation process. When the plasma density reaches the critical value, the energy absorption is mainly determined by the inverse bremsstrahlung and resonance absorption. During the pulse period, the thermalization of electrons makes the ionized free electrons in an unbalanced state, and the conduction electron density, energy absorption and reflection coefficient, and skin depth change with the

laser action time and the laser power density. When the laser irradiation intensity is much higher than the ablation threshold, the strong ablation process is dominant. When the laser irradiation intensity is near the ablation threshold, the weak cupping process caused by Coulomb explosion is dominant. At the same time, however, the ablation threshold and single-pulse ablation depth of the material are directly related to the properties of the material itself, the laser irradiation intensity, and the number of laser pulses.

7.3 Fabricating Micro-hole Arrays on Fused Silica Sheet

7.3.1 Overview of Laser Micro-holes Machining Technology

In fact, each micro-hole precision machining methods have their own advantages and disadvantages. Among them, the mechanical drilling is more common way of processing micro-pores, but it is not widely used in the field of micro-processing. Mechanical drilling needs to rely on drilling tools and other bits, which limit the range of processed materials. While the size of the drill bit and the rigidity of the drill limited the size of the holes made by mechanical processing, the general diameter of micro-holes can only be greater than 30 μm, and depth-to-diameter ratio is generally less than 5 μm. However, due to the micro-holes in the micron or even nanometer order often bring great difficulties to the manufacturing process. At present, there are many methods to precision machining micro-holes, as shown in Fig. 7.3, including electrochemical drilling [9], focusing ion beam drilling [10], mechanical drilling

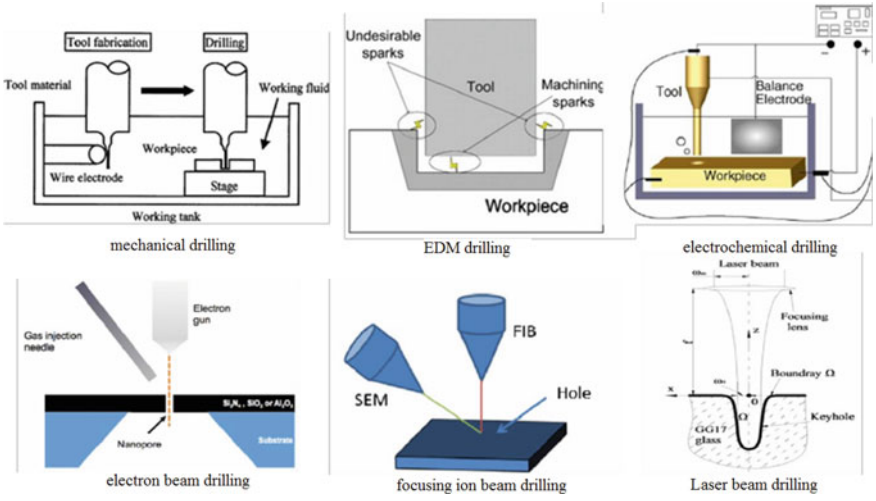

Fig. 7.3 Methods of micro-hole processing [9–13]

[11], electron beam drilling [12], electric discharge machining (EDM) drilling [13], and laser beam drilling [14].

In contrast, electrochemical drilling and EDM drilling are more common. EDM is the way to process by discharge and generally only process shallow holes with diameter greater than 80 μm. Electrochemical drilling is mainly through the electrode-assisted chemical changes to micro-drilling, and the processing of micro-porous by this way is higher in precision. However, two methods above can only be used for micro-processing conductive materials, while it will cause the electrode wear and tear during the process. At present, these two methods are the most common way to process micro-holes, and they are mainly used to process shallow holes with more than 5 μm.

Both electron beam drilling and ion beam drilling are common methods to process submicron-sized micro-holes, but the depth-to-diameter ratio of micro-holes processed by these two methods is generally no more than 10. The two-process methods have harsh conditions that the expensive equipment should be working in the high-vacuum conditions and the processing efficiency is relatively low. Therefore, these two methods are low efficiency and high precision.

Laser beam drilling is widely used in many materials because of its wide applicability, high processing efficiency, low environmental requirements, simple equipment, relatively low cost, and non-contact processing. However, laser drilling usually has shortcomings such as thermal effects and taper. With the rapid development of laser technology, femtosecond laser has the advantages of extremely high peak power and ultrashort pulse width. Therefore, femtosecond laser can process a wide range of materials, and the thermal effect of it is not obvious and even not visible, which is expected to solve the problem of high-quality micro-hole processing.

In 1995, P. P. Pronko et al. of Ultrafast Optical Center of University of Michigan applied femtosecond lasers (central wavelength of 800 nm) to submicron micro-holes fabrication and found that ultrashort pulsed lasers had little thermal impact during the processing. Therefore, the femtosecond laser has advantages of little recast and very high precision during the micro-processing [15]. In 1996, B.N. Chicbkov et al. of the Laser Center in Hanover used a laser with different pulse widths to ablate the solid material [7]. Figure 7.4 shows micro-holes fabricated by using femtosecond, picosecond, and nanosecond lasers on steel foil. It can be seen that the thermal effect

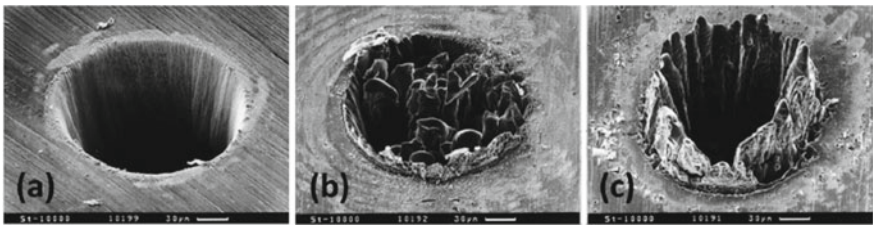

Fig. 7.4 Micro-holes fabricated on 100 μm steel foil using different laser widths were **a** 200 fs, **b** 80 ps, **c** 3.3 ns [7]

near the micro-holes produced by nanosecond and picosecond laser is more obvious, and the recast layer is very obvious. However, the thermal effect of the micro-holes produced by femtosecond laser is not obvious, and the micro-holes are also relatively better. The figure shows the advantages of femtosecond laser micromachining.

In 1997, E. Mazur group of Department of Physical Engineering and Applied Science at Harvard University used focused femtosecond lasers to microburst inside fused silica, sapphire, and other transparent materials, and the material around the focus area was ejected outwardly, so the material within the focus area formed pores [16]. Micro-holes arrays with 2-μm-spacing and diameter of micro-holes ranging from 200 to 250 nm are shown in Fig. 7.5. This is mainly due to the compact focusing and thermal effect of femtosecond laser is not obvious.

In 1999, Xiaonong Zhu et al. of the Femtosecond Science Group at the National Research Council in Canada used femtosecond pulsed lasers to drill micro-holes arrays on the surface of various metal foils, and he found that there was still little thermal damage around the radiation region. In the same year, they also investigated the effects of laser parameters and material properties on femtosecond processing [17, 18]. In 2001–2012, Yan Li et al. of Osaka University in Japan used liquid-assisted method to fabricate micro-holes from the backside of the material to obtain micro-holes with the diameter of 4 μm and the depth of more than 200 μm [19, 20]. As shown in Fig. 7.6, the left-hand column is the cross-section of micro-holes fabricated by the femtosecond laser directly writing from the backside of the quartz in air, and the quartz back has no flowing water, resulting in the diameter of micro-holes about 4 μm and the depth of it about 18 μm. The hole is not very uniform in the internal which is mainly caused by the residues inside the holes that cannot go out. The right-hand column is the cross-section of micro-holes fabricated by the liquid-assisted method. When the laser interacts with the backside of the quartz, the flowing liquid enters into the holes. The flowing liquid removes the debris from the holes which can reduce the scattering of the laser and improve the efficiency of processing. The flowing water can also take away part of the heat which can reduce the heat-affected zone. So, they can obtain deeper holes.

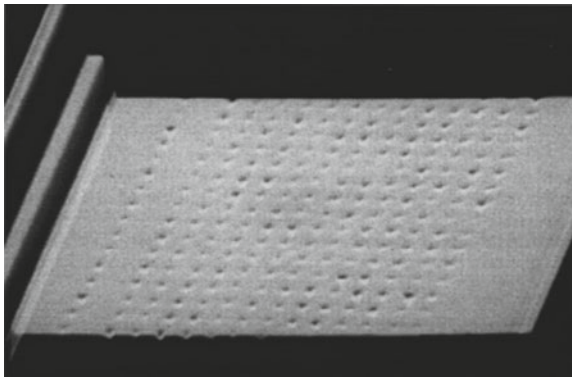

Fig. 7.5 Micro-holes array of 2-μm-spacing produced by micro-explosions inside fused silica. Sample is photographed in reflection using a 1.2 NA objective and is shown in a three-dimensional projection with depth representing intensity of reflected light [16]

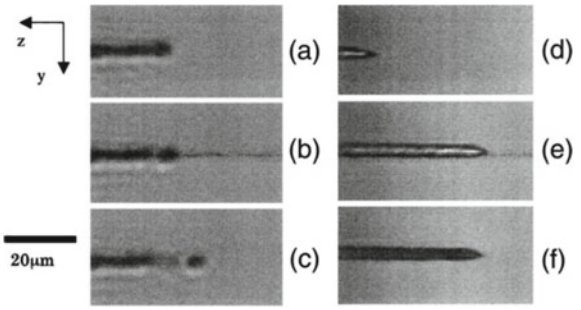

Fig. 7.6 Microdrilling of silica glass from its rear surface in air without and with an inflow of water into the hole. **a**–**c** Drilling without an inflow of water; **d**, **e** drilling with an inflow of water. **f** Image of **e** after the water has receded [19]

In 2002, Choi [21] et al. of the Department of Mechanical Engineering at the University of California studied the physical mechanism of femtosecond laser - induced ablation by using time-resolved microscopy. The formation process of shock wave induced by single beam ablation material is shown in Fig. 7.7, and the spherical shock wave front begins to become apparent at 18.2 ns. Although the initial shock wave transmission is very fast, but after more than 29.8 ns, the ablation becomes slow. At the same time, the energy transfer model was established to predict carrier and lattice temperatures as well as electron and vapor fluxes emitted from the surface.

In the same year, Nakata et al. [22] of the School of Information Science and Electrical Engineering at Kyushu University used a diffraction beam splitter to obtain the interference of femtosecond laser beams to process point arrays. At the same time, arrays of metal dots were fabricated at different scanning speeds and then irradiated by He–Ne laser to obtain the diffraction pattern of the dot arrays, which are shown in Fig. 7.8. In the illustration, we can see that the spot array acts as a grating in the diffraction process, where the distance between the samples to the white screen is 10 cm. In contrast the diffraction pattern to the sample pattern, it can be seen that the larger the distance between the holes, the smaller the distance between the diffractive optical dots. As the spacing between the micro-holes decreases, the spacing between the diffractive optical dots will increase. When the spacing between the holes is equal to 0, the grating diffraction pattern is obtained, and the power at each stage is shown in Fig. 7.8.

In 2003, Kamlage et al. [23] of Hannover Laser Center in Germany studied the effect of femtosecond laser repetition frequency on the morphology of micro-holes

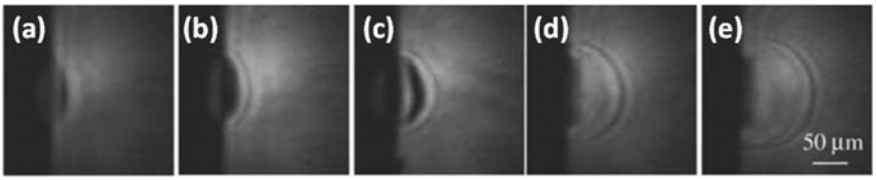

Fig. 7.7 Formation process of shock wave ($F = 1.5$ J/cm^2): **a** 14.9 ns, **b** 18.2 ns, **c** 23.6 ns, **d** 29.8 ns, and **e** 40.4 ns [21]

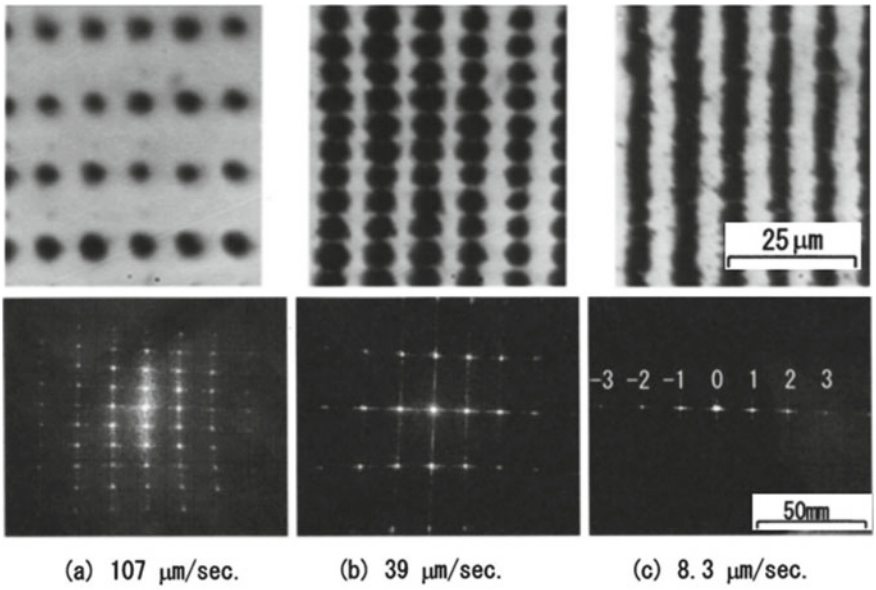

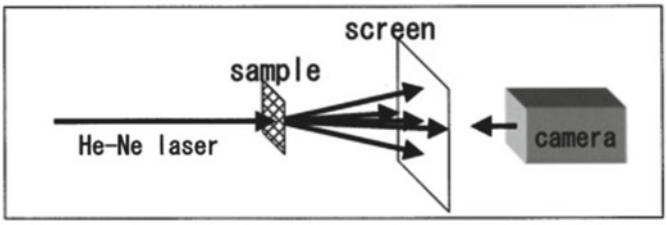

order	-3	-2	-1	0	1	2	3
Power (μw)	0.5	3.7	46.3	102	48.4	4.4	1.0

Fig. 7.8 The sample processed at a scanning speed of **a** 107 μm/s, **b** 39 μm/s, and **c** 8.3 μm/s, respectively, and the corresponding diffraction pattern illustrated is the experimental schematic and the power at each stage [22]

and processed deep hole with better morphology on stainless steel as shown in Fig. 7.9. The experimental results show that the micro-holes outlet diameter increases with increasing repetition frequency when micromachining in the air. Because the melted debris cannot be completely ejected out with increasing repetition frequency which can decrease air ionization threshold will decrease. The plasma and debris remained in the holes act on the wall of the holes again and the divergence and perturbation of the laser, resulting in an increased outlet diameter as shown in Fig. 7.9a. The diameter of micro-holes processed in the vacuum does not change significantly with the repetition frequency as shown in Fig. 7.9b, and the inlet diameter of the micro-holes in the air is ultimately the same as in the vacuum. Because the material and the air are rapidly heated, the gas density is reduced which creates a quasi-vacuum

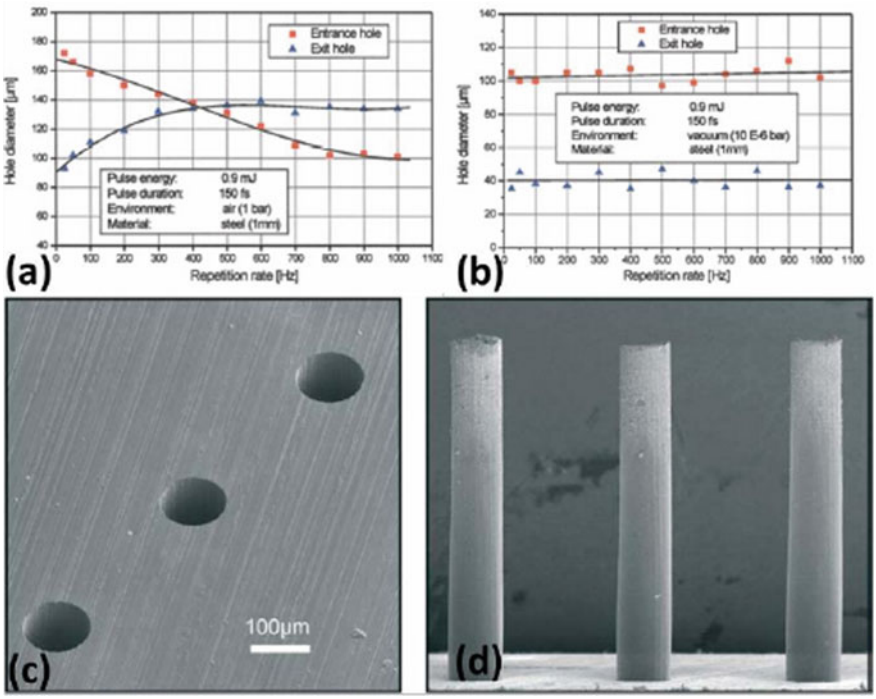

Fig. 7.9 Influence of femtosecond laser repetition frequency on the micro-holes inlet and outlet diameter under the same laser energy **a** the air environment, **b** the vacuum environment, **c** in the air environment, micro-holes on the stainless steel, and **d** a hole replica [23]

environment at the entrance, thus improving the quality of the entrance and reducing the processing taper. Deep holes on a stainless steel with a thickness of 1 mm were fabricated by using a Ti: sapphire femtosecond laser. All processing was performed at atmospheric pressure. As shown in Fig. 7.9c, d, the micro-holes fabricated by femtosecond lasers and their replicas show that the micro-holes have excellent circularity and geometrical morphology, which confirms that the femtosecond laser can be a better way to process metal materials.

In 2015, Hu Zhan group of the Institute of Atomic and Molecular Research at Jilin University reported the morphology of the holes fabricated by femtosecond laser (800 nm, 100 fs) under different ambient pressures [24]. The SEM images of the inlet and outlet of the holes under different ambient pressures are shown in Fig. 7.10. The amount of redeposited material around the inlet holes increases with the increasing of the ambient pressure. When the ambient pressure is 5500 Pa, the amount of redeposited material reaches the maximum. As the ambient pressure increasing, the amount of redeposited material decreases. Under low-pressure conditions, a high degree of expansion of the ablative material results in a clean ablative hole; almost no deposition of particles is observed around the pores. When the ambient pressure is in the range of 40–5500 Pa, the expansion of the ablative material is performed

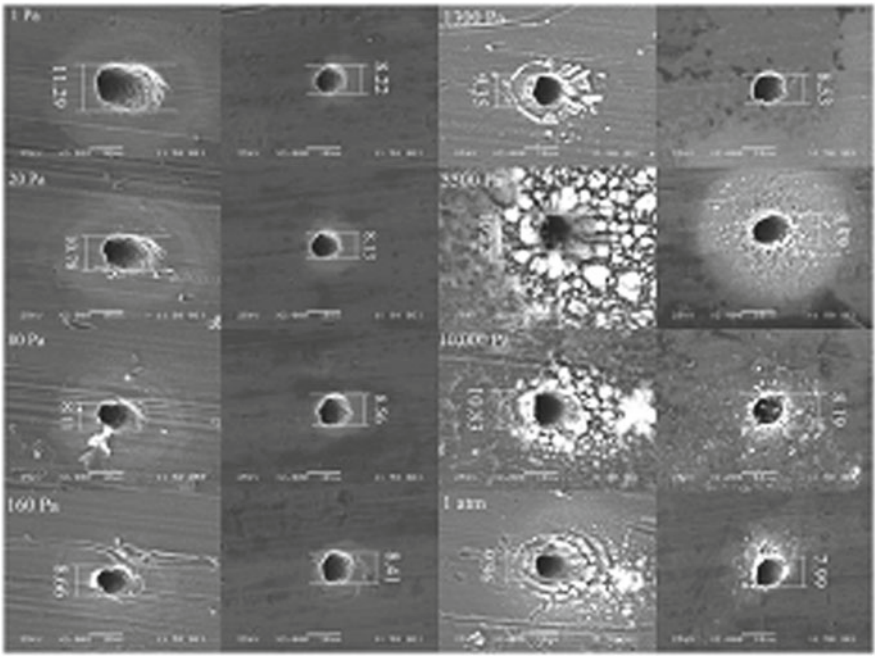

Fig. 7.10 SEM images of the inlet hole (left) and the outlet hole (right) at different ambient pressures [24]

by an increase in ambient pressure, which results in an increase in the amount of redeposited material around the holes. When the ambient pressure is 5500 Pa or higher, the re-deposited ablative material is confined into the ablation holes. This will reduce the amount of ablative material around the hole.

Substrate temperature is an important parameter for controlling the properties of femtosecond laser-induced surface structures besides traditional ways [25]. In 2014, the S. K. Moon group of the School of Mechanical and Aerospace Engineering at Nanyang Technological University evaluated the effects of the hole geometry and the spatter area around the drilled hole on silicon with various temperatures [26]. Figure 7.11 is SEM images of the front side and back side micro-holes array drilled by femtosecond laser with power of 200 mW at different temperatures. The laser drilling efficiency is increased by 56% when the temperature is elevated from 300 to 873 K. The spatter area is found to continuously decrease with increasing substrate temperature; the diameter of inlet holes was reduced by 25% when temperature is 873 K compared to 300 K. The reason for this change is that the elevated temperature of the substrate leads to the increase of the laser energy absorption.

In 2004, P. Simon group of the Laser Laboratory in Göttingen in Germany fabricated a large number of micro-holes patterns on the titanium film using the ultraviolet femtosecond laser interference technique as shown in Fig. 7.12 [27]. Diameter of the holes is about 400 nm, and the micro-holes have good quality. This technology

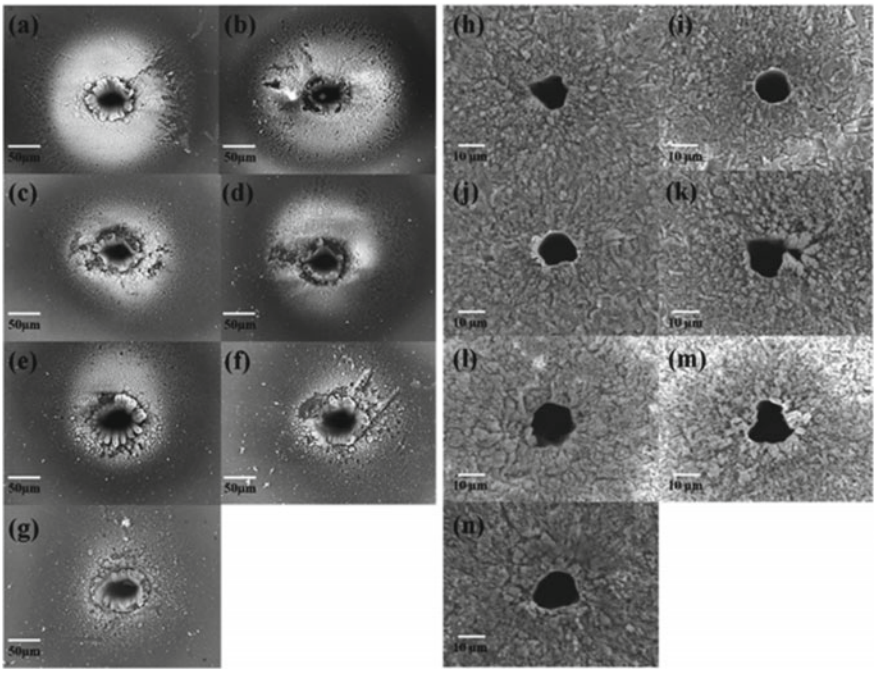

Fig. 7.11 SEM images of the frontside (left two columns) and backside (right two columns) microhole drilled by fs laser at temperature 300 K (**a** and **h**), 373 K (**b** and **i**), 473 K (**c** and **j**), 573 K (**d** and **k**), 673 K (**e** and **l**), 773 K (**f** and **m**), 873 K (**g** and **n**) [26]

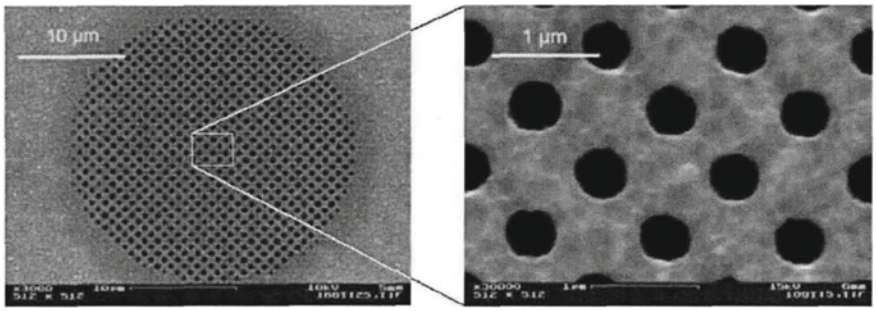

Fig. 7.12 Microstructures on the metal fabricated by using ultraviolet femtosecond laser interference technique [27]

has strong reproducibility and can be processed thousands of sub-micron holes in a flash, so it has a good prospect in the industry.

In 2010, the ZhiZhan Xu group of the Shanghai Institute of Optics and Fine Mechanics in Chinese Academy of Sciences fabricated micro-lens in the internal of the fused silica by using femtosecond laser [28]. The sample was a 1 mm-thick

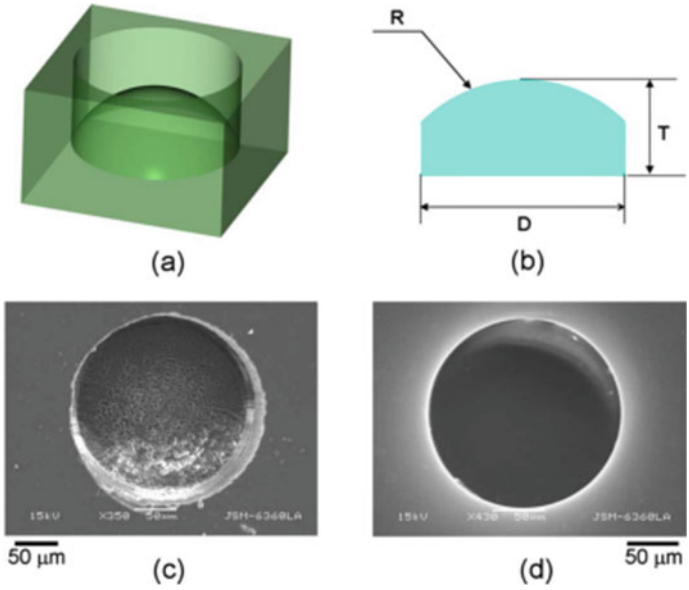

Fig. 7.13 (Color online) **a** Schematic of the micro-lens. **b** Dimensions of a planoconvex micro-lens on a chip: D, R, and T are the diameter of the aperture, radius of the spherical surface, and thickness, respectively. SEM images of micro-lenses **c** before and **d** after OH flame polishing process [28]

polished quartz sheet. The micro-lens had aperture diameter of $D = 200\,\mu$m, spherical surface radius of $R = 300\,\mu$m, and thickness of $T = 500\,\mu$m as illustrated in Fig. 7.13. After processing, the hydrofluoric acid with a solution of 10% was used for ultrasonic bath in 80 min to completely separate the processing area. Then, the surface of the sample is polished by using an oxyhydrogen flame to improve the quality of the lens surface.

In 2014, the Huan Huang group of PolarOnyx, Inc. in California reported micro-holes in different types of materials by using femtosecond fiber lasers in air environments [29]. The holes in stainless steel, bovine bone, soda-lime glass, and bovine tendon fabricated by femtosecond fiber lasers are shown in Fig. 7.14. It can be seen that femtosecond lasers can produce better morphologies on a wide variety of materials. This shows that femtosecond laser can fabricate a wide range of materials.

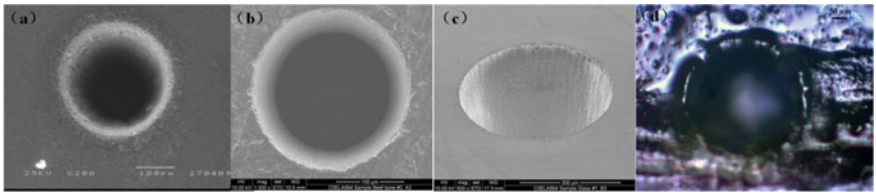

Fig. 7.14 Holes on **a** stainless steel, **b** bovine bone, **c** soda-lime glass, and **d** bovine tendon [29]

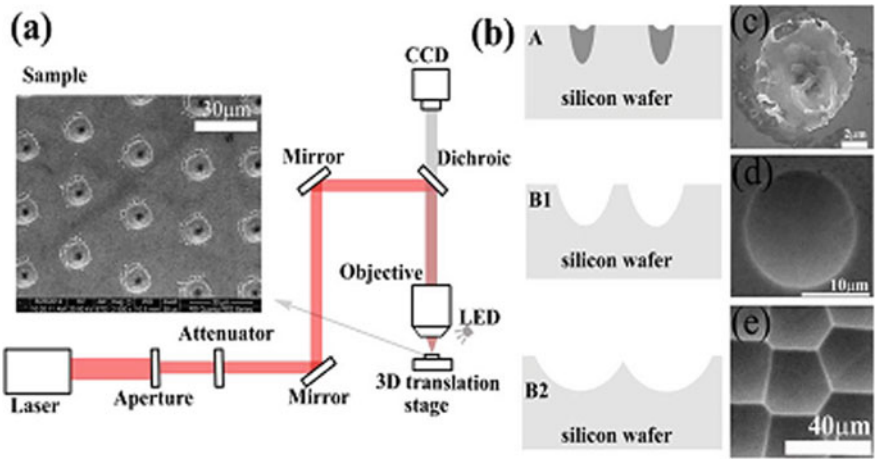

Fig. 7.15 **a** Experimental setup for laser scanning process. Inset, array of pulse-irradiated craters. **b** Process sequence for fabricating close-packed micro-lenses over a silicon wafer. Step A, laser-induced material modification; Step B1, forming concave microstructure by chemical etching; Step B2, etching until adjacent concave microstructures squeeze with each other. **c** SEM image of laser-modification zone. **d** SEM image of circular concave microstructures. **e** SEM images of irregular concave microstructures [30]

In 2015, the Feng Chen group of Xi'an Jiaotong University School of Electronic and Information Engineering reported a novel fabrication method of large-area concave micro-lens array (MLA) on silicon by combination of high-speed laser scanning [30], which would result in single femtosecond laser pulse ablation on surface of silicon and subsequent wet etching. A dimpled lens was fabricated on a 1 cm × 1 cm silicon sheet. The dimensionally adjustable aspheric profile micro-lens array has been developed and can be applied to infrared (IR) optical elements. The processing of the micro-lens array is shown in Fig. 7.15. The processing steps of the microscopic lens on the silicon wafer are listed as follows: Firstly, the material is modified by laser-induced; then, the micro-structure is formed by chemical etching; finally, the adjacent concave micro-structures are pressed against each other.

7.3.2 Preparation of Aluminum Coated Silica

The size of a fused silica sheet is 1 cm × 1 cm × 1 mm. For optimal fabrication, the surface of the silica must be appropriately cleaned to remove contamination. Initially, the fused silica sheet was cleaned with alcohol and deionized water in an ultrasonic bath for 25 min to clear any contamination (loose particles/powder) on the surface. The aluminum film was deposited on the surface of the silica sheet by femtosecond pulsed laser deposition in a high-vacuum chamber (below 5×10^{-4} Pa), as shown in Fig. 7.16. In our experiments, a commercial femtosecond Ti:sapphire

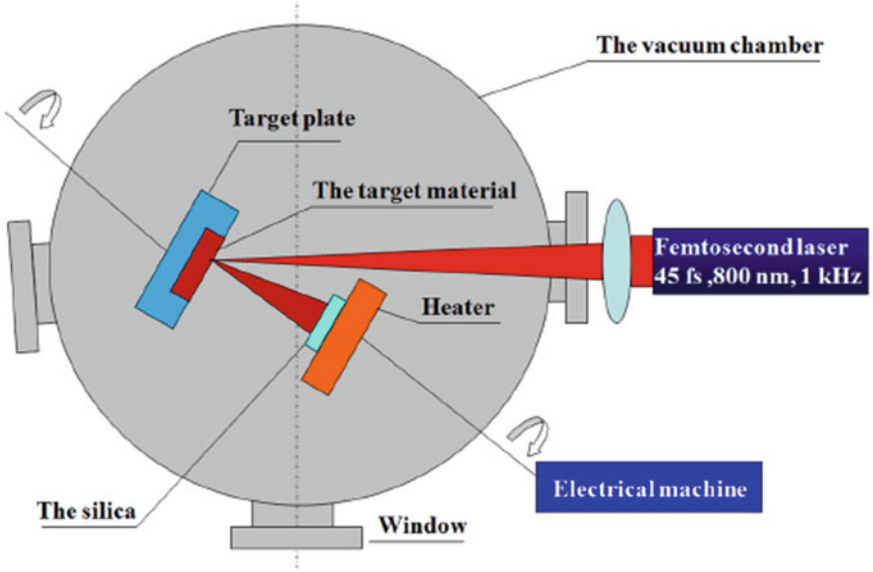

Fig. 7.16 Experimental setup for the preparation of fused silica sheet coated with aluminum film

laser system (Legend Elite, Coherent) based on the chirped-pulse amplification is capable of producing pulses with a duration of 35 fs and an energy of 3.5 mJ, at a center wavelength of 800 nm and a repetition rate of 1 kHz. Then, the fused silica sheet was put onto the heater, and the target material of aluminum was put onto the target plate. Finally, the window was closed, and the electrical machine and heater were turned on. The temperature of the heater was set to 600 °C. The deposition time was 75 min, and the output power of the fs laser was ~1.2 W.

7.3.3 Directly Writing Micro-hole Arrays on Coated-Fused Silica Sheet by Using Femtosecond Laser

The experimental setup of the micro-hole array fabrication process was shown in Fig. 7.17. The fused silica sheet coated with an aluminum film was put on the translation stages. The maximum output power of the femtosecond laser was ~3.5 W. The combination of a half mirror and an attenuator was used to adjust the output radiation power. Then, the attenuated laser beam was focused on the fused silica by using an objective lens with a numerical aperture of 0.4. The femtosecond laser is in direct contact with the sample while the energy of the laser pulses is delivered to the bottom of the hole via multiple reflections. The multi-photon absorption would occur at the focusing voxel in the fused silica sheet. The loss of energy occurs at every step of the reflection process. A high-resolution CCD camera connected to a computer was

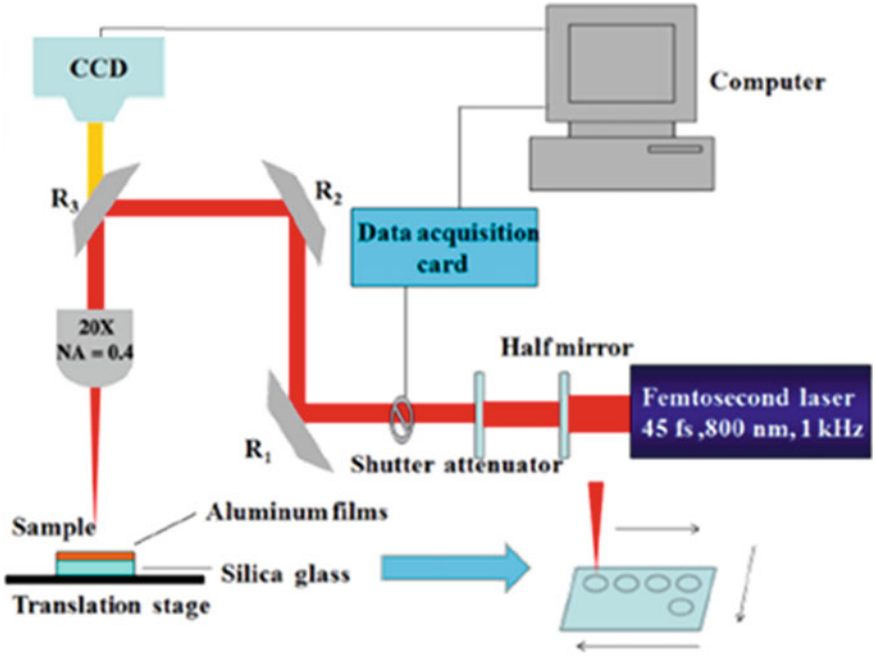

Fig. 7.17 Experimental setup for direct writing micro-holes array on coated-fused silica sheet

also fixed to monitor, the real-time process of the fabrication. The accumulated pulse numbers at each spot were controlled by the opening time of the electronic shutter. All irradiations were performed in air at room temperature. After femtosecond laser irradiation, the sample was cleaned to remove the dust deposited in the ablation area by ultrasonic bath in ethanol and deionized water for 25 min. The microphotographs of the microarray were characterized by using scanning electronic microscope (SEM, Hitachi SU8220) and optical microscopy (OM, Keyence VHX650).

7.3.4 Ablation Threshold of Fused Silica

The ablation threshold fluence of a material could be roughly estimated by the lowest pulsed energy density needed to remove the original material. However, when the laser fluence just exceeds the ablation threshold fluence of a material, it usually is capable of clean and precise material removal. Micro-holes were fabricated on the surface of the sample with different laser pulse energies. The relationship between the diameter D of a crater and the laser fluence was used to estimate the ablation threshold fluence of the fused silica sheet.

The laser fluence F_0 can be estimated from the laser pulse energy E and the local beam diameter d as [31]:

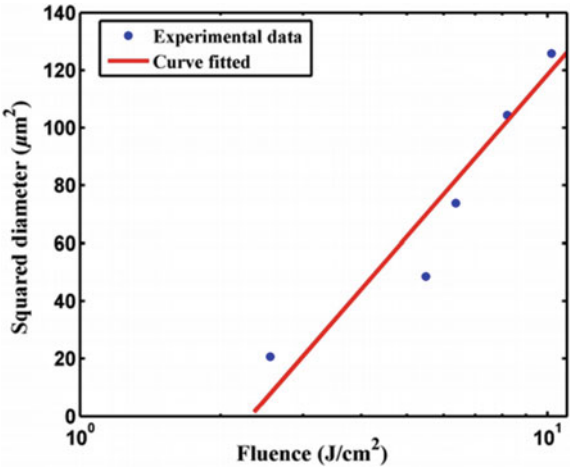

Fig. 7.18 Relationship between squared diameter D_2 and laser fluence

$$F_0 = 2E/\pi d^2 \tag{4}$$

If the fluence F_0 surpasses the ablation threshold fluence F_{th}, the squared diameter D^2 of the ablation crater is associated by

$$D^2 = 2d^2 \ln(F_0/F_{th}) \tag{5}$$

As shown in Fig. 7.18, the single-shot ablation test of the fused silica sheet is investigated and the single-shot irradiation is realized by controlling the repetition rate of the machine. The squared diameter of the micro-holes is a function of the laser fluence. The curve shows that relationship between the squared diameter D^2 and laser fluence F_0 is logarithmic because the X-axis is the logarithm of the laser energy. The curve for the relationship between the squared diameter D_2 and the logarithm of laser energy is linear [31, 32]. The extrapolation to zero of the linear fit obtains the single-shot ablation threshold, and the ablation threshold for the fused silica sheet is calculated as 2.36 J/cm^2. Ablation is a function of the number of pulses. It leads to the definition of an N-pulse ablation threshold when the sample is irradiated by pulsed lasers with the number N_0. $N_0 < N$, no ablation occurs, while if $N_0 > N$, ablation occurs. This effect has been defined as an incubation effect [33, 34]. For the material-dependent "incubation effect," [33] with an increasing number of overlapping pulses, the ablation threshold is anticipated to decrease.

7.3.5 *Average Diameter of the Micro-hole Arrays with Different Fluence*

The number of accumulated laser pulses for drilling each hole was set to 2000 to achieve sufficient repeatability. The dependence of the average diameter of the micro-holes on the fused silica sheet and aluminum coated-fused silica sheet versus the fluence of femtosecond laser is shown in Fig. 7.19.

As shown in Fig. 7.19, the average diameter of the micro-hole arrays on the fused silica sheet and aluminum coated-fused silica sheet increased with increasing femtosecond laser fluence. When the femtosecond laser fluence was between 0.1 and 40 J/cm^2, the average diameter of the micro-holes on the fused silica sheet increased rapidly with the laser fluence. With the fluence higher than 40 J/cm^2, the average diameter seemed to almost reach a maximum and remain unchanged. However, the average diameter of the micro-holes on the fused silica sheet was a little larger than that on the aluminum coated-fused silica sheet.

The morphologies of micro-holes fabricated at different laser fluences for coated and uncoated silica sheets are shown in Fig. 7.20. For coated silica, although the fluence of the laser pulse is changed, the crack and collateral damage around the hole are almost invisible due to the aluminum coating; for uncoated silica, the decrease of the fluence of the laser pulse may decrease the crack and collateral damage around the holes, but cannot make them disappear. Thus, it is a good choice to improve the quality of the femtosecond laser processing by coating with film on the surface of sample.

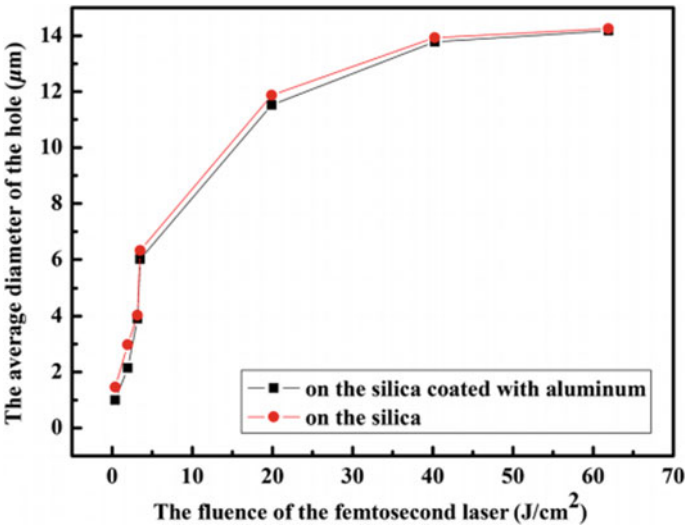

Fig. 7.19 Dependence of the average diameter of the micro-hole arrays on the fused silica sheet and aluminum coated-fused silica sheet versus the fluence of femtosecond laser

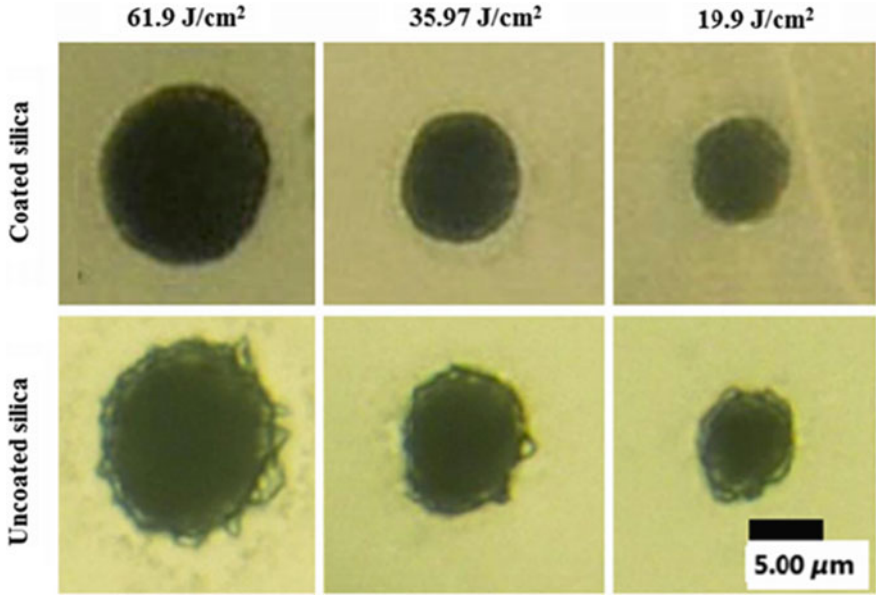

Fig. 7.20 Drilling on coated silica and uncoated silica with different fluences of laser pulse

7.3.6 Micro-hole Arrays on the Surface of Fused Silica Sheet

The micro-hole arrays were fabricated on a fused silica sheet and an aluminum coated-fused silica sheet, respectively. The distance between neighboring hole centers was set to 30 μm. The laser fluence applied for the fabrication was 58.9 J/cm^2. The accumulated pulse numbers at each spot were controlled by the opening time of the electronic shutter, with the opening time of the electric shutter being 2 s. After ablation, a 10% hydrochloric acid (HCl) solution was used to clean the aluminum film on the fused silica sheet. Subsequently, the samples were cleaned to remove the dust deposited in the ablation area by ultrasonic bath in ethanol and deionized water for 25 min.

Figure 7.21 shows the micro-hole arrays fabricated on the fused silica sheet [35, 36]. Figure 7.21a is a microscopic photograph of a micro-hole array pattern on silica, Fig. 7.21b shows a micro-hole array pattern on aluminum coated silica, and there were many burrs and debris around the holes on the fused silica coated aluminum film, which were formed by the molten material ejected from the holes and re-solidifying rapidly. As the insets of Fig. 7.8b show, the fused silica sheets coated with aluminum film were used in the experiment. Figure 7.8c is a SEM image of a micro-hole array on silica. After washing the aluminum film on the fused silica sheet (Fig. 7.21d), the micro-holes on the fused silica sheet were very round and were neatly arranged. The micro-holes were obviously, almost, circular. SEM image of a micro-hole in the holes array on the fused silica sheet is shown in Fig. 7.21e. Figure 7.21f is a SEM

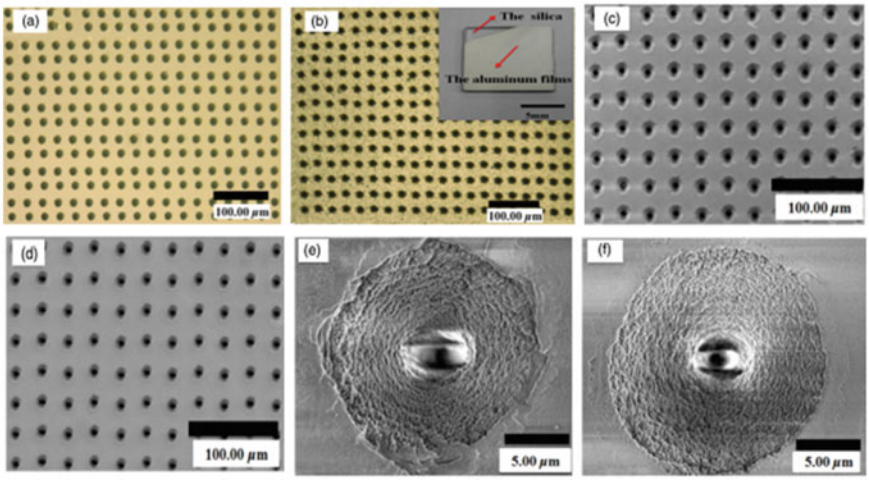

Fig. 7.21 Images of micro-hole on silica (left column) and aluminum coated silica (right column) **a** Microscopic photographs of micro-hole array pattern on silica, **b** micro-hole array pattern on aluminum coated silica, **c** SEM image of micro-hole array on silica, **d** SEM image of micro-hole array after washing the aluminum film, **e** a hole in figure **c**, **f** a hole in figure **d** [36]

image of a randomly selected hole in the holes array, and no debris and recast layer could be discovered around the hole. The microstructures around the hole and the internal walls were very smooth.

In Fig. 7.21**e**, **f**, the microstructures inside the hole were in combination as annulus in shape. That was, because, the multiple femtosecond laser pulses produce multiple shock waves that forced the nanoparticles outward and made the density near the holes increase. Under the action of a series of femtosecond laser pulses, the ring structure was formed inside the holes. Comparing Fig. 7.21e with Fig. 7.21f, there was an evident zone with many cracks around the hole edges in Fig. 7.21e. The zone was formed by the redeposit of the fusant and vaporized fused silica sheet. However, there was a better morphology left in Fig. 7.21f. That may be one benefit of the aluminum film on the fused silica sheet.

Subsequently, the diffraction characteristic of the micro-hole array was examined by using a He–Ne laser beam. In this experiment, the He–Ne laser passed through a lens to form a magnified image of the focused laser beam spot [35]. Then, the focal beam spot passed through the micro-hole array. Parallel light passed through a small hole array, and the image on the screen was regular bright spot array. The micro-hole closer to the central micro-hole in the micro-hole array has the higher brightness in the diffraction characteristic of the micro-hole array. As shown in Fig. 7.22a, the diffraction characteristic of the micro-hole array on silica was obvious, but there were many dark spots that randomly distributed in diffraction light spots. As shown in Fig. 7.22b, the diffraction characteristic of the micro-hole array on silica coated with aluminum was significantly obvious. Compared these two pictures, the micro-hole array on silica coated with aluminum is more uniform than the one on silica.

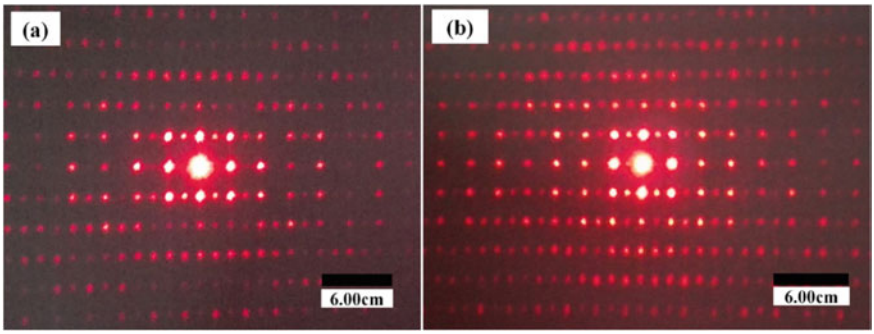

Fig. 7.22 Diffraction pattern of micro-hole array **a** on silica **b** on silica coated with aluminum [35]

7.4 Fabricating Net-Like Structure by Femtosecond Laser Pulses

7.4.1 Overview of Microfluidic Channel Processing Technology

Generally, microfluidic channels can be formed in transparent substrates via FLDW followed by chemical etching [37–40]. However, the morphology of the microchannels fabricated via this way is always conical in shape. This is due to the limited contrast ratio of etching selectivity between the laser exposed and unexposed regions. Since the chemical etching always begins from the surface of the substrate and progresses toward the middle area of the channels, the region close to the entrance of the channels will always suffer a longer etching period compared to the middle region.

The conical feature caused by chemical selective etching is the bottleneck to realize homogeneous channel microfluidic system, so many scholars have devoted themselves to this research. Until now, several methods have been demonstrated to realize homogeneous microchannels within the substrate (shown in Fig. 7.23). (1) Drawing substrate glass after wet chemical etching [41]. The glass drawing process significantly reduces the inner surface roughness of the fabricated channels, and centimeter-level microfluidic channels with an aspect ratio above 1000 can be realized; however, the length of the microfluidic channel fabricated in this way is severely limited. (2) Shape-controlled microchannels [42]. The shape control is achieved by suitable wobbling of the glass substrate during the irradiation process. Cylindrical microchannels with uniform cross-sections are demonstrated with an unprecedented length of 4 mm. But this method increases the diameter of the fabricated microchannel. (3) Segmented chemical etching method to fabricate microchannels with arbitrary length and uniform diameter [43]. A segmented chemical etching method of introducing extra access ports and a secondary power compensation is presented,which enables the fabrication of uniform 3D helical microchannels with

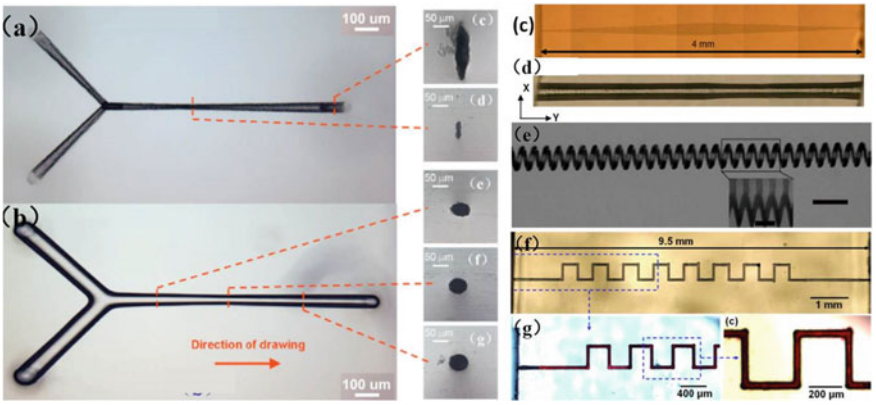

Fig. 7.23 **a**, **b** Optical micrographs of the Y-branched channels before and after drawing, respectively [41]. Microscope image of **c** conical spiral inscribed in the glass and **d** the etched microchannel [42]. **e** Optical micrograph of a helical channel fabricated by segmented chemical etching method [43]. **f**, **g** micrograph of a 1.6-cm-long microchannel embedded in porous glass before postannealing and postannealed, respectively [44].

length of 1.140 cm and aspect ratio of 522. There are some extra corrosion inlets on the microfluidic channel prepared by this method. (4) Fabrication of microfluidic channels using porous glass as substrate [44]. Formation of hollow microchannels in a porous glass substrate immersed in water by FLDW method and postannealing of the glass substrate at ~1150 °C by which the porous glass can be consolidated. A square-wavelike channel with a total length of ~1:4 cm and a diameter of ~64 μm can be easily produced ~250 μm beneath the glass surface. Porous glass is unavailable at the market.

More recently, Feng et al. have developed a new technique which firstly fabricates channel on the surface of the substrate using FLDW followed by chemical etching and then covers a thin layer of PDMS film on substrate to form three-dimensional semi-occlusive microchannels. The conical feature brought by etching selectivity can be effectively reduced, because the channels are fabricated on the surface of substrate; thus, there is no problem of suffering different etching period. Via this technique, various homogeneous networked semi-occlusive microfluidic can be fabricated on the surface of silica.

7.4.2 Fabricating Micro-grid

Micro/nano-surface structures were fabricated using optical diffraction [45, 46]. The obtained diffraction pattern was imprinted on the surface of the ZnSe wafer. In the high-intensity regions, the ZnSe wafer was ablated and generated a surface depression (valley). In the low-intensity regions, a corresponding protrusion (peak) appeared.

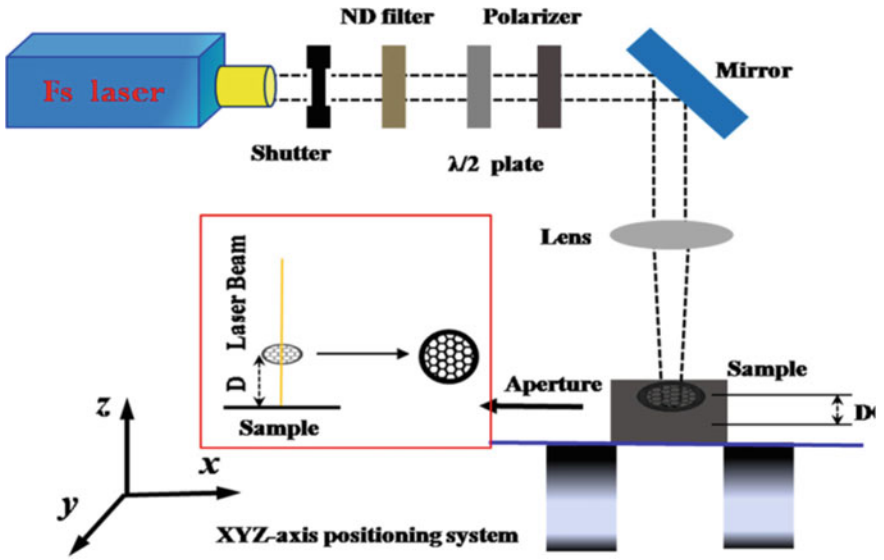

Fig. 7.24 Experimental setup for microsized structure-assisted nanostructure fabrication

The observed micro-patterning is explained with Fresnel's diffraction theory. In addition, two types of spatial frequency surface structures were found, namely laser-induced periodic surface structure (LIPSS) and laser-induced periodic curve surface structure (LIPCSS). LIPCSS appears at the bottom of the ZnSe surface. Unlike LIPSS, LIPCSS is independent of laser polarization. The formation of LIPCSS was because of the interference between the reflected laser field on the valley surface and the incident laser pulse. The microsized structure assisted nanostructure formation opens up the possibility for fabricating the nanosized structure on the wafer surface with ultrashort laser pulses.

The entire diffraction experimental setup is shown in Fig. 7.24. All irradiations were performed in air environment under normal incidence. The experiment is conducted on a commercial Ti:sapphire regenerative amplifier laser system (Legend Elite, Coherent). It generates laser pulses at a center wavelength of 800 nm with pulse duration of 60 fs and pulse energy of 2.0 mJ. The laser system operates at a repetition rate of 1 kHz. The laser beam goes through a lens with a focal length of 150 mm and irradiates on the sample surfaces. The sample is placed at a distance, typically a few hundreds of micrometers behind a hexagonal transmission electron microscope (TEM) mask (the dimension of the TEM mask is 3 mm, and the dimension of a hexagon is 60 μm), which is illuminated at a distance of $Z \approx 120$ mm through the focal lens. The diameter of the laser spot on the sample surface is about 1 mm. The diameter of laser spot is measured and determined with $1/e^2$ intensity level. An electronic shutter is used to control the irradiation pulse numbers, and a neutral density filter, a λ/2 plate, and a polarizer are used to change the laser power continuously. The samples are mounted on an *XYZ*-translation stage controlled by

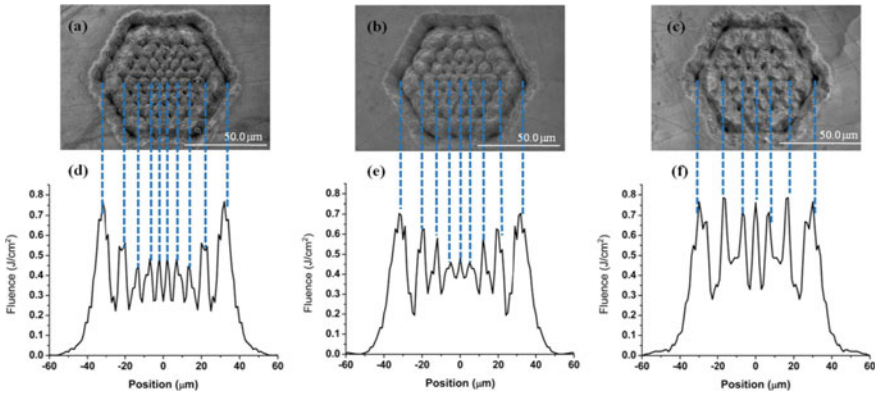

Fig. 7.25 SEM images of the imprinted diffraction structure on ZnSe surface. **a–c** Represent imprinted diffraction structures on ZnSe surface, and the diffraction distance was 375 μm, 405 μm, and 550 μm, respectively. Laser fluence was 0.3 J/m^2, and the number of femtosecond laser pulses was 750 in the experiments. The corresponding calculated fluences along the horizontal midlines in **a–c** are shown in **d–f**, respectively [45]

a computer. Prior to irradiation, the ZnSe wafer is cleaned using ethanol. After the laser irradiation, the sample is dipped in alcohol and cleaned by an ultrasonic bath for 10 min to remove the plume dust deposited in the ablation area. At last, the surface morphology is observed using optical microscopy (OM, Keyence VHX 650) and a scanning electronic microscope (SEM, Hitachi SU8220).

Figure 7.25 shows the SEM images of the diffraction etched structures on the surface of a ZnSe wafer, which was irradiated by femtosecond laser pulses at different diffraction distance, 375, 400, and 550 μm. The laser fluence was 0.3 J/m^2, and the laser pulse number was 750. The etched structure on the ZnSe wafer surface directly reflected the diffraction of femtosecond laser pulses (the wide spectrum). At different diffraction distances, that means a different Fresnel number N_f, the energy distribution of the entire diffraction field is different. If the N_f is larger, the equal energy region (grid area) is greater; the energy density at the grid area is greater than that at the grid lines. Also, a micro-peak structure was found at the surface of the grid area, and a stripe structure was near the grid line. This illustrates that the energy redistribution caused by diffraction plays a key role in the formation of the surface's microsized structure.

7.4.3 Fabricating Microfluidic Channels

Generally, microfluidic channels can be formed in transparent substrates via FLDW followed by chemical etching [37–40]. However, the morphology of the microfluidic channels fabricated via FLDW is always conical in shape. This is due to the limited contrast ratio of etching selectivity between the laser exposed and unexposed regions.

Since the chemical etching always begins from the surface of the substrate and progresses toward the interior of the channels, the region close to the entrance of the channels will always suffer a longer etching period compared to the middle region.

The conical feature caused by chemical selective etching is the obstacle to realize the homogeneous microfluidic channel system. So many researchers have devoted to this study. Several methods have been demonstrated to fabricate homogeneous microchannels within the substrate. (1) Drawing substrate glass after wet chemical etching [41]. The glass drawing process significantly reduces the inner surface roughness of the fabricated channels, and a centimeter-level length of microfluidic channels with an aspect ratio above 1000 can be realized. However, the length of the microfluidic channel fabricated in this way is severely limited. (2) Shape-controlled microchannels [42]. The shape control is achieved by suitable wobbling of the glass substrate during the irradiation process, but this method increases the diameter of the fabricated microchannel. (3) Segmented chemical etching method to fabricate microchannels with arbitrary length and uniform diameter [43]. A segmented chemical etching method of introducing extra access ports and secondary power compensation enables the fabrication of uniform 3D helical microchannels. There are some extra corrosion inlets on the microfluidic channel prepared by this method. (4) Fabrication of microfluidic channels using porous glass as substrate [44]. Formation of hollow microchannels in a porous glass substrate immersed in water by FLDW and post annealing of the glass substrate at ~1150 °C by which the porous glass can be consolidated.

7.4.3.1 Fabricating Net-Like Hexagonal Microfluidic Channels

In the experiment, a fused silica was used as the substrate material which was cut into 10 mm × 10 mm × 1 mm sections with all surfaces polished. Figure 7.26 showed the experimental schematics for fabricating microfluidic channels with FLDW method.

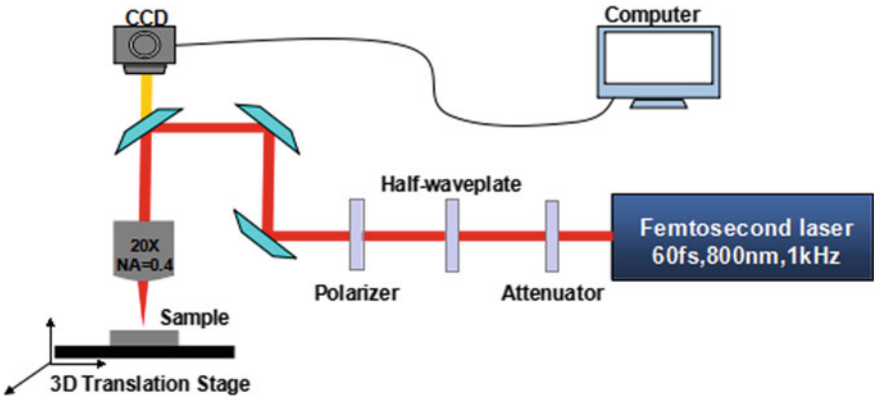

Fig. 7.26 Experimental setup schematic of the FLDW process [47]

The experiment was carried out with a commercial Ti:sapphire regenerative amplifier laser system (Legend Elite, Coherent), which generates laser pulses with center wavelength at 800 nm, pulse duration of 60 fs, and maximum single-pulse energy of 0.3 mJ at a repetition rate of 1 kHz. The average power of the laser beam used to direct writing was controlled by a combination of a polarizer and a wave plate. A x20 objective with a NA of 0.4 was employed to focus the laser beam. The sample could be optionally translated by a PC-controlled XYZ stage (M-111.1DG, Physik Instrumente) with a resolution of 6.9 nm. The average power of femtosecond laser was chosen to be 160 mW, and the translating speed of the stage was 0.01 mm/s (laser fluence was 1.27×10^5 J/cm^2). A charge-coupled device (CCD) was used for monitoring the whole FLDW process in real time.

In the experiment, as shown in Fig. 7.27, the whole process consists of four steps (schematics are shown in Fig. 7.27a–d, respectively): (1) FLDW on the surface of the silica to form a net-like modified region; (2) dipping the laser irradiated substrate in 10% aqueous solution of HF at 25 °C in ultrasonic bath ~30 min for removing the modified material to form homogeneous microfluidic channels; (3) covering a layer of 500 μm thick PDMS film on the substrate; and (4) injecting Rh6G ethylene glycol solution into microfluidic channel in order to test flowing characteristics of the three-dimensional microfluidic. All experiments were conducted in air environment. Prior to irradiation, the fused silica was cleaned in acetone and deionized water in an ultrasonic bath for 15 min. After the laser irradiation, the sample was cleaned in alcohol and deionized water in an ultrasonic bath for 15 min to remove the plume dust deposited in the ablation area. After etching, the substrate was dipped in enough calcium chloride solution to transform residual fluoride and calcium ions to a calcium fluoride precipitation; then 10% sodium hydroxide solution was used to neutralize residual hydrogen ions for 3 min and then douched the substrate with water ~ 10 min. The pH value of substrate was tested by acid–base test papers. Neutralization and douching were conducted until the pH value of substrate was alkalescent. The surface morphology was observed using optical microscopy (OM, Keyence VHX 650) and a scanning electronic microscope (SEM, Hitachi SU8220).

Fabricated net-like hexagonal microfluidic channels and net-like microfluidic triangular channels are shown in Fig. 7.28. Figure 7.28a, b presents a top view of the net-like hexagonal microfluidic channels on the surface of a fused silica substrate.

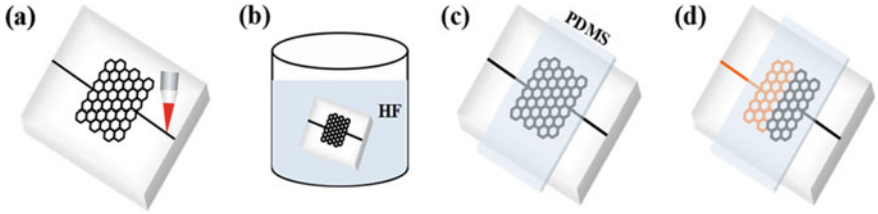

Fig. 7.27 Flow chart of the whole fabrication process. **a** FLDW on the surface of the silica; **b** chemical selective etching with HF; **c** covering a layer of 500 μm thick PDMS film on the substrate; **d** injecting Rh6G ethylene glycol solution into microfluidic channel [47]

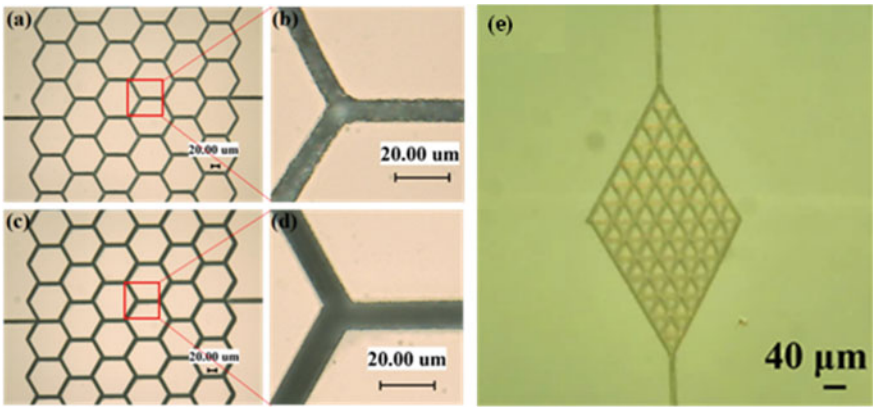

Fig. 7.28 Optical micrographs of microfluidic channels. **a** After direct writing; **b** enlarged image of figure **a**; **c** after selective chemical etching; **d** enlarged image of figure **c**; **e** fabricated net-like triangular microfluidic channels [47]

It can be easily found that there were a handful of recasts around the ablation area, besides the embossment and scallops that existed on the straight channels which seriously impact the roughness of microfluidic channels. After the etching process, top view optical micrographs of microfluidic channels are shown in Fig. 7.28c, d. Recasts have almost disappeared, and besides the microfluidic channels have become more homogeneous. By comparing the optical micrographs of microfluidic channels after direct writing with post-chemical etching, it can be easily found that the roughness and morphology of microfluidic channels both effectively improve after etching. Meanwhile, after etching, the width of microfluidic channels increased to some extent.

The SEM images of the surface morphology of the sample after etching are shown in Fig. 7.29. The overall profile of the net-like microfluidic channel is shown in Fig. 7.29a. Figure 7.29b is an enlarged image of the microfluidic channels with the focus located on the substrate surface. Figure 7.29c shows the morphology of microfluidic channel when the focus is located at the bottom of the microfluidic channel. It is clear that the microfluidic channel after selective chemical etching still shows relatively high surface roughness, which can be attributed to the fact that the SEM has a greater depth of field compared with an optical microscope, and there is always a certain inclination in internal face of the channel particularly near the surface of the substrate (silver zonal region in Fig. 7.29c). The reason why the silver zonal region existed is that the focus position is fixed in the FLDW process; thus, the spot becomes larger with the increase of machining depth. Furthermore, the areas reached the damage threshold will become smaller when the Gaussian femtosecond laser beam becomes larger, and then the width of the channel will decrease with depth increase of channel. Eventually, the fabricated microfluidic channel presents a slope feature in the direction of microfluidic channel depth.

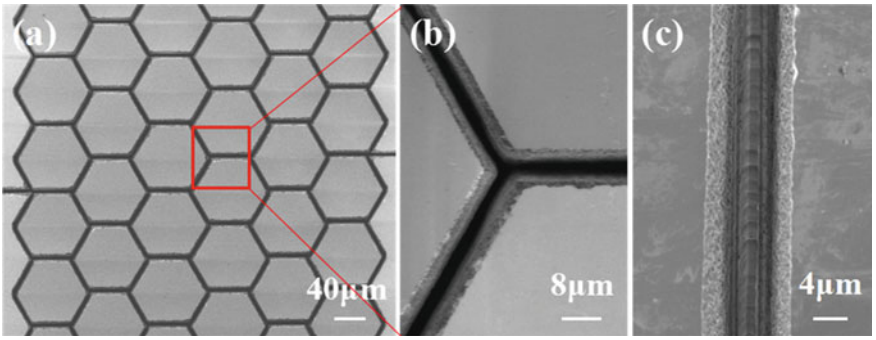

Fig. 7.29 SEM images of net-like microfluidic channels after selective chemical etching. **a** Overall profile; **b** an enlarged image of the microfluidic channel when focus is located on the substrate surface; **c** an enlarged image of the microfluidic channel when focus is located at the bottom of a microfluidic channel [47]

The width of networked microfluidic channel measured at different straight channel is shown in Fig. 7.30, and each data point is the result of the average of five values measured at different positions of the same straight channel. Figure 7.30a is the width of networked microfluidic channel before etching. Obviously, the width of microfluidic channel is about 7.25 μm. Figure 7.30b is the width of networked microfluidic channel after etching, and the width of microfluidic channel is about 8.25 μm. Apparently, etching process increases the width of microfluidic channel about 1 μm. In addition, according to date point and corresponding error distribution, global and regional of microfluidic channel both become more homogeneous after etching.

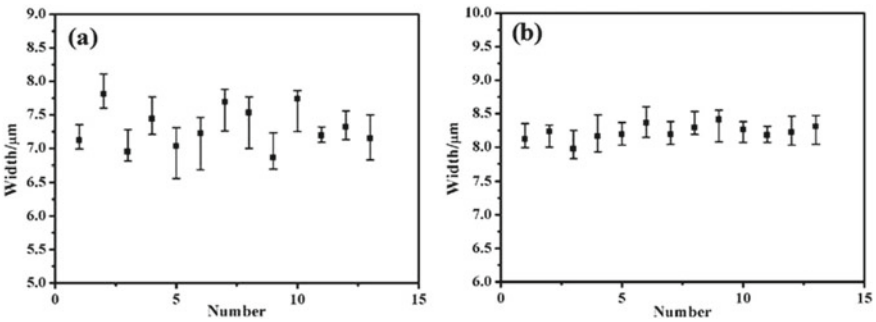

Fig. 7.30 Width of networked microfluidic channel at different straight channel: **a** before etching and **b** after etching [47]

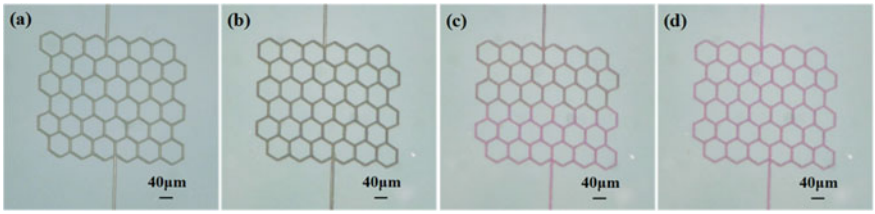

Fig. 7.31 Optical micrographs of net-like microfluidic channels. **a** Fabricated by FLDW on silica substrate after selective chemical etching; **b** covered by a layer of 500 μm thick PDMS film; **c** partially filled with Rh6G ethylene glycol solution; **d** completely filled with Rh6G ethylene glycol solution

7.4.3.2 Liquid Injection Experiment of Hexagonal Net-Like Microchannel

In order to test the flowing characteristics of the semi-occlusive microfluid, the experiment of liquid injection was conducted. The net-like microfluidic channels are fabricated by FLDW on silica substrate. The etched microfluidic channels after selective chemical etching are covered by a 500 μm thin layer of PDMS film. A drop of Rh6G ethylene glycol solution in a pipette drops at the end of the microfluidic channel. The whole process of liquid flow was recorded with an optical microscope with a magnification of 200 times. Some critical moments were captured in the process, as shown in Fig. 7.31.

The mechanism of microfluidic channel fabrication in silica by femtosecond laser writing is that the intense femtosecond laser beam, tightly focused into a confined small area, induces multi-photon absorption within substrate material, leading to material alteration due to an extremely high photon density. Because of the physical and chemical modification associated with multi-photon absorption, the irradiated areas acquire an increased solubility to aqueous hydrofluoric acid [48].

The microfluidic channels were filled with air before injecting Rh6G ethylene glycol solution. As the Rh6G ethylene glycol solution was injected in the microfluidic channels under a capillary force [49], the bottom space of the microfluidic channels was occupied by Rh6G ethylene glycol solution and the air was forced to the top of the microfluidic channels. More liquids in microfluidic channels result in a greater pressure, and more gases dissolve in liquid. So with the increase of Rh6G ethylene glycol solution in microfluidic channels, air gradually dissolves in Rh6G ethylene glycol solution and flows out from the end of microfluidic channels. Eventually, microfluidic channels were completely filled with Rh6G ethylene glycol solution and presented amaranth.

7.5 Applications

Femtosecond lasers are widely used in the fields of ultra-precision processing, microelectronic device manufacturing, medical, high-density information storage, and recording, which are characterized by a small thermal effect, high precision, and wide processing range. These advanced technologies will play an important role in revealing the microscopic world as well as science and technology.

With the development of miniaturized products and application of components, the demand for high-quality micro-holes is increasing in the industry. Among them, high-quality micro-holes are used in aeronautical manufacturing [50], biological devices [51], micro-sensing manufacturing [52, 53], micro-flow devices [54, 55], the new energy field [56], micro-lens [57, 58], ignition target for application to laser-driven inertial confinement fusion (ICF) [59, 60], etc.

During the last two decades, microfluidic systems have attracted considerable attention due to microfluidic system's highly integrating and minimizing. Meanwhile, microfluidic systems can be used for a series of chemical and biological analysis applications [61–63].Microfluidic channels are the key components of a micro-total analysis system (μ-TAS) [64]; thus, the research about them is imminent. So far, photolithography is still a main way of microfluidic channels fabrication which is actually a two-dimensional planar fabrication technology [65, 66]. Therefore, fabrication of three-dimensional (3D) microfluidic structures by photolithography-based techniques requires additional stacking and bonding, leading to an increase in complexity and cost. A main method for achieving 3D microfluidic structures in transparent substrates is to use FLDW as demonstrated by many groups [67, 68]. The microfluidic structures fabricated by FLDW which is a maskless fabrication technique have been found to be comprehensive applications, such as single-cell manipulation, analytics, and label-free protein detection [69], microfluidic waveguide lasers [70], nano-aquarium for dynamic observation of living cells [71], and optofluidic sensors with various functions including refractive index monitoring [72].

References

1. J. Krüger, W. Kautek, Ultrashort pulse-laser interaction with dielectrics and polymers. Adv. Polym. Sci. **168**, 247–290 (2004)
2. R. Le Harzic, N. Huot, E. Audouard, C. Jonin, Comparison of heat-affected zones due to nanosecond and femtosecond laser pulses using transmission electronic microscopy[J]. Appl. Phys. Lett. **80**(21), 3886–3888 (2002)
3. S. Nolte, C. Momma, H. Jacobs, A. Tünnermann, B.N. Chichkov, B. Wellegehausen, H. Welling, Ablation of metals by ultrashort laser pulses[J]. J. Opt. Soc. Am. B **14**(10), 2716–2722 (1999)
4. X. Li, L. Jiang, H.L.T. Cong, Transient localized material properties changes by ultrafast laser-pulse manipulation of electron dynamics in micro/nano manufacturing. Mater. Res. Soc. Symp. Proc. **1365** (2011)
5. H.-B. Sun, S. Kawata, Two-photon laser precision microfabrication and its applications to micro-nano devices and systems[J]. J. Lightwave Technol. **21**(3), 624 (2003)

6. Y. Lawrence Yao, H. Chen, W. Zhang. Time scale effects in laser material removal: a review. Int. J. Adv. Manuf. Technol. **26**(5), 598–608 (2005)
7. B.N. Chichkov, C. Momma, S. Nolte, F. Von Alvensleben, A. Tünnermann, Femtosecond, picosecond and nanosecond laser ablation of solids. Appl. Phys. A **63**(2), 109–115 (1996)
8. J.G. Fujimoto, E.P. Ippen, J.M. Liu, N. Bloembergen, Femtosecond laser interaction with metallic tungsten and nonequilibrium electron and lattice temperatures. Phys. Rev. Lett. **53**(19), 1837–1840 (1984)
9. D.C. Xuan, H.K. Bo, N.C. Chong, Micro-structuring of glass with features less than 100 μm by electrochemical discharge machining. Precis. Eng. **33**(4), 459–465 (2009)
10. E. Kai, K. Mizutani, Micro-drilling of monocrystalline silicon using a cutting tool. Precis. Eng. **26**(3), 263–268 (2002)
11. S.H. Ahn, H.R. Shi, D.K. Choi, N.C. Chong, Electro-chemical micro drilling using ultra short pulses. Precis. Eng. **28**(2), 129–134 (2004)
12. Yi. Zhang, S. Li, G. Chen, J. Mazumder, Experimental observation and simulation of keyhole dynamics during laser drilling. Opt. Laser Technol. **48**(6), 405–414 (2013)
13. P.S. Spinney, D.G. Howitt, R.L. Smith, S.D. Collins, Nanopore formation by low-energy focused electron beam machining. Nanotechnology **21**(37), 2058–2064 (2010)
14. T.H. Maiman, *5–stimulated optical radiation in ruby*. Essent. Lasers 134–136 (1969)
15. P.P. Pronko, S.K. Dutta, J. Squier, J.V. Rudd, D. Du, G. Mourou, Machining of sub-micron holes using a femtosecond laser at 800 nm. Opt. Commun. **114**(1–2), 106–110 (1995)
16. E.N. Glezer, E. Mazur, Ultrafast-laser driven micro-explosions in transparent materials. Appl. Phys. Lett. **71**(7), 882–884 (1997)
17. X. Zhu, A. Yu Naumov, D.M. Villeneuve, P.B. Corkum, Influence of laser parameters and material properties on micro drilling with femtosecond laser pulses. Appl. Phys. A **69**(1), S367–S371 (1999)
18. X. Zhu, D.M. Villeneuve, A. Yu Naumov, S. Nikumb, P.B. Corkum, Experimental study of drilling sub-10 μm holes in thin metal foils with femtosecond laser pulses. Appl. Surf. Sci. **152**(3), 138–148 (1999)
19. Y. Li, K. Itoh, W. Watanabe, K. Yamada, D. Kuroda, J. Nishii, Y. Jiang, Three-dimensional hole drilling of silica glass from the rear surface with femtosecond laser pulses. Opt. Lett. **26**(23), 1912–1914 (2001)
20. N. Muhammad, L. Li, Underwater femtosecond laser micromachining of thin nitinol tubes for medical coronary stent manufacture. Appl. Phys. A **107**(4), 849–861 (2012)
21. T.Y. Choi, D.J. Hwang, C.P. Grigoropoulos (2002) Femtosecond laser induced ablation of crystalline silicon upon double beam irradiation. Appl. Surf. Sci. **197**, 720–725 (2002)
22. Y. Nakata, T. Okada, M. Maeda, Fabrication of dot matrix, comb, and nanowire structures using laser ablation by interfered femtosecond laser beams. Appl. Phys. Lett. **81**(22), 4239–4241 (2002)
23. G. Kamlage, T. Bauer, A. Ostendorf, B.N. Chichkov, Deep drilling of metals by femtosecond laser pulses. Appl. Phys. A **77**(2), 307–310 (2003)
24. Q. Wang, A. Chen, S. Li, H. Qi, Y. Qi, Hu. Zhan, M. Jin, Influence of ambient pressure on the ablation hole in femtosecond laser drilling Cu. Appl. Opt. **54**(27), 8235–8240 (2015)
25. G. Deng, G. Feng, S. Zhou, Experimental and FDTD study of silicon surface morphology induced by femtosecond laser irradiation at a high substrate temperature. Opt. Express **25**(7), 7818–7827 (2017)
26. L.S. Jiao, S.K. Moon, E.Y.K. Ng, H.Y. Zheng, H.S. Son, Influence of substrate heating on hole geometry and spatter area in femtosecond laser drilling of silicon. Appl. Phys. Lett. **104**(18), 181902 (2014)
27. J.H. Klein-Wiele, J. Bekesi, P. Simon, Sub-micron patterning of solid materials with ultraviolet femtosecond pulses. Appl. Phys. A **79**(4), 775–778 (2004)
28. F. He, Y. Cheng, L. Qiao, C. Wang, Z. Xu, K. Sugioka, K. Midorikawa, J. Wu, Two-photon fluorescence excitation with a microlens fabricated on the fused silica chip by femtosecond laser micromachining. Appl. Phys. Lett. **96**(4), 041108-041108-3 (2010)

29. H. Huang, L.-M. Yang, J. Liu, Micro-hole drilling and cutting using femtosecond fiber laser. Opt. Eng. **53**(5), 051513–051513 (2014)
30. Z. Deng, Q. Yang, F. Chen, X. Meng, H. Bian, J. Yong, C. Shan, X. Hou, Fabrication of large-area concave microlens array on silicon by femtosecond laser micromachining. Opt. Lett. **40**(9), 1928–1931 (2015)
31. M.E. Shaheen, J.E. Gagnon, B.J. Fryer, Experimental study on 785 nm femtosecond laser ablation of sapphire in air. Laser Phys. Lett. **12**(6), 066103 (2015)
32. J.M. Liu, Simple technique for measurements of pulsed Gaussian-beam spot sizes. Opt. Lett. **7**(5), 196–198 (1982)
33. D. Gómez, I. Goenaga, On the incubation effect on two thermoplastics when irradiated with ultrashort laser pulses: broadening effects when machining microchannels. Appl. Surf. Sci. **253**(4), 2230–2236 (2006)
34. X. Ni, C. Wang, Z. Wang, M. Hu, Y. Li, L. Chai, The study of nanojoule femtosecond laser ablation on organic glass. Chin. Opt. Lett. **1**(7), 429–431 2003
35. Z. Wang, G. Feng, S. Wang, G. Li, S. Dai, S. Zhou, Improving the quality of femtosecond laser processing micro-hole array by coated with aluminum film on fused silica sheet. Optik **128**, 178–184 (2017)
36. Z. Wang, G. Feng, J. Han, S. Wang, Hu. Ruifeng, G. Li, S. Dai, S. Zhou, Fabrication of microhole arrays on coated silica sheet using femtosecond laser. Opt. Eng. **55**(10), 105101 (2016)
37. V. Maselli, R. Osellame, G. Cerullo, R. Ramponi, P. Laporta, L. Magagnin, P.L. Cavallotti, Fabrication of long microchannels with circular cross section using astigmatically shaped femtosecond laser pulses and chemical etching. Appl. Phys. Lett. **88**(19), 191107 (2006)
38. Y. Bellouard, A. Said, M. Dugan, P. Bado, Fabrication of high-aspect ratio, micro-fluidic channels and tunnels using femtosecond laser pulses and chemical etching. Opt. Exp. **12**(10), 2120–2129 (2004)
39. D.N. Vitek, D.E. Adams, A. Johnson, P.S. Tsai, S. Backus, C.G. Durfee, D. Kleinfeld, J.A. Squier, Temporally focused femtosecond laser pulses for low numerical aperture micromachining through optically transparent materials. Opt. Express **18**(17), 18086–18094 (2010)
40. C. Hnatovsky, R.S. Taylor, E. Simova, P.P. Rajeev, D.M. Rayner, V.R. Bhardwaj, P.B. Corkum, Fabrication of microchannels in glass using focused femtosecond laser radiation and selective chemical etching. Appl. Phys. A **84**(1–2), 47–61 (2006)
41. F. He, Y. Cheng, Z. Xu, Y. Liao, J. Xu, H. Sun, C. Wang, Z. Zhou, K. Sugioka, K. Midorikawa, Direct fabrication of homogeneous microfluidic channels embedded in fused silica using a femtosecond laser. Opt. Lett. **35**(3), 282–284 (2010)
42. K.C. Vishnubhatla, N. Bellini, R. Ramponi, G. Cerullo, R. Osellame, Shape control of microchannels fabricated in fused silica by femtosecond laser irradiation and chemical etching. Opt. Exp. **17**(10), 8685–8695 (2009)
43. S. He, F. Chen, K. Liu, Q. Yang, H. Liu, H. Bian, X. Meng, C. Shan, J. Si, Y. Zhao, Fabrication of three-dimensional helical microchannels with arbitrary length and uniform diameter inside fused silica. Opt. Lett. **37**(18), 3825–3827 (2012)
44. Y. Liao, Y. Ju, L. Zhang, F. He, Q. Zhang, Y. Shen, D. Chen, Y. Cheng, Z. Xu, K. Sugioka, Three-dimensional microfluidic channel with arbitrary length and configuration fabricated inside glass by femtosecond laser direct writing. Opt. Lett. **35**(19), 3225–3227 (2010)
45. S. Wang, G. Feng, S. Zhou, Microsized structures assisted nanostructure formation on ZnSe wafer by femtosecond laser irradiation. Appl. Phys. Lett. **105**, 253110 (2014)
46. S. Wang, G. Feng, Femtosecond laser induced surface structuring on silicon by diffraction-assisted micropatterning. Proc. SPIE **9255**, 925540 (2015)
47. G. Li, G. Feng, S. Wang, H. Zhang, Z. Wang, S. Zhou, Femtosecond laser assisted fabrication of networked semi-occlusive microfluidic channel on fused silica glass surface. **Optik** (2017)
48. S. Kiyama, S. Matsuo, S. Hashimoto, Y. Morihira, Examination of etching agent and etching mechanism on femotosecond laser microfabrication of channels inside vitreous silica substrates†. J. Phys. Chem. C **113**(27), 11560–11566 (2009)

49. M. Gleiche, L.F. Chi, H. Fuchs, Nanoscopic channel lattices with controlled anisotropic wetting. Nature **403**(6766), 173–175 (2000)
50. S. Baheri, S. P. Alavi Tabrizi, B.A. Jubran, Film cooling effectiveness from trenched shaped and compound holes. Heat and Mass Transfer **44**(8), 989–998 (2008)
51. Z. Fei, X. Hu, H.W. Choi, S. Wang, D. Farson, L.J. Lee, Micronozzle array enhanced sandwich electroporation of embryonic stem cells. Anal. Chem. **82**(1), 353–358 (2010)
52. G. Tang, J. Wei, W. Zhou, R. Fan, Wu. Mingyu, Xu. Xiaofeng, Multi-hole plastic optical fiber force sensor based on femtosecond laser micromachining. Chin. Opt. Lett. **12**(9), 090604–090608 (2014)
53. L. Jiang, L. Zhao, S. Wang, J. Yang, H. Xiao, Femtosecond laser fabricated all-optical fiber sensors with ultrahigh refractive index sensitivity: modeling and experiment. Opt. Exp. **19**(18), 17591–17598 (2011)
54. R. An, M.D. Hoffman, M.A. Donoghue, A.J. Hunt, S.C. Jacobson, Water-assisted femtosecond laser machining of electrospray nozzles on glass microfluidic devices. Opt. Exp. **16**(19), 15206–15211 (2008)
55. K. Sugioka, Ya. Cheng, Fabrication of 3d microfluidic structures inside glass by femtosecond laser micromachining. Appl. Phys. A **114**(1), 215–221 (2013)
56. E.H. Lundgren, A.C. Forsman, M.L. Hoppe, K.A. Moreno, A. Nikroo, Fabrication of pressurized 2 mm beryllium targets for ICF experiments. Fusion Sci. Technol. **51**(4), 576–580 (2007)
57. Y. Cheng, H.L. Tsai, K. Sugioka, K. Midorikawa, Fabrication of 3d microoptical lenses in photosensitive glass using femtosecond laser micromachining. Appl. Phys. A **85**(1), 11–14 (2006)
58. Y.-L. Zhang, Q.-D. Chen, H. Xia, H.-B. Sun, Designable 3d nanofabrication by femtosecond laser direct writing. Nano Today **5**(5), 435–448 (2010)
59. T. Wang, Du. Kai, Z. He, X. He, Development of target fabrication for laser-driven inertial confinement fusion at research center of laser fusion. High Power Laser Sci. Eng. **5**, e5 (2017)
60. J.A. Paisner, E.M. Campbell, W.J. Hogan, The national ignition facility project. Fusion Technol. **26**(3), 755–766 (1994)
61. X. Fan, I.M. White, Optofluidic microsystems for chemical and biological analysis. Nature Photon. **5**(10), 591–597 (2011)
62. D. Qin, Y. Xia, J.A. Rogers, R.J. Jackman, X.M. Zhao, G.M. Whitesides, Microsystem technology in chemistry and life science. Top. Curr. Chem. **194**, 1–20 (1999)
63. D.B. Weibel, G.M. Whitesides, Applications of microfluidics in chemical biology. Curr. Opin. Chem. Biol. **10**(6), 584–591 (2006)
64. A. Arora, G. Simone, G.B. Salieb-Beugelaar, J.T. Kim, A. Manz, Latest developments in micro total analysis systems. Anal. Chem. **82**(12), 4830–4847 (2010)
65. Li. Hai-Hua, C. Jian, W. Qing-Kang, Research of photolithography technology based on surface plasmon. Chin. Phys. B **19**(11), 114203 (2010)
66. M.S. Giridhar, K. Seong, A. Schülzgen, P. Khulbe, N. Peyghambarian, M. Mansuripur, Femtosecond pulsed laser micromachining of glass substrates with application to microfluidic devices. Appl. Opt. **43**(23), 4584–4589 (2004)
67. R.R. Gattass, E. Mazur, Femtosecond laser micromachining in transparent materials. Nat. Photon. **2**(4), 219–225 (2008)
68. Xu. Bin-Bin, Y.-L. Zhang, H. Xia, W.-F. Dong, H. Ding, H.-B. Sun, Fabrication and multifunction integration of microfluidic chips by femtosecond laser direct writing. Lab Chip **13**(9), 1677–1690 (2013)
69. W. Hellmich, C. Pelargus, K. Leffhalm, A. Ros, D. Anselmetti, Single cell manipulation, analytics, and label-free protein detection in microfluidic devices for systems nanobiology. Electrophoresis **26**(19), 3689–3696 (2005)
70. D.V. Vezenov, B.T. Mayers, R.S. Conroy, G.M. Whitesides, P.T. Snee, Y. Chan, D.G. Nocera, M.G. Bawendi, A low-threshold, high-efficiency microfluidic waveguide laser. J. Am. Chem. Soc. **127**(25), 8952–8953 (2005)

71. Y. Hanada, K. Sugioka, H. Kawano, I.S. Ishikawa, A. Miyawaki, K. Midorikawa, Nano-aquarium for dynamic observation of living cells fabricated by femtosecond laser direct writing of photostructurable glass. Biomed. Microdev. **10**(3), 403–410 (2008)
72. A. Crespi, Y. Gu, B. Ngamsom, H.J.W.M. Hoekstra, C. Dongre, M. Pollnau, R. Ramponi, H.H. van den Vlekkert, P. Watts, G. Cerullo, Three-dimensional Mach-Zehnder interferometer in a microfluidic chip for spatially-resolved label-free detection. Lab Chip **10**(9), 1167–1173 (2010)

Chapter 8
Femtosecond Laser Direct Writing for 3D Microfluidic Biochip Fabrication

Jian Xu, Felix Sima, and Koji Sugioka

Abstract Microfluidic devices with three-dimensional (3D) configurations and multiple functionalities are exceptionally useful for on-chip construction of artificial biological environments and 3D manipulation of bio-species in microscale spaces. Among the current methods for fabricating these devices, femtosecond (fs) laser direct writing offers several unique advantages, including simple procedures, maskless and resistless processing, and highly flexible 3D fabrication and multifunctional integration in transparent materials such as glass. Direct writing of 3D microstructures having designable functionalities with fs lasers allows the production of microfluidic, microoptic/photonic and microelectronic elements, which can be monolithically integrated into a single glass substrate for the fabrication of high-performance biochips. The principles of fs laser direct writing manufacture of microfluidic, optofluidic, electrofluidic, and ship-in-a-bottle biochips are introduced herein, and practical techniques and recent advances are reviewed. In addition, possible future directions in this field are discussed.

8.1 Introduction

Microfluidic biochips allow high-performance manipulation of small volumes of biological liquids in microscale spaces and have led to new possibilities in biological and medical research [1–3]. Devices such as these having three-dimensional (3D) configurations can provide extraordinary flexibility and functionality with regard to the construction of artificial biological microenvironments, such as organs-on-a-chip

J. Xu · F. Sima · K. Sugioka (✉)
RIKEN Center for Advanced Photonics, RIKEN, Wako, Saitama 351-0198, Japan
e-mail: ksugioka@riken.jp

F. Sima
CETAL, National Institute for Lasers, Plasma and Radiation Physics (INFLPR), Magurele, Ilfov 00175, Romania

J. Xu
School of Physics and Electronic Science, East China Normal University, Shanghai 200241, China

A. Hu (ed.), *Laser Micro-Nano-Manufacturing and 3D Microprinting*, Springer Series in Materials Science 309, https://doi.org/10.1007/978-3-030-59313-1_8

systems [4–6] and the controllable manipulation of bio-species [7–12]. The use of conventional microfabrication methods based on two-dimensional photolithography to produce microfluidic biochips limits the possible 3D geometric designs and also requires highly complex processes. In contrast, femtosecond (fs) laser microfabrication enables the direct fabrication of 3D microstructures inside transparent materials via a maskless, resistless process based on nonlinear multiphoton absorption, and has been shown to represent a superior method of fabricating 3D microfluidic biochips [13–18]. Irradiation of the interior of transparent materials with a focused fs laser beam modifies the physical, chemical, and/or optical properties of the material only within the focal volume of the beam. With translation of the focused laser beam (or the sample, using a high-precision stage), the aforementioned modifications can fabricate a variety of functional microcomponents inside glass substrates, including microoptic/photonic (optical waveguides, optical gratings, etc.), microfluidic (microchannels, microchambers, etc.), and microelectronic (microelectrodes, etc.) elements. In addition, these individual functional elements can be monolithically and seamlessly integrated within a single substrate with high flexibility and compatibility. Consequently, 3D microfluidic biochips fabricated by fs laser direct writing have been applied to diverse applications, including single-cell detection [19] and manipulation [20], functional observation of microorganisms and cells [21–23], cell sorting [24, 25] and cell counting [19, 26, 27], in recent years. In this chapter, we present a comprehensive review of the principles and practical techniques associated with fs laser direct writing, as well as recent advances in the fabrication of 3D microfluidic biochips. Section 8.2 consists of a general introduction of fs laser direct 3D processing, classified according to three different schemes based on volumetric changes at the laser exposed regions. Section 8.3 discusses the fabrication of microfluidic devices by subtractive processing along with the applications of these units. Sections 8.4 and 8.5 detail the monolithic fabrication of optofluidic and electrofluidic biochips, respectively, using various fs laser 3D processing techniques. Section 8.6 presents a new hybrid technique termed “ship-in-a-bottle” integration, by which 3D functionalized polymeric micro/nanocomponents are integrated into 3D glass microfluidic devices. Finally, Sect. 8.7 provides a summary and a discussion of future directions for this technology.

8.2 Femtosecond Laser 3D Processing

Selecting the appropriate processing parameters (such as pulse energy and exposure time) during fs laser irradiation allows localized modification of the interior of transparent materials such as glass, crystals, and polymers, as a result of multiphoton absorption. Coupled with the translation of the focused laser beam (or the sample) in 3D space, these modifications can form 3D functional microstructures, such as optical waveguides (WGs), along the trajectory of the laser beam. In some materials, the chemical or physical properties at the laser-exposed regions can be also modified. Subsequent processing to selectively remove the modified regions by chemical

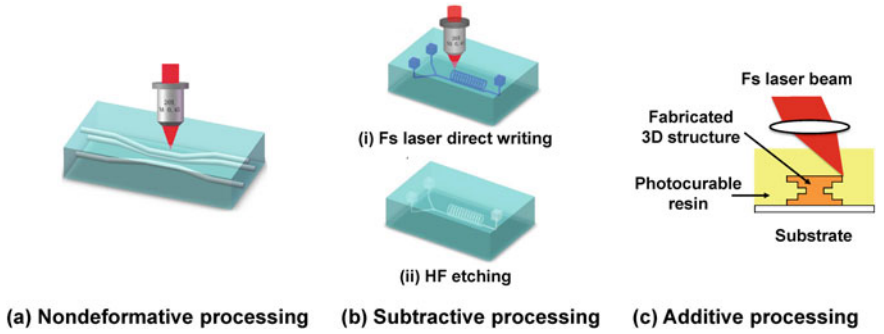

Fig. 8.1 Classification of fs laser 3D processing methods

or physical means can create new 3D microstructures in the bulk material. Multiphoton absorption of the fs laser beam can also induce cross-linking of photocurable resins and negative-photoresists only at the focal volume, enabling the fabrication of solid 3D structures along the beam path. Thus, fs laser 3D processing can potentially accomplish three different tasks, classified as nondeformative, subtractive and additive techniques, as shown in Fig. 8.1.

8.2.1 Nondeformative Processing

The fabrication of functional microstructures without macroscopic volume changes using fs laser 3D processing is defined as nondeformative processing, and is summarized in Fig. 8.1a. A typical nondeformative process is WG writing based on permanent refractive index changes. Since the fs laser inscription of WGs was first reported in 1996 [28], WG fabrication has become one of the most common applications of fs laser 3D processing, with numerous uses in both scientific and engineering fields [29–31]. Compared with conventional fabrication methods, fs laser 3D writing is a very straightforward process for the production of WGs and WG-based photonic devices such as optical splitters and interferometers, since it does not require clean room facilities or multiple procedures. Moreover, the unique 3D processing capabilities resulting from multiphoton absorption allow the fabrication of WGs with significant flexibility at well-controlled depths within the transparent materials, allowing the fabrication of robust devices with small footprints. WGs can be directly created in a wide variety of transparent materials, including glass, crystals, polymers and hydrogels, and has been applied to various microfluidic tasks, including high-sensitivity optofluidic detection [19], optical manipulation [20] and counting of bio-cells [21, 26].

8.2.2 Subtractive Processing

The volumetric removal of laser-exposed regions from transparent materials to form hollow microstructures within bulk glass or polymer specimens via fs laser direct writing is defined as subtractive processing (Fig. 8.1b). Similar to the WG fabrication process, subtractive processing takes advantage of the benefits of laser direct writing to eliminate the need for multiple stacking and bonding during 3D fabrication of microfluidic devices. Currently, two general types of subtractive methods are employed for the creation of 3D microfluidic devices. One is referred to as fs laser-assisted chemical etching (FLAE) or fs laser irradiation followed by chemical etching (FLICE) [32–35]. This method is actually a two-step process (Fig. 8.1b). The initial step involves using focused fs laser irradiation to induce localized modification only over the focal volume within a glass substrate. During this step, direct writing with the focused laser beam can generate modified regions extending from the interior of the sample to the surface in a spatially selective manner. The second step is selective removal of the laser-modified regions by successive chemical etching in diluted hydrofluoric acid (HF) solutions, thus forming hollow 3D structures within the glass. Both photosensitive Foturan glass and fused silica are typically used in conjunction with this approach. The other subtractive method is known as liquid-assisted fs laser 3D drilling (LAFLD), in which a glass substrate immersed in a liquid, such as water, is ablated from the rear surface to the interior by a focused fs laser beam to create hollow 3D microstructures. In this process, the liquid plays an important role by efficiently removing debris from the laser-ablated regions during drilling, potentially producing long channels with complicated 3D structures [36–40]. In contrast to FLAE, this technique can be applied to any material that is transparent to the laser beam. This method can also be used to produce very narrow channels in glass substrates. As an example, channels with diameters of only approximately 700 nm and with arbitrary geometries have been fabricated in fused silica by carefully adjusting the laser pulse energy to near the ablation threshold [40]. However, as the drilling length approaches several hundred micrometers, the debris generated by the ablation process tends to clog the channel, and so in practice, the channel length is limited to approximately 1 cm. The fs laser direct writing ablation of porous glass immersed in water followed by a post-annealing step has been demonstrated as a means of overcoming this limitation [41–43]. In this technique, fs direct writing ablation of porous glass in distilled water is initially performed. During this process, nanopores in the glass form a 3D connective network that allows liquid to flow inside the glass, efficiently removing debris from the ablated regions. Following laser ablation, the sample is annealed to consolidate it into a compact glass. This step completely eliminates the nanopores while retaining the 3D channels inside the glass.

8.2.3 Additive Processing

Additive processing as discussed herein primarily refers to two-photon polymerization (TPP) (Fig. 8.1c) [44–47], which is currently one of the primary approaches to laser-based 3D manufacturing with nanometer-scale precision. Generally, TPP is based on two-photon absorption in a photocurable resin in response to irradiation by a fs laser, which only occurs in the central region of the focal volume at which the laser intensity exceeds the TPP threshold. The width of the solidified region is usually less than the focal spot size and so a fabrication resolution on the order of 100 nm can be achieved when focusing the laser beam with an objective lens having a numerical aperture of approximately 1.4. This technique has been widely applied to the manufacture of 3D functional microdevices for biochip applications, such as micromixers [48, 49], microfilters [49–51], remotely controlled micromachines [52] and cell counters [27]. In addition to TPP, the selective metallization of microchannels [53–56] and fs laser induced photoreduction [57–60] can be also considered as additive processing methods. As an example, using the 3D capabilities of fs laser induced modification, the deposition of thin metal films inside glass channels can be performed in a spatially selective manner [56].

8.3 Fabrication of 3D Microfluidic Devices

Direct writing with a fs laser can prepare microfluidic devices with 3D configurations in many different transparent materials, such as glass [15–18] and polymers [61]. Subtractive processes such as FLAE and LAFLD are typically employed for the fabrication of glass-based devices and, to date, photosensitive Foturan glass and fused silica have been used with FLAE with the greatest degree of success. Foturan is a lithium-aluminosilicate glass doped with trace amounts of silver and cerium ions, and has a relatively low glass transition temperature that allows the fabrication of microfluidic structures with smooth surfaces, in addition to permitting the use of low laser power and higher etching rate. In contrast, fused silica exhibits a wide range optical transmission down to UV ranges, as well as minimal autofluorescence. FLAE processing of Foturan glass by laser-induced photochemical reactions can be described as follows. During fs laser irradiation, silver ions in the focal volume are reduced due to the generation of free electrons by multiphoton absorption, thus precipitating silver atoms. As a result of successive thermal treatment, these precipitated silver atoms fuse together to form silver nanoclusters that act as nuclei for the growth of crystalline lithium metasilicate in the laser-modified regions. The crystallized regions exhibit an etching rate in HF up to 50 times that in the unirradiated areas [34, 62]. Thus, 3D hollow microstructures can be created via the selective chemical etching of the laser-exposed regions using a diluted HF solution. An additional thermal treatment after the etching smooths the etched

surface of the microfluidic structures to ensure sufficient optical quality [63]. Fabrication of hollow microstructures with smooth internal surfaces can also be utilized to obtained 3D buried micro-optical elements such as optical mirrors, microlenses, splitters and fibers in glass substrates [62, 63]. In addition, this technique can form micro-mechanical components, including microvalves and micropumps, to control fluid flow inside microfluidic structures [64]. Unlike FLAE of Foturan, fused silica does not require thermal treatment prior to selective etching. However, it requires higher laser power and longer etching times, since this process relies on photophysical reaction. The etching selectivity of glass substrate has also been enhanced by using a KOH solution instead of HF as the etchant [65, 66]. Obtaining smooth surfaces in fused silica following FLAE is challenging, and several post-thermal treatment methods have been proposed to address this issue, including oxygen/hydrogen flame polishing [67], oven annealing [68], and CO_2 laser annealing [69].

It should be noted that, in many microfluidic biochip applications, control of the cross-sectional shapes of the microchannels is important because it determines the fluid dynamics as well as channel functionality. During fabrication of large channels, the cross-sections can be controlled with significant flexibility by adjusting the multiple laser scanning process in 3D space. However, narrow microchannels fabricated by single scan transverse writing (in which the sample is translated perpendicular to the incident beam) tend to have highly elliptical cross-sections due to elongation of the focal spot in the direction of the incident laser beam. To overcome this problem and thereby fabricate microchannels with circular cross-sections, several beam shaping techniques have been developed, including astigmatic [70], slit [71], crossed [72], and spatiotemporal beam shaping [73].

3D microfluidic devices manufactured by fs laser 3D direct writing have many interesting applications in biological research, such as the determination of microorganism functions, manipulation of bio-cells, and detection and analysis of liquid samples. Hanada et al. reported the FLAE manufacturing of Foturan microchips with embedded 3D hollow microstructures, termed “nano-aquariums,” for the efficient and dynamic observation of living microorganisms and cells in fresh water (Fig. 8.2a) [21]. In this work, a 3D microchannel buried inside a glass substrate was employed to analyze the continuous motion of *Euglena gracilis*. The *Euglena gracilis* were confined to a limited volume in the channel but were still able to move freely, making it much easier to capture images of their movement. These biochips reduced the required observation time by a factor of greater than 10 compared to conventional methods using a Petri dish, and front view images of *Euglena* cell movement were obtained for the first time. In addition, a microchamber integrated with a movable microneedle was used to elucidate the information transmission process in *Pleurosira laevis*. Choudhury et al. demonstrated a 3D mammalian cell separator biochip fabricated by the FLAE of fused silica [24]. Cell sorting in this device was based on differences in the deformability of cell types having varying cytoskeletal architectures. Figure 8.2b illustrates the working principle of the biochip, which consisted of T-junctions formed by two microchannels with narrow constrictions. These constrictions, whose cross-sections were narrower than the average cell size, functioned as filters for sorting. This overall structure enabled accurate, pressure-driven flow

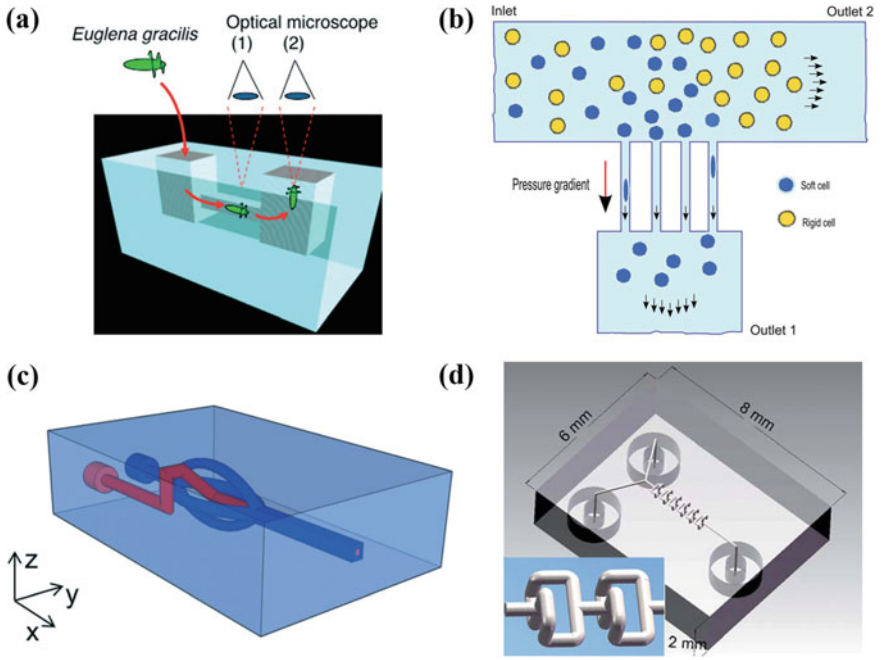

Fig. 8.2 Schematics of 3D microfluidic structures in glass manufactured by fs laser 3D subtractive processing: **a** observation of 3D motion of *Euglena gracilis* [21], **b** cell sorting based on differences in cell deformability [24] (Reproduced with permission from RSC. Copyright 2012, Royal Society of Chemistry), **c** 3D hydrodynamic focusing (red part: sample flow, blue part: sheath flow) [26] (Reproduced with permission from RSC. Copyright 2014, Royal Society of Chemistry), and **d** 3D passive mixing (the inset shows a close-up of two mixing units) [43]

control, resulting in cell deformation that varied with cell characteristics. Following the introduction of a heterogeneous population of cells into this biochip from an inlet, the softer cells were deformed by the pressure gradient maintained across the constrictions and were guided through the constrictions into outlet 1 of the device. The more rigid cells, which were unable to deform sufficiently to pass through the constrictions, flowed toward outlet 2. A T-junction device with 18 constrictions was employed to demonstrate the cell separator biochip concept and achieved throughputs of up to 2800 cells min^{-1} with flow rates as high as 167 $\mu L\ min^{-1}$ using human promyelocytic leukemia cells. After cell sorting, 81% of the population was found to have maintained cellular integrity. Paiè et al. reported 3D hydrodynamic focusing using a microfluidic device fabricated by FLAE of fused silica [26]. As shown in Fig. 8.2c, the input of the device consisted of only two inlets: one for sample flow and the other dividing into four sub-channels to generate sheath flows. Based on the control of the pressure ratio between the sample and the sheath flows, this device allowed ready 3D symmetric flow confinement of cells/particles to a very small area near the center of the focusing channel.

FLAE can be extended to the fabrication of 3D microfluidic devices in polymer substrates. Hanada et al. recently developed a fabrication technique that involves fs laser direct writing followed by wet etching with a dilute fluorinated solvent and annealing to create high-quality 3D microfluidic chips inside a substrate made of the low refractive index fluoric polymer CYTOP [23]. To ensure clear 3D microscopic observations of cell motion near the solid–liquid interface, a minimal mismatch between the refractive indices of the medium and the chip substrate is desirable. The refractive index of CYTOP is 1.34, which is very close to that of water. Thus, these CYTOP microfluidic chips enabled precise observation of the flagellar motion of a *Dinoflagellate* that typically moves in circles near the fluid surface. The CYTOP microfluidic chips are expected to provide opportunities to analyze, in detail, the behavior of various cells near the water–solid interface.

As noted, LAFLD is another method for the manufacture of 3D microfluidic devices [36–40]. FLAE results in some etching of the unexposed regions around the laser-exposed areas due to the limited selectivity of wet chemical etching. In contrast, LAFLD removes only the laser-exposed regions or possibly even smaller zones, since it relies on ablation. Therefore, LAFLD can be applied to the fabrication of 3D nanofluidic devices [40]. Liao et al. demonstrated the rapid fabrication of a passive microfluidic mixer consisting of geometrically complex 3D microchannels via LAFLD of porous glass [43]. This 3D mixer was composed of a Y-shape microchannel embedded 400 μm below the surface of the glass chip in conjunction with a string of mixing units, connected to two opening inlets and one outlet (Fig. 8.2d). Experimental trials demonstrated that two fluorescent dye solutions (fluorescein sodium and Rhodamine B) were well mixed after passing through three mixing units (corresponding to a length of 0.9 mm) over a time span of approximately 10 ms. In contrast, efficient mixing was not achieved in a 1D microfluidic channel over a greater propagation distance of about 1.3 mm. Based on a combination of the threshold effect of fs laser processing using a Gaussian beam and the formation of a periodic nanograting, LAFLD was also used to successfully manufacture buried nanofluidic channels with transverse widths less than 50 nm in porous glass [74]. Integrated devices containing nanofluidic-microfluidic systems with 3D configurations have also been used for the investigation of the stretching of DNA molecules [75].

8.4 Fabrication of Optofluidic Devices

The fs laser 3D process can also integrate certain microoptic/photonic components into microfluidic units to create monolithic optofluidic devices for highly sensitive detection of biochemical species and functional manipulation of living cells. One straightforward strategy involves fs laser direct writing of WGs and WG-based photonic components (such as a Mach-Zehnder interferometer (MZI)) in 3D microfluidic devices fabricated by FLAE. FLAE itself can simultaneously fabricate

certain microoptical components, including optical microlenses and micromirrors in the same microfluidic glass microchip.

Many groups have demonstrated the production of optofluidic devices with integrated WGs for different applications. Kim et al. employed an optofluidic device based on fused silica for single-cell detection [19]. In their study, two optical approaches were used to detect a single red blood cell (RBC) in diluted human blood within a glass microchannel (Fig. 8.3a). In the first technique, the variation in refractive index resulting from the movement of the cell in the channel varied the intensity of WG-delivered He-Ne laser light, thus allowing detection of the cell. The second approach involved detection of fluorescence emission from dyed RBCs excited with Ar ion laser light delivered by the WG. The 5 μm diameter of the microchannels at the neck region was slightly smaller than the size of a RBC (6–8 μm). This configuration

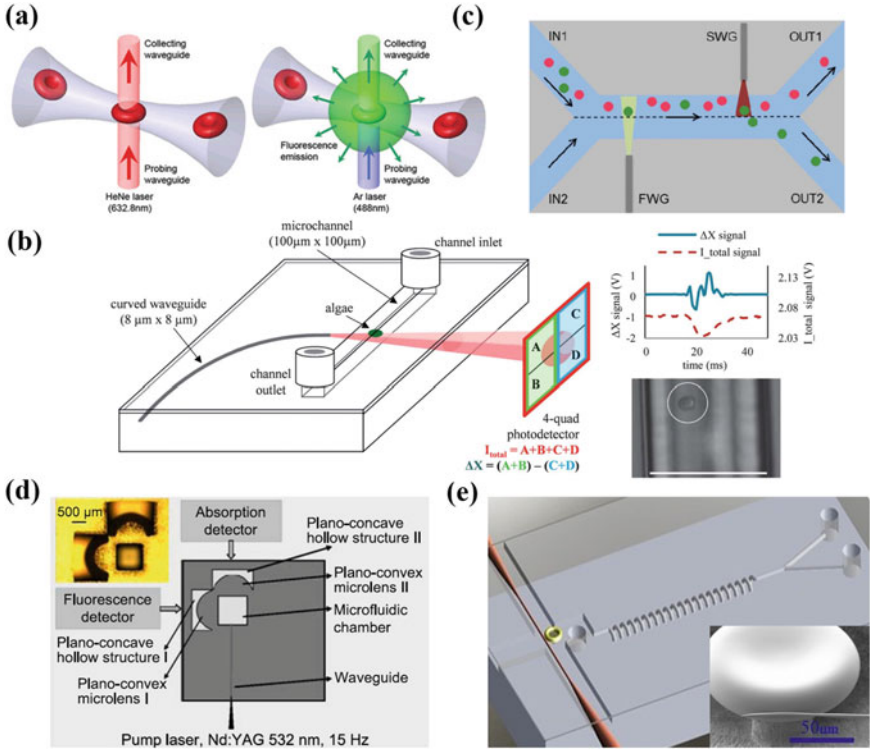

Fig. 8.3 Schematics of 3D optofluidic devices manufactured by fs laser 3D processing, including WG-integrated microfluidic units for **a** single-cell detection [19] (Reproduced with permission from RSC. Copyright 2008, Royal Society of Chemistry), **b** optical classification of algae species [76] (Reproduced with permission from RSC. Copyright 2012, Royal Society of Chemistry), and **c** cell sorting [25] (Reproduced with permission from RSC. Copyright 2012, Royal Society of Chemistry), **d** an integrated microlenses/WG microfluidic device for absorption and fluorescence spectroscopic analyses [77], and **e** WGM microcavity-integrated microfluidic device for highly sensitive analysis of liquid samples [79]

facilitated cell detection to give a sharp, constant, and unambiguous signal because healthy RBCs are able to squeeze through narrow microchannels with diameters as small as 2 μm. Schaap et al. reported the rapid screening, real-time monitoring, and initial classification of algae using a WG-integrated optofluidic device [76]. Rapid identification of algae species is useful for assessing water quality and monitoring adverse events in response to an increase in nutrients such as nitrates or phosphates. The device consisted of a square channel with a cross-section of 100 μm × 100 μm and a 90° curved WG whose end facet was situated perpendicular to the surface of the square channel (Fig. 8.3b). The curvature of the WG prevented uncoupled light from interacting with the photodiode. The radius of curvature was 18 mm, as determined based on laser-induced refractive index change, so as to avoid bending losses. Initially, the sample-containing water was introduced into the channel, after which a laser source delivered by an optical fiber was coupled into the WG to illuminate the entire cross-section of the channel. Finally, the light passing through the channel was analyzed with a four-quadrant photodetector. The movement of a cell or particle through the channel cast a shadow on the photodetector, and the four quadrants of the photodetector generated two specific signals depending on the size and shape of the samples, allowing identification of the species. Using this device, nine different species of algae flowing in the channel could be identified, with an accuracy of 85%. Bragheri et al. performed successive single-cell fluorescence detection and sorting in WG-integrated optofluidic devices based on fused silica [25]. The device design, shown in Fig. 8.3c, was based on an X-shaped channel. Two input channels were merged into a single, center straight channel in which fluorescence detection and sorting were performed in sequence, followed by separation into two output channels. The liquid sample containing cells or particles is introduced from input IN1, while a buffer solution was obtained from input IN2. By appropriately controlling the flow rates of both solutions, a laminar flow was produced such that the entire liquid sample introduced from input IN1 was expelled through output OUT1 along with cells or particles, while the entire buffer solution from the IN2 was sent to OUT2. As a result, the target cells or particles in the sample liquid could be detected by fluorescence measurements using a laser beam delivered via a fluorescence waveguide (FWG). When a specific fluorescence signal from a target cell or particle was detected, the optical force laser beam was switched on to guide the signal to the channel via the sorting waveguide (SWG) with a moderate delay time. As a result, the optical force laser beam pushed the target cell or particle into the buffer solution to eventually sort it into OUT2.

Integration of various other microoptic components, such as microlenses, is possible by FLAE of glass substrates [77, 78]. Wang et al. employed an optofluidic device together with WGs and microlenses for absorption and fluorescence spectroscopic analysis of liquid samples. The device is illustrated in Fig. 8.3d, which shows the long WG connected to a microreservoir formed in Foturan glass [77]. This WG was used to transfer either the fluorescence excitation light from a laser or a broadband beam from a white lamp for absorbance measurements. To avoid divergence of optical signals, two microlenses were also integrated into the device by FLAE, both beside and behind the microreservoir. In this case, the microreservoir

and the microlenses were fabricated simultaneously using a single FLAE procedure, after which the WG was integrated by fs laser direct writing. This design significantly enhanced the sensitivity of both fluorescence and absorption measurements. Whispering-gallery-mode (WGM) microcavities are considered to show exceptional promise with regard to high-sensitivity sensing applications due to their very high Q factors and small mode volumes. Song et al. employed FLAE of fused silica to fabricate a 3D optofluidic device in which a microfluidic structure and an optical microresonator with a Q-factor of 3.21×10^5 in air were monolithically integrated [79]. The fabrication process for this optofluidic device consisted of three main steps: (1) FLAE of fused silica to create a 3D microfluidic channel embedded in glass and a microdisk structure at the outlet of the microchannel; (2) selective reflow of the silica disk structure by CO_2 laser irradiation to create a microresonator with a high Q-factor; and (3) assembly of a fiber taper to the resonator by CO_2 laser welding. The performance of the device (Fig. 8.3e) was demonstrated by measuring the refractive index of purified water containing a very low concentration of NaCl, and a detection limit of approximately 1.2×10^{-4} RIU (refractive index units) was determined.

Another important application of optofluidic devices fabricated by fs laser 3D processing is the investigation of the gliding mechanism of *Phormidium* moving toward a seedling root. *Phormidium* gliding is a useful means of accelerating vegetable growth through the formation of endosymbiotic associations. For this investigation, Hanada et al. first fabricated a T-shaped microfluidic channel formed in Foturan glass having three reservoirs at its ends [22]. When the *Phormidium* was introduced into one reservoir and a seedling root into another, the *Phormidium* was found to always glide toward the seedling rather than toward a third, empty reservoir. In contrast, filling the third reservoir with carbonic water varied the direction of movement of the *Phormidium* depending on the carbonic concentration. Additionally, at a critical CO_2 concentration, the cyanobacterium glided neither toward the seedling root nor toward the carbonic water, indicating that CO_2 secreted by respiration of the root is a possible attractant for the microorganism. To confirm this hypothesis and determine the quantity of CO_2 secreted by the seedling roots, an optofluidic device based on integration of a straight microfluidic channel and WGs were subsequently fabricated. Figure 8.4a shows the schematic of the system. After fabricating a channel in the Foturan glass by FLAE, two WGs that intersected the center of the microfluidic channel were written. The channel was filled with water containing a pH indicator (bromothymol blue (BTB) solution) and white light from a halogen lamp was coupled to the entrance facet of WG I by an objective lens. The white light transmitted by WG I passed through the microchannel, which was filled with a liquid sample, and was then coupled into WG II. The light transmitted by WG II was coupled into a spectrometer by another objective lens to allow collection of the absorption spectrum (Fig. 8.4a). The absorbance was calculated by subtracting the spectrum obtained with the sample in the microfluidic channel from that observed without the sample. The green line in Fig. 8.4b indicates the absorption spectrum of the water containing the BTB solution, having an intense absorption peak at approximately 620 nm. The intensity of this peak decreased with increasing CO_2 concentration in the water due to the concurrent change in pH. The spectrum of

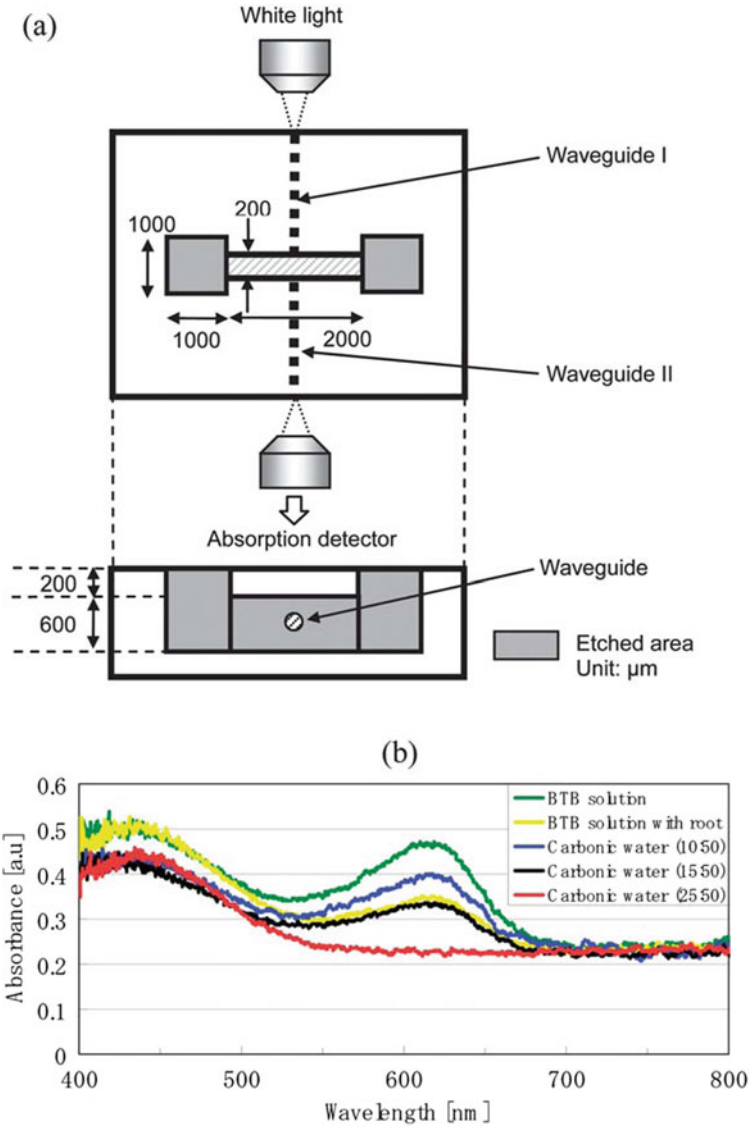

Fig. 8.4 **a** Schematic of a microfluidic chip integrated with a WG for identifying the attractant that induces *Phormidium* gliding, and **b** absorption spectra of water containing a BTB solution (green line), water with a seedling root (yellow line), and carbonic water with varying CO_2 concentrations (blue line: 10 ml CO_2 in 50 ml H_2O, black line: 15 ml CO_2 in 50 ml H_2O, red line: 25 ml CO_2 in 50 ml H_2O) [22]

water containing the seedling root (the yellow line) is comparable to that obtained from 50 ml water mixed with 15 ml CO_2 (the black line). This result implies that the CO_2 concentration generated by root respiration was comparable to that of the carbonic water used in this experiment (15 ml CO_2 in 50 ml H_2O). Interestingly, this CO_2 concentration equaled the critical concentration at which the *Phormidium* did not glide toward the seedling root or the carbonic water in the T-shaped microfluidic channel, confirming that CO_2 is the sole attractant for the *Phormidium.*

8.5 Fabrication of Electrofluidic Devices

Electrical control of biological samples in microfluidic systems is of importance for many biochip applications, such as cell sorting, dielectric measurements of cell properties, and cell manipulation [80, 81]. To this end, the integration of microelectric components into 3D microfluidic devices is highly desirable as a means of fabricating electrofluidic devices. Considering that microfluidic substrates are typically not conductive, one key technology for microelectronic integration is spatially selective metallization of microfluidic structures. Selective metallization of the internal walls of microfluidic structures is possible via fs laser-assisted electroless metal plating. This process consists of two main steps: 3D spatially selective modification by fs laser direct writing and selective metal deposition on the laser-modified regions. Catalytic patterning with metals such as palladium or silver via fs laser irradiation allows selective metallization of the surfaces of many insulators (including fused silica and crystalline lithium niobate) as a result of selective metal deposition [82–86]. It has also been demonstrated that areas in Foturan glass irradiated with a fs laser can be selectively metallized using a commercially-available electroless plating solution without prior catalytic patterning (Fig. 8.5). The associated mechanism may rely on the increased roughness obtained by fs laser-ablation, which induces an anchor effect that selectively adheres metal atoms from the plating solutions [54, 56, 87].

Electrofluidic devices have been produced by first preparing 3D microfluidic structures in Foturan glass using FLAE (Fig. 8.5a). The internal walls of these structures are made highly smooth by an additional thermal treatment following wet chemical etching. Spatially selective metallization of the 3D microfluidic structures is subsequently performed via a two-step process [56, 88–90]. The first step involves fs laser direct writing ablation to create modified patterns at desired positions within the structures, which may include glass chip surfaces and the interior or sidewalls of the microchannels (Fig. 8.5b). This ablation generates the necessary roughness in the laser-exposed regions, enabling the selective deposition of metal structures in these regions by subsequent electroless metal plating due to the anchor effect. The main role of the laser ablation is to homogeneously roughen the glass surface in a highly selective, well-controlled manner at various positions within the 3D structure. However, even careful optimization of laser ablation parameters such as the pulse energy, writing speed, and writing scheme, cannot prevent the generation of

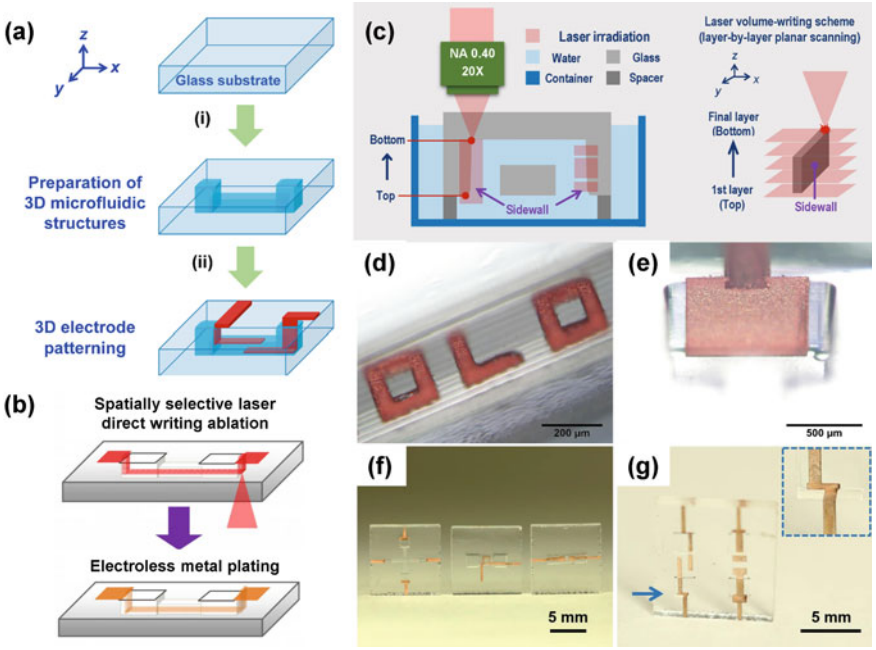

Fig. 8.5 Schematic diagrams of **a** the procedure for the manufacture of electrofluidic devices in glass, **b** spatially selective metallization of glass channels, and **c** water-assisted fs laser ablation of channel sidewalls. **d** 45° and **e** 60° tilted optical micrographs of a metal pattern and an electrode pad formed on sidewall surfaces after electroless copper plating, respectively. **f** Top-view and **g** titled-view photographs of electrode-integrated glass channels with different configurations. The inset shows a close-up of the sidewall indicated by the arrow in **g** [56, 88–90]

microcracks due to the inhomogeneous distribution of induced stress or the redeposition of debris on and around the ablated regions, both of which can degrade the metal patterning produced during the electroless plating step. The introduction of water to the ablation site has been suggested as a means of mitigating this problem (Fig. 8.5c) [88]. In the case of volumetric writing performed by repeating layer-by-layer scanning from the top to the bottom of the sidewalls to produce ablation, the introduction of water during irradiation was found to effectively remove the ablation debris. This allowed the fabrication of crack-free, edged, well-defined structures in a spatially selective manner. The presence of water also compensates the refractive index mismatch at the interface between air and glass, thus improving the focusing geometry during sidewall ablation. For these reasons, water-assisted fs laser ablation greatly improves the ablation quality while ensuring that the ablated surfaces are modified to the extent necessary for selective metallization (Fig. 8.5d, e). An initial application of electroless copper plating is necessary to enhance the adhesion of thin metal films to the glass surface. Subsequently, electroless gold plating is performed to cover the copper films in order to enhance both the chemical stability and biocompatibility of the metal surfaces [91, 92]. In general, the geometric aspects of plated

metals, such as the line width and thickness, can be preciously controlled by tuning the ablation and electroless plating parameters to fit the designs of the desired microelectric elements. This flexible metallization of 3D microchannels may provide a new means for producing precision electric field patterns in microfluidics and thus could have potential uses in many biochip applications. Figure 8.5f, g present some examples of electrode-integrated glass channels fabricated by this technique, in which uniform, continuous metal pads have been selectively deposited from the interior and the sidewalls to the exterior of the channels.

Using the technique described above, electrofluidic devices with different configurations consisting of microfluidic channels integrated with pairs of electrically isolated electrodes were successfully fabricated. These units were subsequently applied to orient the movement direction of *Euglena* cells. To test the electro-orientation performance, *Euglena* cells were introduced into the devices as shown in Fig. 8.6. Figure 8.6a, c, g demonstrate the random motion of the *Euglena* cells in the channels in the absence of an electric field between the integrated microelectrodes. It is also evident that the application of a proper AC electric field dramatically changed the movement of the cells to a bidirectional orientation along the field direction (Fig. 8.6b). This controllable alignment resulted from the interaction between the dipole moments induced in the cells by the electric field and the field itself. As soon as the electric field was turned off, movement of the microorganisms became random again. Electro-orientation in channels using this type of device has been shown to be both reproducible and nondestructive [56, 89]. The single pair of opposing electrodes shown in Fig. 8.6b allowed the 1D orientation of cells along the x-axis. In addition, a four-electrode arrangement with the electrodes at right angles on the base of the channel successfully demonstrated 2D electro-orientation of cell movement in the x–y plane upon varying the direction of the field generated in the microscale space (Fig. 8.6d–f). Furthermore, the swimming direction of the cells could be oriented along the z-direction by using electrodes with square outlines formed at the top and bottom of the channel (Fig. 8.6h). This electrofluidic device allowed the continuous observation of the motion of 45 *Euglena* cells swimming along the z-direction over a span of one minute within an imaging area of approximately 160×120 μm. Due to the electro-orientation effect, the average time required for the continuous observation of five cells swimming along the z-direction was reduced by a factor of approximately 43 as compared with the necessary time interval with no electric field [89]. Although the transparent window at the center of the electrodes was not coated with metal, the surrounding electrode patterns were able to generate sufficiently high electric field intensities for z-directional orientation. This type of manipulation enabled the ready observation of the *Euglena* cells from the front side, potentially providing new insights into the functions of such microorganisms.

Electrotaxis (electro-tactic control) is another interesting phenomenon that can be applied to the electromanipulation of cells. In this process, the locomotion of biological samples towards the cathode or anode is induced under an applied DC electric field. *In-situ* control of electrotaxis in a chip allows precise positioning and manipulation of biological samples. To achieve this, a new type of electrofluidic devices with integrated vertical electrodes on the sidewalls having aspect ratios as

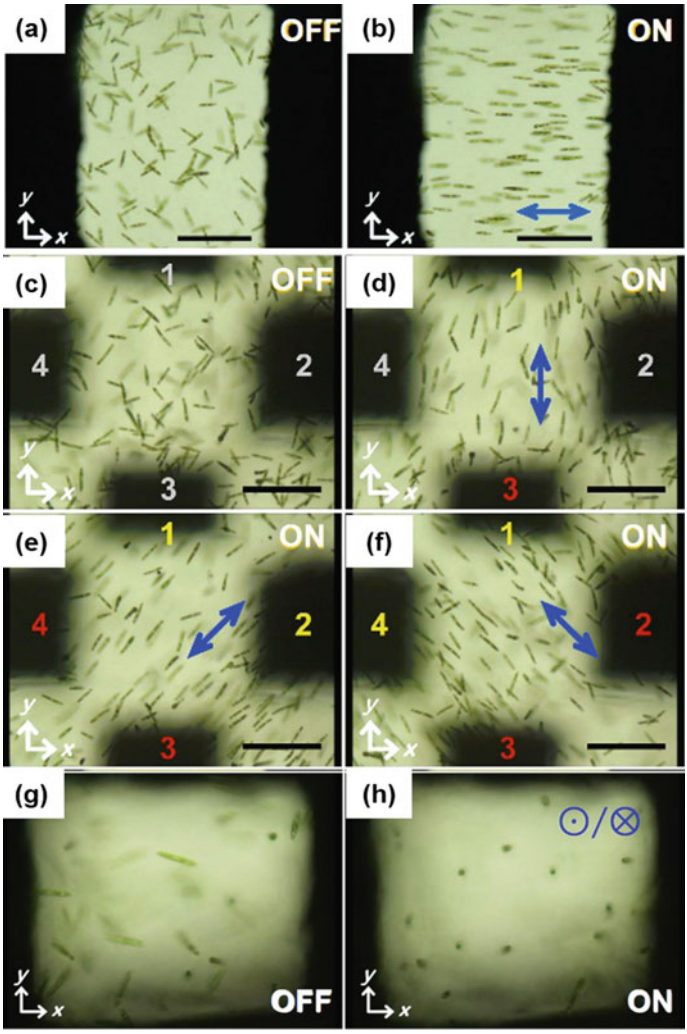

Fig. 8.6 On-chip electro-orientation of *Euglena* cells in 3D space: **a**, **b** a pair of electrodes formed at the bottom of a channel, **c**–**f** four electrodes opposing one other formed at the bottom of a channel, and **g**, **h** electrodes with square outlines formed at the top and bottom of a channel. Black areas correspond to the electrodes. "ON" and "OFF" refer to electric power. The numbers in gray in **c**, **d** indicate that no AC voltage was applied. The numbers in yellow and red in **d**–**f** represent opposite polarities. The arrows indicate the direction of the electric field. The scale bars in **a**–**f** indicate 200 μm. The width of the observation window in **g**, **h** is approximately 500 μm [89, 90]

high as 50 was fabricated using the techniques discussed above [88]. These units were applied to *in-situ* manipulation of the nematode worm *C. elegans* based on electrotaxis. The device is presented in Fig. 8.7, which shows the two metal pads formed on the glass surface and the walls of two open reservoirs connected by an embedded microchannel. The ability of an applied electric force to modify the random omnidirectional swimming of a worm in the channel was assessed by examining the swimming direction of *C. elegans* while switching the polarity of the electric field in the channel. When a DC electric field (−3.5 V/cm) was applied between the two electrodes on the sidewalls (Fig. 8.7b), the *C. elegans* in the microchannel swam from right to left (with the electric field) as indicated by the arrow on the left of

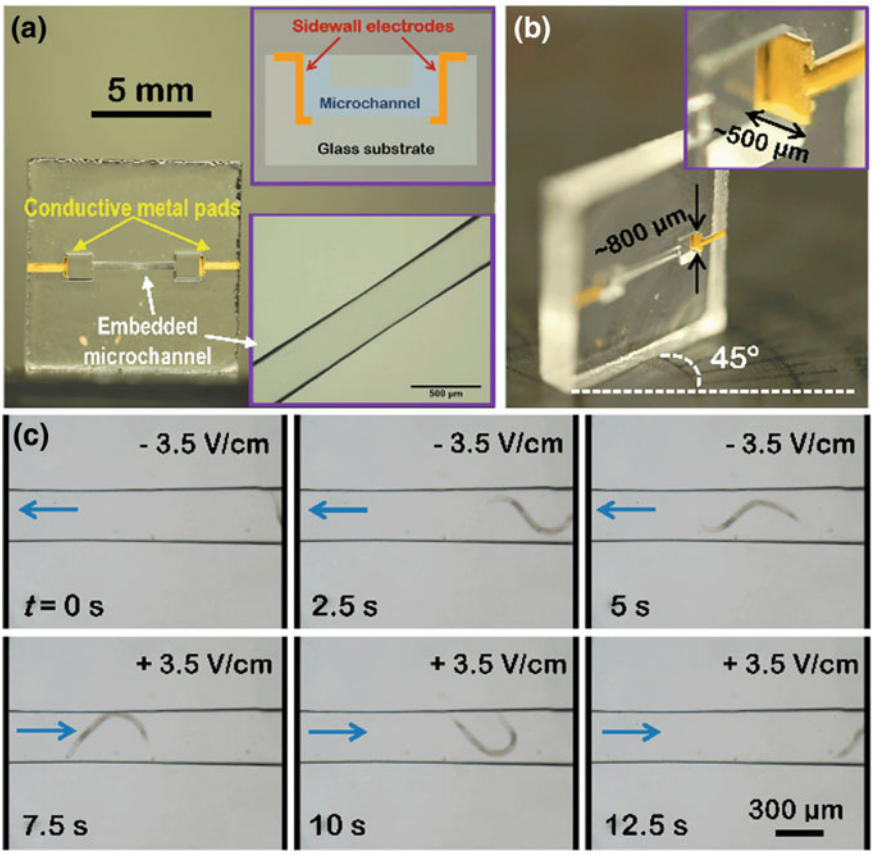

Fig. 8.7 On-chip electro-taxis: **a** a photograph image of the fabricated electrofluidic device (top and bottom insets show a schematic of the device structure and an image of the channel, respectively), **b** a photograph image of the sidewall electrode in **a** taken at an angle of 45° (inset shows a close-up of the electrode surface), and **c** observations of a *C. elegans* worm changing its direction in the channel shown in **a** when the polarity of the electric field is switched at 7.5 s. The arrow in each *in-situ* snapshot image indicates the direction of the electric field [88]

Fig. 8.7c ($t = 0$ s). After approximately 7.5 s, the polarity of the electric field was switched (lower left image in Fig. 8.7c). The worm was then observed to rotate its body and swim from left to right in the new direction of the electric field, clearly demonstrating controllable electrotaxis. Furthermore, the worm continued to move to the right at 12.5 s because the electric field remained in that direction.

8.6 Ship-in-a-Bottle Biochips

Ship-in-a-bottle integration, in which TPP is carried out in a 3D glass microfluidic device to integrate 3D polymeric micro- and nanocomponents, is a novel technique that can be used to enhance the functionality of microfluidic biochips. The devices fabricated by this technique are also known as ship-in-a-bottle biochips [27, 49, 93]. The direct integration of 3D porous filters with a pore size of approximately 1 μm into a sealed planar channel within a commercial microfluidic chip has been achieved by TPP, allowing on-chip separation of nanoscale elements (such as dye molecules) from microscale elements (polystyrene beads) [51]. The filter was fabricated at the intersection of two channels in order to control the flow passing through the filter (Fig. 8.8). A dispersion of microbeads in either buffered or fluorescent solutions was used to demonstrate the ability of the filter to stop the passage of microscale elements while allowing the solution to flow freely. In these trials, a test sample was injected from well 1 (Fig. 8.8a) and a portion of this solution was filtered to well 4, while the remainder was directed to wells 2 and 3. Tests with a suspension of 3 μm polystyrene spheres in a Rhodamine 6G solution showed that 100% of the spheres were stopped and that the fluorescent molecules passed through the filter.

A combination of FLAE and TPP, known as hybrid subtractive and additive fs laser 3D processing, can realize the fabrication of ship-in-a-bottle biochips using a single fs laser micromachining workstation. FLAE was developed as a subtractive laser processing method for the creation of 3D microfluidic structures inside

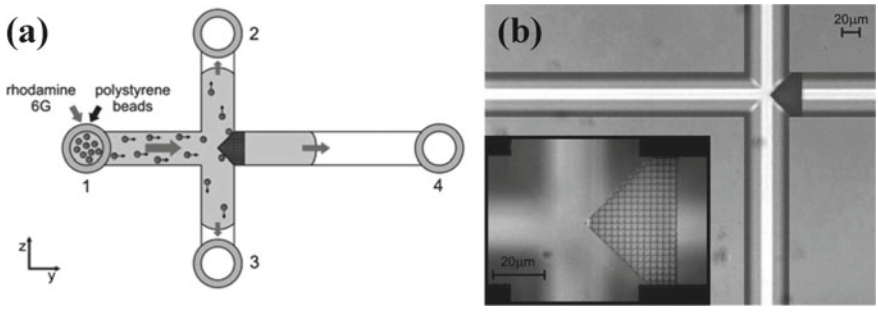

Fig. 8.8 **a** Schematic of a 3D filter in a cross-channel junction and **b** a micrograph of the filter in the channel junction (inset shows a close-up view of the filter) [51]. Reproduced with permission from RSC. Copyright 2012, Royal Society of Chemistry

glass substrates. In contrast, TPP in conjunction with negative-tone photoresists is categorized as an additive laser process and is capable of producing 3D micro- and nanopatterns in biocompatible polymers. This hybrid technique exploits the specific advantages of both processes while avoiding some of the drawbacks of each. Both glass and polymers are transparent materials with good potential for fabrication of functional biochips. This hybrid approach provides both scale-down and scale-up characteristics that allow ready manipulation of the assembled device in conjunction with increased analytical sensitivity by reducing the dimensions of fabricated structures in microfluidic devices. The dimensions of the structures can actually be reduced to below those of a single cell, thus allowing individual cells to be examined and manipulated inside a glass channel. These biochips can therefore permit the exploration of phenomena at cellular levels with sub-micron resolution, representing an excellent opportunity to obtain additional insights into biological processes. Transparent microfluidic and optofluidic biochips are achievable via the integration of microoptical polymer components to build suitable 3D microenvironments for the study of living microorganisms and to improve cell detection or sorting. In addition, there is significant potential for the manufacture of biomimetic structures tailored for specific cellular analyses.

Figure 8.9 illustrates hybrid subtractive and additive fs laser 3D processing [49, 94]. This technique begins with FLAE of a glass substrate to form 3D microfluidic structures. TPP using a negative-tone photoresist (such as SU-8) is then applied inside the 3D glass channels. The polymer being integrated should possess the appropriate mechanical strength, aspect ratio, chemical resistance, and biocompatibility. The same laser setup can be employed for both the FLAE and TPP steps.

Various functional biochips have been successfully fabricated by this hybrid technique. One such device is a multi-functional filter-mixer consisting of two filtering sheets placed at the inlet and outlet of a passive mixer grown inside a microfluidic glass channel [49]. A layered crossing tube configuration was employed in order to guide the flow and allow rapid mixing over a short channel distance, and integration inside a Y-shape closed glass channel was found to lead to highly efficient mixing

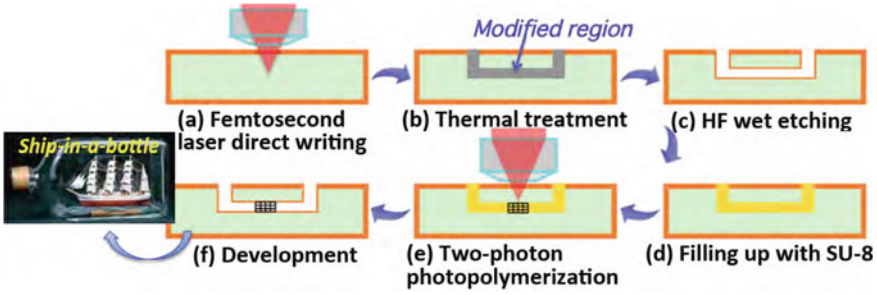

Fig. 8.9 Schematic of hybrid subtractive and additive fs laser 3D processing for ship-in-a-bottle biochip fabrication: **a–c** FLAE of Foturan glass; and **d–f** TPP of an SU-8 photoresist inside a channel [49, 94]

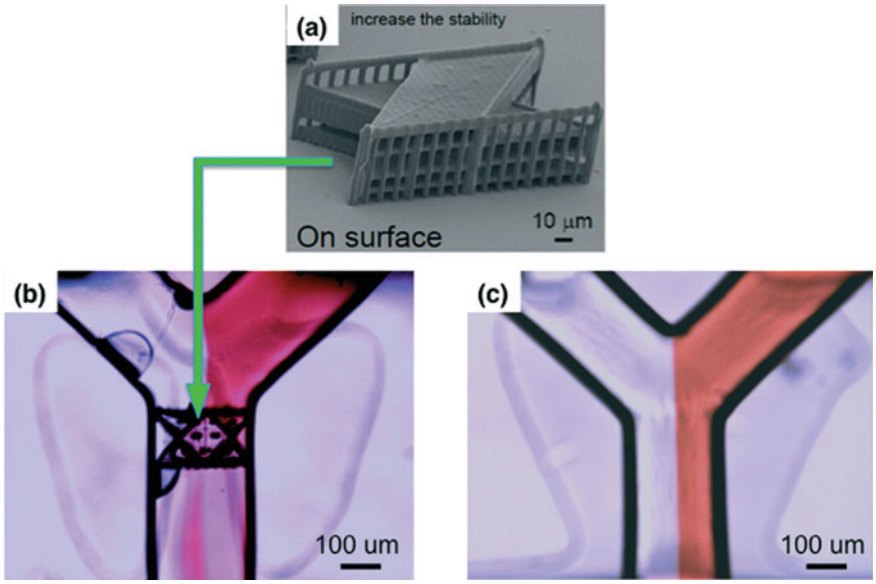

Fig. 8.10 **a** 3D polymeric microcomponents fabricated by TPP for efficient mixing of fluids, showing a comparison of the mixing efficiencies of Y-shaped microfluidic channels **b** with and **c** without integrated microcomponents [49]

of two fluids, with an efficiency of approximately 87% (Fig. 8.10). This hybrid techniques has also been employed to produce an optofluidic device consisting of a 3D microlens array and center pass units. This device was used to count *Euglena* cells, with a 100% success rate [93], by parallel monitoring of intensity changes induced by cells swimming through the center pass units and above the microlenses.

The hybrid method has also been applied to develop biomimetic environments in closed 3D glass microfluidic channels [95]. Sinusoidal polymeric ridges with very high aspect ratios and periodicities that can be modulated have previously been assessed as an approach to cellular studies. In such systems, a dynamic fluid flow in association with pattern sizes reduced to the level at which cells are responsive would mimic a biological environment. Varying the periodicity and amplitude spaces between sinusoidal patterns would also be expected to induce controllable cell migration. Thus, one can foresee various interesting applications for cell manipulation, such as guidance and orientation. Single cell trapping and analysis within small areas are also expected to be possible using such biochips. Another application reported for 3D biomimetic environments with resolutions and hierarchies similar to those of the organism in the biochip is the evaluation of cancer cell migration potentials [96]. In this work, the subtractive FLAE process was employed to fabricate a microchannel with a length of 1 mm and a width of 165 μm inside Foturan glass (Fig. 8.11a–c). Subsequent to this, two polymeric microchannels (40 μm long, 2.5 μm high and 7.5 and 2.7 μm wide), which were narrower than the cancer cell, were introduced inside

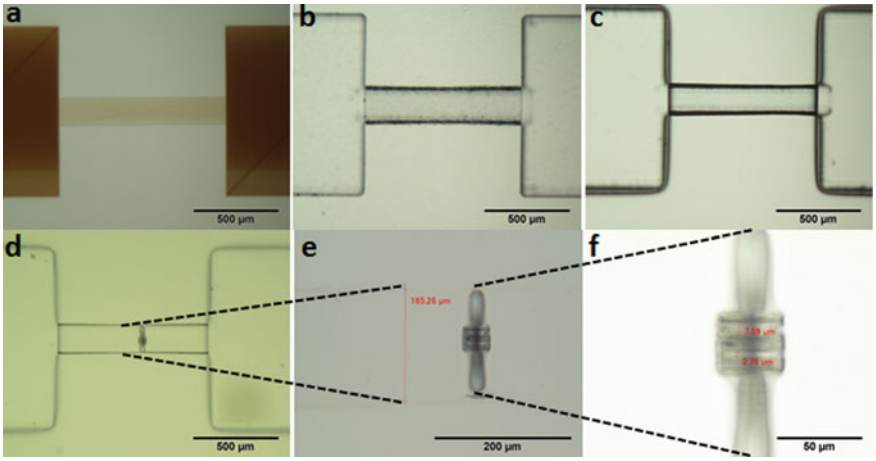

Fig. 8.11 Optical micrographs of a ship-in-a-bottle biochip at different fabrication steps by FLAE and TPP: **a** fs laser irradiation and subsequent initial thermal treatment, **b** chemical etching in a diluted HF solution, **c** smoothing by an additional thermal treatment, and **d**–**f** TPP with an SU-8 photoresist to integrate 3D polymer channel structures into the glass microchannel, **e** and **f** show magnifications of the glass channel/polymeric structures from **d** and the polymeric structures inside the channel, respectively [96]

the glass microchannel via additive TPP using an SU-8 photoresist (Fig. 8.11d–f). The polymeric microchannel supporting scaffold was anchored to the walls of the glass channel to ensure its stability. This scaffold also functioned as a fluid filter to produce a biomimetic dynamic gradient of specific substances and so induce migration of the cancer cell. Consequently, the narrow polymer channels created a biomimetic 3D microenvironment allowing the evaluation of cancer cell migration.

8.7 Summary

In this chapter, we have reviewed the principles and methodology associated with fs laser 3D processing of microfluidic biochips, and have considered recent advances in this field. At present, the merits of fs laser microfabrication have been widely recognized due to the versatility of this technique during materials processing and its capability for innovative device fabrication. Although there have been many achievements in terms of 3D fabrication and multifunctional integration over the past decade, the application of this technique to microfluidic biochip fabrication is still in its infancy and many new directions remain to be explored. The use of new and innovative designs during fs laser direct writing, such as by manipulation of the laser beam, should be evaluated as a means of increasing the functionality of biochips as well as process efficiency. In this regard, the development of new beam shaping techniques [97–99] promises to improve the fabrication quality, 3D spatial

resolution, and speed. Secondly, the introduction of new functional materials into fs laser 3D processing will also increase the possibilities for functionalization of biochips and so increase the range of applications. Lastly, the miniaturization and multi-functionalization of these microsystems, such as in the case of 3D multilayered and multifunctional devices, will ultimately enhance the throughput, sensitivity, and performance of the fabricated biochips. Also, the integration of the present fs laser 3D processing method and other advanced micro/nanoprocessing techniques may lead to the development of novel microfluidic biochips, such as organs-on-chips [4–6], for emerging applications. Currently, fs laser 3D processing is already an attractive technique for constructing tailor-made biomedical devices for fundamental research. Further development and refinements will also make it possible to use this technique for mass production.

References

1. G.M. Whitesides, The origins and the future of microfluidics. Nature **442**, 368–373 (2006)
2. L.Y. Yeo, H.C. Chang, P.P.Y. Chan et al., Microfluidic devices for bioapplications. Small **7**, 12–48 (2011)
3. E.K. Sackmann, A.L. Fulton, D.J. Beebe, The present and future role of microfluidics in biomedical research. Nature **507**, 181–189 (2014)
4. D. Huh, G.A. Hamilton, D.E. Ingber, From 3D cell culture to organs-on-chips. Trends Cell Biol. **21**, 745–754 (2011)
5. J.D. Caplin, N.G. Granados, M.R. James et al., Microfluidic organ-on-a-chip technology for advancement of drug development and toxicology. Adv. Healthc. Mater. **4**, 1426–1450 (2015)
6. A. Balijepalli, V. Sivaramakrishan, Organs-on-chips: research and commercial perspectives. Drug Discov. Today **22**, 397–403 (2017)
7. J. El-Ali, P.K. Sorger, K.F. Jensen, Cells on chips. Nature **442**, 403–411 (2006)
8. H. Yun, K. Kim, W.G. Lee, Cell manipulation in microfluidics. Biofabrication **5**, 022001 (2013)
9. X. Mu, W. Zheng, J. Sun et al., Microfluidics for manipulating cells. Small **9**, 9–21 (2013)
10. A.K. Au, W. Huynh, L.F. Horowitz et al., 3D-printed microfluidics. Angew. Chem. Int. Ed. **55**, 3862–3881 (2016)
11. S. Waheed, J.M. Cabot, N.P. Macdonald et al., 3D printed microfluidic devices: enablers and barriers. Lab Chip **16**, 1993–2013 (2016)
12. C. Chen, B.T. Mehl, A.S. Munshi et al., 3D-printed microfluidic devices: fabrication, advantages and limitations—a mini review. Anal. Methods **8**, 6005–6012 (2016)
13. K. Itoh, W. Watanabe, S. Nolte et al., Ultrafast processes for bulk modification of transparent materials. MRS Bull. **31**, 620–625 (2006)
14. R.R. Gattass, E. Mazur, Femtosecond laser micromachining in transparent materials. Nat. Photonics **2**, 219–225 (2008)
15. K. Sugioka, Y. Cheng, Femtosecond laser processing for optofluidic fabrication. Lab Chip **12**, 3576–3589 (2012)
16. K. Sugioka, J. Xu, D. Wu et al., Femtosecond laser 3D micromachining: a powerful tool for the fabrication of microfluidic, optofluidic, and electrofluidic devices based on glass. Lab Chip **14**, 3447–3458 (2014)
17. R. Osellame, H.J.W.M. Hoekstra, G. Cerullo et al., Femtosecond laser microstructuring: an enabling tool for optofluidic lab-on-chips. Laser Photonics Rev. **5**, 442–463 (2011)
18. B. Xu, Y. Zhang, H. Xia et al., Fabrication and multifunction integration of microfluidic chips by femtosecond laser direct writing. Lab Chip **13**, 1677–1690 (2013)

19. M. Kim, D.J. Hwang, H. Jeon et al., Single cell detection using a glass-based optofluidic device fabricated by femtosecond laser pulses. Lab Chip **9**, 311–318 (2009)
20. F. Bragheri, L. Ferrara, N. Bellini et al., Optofluidic chip for single cell trapping and stretching fabricated by a femtosecond laser. J. Biophotonics **3**, 234–243 (2010)
21. Y. Hanada, K. Sugioka, H. Kawano et al., Nano-aquarium for dynamic observation of living cells fabricated by femtosecond laser direct writing of photostructurable glass. Biomed. Microdevices **10**, 403–410 (2008)
22. Y. Hanada, K. Sugioka, S. Ishikawa et al., 3D microfluidic chips with integrated functional microelements fabricated by a femtosecond laser for studying the gliding mechanism of cyanobacteria. Lab Chip **11**, 2109–2115 (2011)
23. Y. Hanada, T. Ogawa, K. Koike et al., Making the invisible visible: a microfluidic chip using a low refractive index polymer. Lab Chip **16**, 2481–2486 (2016)
24. D. Choudhury, W.T. Ramsay, R. Kiss et al., A 3D mammalian cell separator biochip. Lab Chip **12**, 948–953 (2012)
25. F. Brahheri, P. Minzioni, R.M. Vazquez et al., Optofluidic integrated cell sorter fabricated by femtosecond lasers. Lab Chip **12**, 3779–3784 (2012)
26. P. Paiè, F. Bragheri, R.M. Vazquez et al., Straightforward 3D hydrodynamic focusing in femtosecond laser fabricated microfluidic channels. Lab Chip **14**, 1826–1833 (2014)
27. D. Wu, J. Xu, L. Niu, et al., In-channel integration of designable microoptical devices using flat scaffold-supported femtosecond-laser microfabrication for coupling-free optofluidic cell counting. Light Sci. Appl. **4**, e228 (2015)
28. K.M. Davis, K. Miura, N. Sugimoto et al., Writing waveguides in glass with a femtosecond laser. Opt. Lett. **21**, 1729–1731 (1996)
29. D. Choudhury, J.R. Macdonald, A.K. Kar, Ultrafast laser inscription: perspectives on future integrated applications. Laser Photonics Rev. **8**, 827–846 (2014)
30. F. Chen, J.R. Vázquez de Aldana, Optical waveguides in crystalline dielectric materials produced by femtosecond-laser micromachining. Laser Photonics Rev. **8**, 251–275 (2014)
31. S. Gross, M.J. Withford, Ultrafast-laser-inscribed 3D integrated photonics: challenges and emerging applications. Nanophotonics **4**, 332–352 (2015)
32. Y. Kondo, J. Qiu, T. Mitsuyu et al., Three-dimensional microdrilling of glass by multiphoton process and chemical etching. Jpn. J. Appl. Phys. **38**, L1146 (1999)
33. A. Marcinkevičius, S. Juodkazis, M. Watanabe et al., Femtosecond laser-assisted three-dimensional microfabrication in silica. Opt. Lett. **26**, 277–279 (2001)
34. M. Masuda, K. Sugioka, Y. Cheng et al., 3-D microstructuring inside photosensitive glass by femtosecond laser excitation. Appl. Phys. A **76**, 857–860 (2003)
35. Y. Bellouard, A. Said, M. Dugan et al., Fabrication of high-aspect ratio, micro-fluidic channels and tunnels using femtosecond laser pulses and chemical etching. Opt. Express **12**, 2120–2129 (2004)
36. Y. Li, K. Itoh, W. Watanabe et al., Three-dimensional hole drilling of silica glass from the rear surface with femtosecond laser pulses. Opt. Lett. **26**, 1912–1914 (2001)
37. T.N. Kim, K. Campbell, A. Groisman et al., Femtosecond laser-drilled capillary integrated into a microfluidic device. Appl. Phys. Lett. **86**, 201106 (2005)
38. R. An, Y. Li, Y. Dou et al., Simultaneous multi-microhole drilling of soda-lime glass by water-assisted ablation with femtosecond laser pulses. Opt. Express **13**, 1855–1859 (2005)
39. D.J. Hwang, T.Y. Choi, C.P. Grigoropoulos et al., Liquid-assisted femtosecond laser drilling of straight and three-dimensional microchannels in glass. Appl. Phys. A **79**, 605–612 (2004)
40. K. Ke, E.F. Hasselbrink Jr., A.J. Hunt et al., Rapidly prototyped three-dimensional nanofluidic channel networks in glass substrates. Anal. Chem. **77**, 5083–5088 (2005)
41. Y. Liao, Y. Ju, L. Zhang et al., Three-dimensional microfluidic channel with arbitrary length and configuration fabricated inside glass by femtosecond laser direct writing. Opt. Lett. **35**, 3225–3227 (2010)
42. Y. Ju, Y. Liao, L. Zhang et al., Fabrication of large-volume microfluidic chamber embedded in glass using three-dimensional femtosecond laser micromachining. Microfluid. Nanofluid. **11**, 111–117 (2012)

43. Y. Liao, J. Song, E. Li et al., Rapid prototyping of three-dimensional microfluidic mixers in glass by femtosecond laser direct writing. Lab Chip **12**, 746–749 (2012)
44. S. Maruo, O. Nakamura, S. Kawata, Three-dimensional microfabrication with two-photon-absorbed photopolymerization. Opt. Lett. **22**, 132–134 (1997)
45. E. Stratakis, A. Ranella, M. Farsari et al., Laser-based micro/nanoengineering for biological applications. Prog. Quantum Electron. **33**, 127–163 (2009)
46. M. Farsari, B.N. Chichkov, Materials processing: two-photon fabrication. Nat. Photonics **3**, 450–452 (2009)
47. M. Malinauskas, M. Farsari, A. Piskarskas et al., Ultrafast laser nanostructuring of photopolymers: a decade of advances. Phys. Rep. **533**, 1–31 (2013)
48. T.W. Lim, Y. Son, Y.J. Jeong et al., Three-dimensionally crossing manifold micro-mixer for fast mixing in a short channel length. Lab Chip **11**, 100–103 (2011)
49. D. Wu, S. Wu, J. Xu et al., Hybrid femtosecond laser microfabrication to achieve true 3D glass/polymer composite biochips with multiscale features and high performance: the concept of ship-in-a-bottle biochip. Laser Photonics Rev. **8**, 458–467 (2014)
50. J. Wang, Y. He, H. Xia et al., Embellishment of microfluidic devices via femtosecond laser micronanofabrication for chip functionalization. Lab Chip **10**, 1993–1996 (2010)
51. L. Amato, Y. Gu, N. Bellini et al., Integrated three-dimensional filter separates nanoscale from microscale elements in a microfluidic chip. Lab Chip **12**, 1135–1142 (2012)
52. H. Xia, J. Wang, Y. Tian et al., Ferrofluids for fabrication of remotely controllable micro-nanomachines by two-photon polymerization. Adv. Mater. **22**, 3204–3207 (2010)
53. K. Sugioka, T. Hongo, H. Takai et al., Selective metallization of internal walls of hollow structures inside glass using femtosecond laser. Appl. Phys. Lett. **86**, 171910 (2005)
54. Y. Hanada, K. Sugioka, K. Midorikawa, Selective metallization of photostructurable glass by femtosecond laser direct writing for biochip application. Appl. Phys. A **90**, 603–607 (2008)
55. Z. Zhou, J. Xu, Y. Liao et al., Fabrication of an integrated Raman sensor by selective surface metallization using a femtosecond laser oscillator. Opt. Commun. **282**, 1370–1373 (2009)
56. J. Xu, D. Wu, Y. Hanada et al., Electrofluidics fabricated by space-selective metallization in glass microfluidic structures using femtosecond laser direct writing. Lab Chip **13**, 4608–4616 (2013)
57. T. Tanaka, A. Ishikawa, S. Kawata, Two-photon-induced reduction of metal ions for fabricating three dimensional electrically conductive metallic microstructure. Appl. Phys. Lett. **88**, 08110 (2006)
58. S. Maruo, T. Saeki, Femtosecond laser direct writing of metallic microstructures by photoreduction of silver nitrate in a polymer matrix. Opt. Express **16**, 1174–1179 (2008)
59. Y. Cao, N. Takeyasu, T. Tanaka et al., 3D metallic nanostructure fabrication by surfactant-assisted multiphoton-induced reduction. Small **5**, 1144–1148 (2009)
60. B. Xu, H. Xia, L. Niu et al., Flexible nanowiring of metal on nonplanar substrates by femtosecond-laser-induced electroless plating. Small **6**, 1762–1766 (2010)
61. S.M. Eaton, C.D. Marco, R. Martinez-Vazquez et al., Femtosecond laser microstructuring for polymeric lab-on-chips. J. Biophotonics **5**, 687–702 (2012)
62. K. Sugioka, M. Masuda, T. Hongo et al., Three-dimensional microfluidic structure embedded in photostructurable glass by femtosecond laser for lab-on-chip application. Appl. Phys. A **78**, 815–817 (2004)
63. Y. Cheng, K. Sugioka, K. Midorikawa et al., Three-dimensional micro-optical components embedded in photosensitive glass by a femtosecond laser. Opt. Lett. **28**, 1144–1146 (2003)
64. K. Sugioka, Y. Cheng, Fabrication of 3D microfluidic structures inside glass by femtosecond laser micromachining. Appl. Phys. A **114**, 215–221 (2014)
65. S. Kiyama, S. Matsuo, S. Hashimoto et al., Examination of etching agent and etching mechanism on femtosecond laser microfabrication of channels inside vitreous silica substrates. J. Phys. Chem. C **113**, 11560–11566 (2009)
66. M. Hermans, J. Gottmann, F. Riedel, Selective laser-induced etching of fused silica at high scan-speeds using KOH. J. Laser Micro Nanoeng. **9**, 126–131 (2014)

67. F. He, Y. Cheng, Z. Xu et al., Direct fabrication of homogeneous microfluidic channels embedded in fused silica using a femtosecond laser. Opt. Lett. **35**, 282–284 (2010)
68. F. He, J. Lin, Y. Cheng, Fabrication of hollow optical waveguides in fused silica by three-dimensional femtosecond laser micromachining. Appl. Phys. B **105**, 379–384 (2011)
69. J. Lin, S. Yu, Y. Ma et al., On-chip three-dimensional high-Q microcavities fabricated by femtosecond laser direct writing. Opt. Express **20**, 10212–10217 (2012)
70. R. Osellame, S. Taccheo, M. Marangoni et al., Femtosecond writing of active optical waveguides with astigmatically shaped beams. J. Opt. Soc. Am. B **20**, 1559–1567 (2003)
71. Y. Cheng, K. Sugioka, K. Midorikawa et al., Control of the cross-sectional shape of a hollow microchannel embedded in photostructurable glass by use of a femtosecond laser. Opt. Lett. **28**, 55–57 (2003)
72. K. Sugioka, Y. Cheng, K. Midorikawa et al., Femtosecond laser microprocessing with three-dimensionally isotropic spatial resolution using crossed-beam irradiation. Opt. Lett. **31**, 208–210 (2006)
73. F. He, H. Xu, Y. Cheng et al., Fabrication of microfluidic channels with a circular cross section using spatiotemporally focused femtosecond laser pulses. Opt. Lett. **35**, 1106–1108 (2010)
74. Y. Liao, Y. Shen, L. Qiao et al., Femtosecond laser nanostructuring in porous glass with sub-50 nm feature sizes. Opt. Lett. **38**, 187–189 (2013)
75. Y. Liao, Y. Cheng, C. Liu et al., Direct laser writing of sub-50 nm nanofluidic channels buried in glass for three-dimensional micro-nanofluidic integration. Lab Chip **13**, 1626–1631 (2013)
76. A. Schaap, T. Rohrlack, Y. Bellouard, Optical classification of algae species with a glass lab-on-a-chip. Lab Chip **12**, 1527–1532 (2012)
77. Z. Wang, K. Sugioka, K. Midorikawa, Fabrication of integrated microchip for optical sensing by femtosecond laser direct writing of Foturan glass. Appl. Phys. A **93**, 225–229 (2008)
78. L. Qiao, F. He, C. Wang et al., A microfluidic chip integrated with a microoptical lens fabricated by femtosecond laser micromachining. Appl. Phys. A **102**, 179–183 (2011)
79. J. Song, J. Lin, J. Tang et al., Fabrication of an integrated high-quality-factor (high-Q) optofluidic sensor by femtosecond laser micromachining. Opt. Express **22**, 14792–14802 (2014)
80. J. Voldman, Electrical forces for microscale cell manipulation. Annu. Rev. Biomed. Eng. **8**, 425–454 (2006)
81. L.A. MacQueen, M. Thibault, M.D. Buschmann et al., Electro-manipulation of biological cells in microdevices. IEEE Trans. Dielectr. Electr. Insul. **19**, 1261–1268 (2012)
82. J. Xu, Y. Liao, H. Zeng et al., Selective metallization on insulator surfaces with femtosecond laser pulses. Opt. Express **15**, 12743–12748 (2007)
83. J. Xu, Y. Liao, H. Zeng et al., Mechanism study of femtosecond laser induced selective metallization (FLISM) on glass surfaces. Opt. Commun. **281**, 3505–3509 (2008)
84. Y. Liao, J. Xu, H. Sun et al., Fabrication of microelectrodes deeply embedded in $LiNbO_3$ using a femtosecond laser. Appl. Surf. Sci. **254**, 7018–7021 (2008)
85. J. Song, Y. Liao, C. Liu et al., Fabrication of gold microelectrodes on a glass substrate by femtosecond-laser-assisted electroless plating. J. Laser Micro/Nanoeng. **7**, 334–338 (2012)
86. Y. Liao, L. Qiao, Z. Wang et al., Fabrication of a liquid crystal light modulator by use of femtosecond-laser-induced nanoripples. Opt. Mater. Express **3**, 1698–1704 (2013)
87. G.A. Shafeev, Laser-assisted activation of dielectrics for electroless metal plating. Appl. Phys. A **67**, 303–311 (1998)
88. J. Xu, D. Wu, J.Y. Ip et al., Vertical sidewall electrodes monolithically integrated into 3D glass microfluidic chips using water-assisted femtosecond-laser fabrication for in situ control of electrotaxis. RSC Adv. **5**, 24072–24080 (2015)
89. J. Xu, H. Kawano, W. Liu et al., Controllable alignment of elongated microorganisms in 3D microspace using electrofluidic devices manufactured by hybrid femtosecond laser microfabrication. Microsyst. Nanoeng. **3**, 16078 (2017)
90. J. Xu, K. Midorikawa, K. Sugioka, Femtosecond laser fabricated electrofluidic devices in glass for 3D manipulation of biological samples. Proc. SPIE **9735**, 97350B (2016)

91. J. Yan, Y. Du, J. Liu et al., Fabrication of integrated microelectrodes for electrochemical detection on electrophoresis microchip by electroless deposition and micromolding in capillary technique. Anal. Chem. **75**, 5406–5412 (2003)
92. M. Uncuer, H. Koser, Characterization and application of selective all-wet metallization of silicon. J. Micromech. Microeng. **22**, 015003 (2012)
93. D. Wu, L. Niu, S. Wu et al., Ship-in-a-bottle femtosecond laser integration of optofluidic microlens arrays with center-pass units enabling coupling-free parallel cell counting with a 100% success rate. Lab Chip **15**, 1515–1523 (2015)
94. K. Sugioka, D. Wu, K. Midorikawa, Ship-in-a-bottle biomicrochips fabricated by hybrid femtosecond laser processing. MATEC Web Conf. **8**, 05005 (2013)
95. F. Sima, D. Wu, J. Xu et al., Ship-in-a-bottle integration by hybrid femtosecond laser technology for fabrication of true 3D biochips. Proc. SPIE **9350**, 93500F (2015)
96. F. Sima, D. Serien, D. Wu et al., Micro and nano-biomimetic structures for cell migration study fabricated by hybrid subtractive and additive 3D femtosecond laser processing. Proc. SPIE **10092**, 1009207 (2017)
97. K. Sugioka, Y. Cheng, A tutorial on optics for ultrafast laser materials processing: basic microprocessing system to beam shaping and advanced focusing methods. Adv. Opt. Technol. **1**, 353–364 (2012)
98. M. Duocastella, C.B. Arnold, Bessel and annular beams for materials processing. Laser Photonics Rev. **6**, 607–621 (2012)
99. F. Courvoisier, R. Stoian, A. Couairon, Ultrafast laser micro- and nano-processing with nondiffracting and curved beams. Opt. Laser Technol. **80**, 125–137 (2016)

Chapter 9
Laser-Induced Forward Transfer Towards Additive Manufacturing

S. Papazoglou and I. Zergioti

Abstract The evolution of the printed and flexible electronics has attracted great interest from the academia and the industrial world as well. Due to the wide number of potential materials and emerging applications that may be exploited, laser printing has been studied both for scientific research and commercial purposes. In this context, this chapter discusses the fundamental theory supporting laser printing and specifically Laser-Induced Forward Transfer that is a direct non-contact and non-destructive laser printing technique in an aim to provide a complete overview of the printing mechanism and the jetting dynamics, while in the following paragraphs potential applications are also presented. Moreover, since Laser-Induced Forward Transfer is a technique that could be described as an additive process, in contrary to the subtractive processes such as laser sintering, part of this chapter is focused on the evolution of the technique towards additive manufacturing as well as industrialization activities that have risen in the last 5 years.

Abbreviations

Acronym	Definition
AFA-LIFT	Absorbing film assisted LIFT
BA-LIFT	Blister-actuated LIFT
BioLP	Biological laser printing
CW	Continuous Wave
DRL-LIFT	Dynamic release layer-LIFT
FBARs	Film Bulk Acoustic Resonators
IC	Integrated Circuit

S. Papazoglou · I. Zergioti (✉)
School of Applied Mathematical and Physical Sciences, National Technical University of Athens, Heroon Polytechneiou 9, 157 80, Athens, Greece
e-mail: zergioti@central.ntua.gr

S. Papazoglou
e-mail: simpap@mail.ntua.gr

A. Hu (ed.), *Laser Micro-Nano-Manufacturing and 3D Microprinting*, Springer Series in Materials Science 309, https://doi.org/10.1007/978-3-030-59313-1_9

LEP	Light Emitting Polymer
LIBT	Laser-Induced Backward Transfer
LIFT	Laser-Induced Forward Transfer
MAPLE	Matrix-assisted pulsed laser evaporation
NMP	N methylpyrrolidone
NPs	Nanoparticles
OLEDs	Organic Light-Emitting Diodes
OTFTs	Organic Thin-Film Transistors
PEN	Polyethylene naphthalate
SAW	Surface-Acoustic Wave
TIN-LIFT	Thermal-Induced Nozzle
TP	Triazene polymers
VCSEL	Vertical cavity surface emitting lasers

9.1 Introduction

Recent advancements in organic, inorganic, and flexible electronics have spurred the interest of both the research and the industrial community during the last years since new processes have been developed focusing on the time and cost-effective fabrication of electronic devices. Since device footprint and integration complexity are essential parts of modern technologies, high resolution, selective, and rapid manufacturing techniques are key-enabling factors. Among the main approaches used for the deposition of high quality and functional materials, laser printing has been widely employed owing to its unique characteristics such as the high spatial resolution of the printed features, the versatility of the technique regarding the number of materials that can be transferred, and the non-contact and non-destructive nature of the deposition [1]. In addition, contrary to other deposition methods such as ink-jet printing, LIFT does not suffer from inherent drawbacks like nozzle clogging and it may be applied for the transfer of liquids with viscosities ranging between 1 and 200.000 mPa s [2]. This chapter focuses on the Laser-Induced Forward Transfer (LIFT) technique which is a direct laser printing technique with the aim to present the history as well as latest results-achievements on the application level. Fundamental theory of the technique and experimental results will be also presented in an effort to provide a complete overview for the reader. The last part of the chapter will be devoted to the recent application of the technique on the 3D printing of materials and the evolution of LIFT towards additive manufacturing and industrial exploitation.

9.2 Fundamentals of LIFT

9.2.1 Origins of LIFT

The concept of material transfer using lasers has been a research objective for over 40 years now, where Levene et al. [3] were the first to report the transfer of black ink using a Nd:YAG ($\lambda = 1.06$ μm) laser source in 1970, while almost 15 years later, Bohandy et al. [4, 5], introduced for the first time the term LIFT for the transfer of copper metal features using a pulsed excimer laser source ($\lambda = 193$ nm, 15 ns), on silicon and fused silica substrates, reporting resistivities between 3 and 50 times the resistivity of bulk copper. The experiment was conducted in vacuum conditions, however, LIFT nowadays may be performed in ambient conditions as well [6]. Few years before, in 1979, Deutsch et al. also demonstrated the transfer of metal patterns using "laser-initiated heterogeneous photochemical reactions" through UV photolysis of gas precursors [7], while in 1983 Osgood et al. introduced for the first time to the term "laser initiated chemistry" for the deposition and removal of materials [8, 9]. In brief, the principle idea behind LIFT requires the use of (1) a pulsed laser source, where the wavelength may range between the UV and the IR regions of the spectrum depending on the optical absorption of the material under transfer to the specific wavelength and the type of the application, (2) a donor substrate that is a transparent substrate (sometimes referred to as carrier) coated with a thin film of the material under investigation and (3) a receiver substrate on the surface of which the material is deposited. During LIFT, the donor and receiver substrates are brought closely or in contact to each other and as the laser pulse irradiates the interface between the carrier and the thin-coated film from the back side of the donor substrate, the material is ejected and therefore deposited on the surface of the receiver substrate as it is depicted in Fig. 9.1. The theory and the mechanism of LIFT, regarding liquid and solid-phase printing, will be described in more detail in the next paragraphs.

Apart from the aforementioned basic requirements for LIFT, the system is usually accompanied by mechanical components namely computer-controlled, highly accurate, and fast translation stages that facilitate the transfer of pre-programmed digital patterns as well as optical parts such as galvanometer scanners that enable—if desired—rapid and large area printing.

9.2.2 Limitations of the Technique

Despite the successful implementation of LIFT in a variety of applications, there are certain aspects related to the technique that needs to be addressed before it can be used in massive industrial processes and large-area manufacturing. More specifically, since many LIFT applications involve the printing of metal features namely metal films and metallic nanoparticles (NPs) inks, which are rapidly oxidized when they are exposed to ambient conditions, the fast-melting and evaporation during transfer may

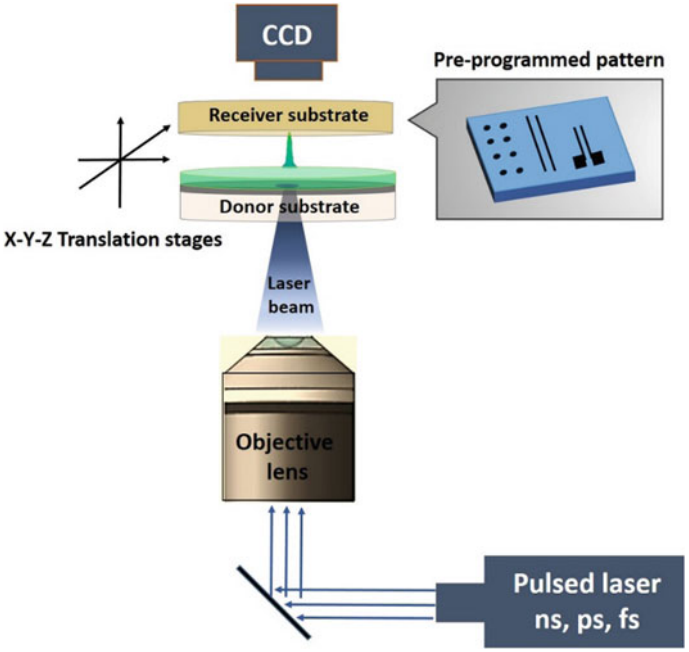

Fig. 9.1 Schematic representation of the LIFT technique

lead to severe alterations in their electrical characteristics. Moreover, the melting of the material under transfer during LIFT may cause irreversible and unwanted phase transformations, directly affecting the structural properties of the printed patterns.

Another important factor for the realization of LIFT, is the preparation and treatment of the donor substrate which is an essential part of the technique, resembling the ribbon in a classic typewriter and it should be highly uniform in thickness and reproducible during preparation, while in the case of pastes and high viscosity inks the evaporation and drying time should be considered since they may affect the jetting dynamics during transfer. There are several methods to prepare a donor substrate, the most important of which are: doctor-blade, spin-coating, sputtering, thermal evaporation, electron gun etc., where each one is used depending on the phase of LIFT (liquid or solid) and the thickness and uniformity requirements. Most of these approaches require vacuum equipment that is expensive and time-consuming, while others (doctor-blade) fail to develop reproducible films when specific thicknesses are required.

Finally, the adhesion of the transferred structures is often an issue, since the quenching of the metallic patterns may lead to the development of intrinsic stresses among the receiver and the material under investigation that subsequently leads to the detachment of the printed structure. However, as it will be presented in the last paragraphs of this chapter, some of these shortcomings have been overcome and

LIFT has been successfully incorporated in industrial processing for electronics and biological applications.

9.2.3 Advancement and Variations of LIFT

In the years that followed its initial use and owing to the technique's simplicity and versatility, LIFT has presented a steady increase in the number of potential applications and materials that could be investigated for organic electronics, bio-electronics, sensors, etc. [10–20]. This is also highlighted in the number of publications [21] and patents that were published during the last 10 years, showing an ever-growing interest in the technique's unique features such as the high-spatial-resolution and the selectivity for drop-on-demand applications (Table 9.1 and Fig. 9.2).

Since 1986, where Bohandy et al. [4] firstly introduced the term "LIFT" and in an effort to overcome the aforementioned LIFT limitations, some alternative methods have been demonstrated. In these contexts, the main techniques that differ from the traditional LIFT (liquid and solid phase, Fig. 9.3) are: Dynamic release layer-LIFT (DRL-LIFT) [22], Laser-Induced Backward Transfer (LIBT) [23], Matrix-assisted pulsed laser evaporation (MAPLE) [24], Blister-actuated LIFT (BA-LIFT) [25], Absorbing film-assisted-LIFT (AFA-LIFT) [26] and Biological laser printing (BioLP) [27]. More specifically, in DRL-LIFT the donor substrate, which in traditional LIFT is a transparent substrate, is usually coated with a thin absorbing layer followed by the deposition of the material under investigation as can be seen in Fig. 9.3 (right). In this case, as the laser beam irradiates the interface between the donor and the thin absorbing layer, vaporization of the thin film occurs leading to the ejection of the material towards the receiver substrate. The dynamic release layer is usually a metallic one, where Au, Cr, Ti, and Cu are often used, however polymeric DRL's may be used as well, with thicknesses ranging between 20 and 100 nm for the metallic and up to 1 μm for the polymeric ones. The first work involving the use of a DRL was reported by Tolbert et al. [22], where multilayer films where used to transfer inks. In the case of the polymeric DRL's, during the irradiation of the donor substrate, decomposition of the organic molecules takes place due to photothermal and photochemical effects that enable the detachment of the material under transfer.

Thus, by adjusting the absorption coefficient of the DRL with respect to the desired wavelength, it is possible to deposit materials with low absorption to the wavelength used and also avoid direct exposure to the laser beam that could possibly alter their structural and morphological characteristics. The most commonly used polymeric DRL's are photopolymers including triazene polymers (TP) that have been reported in several applications [28–30]. AFA-LIFT and BioLP have been employed mainly for the printing of biological materials, since the use of a 1–100 nm thick metallic or metal oxide DRL enables the transfer and avoids the direct interaction of the beam with these sensitive to degrade structures. LIBT on the other hand is an approach that uses a transparent—to the desired—wavelength substrate and is performed in the opposite to traditional LIFT direction. This means that the laser beam propagates

Table 9.1 Overview of works on LIFT

Transferred material	Substrate	Feature size (μm)	Laser source	Wavelength	Pulse duration	Application	Author, year	References
Biomaterials								
Antibodies	Paper		KrF excimer	248 nm	10 ns	Biochemical analysis	Katis (2014)	[105]
Biomaterials such as enzyme patterns	Glass	10–100	Hybrid dye/KrF excimer	248 nm	0.5 ps	Biosensors	Zergioti (2005)	[47]
Mesoscopic patterns of viable *Escherichia coli*	Si, glass, and nutrient agar plates	<10	ArF excimer	193 nm		Biosensors	Ringeisen (2002)	[92]
Salmon sperm DNA	Poly-L-lysine coated glass slides	55–65	Nd:YAG	355 nm	10 ns	Biosensors	Fernandez-Pradas (2004)	[95]
DNA solution	GOPTS functionalized surfaces	100	Nd:YAG	266 nm	10 ns	Capacitive biosensor	Tsekenis (2012)	[107]
Lambda phage DNA	Glass	100	KrF	248 nm	500 fs	Genome functions	Karaiskou (2003)	[94]
Cells	Glass	50–80	Nd:YAG	1064 nm	30 ns	High throughput cell printing	Guillemot (2010)	[98]
Skin cells and human stem cells	Glass	80–140	Nd:YAG	1064 nm	8–9 ns	Human skin regeneration	Koch (2010)	[108]
Peptide-based microarrays	Au-coated glass	20–150	KrF	248 nm	15 ns	Molecular electronics	Dinca (2007)	[88]
Cell containing collagen	Glass slide		Nd:YAG-laser	1064 nm	8–9 ns	Tissue engineering	Michael (2013)	[96]

(continued)

Table 9.1 (continued)

Transferred material	Substrate	Feature size (μm)	Laser source	Wavelength	Pulse duration	Application	Author, year	References
Cell bioink	PCL membrane	2000	Nd:YAG	1064 nm	30 ns	Tissue engineering	Catros (2012)	[97]
Purified and cultured rat Schwann and astroglial cells and pig lens epithelial cells	Glass		KrF	248 nm	30 ns	Controlled transfer of organisms	Hopp (2005)	[26]
Metals, metallic nanoparticle inks								
Silver NP ink	PEN and Si/SiO_2 substrates	50	Nd:YAG	266 nm	10 ns	Conductive interconnects	Boutopoulos (2014)	[37]
Silver paste	Glass, Si, and polyimide substrates	Widths (8–75), heights (1–10), and bond lengths (8–100)	Nd:YVO_4	355 nm	30 ns	Conductive interconnects for electronic and MEMS devices	Wang (2010)	[133]
Silver NP ink	Si wafers	16	Yb:YAG	343 nm	30 ps	Conductive lines	Rapp (2014)	[118]
Silver NP paste	Si substrate	4	Nd:YVO_4	355 nm	30 ns	Customization and repair applications in microelectronics	Auyeung (2011)	[116]
Silver nano ink and paste	Polyimide	Width 11–20	Nd:YVO_4	355 nm	30 ns	Flexible electronics	Auyeung (2007)	[109]
Silver NP ink	Polyimide, SiO_2/Si	25	Nd:YAG	266 nm	10 ns	Flexible electronics	Makrygianni (2014)	[115]

(continued)

Table 9.1 (continued)

Transferred material	Substrate	Feature size (μm)	Laser source	Wavelength	Pulse duration	Application	Author, year	References
Cr, In_2O_3	Glass, silicon	3	KrF	248 nm	500 fs	Diffractive microstructures	Zergioti (1998)	[13]
Silver NP ink	Si wafers	16	Fiber	343 nm	30 ps	Metallic interconnections	Biver (2014)	[39]
Silver nanopaste	Si or c-cut (0001) sapphire wafers	50	Nd:YVO_4	355	65	Microwave interconnects	Breckenfeld (2015)	[121]
Silver NP ink	Glass	5–25	Nd:YVO_4	355 nm	30 ns	OTFT	Kim (2010)	[61]
Silver NP ink	Glass	12, 30, 70	Nd:YVO_4	266 nm	20 ns	Rapid prototyping of microelectronic devices	Duocastella (2012)	[15]
Organic materials-polymers								
PHEMA, PVA, and PVP polymers	Circular Si membranes	20–250	Nd:YAG	266 nm	4 ns	Capacitive chemical sensor	Tsouti (2010)	[78]
Polyethylene	Paper or Mylar		Nd:YAG	1.06 μm		Image recording	Levene (1970)	[3]
Cationic polymer: polyethylenimine (PEI)	Glass coated with PEG polymer	200–300	XeCl	308 nm	30 ns	Cell-based biosensors	Dinca (2011)	[77]
SWCNT suspension	Glass slides or fused silica plates	400	XeCl	308 nm	30 ns	Chemical sensors	Palla-Papavlu (2014)	[81]
Polymer/carbon nanotube (CNT) composite layers	Glass and Al electrodes pre-patterned on SiO_2/Si	70	Nd:YAG	266 nm	4 ns	Chemical sensors	Boutopoulos (2010)	[82]

(continued)

Table 9.1 (continued)

Transferred material	Substrate	Feature size (μm)	Laser source	Wavelength	Pulse duration	Application	Author, year	References
Liquid-phase exfoliated graphene	Si/SiO_2 and flexible polymer substrates	180–200	Nd:YAG	266 nm	10 ns	Organic electronics	Papazoglou (2014)	[122]
Organic semiconductor (P3HT)	SiO_2/Si	60–130	Nd:YAG	266 nm	4 ns	OTFT	Zergioti (2011)	[56]
Organic semiconductor P3HT	Si/SiO_2	250	Nd:YAG	266 nm	4 ns	OTFT	Makrygianni (2013)	[58]
PIB, PECH, and PEI chemoselective polymers	SMR devices	350	XeCl	308 nm		Sensors	Cannatà (2012)	[79]
Chemoselective polymers: PECH, PIB, and PEI	SAW resonators		XeCl	308 nm		Sensors	Pietrantonio (2012)	[80]
PEDOT:PSS	BK7 or Si, or flexible	150	Nd:YAG, S pulse amplitude systems, LPX 210i Lambda Physics	1064, 532, 1025, 248 nm	8 ns, 50 ps, 400 fs, 25 ns	Plastic electronics	Thomas (2007)	[31]
Inorganic materials-oxides								
$SnCl_2(acac)_2$, SnO_2 NP	Metal electrodes sputtered onto glass	500 or 1000	XeCl excimer	308 nm	30 ns	Gas sensors	Mattle (2013)	[84]
$LiCoO_2$ cathode and carbon anode	Al and Cu current collectors	50	$Nd:YVO_4$	355 nm		Microbatteries	Kim (2007)	[68]

(continued)

Table 9.1 (continued)

Transferred material	Substrate	Feature size (μm)	Laser source	Wavelength	Pulse duration	Application	Author, year	References
Silicon nanoparticles	Glass	160–240 nm	Ti:Sapphire	800 nm	50 fs	Nanoantennas, nanolasers, metamaterials	Zywietz (2014)	[14]
Small molecule Alq_3	Pre-patterned ITO glass slides	600 × 500	XeCl excimer	308 nm	30 ns	OLED pixels	Shaw-Stewart (2013)	[28]
nc-TiO_2 paste	SnO_2 coated glass	250	Nd:YVO_4	355 nm		Solar cells	Kim (2004)	[65]
Al_2O_3			Nd:YAG	1.06 μm		Surface acoustic wave resonators	Greer (1988)	[10]

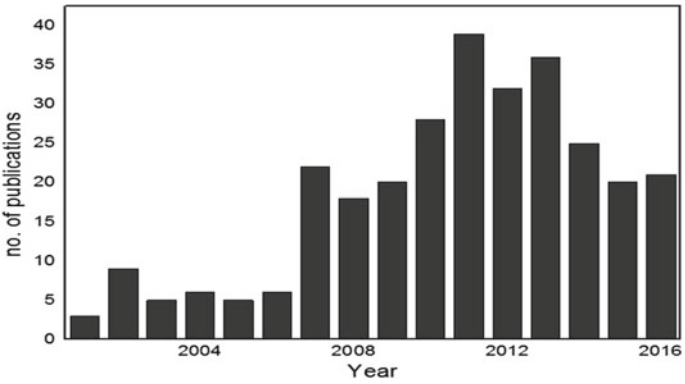

Fig. 9.2 Number of publications associated with LIFT since 2000. Obtained from Scopus search results [21]

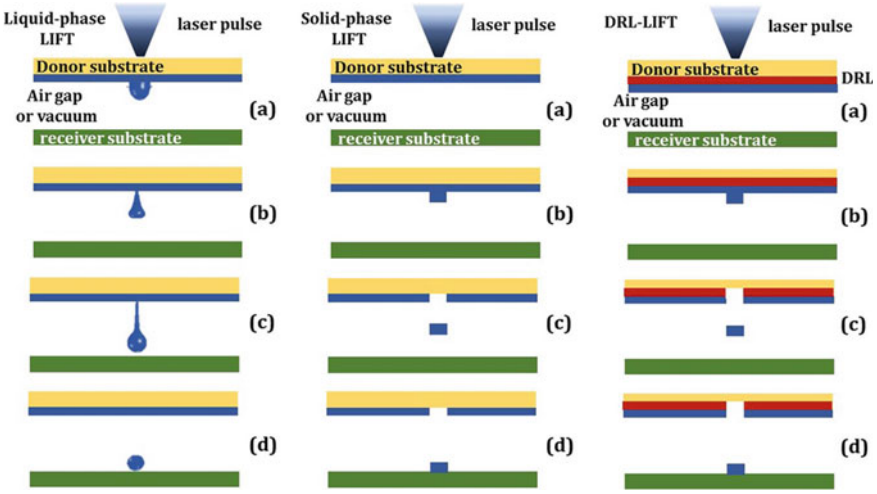

Fig. 9.3 Schematics of liquid-phase LIFT (left), solid-phase LIFT (middle), DRL-LIFT (right)

through the transparent receiver substrate and irradiates the surface of the material under transfer that is coated on the donor substrate, propelling it towards the beam originating direction and on the receiver substrate. Finally, MAPLE, is an approach very similar to LIFT but the laser fluences that are being used are below the ablation threshold of the materials under investigation, therefore no vaporization is observed an advantage that may be used for the deposition of complex structures.

9.3 Mechanism of Transfer in LIFT

The dynamics of the liquid and solid deposits that are transferred during LIFT have been studied by several groups through time-resolved imaging with the aim to provide a deeper understanding of the phenomena that occur at different timescales starting from the moment that the laser pulse irradiates the donor substrate until the material finally impacts the receiver substrate. In the next paragraphs, these studies will be presented including the jetting dynamics of different materials namely metallic NP inks, pastes, and biological materials.

9.3.1 Mechanism of Liquid Phase LIFT

Many research groups have been involved in the study of LIFT dynamics so as to investigate the jetting mechanism regarding various materials and viscosities [31–33]. Briefly, the mechanism in liquid phase LIFT can be described as follows: (1) at the low laser fluence regime, the free surface of the coated material is displaced due to the formation of a bubble of vaporized material that consequently collapses back on the donor substrate and no transfer is observed, (2) at an intermediate—above threshold—laser fluence regime successful transfer of well-defined droplets is observed and the released material is confined within a narrow jet, while no satellite droplets and material debris are observed, (3) finally above a certain laser fluence threshold (high fluence regime) the vapor bubble bursts violently and the released jet can be described as divergent leading to splashing and uncontrolled deposition [32].

The ejection mechanism and dynamics of a viscous nanopowder transferred by MAPLE have been investigated in an early attempt using time-resolved microscopy [34]. In this work, an Nd:YAG laser source using the 3rd harmonic (355 nm) has been employed for the investigation of the transfer process at different laser fluences. In another work, the ejection dynamics of the nanosecond laser transfer of a 200 nm thick gold layer have been demonstrated [35], revealing two jetting regimes with single droplet ejection at low fluences (>140 mJ/cm^2) and undesirable multiple droplet formation at higher fluences (>400 mJ/cm^2). Moreover, the ejection mechanism of complex solutions (Ag NP inks) [36] and metallic pastes [37] has also been reported, whereas for low viscosity Ag NP inks, the incorporation of a metallic (Ti) DRL lead to a "low velocity" jetting behavior ranging between 9 and 77 m/s for a fluence window between 100 and 230 mJ/cm^2. Regarding high viscosity pastes (>500 cP) the jetting behavior resembles that of solid-phase LIFT, where the ejected material from the donor substrate travels rather slowly (<1 m/s) towards the receiver substrate resulting in a smooth landing and avoiding the formation of fragments and debris upon impact. Jetting dynamics studies during printing at high repetition rates (500 kHz) has been also demonstrated for the transfer of Ag Np ink using a frequency tripled fiber laser ($\lambda = 343$ nm, $\tau = 30$ ps). An intriguing observation in this work was that for a given spacing of 20 μm or smaller between adjacent pulses, interaction

between the bubbles at the bottom of the jets occurs leading to a non-uniform droplet deposition [38]. Adjacent laser pulse interaction has been also studied by another group [39], where it was reported that the second jet shows the tendency to be tilted towards or away from the first one, an effect that depends on the time delay between the two pulses. At this point it is important to mention, that significant jet to jet interactions are also observed at specific interbeam distances, a phenomenon that is not observed in single beam LIFT and was reported by Patrascioiu et al. [40]. Time-resolved imaging of an alginate-based hydrogel laser printing using LIFT has been also demonstrated [41], where two different laser fluences have been used (1.6 and 2.7 J/cm^2) with a gap between donor and receiver substrates of 450 μm. It was shown, that the liquid jet widens in diameter at higher impact velocities while at lower impact velocities caused a disk-lie spreading as well as a subsequent diameter oscillation in a phenomenon that occurs at microsecond timescale (Figs. 9.4 and 9.5).

Moreover, studies regarding DRL and BA-LIFT have explained the differences of the mechanism among the two approaches, whereas in the case of BA-LIFT using a polyimide DRL [20, 42], it was shown that the laser energy was absorbed within a small area and resulted in a confined high-temperature pocket and at low laser fluences the expanding gases that occur remain covered within the DRL film resulting in a deformed and rapidly inflating blister. On the other hand, DRL LIFT differs from BA-LIFT since the blister remains sealed at all times during transfer, thus the ejected

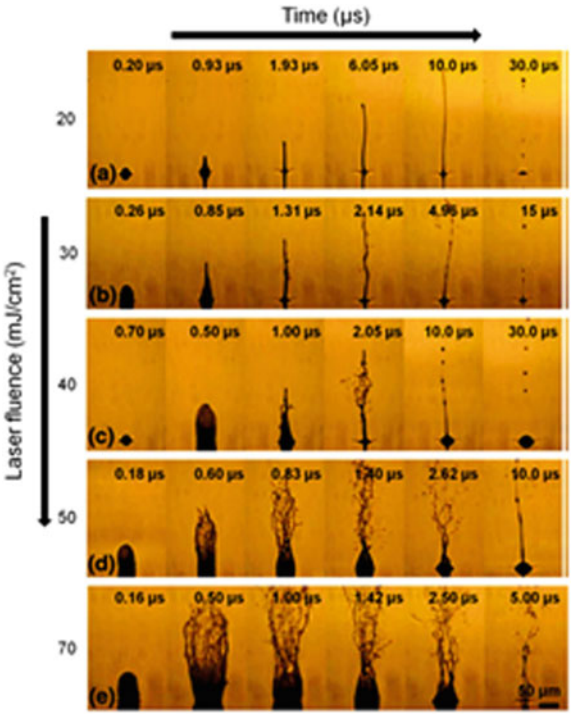

Fig. 9.4 Time-resolved images of Ag nanoparticles ink at different laser fluences: **a** 20 mJ/cm^2, **b** 30 mJ/cm^2, **c** 40 mJ/cm^2, **d** 50 mJ/cm^2, **e** 70 mJ/cm^2. Reprinted with permission from [36]. Copyright 2014, with kind permission from Springer Science and Business Media

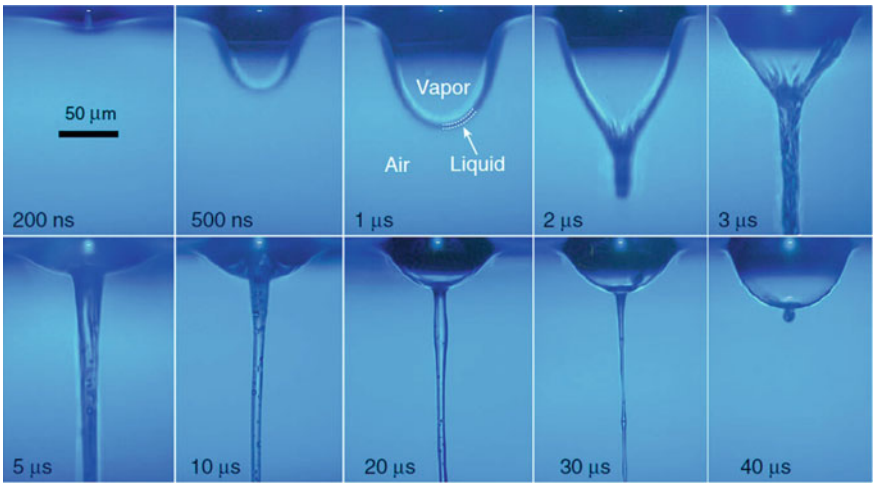

Fig. 9.5 Time-resolved images of liquid ejection into the ambient air using a 50-nm titanium absorbing layer. Reprinted with permission from [43]. Copyright 2011, with kind permission from Springer Science and Business Media

material is not irradiated directly from the laser pulse, minimizing any potential degradation effects that could occur under direct exposure [43]. Recently, since laser printing of biological materials has attracted great interest, Ali et al. [44], have studied the jetting dynamics during the laser printing of mesenchymal stem cells so as to promote the deposition at low kinetic energies that favors the successful deposition of the biological material. In this work, the transition from the subthreshold regime to the jetting regime has been associated with a geometrical parameter (vertex angle) that can be exploited to promote the deposition of cells with high viability at slow velocities.

9.3.2 Mechanism of Solid Phase LIFT

The transfer of solid structures using LIFT has been studied by several groups [45–51] since the ejection mechanism differs from that of liquid-phase LIFT. In solid-phase LIFT, the material under investigation is usually coated on the donor substrate and is left to dry (using hot plate or oven), so as to evaporate the remaining solvent and obtain a solid thin film. Subsequently, the two substrates (donor and receiver) are brought in close proximity or in contact with each other—as in the case of liquid-phase LIFT—and the laser pulse irradiates the interface between the transparent carrier of the donor substrate and the coated material. As a consequence, part of the irradiated material is transferred towards the receiver substrate when a laser pulse of sufficient fluence (above threshold) is used. During the transfer of a solid film and for small distances between the donor and the receiver substrates (<500 µm),

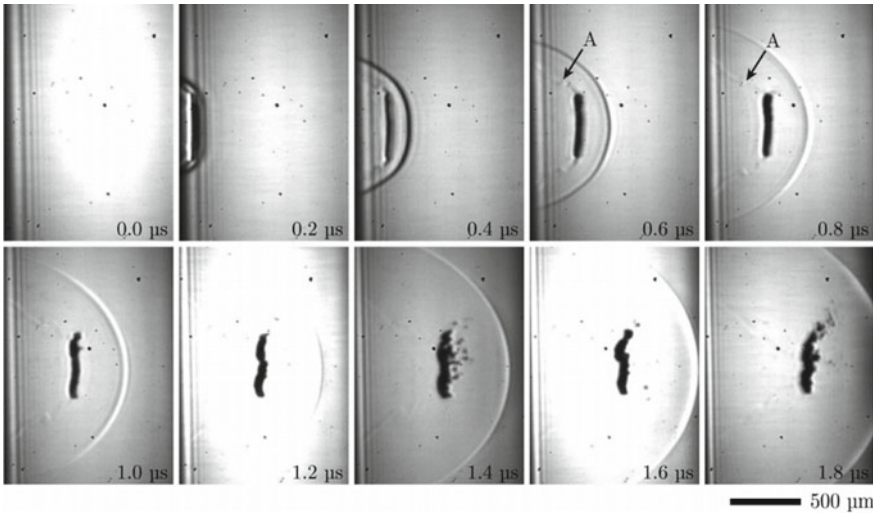

Fig. 9.6 Sequence of images taken for a 350 nm TP/80 nm Al sample at a fluence of 360 mJ/cm^2. The arrow A shows a gas flow behind the flyer. Reprinted with permission from [48]. Copyright 2010, with kind permission from ACS Publications

damages and disintegration of the deposited flyer may occur due to the presence of the shockwave that is produced as the laser pulse impacts the donor substrate. This shockwave is initially in a flat-shaped form and rapidly evolves in a hemispherically propagating form that precedes the traveling flyer during transfer. In a study by Fardel et al. [48], it was shown that this shockwave reaches first the receiver substrate and is reflected back towards the traveling flyer, a collision that may have detrimental effects on the transferred material (Fig. 9.6).

First reports on the study of solid-phase LIFT was demonstrated by Nakata and Okada [45], where the deposition of emissive particles from a gold thin film was investigated. The dynamics of DNA thin films transfer have been also studied in a comparative study using stroboscopic schlieren imaging where nanosecond and femtosecond laser pulses were employed [46]. In this work, it was reported that the use of ultrashort pulses (fs) results in a more directional material ejection with small angular divergence that enables high spatial resolution regarding the transferred pixels as compared to the use of short pulses (ns). Moreover, the dynamics of an aryltriazene polymer deposition has been demonstrated using time-resolved shadowgraphy, where it was shown that the traveling flyer evolves with time from a flat-shaped pixel in a distorted and expanded structure [47]. Apart from the shockwave effect that was mentioned earlier, the melting of the transferred material is often a crucial factor that leads to the surface disintegration of the printed structures. To avoid this, DRL LIFT is often used with triazene polymers being the most widely employed polymeric DRL, for the transfer of polymer and metal features [52].

9.4 Applications of LIFT

The rapid evolution of the LIFT technique and the development of various alternative approaches for the realization of the transfer has lead to the incorporation of LIFT into the fabrication of different devices for Organic Thin-Film Transistors (OTFTs), Organic Light-Emitting Diodes (OLEDs), electrical interconnects in integrated circuits (IC), chemical, and biological sensors applications. Since resolution and reproducibility are among the current market trends, LIFT has shown great promise in achieving both targets through the minimization of the printed features and the repeatability of the process. This is further highlighted by the number of publications that have been reported as well as from the establishment of the technique in industrial processes as it will be described in the next paragraphs.

9.4.1 Laser Printing for Organic Electronics and Micropower Devices

The market needs in the organic electronics community require a decrease in the device footprint while at the same time integration complexity and increase in the number of the active components are also required. Laser printing enables the high speed, contactless, and high resolution transfer of a wide range of organic materials of varying viscosities providing certain advantages compared to conventional deposition techniques such as inkjet printing that suffers from inherent limitations namely nozzle clogging when it comes to high viscosity solutions and the need for masks and clean room facilities in the case of lithographic processes, where highly toxic etchants and developer solutions are also used [53]. LIFT has been successfully used for OTFTs applications [19, 54–60], OLEDs [28, 61–63], solar cells/photovoltaics [64–66], microbatteries [67–70] and ultra and microcapacitors [51, 71, 72]. More specifically, OTFTs devices via LIFT have been demonstrated for the simultaneous multilayer transfer of diPhAc-3T (p-type semiconductor), parylene-C as the dielectric layer and a thin silver layer that served as the gate electrode that resulted in a functional top gate OTFT [30] (Fig. 9.7).

In another work, OTFTs using pentacene with bottom-contact and top-contact configurations have been reported using LIFT. The source-drain electrodes were formed using silver NPs inks—printed with a Nd:YVO_4 laser source ($\lambda = 355$ nm, 30 ns)—with reporting field-effect mobilities at the order of 0.11 cm^2/V s [60]. Air-stable high performing OTFTs have been also reported by Rapp et al. [19], with hole mobilities up to 0.04 cm^2/V s, threshold voltage Vt near 0 V and Ion/Ioff ratio up to 2.8×10^5. Additionally, tricolor OLEDs have been transferred using LIFT in a multilayer stack approach that consisted of the aluminum cathode and the blue, red or green light-emitting polymer (LEP) layer. The device showed good efficiencies comparable to that of conventional spin-coated devices [73]. BA-LIFT has been also employed for the fabrication of OLEDs with electroluminescence emission and

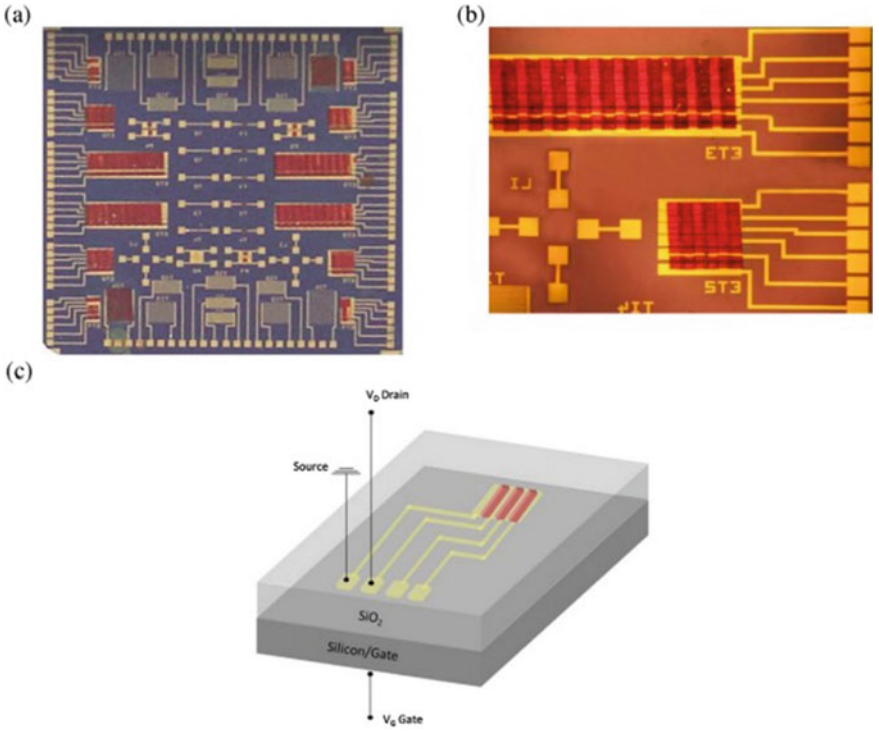

Fig. 9.7 Optical images of LIFT printed PQT-12 OTFTs (PQT-12 printed on Pt electrodes) at increasing magnification, showing the whole chip (**a**), and small regions (**b**). **c** Schematic representation of the fabricated OTFTs and the relevant applied voltages. Reprinted with permission from [58]. Copyright 2016, with kind permission from Elsevier

diode behavior and reporting lifetime comparable with literature reports for spin-coated devices [25]. Moreover, microcapacitors with controlled electrical capacity in the pF-nF range have been reported using LIFT, where micrometric-sized pixels of hybrid organic–inorganic thin films (Ag/parylene-C) have been transferred [74]. In the same context, Rapp et al. [72], have demonstrated multilayer capacitor pixels using picosecond LIFT along with a smart beam shaping technique that included a double mask setup.

9.4.2 Laser Printing for Chemical Sensors and Biosensors

The ability of LIFT to transfer a wide range of materials has enabled the academic community to investigate the printing of materials—other than metals—such as polymers [17, 18, 75–79], carbon nanotubes [80], carbon nanotube/polymer nanocomposites [81], oxides [82, 83], and biomaterials [26, 27, 46, 84–106] for the fabrication

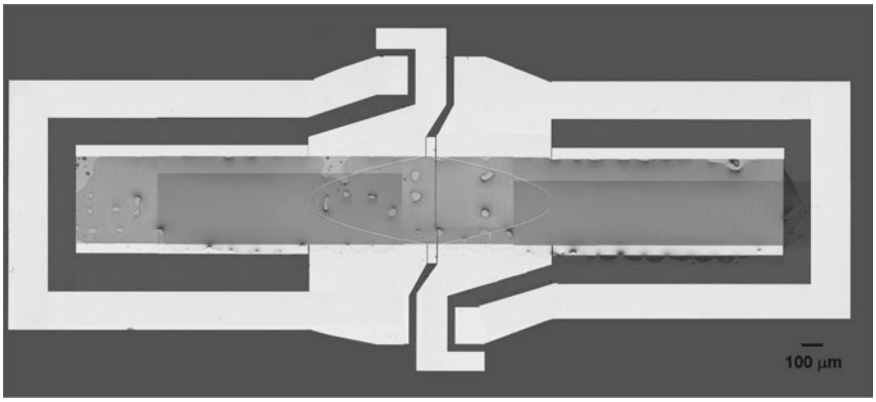

Fig. 9.8 Optical microscopy images of SAW devices coated by overlapping droplets printed through LIFT with a laser fluence of 650 mJ/cm^2. Reprinted with permission from [86]. Copyright 2014, with kind permission from Elsevier

of chemical sensors and biosensors, where laser printing may be used to deposit both the sensing elements and the conductive electrodes of the sensor device. Among the signal transduction mechanisms one may find resistive, capacitive, surface-acoustic wave (SAW), film bulk acoustic resonators (FBARs) and amperometric sensors that exhibit high sensitivity and selectivity towards the analytes under detection. In addition, the high spatial resolution of the technique enables for the dense and precise deposition of array patterns for simultaneous multi-analyte measurements (Fig. 9.8).

More specifically, regarding chemical sensors, Tsouti et al. [77] have demonstrated the development of a capacitive chemical sensor array, able to host up to 256 sensing sites using LIFT. Various polymers have been laser transferred in this work namely poly(2-hydroxyethyl methacrylate) (PHEMA), polyacrylic acid (PAA), poly(4-vinylpyridine) (P4VP), poly(vinylpyrrolidone) (PVP), poly(vinyl chloride-co-vinyl acetate) (PVC-co-PVA), poly(hydroxyl styrene) (PHS) and poly(methyl methacrylate) (PMMA) on thin silicon/LTO membrane substrates. The sensor arrays have been tested upon exposure to different analytes such as methanol, water, and ethanol vapors and exhibited good sensitivity depending on the analyte under investigation. In another work by Dinca et al. [17], polyethylenimine (PEI) and polyisobutylene (PIB) sensitive polymers have been laser printed on SAW substrates for the fabrication of chemical sensors. In this case, solid-phase DRL-LIFT has been used and it was shown that in order to avoid damage to the interdigital transducers a laser fluence under 625 mJ/cm^2 should be applied. In addition, the sensor devices were tested upon exposure to acetone and it was highlighted that LIFT may be used for the transfer of sensitive polymers for the fabrication of chemical sensors. Furthermore, oxides (SnO_2) have been transferred using LIFT and employed different precursor systems based on UV absorbing metal complex precursors namely, $SnCl_2(acac)_2$ for the preparation of the donor substrate. The devices showed good response and the deposited polymers showed changes in their electrical

conductivity upon testing with acetone, methane, and ethanol [83]. Chemoselective polymers have been also printed with LIFT on SAW sensors for the detection of toxic volatile organic compounds (sarin, GB) [79]. In this work, chemical sensors based on FBARs, in the solidly mounted resonator (SMR) configuration have been reported, exploiting three polymer sensitive layers (LIFT printed) namely, polyepichlorohydrin (PECH), polyethyleneimine (PEI), and polyisobutylene (PIB), with a detection limit of 9.24 ppb for the PECH coated sensor when exposed to GB. Recently, graphene oxide ink has been laser printed on Au electrodes on SiO_2 substrates, using the 4rth harmonic of a pulsed Nd:YAG laser source and the printed features subsequently underwent a thermal reduction step to restore the electrical properties of the graphitic material [82]. The resistive chemical sensor devices were tested upon exposure to water, ethanol, and p-xylene vapors and showed good response with a sensitivity of 5000 ppm for water vapors and 700 ppm for p-xylene vapors.

Regarding the incorporation of LIFT into the fabrication of biosensor devices, the first work was reported by Karaiskou et al. [93], where lambda phage DNA microarrays were printed on glass substrates using LIFT. The ultrafast laser pulses were generated by a sub-ps laser source ($\lambda = 248$ nm, $f = 500$ fs) and the transferred structures had a 100 μm $\times$ 100 μm size. One year earlier, Ringeisen and co-workers [91], have demonstrated the transfer of active proteins, viable *Escherichia coli* and mammalian Chinese hamster ovary cells using a laser direct-write technique that combined the LIFT and MAPLE techniques. After its first demonstration in biosensors fabrication, LIFT has been often used for the printing of biomaterials as in the case of [92], where a novel laser printing approach has been reported. More specifically, proteins and DNA have been laser transferred using a diode-pumped ytterbium femtosecond laser ($\lambda = 1027$ nm, $\tau = 450$ fs) from a tank that contained the biomaterial solution and not a donor substrate as in the case of traditional LIFT. In this case, the receiver substrate was transparent to the wavelength used and the laser pulse went through the receiver substrate and was subsequently focused in the tank containing the liquid solution causing micro-droplets to be ejected back towards the receiver substrate (printing direction is in the opposite direction with respect to the initial beam direction) in an approach similar to LIBT (Fig. 9.9).

Furthermore, skin cell lines (fibroblasts/keratinocytes) and human mesenchymal stem cells have been transferred using LIFT owing to their potential use in regeneration of human skin applications as well as stem cell therapy [107]. In another work involving the laser printing of cells, high throughput laser printing has been demonstrated [97], for the transfer of the biopolymer (sodium alginate), and biomaterials (nano-sized hydroxyapatite synthesized by wet precipitation) and human endothelial cells (EA.hy926). This study demonstrated the potential of BioLP for three-dimensional tissue construction applications. For the experiments, a rapid prototyping workstation equipped with an IR pulsed laser ($\tau = 30$ ns, $\lambda = 1064$ nm) was used. The transferred structures were 70 μm in diameter, where each droplet contained 5–7 living cells. Another application that LIFT has been used, is point-of-care medical diagnostics [104], where antibodies were laser transferred on cellulose paper substrates that is an ideal receiver because of its bio-compatibility and liquid transport properties. A calibration curve that related to the intensity of the color

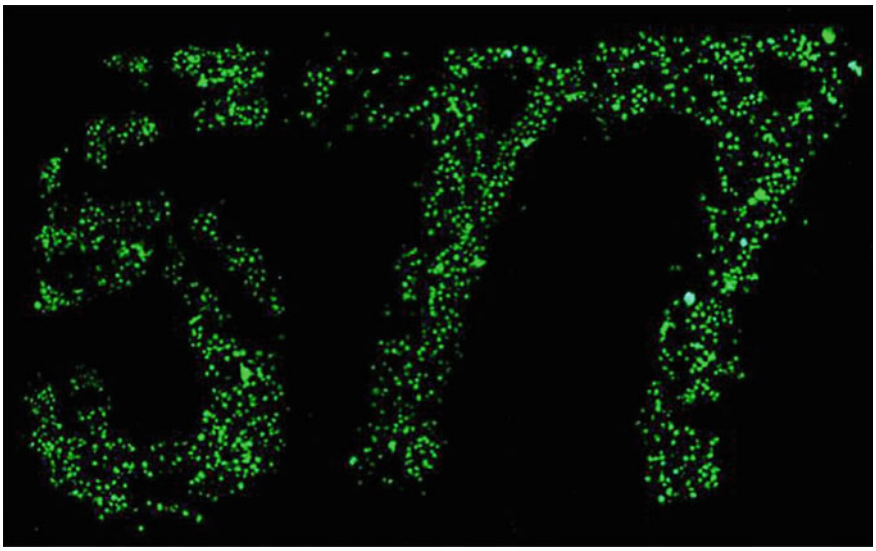

Fig. 9.9 A laser printed pattern of EA.hy926 cells after live/dead assay. Reprinted with permission from [97]. Copyright 2010, with kind permission from Elsevier

obtained to the concentration of active antibodies was determined so as to enable a quantitative assessment of the device performance.

9.4.3 Laser Printing of Organic/inorganic Inks, Nanoparticles, and Pastes

Metallic NPs inks are commonly employed for the formation of electrical interconnects and conductive patterns in IC technology, where silver, gold, and copper NPs inks are often used. Metallic NPs present a significant decrease in their melting point owing to the high surface-area-to-volume ratio, therefore enabling their sintering in low temperatures that makes them compatible with flexible and sensitive to high-temperature substrates (paper, polymers) [108]. In addition, they present strong light absorption and unique optical properties within the visible range facilitating their post-processing [109]. Moreover, the NPs after their coalescence in conductive and rigid patterns show high electrical conductivity, almost half the electrical conductivity of the bulk material as well as air stability in ambient environments [110, 111]. Conductive inks are usually found in aqueous or organic solvent dispersions, where alcohols, ethylene and diethylene glycol, glycol ether and cyclohexanone are commonly employed solvents for printable inks [112] (Fig. 9.10).

LIFT has been used for the printing of conductive inks of Ag NPs for over a decade now [108], where silver NPs inks with widths <20 μm and heights of ~0.5 μm have

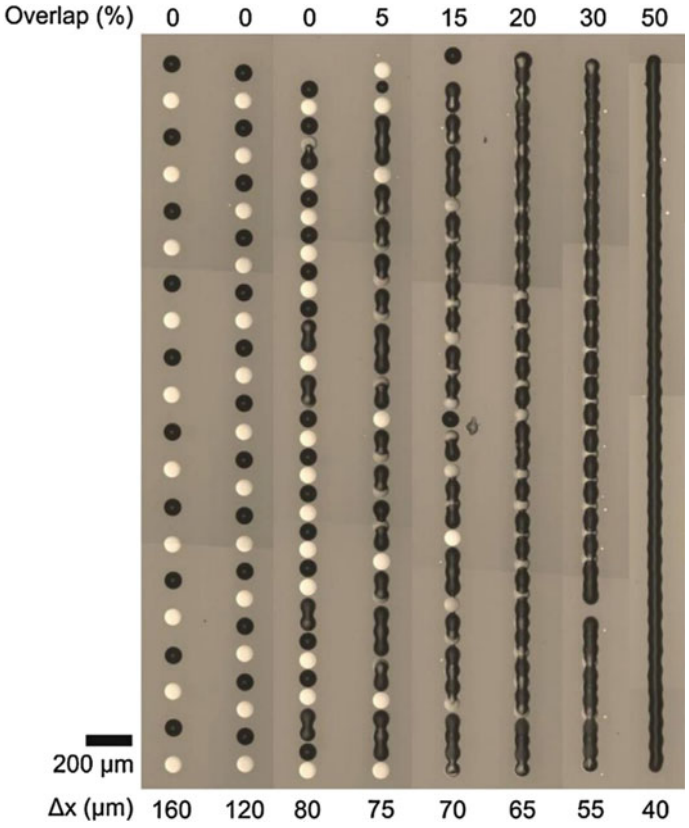

Fig. 9.10 Optical microscopy photo of silver ink lines printed with different printing distances between adjacent droplets. Reprinted with permission from [119]. Copyright 2015, with kind permission from Elsevier

been deposited on polyimide substrates exhibiting electrical resistivities that were below 10× the bulk silver using oven or laser curing. Recently, several works have presented the transfer of metallic NPs inks and pastes for electronic applications, a factor that later leads to the incorporation of LIFT in additive manufacturing processes as it will be described in the next paragraphs [2, 13, 15, 113–120]. More specifically, in [119] conductive silver NPs inks have been transferred in line patterns using a Yb:KYW laser with an output wavelength at 1027 nm and a pulse duration of 450 fs. Since bulging and irregular shape of the printed lines is often observed in line printing, in this work, a different approach was followed. This was based on printing adjacent droplets in alternate sequences, therefore printing two overlapping sets of droplets with an intermediate drying step allowing the formation of functional continuous lines without bulging (Fig. 9.11).

In another work [2], the transfer mechanism of a high viscosity (280–400 Pa s) silver paste was investigated with fluences in the range between 0.6 and 14.4 J/cm^2

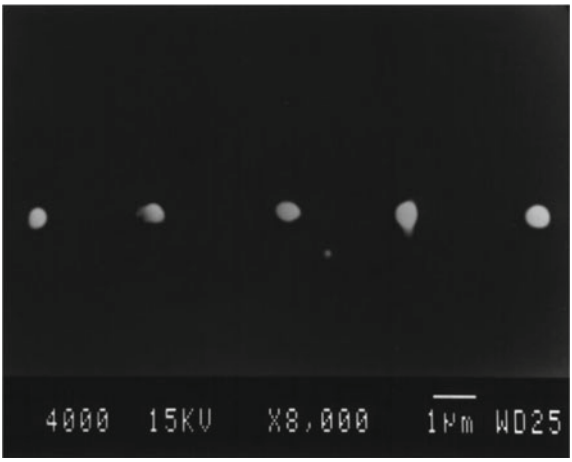

Fig. 9.11 SEM image of chromium dots laser printed on glass using fs laser pulses. Reprinted with permission from [13]. Copyright 1998, with kind permission from Springer Science and Business Media

using a 532 nm pulsed ns laser source. Four different ejection regimes were reported namely (i) non-dot transfer for laser fluence below the thickness-dependent transfer threshold, (ii) cluster-dot transfer where the paste fragments in larger clusters, (iii) concrete-dot transfer, where the paste is transferred in a well-defined manner, and (iv) explosive transfer, where for the high laser fluence regime a bursting transfer is observed. Furthermore, the high-speed laser printing of silver NPs ink has been investigated by Rapp et al. [117], where a picosecond laser emitting at 343 nm at 500 kHz was used to transfer silver lines of 30 μm width and thinner than 500 nm, with millimeter length and printing velocities up to 4 m/s.

Recently, apart from the aforementioned metallic nanoparticles, silicon nanoparticles [14] and liquid phase exfoliated graphene ink [121] have been transferred using LIFT. In the first case, femtosecond laser printing of silicon nanoparticles onto glass substrates has been reported. The laser-printed nanoparticles have been arranged both in periodic and complex structures, allowing for the generation of individual amorphous and crystalline spherical silicon NPs, whose optical properties could be precisely controlled (Fig. 9.12).

In the latter case, a graphene ink in N-methylpyrrolidone (NMP) with a concentration of 0.078 mg/ml has been printed on SiO_2 and flexible polymeric substrates (polyethylene naphthalate, PEN) in array and line patterns using the fourth harmonic ($\lambda = 266$ nm, $\tau = 4$ ns) of an Nd:YAG laser source. The printed features were investigated using micro-Raman spectroscopy and presented good structural properties comparable to that of the reference drop casted samples, while electrical conductivity values were at the order of 1 S/m slightly lower than those reported by inkjet printing possibly due to the rapid oxidation of NMP when heated in ambient conditions.

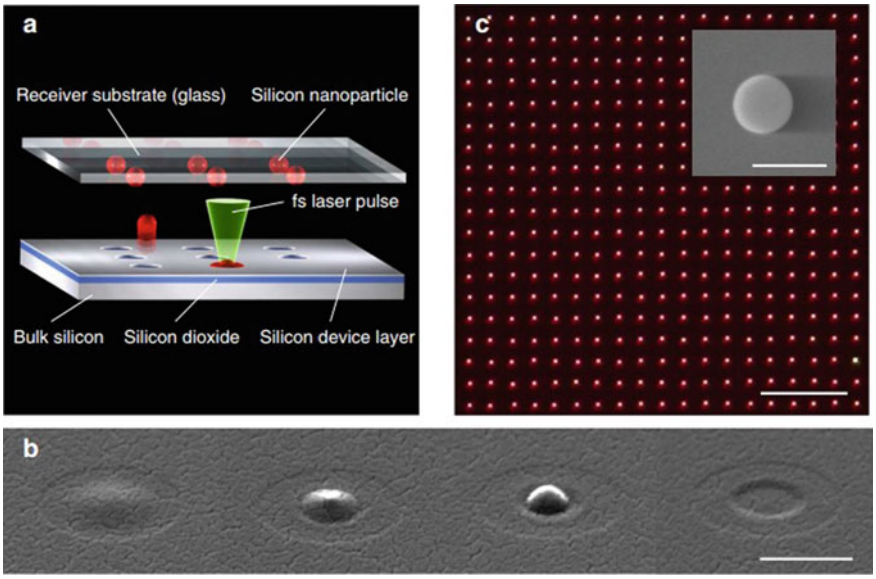

Fig. 9.12 **a** Schematic of femtosecond laser printing of silicon nanoparticles, **b** SEM images of the target before and after the silicon nanoparticle ejection. From left to right, the laser pulse energy is increased (scale bar, 400 nm), **c** array of amorphous Si nanoparticles (diameter of 160 nm) (scale bar, 20 mm). Reprinted by permission from Macmillan Publishers Limited [Nature Communications] [14]. Copyright (2014)

9.5 Complementarity of LIFT with Other Laser Processes for Device Fabrication and Manufacturing

Although laser printing may serve as a stand-alone technique for device fabrication in various applications, it may also be used in complement to other laser processes such as laser sintering and laser ablation. This enables the all laser fabrication of functional components in IC technologies, since lasers enable not only the rapid and low-cost processing but also substrate selectivity, as in the case of temperature-sensitive substrates. In this context, laser sintering has been widely employed especially in the case of metallic NPs inks [122–130] to enable the coalescence of the particles into conductive patterns. According to the study performed by Zenou et al. [124], the sintering of the metallic NPs may be structured in three main steps that involve: (i) the evaporation of the solvent, (ii) the removal of dispersants and binder materials through thermal decomposition, and (iii) the neck formation and grain growth, whereas the NPs size and the decomposition temperatures of the organic binders play an important role in the sintering parameters. In these frames, in [122] gold nanoparticles in solution have been laser sintered using an argon-ion laser at 488 nm, with reported specific electrical resistivities of the laser-cured gold conductors at the order of 1.4×10^{-7} Ω m. Moreover, in [124] copper NPs inks have been laser sintered using a

532 nm continuous wave (CW) laser source in ambient conditions and the reported resistivities were 2–3 times lower than that of the bulk copper, similar to the values for non-oxidizing atmospheres and linewidths of <5 μm, whereas the process was monitored through reflectivity measurements that facilitated the evaluation of the sintered structures. Moreover, a comparative study on the use of CW, ns and ps pulsed laser sources has been demonstrated in [126], using both 532 and 1064 nm wavelengths for the laser sintering of Ag NPs inks on PEN and showed that the optimum electrical properties were obtained with 1064 nm and ns pulses due to the lower optical absorption of the NPs at this wavelength. The laser wavelength effect on the sintering of silver NPs inks was also reported by Paeng et al. [128]. In this work, Ag NPs inks spin-coated on soda lime glass substrates were irradiated using three different wavelengths namely 405, 514.5, and 817 nm at different laser intensities and scanning speeds. One important finding was that while the optical response of the processed inks was mainly determined by the laser wavelength it was the beam intensity and the scanning speed that controlled the induced temperature fields. The lowest electrical resistivity in this work was reported for the 514.5 nm wavelength and 2 mm/s scanning speed (100 mW laser power) at 5.28 μΩ cm, while it was slightly higher for the 405 and 817 nm wavelengths, where the resistivities were 5.7 and 8.9 μΩ cm respectively.

9.6 LIFT Towards 3D Printing and Additive Manufacturing

The evolution of the laser printing technology during the last decade has allowed for the printing of more complex structures towards the development of electrical interconnects and rapid prototyping processes. The ability that the LIFT technique offers relies on the fact that it can print virtually any material on any substrate and this can be also exploited in applications where different surface topologies are used. In these frames, Kaur et al. [131], have demonstrated the flip-chip bonding of vertical cavity surface-emitting lasers (VCSEL), using LIFT (Fig. 9.13).

More specifically, this work involved the deposition of indium micro-bumps onto bond pads including a successive deposition of additional printed layers so as to create a final structure of 1.5 μm in height and 20 μm in diameter. Performance evaluation of the developed chips showed a variation in optical power of less than 0.3 dB after 350 h. of testing at 85 °C and 85% relative humidity, a minimal degradation that could be attributed to moisture penetration. In a different work, Wang et al. [132], reported the laser 3-dimensional printing of silver nanopastes for the formation of interconnects including voxels crossing 100 μm wide silicon channels, multilayer scaffold structures and high aspect ratio micro pyramids and micro pillars. Furthermore, Zenou et al. [133], also showed the 3D printing of micro-objects using a variation of LIFT entitled Thermal Induced Nozzle-LIFT (TIN-LIFT) that employs sub-nanosecond pulses to enable the transfer of thick metal structures through the

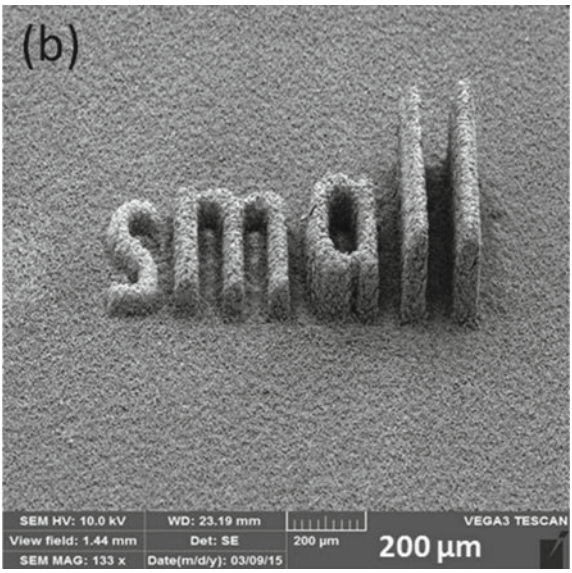

Fig. 9.13 SEM photo of laser-printed copper logo with different heights between adjacent letters as: "s" is 40 μm, then, "m" = 70 μm, "a" = 120 μm, "l" 190 μm. Reprinted with permission from [134]. Copyright 2015, with kind permission from Wiley-VCH Verlag GmbH & Co. KGaA, Weinheim

formation of nozzle like structures that enable high directionality of the transferred materials. Thus, in this work, copper metal pillars were formed using TIN-LIFT with a height of 106 μm and a width of 9 μm, where each pillar consisted of 200 printed copper droplets, while conformal, laser micro-cladding of 3D micro-parts was demonstrated as well. In another work, Zenou et al. [134], developed copper laser printed logos, where each letter had a different height ranging between 40 and 190 μm. This work also showed for the first time the laser printing of copper in ambient conditions that enable the transfer on heat-sensitive substrates and could eliminate the need for post-printing processes such as thermal sintering. Similar to the aforementioned works, Visser et al. [135], deposited copper pillars with a maximum height of 2.1 mm, showing the potential use of the technique for out-of-plane interconnects between different layers of stacked electronics. The unique characteristics of LIFT are not limited only in integrated circuits and interconnects applications but also in biological applications. In the work by Gruene et al. [136], the laser printing of three-dimensional multicellular arrays was presented for the study of cell-cell and cell-environment interactions. Additional experiments on cell survival, proliferation and cytotoxicity were performed and possible negative effects of the laser printing technique have been excluded.

9.7 Industrialization of LIFT

The ever-growing research interest in the unique advantages that LIFT presents has enabled the constant growth of the technique and the evolution in terms of

printing resolution, speed, and reproducibility for a wide variety of materials. This was exploited not only by the academia but from the industry as well since in the last 5 years the technique has been exploited for commercial purposes. For example in 2011, Daetwyler launched a digital laser printing solution called LaserSonic [137] under the banner "DI Project AG," which was a joint venture of the companies Interprint and Daetwyler. In addition, Orbotech Ltd. has launched the Precise™ 800 system [138] that is the first solution for advanced High-Density Interconnect (HDI) and complex multi-layer PCB manufacturing and is capable of both removing excess copper and also depositing missing copper. Moreover, in the biomaterial industry Poietis offers a laser-assisted bioprinting solution [139] that relies on the principles of 3D printing and allows the precise 3D positioning of cells as well as extracellular matrix via a layer by layer assembly approach with micrometer resolution. Finally, ALPhaNOV [140] is already participating in a research project, where its main goal is to validate the methodology for laser-assisted biological materials printing for in vivo bone tissue engineering in mice.

9.8 Conclusions

The progress of laser printing technology and specifically of the LIFT technique was presented in this chapter with the aim to provide a complete overview on the important findings and applications that have been made up to date. The evolution that has been made since LIFT's first reporting has enabled LIFT to be incorporated into the development of several different applications such as chemical and biological sensors, OLEDs, OTFTs, electrical interconnects etc. Moreover, the unique advantages of LIFT namely selectivity, high-spatial resolution and versatility along with the complementarity of the technique with other laser processes including laser sintering, ablation, etc. enable the fabrication of all-laser printed devices in a rapid and cost-effective way and this has been already exploited for industrial purposes as it was mentioned in the last paragraph.

Acknowledgements The authors kindly acknowledge funding from the "Research Projects for Excellence IKY/SIEMENS" Program.

References

1. C.B. Arnold, P. Serra, A. Pique, MRS Bull. **32**, 23–31 (2007)
2. D. Munoz-Martina, C.F. Brasz, Y. Chena, M. Morales, C.B. Arnold, C. Molpeceres, Appl. Surf. Sci. **366**, 389–396 (2016)
3. M.L. Levene, R.D. Scott, B.W. Siryj, Material transfer recording. Appl. Opt. **9**(10), 2260–2265 (1970)
4. J. Bohandy, B. Kim, F.J. Adrian, J. Appl. Phys. **60**, 1538 (1986)

5. F.J. Adrian, J. Bohandy, B.F. Kim, A.N. Jette, P. Thompson, J. Vac. Sci. Technol. B **5**(5), 1490 (1987)
6. A. Pique, in *Laser Precision Microfabrication*, ed. by K. Sugioka, M. Meunier, A. Pique (Springer, Berlin Heidelberg New York, 2010), pp. 259–291
7. T.F. Deutsch, D.J. Ehrlich, R.M. Osgood Jr., Appl. Phys. Lett. **35**(2), 175–177 (1979)
8. R.M. Osgood Jr., Ann. Rev. Phys. Chem. **34**(77), 77–101 (1983)
9. R.M. Osgood Jr., J. Phys. **44**, C5133–C5138 (1983)
10. J.A. Greer, T.E. Parker, SPIE Proc. **998**, 113–125 (1988)
11. L. Rapp, C. Cibert, A.P. Alloncle, P. Delaporte, Appl. Surf. Sci. **255**, 5439–5443 (2009)
12. A. Palla-Papavlu, V. Dinca, C. Luculescu, J. Shaw-Stewart, M. Nagel, T. Lippert, M. Dinescu, J. Opt. **12**, 124014 (2010)
13. I. Zergioti, S. Mailis, N.A. Vainos, P. Papakonstantinou, C. Kalpouzos, C.P. Grigoropoulos, C. Fotakis, Appl. Phys. A **66**, 579 (1998)
14. U. Zywietz, A.B. Evlyukhin, C. Reinhardt, B.N. Chichkov, Nat. Commun. **5**, 3402 (2014)
15. M. Duocastella, H. Kim, P. Serra, A. Piqué, Appl. Phys. A **106**, 471–478 (2012)
16. J.A. Grant-Jacob, B. Mills, M. Feinaeugle, C.L. Sones, G. Oosterhuis, M.B. Hoppenbrouwers, R.W. Eason, Opt. Mater. Express **3**(6), 747–754 (2013)
17. V. Dinca, A. Palla-Papavlu, M. Dinescu, J. Shaw Stewart, T.K. Lippert, F. Di Pietrantonio, D. Cannata, M. Benetti, E. Verona, Appl. Phys. A **101**, 559–565 (2010)
18. C. Boutopoulos, V. Tsouti, D. Goustouridis, S. Chatzandroulis, I. Zergioti, Appl. Phys. Lett. **93**, 191109 (2008)
19. L. Rapp, F. Serein-Spirau, J.-P. Lere-Porte, A.P. Alloncle, P. Delaporte, F. Fages, C. Videlot Ackermann, Org. Electron. **13**, 2035–2041 (2012)
20. N.T. Kattamis, P.E. Purnick, R. Weiss, C.B. Arnold, Appl. Phys. Lett. **91**, 171120 (2007)
21. https://www.scopus.com/
22. W.A. Tolbert, I.Y.S. Lee, M.M. Doxtader, E.W. Ellis, D.D. Dlott, J. Imaging Sci. Technol **37**, 411 (1993)
23. A.I. Kuznetsov, J. Koch, B.N. Chichkov, Opt. Express **17**(21), 18820–18825 (2009)
24. K.B. Shepard, Y. Guo, C.B. Arnold, R.D. Priestley, Appl. Phys. A (2012). https://doi.org/10.1007/s00339-012-7151-8
25. N.T. Kattamis, N.D. McDaniel, S. Bernhard, C.B. Arnold, Org. Electron. **12**, 1152–1158 (2011)
26. B. Hopp, T. Smausz, N. Kresz, N. Barna, Z. Bor, L. Kolozsvari, D.B. Chrisey, A. Szabo, A. Nogradi, Tissue Eng. **11**, 1181 (2005)
27. J.A. Barron, P. Wu, H. Ladouceur, B.R. Ringeisen, Biomed. Microdevices **6**, 139–147 (2004)
28. J.R.H. Shaw-Stewart, T. Mattle, T.K. Lippert, M. Nagel, F.A. Nuesch, A. Wokaun, J. Appl. Phys. **113**, 043104 (2013)
29. J. Stebani, O. Nuyken, T. Lippert, A. Wokaun, Makromol. Chem. Rapid Commun. **14**, 365 (1993)
30. C. Constantinescu, A.K. Diallo, L. Rapp, P. Cremillieu, R. Mazurczyk, F. Serein-Spirau, J.P. Lere-Porte, P. Delaporte, A.P. Alloncle, C. Videlot-Ackermann, Appl. Surf. Sci. **336**, 11–15 (2015)
31. B. Thomas, A.P. Alloncle, P. Delaporte, M. Sentis, S. Sanaur, M. Barret, P. Collot, Appl. Surf. Sci. **254**, 1206 (2007)
32. M. Duocastella, J.M. Fernandez-Pradas, J.L. Morenza, P. Serra, J. Appl. Phys. **106**, 084907 (2009)
33. A. Patrascioiu, J.M. Fernandez-Pradas, A. Palla-Papavlu, J.L. Morenza, P. Serra, Microfluid. Nanofluid. **16**, 55–63 (2014)
34. D. Young, R.C.Y. Auyeung, A. Pique, D.B. Chrisey, D.D. Dlott, Appl. Surf. Sci. **197–198**, 181–187 (2002)
35. R. Pohl, C.W. Visser, G.R.B.E. Römer, C. Sun, A.J. Huis in't Veld, D. Lohse, J. Laser Micro/Nanoeng. **10**(2), 154–157 (2015)
36. C. Boutopoulos, I. Kalpyris, E. Serpetzoglou, I. Zergioti, Microfluid. Nanofluid **16**, 493–500 (2014)

37. S.A. Mathews, R.C.Y. Auyeung, H. Kim, N.A. Charipar, A. Pique, J. Appl. Phys. **114**, 064910 (2013)
38. E. Biver, L. Rapp, A.P. Alloncle, P. Delaporte, Appl. Surf. Sci. **302**, 153–158 (2014)
39. C.F. Brasz, J.H. Yang, C.B. Arnold, Microfluid. Nanofluid. **18**(2), 185–197 (2015)
40. A. Patrascioiu, C. Florian, J.M. Fernandez-Pradas, J.L. Morenza, G. Hennig, P. Delaporte, P. Serra, Appl. Phys. Lett. **105**, 014101 (2014)
41. C. Unger, M. Gruene, L. Koch, J. Koch, B.N. Chichkov, Appl. Phys. A **103**, 271–277 (2010)
42. N.T. Kattamis, M.S. Brown, C.B. Arnold, J. Mater. Res. **26**(18), 2438–2449 (2011)
43. M.S. Brown, N.T. Kattamis, C.B. Arnold, Microfluid. Nanofluid. **11**, 199–207 (2011)
44. M. Ali, E. Pages, A. Ducom, A. Fontaine, F. Guillemot, Biofabrication **6**, 045001 (2014)
45. Y. Nakata, T. Okada, Appl. Phys. A **69**(Suppl.), S275–S278 (1999)
46. I. Zergioti, A. Karaiskou, D.G. Papazoglou, C. Fotakis, M. Kapsetaki, D. Kafetzopoulos, Appl. Surf. Sci. **247**, 584–589 (2005)
47. R. Fardel, M. Nagel, F. Nuesch, T. Lippert, A. Wokaun, Appl. Surf. Sci. **255**, 5430–5434 (2009)
48. R. Fardel, M. Nagel, F. Nuesch, T. Lippert, A. Wokaun, J. Phys. Chem. C **114**, 5617–5636 (2010)
49. J. Shaw-Stewart, B. Chu, T. Lippert, Y. Maniglio, M. Nagel, F. Nuesch, A. Wokaun, Appl Phys A **105**, 713–722 (2011)
50. R. Pohl, M. Jansink, G.R.B.E. Römer, A.J. Huis in't Veld, Appl. Phys. A Mater. Sci. Process. **120**(2), 427–434 (2015)
51. C.D.G. Constantinescu, L. Rapp, P. Rotaru, A.P. Alloncle, J. Phys. D Appl. Phys. **49**(15), 155301 (2016). https://doi.org/10.1088/0022-3727/49/15/155301
52. R. Fardel, M. Nagel, F. Nuesch, T. Lippert, A. Wokaun, Appl. Surf. Sci. **254**, 1322–1326 (2007)
53. S.H. Ko, C.P. Grigoropoulos, in ed. by S.H. Ko (InTech, 2011). ISBN: 978-953-307-273-9
54. L. Rapp, S. Nenon, A.P. Alloncle, C. Videlot-Ackermann, F. Fages, P. Delaporte, Appl. Surf. Sci. **257**, 5152–5155 (2011)
55. I. Zergioti, M. Makrygianni, P. Dimitrakis, P. Normand, S. Chatzandroulis, Appl. Surf. Sci. **257**, 5148–5151 (2011)
56. L. Rapp, A.K. Diallo, S. Nenon, A.P. Alloncle, C. Videlot-Ackermann, F. Fages, M. Nagel, T. Lippert, P. Delaporte, Thin Solid Films **520**, 3043–3047 (2012)
57. M. Makrygianni, E. Verrelli, N. Boukos, S. Chatzandroulis, D. Tsoukalas, I. Zergioti, Appl. Phys. A **110**, 559–563 (2013)
58. M. Makrygianni, A. Ainsebaa, M. Nagel, S. Sanaur, Y.S. Raptis, I. Zergioti, D. Tsamakis, Appl. Surf. Sci. **390**, 823–830 (2016)
59. L. Rapp, A.K. Diallo, A.P. Alloncle, C. Videlot-Ackermann, F. Fages, P. Delaporte, Appl. Phys. Lett. **95**, 171109 (2009)
60. H. Kim, R.C.Y. Auyeung, S.H. Lee, A.L. Huston, A. Piqué, J. Phys. D Appl. Phys. **43**(8), 085101 (2010)
61. R. Fardel, M. Nagel, F. Nuesch, T. Lippert, A. Wokaun, Appl. Phys. Lett. **91**, 061103 (2007)
62. J.S. Stewart, T. Mattle, T. Lippert, M. Nagel, F. Nüesch, A. Wokaun, Appl. Surf. Sci. **278**, 341–346 (2013)
63. J.S. Stewart, T. Lippert, M. Nagel, F. Nüesch, A. Wokaun, ACS Appl. Mater. Interfaces **4**(7), 3535–3541 (2012)
64. H. Kim, G. Kushto, C.B. Arnold, Z.H. Kafafi, A. Pique, Appl. Phys. Lett. **85**, 464 (2004)
65. M.I. Sanchez-Aniorte, B. Mouhamadou, A.P. Alloncle, T. Sarnet, P. Delaporte, Appl. Phys. A **122**, 595 (2016). https://doi.org/10.1007/s00339-016-0113-9
66. M. Colina, A. Morales-Vilches, C. Voz, I. Martín, P. Ortega, A. Orpella, G. López, R. Alcubilla, Appl. Surf. Sci. **336**, 89–95 (2015)
67. H. Kim, R.C.Y. Auyeung, A. Pique, J. Power Sources **165**, 413–419 (2007)
68. H. Kim, J. Proell, R. Kohler, W. Pfleging, A. Pique, J. Laser Micro/Nanoeng. **7**, 3 (2012)
69. A.C. Atre, C.B. Arnold, Proc. SPIE **7921** (2011). https://doi.org/10.1117/12.876467
70. A. Pique, et al., Proc. SPIE 27–31 (2002). https://doi.org/10.1117/12.486567

71. C.B. Arnold, T. Sutto, H. Kim, A. Pique, Laser Focus World **40**, 9–12 (2004)
72. L. Rapp et al., Sens. Actuators A Phys. **224**, 111–118 (2015)
73. J.S. Stewart, T. Lippert, M. Nagel, F. Nuesch, A. Wokaun, Appl. Phys. Lett. **100**, 203303 (2012)
74. C.D.G. Constantinescu, L. Rapp, A.K. Diallo, C.V. Ackerman, P. Delaporte, P. Alloncle, Org. Electron. **20**, 1–7 (2015)
75. M. Kandyla, S. Chatzandroulis, I. Zergioti, Opto-Electron. Rev. **18**(4), 345–351 (2010)
76. V. Dinca, A. Palla-Papavlu, I. Paraico, T. Lippert, A. Wokaun, M. Dinescu, Appl. Surf. Sci. **257**, 5250–5254 (2011)
77. V. Tsouti, C. Boutopoulos, D. Goustouridis, I. Zergioti, P. Normand, D. Tsoukalas, S. Chatzandroulis, Sens. Actuators B **150**, 148–153 (2010)
78. D. Cannata et al., Sens. Actuators B **173**, 32–39 (2012)
79. F. Di Pietrantonio, M. Benetti, D. Cannata, E. Verona, A. Palla-Papavlu, V. Dinca, M. Dinescu, T. Mattle, T. Lippert, Sens. Actuators B **174**, 158–167 (2012)
80. A. Palla-Papavlu, M. Dinescu, A. Wokaun, T. Lippert, Appl. Phys. A **117**, 371–376 (2014)
81. C. Boutopoulos, C. Pandis, C. Giannakopoulos, P. Pissis, I. Zergioti, Appl. Phys. Lett. **96**, 041104 (2010)
82. S. Papazoglou, V. Tsouti, S. Chatzandroulis, I. Zergioti, Opt. Laser Technol. **82**, 163–169 (2016)
83. T. Mattle, A. Hintennach, T. Lippert, A. Wokaun, Appl. Phys. A **110**, 309–316 (2013)
84. P. Serra, M. Colina, J.M. Fernandez-Pradas, L. Sevilla, J.L. Morenza, Appl. Phys. Lett. **85**, 1639–1641 (2004)
85. J.A. Barron, H.D. Young, D.D. Dlott, M.M. Darfler, D.B. Krizman, B.R. Ringeisen, Proteomics **5**, 4138 (2005)
86. A.P. Papavlu, et al., Sens. Actuators B **192**, 369–377 (2014)
87. V. Dinca, E. Kasotakis, J. Catherine, A. Mourka, A. Mitraki, A. Popescu, M. Dinescu, M. Farsari, C. Fotakis, Appl. Surf. Sci. **254**, 1160–1163 (2007)
88. V. Dinca, M. Farsari, D. Kafetzopoulos, A. Popescu, M. Dinescu, C. Fotakis, Thin Solid Films **516**, 6504–6511 (2008)
89. V. Dinca, A. Ranella, M. Farsari, D. Kafetzopoulos, M. Dinescu, A. Popescu, C. Fotakis, Biomed. Microdevices **10**, 719–725 (2008)
90. M. Colina, M. Duocastella, J.M. Fernandez-Pradas, P. Serra, J.L. Morenza, J. Appl. Phys. **99**, 084909 (2006)
91. B.R. Ringeisen, D.B. Chrisey, A. Pique, H.D. Young, R. Modi, M. Bucaro, J. Jones-Meehan, B.J. Spargo, Biomaterials **23**, 161–166 (2002)
92. M. Duocastella, J.M. Fernandez-Pradas, J.L. Morenza, D. Zafra, P. Serra, Sens. Actuators B **145**, 596–600 (2010)
93. A. Karaiskou, I. Zergioti, C. Fotakis, M. Kapsetaki, D. Kafetzopoulos, Appl. Surf. Sci. **208–209**, 245–249 (2003)
94. J.M. Fernandez-Pradas, M. Colina, P. Serra, J. Dominguez, J.L. Morenza, Thin Solid Films **453–454**, 27–30 (2004)
95. S. Michael, H. Sorg, C.-T. Peck, L. Koch, A. Deiwick, B. Chichkov, P.M. Vogt, K. Reimers, PLoS ONE **8**(3), e57741 (2013)
96. S. Catros, F. Guillemot, A. Nandakumar, S. Ziane, L. Moroni, P. Habibovic, C. van Blitterswijk, B. Rousseau, O. Chassande, J. Amedee, J.-C. Fricain, Tissue Eng. Part C Methods **18**(1), 62–70 (2012)
97. F. Guillemot et al., Acta Biomater. **6**(7), 2494–2500 (2010)
98. S. Catros et al., Biofabrication **3**(2), 025001 (2011)
99. J. Yan, Y. Huang, D.B. Chrisey, Biofabrication **5**(1), 015002 (2013)
100. H. Gudapati, J. Yan, Y. Huang, D.B. Chrisey, Biofabrication **6**(3), 035022 (2014)
101. L. Koch, M. Gruene, C. Unger, B. Chichkov, Curr. Pharm. Biotechnol. **14**(1), 91–97 (2013)
102. M. Gruene et al., Tissue Eng. Part C Methods **17**(1), 79–87 (2011)
103. B. Guillotin et al., Biomaterials **31**(28), 7250–7256 (2010)
104. I.N. Katis et al., Biomicrofluidics **8**, 036502 (2014)

105. Z. Zhang, R. Xiong, R. Mei, Y. Huang, D.B. Chrisey, Langmuir **31**(23), 6447–6456 (2015)
106. G. Tsekenis, M. Chatzipetrou, J. Tanner, S. Chatzandroulis, D. Thanos, D. Tsoukalas, I. Zergioti, Sens. Actuators B **175**, 123–131 (2012)
107. L. Koch, et al., Tissue Eng. Part C Methods **16**(5), 847–854 (2010)
108. R.C.Y. Auyeung, H. Kim, S.A. Mathews, A. Pique, J. Las, Micro/Nanoeng. **2**(1), 21–25 (2007)
109. Y. Son, J. Yeo, H. Moon, T.W. Lim, K.H. Nam, S. Yoo, C.P. Grigoropoulos, D. Yang, S.H. Ko, Adv. Mater. **23**, 3176–3181 (2011)
110. W. Cui, W. Lu, Y. Zhang, G. Lina, T. Wei, L. Jiang, Colloids Surf A Physicochem. Eng. Asp. **358**, 35–41 (2010)
111. D. Kim, J. Moon, Electrochem. Solid State Lett. **8**(11), J30–J33 (2005)
112. K. Rajan, I. Roppolo, A. Chiappone, S. Bocchini, D. Perrone, A. Chiolerio, Nanotechnol. Sci. Appl. **9**, 1–13 (2016)
113. L. Rapp, J. Ailuno, A.P. Alloncle, P. Delaporte, Opt. Express **19**(22), 21563–21574 (2011)
114. M. Makrygianni, I. Kalpyris, C. Boutopoulos, I. Zergioti, Appl. Surf. Sci. **297**, 40–44 (2014)
115. R.C.Y. Auyeung, H. Kim, N.A. Charipar, A.J. Birnbaum, S.A. Mathews, A. Pique, Appl. Phys. A **102**, 21–26 (2011)
116. D. Kim, S. Jeong, B.K. Park, J. Moon, Appl. Phys. Lett. **89**, 264101 (2006)
117. L. Rapp, E. Biver, A.P. Alloncle, P. Delaporte, JLMN J. Laser Micro/Nanoeng. **9**, 5–9 (2014)
118. T. Inui et al., RSC Adv. **5**, 77942 (2015)
119. C. Florian, F.C. Lucas, J.M.F. Pradas, R. Artigas, S. Ogier, D. Karnakis, P. Serra, Appl. Surf. Sci. **336**, 304–308 (2015)
120. E. Breckenfeld, H. Kim, R.C.Y. Auyeung, N. Charipar, P. Serra, A. Piqué, Appl. Surf. Sci. **331**, 254–261 (2015)
121. S. Papazoglou, Y.S. Raptis, S. Chatzandroulis, I. Zergioti, Appl. Phys. A **117**(1), 301–306 (2014)
122. N.R. Bieri, J. Chung, S.E. Haferl, D. Poulikakos, C.P. Grigoropoulos, Appl. Phys. Lett. **82**(20), 3529 (2003)
123. E. Halonen, E. Heinonen, M. Mäntysalo, Opt. Photonics J. **3**, 40–44 (2013)
124. M. Zenou, O. Ermak, A. Saar, Z. Kotler, J. Phys. D Appl. Phys. **47**, 025501 (2014)
125. S.H. Ko, J. Chung, H. Pan, C.P. Grigoropoulos, D. Poulikakos, Sens. Actuators A **134**, 161–168 (2007)
126. I. Theodorakos, F. Zacharatos, R. Geremia, D. Karnakis, I. Zergioti, Appl. Surf. Sci. **336**, 157–162 (2015)
127. P. Peng, A. Hu, Y. Zhou, Appl. Phys. A **108**, 685–691 (2012)
128. D. Paeng, J. Yeo, D. Lee, S.-J. Moon, C.P. Grigoropoulos, Appl. Phys. A **120**, 1229 (2015)
129. J. Yeo, S. Hong, D. Lee, N. Hotz, M.-T. Lee, C.P. Grigoropoulos, S.H. Ko, PLoS ONE **7**(8), e42315 (2012)
130. C.W. Cheng, J.K. Chen, Appl. Phys. A **122**, 289 (2016)
131. K.S. Kaur, J. Missinne, G. Van Steenberge, Appl. Phys. Lett. **104**, 061102 (2014)
132. J. Wang, R.C.Y. Auyeung, H. Kim, N.A. Charipar, A. Piqué, Adv. Mater. **22**, 4462–4466 (2010)
133. M. Zenou, Z. Kotler, Opt. Express **24**(2), 1431 (2016)
134. M. Zenou, A. Sa'ar, Z. Kotler, Small (2015). https://doi.org/10.1002/smll.201500612
135. C.W. Visser, R. Pohl, C. Sun, G.-W. Römer, B. Huis in't Veld, D. Lohse, Adv. Mater. (2015). https://doi.org/10.1002/adma.201501058
136. M. Gruene, et al., Tissue Eng. Part C Methods **17**(10) (2011). https://doi.org/10.1089/ten.tec.2011.0185
137. https://www.daetwyler-usa.com/pressroom/en/information/History
138. https://www.orbotech.com/news-events/press-releases/orbotechs-precise-800-automated-optical-shaping-system-wins-prestigious-award
139. https://poietis.com/ngb/
140. https://www.alphanov.com/en/collaborative-projects/boneprinting-laser-assisted-bioimpression

S. Papazoglou was born in 1983 in Athens, Greece and received his bachelor's degree in 2010 from the Department of Material Science, University of Patras Greece. In 2013 he received his Master's Degree in Microsystems and Nanodevices and in 2018 he received his Ph.D. on the laser processing of nanomaterials for organic electronic applications from the National Technical University of Athens where he is currently a Postdoctoral Researcher.

I. Zergioti is a Professor at the National Technical University of Athens, School of Applied Mathematical and Physical Sciences. She studied Physics at the University of Crete and she received the Ph.D. degree at the FORTH-IESL. She did her postdoctoral work at the Max Planck Institute for Biophysikalische Chemie, and at Philips CFT. She is among the world leaders on the Laser-Induced Forward Transfer work and has co-authored more than 80 publications in international refereed journals, 90 publications in conference proceedings, three chapters in scientific books, three granted Greek patents, one European patent, one PCT on LIFT process and applications.

Chapter 10
Laser Scanning Stereolithography

Soshu Kirihara

Abstract Laser scanning stereolithography of additive manufacturing techniques has been developed to create metal and ceramic components with dendritic geometries and ordered microcavities. The microlattice patterns were propagated spatially in the computer graphic space. The photosensitive resin pastes with metal and ceramic particles were photo-polymerized using an ultraviolet laser. As a practical demonstration of stereolithographic lamination process, solid electrolyte dendrites of yttria-stabilized zirconia were fabricated for fuel cell miniaturization. Subsequently, metallodielectric photonic crystals with diamond lattice structures were fabricated. Moreover, artificial bones of hydroxyapatite scaffolds were modeled to realize excellent biocompatibility. The graded porous structures in the artificial bones were processed.

10.1 Introduction

Laser scanning stereolithography of additive manufacturing techniques has been developed to create metal and ceramic components with dendritic geometries and ordered microcavities [1, 2]. The microlattice patterns were propagated spatially in the computer graphic space. The photosensitive resin pastes with metal and ceramic particles were photo-polymerized using an ultraviolet laser. Using a stereolithographic lamination process, solid electrolyte dendrites of yttria-stabilized zirconia (YSZ) were fabricated for fuel cell miniaturization. The gaseous fluid profiles and pressure distributions were visualized and analyzed. Subsequently, metallodielectric photonic crystals with diamond lattice structures were fabricated. The electromagnetic wave properties were measured using terahertz time-domain spectroscopy. Moreover, artificial bones of hydroxyapatite scaffolds were modeled to realize excellent biocompatibility. The graded porous structures in the artificial bones were processed.

S. Kirihara (✉)
Joining and Welding Research Institute, Osaka University, Ibaraki City, Japan
e-mail: kirihara@jwri.osaka-u.ac.jp

A. Hu (ed.), *Laser Micro-Nano-Manufacturing and 3D Microprinting*, Springer Series in Materials Science 309, https://doi.org/10.1007/978-3-030-59313-1_10

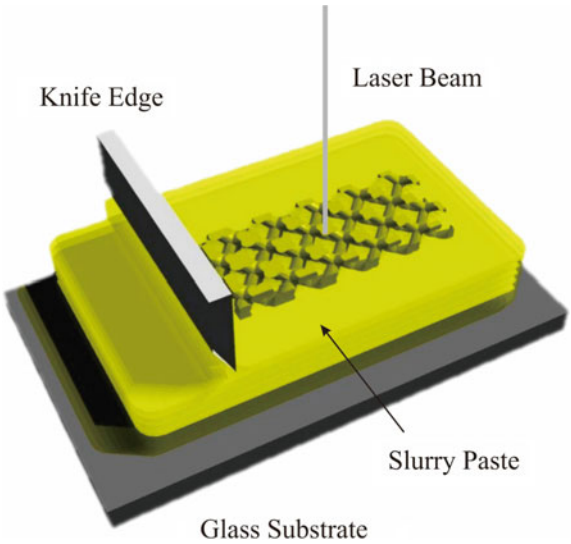

Fig. 10.1 Schematic illustration of the laser scanning stereolithography supported by computer-aided design, manufacture, and evaluation

10.2 Laser Processing

The graphic models were successfully designed using commercial applications. The three-dimensional solid models were sliced into two-dimensional layers. Numerical data for the laser operation were processed according to the cross-sectional outlines. Laser scanning stereolithography is schematically illustrated in Fig. 10.1. Metal or ceramic particles of 200–800 nm diameters were dispersed (at 40–60% volume fraction) in the photosensitive acrylic resins. Further, the fabricated pastes were spread on the substrate with layer thicknesses of 30–70 μm using a mechanical knife edge, and an ultraviolet laser beam of 355 nm wavelength is scanned over the paste surface according to the processing data. The spot size of laser beam can be adjusted from 10 to 100 μm in variable range. The irradiation power was maintained between 100 and 300 mW. The photosensitive resin paste was polymerized with the nanoparticles. Through the continuous layer laminations, solid objects were fabricated successfully. The complex geometric patterns were obtained within 5–10 μm in size tolerance. The composite precursors were dewaxed at 600 °C and sintered at temperatures above 1000 °C according to the materials used in the controlled atmospheres.

10.3 Metal and Ceramic Components

Solid oxide fuel cells (SOFCs) are expected to be the next-generation energy conversion systems owing to their higher efficiency. Yttria-stabilized zirconia (YSZ)—added nickel (Ni) possesses many desirable properties for an anode, such as high

electronic and ionic conductivities, and chemical and mechanical stabilities at high operating temperatures. The energy efficiency is influenced by the anode microstructure, and the fuel gas diffusion and electrochemical reactions on the electrode surfaces composed of YSZ/Ni/Gas triple-phase boundary proceed simultaneously. YSZ-Ni porous anodes have been fabricated to realize large surface areas and high activations [3–5].

In this study, solid electrodes with dendritic microstructures and wide surface areas were used to realize effective gas diffusion and appropriate mechanical strength. The permeability of the cavity network design and fluid implementation was optimized through the finite element method. The dendritic structures constructed from micrometer-order ceramic rods with coordination numbers of 4, 6, 8, and 12 were designed in a computer application. The aspect ratios of the rod diameter to length were valued from 0.75 to 3.00. The gaseous fluid properties and stress distributions in dendritic electrodes were simulated and visualized.

The dendritic lattice with coordination number 12 and 2.18 aspect ratio exhibited the maximum surface area. The designed graphic model of a lattice unit is presented in Fig. 10.2. The solid electrolyte texture is expected to increase the triple-phase boundaries and lower the activation over-potential in the electrode. The fluid behavior of the dendritic structure is shown in Fig. 10.3, where smooth streamlines according to cyclical vacancies are indicated. The lattice structures are expected to enable the prompt fuel gas diffusion.

The real dendritic structures composed of YSZ and nickel oxide (NiO) are displayed in Fig. 10.4. Micrometer-order ceramic lattices with coordination number 12 were successfully formed by the laser scanning stereolithography and sintering [6]. The optimized dendritic structure of lattice constant 100 μm was fabricated through the lamination process with layer thickness of 10 μm. The composite precursors were dewaxed at 600 °C for 2 h and sintered at 1400 °C for 2 h in air. Microstructures and composite distributions were observed using scanning electron microscopy and energy-dispersive X-ray spectroscopy, and the fine grains of YSZ and NiO were found to be well-connected.

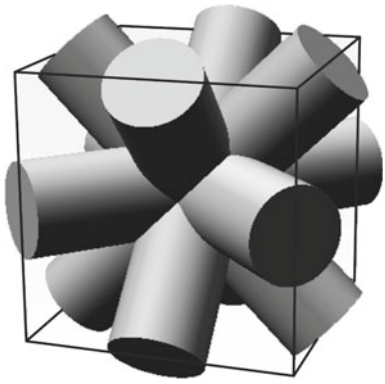

Fig. 10.2 Graphically designed lattice model with coordination number 12 to optimize and reconcile wide surface areas and high porosity

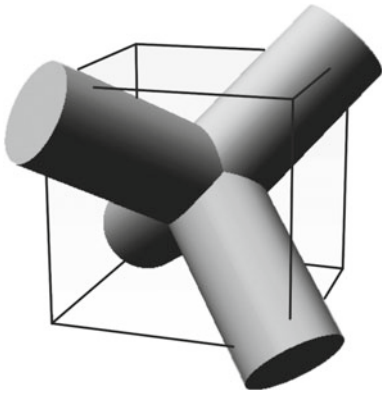

Fig. 10.3 Gaseous streamlines in the dendritic lattices with coordination number 12, simulated and visualized by the finite element volume method

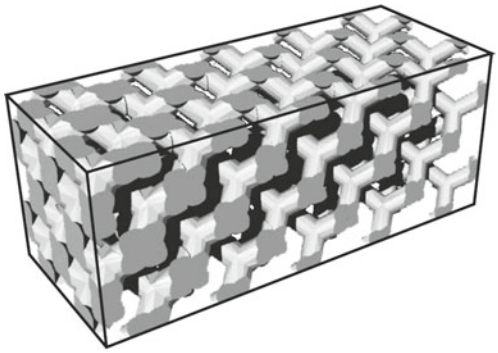

Fig. 10.4 Yttria-stabilized zirconia texture including nickel oxide particles as electrochemical activation points of the triple-phase boundaries

10.4 Metal and Glass Components

Metallodielectric photonic crystals are composed of periodically arranged magnetic materials. These crystals form forbidden bands to reflect electromagnetic waves of wavelengths comparable to the lattice constant through Bragg diffraction [7, 8]. The electromagnetic waves in terahertz frequency ranges were verified to synchronize with the collective vibration modes of various harmful substances; therefore, spectroscopic technologies are expected to be applied to sensors for real-time detection of toxic materials [9]. Diamond photonic crystals with coordination number 4 composed of the metallic glass dispersed oxide glass were fabricated by laser scanning stereolithography and applied to the terahertz wave sensor devices.

The diamond lattice structures composed of magnetic rods with an aspect ratio of 1.5 were designed using the computer graphic software, as shown in Fig. 10.5. The lattice constant was 500 μm in length. The whole structure was 5 × 5 × 5 mm consisting of 10 × 10 × 10 unit cells. The electromagnetic wave propagation and spatial wave diffractions were simulated along Maxwell's equations using the plane

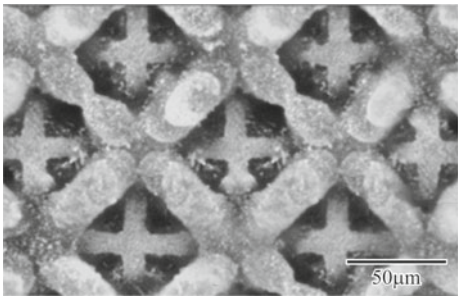

Fig. 10.5 Designed graphic model of the diamond structure with coordination number 4 for opening perfect bandgaps by electromagnetic wave diffractions

wave expansion method. The electromagnetic energy distributions in the periodic arrangements were visualized by the transmission line modeling.

The diamond lattices were fabricated with size tolerance of ±5 μm by the laser scanning stereolithography [10]. The sintered diamond structures with a lattice constant of 500 μm are shown in Fig. 10.6. The micrometer-order lattice pattern was successfully formed. In the paste material preparation, the metallic glass ($Fe_{72}B_{14.4}Si_{9.6}Nb_4$) and oxide glass ($B_2O_3{\cdot}Bi_2O_3$) particles of 2.6 and 1.0 μm diameter were dispersed in the photosensitive acrylic resin at 17 and 23% volume fraction, respectively. In the lamination process, the thickness of each layer was set to 10 μm. The formed precursor was dewaxed at 420 °C for 8.0 h with 1.0 ºC/min and sintered at 460 °C for 0.5 h with 2.0 ºC/min in an Ar atmosphere.

The comparison of X-ray diffraction patterns before and after the heat treatments indicated that the metallic glass did not crystallize through the heating process. The linear shrinkage ratios of the horizontal and vertical axes were 10.2 and 12.5%, respectively. The lattice model was corrected and redesigned according to the liner shrinkage ratios. The terahertz wave transmission behavior measured by time-domain spectroscopy is shown in Fig. 10.7. The electromagnetic bandgap was formed in the frequency range of 0.19–1.02 THz, and the measured results were in good agreement with the simulated results.

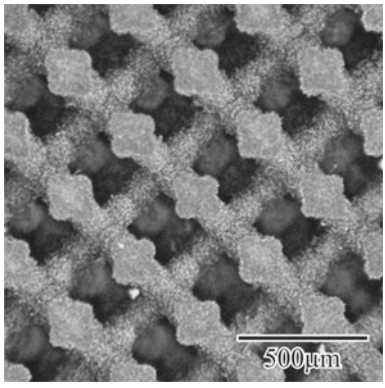

Fig. 10.6 Metallodielectric photonic crystal with microlattices of metal and oxide glasses to modulate the electromagnetic wave propagations

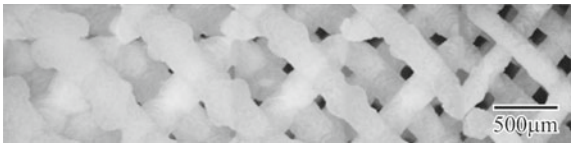

Fig. 10.7 Transmission attenuation of terahertz waves for the metallodielectric photonic crystal with diamond lattice structure

10.5 Full Ceramic Components

Natural human bones have compact and cancellous structures to realize effective compatibilities for physical activities and biological metabolism. The inner porous structures show graded distributions from 50 to 90% in volume fractions, which are mimicked in the fabrication of artificial bones. Conventional artificial bones have homogeneous cancellous patterns of 75% porosity [11, 12]. By using the laser scanning stereolithography, the hydroxyapatite artificial bones with the graded lattice patterns were fabricated to realize effective biocompatibility and high mechanical strength [13].

The graphic model of the graded porous structure was designed, as shown in Fig. 10.8. The solid rods are connected regularly to create a tetra-pot structure of four-coordinate lattices [14]. Because relationship between the scaffold porosities and rod aspect ratios shows a simple proportionality, by changing the aspect ratio from 1.2 to 2.0, the structural porosity can be controlled from 53 to 80% comparing with the natural bone. The fluid flow properties in the scaffold structure were simulated using the computer fluid dynamic method, as shown in Fig. 10.9. The streamline distribution of the biological fluid shows omni-azimuth propagation.

The resin components with bioceramic dispersions were fabricated successfully by computer-aided design, manufacture, and evaluation. Photosensitive acrylic resin with hydroxyapatite particles of diameter 10 μm at 45 vol. % was used as the ink material in the printing process. Paste layers of 30 μm thickness were laminated, and the composite lattices were created precisely in the micrometer order. In addition, the part accuracies of the lattices were measured under a 25 μm size difference.

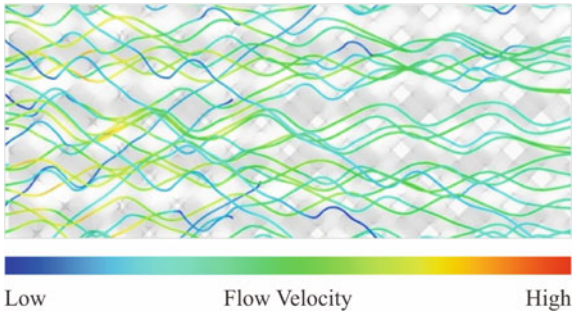

Fig. 10.8 Four-coordination lattice model designed to realize graded porosities as an artificial bone of biological scaffold

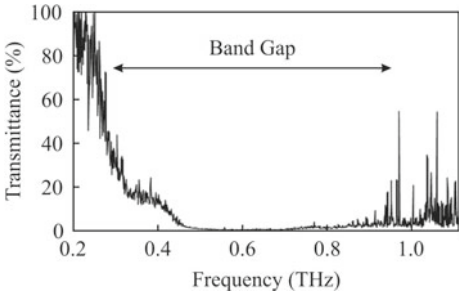

Fig. 10.9 Fluid streamlines in continuous and connected cavities to disperse biological fluid flows for osseointegration as natural metabolism

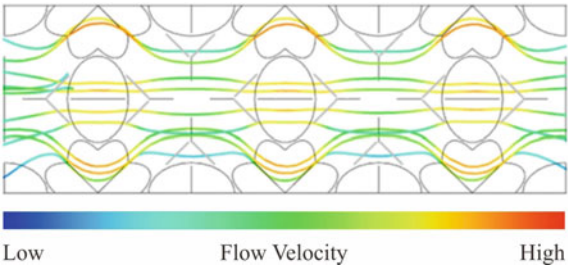

Fig. 10.10 Biological ceramic components of sintered hydroxyapatite lattices with a high relative density and fine microstructure

The precursor was dewaxed at 600 °C for 2 h at a heating rate of 1.0 °C/min and sintered at 1250 °C for 2 h at a rate of 5.0 °C/min in air. The sintered scaffold of the hydroxyapatite ceramic with graded lattices is shown in Fig. 10.10. The linear shrinkage ratios for the horizontal and vertical axes were 23 and 25%, respectively. Smaller lattice structures could be obtained through controlled body shrinkages during the optimized sintering process. In the ceramic microstructure of sintered hydroxyapatite, cracks and pores were absent. The grain size was approximately 4 μm, and the relative densities of these ceramic components were measured as 99% using the Archimedean method.

10.6 Conclusions

The fabrication of practical material components with functional geometries by laser scanning stereolithography was demonstrated. Dendritic electrodes composed of yttria-stabilized zirconia and nickel oxide were successfully processed. Ceramic electrodes with large effective reaction area can exhibit smooth fuel gas transparent characteristics to promote effective anode reactions. Metallodielectric photonic crystals composed of metallic glass particles dispersed in an oxide glass matrix were processed. The artificial crystals formed are expected to be used in real-time sensing of harmful substances in the aqueous phase environments. Hydroxyapatite scaffolds of four-coordinate lattices with graded porosities were processed. The designed

porous structures can realize appropriate biological fluid circulations and promote the regeneration of new bones.

References

1. S. Kirihara, Ultraviolet laser lithography of titania photonic crystals for Terahertz-wave modulation. Materials **11**(5), 835–845 (2018)
2. S. Kirihara, Additive manufacturing of ceramic components using laser scanning stereolithography. Weld World **60**(4), 697–702 (2016)
3. H. Koide, Y. Someya, T. Yoshida, T. Maruyama, Properties of Ni/YSZ cermet as anode for SOFC. Solid State Ionics **132**(3–4), 253–260 (2000)
4. T. Fukui, S. Ohara, M. Naito, K. Nogi, Performance and Stability of SOFC Anode Fabricated from NiO-YSZ Composite Particles. J. Power Sour. **110**(1), 91–95 (2002)
5. J.H. Yu, G.W. Park, S. Lee, S.K. Woo, Microstructural effects on the electrical and mechanical properties of Ni-YSZ cermet for SOFC anode. J Power Sourc **163**(2), 926–932 (2007)
6. S. Kirihara, Y. Uehara, N. Komori, M. Nakano, S. Tasaki, Freeform fabrication of ceramics dendrites for fluctuation modulations in energy and material flows. Int. J. Modern Manuf. Technol. **4**(1), 65–68 (2012)
7. E. Yablonovitch, Inhibited spontaneous emission in solid-state physics and electronics. Phys. Rev. Lett. **58**(20), 2059–2062 (1987)
8. M. Inoue, R. Fujikawa, A. Baryshev, A. Khanikaev, P.B. Lim, H. Uchida, O. Aktsipetrov, A. Fedyanin, T. Murzina, A. Granovsky, Magnetophoton. Cryst. J. Phys. D Appl. Phys. **39**(8), R151–R161 (2006)
9. N. Hoshi, Y. Nikawa, K. Kawai, S. Ebisu, Application of microwaves and millimeter waves for the characterization of teeth for dental diagnosis and treatment. Microwave Theory Techn. **46**, 834–838 (1998)
10. S. Kirihara, M. Nakano, Freeform fabrication of magnetophotonic crystals with diamond lattices of oxide and metallic glasses for terahertz wave control by micro patterning stereolithography and low temperature sintering. Micromachines **4**(2), 149–156 (2013)
11. C. Shengyong, Xi. Juntong, A control approach for pore size distribution in the bone scaffold based on the hexahedral mesh refinement. Comput. Aided Des. **40**(10–11), 1040–1050 (2008)
12. S. Itoh, S. Nakamura, M. Nakamura, K. Shinomiya, K. Yamashita, Enhanced bone ingrowth into hydroxyapatite with interconnected pores by electrical polarization. Biomaterials **27**(32), 5572–5579 (2006)
13. I. Sopyan, M. Mel, S. Ramesh, K.A. Khalid, Porous hydroxyapatite for artificial bone applications. Sci. Technol. Adv. Mater. **8**(1–2), 116–123 (2007)
14. C. Maeda, S. Tasaki, S. Kirihara, Accurate fabrication of hydroxyapatite bone models with porous scaffold structures by using stereolithography. Mater. Sci. Eng. **18**(7), 072017-1-4 (2011)

Chapter 11
Lithium-Ion Battery—3D Micro-/Nano-Structuring, Modification and Characterization

Wilhelm Pfleging, Petronela Gotcu, Peter Smyrek, Yijing Zheng, Joong Kee Lee, and Hans Jürgen Seifert

Abstract Laser processing technologies for micro-/nanostructuring of electrode materials have a great potential in improving the electrochemical performance and operational lifetime of lithium-ion cells. Different types of laser structuring were used on different surfaces such as metallic current collectors and thin or thick film electrodes. For thin metallic current collector foils, at anode and cathode sides, the self-organized structuring by laser-induced periodical surface structures and laser interference methods were successfully applied for improving electrode film adhesion and cell impedance. For thin and thick film electrode layers direct laser ablation with structure sizes down to the micrometer range and high aspect ratios were found most powerful in order to create three-dimensional (3D) cell architectures with benefits regarding cell performance and a homogenous wetting of composite electrodes with liquid electrolyte. A huge impact of laser formed 3D batteries regarding capacity retention and cell lifetime at high charging and discharging rates was detected. The impact on diffusion kinetics of laser structured 3D electrodes was studied using classical methods such galvanostatic intermittent titration technique and cyclic voltammetry. A further improvement of 3D battery performance due to an operation in high potential regime and for advanced high energy silicon anode material was achieved by joining of laser structuring and thin-film passivation either of active particles before laser patterning or by passivating of complete 3D electrodes after laser processing. Finally, laser-induced breakdown spectroscopy will be presented as a powerful tool for elemental mapping of entire 2D and 3D electrodes. The impact of 3D architectures on lithium distribution and chemical degradation processes in 2D batteries was investigated and analyzed.

W. Pfleging (✉) · P. Gotcu · P. Smyrek · Y. Zheng · H. J. Seifert
Karlsruhe Institute of Technology, IAM-AWP, P.O. Box 3640, 76021 Karlsruhe, Germany
e-mail: wilhelm.pfleging@kit.edu

J. K. Lee
Department of Energy and Environmental Engineering, Korea University of Science and Technology, 176 Gajungro Yuseong-gu, Daejeon 305-350, Republic of Korea

Center for Energy Convergence, Green City Research Institute, Korea Institute of Science and Technology, Hwarangno 14 gil 5, Seoul 136-791, Republic of Korea

A. Hu (ed.), *Laser Micro-Nano-Manufacturing and 3D Microprinting*, Springer Series in Materials Science 309, https://doi.org/10.1007/978-3-030-59313-1_11

11.1 Introduction

11.1.1 Lithium-Ion Batteries

Almost 30 years ago Sony introduced the commercial lithium-ion battery (LIB) designed for portable electronic applications containing amorphous carbon as anode, lithium cobalt oxide ($LiCoO_2$) as cathode and non-aqueous liquid electrolyte. Nowadays, LIBs became the most feasible electric energy storage tool [1–3]. For stationary or high power applications batteries contain thick film electrodes as complex systems with determined stoichiometry and material phases yielding to capacities even higher than 60 Ah [4]. New transportation concepts support electromobility, which appears to be the most appropriate solution in terms of sustainability use of energy resources and environmental stability. Further development of LIB technology is directed towards energy storage concepts which will meet the requirements of e-transportation, in terms of energy and power density [5].

11.1.2 3D Battery Concept

The state-of-art LIB electrodes are two-dimensional (2D) materials with relative limited film thickness. Therefore the total amount of energy stored in 2D LIB electrodes is restricted by their areal footprint. Efforts are directed towards the development of advanced lithium-ion electrodes, e.g., modified surface architectures. The development of 3D architectures in LIB electrodes is a relatively new approach for overcoming battery power losses during operation, high interelectrode ohmic resistances [6, 7], and further chemical or mechanical degradation. The latter one occurs due to lithium-ion insertion producing high volume changes within the composite layers [8]. Electrodes with 3D architecture are developed in order to enhance the surface area and improve the electrolyte filling process [9–12]. The goal of the 3D battery concept is to design cell and electrode architectures, which maximize the power performance and high power capability, and improve the high cycle lifetime through evolution of new and shorter lithium-ion pathways [6]. In recent concepts [13–15], the 3D micro- and nanostructured architectures will make use of the complete available space thus increasing the energy density of the battery by 200%. A common approach is 3D structuring of the electrode substrate, the current collector, prior to electrode film deposition. Baggetto et al. [16] and Notten et al. [17] adopted an approach which complies with state-of-the-art integrated circuits (IC) technologies such as standard lithography, etching technologies and thin-film deposition. Furthermore, the 3D electrode architectures could also be achieved by using template materials such as anodic aluminum oxides, colloidal crystals and bio-templates, 3D printing, and laser structuring [18, 19]. In comparison to all above methods, the laser-assisted approach is a simple, rapid, and easily scalable process for the 3D electrode industrial production [12, 20].

11.1.3 Laser Materials Processing

Laser materials processing in manufacturing of LIB is a rather new technological approach, which enables rapid manufacturing, high reliability, and a significant reduction of lithium-ion battery manufacturing costs. Cost-efficient ns-laser cutting of electrodes was one of the first laser technologies, which were successfully transferred to industrial high energy battery production [21–25]. A rather new technical approach is the laser patterning of battery materials, namely current collectors (aluminum or copper), separator materials, and thin and thick film electrodes [e.g., $LiNi_{1/3}Mn_{1/3}Co_{1/3}O_2$ (NMC), $LiFePO_4$ (LFP), $LiCoO_2$ (LCO), $LiMn_2O_4$ (LMO), silicon (Si)] [12, 18, 26–28]. For each type of battery materials, laser structuring can improve the battery lifetime, cycle stability, and high rate capability. The structuring of the current collector foils can improve the electrode film adhesion which is a critical aspect for high energy and thick film electrodes [29]. The 3D battery concept introduced to microbatteries by Notten et al. [30] and summarized in a review article by Ferrari et al. [11] was transferred by the researchers at KIT to a new battery concept by direct structuring of thick and thin-film electrodes for batteries with high energy and power densities. A defined thermal impact can be advantageous in electrode manufacturing, already confirmed by laser annealing of thin-film electrodes for adjusting of battery active crystalline phases [31–33]. Nanosecond laser or ultrafast laser for direct structuring or printing of electrode materials can be used to realize three-dimensional (3D) electrode architectures. Furthermore, it was shown that introducing 3D micro-/nano-structures will improve the electrolyte wetting even of thick film composite electrodes. Laser structuring can modify electrodes and separators into superwicking materials, enhancing the battery lifetime and its performance [12]. A main issue in laser materials processing is the process up-scaling with respect to large electrode footprint areas, e.g., for batteries with pouch cell design, and the laser processing speed, which should be adapted to the standards in battery manufacturing for high energy and high power lithium-ion cells.

11.2 Micro-/Nano-Structuring of Current Collectors

The electrode film has to withstand mechanical demands during cell assembling, and thereafter, during repeated cell operation, when lithium-ion intercalation and de-intercalation occur, due to expansion and shrinkage of the electrochemically active material particles. Within state-of-the-art LIBs, graphite anodes with a practical capacity in the range of 330–372 mAh/g are applied. During charging and discharging the graphite anode undergoes a volume expansion of about 10% [34]. For next generation LIBs, silicon (Si) or silicon-doped graphite (Si/C) have been regarded as the most promising anode material due to a high theoretical energy density of Si of about 4200 mAh/g [35]. High energy batteries using a significant

amount Si on anode side are not commercialized so far because of their short operational lifetime. The formation of silicon-lithium alloys during battery operation results in tremendous volume change of up to 300–400% in dependence on the applied voltage window [8, 29, 36]. Failure mechanisms based on film or Si particle cracking, Si particle pulverization, and delamination of the active layer from the copper current collector leading to a significant drop in capacity [37, 38]. In recent studies, it was confirmed that new binder materials, such as polyacrylic acid (PAA) improve the adhesive force among silicon particles [39, 40]. Alternatively, chemical or topographical modification of current collector surfaces could provide an improving of the interfacial adhesion between the composite active material and the metallic substrate foil [41]. Prior to electrode coating processes by tape casting or slot die coating, laser micro/nano-structuring of current collectors is performed in order to improve the mechanical anchoring between active particles, binder, and the metallic substrate. For laser micro-/nano-structuring of current collector surfaces two process strategies are proposed: direct laser interference patterning (DLIP) and laser-induced periodic surface structures (LIPSS) [41].

11.2.1 Direct Laser Interference Patterning (DLIP)

DLIP describes a very prominent method to realize micron and sub-micron patterns by using interference-effect. Hereby, two, three, or more coherent laser beams are superimposed in order to generate a high-intensity interference pattern along the sample surface. In general, a single laser beam is split into two or more beams by using beam splitters or phase shift masks, as described in [42, 43], respectively. The number and arrangement of applied laser beams defines the submicron resolution and type of interference pattern, e.g. intensity maxima along lines or dots for a two-beam or a four beam configuration, respectively [42, 44]. As an example, the stationary intensity distribution resulting from four-beam interference can be calculated as follows:

$$I = \left|\vec{E}_1 + \vec{E}_2 + \vec{E}_3 + \vec{E}_4\right|^2$$

$$\vec{E}_1 = \vec{E}_1^0 \cdot \cos\left(\vec{k}_1 \cdot \vec{r} - \omega \cdot t + \phi_1\right)$$

$$\vec{E}_j = \vec{E}_j^0 \cdot \mathrm{e}^{(\vec{k}_j \cdot \vec{r} - i\omega t + \phi_j)}$$

$$\vec{E}_j = \vec{E}_j^0 \cdot \mathrm{e}^{-i\omega t} \cdot \mathrm{e}^{(\vec{k}_j \cdot \vec{r} + \phi_j)}$$

$$I = \left|\sum_{j=1}^{4} \vec{E}_j^0 \cdot \mathrm{e}^{(\vec{k}_j \cdot \vec{r} + \phi_j)}\right|^2$$

$$I = I_0 \left| \sum_{j=1}^{4} \cos\left(\vec{k}_j \cdot \vec{r} + \phi_j\right) + i \cdot \sin\left(\vec{k}_j \cdot \vec{r} + \phi_j\right) \right|^2$$

$$\Rightarrow \quad \frac{I}{I_0} = \left[\sum_{j=1}^{4} \cos\left(\vec{k}_j \cdot \vec{r} + \phi_j\right) \right]^2 + \left[\sum_{j=1}^{4} \sin\left(\vec{k}_j \cdot \vec{r} + \phi_j\right) \right]^2 \tag{11.1}$$

where $\vec{E}_j^0$ are electric field amplitude vectors, $\vec{k}_j$ the wave vectors, and ϕ_j the optical phases of the interfering beams. For $\vec{r} = (x, y, 0)$, a symmetrical arrangement of the laser beams, and 2θ as angle between two opposite oriented laser beams, one get the following description of the interference pattern

$$\frac{I}{I_0} = [2 \cdot \cos(\phi) \cdot \cos(-k \sin(\theta) \cdot x) + 2 \cdot \cos(-k \sin(\theta) \cdot y)]^2 + [2 \cdot \sin(\phi) \cdot \cos(-k \sin(\theta) \cdot x)]^2 \tag{11.2}$$

For $\Phi = 0, \theta = 13.8°, \lambda = 193$ nm the intensity pattern and related ablation profile were calculated (Fig. 11.1a) and applied for texturing of thin films (Fig. 11.1b) [44].

A two-beam interference pattern is producing a line structure with a periodicity Λ, which can be adjusted by varying the angle 2θ between two coherent laser beams and the wavelength λ [42]:

$$\Lambda = \frac{\lambda}{2 \cdot \sin(\theta)} \tag{11.3}$$

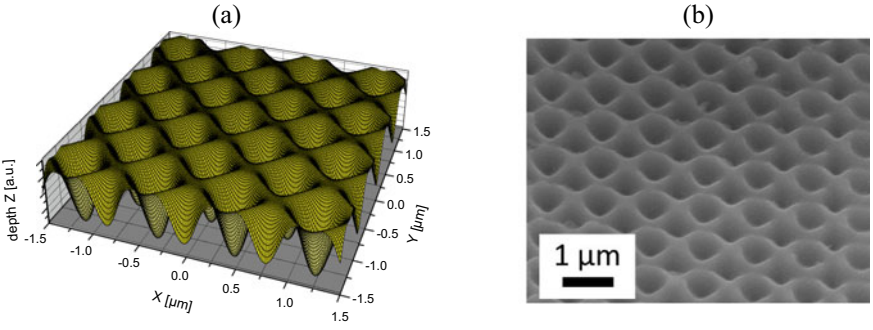

Fig. 11.1 Comparison between calculated submicron-pattern (**a**) and laser structured carbon thin film (**b**)

11.2.2 Laser-Induced Periodic Surface Structures (LIPPS)

The formation mechanisms and applications of LIPSS, often termed as ripples, are under intense investigation. LIPSS are nano-scaled surface structures composed of wave-like structures, which exhibit a clear correlation to the incident laser wavelength and polarization. LIPSS can be generated on almost any type of material such as metal, glass, polymer, or semiconductors. A complete understanding of the comprehensive mechanism of LIPSS formation is currently not available.

Regarding the structure periodicity of LIPSS, one distinguishes two different LIPSS categories: low spatial frequency LIPSS (LSFL) and high spatial frequency LIPSS (HSFL). For LSFL, one of the proposed mechanisms for strong absorbing materials, such as semiconductors and metal, is the so-called interference theory: the structures are formed by interaction of the incident laser beam and excited surface plasmon polaritons (SPP) [45–47]. SPP are surface electromagnetic waves, which are excited by the incident laser beam. The LSFL is usually perpendicular oriented to the laser beam polarization and exhibits a periodicity that is a bit smaller than the laser wavelength. The structure periodicity Λ_{LSFL} equates to the SPP wavelength Λ_{SPP} and can be related to the normal incident laser wavelength λ:

$$\Lambda_{\mathrm{LSFL}} = \Lambda_{\mathrm{SPP}} = \frac{\lambda}{\mathrm{Re}(\eta)\cdot} \tag{11.4}$$

where $\eta = [\varepsilon_{\mathrm{d}}\varepsilon_{\mathrm{metal}}/(\varepsilon_{\mathrm{metal}} + \varepsilon_{\mathrm{d}})]^{1/2}$ is the effective refractive index of the dielectric-metal interface for surface plasmons, ε_{d} is the dielectric constant of the ambient dielectric medium, and $\varepsilon_{\mathrm{metal}}$ is the dielectric constant of the metal [45].

With the further development of femtosecond laser sources, LIPSS with a period smaller than half of the wavelength of the so-called HSFL were observed. Femtosecond laser pulses enable to provide high intensity along the entire irradiated area. An increasing number of laser pulses enhances the intensity of the SPP which leads to the formation of spatial harmonics of SPP. HSFL with structure periodicities smaller than fractions of the incident laser wavelength ($<\lambda/2$, $\lambda/4$, $\lambda/8$, …) are formed by interference between the spatial harmonics of the SPP and the incident laser beam [48].

To summarize, LIPSS formation is based on a dynamic process, which strongly depends on a multiplicity of parameters such as laser wavelength, pulse duration, pulse number, laser fluence, material properties, and ambient gas.

11.2.3 Adhesion Properties of Composite Electrodes on Laser Nanostructured Current Collectors

Figure 11.2a shows periodic line structures on the aluminum current collector (cathode) generated by DLIP with a laser source operating at a wavelength of

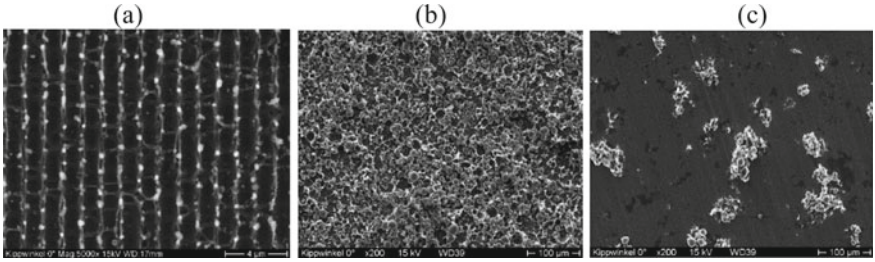

Fig. 11.2 Film adhesion of NMC on DLIP modified aluminum foils: SEM images of **a** DLIP surface structure on aluminum ($\Lambda = 1.3$ µm), and **b** residual NMC-particles after 90° peel-off testing. **c** residual NMC-particles after 90° peel-off testing using an untreated aluminum foil

1064 nm. A line periodicity of 1.3 µm with an average surface roughness *R*a of 109 nm could be measured by atomic force microscopy (AFM). Tape casting of composite material made of lithium nickel manganese cobalt oxide was performed using structured and unstructured aluminum foils as substrate. The film adhesion was characterized by 90° peel-off tests as described elsewhere [49]. A significant increase of adhesion of about 250 N/m could be detected on aluminium surface. The reference value for unstructured aluminum was 140 N/m. After the peel-off tests, the NMC-particles and binder were tightly stuck on the modified aluminum surface (Fig. 11.2b). On contrary, the coating of the reference samples was almost completely removed from the unstructured current collector surface (Fig. 11.2c), which indicates, that the intrinsic film adhesion among the active particles is more stable than the adhesion of the coating towards the unstructured surface.

The formation of LIPSS on copper current collectors (anode) was explored as function of laser fluence, pulse number, and scanning speed for a laser pulse duration of 350 fs and a laser wavelength of 515 nm. For single pulse laser ablation, the copper surface was exposed to the laser beam at a fluence of 10.35 J/cm^2 (Fig. 11.3a). Randomly distributed nano-pores and nano-sized ripples were formed on the surface. Elemental analysis by using energy-dispersive X-ray spectroscopy revealed that no oxide formation took place due to laser exposure. Well defined periodic ripples could

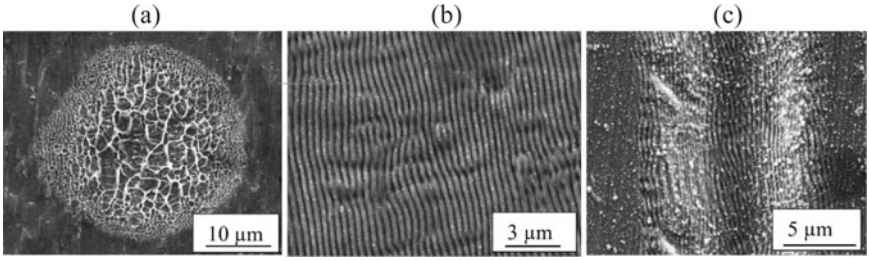

Fig. 11.3 SEM-images of ultrafast laser-induced nano-sized surface structures: **a** nano-pores, **b** LIPSS, and **c** micro-structure combined with nano-ripples

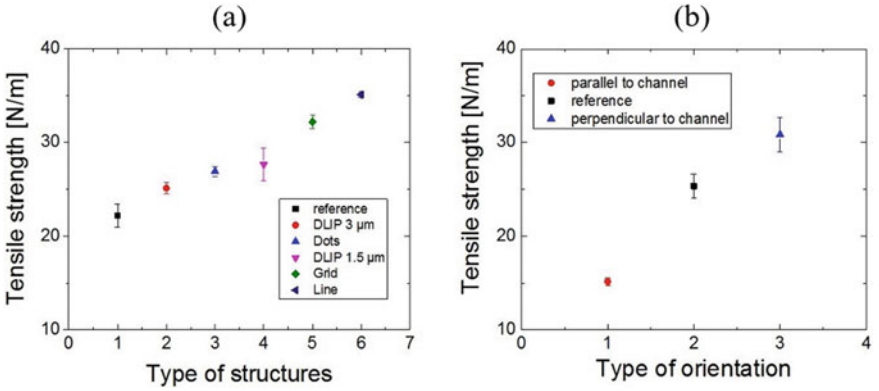

Fig. 11.4 Tensile strength of graphite film (anode) on laser structured copper current as function of **a** surface structures and **b** structure orientation

be achieved by applying a laser fluence of $\varepsilon = 0.16$ J/cm^2 and a laser scanning speed of $v = 50$ mm/s (Fig. 11.3b), which corresponds to an overlap of 80 laser pulses per irradiated area. A surface roughness Ra of 181 nm and a LIPSS depth of 500 nm could be measured by AFM. In general, LIPSS were formed on copper by applying a laser fluence which is close to the ablation threshold of about 0.41 J/cm^2. However, by using an appropriate combination of laser fluence and scanning speed, micro-ablation combined with nano-ripple formation could be realized (Fig. 11.3c). Based on these parameter studies, nano-pores, nano-ripples, and line-/grid-patterns with a pitch distance of 50 µm were created on copper foils for subsequent analysis of electrode film adhesion.

The adhesive strength of graphite anode composite thick films on surfaces of copper current collector foils is in the range of 20–35 N/m (Fig. 11.4a), which is almost one order of magnitude lower than the measured values of 140–250 N/m for composite NMC cathode films on surfaces of aluminum current collector foils. This difference in adhesion strength is related to different sizes and shapes of graphite and NMC particles. However, laser structured copper surfaces led to an improved anode film adhesion (Fig. 11.4a). The type of surface structure design has a great influence on the adhesive properties. The most appropriate results were achieved for copper surfaces with hierarchical surface structures that contain micro-sized line/lattice patterns and nano-sized ripples (Fig. 11.3c). The depth of the laser-generated line structures was 5 µm. The main impact of current collector surface structures is related to an increased contact area and structure orientation and their interaction with graphite particles and polymer binder. In order to investigate the impact of structure orientation on the tensile strength, two types of experiments with line patterns were designed with different peel-off directions: line patterns are parallel and perpendicular to peel-off direction, respectively. It was clearly demonstrated that an enhanced film adhesion with peel-off direction perpendicular to line pattern direction is achieved (Fig. 11.4b) in comparison to the reference measurement without

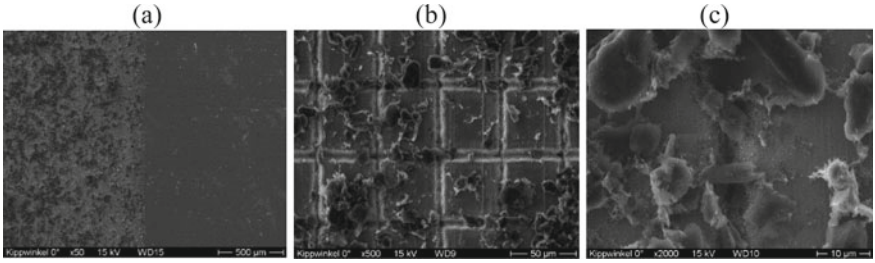

Fig. 11.5 SEM images of copper foil with different surface structures after peel-off testing: **a** DLIP-structured ($\Lambda = 1.3$ μm) copper (left) and unstructured copper (right), **b** grid-pattern in overview and **c** grid-pattern in detail view

laser modification of the current collector. On the other hand, the anode film could be peeled-off from the substrate much easier, if the line pattern is oriented in parallel to the peel-off direction. This phenomenon can be of great interest in recycling of LIBs.

SEM studies (Fig. 11.5a–c) after peel-off tests reveal that graphite particles and binder were anchored inside of the line structures (Fig. 11.5b, c), which can explain the increased film adhesion strength on micro/nano-scaled line/grid structures in comparison to those with nano-sized surface structures. However, the largest adhesion strength could not be achieved by applying a grid structure, which would provide the largest increase of contact area. The line structure orientation and the peel-off direction during adhesion tests have to be taken into account as well.

11.2.4 Impact of Laser Structured Current Collector on Electrochemical Performance

The electrochemical performance of graphite anodes which were deposited on unstructured and laser structured current collectors was characterized by galvanostatic measurements. Dot patterns (Fig. 11.3a) with different pitch distances (25, 50, 75 μm) were generated on copper current collectors. Electrochemical impedance spectroscopy (EIS) was applied in order to study the impact on internal cell resistance.

Figure 11.6 shows EIS spectra (Nyquist plot) of full cells in coin cell design, which were assembled with graphite anodes deposited either on untreated ("reference") or laser structured copper current collectors. For this purpose, different dot patterns with pitch distance of 25, 50, and 75 μm were applied. All Nyquist plots show a similar configuration with one semicircle. Nevertheless, the pitch of the laser-generated pattern can be used to control the electrochemical impedance. The cell with the 50 μm dot pattern on the copper current collector exhibits the lowest impedance (~210 Ω), i.e., charge transfer resistance, in comparison to the reference sample (410 Ω). Contrary to this result, a pitch distance of 25 μm provided the largest

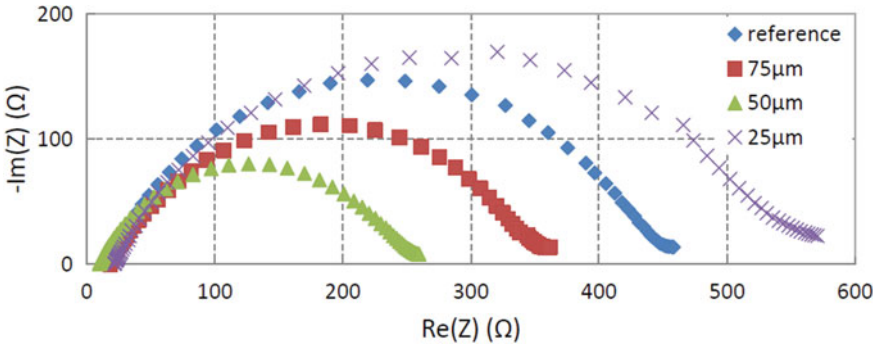

Fig. 11.6 EIS measurements of graphite anode with unstructured and structured current collectors as function of pitch distance (surface structure: dots patterns, coin cell design) [50]

impedance. This might be ascribed to a reduced metallic electrical conductivity of Cu due to an increased amount of laser-induced nano-pores at the copper surface. The results indicate that a balance is required to be found between the advantages of an increased graphite-copper interface area and a decreased electrical conductivity. Furthermore, on base of XRD measurements, it could be found that the reduced charge transfer resistance corresponds to a change in the orientation of graphite particles for anodes deposited on micro-/nano-structured Cu current collector foils [50].

In order to investigate the electrochemical degradation and capacity retention, cells with unstructured and laser structured current collectors were cycled at 0.5 C. It was shown, that after 100 cycles the graphite anode with 50 µm dot pattern exhibits the highest capacity retention (258 mAh/g) in comparison to the reference cell (198 mAh/g) [50]. This result is well consistent with EIS measurements in Fig. 11.6. The optimized interface area between active materials towards current collector and the induced graphite particle orientation can minimize the impedance of the cell and further contribute to the improvement of the battery performance, capacity retention, and battery lifetime, especially at high C-rate.[1]

11.3 Impact of Electrode Surface Modification on Li-Ion Kinetics[2]

Our previous studies [52] showed that direct laser patterning of the surface of thick film electrode materials enables an increase of capacity retention especially for high

[1] C-rate of "1C" or "2C" is defined as complete theoretical lithium charge/discharge in 1 or 1/2 h, respectively.

[2] Portions of the following text have been reprinted from [51] under the open access license (CC BY).

charging and discharging rates. For a better understanding of electrochemical intercalation/deintercalation processes in laser modified electrodes, quantitative experiments of lithiation/delithiation rates were considered. The simplest quantitative approach to determine the rate of effective Li-ion insertion in the active material and the rate of Li-ion transport in the electrolyte is expressed by so-called chemical diffusion coefficient values. For this purpose, one of the most common coulometric titration techniques, the galvanostatic intermittent titration technique (GITT) has been involved.

The focus is set on composite thick film commercial cathode materials (MTI Corporation, USA) based on current collector layer represented by the aluminum foil single side coated by a composite layer, with determined properties as described previously [53]. Such cathode materials are produced by a tape cast process, followed by calendering (final thickness of composite layer of 95 μm), during which the particle–particle contact and the composite adhesion to the current collector are substantially improved. The composite layer contains binder, conductive carbon, and active material rich in lithium cobalt oxide ($LiCoO_2$) as shown by the scanning electron microscopy (SEM) analysis in Fig. 11.7. The main drawbacks of $LiCoO_2$ cathodes, e.g., the high costs, the limited practical capacity due to structural and chemical instabilities at deep charge ($x < 0.5$ in Li_xCoO_2), and the susceptibility to thermal runaway, is compensated by the addition of $LiMn_2O_4$, with lower costs and sufficiently high charge voltage [54]. The advantages of the new chemistries are a more balanced performance and an increased thermal stability of these cathode materials in comparison to that of the individual component.

The surface of the cathode layer was modified by laser ablation with an ultrafast fiber laser (Tangerine, Amplitude Systèmes, France), performed in ambient air down to the current collector. The applied laser process parameters were: 515 nm wavelength, 330 fs pulse duration, 200 kHz repetition rate, $1.5 \cdot 10^9$ W peak power, 100 mm/s laser scan speed and 2 scans, 100 μm pitch. Beside SEM, light microscopy

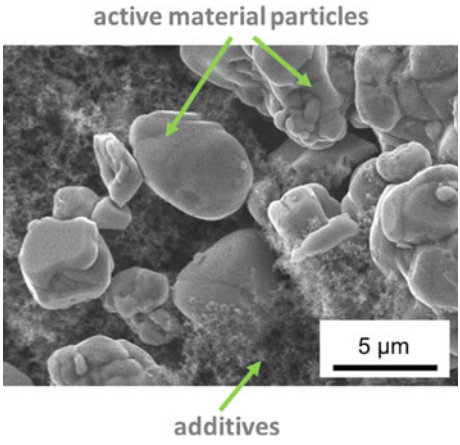

Fig. 11.7 SEM image (top view) of the composite layer, part of the cathode sample

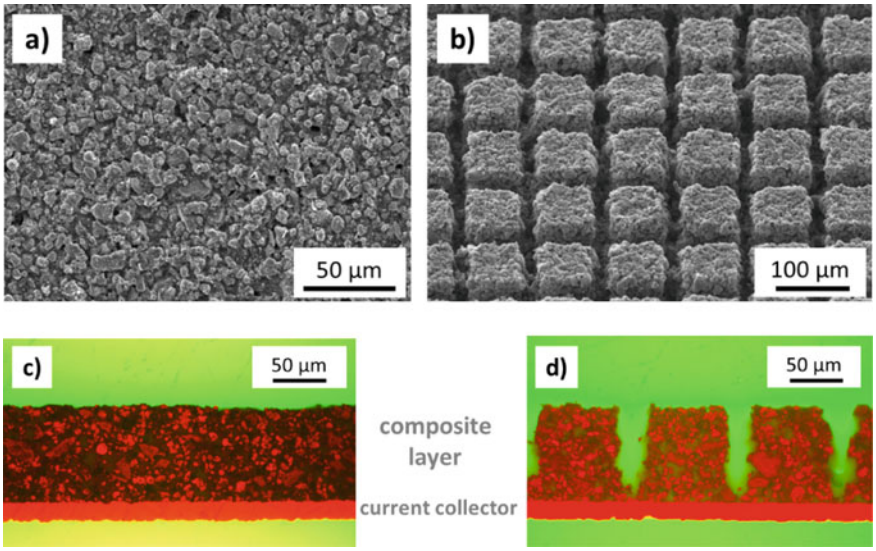

Fig. 11.8 Lithium-ion battery cathode samples—**a**, **c** unstructured and **b**, **d** structured-based on aluminum foil single side coated by $LiCoO_2$ rich composite layer. **a**, **b** SEM images (top view); **c**, **d** LM images (cross section view) [51]

(LM) was also used in structural investigations. Figure 11.8 shows the top view and the cross-section view of both, unstructured and structured cathodes, (a) and (c) for the unstructured sample, (b) and (d) for the laser structured sample, respectively.

Electrochemical measurements were performed using coin cell design for half-cell types. The cells were assembled in a glove box maintained under argon gas (mass fraction purity 0.999999, water and oxygen levels each below 0.101×10^{-7}). Lithium metal with a thickness of 0.38 mm (mass fraction purity 0.999, from Sigma Aldrich, Germany) was used as counter electrode. The separator was a glass fibre separator (GF/A Whatman) and the electrolyte was a commercial mixture of ethylene carbonate: dimethyl carbonate (1:1 volume ratio) containing 1 M $LiPF_6$ (BASF, Germany). Electrochemical characterization of similar cells was previously carried out in our facility labs and described elsewhere [55, 56]. In this study, each measurement was performed on a minimum of three identically made cells. For simplicity, we further refer to a cell containing unstructured or structured cathode materials as reference-cell and laser-cell, respectively.

After initial capacity determination, the cell was initially discharged down to 3.0 V versus Li/Li^+ using a constant current—constant voltage (CC-CV) procedure, followed by GITT. A set of current pulses were applied up to 4.2 V versus Li/Li^+ for a known period of time τ, followed by a relaxation period, while the potential was continuously measured. Finding suitable measurement parameters such as current pulse length, charge/discharge rate and relaxation time was main challenge for this technique.

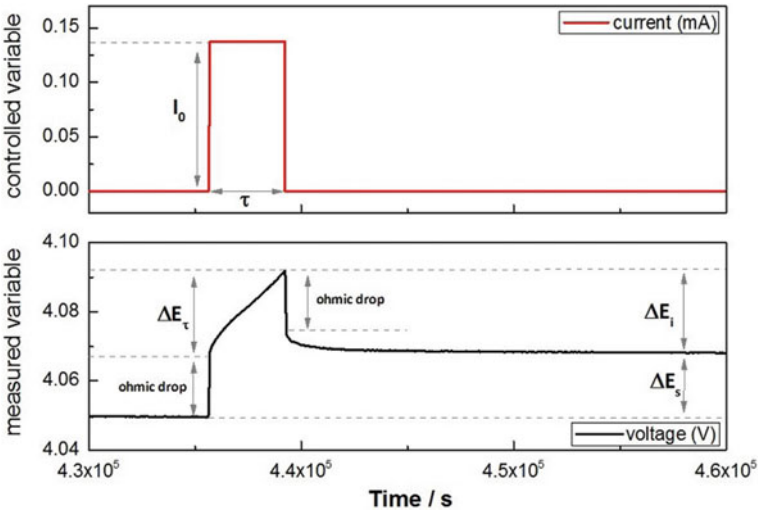

Fig. 11.9 Example of a constant current pulse applied for a known interval of time τ followed by a relaxation time, while the corresponding potential was measured [51]

Figure 11.9 reports a typical current pulse corresponding to a current rate of C/20 applied for τ of 1 h, and the measured voltage in a relaxation period of 6 h. The diffusion coefficient of Li-ions D_{Li^+} was calculated for each titration step using the following equation recommended by Weppner and Huggins [57] for solid-mixed conducting electrodes:

$$D_{\mathrm{Li}^+} = \frac{4}{\pi} \cdot \left(\frac{V_{\mathrm{m}} \cdot I_0}{S \cdot F \cdot z_{\mathrm{Li}}} \right)^2 \cdot \left(\frac{\frac{\mathrm{d}E_s}{\mathrm{d}x}}{\frac{\mathrm{d}E_\tau}{\mathrm{d}\tau^{0.5}}} \right)^2, \tag{11.5}$$

valid when $\tau \cdot D_{\mathrm{Li}^+} \ll L^2$, where: V_{m} is the molar volume of the electrode (considering the density of composite layer of 2.29 ± 0.03 g cm^{-3} [53]), I_0 is the current pulse, S is the electrochemically active area of the electrode–electrolyte interface, given by the product of BET surface area and the active material mass, F is the Faraday constant, z_{Li} is the charge number of Li, E_s and E_τ are the steady-state and the transient voltages, respectively, L is the composite thickness (95 μm, [53]). After each titration step, the change in stoichiometry Δx of active material is given by (11.6):

$$\Delta x = \frac{I_0 \cdot \tau}{z_{Li} \cdot n \cdot F} \tag{11.6}$$

The typical behaviors of the transient and steady-state voltages for a reference-cell is presented in Fig. 11.10. As a function of square root of time, the transient voltage change shows usually a linear trend. Using these parameters, the diffusion coefficient for each change in stoichiometry is reported in Fig. 11.11. The electrochemical active area defined by the product of BET surface area and the active material mass is valid for a description of the 2D surface area (dashed line in Fig. 11.11). The impact of the free-standing structures on the electrode surface needs to be included in a 3D description, for which their contribution relates to the top and surrounding walls of every single structure. Based on the laser parameters used for the 3D structure

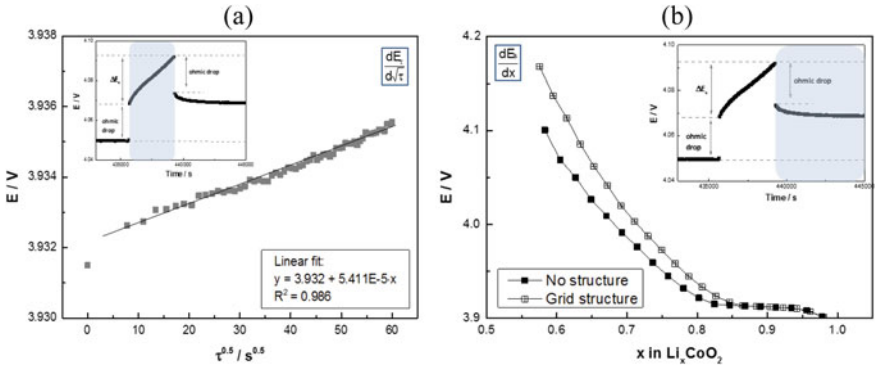

Fig. 11.10 Measured variables in the GITT for the evaluation of diffusion coefficient: **a** transient E_τ and **b** equilibrium E_s potentials [51]

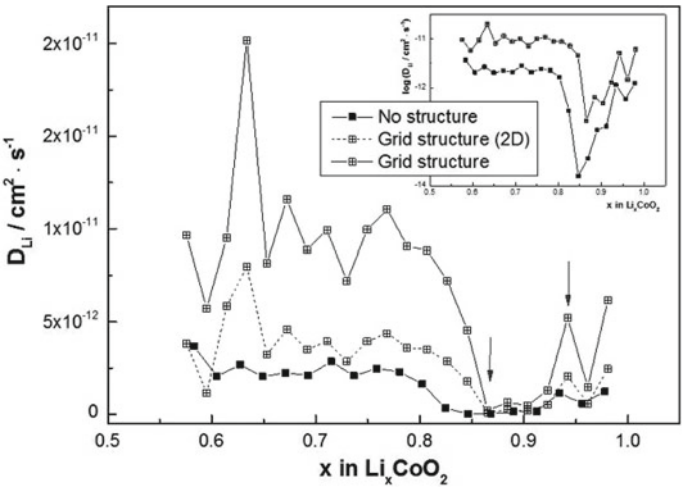

Fig. 11.11 Diffusion coefficient of Li-ions obtained by GITT as a function of stoichiometry [51]

generation, a decrease of 36% in surface area (2D) is expected along with an increase of over 300% due to the lateral wall contribution (3D) for the structured cathode layer.

The titration technique offers information in relation to the phase diagram, i.e., the existing phases in the system. The diffusion coefficient corresponding to the laser structured material tends to be more sensitive to the phase transitions. At $x \sim 0.94$ a clear change in the slope is observed, which according to [58, 59] is related to the first order insulator–metal transition. For the x range between 0.94 and 0.86, the diffusion coefficient is described by a plateau in quite good agreement with the two-phase region described in the previous electrochemical studies. The measurements by Reynier et al. [60] found this two-phase region in the x range from 0.95 to 0.83, whereas lower concentration for $x = 0.75$ or 0.80 was reported by [58, 61] respectively. For a more precise determination of the phase boundaries composition, smaller titration steps are needed. Nevertheless, in this region, the diffusion coefficients of the two different material types are the lowest achieved (insert graph in Fig. 11.11). Below $x \sim 0.86$ the diffusion coefficient determined for laser structured sample is 5 times higher than for the unstructured. This range in stoichiometry corresponds to the layered hexagonal single phase [60, 62], where the 3D structures seem to have an impact on the kinetic properties. Approaching a lower x, i.e. the order–disorder transition known for $x \sim 0.5$, the diffusion coefficient of the laser-cell tends to be more sensitive and shows a change in slope.

A closer look to the titration steps (Fig. 11.12) enables us to distinguish dissimilarities in the voltage changes of each cell. At $x = 0.96$ and at a close value of the determined diffusion coefficient for each cathode material, the voltage drop in the reference-cell is significantly higher than in the laser-cell. This is also noticed in the hexagonal phase at $x = 0.63$, however with a slight smaller effect. The equilibrium

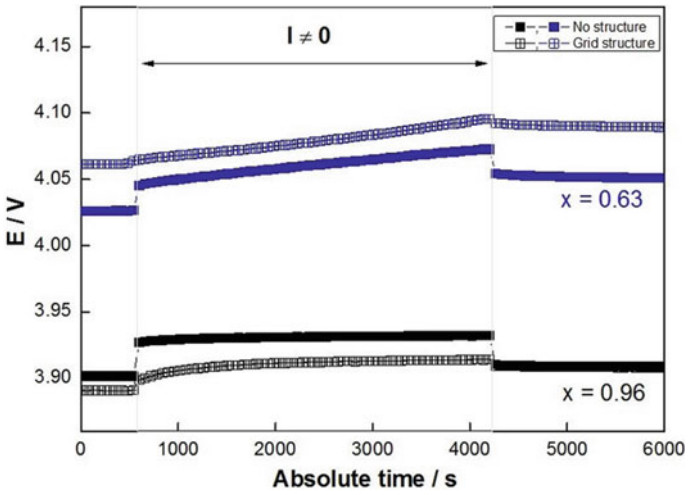

Fig. 11.12 Relaxation and transient voltages characteristic for GITT steps performed on cells with unstructured and laser structured materials at defined stoichiometry for $x = 0.96$ and $x = 0.63$ [51]

potential behavior at this point clearly indicates a different diffusion-rate yielding to a four times higher diffusion coefficient.

In order compare the influence of each specific cell design characteristics, the voltage loss ΔE_i was determined. Immediately after the current was interrupted, we measured a steep drop in voltage. This instantaneous drop is mainly due to the ohmic resistance of the cell (ohmic drop), to which is added a contribution of the polarization effects. Since the ohmic drop is a very fast process, it could not be here separated. The instantaneous cell impedance, calculated as the ratio of the instantaneous voltage drop and current, of reference-cell is factor 3 higher than of the laser-cell (Fig. 11.13). As the cell impedance is dependent on current, this is expected to increase with increasing current densities.

Whereas GITT enables the determination of the diffusion coefficient of Li-ions at a certain modified stoichiometry, cyclic voltammetry (CV) offers an overall diffusion coefficient in the measured voltage range. In order to validate our GITT data, CV measurements were carried out using a scan rate ϑ between 0.02 and 0.07 mV s^{-1}, in the same voltage range from 3.0 to 4.2 V. The chemical diffusion coefficient was calculated using the Randles-Ševčík equation applied for room temperature [63]:

$$D_{\mathrm{Li}^+} = \left(\frac{I_\mathrm{P}}{\vartheta^{0.5}}\right)^2 \cdot \left(2.69 \cdot 10^5 \cdot z_{\mathrm{Li}}^{3/2} \cdot S \cdot C^*\right)^{-2}, \tag{11.7}$$

where I_P is the peak current, C^* is the concentration of active ions. The results of Li-ions diffusion rates for GITT and CV are presented in Table 11.1 for unstructured and laser structured cathode materials. The results between the two techniques agree

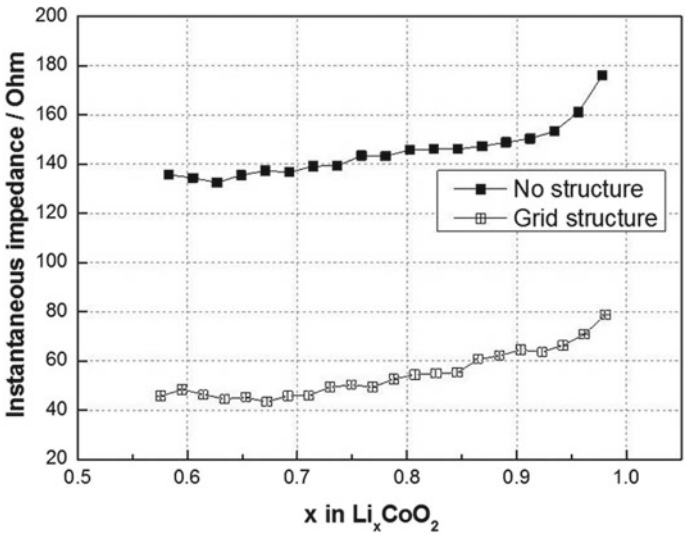

Fig. 11.13 Instantaneous impedance as a function of stoichiometry [51]

Table 11.1 Li-ion diffusion coefficients measured in cells with unstructured and laser structured materials

Method	Diffusion coefficient (cm s^2)	
	No structure	Laser structured
GITT	1.57×10^{-12}	7.13×10^{-12}
CV	1.54×10^{-12} (charge) 1.11×10^{-12} (discharge)	7.4×10^{-12} (charge) 4.0×10^{-12} (discharge)

well, especially when the charge process for CV measurements is considered, and are consistent with the already determined diffusion coefficient for such active material. The values of the diffusion coefficients are in the range given by previous studies [64], which are influenced by the measurement parameters, voltage range, electrolyte properties, etc. However, the goal of this work was to determine relative values with respect to the specific design characteristics of reference and laser-cells.

The laser-cells seem to have generally a higher kinetic performance, independent of the cathode material. This observation was made on cells with structured $LiFePO_4$ [65], for which the difference in diffusion coefficient was about one order of magnitude. The corresponding 3D microstructures were generated with an ablation depth of 39 μm down to the current collector.

The CV of a reference-cell compared to the one of a laser-cell is shown in Fig. 11.14. The peak current of the laser cell was significantly increased in comparison to the reference cell with unstructured electrode. During charging, the laser-cell reaches 3.88 mA, while a current of 1.65 mA could be obtained for the reference-cell. The voltage corresponding to the CV peak for all the cells shifted slightly to higher values. For discharge processes, the voltage shift was found to decrease only for the laser-cell. The over-potentials, namely the charge-transfer resistance and concentration polarization, were significantly reduced for cells having laser structured composited electrodes. Figure 11.15 shows the current maxima extracted from the cyclic voltammograms depending on the root function of the scan rate during

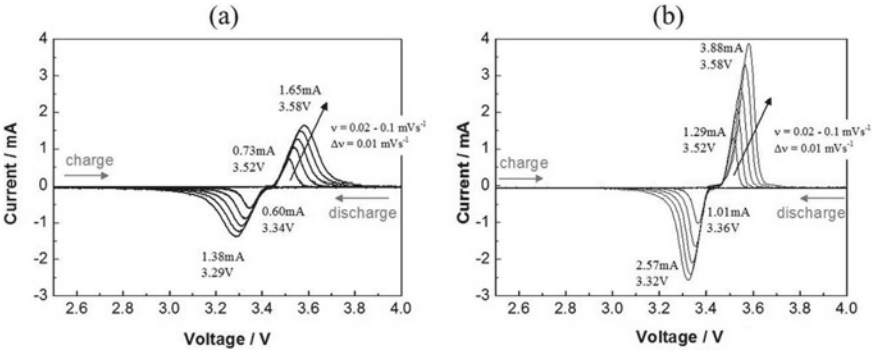

Fig. 11.14 Cyclic voltammograms of **a** reference-cell and **b** laser-cell

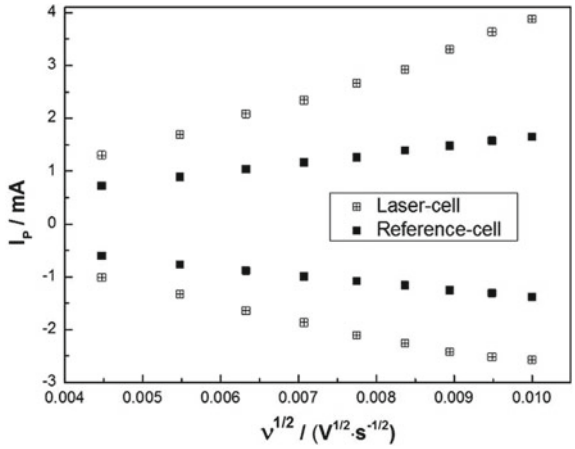

Fig. 11.15 Peak current I_P as a function of the square root of the scan rate ν of reference- and laser-cells

charging (oxidation) and discharging (deoxidation). It is obvious, that the current maxima achieved for the laser-cell show always the highest values. Furthermore, the current maxima values were linearly proportional to the square root of the scan rate, which indicates that a diffusion-controlled process takes place [66]. To summarize, a 3D microstructure represents an increased active surface area which is in direct contact with the free liquid electrolyte leading to an enhanced lithium-ion diffusion transport rate.

After GITT and CV measurements, the cell rate capability was determined by applying successively increased C-rates from C/10 up to 2C (Fig. 11.16). Galvanostatic testing measurements were performed in a voltage range between 3.0 and 4.2 V versus Li/Li^+. Since already at low current densities of GITT the resistance of the reference-cell was much higher than of the laser-cell, at high C-rates this effect imposes a significant capacity loss. It was observed that the capacity of the

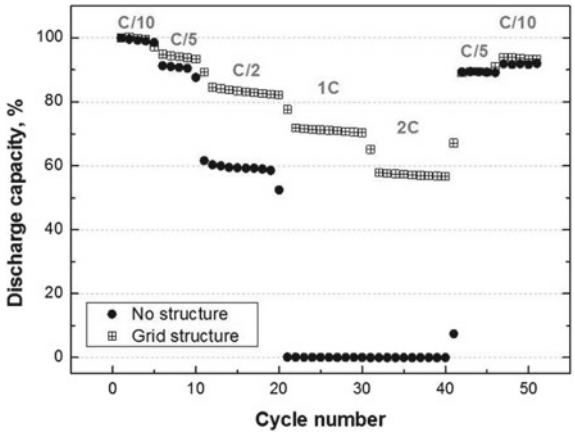

Fig. 11.16 Discharge capacity determined by galvanostatic cycling with potential limitation using different C-rates, performed on reference- and laser-cells [51]

reference-cell is significantly decreased, i.e. at C/2, its retained capacity is only at 60%, and furthermore, at 1C and 2C such cell shows no capacity. At 2C, the laser-cell still retains about 60% of its initial capacity. As a final cycling step, the C-rate was set back to C/10 to determine whether any cell degradation occurred during these galvanostatic measurements. A small capacity loss was observed at the end of the measurements: the cell capacity decreased by 6% and 8% for laser- and reference-cells, respectively.

11.4 Passivation Coatings on Three-Dimensional Electrodes

After introducing the first commercial lithium-ion batteries (LIB) in 1991 by Sony, lithium cobalt oxide (LCO) became the most used cathode material for LIB for at least two decades due to its excellent lithium-ion diffusion kinetics and simple type of synthesis [67]. The laser-assisted formation of conical 3D microstructures in thick composite LCO films but also thin-film LCO cathodes was discovered by Pfleging et al. [26]. They could achieve significant electrochemical improvements such as enhanced capacity retention at high C-rates. By applying a voltage window of 3.0–4.2 V, LCO cells cannot provide more than half of their theoretical capacity of about 274 mAh/g [68]. One popular approach to increase the specific capacity of lithium-ion batteries is to increase the upper voltage, e.g. to values of about 4.5 V. In the case of LCO, however, a structural phase transition from the hexagonal to the monoclinic phase occurs for electrochemical cycles at higher voltages, which leads to structural damage to the electrode material. In addition, side reactions due to electrolyte decomposition and co-dissolution contribute significantly to a rapid fading of specific capacity with increasing cycle number [68–70].

In order to improve the structural stability of LCO materials in widened voltage windows with upper voltages above 4.2 V, surface coatings with metal oxides such as Al_2O_3 [71], $AlPO_4$ [72], SnO_2 [73], ZrO_2 [74], ZnO [75], CuO [69], and MgO [76] have been suggested. Other technical approaches have dealt with coatings based on carbon such as sucrose [77] or carbon black [78]. As far as we know, the carbon coating on the surface of a compact LCO thin-film electrode is quite a new research field. In particular, the role of carbon coating in preventing co-dissolution has not been disclosed. Lee et al. [79–81] have applied fullerene C60 thin films as functional coating layers for silicon- and tin-based anodes and for composites for lithium-ion batteries and an excellent electrochemical improvement could be proven. By applying plasma processing condition, C60 formed a polymerization [82]. It could be shown that the C60 films were polymerized along the anode surfaces forming an artificial solid electrolyte interphase layer (SEI) which was mechancial stable during volume changes of the cathode while lithiation/de-lithiation takes place; and also chemical side reactions between electrode material and liquid electrolyte could be suppressed [79–81]. Lee et al. [83] demonstrated a new approach by applying the polymerized C60 coating to the laser-generated 3D LCO microstructure. Prior to C60

coating the laser structured LCO thin films were laser annealed to synthesize the high-temperature phase (HT-LCO). The passivated electrode (C_{60}@3D-HT-LCO) could finally counteract the above-mentioned problems for a widened voltage window of about 3.0–4.5 V. The dissolution of Co could be prevented while maintaining the interface kinetics which led to improved electrochemical performance of the special designed cathode material.

11.4.1 Experimental Approach

The process for the production of passivated and structured thin-film cathode materials is shown schematically in Fig. 11.17. In an Ar atmosphere, radio-frequency (RF) magnetron sputtering using a Leybold Z550 coating system is applied to deposit

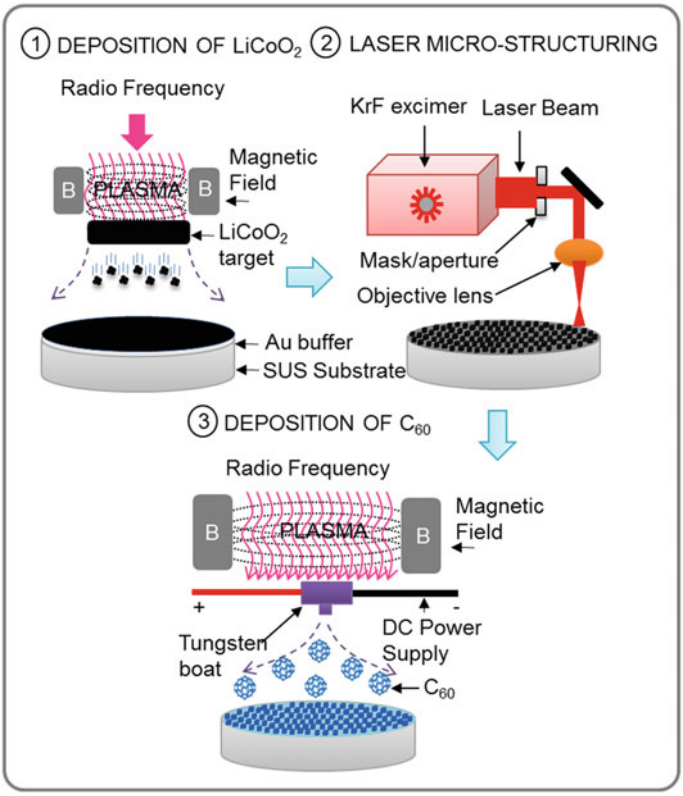

Fig. 11.17 Schematic illustration for the preparation of C_{60}@3D HT-LCO including the deposition of $LiCoO_2$ by magnetron sputtering, laser structuring/annealing and deposition of plasma-polymerized C_{60} thin film on laser-structure $LiCoO_2$ performed by plasma-assisted thermal evaporation. Reprinted from [83], with permission from Elsevier

compact LCO thin films on stainless steel substrates (Fig. 11.17a). Subsequently, laser microstructuring of the deposited LCO thin films was investigated using short-pulsed excimer laser sources (ATLEX-1000-I, ATL Lasertechnik GmbH, Germany), which operated at a wavelength of 248 nm (Fig. 11.17b). The laser pulse repetition rate could be varied from single pulse up to 1000 Hz and the laser pulse duration at FWHM was 5 ns. The excimer laser sources were implemented in Promaster and Micromaster micromachining laser workstations (Optec s.a., Belgium). The laser fluences could be varied from 0.5 to 10 J/cm^2. All laser ablation processes were carried out in ambient air in order to enable the formation of self-organized microstructures, so-called cones, on the cathode thin film material. The loss of active material was quite low and is in the range of 0–10 wt% [26]. After structuring laser annealing of unstructured and laser-structured thin films was carried out to synthesize the required battery phase (HT-LCO) applying a high-power diode laser (FLS IronScan, Fisba Optik AG) with a maximum average laser power of 50 W at an operating wavelength of 940 nm. The laser beam had a focus diameter of 1 mm on the sample surface. The temperature on the sample surface could be controlled inline whereby a pyrometer (FLS PyroS, Fisba Optik AG) was connected to the laser power management system. The annealing temperature could be adjusted and precisely controlled from 120 to 700 °C. Finally, a C60 coating was realized on 3D-HT-LCO by applying RF plasma-assisted thermal evaporation (RF-PATE, Fig. 11.17c). The deposition of C60 thin films took about 5 min. The mode of operating of RF-PATE has been described in detail elsewhere [79, 82].

After laser annealing, the surface morphology of the cathode thin film consists of small grains with a size in the range of 100–200 nm in diameter. The laser annealing process was performed at 500 °C for a duration of 17 min [26, 31]. The precise control of the thickness of the C60 coating on top of the 3D-HT-LCO cathode is a critical parameter, since it determines both the solid electrolyte interface and the electronic conductivity and it should enable high mechanical strength during electrochemical cycling [76]. It was shown in previous studies by Lee et al. [80, 84] that a C60-thickness of about 80 nm is most appropriate for cell operation.

11.4.2 Electrochemical Performance of Passivated LCO Thin Film

The cathodes were assembled in coin cells with lithium as counter electrode and electrolyte made of 1 M LiPF6 in ethylene carbonate, ethyl methyl carbonate, and dimethyl carbonate (volume ratio 1:1:1). The galvanostatic cycling was performed in a widened voltage window of 3.0–4.5 V which delivers initial discharge capacities of 150, 159, and 175 mAh/g for HT-LCO, 3D HT-LCO, and C_{60}@3D HT-LCO, respectively. The coulombic efficiency (CE) of C_{60}@3D HT-LCO is highest (94%), followed by 3D HT-LCO (92%) and pristine HT-LCO (88%). A higher CE value reflects a lower irreversible loss of capacity, which is mainly due to a suppression of

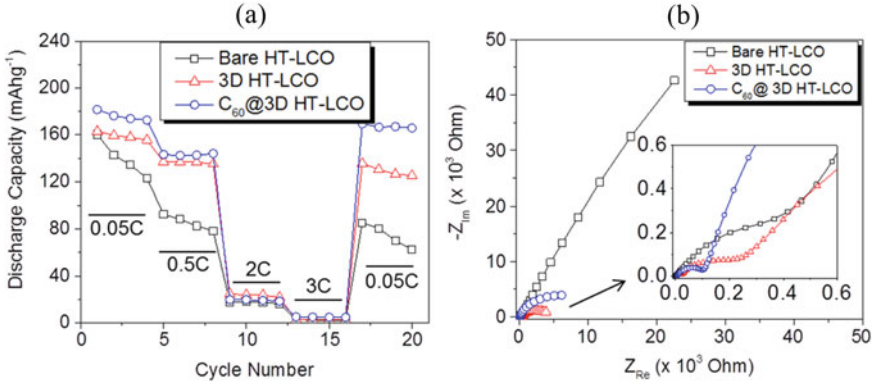

Fig. 11.18 **a** Rate capability tests at different current densities, and **b** EIS analysis of bare HT-LCO, 3D HT-LCO, and C_{60}@3D HT-LCO. Reprinted from [83], with permission from Elsevier

irreversible lithium-ion loss caused by side reactions like electrolyte decomposition during charging or kinetic interface problems during discharge process [85, 86]. In addition, it was observed that the C_{60}@3D HT-LCO reveals a lower overpotential, which indicates a lower cell impedance. The rate capability tests were carried out for different C rates within a voltage window of 3.0–4.5 V (Fig. 11.18a). Among the cathodes tested, the C_{60}@3D HT-LCO electrodes provide the best electrochemcial performance. The initial discharge capacities of pristine HT-LCO, 3D-HT-LCO, and C_{60}@3D HT-LCO at 0.05C are 160, 163 and 181 mAh/g, respectively. At higher C-rates of 2C and 3C a significant drop in capacity is observed for all types of electrodes. However, applying a C-rate of 0.05C (C/20) after the C-rate performance test enables a comparison with the initial capacities: the cell with C_{60}@3D HT-LCO cathode achieve still 91% of initial capacity, while the cells with pristine (bare) and uncoated 3D-HT-LCO achieve only 77% and 38% of initial capacity, respectively. Significant less cell degradation with C_{60}@3D HT-LCO electrodes can be attributed to a stable layer structure of the cathode, in particular to the stabilization at the interface between the electrode and the liquid electrolyte [67].

Electrochemical impedance spectroscopy (EIS) measurements were applied directly after C-rate performance tests in order to study the interfacial kinetics of the electrodes mainly influencing the battery operation. EIS was carried out in a frequency range from 100 kHz to 10 MHz with a voltage amplitude of 5 mV. The resulting Nyquist plot (Fig. 11.18b) shows a semicircle for high-frequencies which represents RC-circuit of the charge transfer resistance (R_{CT}) and the slope curve measured at low frequencies is caused by lithium-ion diffusion processes and corresponds to the so-called Warburg impedance [87]. It is quite obvious, that for all types of studied electrodes, C_{60}@3D HT-LCO provides the lowest value of charge transfer resistance (see inset, Fig. 11.18b). The presented studies confirm that it is beneficial to combine laser-induced 3D architectures and plasma-assisted C60 coating in order

to reduce significantly the overall cell impedance, to enhance capacity retention at high C-rates, and to reduce cell degradation.

11.4.3 Electrochemical Performance of 3D Silicon/carbon Core–Shell Electrodes

In a very similar approach as described in Fig. 11.17, the passivation of silicon (Si) anode nanomaterials and their electrochemical impact in 3D electrodes was studied [28]. For this purpose Si nanoparticles (particle size 10–250 nm) were passivated with a 5–7 nm thick carbon layer by applying thermal decomposition at 700 °C in an atmosphere of 10% C_3H_6 and 90% Ar. The so-called silicon/carbon core–shell particles (Si@C) were used as active material (60 wt%) in a slurry which is coated via tape casting on a copper current collector foil (Fig. 11.19a). An electrode film thickness of 24 µm was adjusted with a mass load in the range of 0.6–1 mg/cm^2. Subsequent ultrafast laser structuring (pulse length 370 fs) was performed at a wavelength of

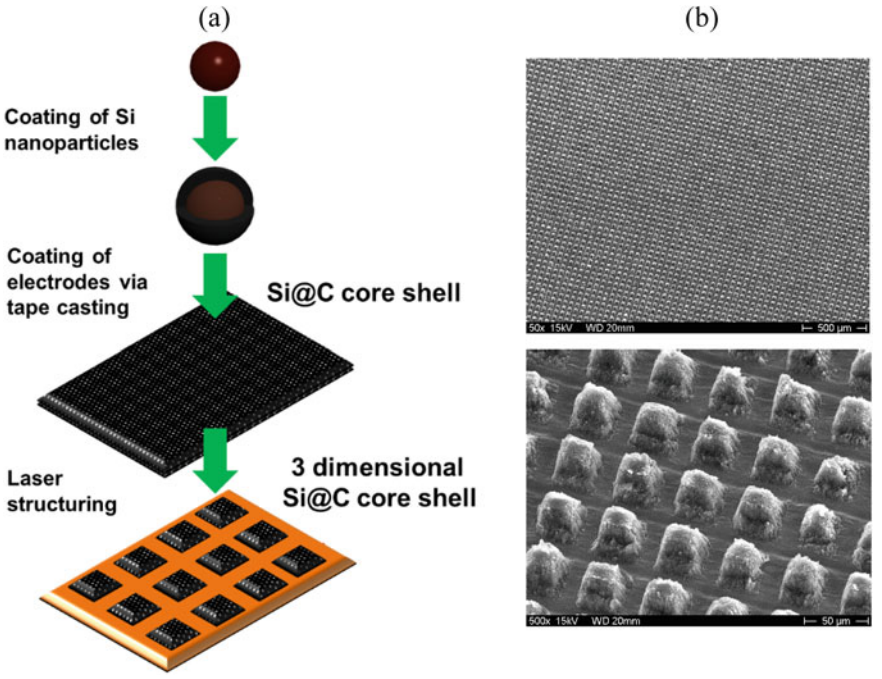

Fig. 11.19 Fabrication of 3D Si@C core–shell electrodes: **a** schematic view of preparation process; **b** SEM images (overview and detail view) of 3D Si@C core–shell electrodes

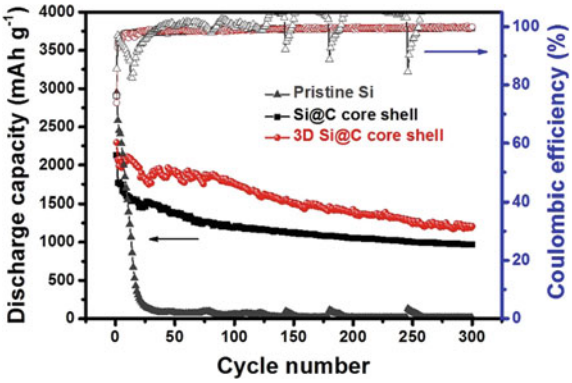

Fig. 11.20 Discharge capacity of pristine Si, Si@C, and 3D Si@C core–shell electrodes at a current density of 200 mA/g in the potential range 0–2 V. Reprinted from [28], with permission from Elsevier

515 nm, an average laser power 0.28 W, and a laser repetition rate of 200 kHz. Free-standing structures down to the current collector were fabricated along the complete electrode area with a pitch of 50 μm and a line width of 15 μm (Fig. 11.19b).

The electrochemical performances of 3D Si@C, Si@C, and pristine Si, which were used as anode materials for lithium-ion batteries, were investigated in order to identify the impact of material and 3D electrode design (Fig. 11.20). The discharge capacity of the pristine Si exhibits a rapid decrease within the first 25 cycles, decreasing to 0 mAh/g. The coulombic efficiency of the pristine Si shows an unstable behavior. During cycling, the volume change in Si leads to a continuous crack formation, and therefore the pristine Si surface is exposed to the electrolyte at each cycle, resulting in repetitive formation of new SEI layers, which is called "unstable SEI formation". The Si@C core–shell electrodes obtained by the thermal decomposition improve the reversible capacity and cycle retention because of the conformal carbon coating. More interestingly, the reversible capacity of the 3D Si@C core–shell electrode is higher than that of the pristine Si@C core–shell electrode after 300 cycles. Apparently, the unique 3D architecture is responsible for the improved cycle performance with a larger active surface area to reduce the polarization effect and provide enough space to release physical stress occurring during the Li-ion insertion and extraction processes. By the introduction of a carbon coating and the laser structuring, an enhanced performance of Si anode materials exhibiting high specific capacity (>1200 mAh/g over 300 cycles), good rate capability (1170 mAh/g at 8 A/g), and a stable cycle retention was achieved.

11.5 Laser-Induced Breakdown Spectroscopy of 3D Electrodes

For achieving an optimized three-dimensional (3D) electrode design a sophisticated analytical tool is necessary which enables a rapid screening of the chemical composition of complete electrodes (surface and bulk) after electrochemical cycling. This

analytic tool should act as feedback control between electrochemical performance and the generated laser-assisted 3D architectures. Laser-induced breakdown spectroscopy (LIBS) seems to be a powerful item and was therefore intensively applied to characterize 3D structures on thick film electrodes *post-mortem* (after battery tests). LIBS is an analysis method which offers the possibility to characterize the elemental composition very fast [88] and it is capable of performing direct 3D analysis with micrometric [89] or nanometric resolution [90]. Only one single laser pulse under ambient air is required in order to generate a laser-induced plasma and the achieved chemical information can be directly correlated with a local State-of-Health (SOH). Characterization methods such as bulk analysis, depth profiling, elemental mapping as well as layer-by-layer analysis can be performed at atmospheric pressure condition [91, 92]. In the field of lithium-ion batteries, LIBS is a rather new approach in order to obtain *post-mortem* critical information on surface phenomena that define and control the performance of Li-based battery systems. As a powerful analytical tool, LIBS can be used for an entire analysis of large-areal 3D battery sheets. Besides a large area surface characterization also an elemental mapping of the complete electrode bulk material down to the current collector can be realized. Post-lithium concepts, 3D battery concepts, and thick film electrode concepts can be investigated in order to achieve advanced high energy and high power batteries. This new research field has great potential to study aging effects as a function of electrochemical performance, (e.g., lifetime, cycle retention), cycle parameters, and 3D-concept parameter (aspect ratio, active surface area, porosity). Finally, LIBS is a flexible analytical method for measuring of chemical patterns that are induced by 3D topographies, degradation, or aging processes.

In recent research studies, it could be shown for the first time that LIBS can be successfully applied to analyze chemical compositions along complete electrode surfaces of cycled or uncycled cells. Element mapping and element depth-profiling were applied for characterizing the electrode as function of SoH and cell architecture [56, 93–95]. This new approach for cell characterization requires a specialized calibration procedure based on electrochemical titration in order to produce NMC samples with defined lithium amount [55]. In the current chapter we describe the manufacturing of 3D NMC electrodes, their electrochemical cycling behavior, and subsequent *post-mortem* elemental characterization by using LIBS.

11.5.1 Manufacturing Route for 3D Electrodes

The fabrication of 3D electrodes can be divided into four main processing steps (Fig. 11.21a-d): (a) slurry preparation, (b) coating/drying, (c) calendering, and (d) ultrashort laser structuring.

The cathode slurry was prepared by mixing 90 wt% of lithium nickel manganese cobalt oxide ($LiMeO_2$, Me = Ni:Mn:Co = 1:1:1), 5 wt% of conductive additive (TIMCAL SUPER C65) and 5 wt% of polyvinylidene fluoride (PVDF) binder. *N*-Methyl-2-pyrrolidone (NMP) was used as solvent. Additionally, the slurry was

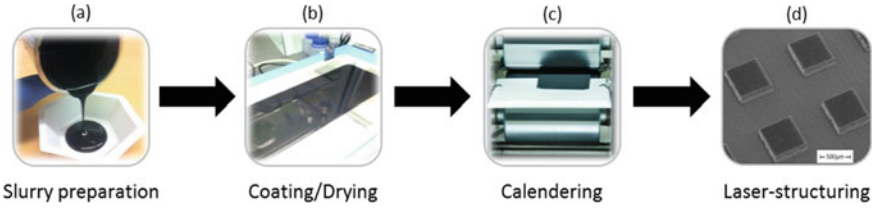

Fig. 11.21 Processing steps for manufacturing of 3D electrodes: **a** slurry preparation, **b** coating/drying, **c** calendering and **d** ultrashort laser structuring

deposited onto a 20 μm thick aluminum foil, which is denoted as current collector. The coating procedure was carried out using a tape-casting film coater with an integrated heating lid. Subsequently, the electrode sheets were dried for 2 h at elevated temperatures. All cathodes were calendered for improving the particle-to-particle contact (Fig. 11.23a) and for realizing a good film adhesion between the NMC composite material and the current collector. Furthermore, calendering is an essential processing step to increase the volumetric energy density of the entire cell [96]. Within the next step, free-standing micro-pillars were generated with a dimension of 600 μm × 600 μm by removing the composite material down to the substrate (Fig. 11.24a). A micromachining workstation (PS450-TO, Optec s.a., Belgium) equipped with an ultrafast fiber laser (Tangerine, Amplitude Systèmes, France) was used. The pitch distance was set to 1200 μm. Finally, two types of electrodes (unstructured/laser structured NMC cathodes) were laser cut in circular disks with 12 mm in diameter. Prior to cell assembly, the electrodes were dried in a vacuum oven for 24 h at 130 °C. Swagelok® cell design was applied for the subsequent battery tests.

11.5.2 Post-mortem LIBS Investigation of Lithium Distribution in NMC Thick Film Electrodes

Unstructured and laser patterned NMC cathodes were characterized *post-mortem* by LIBS in order to study the lithium amount at the sample surface at different SoH. For this purpose, the Swagelok® cells were electrochemically cycled using the following testing procedure: In a first approach (electrochemical formation) both Swagelok® cells were cycled for three cycles using a C-rate of C/10 in a voltage range of 3.0–4.2 V. For investigation of lithium distribution in electrodes, which operate at high electrical currents, the C-rate was increased up to C/2 for 100 cycles. Additionally, both types of Swagelok® cells were disassembled in an argon-filled glovebox and the NMC electrodes were washed two times for each 30 min in fresh dimethylcarbonate. Finally, an elemental mapping of lithium was carried out for both electrodes in order to investigate the lithium distribution at different SoH.

The experimental setup of LIBS used in this work is illustrated in Fig. 11.22. LIBS measurements were performed using a dot matrix with a point-to-point distance of

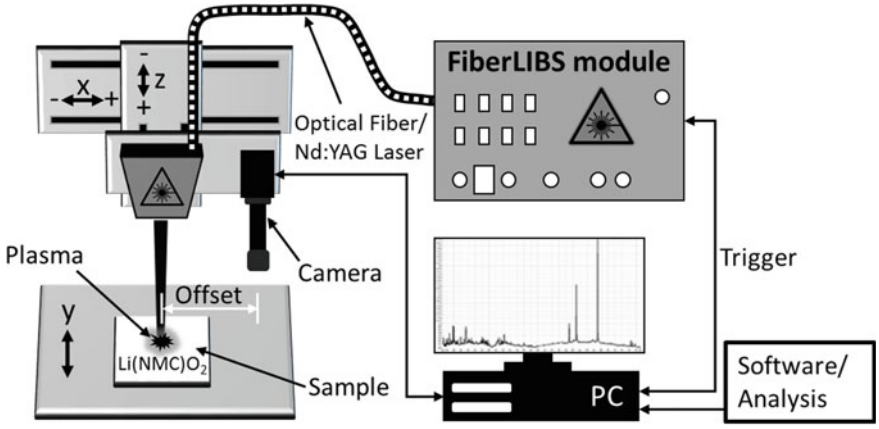

Fig. 11.22 Scheme of the experimental setup of LIBS for the characterization of NMC electrodes. Reprinted from [55] with permission from IOP Publishing

100 μm. The measurement area of each NMC electrode surface was set to 13 mm × 13 mm. A calibration-file was used for enabling an elemental mapping of lithium for both NMC electrodes. The detailed calibration procedure is described elsewhere [55]. Briefly, nine individual cells were galvanostatic cycled up to 3.0, 3.25, 3.5, 3.75, 4.0, 4.25, 4.5, 4.75, and 5.0 V. By this measure NMC electrodes with different SoC were produced acting as reference samples for subsequent LIBS calibration procedure.

In a first approach, LIBS measurements were performed on a calendered and unstructured NMC electrode with a thickness of 100 μm. The local SoH was controlled by electrochemical cycling in a voltage range of 3.0–4.2 V (Fig. 11.23b). It could be clearly demonstrated that the discharge capacity provides a big drop at cycle 92. The value drops down from 63.6 to 9%. Finally, the cell leads to a spontaneous cell failure at cycle 93. After an elemental mapping of lithium, the amount was locally increased at position $X = 4.8$ mm and $Y = 7.2$ mm (Fig. 11.23c). This lithium amount can be assigned to local lithium plating. A possible reason for this inhomogeneity in lithium concentration might be an insufficient wetting of the electrode with liquid electrolyte. Dry electrode areas can lead to a reinforced degradation of active material and finally to a spontaneous drop in capacity and subsequent cell failure. Homogeneous wetting is quite important for sufficient electrochemical cyclability, especially for calendered NMC electrodes with film thicknesses >100 μm and those with low porosity (<30%). Two aspects have to be considered, first, the electrode footprint area will have an impact on cell degradation processes, and second, the electrode surfaces having an inhomogeneous lithium distribution will induce a variation of electrical current densities along the surface, which in turn will reinforce the chemically driven aging and cell failure process.

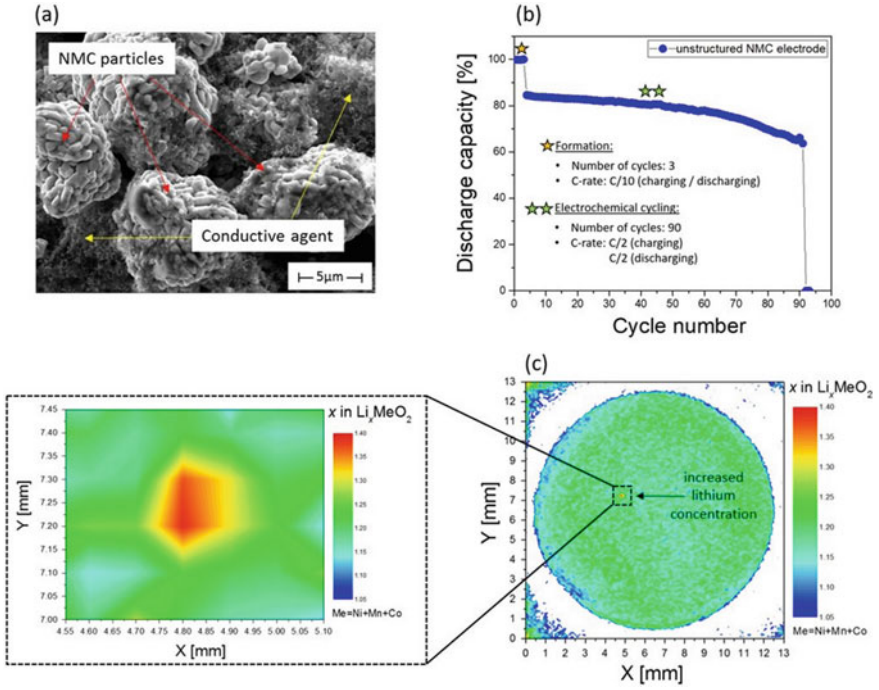

Fig. 11.23 Characterization of NMC electrode material: **a** SEM image (top view) of an as-deposited, calendered, and unstructured NMC electrode, **b** electrochemical performance [discharge capacity (%) vs. cycle number and spontaneous cell failure at cycle 93] [97], **c** LIBS lithium mapping (survey and detail) of a cycled and unstructured NMC electrode

In a second approach, LIBS measurements were performed on laser structured NMC electrodes in order to investigate the lithium distribution in free-standing micro-pillars (Fig. 11.24a). It could be shown, that for charging- and discharging C-rates $\geq$C/2, the lithium concentration is significantly increased along the contour of each micro-pillar (Fig. 11.24b). It seems to be quite clear that for high current densities this becomes an important matter leading to a measurable local variation of lithium concentration along the surface of each free-standing micro-pillar. For elevated C-rates (>1C) the rate of lithium intercalation will increase along the sidewalls of each micro-pillar as illustrated schematically in Fig. 11.24c. The C-rate performance depends mainly on the lithium-ion diffusion kinetics within the active material and the liquid electrolyte [98]. Thus, the presented results clearly show, that 3D architectures act as attractor for lithium-ions and boost the battery performance regarding high rate capability (cell power) and cell lifetime.

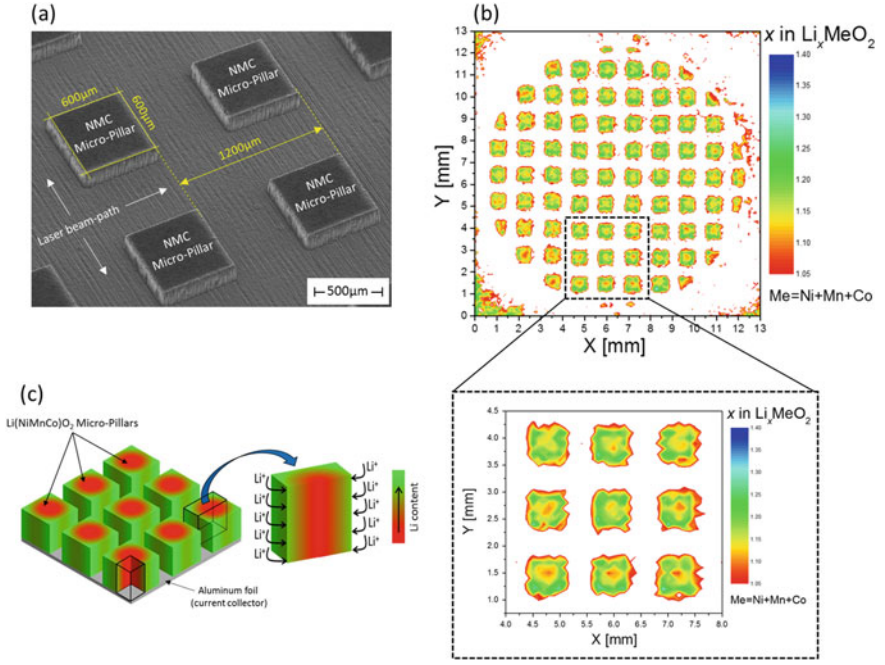

Fig. 11.24 Characterization of NMC electrode material: **a** SEM image (top view) of a calendered and laser-structured NMC electrode with micro-pillars of 600 µm × 600 µm [97]. **b** LIBS lithium mapping (survey and detail) of a cycled and laser structured NMC electrode, **c** schematic view of a model for laser structured NMC electrodes with 3D micro-pillars during electrochemical cycling at high discharging C-rates

11.6 Conclusion

Laser-assisted processes can be easily integrated into existing battery production lines with the intention to achieve a significant impact on reducing cell manufacturing costs. For laser welding of bus bars and high-speed cutting of individual electrodes a mature level is achieved. Both technologies are already being partially introduced in cell production and in pilot lines. Up to now, nanosecond laser systems have been preferred for electrode cutting for economic reasons. However, it was shown in several studies that ultrafast laser processing of electrodes offers significantly improved qualities and a higher ablation efficiency, which can be introduced in a new laser-based 3D battery generation. For the manufacture of lithium-ion batteries, the laser structuring of composite thick film electrodes and thin metal current collectors offer great advantages in terms of improving cell performance, such as a longer battery lifetime and an improved cycle retention for high charge and discharge rates. A suitable 3D surface topography has been shown to influence the lithium-ion diffusion kinetics within the electrolyte filled composite electrode materials, while avoiding critical mechanical stresses during charging/discharging and

significantly reducing overall cell impedance. Laser nanostructured current collector surfaces will enable the practical use of thick films and new high energy materials such as silicon anodes or silicon doped graphite anodes in lithium-ion batteries. A combination of the 3D battery concept, thick film concept, and thin film passivation of electrodes will enable the development of a new generation of lithium-ion cells, which will provide high energy density and high power density at the same time. Furthermore, due to enhanced cell lifetime, second life applications become realistic and economic relevance. Laser plasma spectroscopy offers an excellent analytical tool for coating quality control and for further optimization of the 3D electrode architecture regarding cell performance and cell degradation even for pouch cell geometries. Future work will focus on appropriate designs and selections of advanced active materials for high-performance batteries and future battery concepts. Process up-scaling for large electrode areas leads to a significant reduction in manufacturing costs while maintaining or improving the overall performance and safety of the battery.

Acknowledgements We thank the financial support by the German Federal Ministry of Education and Research (BMBF) in frame of the Korea-Germany Mobility Programme (01DR14018). Furthermore, this work was supported by KIST institutional program and research grants of NRF (NRF-2012M1A2A2671792) funded by the National Research Foundation under the Ministry of Science, ICT & Future, Korea. The work on laser processing and 3D battery has received funding from the German Research Foundation (DFG, Project No. 392322200). The authors thank to Dr. Melanie Mangang, Dr. Robert Kohler, Dr. Johannes Pröll, Dr. Jung Sub Kim, and Prof. Dr. Chairul Hudaya for their scientific and technical contributions of many years to the 3D battery concept.

References

1. J.B. Goodenough, Y. Kim, Challenges for rechargeable Li batteries. Chem. Mater. **22**(3), 587–603 (2010). https://doi.org/10.1021/cm901452z
2. B. Scrosati, J. Garche, Lithium batteries: status, prospects and future. J. Power Sources **195**(9), 2419–2430 (2010). https://doi.org/10.1016/j.jpowsour.2009.11.048
3. G. Amatucci, A. Du Pasquier, A. Blyr, T. Zheng, J.M. Tarascon, The elevated temperature performance of the $LiMn_2O_4$/C system: failure and solutions. Electrochim. Acta **45**(1–2), 255–271 (1999). https://doi.org/10.1016/S0013-4686(99)00209-1
4. A. Sakti, Quantification of performance and cost trajectory of Li-ion battery designs for personal vehicle electrification in the near future. Dissertation, Carnegie Mellon University (2013)
5. D. Andre, S.-J. Kim, P. Lamp, S.F. Lux, F. Maglia, O. Paschos, B. Stiaszny, Future generations of cathode materials: an automotive industry perspective. J. Mater. Chem. A **3**(13), 6709–6732 (2015). https://doi.org/10.1039/c5ta00361j
6. J.W. Long, B. Dunn, D.R. Rolison, H.S. White, Three-dimensional battery architectures. Chem. Rev. **104**(10), 4463–4492 (2004)
7. J.F.M. Oudenhoven, L. Baggetto, P.H.L. Notten, All-solid-state lithium-ion microbatteries: a review of various three-dimensional concepts. Adv. Energy Mater. **1**(1), 10–33 (2011). https://doi.org/10.1002/aenm.201000002
8. R. Kohler, H. Besser, M. Hagen, J. Ye, C. Ziebert, S. Ulrich, J. Pröll, W. Pfleging, Laser microstructuring of magnetron-sputtered SnO_x thin films as anode material for lithium ion batteries. Microsyst. Technol. **17**(2), 225–232 (2011). https://doi.org/10.1007/s00542-011-1259-1

9. H. Xia, Y.H. Wan, W. Assenmacher, W. Mader, G.L. Yuan, L. Lu, Facile synthesis of chain-like $LiCoO_2$ nanowire arrays as three-dimensional cathode for microbatteries. NPG Asia Mater. **6** (2014). https://doi.org/10.1038/am.2014.72
10. W. Xiong, Q.Y. Xia, H. Xia, Three-dimensional self-supported metal oxides as cathodes for microbatteries. Funct. Mater. Lett. **7**(5) (2014). https://doi.org/10.1142/S1793604714300035
11. S. Ferrari, M. Loveridge, S.D. Beattie, M. Jahn, R.J. Dashwood, R. Bhagat, Latest advances in the manufacturing of 3D rechargeable lithium microbatteries. J. Power Sources **286**, 25–46 (2015). https://doi.org/10.1016/j.jpowsour.2015.03.133
12. W. Pfleging, J. Pröll, A new approach for rapid electrolyte wetting in tape cast electrodes for lithium-ion batteries. J. Mater. Chem. A **2**(36), 14918–14926 (2014). https://doi.org/10.1039/c4ta02353f
13. D.G. Lim, D.W. Chung, R. Kohler, J. Pröll, C. Scherr, W. Pfleging, R.E. Garcia, Designing 3D conical-shaped lithium-ion microelectrodes. J. Electrochem. Soc. **161**(3), A302–A307 (2014). https://doi.org/10.1149/2.013403jes
14. J.H. Pikul, H.G. Zhang, J. Cho, P.V. Braun, W.P. King: High-power lithium ion microbatteries from interdigitated three-dimensional bicontinuous nanoporous electrodes. Nat. Commun. **4** (2013). https://doi.org/10.1038/Ncomms2747
15. H.G. Zhang, X.D. Yu, P.V. Braun, Three-dimensional bicontinuous ultrafast-charge and -discharge bulk battery electrodes. Nat. Nanotechnol. **6**(5), 277–281 (2011). https://doi.org/10.1038/Nnano.2011.38
16. L. Baggetto, R.A.H. Niessen, F. Roozeboom, P.H.L. Notten, High energy density all-solid-state batteries: a challenging concept towards 3D integration. Adv. Funct. Mater. **18**(7), 1057–1066 (2008). https://doi.org/10.1002/adfm.200701245
17. J. Xie, J.F.M. Oudenhoven, D.J. Li, C.G. Chen, R.A. Eichel, P.H.L. Notten, High power and high capacity 3D-structured TiO_2 electrodes for lithium-ion microbatteries. J. Electrochem. Soc. **163**(10), A2385–A2389 (2016). https://doi.org/10.1149/2.1141610jes
18. J. Pröll, H. Kim, A. Piqué, H.J. Seifert, W. Pfleging, Laser-printing and femtosecond-laser structuring of $LiMn_2O_4$ composite cathodes for Li-ion microbatteries. J. Power Sources **255**, 116–124 (2014). https://doi.org/10.1016/j.jpowsour.2013.12.132
19. S. Rosenberg, A. Hintennach, Laser-printed lithium-sulphur micro-electrodes for Li/S batteries. Russ. J. Electrochem. **50**(4), 327–335 (2014). https://doi.org/10.1134/S1023193514040065
20. E. Mottay, X.B. Liu, H.B. Zhang, E. Mazur, R. Sanatinia, W. Pfleging, Industrial applications of ultrafast laser processing. MRS Bull. **41**(12), 984–992 (2016). https://doi.org/10.1557/mrs.2016.275
21. M. Luetke, V. Franke, A. Techel, T. Himmer, U. Klotzbach, A. Wetzig, E. Beyer, A comparative study on cutting electrodes for batteries with lasers. Phys. Proc. **12**, 286–291 (2011). https://doi.org/10.1016/j.phpro.2011.03.135
22. B. Schmieder, Laser cutting of graphite anodes for automotive lithium-ion secondary batteries: investigations in the edge geometry and heat affected zone. Proc. SPIE **8244**, 0R1–0R7 (2012)
23. A.G. Demir, B. Previtali, Remote cutting of Li-ion battery electrodes with infrared and green ns-pulsed fibre lasers. Int. J. Adv. Manufact. Technol. **75**(9), 1557–1568 (2014). https://doi.org/10.1007/s00170-014-6231-7
24. A.H.A. Lutey, A. Fortunato, S. Carmignato, A. Ascari, E. Liverani, G. Guerrini, Quality and productivity considerations for laser cutting of $LiFePO_4$ and $LiNiMnCoO_2$ battery electrodes. Proc. CIRP **42**, 433–438 (2016). https://doi.org/10.1016/j.procir.2016.02.227
25. J. Kurfer, M. Westermeier, C. Tammer, G. Reinhart, Production of large-area lithium-ion cells—preconditioning, cell stacking and quality assurance. CIRP Ann. Manufact. Technol. **61**(1), 1–4 (2012). https://doi.org/10.1016/j.cirp.2012.03.101
26. R. Kohler, J. Pröll, M. Bruns, S. Ulrich, H.J. Seifert, W. Pfleging, Conical surface structures on model thin-film electrodes and tape-cast electrode materials for lithium-ion batteries. Appl. Phys. A **112**(1), 77–85 (2013). https://doi.org/10.1007/s00339-012-7205-y
27. H. Kim, J. Pröll, R. Kohler, W. Pfleging, A. Pique, Laser-printed and processed $LiCoO_2$ cathodethick films for LI-ion microbatteries. J. Laser Micro Nanoeng. **7**(3), 320–325 (2012). https://doi.org/10.2961/jlmn.2012.03.0016

28. J.S. Kim, W. Pfleging, R. Kohler, H.J. Seifert, T.Y. Kim, D. Byun, H.G. Jung, W.C. Choi, J.K. Lee, Three-dimensional silicon/carbon core-shell electrode as an anode material for lithium-ion batteries. J. Power Sources **279**, 13–20 (2015). https://doi.org/10.1016/j.jpowsour.2014.12.041
29. X.-X. Tang, W. Liu, B.-Y. Ye, Y. Tang, Preparation of current collector with blind holes and enhanced cycle performance of silicon-based anode. Trans. Nonferrous Met. Soc. China **23**(6), 1723–1727 (2013). https://doi.org/10.1016/S1003-6326(13)62654-0
30. P.H.L. Notten, F. Roozeboom, R.A.H. Niessen, L. Baggetto, 3-D integrated all-solid-state rechargeable batteries. Adv. Mater. **19**(24), 4564–4567 (2007)
31. R. Kohler, P. Smyrek, S. Ulrich, M. Bruns, V. Trouillet, W. Pfleging, Patterning and annealing of nanocrystalline $LiCoO_2$ thin films. J. Optoelectron. Adv. Mater. **12**(3), 547–552 (2010)
32. J. Pröll, R. Kohler, M. Torge, S. Ulrich, C. Ziebert, M. Bruns, H.J. Seifert, W. Pfleging, Laser microstructuring and annealing processes for lithium manganese oxide cathodes. Appl. Surf. Sci. **257**, 9968–9976 (2011)
33. J. Pröll, P.G. Weidler, R. Kohler, A. Mangang, S. Heissler, H.J. Seifert, W. Pfleging, Comparative studies of laser annealing technique and furnace annealing by X-ray diffraction and Raman analysis of lithium manganese oxide thin films for lithium-ion batteries. Thin Solid Films **531**, 160–171 (2013). https://doi.org/10.1016/j.tsf.2013.01.015
34. K.-Y. Oh, J.B. Siegel, L. Secondo, S.U. Kim, N.A. Samad, J. Qin, D. Anderson, K. Garikipati, A. Knobloch, B.I. Epureanu, C.W. Monroe, A. Stefanopoulou, Rate dependence of swelling in lithium-ion cells. J. Power Sources **267**, 197–202 (2014). https://doi.org/10.1016/j.jpowsour.2014.05.039
35. X. Su, Q.L. Wu, J.C. Li, X.C. Xiao, A. Lott, W.Q. Lu, B.W. Sheldon, J. Wu, Silicon-based nanomaterials for Lithium-ion batteries: a review. Adv. Energy Mater. **4**(1) (2014). https://doi.org/10.1002/Aenm.201300882
36. D. Chen, S. Indris, M. Schulz, B. Gamer, R. Mönig, In situ scanning electron microscopy on lithium-ion battery electrodes using an ionic liquid. J. Power Sources **196**(15), 6382–6387 (2011). https://doi.org/10.1016/j.jpowsour.2011.04.009
37. T. Yoon, C.C. Nguyen, D.M. Seo, B.L. Lucht, Capacity fading mechanisms of silicon nanoparticle negative electrodes for lithium ion batteries. J. Electrochem. Soc. **162**(12), A2325–A2330 (2015). https://doi.org/10.1149/2.0731512jes
38. H. Wu, Y. Cui, Designing nanostructured Si anodes for high energy lithium ion batteries. Nano Today **7**(5), 414–429 (2012). https://doi.org/10.1016/j.nantod.2012.08.004
39. A. Magasinski, B. Zdyrko, I. Kovalenko, B. Hertzberg, R. Burtovyy, C.F. Huebner, T.F. Fuller, I. Luzinov, G. Yushin, Toward efficient binders for Li-ion battery si-based anodes: polyacrylic acid. ACS Appl. Mater. Interfaces **2**(11), 3004–3010 (2010). https://doi.org/10.1021/am100871y
40. C. Erk, T. Brezesinski, H. Sommer, R. Schneider, J. Janek, Toward silicon anodes for next-generation lithium ion batteries: a comparative performance study of various polymer binders and silicon nanopowders. ACS Appl. Mater. Interfaces **5**(15), 7299–7307 (2013). https://doi.org/10.1021/am401642c
41. Y. Zheng, Z. An, P. Smyrek, H.J. Seifert, T. Kunze, V. Lang, A.F. Lasagni, W. Pfleging, Direct laser interference patterning and ultrafast laser-induced micro/nano structuring of current collectors for lithium-ion batteries. Proc. SPIE **9736**, 1B1–1B7 (2016)
42. A.F. Lasagni, C. Gachot, K.E. Trinh, M. Hans, A. Rosenkranz, T. Roch, S. Eckhardt, T. Kunze, M. Bieda, D. Günther, V. Lang, F. Mücklich, Direct laser interference patterning, 20 years of development: from the basics to industrial applications. Proc. SPIE **10092**, 11 (2017)
43. J.H. Klein-Wiele, P. Simon, Fabrication of periodic nanostructures by phase-controlled multiple-beam interference. Appl. Phys. Lett. **83**(23), 4707–4709 (2003). https://doi.org/10.1063/1.1631746
44. W. Pfleging, R. Kohler, M. Torge, V. Trouillet, F. Danneil, M. Stüber, Control of wettability of hydrogenated amorphous carbon thin films by laser-assisted micro- and nanostructuring. Appl. Surf. Sci. **257**(18), 7907–7912 (2011). https://doi.org/10.1016/j.apsusc.2011.02.126
45. A.Y. Vorobyev, C. Guo, Direct femtosecond laser surface nano/microstructuring and its applications. Laser Photonics Rev. **7**(3), 385–407 (2013). https://doi.org/10.1002/lpor.201200017

46. J. Bonse, S. Höhm, S.V. Kirner, A. Rosenfeld, J. Krüger, Laser-induced periodic surface structures—a scientific evergreen. IEEE J. Sel. Top. Quantum Electron. **23**(3), 1–15 (2017). https://doi.org/10.1109/jstqe.2016.2614183
47. J. Bonse, A. Rosenfeld, J. Krüger, On the role of surface plasmon polaritons in the formation of laser-induced periodic surface structures upon irradiation of silicon by femtosecond-laser pulses. J. Appl. Phys. **106**(10), 104910 (2009). https://doi.org/10.1063/1.3261734
48. V.S. Makin, R.S. Makin, A.Y. Vorobyev, C. Guo, Dissipative nanostructures and Feigenbaum's universality in the "metal-high-power ultrashort-pulsed polarized radiation" nonequilibrium nonlinear dynamical system. Tech. Phys. Lett. **34**(5), 387–390 (2008). https://doi.org/10.1134/s1063785008050088
49. Y. Zheng, Z. An, P. Smyrek, H.J. Seifert, T. Kunze, V. Lang, A.F. Lasagni, W. Pfleging, Laser interference patterning and laser-induced periodic surface structure formation on metallic substrates, in *2016 IEEE International Conference on Manipulation, Manufacturing and Measurement on the Nanoscale* (*3M-NANO*) (2016), pp. 159–163. https://doi.org/10.1109/3m-nano.2016.7824955
50. N. Zhang, Y. Zheng, A. Trifonova, W. Pfleging, Laser structured Cu foil for high-performance lithium-ion battery anodes. J. Appl. Electrochem., 1–9 (2017). https://doi.org/10.1007/s10800-017-1086-x
51. W. Pfleging, P. Gotcu, Femtosecond laser processing of thick film cathodes and its impact on lithium-ion diffusion kinetics. Appl. Sci. **9**(17), 3588 (2019)
52. J. Pröll, R. Kohler, A. Mangang, S. Ulrich, C. Ziebert, W. Pfleging, 3D structures in battery materials. J. Laser Micro Nanoeng. **7**(1), 97–104 (2012). https://doi.org/10.2961/jlmn.2012.01.0019
53. P. Gotcu, H.J. Seifert, Thermophysical properties of $LiCoO_2$–$LiMn_2O_4$ blended electrode materials for Li-ion batteries. Phys. Chem. Chem. Phys. **18**(15), 10550–10562 (2016). https://doi.org/10.1039/c6cp00887a
54. A. Manthiram, T. Muraliganth, Lithium intercalation cathode materials for lithium-ion batteries, in *Handbook of Battery Material*. ed. by C. Daniel, J.O. Besenhar (Wiley-VCH Verlag GmbH & Co., Weinheim, 2011), pp. 343–375
55. P. Smyrek, J. Pröll, H.J. Seifert, W. Pfleging, Laser-induced breakdown spectroscopy of laser-structured $Li(NiMnCo)O_2$ electrodes for lithium-ion batteries. J. Electrochem. Soc. **163**(2), A19–A26 (2016). https://doi.org/10.1149/2.0981514jes
56. P. Gotcu, W. Pfleging, P. Smyrek, H.J. Seifert, Thermal behaviour of Li_xMeO_2 (Me = Co or Ni + Mn + Co) cathode materials. Phys. Chem. Chem. Phys. **19**, 11920–11930 (2017). https://doi.org/10.1039/c7cp00513j
57. W. Weppner, R.A. Huggins, Determination of the kinetic parameters of mixed-conducting electrodes and application to the system Li_3Sb. J. Electrochem. Soc. **124**(10), 1569–1578 (1977). https://doi.org/10.1149/1.2133112
58. J.N. Reimers, J.R. Dahn, Electrochemical and in situ X-ray-diffraction studies of lithium intercalation in Li_xCoO_2. J. Electrochem. Soc. **139**(8), 2091–2097 (1992). https://doi.org/10.1149/1.2221184
59. Z.H. Chen, J.R. Dahn, Methods to obtain excellent capacity retention in $LiCoO_2$ cycled to 4.5 V. Electrochim. Acta **49**(7), 1079–1090 (2004). https://doi.org/10.1016/j.electacta.2003.10.019
60. Y. Reynier, J. Graetz, T. Swan-Wood, P. Rez, R. Yazami, B. Fultz, Entropy of Li intercalation in Li_xCoO_2. Phys. Rev. B **70**(17), 174304 (2004)
61. J.N. Reimers, J.R. Dahn, U. Vonsacken, Effects of impurities on the electrochemical properties of $LiCoO_2$. J. Electrochem. Soc. **140**(10), 2752–2754 (1993). https://doi.org/10.1149/1.2220905
62. K. Chang, B. Hallstedt, D. Music, J. Fischer, C. Ziebert, S. Ulrich, H.J. Seifert, Thermodynamic description of the layered O_3 and O_2 structural $LiCoO_2$–CoO_2 pseudo-binary systems. Calphad **41**, 6–15 (2013). https://doi.org/10.1016/j.calphad.2013.01.001
63. G. Denuault, M. Sosna, K.-J. Williams, 11—classical experiments A2—Zoski, Cynthia G, in *Handbook of Electrochemistry* (Elsevier, Amsterdam, 2007), pp. 431–469

64. J.S. Hong, J.R. Selman, Relationship between calorimetric and structural characteristics of lithium-ion cells—II. Determination of Li transport properties. J. Electrochem. Soc. **147**(9), 3190–3194 (2000). https://doi.org/10.1149/1.1393882
65. M. Mangang, P. Gotcu-Freis, H.J. Seifert, W. Pfleging, Electrochemical and kinetic studies of ultrafast laser structured $LiFePO_4$ electrodes. Proc. SPIE **9351**, 0K1–0K12 (2015). https://doi.org/10.1117/12.2078900
66. K. Tang, X. Yu, J. Sun, H. Li, X. Huang, Kinetic analysis on $LiFePO_4$ thin films by CV, GITT, and EIS. Electrochim. Acta **56**(13), 4869–4875 (2011). https://doi.org/10.1016/j.electacta.2011.02.119
67. T. Teranishi, Y. Yoshikawa, R. Sakuma, H. Hashimoto, H. Hayashi, A. Kishimoto, T. Fujii, High-rate performance of ferroelectric $BaTiO_3$-coated $LiCoO_2$ for Li-ion batteries. Appl. Phys. Lett. **105**(14), 143904-1–143904-3 (2014). https://doi.org/10.1063/1.4898006
68. Q. Hao, C.X. Xu, S.Z. Jia, X.Y. Zhao, Improving the cycling stability of $LiCoO_2$ at 4.5 V through surface modification by Fe_2O_3 coating. Electrochim. Acta **113**, 439–445 (2013). https://doi.org/10.1016/j.electacta.2013.09.105
69. Q. Hao, H.Y. Ma, Z.C. Ju, G.D. Li, X.W. Li, L.Q. Xu, Y.T. Qian, Nano-CuO coated $LiCoO_2$: synthesis, improved cycling stability and good performance at high rates. Electrochim. Acta **56**(25), 9027–9031 (2011). https://doi.org/10.1016/j.electacta.2011.04.097
70. Y. Bai, K. Jiang, S.W. Sun, Q. Wu, X. Lu, N. Wan, Performance improvement of $LiCoO_2$ by MgF_2 surface modification and mechanism exploration. Electrochim. Acta **134**, 347–354 (2014). https://doi.org/10.1016/j.electacta.2014.04.155
71. H.M. Cheng, F.M. Wang, J.P. Chu, R. Santhanam, J. Rick, S.C. Lo, Enhanced cycleabity in lithium ion batteries: resulting from atomic layer depostion of Al_2O_3 or TiO_2 on $LiCoO_2$ electrodes. J. Phys. Chem. C **116**(14), 7629–7637 (2012). https://doi.org/10.1021/jp210551r
72. E. Jung, Y.J. Park, Characterization of thermally aged $AlPO_4$-coated $LiCoO_2$ thin films. Nanoscale Res. Lett. **7**, 1–4 (2012). https://doi.org/10.1186/1556-276x-7-12
73. C. Hudaya, J.H. Park, J.K. Lee, W. Choi, SnO_2-coated $LiCoO_2$ cathode material for high-voltage applications in lithium-ion batteries. Solid State Ionics **256**, 89–92 (2014). https://doi.org/10.1016/j.ssi.2014.01.016
74. B.J. Hwang, C.Y. Chen, M.Y. Cheng, R. Santhanam, K. Ragavendran, Mechanism study of enhanced electrochemical performance of ZrO_2-coated $LiCoO_2$ in high voltage region. J. Power Sources **195**(13), 4255–4265 (2010). https://doi.org/10.1016/j.jpowsour.2010.01.040
75. X.Y. Dai, L.P. Wang, J. Xu, Y. Wang, A.J. Zhou, J.Z. Li, Improved electrochemical performance of $LiCoO_2$ electrodes with ZnO coating by radio frequency magnetron sputtering. ACS Appl. Mater. Interfaces **6**(18), 15853–15859 (2014). https://doi.org/10.1021/am503260s
76. Y. Orikasa, D. Takamatsu, K. Yamamoto, Y. Koyama, S. Mori, T. Masese, T. Mori, T. Minato, H. Tanida, T. Uruga, Z. Ogumi, Y. Uchimoto, Origin of surface coating effect for MgO on $LiCoO_2$ to improve the interfacial reaction between electrode and electrolyte. Adv. Mater. Interfaces **1**(9) (2014). https://doi.org/10.1002/Admi.201400195
77. Q. Cao, H.P. Zhang, G.J. Wang, Q. Xia, Y.P. Wu, H.Q. Wu, A novel carbon-coated $LiCoO_2$ as cathode material for lithium ion battery. Electrochem. Commun. **9**(5), 1228–1232 (2007). https://doi.org/10.1016/j.elecom.2007.01.017
78. J. Kim, B. Kim, J.G. Lee, J. Cho, B. Park, Direct carbon-black coating on $LiCoO_2$ cathode using surfactant for high-density Li-ion cell. J. Power Sources **139**(1–2), 289–294 (2005). https://doi.org/10.1016/j.jpowsour.2004.07.008
79. J.H. Park, C. Hudaya, A.Y. Kim, D.K. Rhee, S.J. Yeo, W. Choi, P.J. Yoo, J.K. Lee, Al-C hybrid nanoclustered anodes for lithium ion batteries with high electrical capacity and cyclic stability. Chem. Commun. **50**(22), 2837–2840 (2014). https://doi.org/10.1039/c3cc47900e
80. C. Hudaya, B. Kang, H.G. Jung, W. Choi, B.J. Jeon, J.K. Lee, Plasma-polymerized C-60 as a functionalized coating layer on fluorine-doped tin oxides for anode materials of lithium-ion batteries. Carbon **81**, 835–838 (2015). https://doi.org/10.1016/j.carbon.2014.09.015
81. A.A. Arie, J.K. Lee, Fullerene C-60 coated silicon nanowires as anode materials for lithium secondary batteries. J. Nanosci. Nanotechnol. **12**(4), 3547–3551 (2012). https://doi.org/10.1166/jnn.2012.5557

82. A.A. Arie, O.M. Vovk, J.K. Lee, Surface-coated silicon anodes with amorphous carbon film prepared by fullerene C-60 sputtering. J. Electrochem. Soc. **157**(6), A660–A665 (2010). https://doi.org/10.1149/1.3363531
83. C. Hudaya, M. Halim, J. Proll, H. Besser, W. Choi, W. Pfleging, H.J. Seifert, J.K. Lee, A polymerized C60 coating enhancing interfacial stability at three-dimensional $LiCoO_2$ in high-potential regime. J. Power Sources **298**, 1–7 (2015). https://doi.org/10.1016/j.jpowsour.2015.08.044
84. A.A. Arie, J.O. Song, J.K. Lee, Structural and electrochemical properties of fullerene-coated silicon thin film as anode materials for lithium secondary batteries. Mater. Chem. Phys. **113**(1), 249–254 (2009). https://doi.org/10.1016/j.matchemphys.2008.07.082
85. J. Mun, T. Yim, J.H. Park, J.H., Ryu, S.Y. Lee, Y.G. Kim, S.M. Oh, Allylic ionic liquid electrolyte-assisted electrochemical surface passivation of $LiCoO_2$ for advanced, safe lithium-ion batteries. Sci. Rep. **4** (2014). https://doi.org/10.1038/Srep05802
86. J.P. Yu, Z.H. Han, X.H. Hu, H. Zhan, Y.H. Zhou, X.J. Liu, The investigation of Ti-modified $LiCoO_2$ materials for lithium ion battery. J. Power Sources **262**, 136–139 (2014). https://doi.org/10.1016/j.jpowsour.2014.03.073
87. H. Castaneda, The impedance response of different mechanisms for $LiCoO_2$/acetylene carbon electrodes in alkaline solutions under polarization conditions. Electrochim. Acta **112**, 562–576 (2013). https://doi.org/10.1016/j.electacta.2013.08.177
88. F. Boue-Bigne, Laser-induced breakdown spectroscopy applications in the steel industry: rapid analysis of segregation and decarburization. Spectrochim. Acta Part B Atom. Spectrosc. **63**(10), 1122–1129 (2008). https://doi.org/10.1016/j.sab.2008.08.014
89. J.M. Vadillo, J.J. Laserna, Laser-induced plasma spectrometry: truly a surface analytical tool. Spectrochim. Acta Part B Atom. Spectrosc. **59**(2), 147–161 (2004). https://doi.org/10.1016/j.sab.2003.11.006
90. J.M. Vadillo, C.C. Garcia, S. Palanco, J.J. Laserna, Nanometric range depth-resolved analysis of coated-steels using laser-induced breakdown spectrometry with a 308 nm collimated beam. J. Anal. At. Spectrom. **13**(8), 793–797 (1998). https://doi.org/10.1039/A802343c
91. V. Zorba, J. Syzdek, X.L. Mao, R.E. Russo, R. Kostecki, Ultrafast laser induced breakdown spectroscopy of electrode/electrolyte interfaces. Appl. Phys. Lett. **100**(23) (2012). https://doi.org/10.1063/1.4724203
92. H.M. Hou, L. Cheng, T. Richardson, G.Y. Chen, M. Doeff, R. Zheng, R. Russo, V. Zorba, Three-dimensional elemental imaging of Li-ion solid-state electrolytes using FS-laser induced breakdown spectroscopy (LIBS). J. Anal. At. Spectrom. **30**(11), 2295–2302 (2015). https://doi.org/10.1039/c5ja00250h
93. P. Smyrek, Y. Zheng, J.H. Rakebrandt, H.J. Seifert, W. Pfleging, Investigation of micro-structured $Li(Ni_{1/3}Mn_{1/3}Co_{1/3})O_2$ cathodes by laser-induced breakdown spectroscopy. Proc. SPIE **10092**, 0S1–0S7 (2017). https://doi.org/10.1117/12.2253894
94. P. Smyrek, Y. Zheng, H.J. Seifert, W. Pfleging, Post-mortem characterization of FS laser-generated micro-pillars in $Li(Ni_{1/3}Mn_{1/3}Co_{1/3})O_2$ electrodes by laser-induced breakdown spectroscopy. Proc. SPIE **9736**, 1C1–1C6 (2016)
95. P. Smyrek, Y. Zheng, H.J. Seifert, W. Pfleging, Laser-induced breakdown spectroscopy as a powerful tool for characterization of laser modified composite materials, in *2016 IEEE International Conference on Manipulation, Manufacturing and Measurement on the Nanoscale* (*3M-NANO*), 18–22 July 2016, pp. 164–167
96. H.H. Zheng, G. Liu, X.Y. Song, P. Ridgway, S.D. Xun, V.S. Battaglia, Cathode performance as a function of inactive material and void fractions. J. Electrochem. Soc. **157**(10), A1060–A1066 (2010). https://doi.org/10.1149/1.3459878
97. P. Smyrek, T. Bergfeldt, H.J. Seifert, W. Pfleging, Laser-induced breakdown spectroscopy for the quantitative measurement of lithium concentration profiles in structured and unstructured electrodes. J. Mater. Chem. A **7**(10), 5656–5665 (2019). https://doi.org/10.1039/c8ta10328c
98. S.L. Wu, W. Zhang, X. Song, A.K. Shukla, G. Liu, V. Battaglia, V. Srinivasan, High rate capability of $Li(Ni_{1/3}Mn_{1/3}Co_{1/3})O_2$ electrode for Li-ion batteries. J. Electrochem. Soc. **159**(4), A438–A444 (2012). https://doi.org/10.1149/2.062204jes

Index

A. Hu (ed.), *Laser Micro-Nano-Manufacturing and 3D Microprinting*, Springer Series in Materials Science 309, https://doi.org/10.1007/978-3-030-59313-1

N

O

P

T